Transactions of the ASME®

Technical Editor, LEWIS T. WHEELER (1997)

Department of Mechanical Engineering,
University of Houston,
Houston, TX 77204-4792

Transactions of the ASME, Journal of Applied Mechanics (ISSN 0021-8936) is published quarterly (Mar., June, Sept., Dec.) for $165.00 per year by The American Society of Mechanical Engineers, 345 East 47th Street, New York, NY 10017. Second class postage paid at New York, NY and additional mailing office. POSTMASTER: Send address changes to Transactions of the ASME, Journal of Applied Mechanics, c/o THE AMERICAN SOCIETY OF MECHANICAL ENGINEERS, 22 Law Drive, Box 2300, Fairfield, NJ 07007-2300.

CHANGES OF ADDRESS must be received at Society headquarters seven weeks before they are to be effective. Please send old label and new address.

PRICES: To members, $40.00, annually: to nonmembers, $165.00.
Add $24.00 for postage to countries outside the United States and Canada.

INDEXED by Applied Mechanics Reviews and Engineering Information, Inc. Canadian Goods & Services Tax Registration #126148048

Journal of Applied Mechanics

Published Quarterly by The American Society of Mechanical Engineers

VOLUME 60 • NUMBER 3 • SEPTEMBER 1993

(Contents continued on Inside Back Cover)

CONTENTS (CONTINUED)

BRIEF NOTES

DISCUSSIONS

BOOK REVIEW

ERRATUM

ANNOUNCEMENTS AND SPECIAL NOTES

C. H. Jenkins
Assoc. Professor,
Department of Mechanical Engineering,
South Dakota School of Mines
and Technology,
Rapid City, SD 57701
Mem. ASME

J. W. Leonard
Professor and Head,
Department of Civil Engineering,
University of Connecticut,
Storrs, CT 06269

Dynamic Wrinkling of Viscoelastic Membranes

Problems associated with viscoelastic membrane structures have been documented, e.g., dynamic wrinkling and its effects on fatigue analysis and on snap loading. In the proposed analysis method, the constitutive equation is approximated by a finite difference equation and embedded within a nonlinear finite element spatial discretization. Implicit temporal integration and a modified Newton-Raphson method are used within a time increment. The stress-strain hereditary relation is formally derived from thermodynamic considerations. Use of modified strain-energy and dissipation functions facilitates the description of wrinkling during the analysis. Applications are demonstrated on an inflated cylindrical cantilever and on a submerged cylindrical membrane excited by waves.

1 Introduction

1.1 Background. Thin membranes are inherently no-compression structures. Compressive stress, of sufficient magnitude to overcome tensile prestress, will be handled via changes in membrane geometry, i.e., by an out-of-plane deformation or localized buckling called "wrinkling." Analysis of wrinkling is important to the prediction of membrane structural response. In long-term loading situations, the creep/relaxation response of viscoelastic materials will tend to decrease the level of prestress, thus increasing the formation of wrinkles. Problems of dynamic wrinkling (e.g., panel flutter) are of interest for the effects on fatigue analysis (e.g., tension field effects on mean stress distribution) and on snap loading (e.g., when a wrinkled region suddenly regains the lost principal stress). (Such considerations are beyond the scope of the present work, however.)

1.2 Prior Research. Wagner (1929) introduced the ideas of wrinkling and "tension field theory" in connection with flat sheet metal girders in the very thin metal webs used in airplane construction. Under the action of a specific loading, one of the principal stresses goes to zero while the other remains non-negative. If the non-negative principal stress remains greater than zero, a "tension field" is defined; if it is zero, a "slack" region results. The crests and troughs of "wrinkle waves" align with the direction of the nonzero principal stress. In typical wrinkling analysis, results are only in terms of average strains and displacements, while no detailed information is generated for each wrinkle. Furthermore, a membrane need not be wrinkled over its entire surface. (A review of membrane wrinkling research is given by Jenkins and Leonard (1991a).)

The formation of a finite number of wrinkles during membrane deformation relies on the inherent (albeit small) bending stiffness of the material. Detailed description of the wrinkling phenomena is absent in membrane analysis since the bending stiffness is disregarded. Pipkin (1986) and Steigmann and Pipkin (1989a, b, c) discuss this further and postulate the existence of a "relaxed strain-energy density," which represents the average energy per unit initial area over a region containing many wrinkles. The relaxed energy density is constrained such that its derivatives (stresses) are non-negative, thus incorporating tension field theory into membrane theory automatically.

1.3 Conventions. The following conventions are used: the summation convention is implied unless explicitly stated otherwise; Latin indices take the values 1, 2, 3 unless explicitly stated otherwise; Greek indices take the values 1, 2; capital and lower case Latin letters (except indices and symbols with a tilde) refer to the undeformed and deformed state, respectively; bold type indicates vector or tensor quantities; superscripts or subscripts enclosed in parentheses indicate no sum, and the overdot symbol represents differentiation with respect to time.

1.4 Strain and Stress Measure. Consider the Cartesian coordinates X_i of a point X on the undeformed membrane midsurface which becomes point x with coordinates x_i on the deformed midsurface. Also define convected curvilinear midsurface coordinates $\Theta^i = \theta^i$, i.e., the Θ^i coordinates of X are numerically equal to the θ^i coordinates of x. The metric tensor in the deformed state is $g_{kl} = \mathbf{g}_k \cdot \mathbf{g}_l$, $\mathbf{g}_i = \partial \mathbf{r}/\partial\theta^i$, and $\mathbf{r}$ is the position vector from o to x; similarly, in the undeformed state, $G_{kl} = \mathbf{G}_k \cdot \mathbf{G}_l$, where $\mathbf{G}_i = \partial \mathbf{R}/\partial\theta^i$, and $\mathbf{R}$ is the position vector from 0 to X. The convected Green-Lagrange strain tensor components, E_{kl}, are given by (Green and Zerna, 1968)

$$E_{kl} = \frac{1}{2}(g_{kl} - G_{kl}). \tag{1}$$

Contributed by the Applied Mechanics Division of THE AMERICAN SOCIETY OF MECHANICAL ENGINEERS for publication in the ASME JOURNAL OF APPLIED MECHANICS.

Discussion on this paper should be addressed to the Technical Editor, Professor Lewis T. Wheeler, Department of Mechanical Engineering, University of Houston, Houston, TX 77204-4792, and will be accepted until four months after final publication of the paper itself in the ASME JOURNAL OF APPLIED MECHANICS.

Manuscript received by the ASME Applied Mechanics Division, Aug. 6, 1991; final revision, Aug. 17, 1992. Associate Technical Editor: A. K. Noor.

2 Viscoelastic Finite Elements

2.1 Nonlinear Finite Element Method. We follow a finite element discretization for a combined incremental/iterative method with a "modified" Newton-Raphson iteration, using an isoparametric formulation. With the notation that the increment of time is Δt, Ψ_I = isoparametric shape function for node I, X_i^I = ith initial coordinate of node I, U_i^I = ith displacement of node I, ξ_i = natural coordinate of the element, $I = 1, \ldots,$ number of nodes (per element), and $k = 1, \ldots,$ number of iterations per time step, we write the combined incremental/iterative membrane equation of motion as (Jenkins, 1991):

$$[\tilde{M}_{ijIJ}]\{\ddot{U}_j^J(t+\Delta t;\, k+1)\} + [\tilde{K}_{ijIJ}(t+\Delta t)]\{\Delta U_j^J(t+\Delta t)\} = \{\tilde{P}_{iI}(t+\Delta t;\, k+1)\} - \{\tilde{F}_{iI}(t+\Delta t;\, k)\} \quad (2)$$

where $[\tilde{M}_{ijIJ}]$ = consistent mass matrix, $[\tilde{K}_{ijIJ}(t + \Delta t)]$ = tangent stiffness matrix, $\{\tilde{P}_{iI}(t + \Delta t; k + 1)\}$ = external force vector, $\{\tilde{F}_{iI}(t + \Delta t; k)\}$ = internal force vector, and $\{\Delta U_j^J(t + \Delta t)\}$ = incremental displacement vector between iterations k and $k + 1$. Note that, by use of the modified Newton-Raphson method, $[\tilde{K}_{ijIJ}(t + \Delta t)]$ is constant during a time step.

2.2 Constitutive Equation—General. The method of "local state" (see Germain, 1973; Lemaitre and Chaboche, 1990) postulates that the thermodynamic state of a continuum at a specific location and time is completely defined by the values of certain variables (state variables) at that time and location. The "observable" state variables, temperature and deformation, define elastic (reversible) phenomena uniquely as a function of time. "Internal" state variables (e.g., deformation rate) are required for the representation of dissipative phenomena, since the current state also depends on the state history. State laws are derived from postulated thermodynamic potentials which are functions of the state variables. In order to satisfy the Clausius-Duhem inequality (second law of thermodynamics), potentials must be non-negative, convex functions with zero values at the origin of state variable space; a typical choice is that of a positive-definite quadratic form.

In light of the above discussion, we postulate the existence of strain energy and dissipation functions $\tilde{W} = \tilde{W}(\boldsymbol{E}, \tilde{\boldsymbol{C}}, t)$ and $\tilde{V} = \tilde{V}(\dot{\boldsymbol{E}}, \tilde{\boldsymbol{C}}, t)$, respectively, such that

$$S^{ij}(t) = \frac{\partial \tilde{W}}{\partial E_{ij}}(t) + \frac{\partial \tilde{V}}{\partial \dot{E}_{ij}}(t) \quad (3)$$

where S^{ij} is the convected, second Piola-Kirchoff stress tensor, and $\tilde{\boldsymbol{C}}$ is the constitutive tensor. In Appendix A we show the connection between (3) and the linear hereditary constitutive equation. We now generalize as follows: for suitable choices of state variables in $\tilde{W}$ and $\tilde{V}$, and for a suitable material function approximation by a Prony series, the following finite linear viscoelastic constitutive relation is obtained from (3) (where the dependence of the material function on current strain has been neglected)

$$S^{\alpha\beta}(t) = \tilde{C}^{\alpha\beta\gamma\zeta}(0)E_{\gamma\zeta}(t) - \int_0^t \frac{d\tilde{C}^{\alpha\beta\gamma\zeta}(t-\tau)}{d\tau} E_{\gamma\zeta}(\tau)d\tau. \quad (4)$$

2.3 Constitutive Equation—Computational Form. Solution of complicated viscoelastic problems will generally require numerical techniques. (For a review of computational methods in viscoelasticity, see Jenkins and Leonard, 1991b.) In the direct method proposed by White (1968), the governing integro-differential constitutive equation is approximated by a finite-difference equation and embedded within the spatial discretization, thus making a viscoelastic finite element; this is the method followed in the present work.

In summary, we rewrite (4) in incremental form based on a Taylor series approximation, then descretize with a trapezoidal approximation. A three-term Prony series approximates the relaxation modulus to reduce computational memory requirements (the adequacy of this double exponential model for solid polymers has previously been discussed by Garbarski, 1989). Finally, after considerable algebra, we rewrite (2) as

$$[\tilde{M}_{ijIJ}\{\ddot{U}_j^J(t+\Delta t;\, k+1)\} + [\tilde{K}_{ijIJ}(t+\Delta t)]\{\Delta U_j^J(t+\Delta t)\} = \{\tilde{P}_{iI}(t+\Delta t;\, k+1)\} - \{\tilde{F}_{iI}(t+\Delta t;\, k)\} + \{\tilde{Q}_{iI}(t+\Delta t)\} \quad (5)$$

where $\{\tilde{Q}_{iI}(t + \Delta t)\}$ = memory load vector. (For details see Jenkins and Leonard, 1991b.)

3 Wrinkling Analysis

3.1 Formulation. For wrinkling under a plane stress assumption, we define principal stresses S^β (see Appendix B):

$$S^1(t) = \frac{\partial \tilde{W}}{\partial E_1(t)} + \frac{\partial \tilde{V}}{\partial \dot{E}_1(t)},\quad S^2(t) = \frac{\partial \tilde{W}}{\partial E_2(t)} + \frac{\partial \tilde{V}}{\partial \dot{E}_2(t)} \quad (6)$$

where E_β are the principal strains. Following Steigmann and Pipkin (1989a, b, c), a "natural width" (in simple tension), $\overset{*}{E}_2[E_1(t)]$, is defined such that when $S^2(t) \to \overset{*}{S}^2 = 0$, $E_2(t) = \overset{*}{E}_2[E_1(t)]$, and $S^1 \to \overset{*}{S}^1[E_1, \overset{*}{E}_2, t]$, where starred quantities denote values at wrinkling. When $E_2(t) \le \overset{*}{E}_2[E_1(t)]$ (with $E_1 > 0$), $E_2 \to \overset{*}{E}_2$, and "relaxed" strain energy and dissipation functions are defined as

$$\tilde{W}^* = \tilde{W}^*(\tilde{\boldsymbol{C}}, E_1, \overset{*}{E}_2, t),\quad \tilde{V}^* = \tilde{V}^*(\tilde{\boldsymbol{C}}, \dot{E}_1, \overset{*}{E}_2, t) \quad (7)$$

from which the stresses during wrinkling may be formally found. We note that the above differs from the approach of some authors (see, e.g., Contri and Schrefler, 1988) who assume S^1 remains fixed instead of E_1 above. In either case, the strain energy after wrinkling is never greater than the strain energy before wrinkling.

For the moderate deformation of compressible isotropic *elastic* membranes (dissipation function equals zero), the wrinkling condition is shown to be (see Appendix B):

$$\overset{*}{E}_2(E_1) = -\frac{\tilde{C}^{21}}{\tilde{C}^{22}} E_1. \quad (8)$$

The wrinkling condition for isotropic finite linear *viscoelastic* membranes under plane stress is found from

$$\overset{*}{S}^2(t) = \tilde{C}^{2\beta}(0)\overset{*}{E}_\beta(t) - \int_0^t \frac{d\tilde{C}^{2\beta}(t-\tau)}{d\tau} \overset{*}{E}_\beta(\tau)d\tau = 0 \quad (9)$$

or

$$\tilde{C}^{22}(0)\overset{*}{E}^2(t) - \int_0^t \frac{d\tilde{C}^{22}(t-\tau)}{d\tau} \overset{*}{E}_2(\tau)d\tau = -\tilde{C}^{21}(0)E_1(t) + \int_0^t \frac{d\tilde{C}^{21}(t-\tau)}{d\tau} E_1(\tau)d\tau. \quad (10)$$

Then $S^1 \to \overset{*}{S}^1[E_1, \overset{*}{E}_2, t]$ in the wrinkling region, or

$$\overset{*}{S}^1(t) = \tilde{C}^{11}(0)E_1(t) + \tilde{C}^{12}(0)\overset{*}{E}_2(t) - \int_0^t \frac{d}{d\tau}[\tilde{C}^{11}(t-\tau)E_1(\tau) + \tilde{C}^{12}(t-\tau)\overset{*}{E}_2(t-\tau)]d\tau$$

$$= \tilde{C}^{11}(0)E_1(t) - \int_0^t \frac{d\tilde{C}^{11}(t-\tau)}{d\tau} E_1(\tau)d\tau + \tilde{C}^{12}(0)\overset{*}{E}_2(t) - \int_0^t \frac{d\tilde{C}^{12}(t-\tau)}{d\tau} \overset{*}{E}_2(\tau)d\tau. \quad (11)$$

For constant Poisson's ratio, ν,

$$\tilde{C}^{12}(t) = \nu \frac{\overset{*}{G}^{11}}{\overset{*}{G}^{22}} \tilde{C}^{22}(t) = \nu \frac{\overset{*}{G}^{22}}{\overset{*}{G}^{11}} \tilde{C}^{11}.$$

Then

$$\overset{*}{S}^{1}(t) = \tilde{C}^{11}(0)E_1(t) - \int_0^t \frac{d\tilde{C}^{11}(t-\tau)}{d\tau} E_1(\tau)d\tau + \nu \frac{\overset{*}{G}^{11}}{\overset{*}{G}^{22}} \left[C^{22}(0)\overset{*}{E}_2(t) - \int_0^t \frac{d\tilde{C}^{22}(t-\tau)}{d\tau} \overset{*}{E}_2(\tau)d\tau \right]. \quad (12)$$

Now, substituting (10) into (12) gives

$$= \tilde{C}^{11}(0)E_1(t) - \int_0^t \frac{d\tilde{C}^{11}(t-\tau)}{d\tau} E_1(\tau)d\tau + \nu \frac{\overset{*}{G}^{11}}{\overset{*}{G}^{22}} \left[-C^{21}(0)E_1(t) - \int_0^t \frac{d\tilde{C}^{21}(t-\tau)}{d\tau} E_1(\tau)d\tau \right]. \quad (13)$$

Finally,

$$\overset{*}{S}_1(t) = (1-\nu^2)\tilde{C}^{11}(0)E_1(t) - (1-\nu^2) \int_0^t \frac{d\tilde{C}^{11}(t-\tau)}{d\tau} E_1(\tau)d\tau. \quad (14)$$

4 Computer Implementation

In what follows, use is made of quadratic, isoparametric quadrilateral (8-node) curved membrane elements. (For convenience, straight lines are shown connecting nodal points in Figs. 1 and 5.) To determine the initial equilibrium configuration of a structure to applied static loads, a viscous relaxation technique is used. Newmark's method is used to solve the dynamical equations of motion. Pressure loads, a specific example of nonconservative loads, are accounted for by iteration, thus eliminating the need to compute nonsymmetric matrices. For validation purposes, the problems of the uniform inflation of initially plane elastic and viscoelastic rectangular membranes were considered. (See Jenkins (1991) for further program details and validation results.)

The present analysis method is used for the specific case of a plasticized PVC membrane material with the following relevant properties:

Thickness = 1.3 mm (0.050 in.); initial elastic modulus = 55.16 MPa (8000 psi);
relaxation modulus = $[23 + 26\exp(-2.6 \times 10^{-2}\ t) + 6.2\exp(-1.8 \times 10^{-3})]$ MPa
($[3.4 + 3.7\exp(-2.6 \times 10^{-2}\ t) + 0.90\exp(-1.8 \times 10^{-3})] \times 10^3$ psi);
Poisson's ratio = 0.45;
mass density = 1068 N s^2/m^4 (1.0×10^{-4} lb s^2/in.^{4}).

We note that only quasi-static values of moduli were available to us. For harmonic loading (as in the examples that follow), the use of "complex" moduli is indicated. Incorporation of such effects into the formulation is ongoing and will be reported subsequently.

Principal stress results are plotted at selected integration

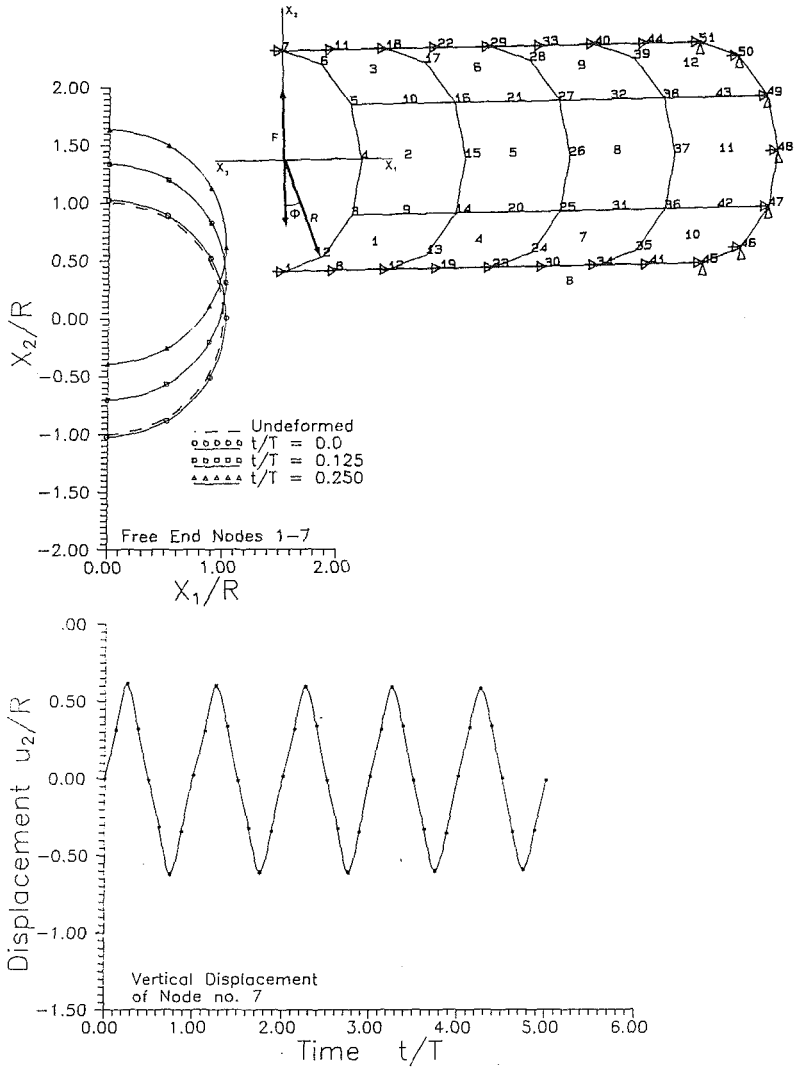

Fig. 1 Displacement results for sinusoidal loading of cantilever cylinder

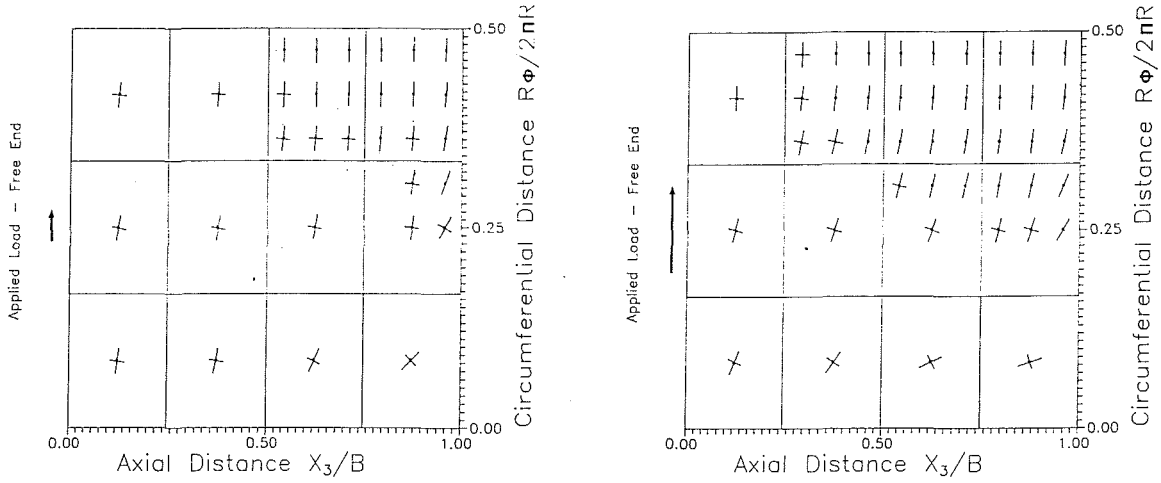

Fig. 2 Principal stress results, sinusoidal loading: $t/T = 0.125$; $t/T = 0.25$

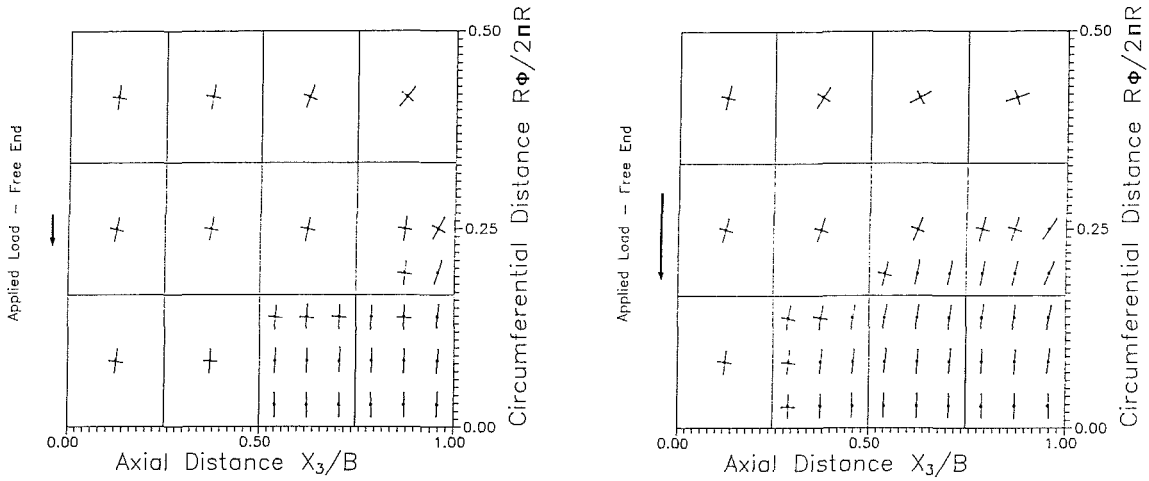

Fig. 3 Principal stress results, sinusoidal loading: $t/T = 0.625$; $t/T = 0.75$

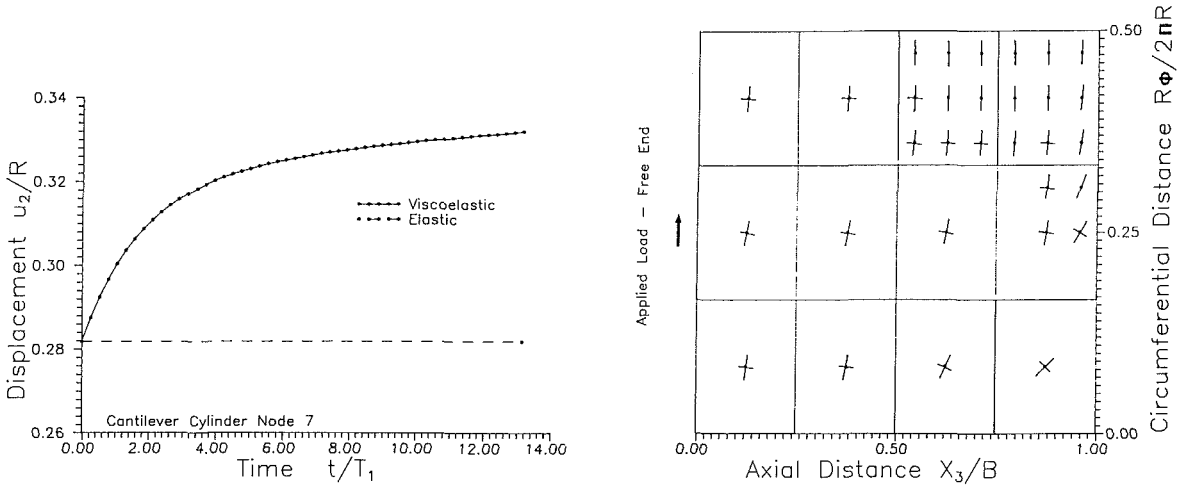

Fig. 4 Quasi-static displacement and principal stress results

points as follows: wherever uniaxial stress ("tension field") occurs, it is shown; biaxial stress is shown only where required for clarity; magnitudes are not indicated, although the longer line corresponds to the larger principal stress; orientation of principal stress is as shown; a circle enclosing an integration point indicates a "slack" region; the finite element model is "unrolled" into a plane surface for viewing.

5 Applications

5.1 Deformation of an Inflated Cylindrical Membrane Cantilever. Various investigators have considered the inflated cylindrical membrane structure, with particular interest in the stability of equilibrium (see Jenkins, 1991, for review). In the present work, we first apply a sinusoidal tip load of

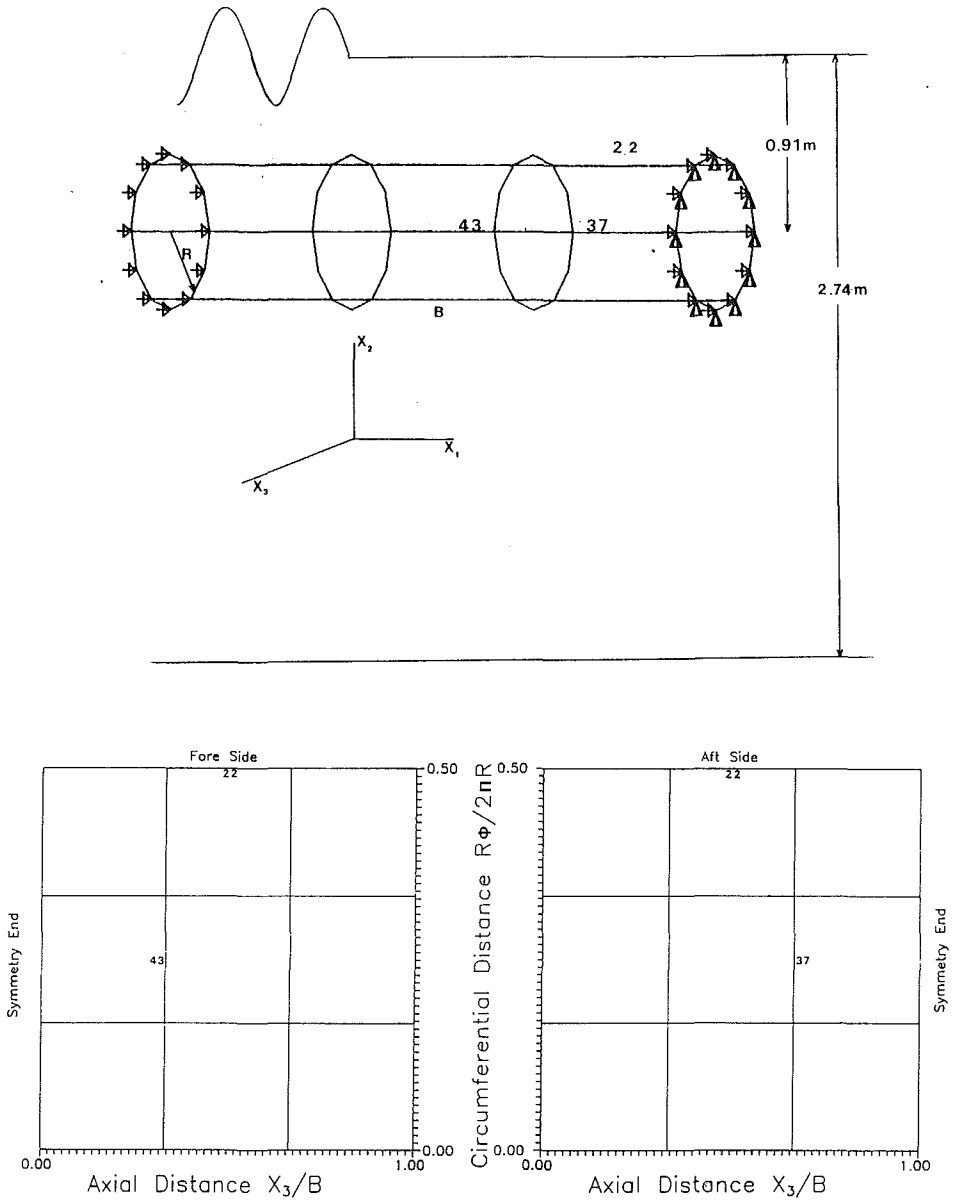

Fig. 5 Submerged cylinder configuration

amplitude 1.17 kN (264 lb) and period $T = 1.0\,s$ to a viscoelastic cylindrical cantilever beam initially inflated to a pressure of 4.76 kPa (0.694 psi). (Advantage is taken of axial symmetry as shown in Fig. 1.) Cylinder dimensions are radius $R = 0.46$ m (1.5 ft) and length $B = 2.4$ m (8.0 ft). The displacement of a free-end node with time is also given in Fig. 1, as well as a deformation profile of the free end at various times. Figures 2 and 3 indicate the principal stresses at selected integration points at various times. Wrinkling results are as expected: as the load forces the free end up, compressive stresses build in the upper half of the cylinder causing wrinkling waves aligned perpendicular to the compressive stress; the same follows as the load forces the free end down and wrinkling develops in the bottom half of the cylinder. We note that the stress at $t/T = 0.0, 0.5, 1.0, \ldots$, are purely biaxial.

Then we apply a constant tip load (587 N) to the above cantilever cylinder. Time-dependent displacement and wrinkling results are given in Fig. 4, where the time has been nondimensionalized by the first relaxation time constant T_1 ($= 1/0.0262\,s^{-1} = 38.2\,s$) of the viscoelastic constitutive relation. Corresponding static elastic results are also shown for comparison purposes. Wrinkling results are shown for $t/T_1 = 13$.

5.2 Hydrodynamic Loading of a Submerged Membrane Cylinder. Membrane structures have been considered for use in the marine environment in a variety of situations including storage containers, dwellings, and breakwaters (Jenkins and Leonard, 1991a). To examine the latter case, the numerically predicted response of an experimental cylindrical breakwater model was considered. (For experimental details, see Broderick, 1991.) A 0.91 m (3.0 ft) diameter right circular viscoelastic PVC cylinder of length $2B = 3.7$ m (12 ft) is submerged in 2.7 m (9.0 ft) of water depth with the (X_3) axis of the cylinder 3 feet below the still water level and parallel to it (see Fig. 5). Due to symmetry of loading, only 1/2 the length of the cylinder is modeled; one end has a fixed boundary condition, the other is fixed only in the axial direction. The cylinder contains water and is subjected to an over-pressure of 0.48 kPa (10 psf), a value corresponding to the experimentally observed mean value. Surface waves of 0.15 m (0.5 ft) height and period $T = 2\,s$ are incident on the cylinder in the positive X_1-direction. Incident wave pressure on the cylinder is accounted for in the numerical model by a linear Froude-Krylof model, i.e., no diffraction or radiation effects are considered to modify the incident wave field. Internal pressure of the

cylinder is assumed constant. The mass of the contained fluid is distributed to the cylinder as lumped masses at the corner of the elements.

A selected finite element vertical displacement result at the membrane top are compared to experimental values in Fig. 6 for approximately seven cycles of loading (results are nondimensionalized by 1/2 the wave height to match experimental data); corresponding cross-section profiles for two cycles are also shown. The comparison is quite good, considering the lack of a more sophisticated hydrodynamic model.

Figures 7 and 8 indicate the associated principal stresses for selected times. Both fore and aft sides (left and right sides of figures, respectively) are represented in plane "unwrapped" view; the symmetry end corresponds to the tank centerline. A significant amount of the membrane is wrinkled, which is indicative of the complexity of the loading environment. We would expect increased internal pressure to decrease the amount of wrinkling to some extent. Comparison with experimental video data shows that the essential description of the wrinkled

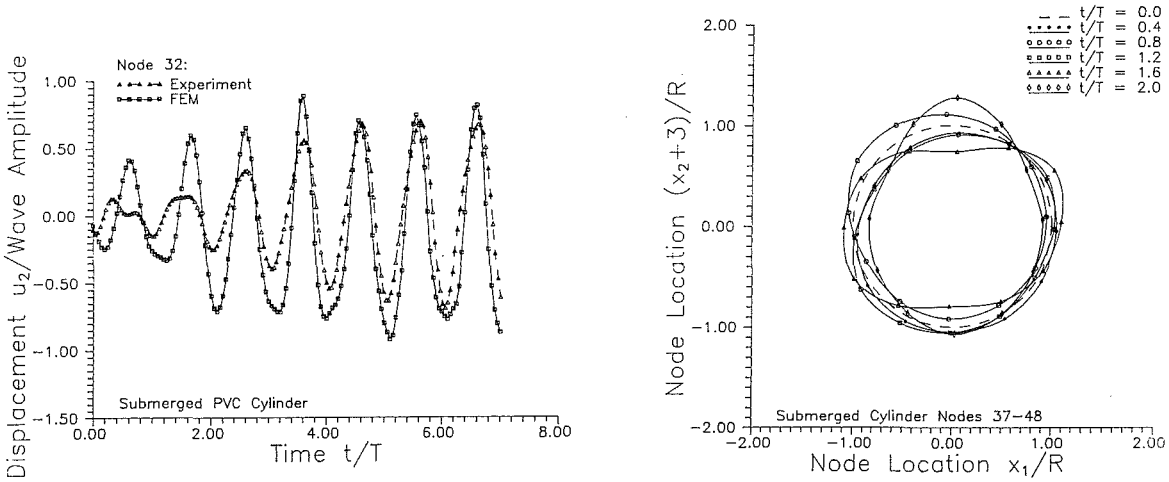

Fig. 6 Submerged cylinder: vertical displacement validation; cross-section profiles

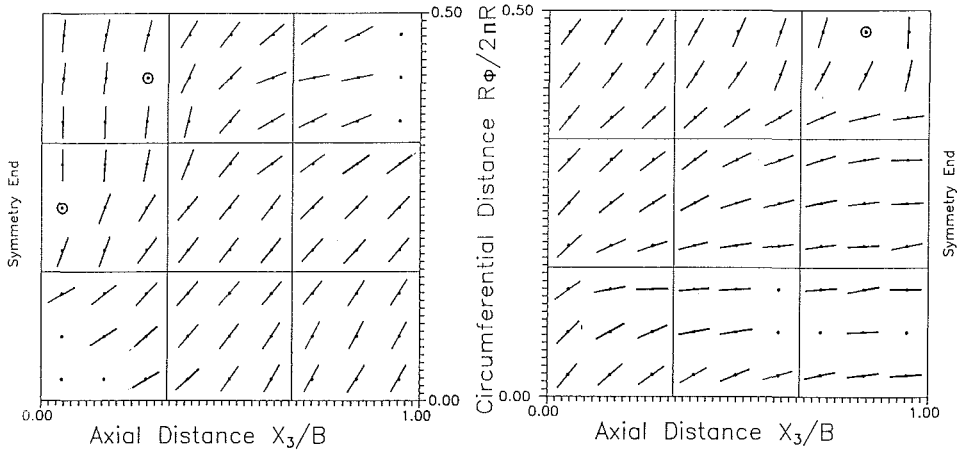

Fig. 7 Submerged cylinder principal stress results, *t/T* = 0.4

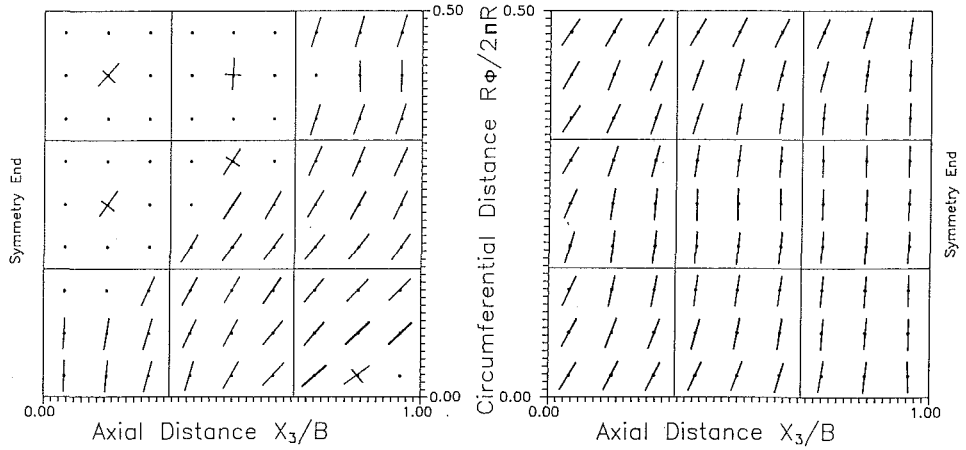

Fig. 8 Submerged cylinder principal stress results, *t/T* = 0.8

surface has been captured (see Jenkins, 1991, for additional details and results).

6 Acknowledgment

This material is based upon work supported by the USN Office of Naval Research under the University Research Initiative (URI) Contact No. N00014-86-K-0687. We gratefully acknowledge this support.

7 References

Broderick, L., 1991, "Interaction of Water Waves and Deformable Bodies," Ph.D. dissertation, Oregon State University, Corvallis, OR.

Contri, P., and Schrefler, B. A., 1988, "A Geometrically Nonlinear Finite Element Analysis of Wrinkled Membrane Surfaces by a No-Compression Material Model," *Comm. in Appl. Num. Meth.*, Vol. 4, pp. 5–15.

Garbarski, J., 1989, "Application of the Exponential Function to the Description of Viscoelasticity in Some Solid Polymers," *Int. J. Mech. Sci.*, Vol. 31, pp. 165–178.

Germain, P., 1973, *Cours de Mecanique de Milieux Continus*. Masson, Paris.

Green, A. E., and Zerna, W., 1968, *Theoretical Elasticity*, 2nd ed., Oxford University Press, London.

Jenkins, C., 1991, "Transient Nonlinear Deformations of Viscoelastic Membranes," Ph.D. dissertation, Oregon State University, Corvallis, OR.

Jenkins, C., and Leonard, J. W., 1991, "Nonlinear Dynamic Response of Membranes: State of the Art," ASME *Appl. Mech. Rev.*, Vol. 44, pp. 319–328.

Jenkins, C., and Leonard, J. W., 1991b, "Transient Nonlinear Deformation of Viscoelastic Membrane Structures," *Struct. Eng. Rev.* (in press).

Lemaitre, J., and Chaboche, J.-L., 1990, *Mechanics of Solid Materials*, Cambridge University Press, Cambridge, UK.

LeTallec, P., and Rahier, C., 1989, "Numerical Modeling of Viscoelastic Structures in Large Strains and Rolling Motions," *Proc. 5th Int. Symp. Num. Mthds. Engrg.*, Lausanne, Switzerland.

Malvern, L. E., 1969, *Introduction to the Mechanics of a Continuous Medium*, Prentice-Hall, Englewood Cliffs, NJ.

Pipkin, A. C., 1986a, "The Relaxed Energy Density for Isotropic Elastic Membranes," *IMA J. Appl. Math.*, Vol. 36, pp. 85–99.

Steigmann, D. J., and Pipkin, A. C., 1989a, "Axisymmetric Tension Fields," *Z. Angew. Math. Phys.*, Vol. 40, pp. 526–542.

Steigmann, D. J., and Pipkin, A. C., 1989b, "Finite Deformations of Wrinkled Membranes," *Quart J. Mech. Appl. Math.*, Vol. 42, pp. 427–440.

Steigmann, D. J., and Pipkin, A. C., 1989c, "Wrinkling of Pressurized Membranes," ASME JOURNAL OF APPLIED MECHANICS, Vol. 56, pp. 624–628.

Wagner, H., 1929, "Flat Sheet Girder with Very Thin Metal Web," *Z. Flugtech. Motorluft-Schiffahrt*, Vol. 20, pp. 200–207; 227–231; 281–284; 306–314 (reprinted as NACA Technical Memorandum 604–606, NACA, Washington, 1931.)

White, J. L., 1968, "Finite Elements in Linear Viscoelasticity," *Proc. 2nd Conf. Matrix Mthds. Struct. Mech.*, AFFDLTR-150.

APPENDIX A

Viscoelastic Constitutive Relation

Following Lemaitre and Chaboche (1990), we consider the specific plane stress case when, for small strain,

$$\tilde{W}=\frac{1}{2}\left[\frac{\nu\tilde{E}}{(1-\nu^2)}E_{\alpha\alpha}E_{\beta\beta}+2\frac{\tilde{E}}{(1+\nu)}E_{\gamma\zeta}E_{\gamma\zeta}\right] \quad \text{(A1}a\text{)}$$

$$\tilde{V}=\frac{1}{2}\left[\frac{\nu\tilde{E}T}{(1-\nu^2)}\dot{E}_{\alpha\alpha}\dot{E}_{\beta\beta}+2\frac{\tilde{E}T^*}{(1+\nu)}\dot{E}_{\gamma\zeta}\dot{E}_{\gamma\zeta}\right], \quad \text{(A1}b\text{)}$$

where T and T^* are characteristic retardation times in tension and shear, respectively, $\tilde{E}$ is the initial elastic modulus, and ν is the Poisson's ratio. The stress can now be shown to be

$$S_{\alpha\beta}=\left[\frac{\nu\tilde{E}}{(1-\nu^2)}E_{\gamma\gamma}\delta_{\alpha\beta}+\frac{\tilde{E}}{(1+\nu)}E_{\alpha\beta}\right]+\left[\frac{\nu\tilde{E}T}{(1-\nu^2)}\dot{E}_{\zeta\zeta}\delta_{\alpha\beta}+\frac{\tilde{E}T^*}{(1+\nu)}\dot{E}_{\alpha\beta}\right]$$
$$=\frac{\nu\tilde{E}}{(1-\nu^2)}(E_{\gamma\gamma}+T\dot{E}_{\zeta\zeta})\delta_{\alpha\beta}+\frac{\tilde{E}}{(1+\nu)}(E_{\alpha\beta}+T^*\dot{E}_{\alpha\beta}). \quad \text{(A2)}$$

The shear retardation time, T^*, can be determined during a shear test, i.e., when

$$S_{\alpha\beta}=\text{constant}=\frac{\tilde{E}}{(1+\nu)}(E_{\alpha\beta}+T^*\dot{E}_{\alpha\beta}),\ \alpha\neq\beta. \quad \text{(A3)}$$

The solution of this differential equation is readily shown to be

$$E_{\alpha\beta}(t)=\frac{1+\nu}{\tilde{E}}S_{\alpha\beta}[1-\exp(-t/T^*)],\ \alpha\neq\beta. \quad \text{(A4)}$$

Similarly, T is identified through a tension test, viz.,

$$S_{(\alpha)(\alpha)}=\text{constant}$$
$$=\frac{\tilde{E}\nu}{(1-\nu^2)}(E_{\gamma\gamma}+T\dot{E}_{\zeta\zeta})\delta_{(\alpha)(\alpha)}+\frac{\tilde{E}}{(1+\nu)}[E_{(\alpha)(\alpha)}+T^*\dot{E}_{(\alpha)(\alpha)}]. \quad \text{(A5)}$$

Using the facts that $E_{(\beta)(\beta)}=-\nu E_{(\alpha)(\alpha)}$, where $\upsilon=$ constant, and $1-\nu^2=(1-\nu)(1+\nu)$, we combine terms to get

$$S_{(\alpha)(\alpha)}=\tilde{E}E_{(\alpha)(\alpha)}+\frac{\tilde{E}}{(1+\nu)}(\nu T+T^*)\dot{E}_{(\alpha)(\alpha)}$$
$$=\tilde{E}E_{(\alpha)(\alpha)}+\eta\dot{E}_{(\alpha)(\alpha)},\ \eta=\frac{\tilde{E}}{(1+\nu)}(\nu T+T^*). \quad \text{(A6)}$$

We recognize (A6) as the governing equation for a Kelvin-Voigt mechanical-analogic model with response

$$E_{(\alpha)(\alpha)}(t)=\frac{1}{\tilde{E}}S_{(\alpha)(\alpha)}[1-\exp(-\tilde{E}t/\eta)]. \quad \text{(A7)}$$

The model can be generalized by forming assemblies of Kelvin-Voigt models; for linear viscoelasticity, the strain responses may be summed, e.g.,

$$E_{(\alpha)(\alpha)}(t)=\left\{\frac{1}{\tilde{E}_1}+\frac{1}{\tilde{E}_2}[1-\exp(-\tilde{E}_2t/\eta_2)]+\frac{1}{\tilde{E}_3}[1-\exp(-\tilde{E}_3t/\eta_3)]\right\}S_{(\alpha)(\alpha)} \quad \text{(A8)}$$

This result can also be reached by use of the Prony series representation of the material function in the hereditary constitutive relation. Consider the three-term Prony series

$$\tilde{J}(t)=\tilde{A}_1+\tilde{A}_2\exp(-\tilde{B}_2t)+\tilde{A}_3\exp(-\tilde{B}_3t) \quad \text{(A9)}$$

substituted into the linear hereditary integral

$$E_{\alpha\beta}(t)=\tilde{J}(0)S_{\alpha\beta}(t)-\int_0^t\frac{d\tilde{J}(t-\tau)}{d\tau}S_{\alpha\beta}(\tau)d\tau. \quad \text{(A10)}$$

For constant $S_{\alpha\beta}$ in (A10) we integrate to get Eq. (A8) where

$$\frac{1}{\tilde{E}_1}=\tilde{A}_1+\tilde{A}_2+\tilde{A}_3,\ \frac{1}{\tilde{E}_2}=\tilde{A}_2,\ \frac{1}{\tilde{E}_3}=\tilde{A}_3,\ \tilde{B}_2=\frac{\tilde{E}_2}{\eta_2},\ \tilde{B}_3=\frac{\tilde{E}_3}{\eta_3}.$$

APPENDIX B

Wrinkling Condition

Define principal stresses and strains

$$S^\alpha\equiv[S^{(\alpha)(\alpha)}]_{\max,\min},\ E_\beta\equiv[E_{(\beta)(\beta)}]_{\max,\min}$$

where $S^1>S^2$, $E_1>E_2$ and parentheses around superscripts or subscripts indicate no sum. Now also define

$$\tilde{C}^{\alpha\beta}\equiv\tilde{C}^{(\alpha)(\alpha)(\beta)(\beta)}.$$

* In general, the principal axes (defined by the basis vectors G_α) will differ from the local coordinate axes (defined by the basis vectors G_α), and the metric tensor components $G^{\alpha\beta}$ transformed to the principal coordinates are given by

$$\overset{*}{G}^{\alpha\beta} = \lambda^{\alpha}_{\gamma}\lambda^{\beta}_{\xi}G^{\gamma\xi} \tag{B1}$$

where the backward change of basis coefficients $\lambda^{\alpha}_{\gamma}$ (Malvern, 1969) are given by the transformation

$$G_{\gamma} = \lambda^{\alpha}_{\gamma}\overset{*}{G}_{\alpha}. \tag{B2}$$

For an isotropic Hookean material,

$$S^{\alpha} = \tilde{C}^{\alpha\beta}E_{\beta}. \tag{B3}$$

Now for wrinkling, $S^2 = 0$, then

$$0 = \tilde{C}^{21}E_1 + \tilde{C}^{22}E_2 \tag{B4}$$

and the wrinkling condition is given by

$$\overset{*}{E}_2(E_1) = -\frac{\tilde{C}^{21}}{\tilde{C}^{22}}E_1. \tag{B5}$$

The principal stress under wrinkling is then given by

$$\overset{*}{S}^1 = \tilde{C}^{11}E_1 + \tilde{C}^{12}\overset{*}{E}_2 = \left(\tilde{C}^{11} - \frac{\tilde{C}^{12}\tilde{C}^{12}}{\tilde{C}^{22}}\right)E_1. \tag{B6}$$

ERRATA

Errata on "The Spherical Inclusion with Imperfect Interface," by Z. Hashin, published in the June 1991 issue of JOURNAL OF APPLIED MECHANICS, Vol. 58, pp. 444–449.

On page 446, the last two Eqs. (19) should read:

$$\sigma_{\theta\theta} = 2G\beta\left\{3(7+\nu)A\rho^2 + 2B + (1-2\nu)C/\rho^3 + \frac{9}{2}D/\rho^5 + \left[-7(2+\nu)A\rho^2 - B + (1-2\nu)C/\rho^3 - \frac{7}{2}D/\rho^5\right]3\cos^2\theta.\right\}$$

$$\sigma_{\phi\phi} = 2G\beta\left\{15\nu A\rho^2 - B - 5(1-2\nu)C/\rho^3 + \frac{3}{2}D/\rho^5 + \left[-(11+7\nu)A\rho^2 + 3(1-2\nu)C/\rho^3 - \frac{5}{2}D/\rho^5\right]3\cos^2\theta\right\}.$$

Equation (20) should read:

$$A_1 = C_2 = D_2 = 0 \quad B_1 = 1.$$

The last two Eqs. (25) should read:

$$\frac{\sigma^{(1)}_{\theta\theta}(a,\theta)}{\sigma_0} = \frac{K_2(3K_1 - 2G_1) + 6K_1G_1(1+3p)}{3K_1[3K_2 + 4G_2(1+3p)]} + \frac{1}{3}\left\{2 + (1-2\nu_1)C_1 + \frac{9}{2}D_1 + \frac{3}{2}[-2 + 2(1-2\nu_1)C_1 - 7D_1]\cos^2\theta\right\}$$

$$\frac{\sigma^{(1)}_{\phi\phi}(a,\theta)}{\sigma_0} = \frac{K_2(3K_1 - 2G_1) + 6K_1G_1(1+3p)}{3K_1[3K_2 + 4G_2(1+3p)]} + \frac{1}{3}\left\{-1 - 5(1-2\nu_1)C_1 + \frac{3}{2}D_1 + \frac{3}{2}[6(1-2\nu_1)C_1 - 5D_1]\cos^2\theta\right\}.$$

The help of Mr. Uri Schur in correcting these errors is gratefully acknowledged.

Green's Functions for Generalized Plane Problems of Anisotropic Bodies With a Hole or a Rigid Inclusion

Yung-Ming Wang

Jiann-Quo Tarn

Department of Civil Engineering,
National Cheng Kung University,
Tainan, Taiwan 70101,
Republic of China

Green's function solutions are presented for the generalized plane problems of a point force and an edge dislocation located in the general anisotropic elastic medium with a hole or with a rigid inclusion. The Lekhnitskii's complex potential approach is used and a general expression of the solutions is obtained. Particular attention is paid to the determination of appropriate mapping functions that map the exterior of the hole or the inclusion onto the exterior of a unit circle. The conditions under which the conformal mapping is possible are explored. Examples using the Green's functions for the solution of notch problem are given.

Introduction

The solution of a point force or a dislocation located in an elastic medium of infinite extent is known as the Green's function solution or the fundamental solution. Among its wide applications, the Green's function is essential in the boundary element method (Brebbia, Telles, and Wrobel, 1984). In studying elasticity problems involving geometrical disturbance, such as a hole or an inclusion, it is preferable to employ a special Green's function which satisfies the boundary conditions at the hole or the inclusion in the formulation so as to avoid disturbance of the stress distribution in the vicinity of the high stress concentration region.

Considerable research on the related topics can be found in the literature. The use of special Green's function in the crack problems have received much attention (Snyder and Cruse, 1975; Clements and Haselgrove, 1983; Ang and Clements, 1987; Kamel and Liaw, 1989). Interactions between point singularities and a rigid inclusion have been a topic of considerable interest because of their practical importance (Mura, 1982; Santare and Keer, 1986; Dundurs and Markenscoff, 1989; Li and Ting, 1989). To the authors' knowledge, earlier studies on the Green's functions of anisotropic elasticity are for anisotropy of special kinds, and for a hole or an inclusion of elliptic shape which includes its geometric limits, such as a circle, a crack, or a line inclusion. Recently, using the Stroh formalism (Stroh, 1958), Hwu and Yen (1991) studied the Green's function for the case of a point force in two-dimensional anisotropic medium containing an elliptic hole. Ting and Yan (1991) studied the problem of general anisotropic medium with an elliptic hole subjected to prescribed traction on the hole surface and an elliptic rigid inclusion subjected to a concentrated force. While certain identities concerning eigenvalues and eigenvectors developed in the Stroh formalism may be useful in simplifying and interpreting the solutions, as discussed by Suo (1990), the formalism is essentially an alternative derivation of the classical Lekhnitskii's approach (1963). Due to its explicitness, the Lekhnitskii's complex potential formulation is employed in this paper to obtain the Green's function solutions for the generalized plane problems in the cases of a point force and an edge dislocation located in the anisotropic elastic medium with a hole or with a rigid inclusion. The anisotropy considered herein is completely general, without assuming elastic symmetry of the materials.

It is well known that the use of the complex potential approach to the notch problem involves conformal mapping. While it is relatively simple in the case of isotropic materials because a single mapping function is required, the solution is considerably more difficult to obtain in the case of general anisotropic materials, since it requires finding three conformal mapping functions which transform the complex parameter regions onto the exterior of a unit circle. Analytic solutions for the notch problems in anisotropic elasticity appear to be available only for the hole of elliptic shape (Savin, 1961; Lekhnitskii, 1963). For a hole contour of a general shape, many numerical solution methods were devised (Sih, 1978). Approximate solutions based on perturbation method valid in restrictive conditions for orthotropic materials can be found in Lekhnitskii (1968). In this paper, a general expression of the solutions for hole of arbitrary shape is derived and particular attention is paid to the determination of appropriate

Contributed by the Applied Mechanics Division of THE AMERICAN SOCIETY OF MECHANICAL ENGINEERS for publication in the ASME JOURNAL OF APPLIED MECHANICS.

Discussion on this paper should be addressed to the Technical Editor, Professor Lewis T. Wheeler, Department of Mechanical Engineering, University of Houston, Houston, TX 77204-4792, and will be accepted until four months after final publication of the paper itself in the ASME JOURNAL OF APPLIED MECHANICS.

Manuscript received by the ASME Applied Mechanics Division, Nov. 15, 1991; final revision, June 4, 1992. Associate Technical Editor: R. Abeyaratne.

mapping functions. The conditions under which the conformal mapping is possible are explored. It is shown that the conformal mapping in the entire region outside the unit circle is indeed possible only for elliptic contour or for anisotropy of a special kind. Nevertheless, useful mapping functions which are conformal and single-valued within a local region containing the arbitrary contour can be obtained in a simple manner. Application of the special Green's functions to the solutions of problems involving holes or rigid inclusions of arbitrary shape is then discussed and examples are given to examine the validity and generality of the present solution.

Basic Equations and General Solutions

The stress and displacement components for a generalized plane deformation of a general anisotropic elastic medium can be expressed in terms of three complex potentials (Lekhnitskii, 1963) as

$$\sigma_{11} = 2\mathrm{Re}(\mu_1^2\phi_1' + \mu_2^2\phi_2' + \mu_3^2\lambda_3\phi_3') \tag{1}$$

$$\sigma_{22} = 2\mathrm{Re}(\phi_1' + \sigma_2' + \lambda_3\phi_3') \tag{2}$$

$$\sigma_{12} = -2\mathrm{Re}(\mu_1\phi_1' + \mu_2\phi_2' + \mu_3\lambda_3\phi_3') \tag{3}$$

$$\sigma_{13} = 2\mathrm{Re}(\mu_1\lambda_1\phi_1' + \mu_2\lambda_2\phi_2' + \mu_3\phi_3') \tag{4}$$

$$\sigma_{23} = -2\mathrm{Re}(\lambda_1\phi_1' + \lambda_2\phi_2' + \phi_3') \tag{5}$$

$$u_1 = 2\mathrm{Re}\left(\sum_{k=1}^{3} p_k\phi_k\right) \tag{6}$$

$$u_2 = 2\mathrm{Re}\left(\sum_{k=1}^{3} q_k\phi_k\right) \tag{7}$$

$$u_3 = 2\mathrm{Re}\left(\sum_{k=1}^{3} r_k\phi_k\right) \tag{8}$$

in which $\phi_k = \phi_k(z_k)$, $(k = 1, 2, 3)$ are the complex potentials, $z_k = x + \mu_k y$, Re stands for the real part, and prime ($'$) denotes differentiation with respect to the argument. The rigid-body displacements were omitted. μ_k are the three complex conjugate roots with positive imaginary part of the characteristic equation:

$$l_4(\mu)l_2(\mu) - l_3^2(\mu) = 0 \tag{9}$$

where
$$l_2(\mu) = \beta_{55}\mu^2 - 2\beta_{45}\mu + \beta_{44},$$
$$l_3(\mu) = \beta_{15}\mu^3 - (\beta_{14} + \beta_{56})\mu^3 + (\beta_{25} + \beta_{46})\mu - \beta_{24},$$
$$l_4(\mu) = \beta_{11}\mu^4 - 2\beta_{16}\mu^3 + (2\beta_{12} + \beta_{66})\mu^2 - 2\beta_{26}\mu + \beta_{22}.$$

β_{ij} are the coefficients of deformation of the material. The expressions for the complex parameters λ_k, P_k, q_k, and r_k in terms of β_{ij} and μ_k can be found in Lekhnitskii's book. The basic equations for the generalized plane stress problem are obtained by replacing β_{ij} with the compliances a_{ij} of the material.

When the material possesses one plane of elastic symmetry normal to the x_3-axis (monoclinic material), or the material is orthotropic with axes 1, 2 as its principal material axes, then $l_3(\mu) = 0$ and $\lambda_1 = \lambda_2 = \lambda_3 = 0$. Determination of ϕ_3 is not coupled with ϕ_1 and ϕ_2. The in-plane and antiplane deformations can be treated independently.

For the expedience of exposition, let us adopt the following matrix notations similar to those given by Stroh (1958) and Suo (1990),

$$\boldsymbol{\phi} = \begin{Bmatrix} \phi_1 \\ \phi_2 \\ \phi_3 \end{Bmatrix}, \quad \mathbf{u} = \begin{Bmatrix} u_1 \\ u_2 \\ u_3 \end{Bmatrix}, \quad \sigma_1 = \begin{Bmatrix} \sigma_{11} \\ \sigma_{12} \\ \sigma_{13} \end{Bmatrix}, \quad \sigma_2 = \begin{Bmatrix} \sigma_{21} \\ \sigma_{22} \\ \sigma_{23} \end{Bmatrix},$$

$$\mathbf{A} = \begin{bmatrix} p_1 & p_2 & p_3 \\ q_1 & q_2 & q_3 \\ r_1 & r_2 & r_3 \end{bmatrix}, \mathbf{L} = \begin{bmatrix} -\mu_1 & -\mu_2 & -\mu_3\lambda_3 \\ 1 & 1 & \lambda_3 \\ -\lambda_1 & -\lambda_2 & -1 \end{bmatrix},$$

$$\boldsymbol{\mu} = \begin{bmatrix} \mu_1 & 0 & 0 \\ 0 & \mu_2 & 0 \\ 0 & 0 & \mu_3 \end{bmatrix}.$$

Then Eqs. (1)–(8) can be recast into compact forms as follows:

$$\sigma_1 = -\mathbf{L}\boldsymbol{\mu}\boldsymbol{\phi}' - \bar{\mathbf{L}}\,\bar{\boldsymbol{\mu}}\,\bar{\boldsymbol{\phi}}' \tag{10}$$

$$\sigma_2 = \mathbf{L}\boldsymbol{\phi}' + \bar{\mathbf{L}}\,\bar{\boldsymbol{\phi}}' \tag{11}$$

$$\mathbf{u} = \mathbf{A}\boldsymbol{\phi} + \bar{\mathbf{A}}\,\bar{\boldsymbol{\phi}} \tag{12}$$

where the overbar denotes the complex conjugate.

In addition, the resultant forces $\mathbf{T}$ on an arc can be expressed by

$$\mathbf{T} = -\mathbf{L}\boldsymbol{\phi} - \bar{\mathbf{L}}\,\bar{\boldsymbol{\phi}}. \tag{13}$$

Consider an infinite region with a traction-free hole or a rigid inclusion. The boundary conditions on the contour of the interior boundary Γ can be written as follows:

(1) When Γ is a traction-free boundary,

$$\mathbf{L}\boldsymbol{\phi} + \bar{\mathbf{L}}\,\bar{\boldsymbol{\phi}} = 0 \qquad \text{on } \Gamma. \tag{14}$$

(2) When Γ is a rigid boundary,

$$\mathbf{A}\boldsymbol{\phi} + \bar{\mathbf{A}}\,\bar{\boldsymbol{\phi}} = 0 \qquad \text{on } \Gamma. \tag{15}$$

Suppose that exterior of Γ in the ζ_k planes can be mapped conformally onto the exterior of a unit circle, $\sigma = e^{i\theta}$, by the mapping functions

$$z_k = w_k(\zeta_k), \quad k = 1, 2, 3. \tag{16}$$

Then, the boundary condition on the unit circle in the ζ_k plane becomes

$$\mathbf{L}\boldsymbol{\Phi}(\sigma) + \bar{\mathbf{L}}\,\bar{\boldsymbol{\Phi}}(\sigma) = 0, \tag{17}$$

$$\mathbf{A}\boldsymbol{\Phi}(\sigma) + \bar{\mathbf{A}}\,\bar{\boldsymbol{\Phi}}(\sigma) = 0, \tag{18}$$

where $\boldsymbol{\Phi}(\zeta_k) = \boldsymbol{\phi}(w_k(\zeta_k))$.

When the medium contains point singularities due to the presence of a concentrated force and an edge dislocation, $\boldsymbol{\Phi}$ must be holomorphic in $|\sigma| > 1$ except at the point singularities and at infinity.

Let $\boldsymbol{\Phi}$ consist of a function $\mathbf{f}$ which contains the point singularities but is holomorphic in $|\sigma| < 1$, and function $\mathbf{g}$ holomorphic everywhere in $|\sigma| > 1$,

$$\boldsymbol{\Phi}(\zeta) = \mathbf{f}(\zeta) + \mathbf{g}(\zeta). \tag{19}$$

Note that $\bar{\sigma} = \sigma^{-1}$ on the unit circle, and $\bar{\mathbf{f}}(\sigma^{-1})$ is the boundary value of $\bar{\mathbf{f}}(\zeta^{-1})$ which is holomorphic in $|\sigma| > 1$, and $\bar{\mathbf{g}}(\sigma^{-1})$ is the boundary value of $\bar{\mathbf{g}}(\zeta^{-1})$ which is holomorphic in $|\sigma| < 1$. Substituting (19) into (17), (18), multiplying them by $1/2\pi i(\sigma - \zeta)$, and integrating around the unit circle, we obtain according to the Cauchy's formula for the infinite region (Muskhelishvili, 1954)

$$\mathbf{L}\mathbf{g}(\zeta) = -\bar{\mathbf{L}}\,\bar{\mathbf{f}}(\zeta^{-1}), \quad |\zeta| > 1 \tag{20}$$

for the case of a traction-free hole and

$$\mathbf{A}\mathbf{g}(\zeta) = -\bar{\mathbf{A}}\,\bar{\mathbf{f}}(\zeta^{-1}), \quad |\zeta| > 1 \tag{21}$$

for the case of a rigid inclusion.

Then by (19) we obtain

$$\boldsymbol{\Phi}(\zeta) = \mathbf{f}(\zeta) - \mathbf{L}^{-1}\bar{\mathbf{L}}\,\bar{\mathbf{f}}(\zeta^{-1}) \tag{22}$$

for the case of a fraction-free hole, and

$$\boldsymbol{\Phi}(\zeta) = \mathbf{f}(\zeta) - \mathbf{A}^{-1}\bar{\mathbf{A}}\,\bar{\mathbf{f}}(\zeta^{-1}) \tag{23}$$

for the case of a rigid inclusion.

Equations (22), (23) are the general expressions of the complex potentials satisfying the boundary conditions (17) or (18). It can be applied to various problems involving a notch or an inclusion. Determination of $\mathbf{f}(\zeta)$ for a given boundary value problem requires that it be holomorphic in the unit circle. Once the solution of $\mathbf{f}(\zeta)$ is determined for the problem, the pertinent field quantities can be obtained from (1)–(8) by replacing ζ in each component functions with ζ_1, ζ_2, and ζ_3, respectively.

Green's Function Solutions

Consider a concentrated force $P=(p_x, p_y, 0)$ and an edge dislocation with Burgers vector $\mathbf{b}=b_x\mathbf{i}+b_y\mathbf{j}$ both located at the point (x^*, y^*) in the medium. When the point singularities are acting in an unbounded region without the geometrical disturbance, the stress and displacement fields can be determined from ϕ_k^∞

$$\phi_k^\infty(z)=c_k \log(z-z_k^*) \tag{24}$$

where $z_k^*=x^*+\mu_k y^*$, the coefficient vectors $\mathbf{c}=\{c_1, c_2, c_3\}$ are obtained from the condition that integrations of the force and displacement determined by (24) over a simple closed contour encircled z_k^* produce the resultant forces equal to $(p_x, p_y, 0)$ and the displacement increments $(b_x, b_y, 0)$. The conditions provide

$$\begin{bmatrix} \mathbf{L} & -\overline{\mathbf{L}} \\ \mathbf{A} & -\overline{\mathbf{A}} \end{bmatrix} \begin{Bmatrix} \mathbf{c} \\ \overline{\mathbf{c}} \end{Bmatrix} = \frac{1}{2\pi i} \begin{Bmatrix} \mathbf{p} \\ \mathbf{b} \end{Bmatrix}. \tag{25}$$

When the point singularities are acting in the unbounded region containing a hole or an inclusion, the stress and displacement field must be perturbed by the presence of the hole or the inclusion. Consequently, in addition to ϕ_k^∞, a modified term ϕ_k^mwhich is holomorphic outside the unit circle should be included. Thus, in the ζ_k plane,

$$\Phi_k(\zeta)=c_k \log(\zeta-\zeta_k^*)+\Phi_k^m(\zeta) \tag{26}$$

where $\zeta_k^*=w_k^{-1}(z_k^*)$.

Comparison of (26) with (22), (23) immediately gives

$$f_k(\zeta)=c_k \log(\zeta-\zeta_k^*). \tag{27}$$

It follows from (22), (23) that

$$\Phi_k(\zeta_k)=c_k \log(\zeta_k-\zeta_k^*)-\sum_{j=1}^{3} M_{kj}\bar{c}_j \log(\zeta_k^{-1}-\bar{\zeta}_j^*), \tag{28}$$

where $\mathbf{M}=\mathbf{L}^{-1}\overline{\mathbf{L}}$ for the case of a traction-free hole and $\mathbf{M}=\mathbf{A}^{-1}\overline{\mathbf{A}}$ for the case of a rigid inclusion.

The Mapping Functions

Determination of the Green's function solutions (28) is based on the existence of the conformal mapping functions (16). In practice, however, it is very difficult to find the suitable mapping functions that transform conformally the ζ_k parameter regions onto the exterior of a unit circle. In the following, the conditions under which the conformal mapping is possible are explored.

Consider a hole of arbitrary shape in the infinite region. The Fourier series representation of the contour can be expressed by

$$x(\theta)=A_0+\sum_{n=1}^{\infty} A_n \cos n\theta+\sum_{n=1}^{\infty} B_n \sin n\theta, \tag{29}$$

$$y(\theta)=C_0+\sum_{n=1}^{\infty} C_n \cos n\theta+\sum_{n=1}^{\infty} D_n \sin n\theta, \tag{30}$$

where $0\le\theta\le 2\pi$. It is shown in the Appendix that the family of elliptic contours can be represented by (29), (30) with $A_n=B_n=C_n=D_n=0$ for $n\ge 2$.

On the z_k planes, the contour is given by

$$z_k=x+\mu_k y=(A_0+\mu_k C_0)+\sum_{n=1}^{\infty}(A_n+\mu_k C_n)\cos n\theta + \sum_{n=1}^{\infty}(B_n+\mu_k D_n)\sin n\theta. \tag{31}$$

It is necessary that the mapping functions be holomorphic and single-valued outside the unit circle. Equation (16) thus may be represented by a Laurent's series in the form

$$z_k=w_k(\zeta_k)=m_{0k}+m_{1k}\zeta_k+\sum_{n=1}^{\infty} m_{-nk}\zeta_k^{-n}. \tag{32}$$

In addition, all the roots of $w_k'(\zeta_k)=0$ are required to locate inside the unit circle.

On the unit circle, $\zeta_k=e^{i\theta}$, then

$$z_k=m_{0k}+(m_{1k}+m_{-1k})\cos\theta+\sum_{n=2}^{\infty} m_{-nk}\cos n\theta + i(m_{1k}-m_{-1k})\sin\theta-\sum_{n=2}^{\infty} m_{-nk}\sin n\theta. \tag{33}$$

Comparing (33) with (31), we obtain

$$m_{0k}=A_0+\mu_k C_0, \tag{34}$$

$$m_{1k}=[A_1-iB_1+\mu_k(C_1-iD_1)]/2, \tag{35}$$

$$m_{-1k}=[A_1+iB_1+\mu_k(C_1+iD_1)]/2, \tag{36}$$

$$m_{-nk}=A_n+\mu_k C_n=i(B_n+\mu_k D_n), \quad n\ge 2. \tag{37}$$

Since μ_k are always complex, let $\mu_k=\alpha_k+i\beta_k$, α_k and β_k being real numbers, $\beta_k>0$. From (37), we have for $n\ge 2$,

$$\alpha_k C_n+\beta_k D_n=-A_n, \qquad k=1, 2, 3.$$

$$\beta_k C_n-\alpha_k D_n=-B_n, \tag{38}$$

Equations (38) are compatible only under two possible conditions:

(1) $A_n=B_n=C_n=D_n=0$ for $n\ge 2$,

then $m_{-nk}=0$ for $n\ge 2$.

The contour is a family of ellipses. Furthermore, it is shown in the Appendix if $A_1D_1-B_1C_1>0$, the exterior of the ellipse is mapped onto the exterior of the unit circle by (32) with the branch points located inside the unit circle. If $A_1D_1-B_1C_1<0$, the appropriate mapping functions are

$$w(\zeta_k)=m_{0k}+m_{1k}\zeta_k^{-1}+m_{-1k}\zeta_k. \tag{39}$$

By prescribing appropriate parameters in the mapping functions for the elliptic hole, the Green's functions for a circular hole, for a crack, can be readily obtained.

(2) $\alpha_1=\alpha_2=\alpha_3$, $\beta_1=\beta_2=\beta_3$, hence $\mu_1=\mu_2=\mu_3$.

This means that the characteristic Eq. (9) has repeated complex roots. Note that the basic forms of complex potential representation of stresses and displacements are different from those given by Eqs. (1)–(8) in this case. The isotropy is a well-known degenerate case of this kind with $\mu_1=\mu_2=i$.

Equations (38) contradict for any other situation. Consequently, the mapping functions which is conformal and single-valued everywhere outside the unit circle can not be found for a nonelliptic contour with distinct μ_k.

On the other hand, a mapping which is conformal and single-valued within a local region containing the hole of arbitrary shape can be determined by using a complete Laurent's series representation

$$z_k=w_k(\zeta_k)=\sum_{n=-\infty}^{\infty} m_{nk}\zeta_k^n. \tag{40}$$

Comparing (40) with (31), we obtain

$$m_{0k} = A_0 + \mu_k C_0, \tag{41}$$

$$m_{nk} = [A_n - iB_n + \mu_k (C_n - iD_n)]/2, \tag{42}$$

$$m_{-nk} = [A_n + iB_n + \mu_k (C_n + iD_n)]/2. \tag{43}$$

The mapping functions (40) are not single-valued in the entire region outside the unit circle because branch points where $w_k'(\zeta_k) = 0$ in general exist outside the unit circle.

In spite of the fact that the branch points of (40) are not always located inside the unit circle, the mapping functions are holomorphic and single-valued within a finite region between the interior contour and the branch cuts. The corresponding Green's functions satisfying the boundary conditions at the interior contour are useful in the numerical solution of the pertinent problems. When using a numerical procedure such as the boundary element method to analyze a problem involving an interior contour of arbitrary shape, it is advantageous to determine first the local region containing the hole or the inclusion in which (40) is holomorphic and single-valued. Then the problem region is divided into subregions, and the special Green's functions (28) can be employed in the subregion containing the hole or the inclusion, with its boundary not intersecting the branch cut. The Green's functions (24) for an unbounded region can be used for the remaining subregions of the problem. Thus, the boundary conditions on the interior contour are satisfied exactly and can be eliminated from the path of integration, and only the remote boundaries away from the hole or the inclusion are required to include in the boundary integral equation. The continuity between the interfaces of the subregions can be implemented easily according to the boundary element method procedure (Brebbia, Telles, and Wrobel, 1984).

Examples

To show the validity and generality of (22), (23) and the Green's functions derived herein, the following examples are presented:

(1) An Infinite Plate With an Elliptic Hole Under Remote Loading. The load considered is a linearly varying normal force applied at infinity, which includes the cases of a uniform tension and a bending force. Solutions obtained by superposition and series expansions in these two cases for monoclinic materials were given in Lekhnitskii (1963).

In the present solution, the prescribed condition at infinity is

$$\sigma_x^\infty = ky + p_x,$$

$$\sigma_y^\infty = \sigma_{xy}^\infty = \sigma_{xz}^\infty = \sigma_{yz}^\infty = 0, \tag{44}$$

where k, p_x are the constants characterize the applied load.

The complex potentials corresponding to the prescribed loading condition for the infinite plate without a hole are in the form of

$$\boldsymbol{\phi}^\infty(z) = \mathbf{a}z^2 + \mathbf{b}z. \tag{45}$$

The coefficients **a** and **b** can be determined by substituting (45) into (10), (11) and using the condition (44).

According to (32), the mapping functions that map the exterior of an elliptic hole with semi-axes **a**, **b** coincident with x, y-axes onto the exterior of a unit circle are

$$z_k = m_{1k}\zeta_k + m_{-1k}\zeta_k^{-1} \tag{46}$$

where

$$m_{1k} = (a - i\mu_k b)/2, \quad m_{-1k} = (a + i\mu_k b)/2.$$

Substituting (47) into (45) gives Φ_k^∞ in the ζ_k plane,

$$\Phi_k^\infty(\zeta) = m_{1k}^2 a_k \zeta^2 + m_{1k} b_k \zeta + 2m_{1k}m_{-1k}a_k + m_{-1k}b_k\zeta^{-1} + m_{-1k}^2 a_k \zeta^{-2}. \tag{47}$$

In the presence of an elliptic hole in the medium, a modified term $\Phi_k^m(\zeta)$ holomorphic in $|\sigma| > 1$ must be added to Φ_k^∞. Comparing with (19) and retaining only the terms in (47) which are single valued and holomorphic in $|\phi| < 1$, we obtain

$$\mathbf{f}(\zeta) = \mathbf{a}^*\zeta^2 + \mathbf{b}^*\zeta$$

where

$$a_k^* = m_{1k}^2 a_k, \quad b_k^* = m_{1k} b_k.$$

Thus, a direct application of (22) gives the required complex potentials for the problem:

$$\boldsymbol{\Phi}(\zeta) = a^*\zeta^2 + \mathbf{b}^*\zeta - \mathbf{L}^{-1}\overline{\mathbf{L}}(\overline{\mathbf{b}}^*\zeta^{-1} + \overline{\mathbf{a}}^*\zeta^{-2}). \tag{48}$$

The general solution is now examined by comparing with the available solution given in Lekhnitskii (1963) for the special case of monoclinic materials. When the material has one plane of elastic symmetry normal to x_3-axis, then $\lambda_1 = \lambda_2 = \lambda_3 = 0$. **a**, **b** in (45) are determined as

$$a_1 = \frac{k}{2p'(\mu_1)}, \quad a_2 = \frac{k}{2p'(\mu_2)}, \quad a_3 = 0,$$

$$b_1 = \frac{\mu_1 p_x}{p'(\mu_1)}, \quad b_2 = \frac{\mu_2 p_x}{p'(\mu_2)}, \quad b_3 = 0,$$

where

$$p(\mu) = (\mu - \mu_1)(\mu - \mu_2)(\mu - \overline{\mu}_1)(\mu - \overline{\mu}_2).$$

Then from (48),

$$\Phi_1(\zeta_1) = a_1^*\zeta_1^2 + b_1^*\zeta_1 + \left(\frac{\mu_2 - \overline{\mu}_1}{\mu_1 - \mu_2}\overline{b}_1^* + \frac{\mu_2 - \overline{\mu}_2}{\mu_1 - \mu_2}\overline{b}_2^*\right)\zeta_1^{-1} + \left(\frac{\mu_2 - \overline{\mu}_1}{\mu_1 - \mu_2}\overline{a}_1^* + \frac{\mu_2 - \overline{\mu}_2}{\mu_1 - \mu_2}\overline{\alpha}_2^*\right)\zeta_1^{-2}, \tag{49}$$

$$\Phi_2(\zeta_2) = a_2^*\zeta_2^2 + b_2^*\zeta_2 - \left(\frac{\mu_1 - \overline{\mu}_1}{\mu_1 - \mu_2}\overline{b}_1^* + \frac{\mu_1 - \overline{\mu}_2}{\mu_1 - \mu_2}\overline{b}_2^*\right)\zeta_2^{-1} - \left(\frac{\mu_1 - \overline{\mu}_1}{\mu_1 - \mu_2}\overline{a}_1^* + \frac{\mu_1 - \overline{\mu}_2}{\mu_1 - \mu_2}\overline{a}_2^*\right)\zeta_2^{-2}, \tag{50}$$

$$\Phi_3(\zeta_3) = 0. \tag{51}$$

Lekhnitskii's solution for the problem was obtained by a superposition of a modified stress field determined by Fourier series expansion upon the uniform stress field valid for the infinite plate without the hole. Corresponding to the present solution, the modified stresses are determined from the functions

$$\Phi_k^m = \Phi_k(\zeta_k) - \Phi_k^\infty(\zeta_k).$$

A little algebra gives

$$\Phi_1^m(\zeta_1) = \frac{1}{\mu_1 - \mu_2}\left(-\frac{ip_x b}{2}\zeta_1^{-1} + \frac{kb^2}{8}\zeta_1^{-2}\right),$$

$$\Phi_2^m(\zeta_2) = \frac{-1}{\mu_1 - \mu_2}\left(-\frac{ip_x b}{2}\zeta_2^{-1} + \frac{kb^2}{8}\zeta_2^{-2}\right),$$

which are exactly the solutions provided by Lekhnitskii.

(2) A Plate With a Square-Like Hole Under Uniform Tension. The contour of the square-like hole (Fig. 1) is represented by

$$x = a(\cos\theta + \epsilon\cos 3\theta), \tag{52}$$

$$y = a(\sin\theta - \epsilon\sin 3\theta). \tag{53}$$

An approximate solution using perturbation method was given by Lekhnitskii (1968) for the case of an orthotropic material and small values of the parameter ϵ. To compare the present solution with the perturbation solution valid for small ϵ we made the computation by selecting $a = 10$, $\epsilon = 1/9$ and used the same material properties $E_1 = 1.2 * 10^5 \text{kg/cm}^2$,

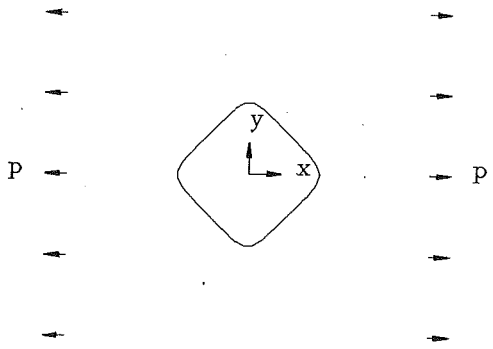

Fig. 1 Geometry and loading of Example 2

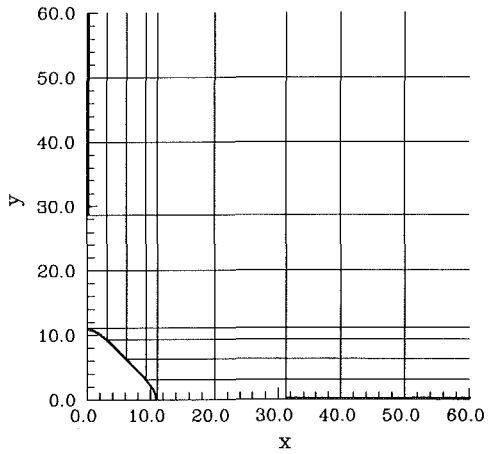

Fig. 2 Branch cuts in the first quadrant of the physical plane (branch points are at $z = \pm 31.22$ and $z = \pm 28.64i$, heavy lines indicate branch cuts)

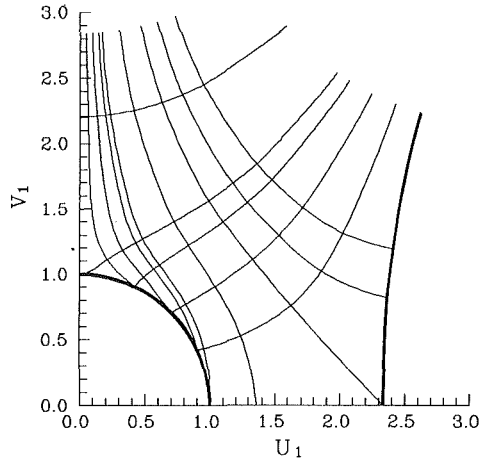

Fig. 3 Conformal mapping and branch cut in the ζ_1 plane

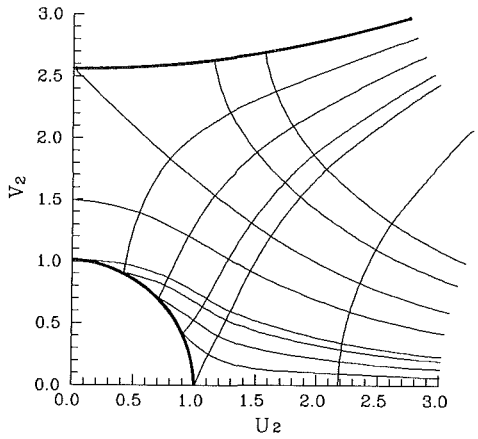

Fig. 4 Conformal mapping and branch cut in the ζ_2 plane

$E_2 = 0.6 * 10^5 \text{kg/cm}^2$, $G_{12} = 0.07 * 10^5 \text{kg/cm}^2$, $\nu_{12} = 0.071$. The corresponding complex parameters are found to be $\mu_1 = 4.11i$, $\mu_2 = 0.344i$. The mapping functions obtained according to (40)–(43) are

$$z_1 = -1.73\ \zeta_1^3 + 25.5\ \zeta_1 - 15.5\ \zeta_1^{-1} - 2.84\ \zeta_1^{-3}, \quad (54)$$

$$z_2 = 0.364\ \zeta_2^3 + 6.72\ \zeta_2 + 3.28\ \zeta_2^{-1} + 0.747\ \zeta_2^{-3}. \quad (55)$$

The branch points are located at $\zeta_1 = \pm 2.33$, $\zeta_2 = \pm 2.56i$, which correspond to $z = \pm 31.22$ and $z = \pm 28.64i$ in the physical plane, respectively. Figure 2 shows the branch cuts and only the first-quadrant region is shown because of symmetry. Figures 3 and 4 show the region of conformal mapping in the ζ_1 and ζ_2 planes. Indeed, the contour described by (53) is mapped into a unit circle in the ζ_k planes by the mapping functions (54), (55).

Numerical solution of the problem using the boundary element method can be obtained by dividing the problem region into two subregions. In the subregion in between the hole and $|x| \le 20$, $|y| \le 20$, the special Green's functions (28) with mapping functions (54), (55) were used. The Green's functions for the infinite region (Eq. (24)) were used in the remaining region. Sixteen quadratic boundary elements along the interface $|x| = 20$, $|y| = 20$ and four quadratic boundary elements in the remote boundary were used in the computation. Comparisons of the results with the Lekhnitskii's solution are given in Fig. 5, in which the cases of uniform tension in direction of E_1 and in direction of E_2 were calculated. The results are in excellent agreement.

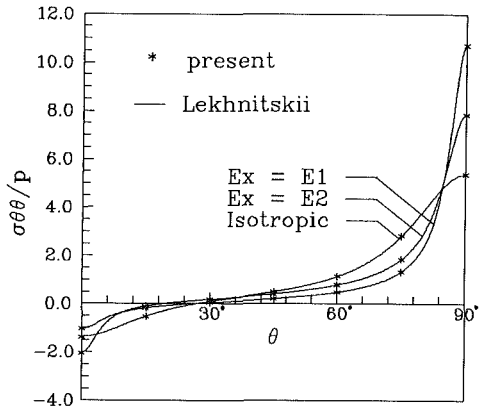

Fig. 5 Comparisons of the present solution with the approximate solution for Example 2

In the case of isotropy, the solution form is different. In practice, nevertheless, isotropy may be considered as a special case of anisotropy by assuming $\mu_1 = i$, and $\mu_2 = i + \epsilon$, ϵ being a very small constant, here we use $\epsilon = 10^{-6}$. Then the present Green's functions are still applicable. It is not difficult to show that the branch points generally are located at a distance far away from the hole. Hence, often there is no need to consider the branch cut. The boundary element method solutions for the problem shown in Fig. 1, using only four quadratic boundary elements in the remote boundary in comparison with the

solution given in Lekhnitskii (1968), are shown in Fig. 5. Practically identical results were obtained.

Acknowledgment

This work is supported by the National Science Council of Republic of China through Grant NSC-82-0410-E006-086.

References

Ang, W. T., and Clements, D. L., 1987, "A Boundary Integral Equation Method for the Solution of a Class of Crack Problems," *J. Elasticity*, Vol. 17, pp. 9–21.

Brebbia, C. A., Telles, J. C. F., and Wrobel, L. C., 1984, *Boundary Element Techniques*, Springer-Verlag, New York.

Clements, D. L., and Haselgrove, M. A., 1983, "A Boundary Integral Equation for a Class of Crack Problems in Anisotropic Elasticity," *Int. J. Comp. Math.*, Vol. 12, pp. 267–278.

Dundurs, J., and Markenscoff, X., 1989, "A Green's Function Formulation of Anticracks and Their Interaction with Load-Induced Singularities," ASME JOURNAL OF APPLIED MECHANICS, Vol. 56, pp. 550–555.

Hildebrand, F. B., 1965, *Methods of Applied Mathematics*, 2nd ed., Prentice-Hall, Englewood Cliffs, NJ.

Hwu, C., and Yen, W. J., 1991, "Green's Functions of Two-Dimensional Anisotropic Plates Containing an Elliptic Hole," *Int. J. Solids Structures*, Vol. 27, pp. 1705–1719.

Kamel, M., and Liaw, B. M., 1989, "Green's Functions Due to Concentrated Moments Applied in Anisotropic Plane with an Elliptic Hole or a Crack," *Mech. Res. Commans.*, Vol. 16, pp. 311–319.

Lekhnitskii, S. G., 1963, *Theory of Elasticity of an Anisotropic Elastic Body*, Holden-Day, San Francisco, CA.

Lekhnitskii, S. G., 1968, *Anisotropic Plates*, Gordon and Brench, New York.

Li, Q., and Ting, T. C. T., 1989, "Line Inclusions in Anisotropic Elastic Solids," ASME JOURNAL OF APPLIED MECHANICS, Vol. 56, pp. 556–563.

Mura, T., 1982, *Micromechanics of Defects in Solids*, Martinus Nijhoff, The Hague.

Muskhelishvili, N. I., 1954, *Some Basic Problems in the Mathematical Theory of Elasticity*, 4th ed., Noordhoff, Groningen, The Netherlands.

Santare, M. H., and Keer, L. M., 1986, "Interaction Between an Edge Dislocation and a Rigid Elliptical Inclusion," ASME JOURNAL OF APPLIED MECHANICS, Vol. 53, pp. 382–385.

Savin, G. N., 1961, *Stress Concentration Around Holes*, Pergamon Press, London.

Sih, G. C., ed., 1978, *Stress Analysis of Notch Problems*, Noordhoff, Alphen aan den Rijn, The Netherlands.

Stroh, A. N., 1958, "Dislocations and Cracks in Anisotropic Elasticity," *Phil. Mag.*, Vol. 7, pp. 625–646.

Suo, Z., 1990, "Singularities, Interfaces and Cracks in Dissimilar Anisotropic Media," *Proc. Royal Society London*, Vol. A427, pp. 331–358.

Snyder, M. D., and Cruse, T. A., 1975, "Boundary-Intergal Equation Analysis of Cracked Anisotropic Plates," *Int. J. Fracture*, Vol. 11, pp. 315–328.

Ting, T. C. T., and Yan, G., 1991, "The Anisotropic Elastic Solid with an Elliptical Hole or Rigid Inclusion," *Int. J. Solids Structures*, Vol. 27, pp. 1879–1894.

APPENDIX

Consider the contour given by

$$x = A_0 + A_1 \cos\theta + B_1 \sin\theta, \tag{A1}$$

$$y = C_0 + C_1 \cos\theta + D_1 \sin\theta. \tag{A2}$$

Expressing $\cos\theta$, $\sin\theta$ in terms of x, y, we can represent the contour by the following quadratic equation:

$$(C_1^2 + D_1^2)(x - A_0)^2 - 2(A_1C_1 + B_1D_1)(x - A_0)(y - C_0) + (A_1^2 + B_1^2)(y - C_0)^2 = (A_1D_1 - B_1C_1)^2. \tag{A3}$$

The canonical form (Hildebrand, 1965) of (A3) is given by

$$\lambda_1(X - A_0)^2 + \lambda_2(Y - C_0)^2 = (A_1D_1 - B_1C_1)^2 \tag{A4}$$

where λ_1, λ_2 denote the eigenvalues of the matrix $\mathbf{A}$,

$$\mathbf{A} = \begin{bmatrix} C_1^2 + D_1^2 & -(A_1C_1 + B_1D_1) \\ -(A_1C_1 + B_1D_1) & A_1^2 + B_1^2 \end{bmatrix} \tag{A5}$$

$$\lambda_{1,2} = (A_1^2 + B_1^2 + C_1^2 + D_1^2) \pm ([(A_1 - D_1)^2 + (B_1 + C_1)^2][(A_1 + D_1)^2 + (B_1 - C_1)^2])^{1/2}. \tag{A6}$$

Equation (A4) is an ellipse in a rotated plane with the center at (A_0, C_0) and the semi-axes are $(A_1D_1 - B_1C_1)^2/\lambda_1$, $(A_1D_1 - B_1C_1)^2/\lambda_2$. Hence, (A1) and (A2) represent a family of elliptic contours.

The mapping functions that map conformally the ellipse represented by (A1), (A2) in the physical plane into a unit circle in the ζ_k planes are

$$z_k = w_k(\zeta_k) = m_{0k} + m_{1k}\zeta_k + m_{-1k}\zeta_k^{-1} \tag{A7}$$

where

$$m_{0k} = A_0 + \mu_k C_0,$$

$$m_{1k} = [A_1 - iB_1 + \mu_k(C_1 - iD_1)]/2,$$

$$m_{1k} = [A_1 + iB_1 + \mu_k(C_1 + iD_1)]/2.$$

The branch points where $w_k'(\zeta_k) = 0$ are located at

$$\zeta_k = \pm(m_{-1k}/m_{1k})^{1/2}, \tag{A8}$$

and the requirement that the branch points be inside the unit circle produces the following condition:

$$A_1D_1 - B_1C_1 > 0. \tag{A9}$$

Let the origin be located at the center of the ellipse. Then at the point $x = x_0 > 0$, $y = 0$ on the ellipse,

$$\frac{dy}{d\theta} = \frac{x_0(C_1^2 + D_1^2)}{A_1D_1 - B_1C_1}. \tag{A10}$$

If $A_1D_1 - B_1C_1 > 0$, as θ increases counterclockwise in the ζ_k plane, $dy/d\theta > 0$, the point x_0, y_0 also travels counterclockwise in the z plane. Therefore, the exterior of the ellipse is mapped onto the exterior of the unit circle by (A7). On the contrary, if $A_1D_1 - B_1C_1 < 0$, then $dy/d\theta < 0$, the exterior of the ellipse is mapped into the interior of the unit circle by (A7), with branch points outside the unit circle. In this case, the mapping functions that map the exterior of the ellipse onto the exterior of the unit circle are

$$\zeta_k = w_k(\zeta_k) = m_{0k} + m_{1k}\zeta_k^{-1} + m_{-1k}\zeta_k. \tag{A11}$$

The branch points $\zeta_k = \pm(m_{1k}/m_{-1k})^{1/2}$ of (A11) then are located inside the unit circle.

G. Anlas

M. H. Santare

Department of Mechanical Engineering
and Center for Composite Materials,
University of Delaware,
Newark, DE 19716

Arbitrarily Oriented Crack Inside an Elliptical Inclusion

The plane problem of an elastic elliptic inclusion containing a crack is solved. Complex potentials presented by Qaissaunee (1992) for an edge dislocation inside an elastic elliptical inclusion are used to obtain the Green's function for this problem. The problem is formulated in terms of systems of singular integral equations which are solved numerically. Some detailed results are given for various crack inclusion geometries and material combinations.

1 Introduction

Crack fiber interactions in short fiber composites have been a topic of considerable research. Experimental work has shown that, in some cases, overall material fracture doesn't occur until after the individual fibers begin to fracture, as shown by Clegg et al. (1988). In other words, in these cases, cracks first appear in the fibers. To gain insight into this and related problems, the solution for an arbitrarily oriented crack inside an elliptic inclusion is solved. The crack in the inclusion is formulated in terms of a distribution of dislocations. Resulting integral equations are solved to find the stress intensity factors.

The problem of edge dislocation-circular inclusion interaction was first solved by Dundurs and Mura (1964). Dundurs and Sendeckyj (1965) solved the case where the edge dislocation was inside the circular inclusion. In both cases Airy's stress functions were used to formulate the problem. Atkinson (1972) used the results of Dundurs and Mura to analyze the interaction between a crack and a circular inclusion. He set up the problem in terms of a distribution of dislocations and solved the resulting integral equations. Erdogan, Gupta, and Ratwani (1974) studied the interaction between a circular inclusion and an arbitrarily oriented crack. They used a method similar to that of Atkinson's. Erdogan and Gupta (1975) later solved the case where the crack crosses the interface.

Elliptic inclusions were considered later than circular inclusions. Warren (1983) used an infinite series to formulate the case where the edge dislocation was inside the elliptic inclusion. He later used the solution to study the crack at the tip of a craze (1984). Stagni and Lizzio (1983) solved the case where the edge dislocation was located outside an elliptic inclusion. Santare and Keer (1986) presented the solution for the interaction of an edge dislocation outside a rigid elliptic inclusion. Using that solution to formulate the Green's functions, Patton and Santare (1990) studied the effect of a rigid elliptic inclusion on a straight crack. Wu and Chen (1990) solved the case where the crack is inside an ellipse, extending from one focus to the other of the ellipse. In a more extensive survey, Mura (1988) reviews the studies on crack inclusion interaction problems in his paper on inclusion problems.

2 The Stress Field for a Dislocation Inside the Elliptic Inclusion

Consider an elastic matrix, denoted as region 1, with elastic constants μ_1 and κ_1 containing a perfectly bonded elastic elliptic inclusion, denoted as region 2, with elastic constants κ_2 and μ_2 where μ_i is the shear modulus, and $\kappa_i = 3 - 4\nu_i$ for plane strain and $\kappa_i = (3 - \nu_i)/(1 + \nu_i)$ for plane stress, where ν_i is the Poisson's ratio. The elliptic elastic inclusion contains an edge dislocation at point z_0 (see Fig. 1). The stress field in the inclusion with the dislocation has been solved in terms of the complex potentials ϕ and ψ by Qaissaunee (1992).

Stresses and displacements can be written in terms of the complex potential as defined by Muskhelishvili (1954).

$$\sigma_{xx} = \sigma_{yy} = 2[\phi'(z) + \phi'(z)], \tag{1}$$

$$\sigma_{yy} - \sigma_{xx} + 2i\sigma_{xy} = 2[\bar{z}\phi''(z) + \psi'(z)], \tag{2}$$

$$2\mu(u + iv) = \kappa\phi(z) - z\phi'(z) - \psi'(z). \tag{3}$$

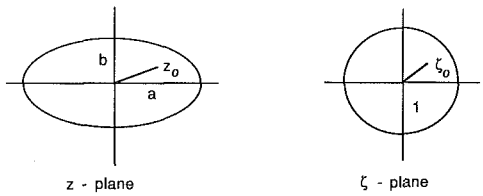

Fig. 1 Geometry of the problem; (*a*) physical; (*b*) mapped plane

Contributed by the Applied Mechanics Division of THE AMERICAN SOCIETY OF MECHANICAL ENGINEERS for publication in the ASME JOURNAL OF APPLIED MECHANICS.

Discussion on this paper should be addressed to the Technical Editor, Professor Lewis T. Wheeler, Department of Mechanical Engineering, University of Houston, Houston, TX 77204-4792, and will be accepted until four months after final publication of the paper itself in the ASME JOURNAL OF APPLIED MECHANICS.

Manuscript received by the ASME Applied Mechanics Division, Apr. 22, 1992; final revision, Apr. 23, 1992. Associate Technical Editor: C. F. Shih.

The primes denote the derivatives with respect to z where $z = x + iy$ and the overbar denotes the complex conjugate and i is the imaginary number.

The geometry of the problem is simplified by mapping the ellipse into the unit circle as shown on Fig. 1, the function used is $z = w(\zeta) = R(\zeta + m/\zeta)$, where $m = (a-b)/(a+b)$ and $R = (a+b)/2$. The complex potentials ϕ_2 and ψ_2 for region 2 are

$$\phi_2(\zeta) = \gamma_2 \ln\left[\frac{(\zeta-\zeta_0)\left(\zeta-\frac{m}{\zeta_0}\right)}{\zeta}\right] + \sum_{-\infty}^{\infty} c_k \zeta^k,$$

$$\psi_2(\zeta) = \overline{\gamma_2}\ln\left[\frac{(\zeta-\zeta_0)\left(\zeta-\frac{m}{\zeta_0}\right)}{\zeta}\right] + \gamma_2 \frac{\zeta\left(\frac{1}{\zeta}+m\zeta-\overline{\zeta_0}-m/\overline{\zeta_0}\right)}{(\zeta-\zeta_0)(\zeta-m/\zeta_0)} + \sum_{-\infty}^{\infty} d_k\zeta^k - \gamma_2 \frac{\zeta(1+m\zeta^2)}{\zeta^2-m}\,\zeta_0 \frac{\zeta^2-m\zeta_0}{\zeta_0\zeta^3-(m+\zeta_0^2)\zeta^2+\zeta_0 m\zeta} - \frac{\zeta(1+m\zeta^2)}{(\zeta^2-m)}\sum_{-\infty}^{\infty} c_k k\zeta^{k-1}. \quad (4)$$

In these expressions, $\gamma_2 = \mu_2 \mathbf{b}/i\pi(\kappa_2+1)$, where $\mathbf{b} = b_x + ib_y$, and b_x and b_y are the Cartesian components of the Burgers vector.

The constants are

$$c_k = (1-\beta)\frac{p_k r_k - (\beta-1)q_k\overline{r_k}}{p_k^2-(\beta-1)^2 q_k^2} \quad (5)$$

$$c_{-k} = m^k c_k \quad (6)$$

$$d_k = -\alpha(m^k\overline{c_k} + \overline{\gamma_2}\,\overline{A_k}) \quad (7)$$

$$d_{-k} = m^k d_k + q_k c_k \quad (8)$$

where

$$p_k = (\beta-\alpha) - (\beta-1)\alpha m^{2k},$$
$$q_k = (1-m^2)km^{(k-1)}$$
$$r_k = -\alpha m^k A_k + \overline{B_k}$$

and

$$A_k = \frac{1}{k}\left[\zeta_0^k + \left(\frac{m}{\zeta_0}\right)^k\right],$$
$$A_{-k} = \gamma_2 A_k,$$
$$B_k = \left[\frac{mq-m^3/\zeta_0-\zeta_0}{\zeta_0^2-m}\left(\frac{m}{\zeta_0}\right)^{k-1} + \frac{m\zeta_0^3-q\zeta_0^2+\zeta_0}{\zeta_0^2-m}\,\xi_0^{k-1}\right],$$
$$B_{-k} = \overline{\gamma_2}\,A_k + \gamma_2 B_k,$$
$$q = \overline{\zeta_0} + m/\overline{\zeta_0}$$
$$\alpha = \frac{\Gamma\kappa_1-\kappa_2}{\Gamma\kappa_1+1},$$
$$\beta = \frac{\Gamma(\kappa_1+1)}{\Gamma\kappa_1+1}.$$
$$\Gamma = \mu_2/\mu_1$$

Therefore, after some manipulations, one can write the stresses inside the inclusion

$$\sigma_{xx} = 2\mathrm{Re}\left[\gamma_2\frac{\zeta\zeta_0}{R(\zeta-\zeta_0)(\zeta\zeta_0-m)} + \frac{\zeta^2}{R(\zeta^2-m)}\sum_{-\infty}^{\infty} c_k k\zeta^{k-1}\right] + \mathrm{Re}\left[\gamma_2\frac{(m+\overline{\zeta}^2)\zeta_0^2\zeta^2}{\overline{\zeta}R(\zeta-\zeta_0)^2(\zeta_0\zeta-m)^2} + \frac{2m\zeta^3(\overline{\zeta}^2+m)}{R\overline{\zeta}(\zeta^2-m)^3}\sum_{-\infty}^{\infty} c_k k\zeta^{k-1} - \frac{(\overline{\zeta}^2+m)\zeta^4}{R(\zeta^2-m)^2\overline{\zeta}}\sum_{-\infty}^{\infty} c_k k(k-1)\zeta^{k-2} - \overline{\zeta}^2\frac{\zeta\zeta_0}{R(\zeta-\zeta_0)(\zeta\zeta_0-m)} - \gamma_2\frac{(m+\overline{\zeta_0}^2)\zeta_0^2\zeta^2}{\overline{\zeta_0}R(\zeta-\zeta_0)^2(\zeta_0\zeta-m)^2} - \frac{\zeta^2}{R(\zeta^2-m)}\sum_{-\infty}^{\infty} d_k k\zeta^{k-1} + \frac{\zeta^2(m\zeta^4-3m^2\zeta^2-\zeta^2-m)}{R(\zeta^2-m)^3}\sum_{-\infty}^{\infty} c_k k\zeta^{k-1} + \frac{\zeta^3(1+m\zeta^2)}{R(\zeta^2-m)^2}\sum_{-\infty}^{\infty} c_k k(k-1)\zeta^{k-2}\right], \quad (9)$$

$$\sigma_{yy} = 2\mathrm{Re}\left[\gamma_2\frac{\zeta\zeta_0}{R(\zeta-\zeta_0)(\zeta\zeta_0-m)} + \frac{\zeta^2}{R(\zeta^2-m)}\sum_{-\infty}^{\infty} c_k k\zeta^{k-1}\right] - \mathrm{Re}\left[\gamma_2\frac{(m+\overline{\zeta}^2)\zeta_0^2\zeta^2}{\overline{\zeta}R(\zeta-\zeta_0)^2(\zeta_0\zeta-m)^2} + \frac{2m\zeta^3(\overline{\zeta}^2+m)}{R\overline{\zeta}(\zeta^2-m)^2}\sum_{-\infty}^{\infty} c_k k\zeta^{k-1} - \frac{(\overline{\zeta}^2+m)\zeta^4}{R(\zeta^2-m)^2\overline{\zeta}}\sum_{-\infty}^{\infty} c_k k(k-1)\zeta^{k-2} - \overline{\gamma^2}\frac{\zeta\zeta_0}{R(\zeta-\zeta_0)(\zeta\zeta_0-m)} - \gamma_2\frac{(m+\overline{\zeta_0}^2\zeta_0^2\zeta^2}{\overline{\zeta_0}R(\zeta-\zeta_0)^2(\zeta_0\zeta-m)^2} - \frac{\zeta^2}{R(\zeta^2-m)}\sum_{-\infty}^{\infty} d_k k\zeta^{k-1} + \frac{\zeta^2(m\zeta^4-3m^2\zeta^2-\zeta^2-m)}{R(\zeta^2-m)^3}\sum_{-\infty}^{\infty} c_k k\zeta^{k-1} + \frac{\zeta^3(1+m\zeta^2)}{R(\zeta^2-m)^2}\sum_{-\infty}^{\infty} c_k k(k-1)\zeta^{k-2}\right], \quad (10)$$

$$\sigma_{xy} = \mathrm{Im}\left[-\gamma_2\frac{(m+\overline{\gamma}^2)\zeta_0^2\zeta^2}{\overline{\zeta}R(\zeta-\zeta_0)^2(\zeta_0-\zeta-m)^2} - \frac{2m\zeta^3(\overline{\zeta}^2+m)}{R\overline{\zeta}(\zeta^2-m)^3}\sum_{-\infty}^{\infty} c_k k\zeta^{k-1} + \frac{(\overline{\zeta}^2+m)\zeta^4}{R(\zeta^2-m)^2\overline{\zeta}}\sum_{-\infty}^{\infty} c_k k(k-1)\zeta^{k-2} + \overline{\gamma^2}\frac{\zeta\zeta_0}{R(\zeta-\zeta_0)(\zeta\zeta_0-m)} + \gamma_2\frac{(m+\overline{\zeta_0}^2)\zeta_0^2\zeta^2}{\overline{\zeta_0}R(\zeta-\zeta_0)^2(\zeta_0\zeta-m)^2} + \frac{\zeta^2}{R(\zeta^2-m)}\sum_{-\infty}^{\infty} d_k k\zeta^{k-1} - \frac{\zeta^2(m\zeta^4-3m^2\zeta^2-\zeta^2-m)}{R(\zeta^2-m)^3}\sum_{-\infty}^{\infty} c_k k\zeta^{k-1} - \frac{\zeta^3(1+m\zeta^2)}{R(\zeta^2-m)^2}\sum_{-\infty}^{\infty} c_k k(k-1)\zeta^{k-2}\right]. \quad (11)$$

These stresses can be separated into bounded and singular portions. The singular portion represents the dislocation and its image points and the bounded portion represent the interaction for the case where the crack is fully imbedded in the inclusion without touching the interface. The bounded parts of the stresses are calculated matching the tractions and displacements along the elliptical contour which is mapped to the unit circle. The resulting terms are the series terms of the expressions above:

$$\sigma_{xxb} = \frac{\zeta^2}{R(\zeta^2-m)}\sum_{-\infty}^{\infty} c_k k\zeta^{k-1} + \mathrm{Re}\left[\frac{2m\zeta^3(\overline{\zeta}^2+m)}{R\overline{\zeta}(\zeta^2-m)^3}\sum_{-\infty}^{\infty} c_k k\zeta^{k-1}\right.$$

$$-\frac{(\bar{\zeta}^2+m)\zeta^4}{R(\zeta^2-m)^2\bar{\zeta}}\sum_{-\infty}^{\infty}c_k k(k-1)\zeta^{k-2}-\frac{\zeta^2}{R(\zeta^2-m)}\sum_{-\infty}^{\infty}d_k k\zeta^{k-1}$$
$$+\frac{\zeta^2(m\zeta^4-3m^2\zeta^2-\zeta^2-m)}{R(\zeta^2-m)^3}\sum_{-\infty}^{\infty}c_k k\zeta^{k-1}$$
$$+\frac{\zeta^3(1+m\zeta^2)}{R(\zeta^2-m)^2}\sum_{-\infty}^{\infty}c_k k(k-1)\zeta^{k-2}\Bigg], \quad (12)$$

$$\sigma_{yyb}=2\frac{\zeta^2}{R(\zeta^2-m)}\sum_{-\infty}^{\infty}c_k k\zeta^{k-1}-\mathrm{Re}\Bigg[\frac{2m\zeta^3(\bar{\zeta}^2+m)}{R\bar{\zeta}(\zeta^2-m)^3}\sum_{-\infty}^{\infty}c_k k\zeta^{k-1}$$
$$-\frac{(\bar{\zeta}^2+m)\zeta^4}{R(\zeta^2-m)^2\bar{\zeta}}\sum_{-\infty}^{\infty}c_k k(k-1)\zeta^{k-2}-\frac{\zeta^2}{R(\zeta^2-m)}\sum_{-\infty}^{\infty}d_k k\zeta^{k-1}$$
$$+\frac{\zeta^2(m\zeta^4-3m^2\zeta^2-\zeta^2-m)}{R(\zeta^2-m)^3}\sum_{-\infty}^{\infty}c_k k\zeta^{k-1}$$
$$+\frac{\zeta^3(1+m\zeta^2)}{R(\zeta^2-m)^2}\sum_{-\infty}^{\infty}c_k k(k-1)\zeta^{k-2}\Bigg], \quad (13)$$

$$\sigma_{xyb}=\mathrm{Im}\Bigg[\frac{2m\zeta^3(\bar{\zeta}^2+m)}{R\bar{\zeta}(\zeta^2-m)^3}\sum_{-\infty}^{\infty}c_k k\zeta^{k-1}$$
$$-\frac{(\bar{\zeta}^2+m)\zeta^4}{R(\zeta^2-m)^2\bar{\zeta}}\sum_{-\infty}^{\infty}c_k k(k-1)\zeta^{k-2}$$
$$-\frac{\zeta^2}{R(\zeta^2-m)}\sum_{-\infty}^{\infty}d_k k\zeta^{k-1}$$
$$+\frac{\zeta^2(m\zeta^4-3m^2\zeta^2-\zeta^2-m)}{R(\zeta^2-m)^2}\sum_{-\infty}^{\infty}c_k k\zeta^{k-1}$$
$$+\frac{\zeta^3(1+m\zeta^2)}{R(\zeta^2-m)^2}\sum_{-\infty}^{\infty}c_k k(k-1)\zeta^{k-2}\Bigg]. \quad (14)$$

The singular portions of the stresses are the remaining terms which are not represented in infinite series.

3 Integral Equations

A crack can be represented by a distribution of dislocations. In this case the distribution is unknown, but the resulting crack faces are assumed to be traction-free. This condition can be expressed by the following integral equations:

$$\int_{z_1}^{z_2}\frac{b_n(z_0)}{z-z_0}dz_0+\int_{z_1}^{z_2}K_n(z,z_0)b_n(z_0)dz_0=\frac{\pi(\kappa_2+1)}{\mu_2}F_n, \quad (15)$$

$$\int_{z_1}^{z_2}\frac{b_t(z_0)}{z-z_0}dz_0+\int_{z_1}^{z_2}K_t(z,z_0)b_t(z_0)dz_0=\frac{\pi(\kappa_2+1)}{\mu_2}F_t. \quad (16)$$

n and t refer to the positive normal and tangential directions to the crack. b_n and b_t are

$$b_n=b_y\cos\theta-b_x\sin\theta \quad (17)$$

$$b_t=b_n\sin\theta+b_x\cos\theta \quad (18)$$

where θ is the angle of crack as shown in Fig. 2.

The first integrals contain the Cauchy singular portion of the stresses due to distribution of dislocations. In the second integrals, K_n and K_t are the bounded kernels which represent the interaction between the crack and elliptical inclusion. They are in the n and t directions, respectively. Some portions of K_n and K_t become unbounded when the crack touches the interface between the inclusion and the matrix. This situation requires a separate analysis as discussed in Erdogan and Gupta (1975) and is not treated here. K_n and K_t can be obtained from Eqs. (12)–(14) by calculating the normal and the tangential components.

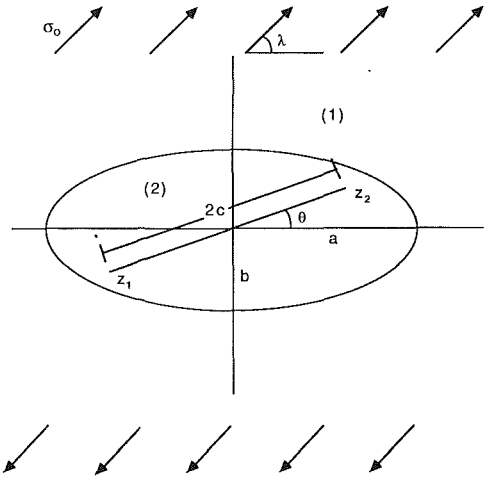

Fig. 2 Problem geometry

The right-hand side of the equations are the constant stresses in the elliptic inclusion, in the absence of the crack, induced by the loading σ_0 at infinity. They are derived by using the solution given by Hardimann (1954).

$$F_n=F_{yy}\cos^2\theta+F_{xx}\sin^2\theta-2F_{xy}\sin\theta\cos\theta \quad (19)$$

$$F_t=(F_{xx}-F_{yy})\sin\theta\cos\theta+F_{xy}(\sin^2\theta-\cos^2\theta) \quad (20)$$

where

$$F_{xx}=(A_1-B_1)/2$$
$$F_{yy}=(A_1+B_1)/2$$
$$F_{xy}=-B_2/2$$
$$A_1=\frac{r\sigma_0[r(a+b)^2-2p(a^2+b^2)]-2p(a^2-b^2)G_1 r}{r(a+b)^2-4abp(1+2p-2r)}$$
$$B_1=\frac{r\sigma_0(a^2-b^2)(1+2p-r)+rG_1(a+b)^2(1+2p)}{r(a+b)^2-4abp(1+2p-2r)}$$
$$B_2=\frac{rG_2(a+b)^2}{r(a+b)^2-4abp}$$

and

$$a=R(1+m)$$
$$b=R(1-m)$$
$$G_1=-\sigma_0\cos2\lambda$$
$$G_2=\sigma_0\sin2\lambda$$
$$r=E_1/E_2$$
$$p=E-1/8(1/\mu_1-1/\mu_2).$$

4 Solution

The integration equations can be reduced to a standard form by the substitutions

$$z_0=\frac{z_2-z_1}{2}\xi_0+\frac{z_2+z_1}{2} \quad (21)$$

Table 1 Stress intensity factors for a crack located in a circular inclusion, $m = 0.0$, $\theta = 30.0$ deg, $\kappa_1 = \kappa_2 = 1.8$, λ; = 90.0 deg

	$\mu_2/\mu_1 = 3.0$		$\mu_2/\mu_1 = 1/3$	
a/d	$K_I/\sigma_0 c^{1/2}$	$K_{II}/\sigma_0 c^{1/2}$	$K_I/\sigma_0 c^{1/2}$	$K_{II}/\sigma_0 c^{1/2}$
$\rightarrow \infty$	0.9458	0.5683	0.4640	0.2526
40	0.9462	0.5685	0.4638	0.2525
20	0.9475	0.5690	0.4630	0.2523
10	0.9528	0.5709	0.4600	0.2515
5	0.9735	0.5784	0.4488	0.2485
2	1.1067	0.6273	0.3914	0.2316
1.25	1.3585	0.7337	0.3526	0.2046
1.11	1.5312	0.8195	0.2963	0.1888
1.05	1.7132	0.9140	0.2768	0.1742

Table 2 Stress intensity factors for a crack located in an elliptic inclusion, $m = 0.5$, $\theta = 0.0$ deg, $\kappa_1 = \kappa_2 = 1.8$, $\lambda = 90.0$ deg

	$\mu_2/\mu_1 = 3.0$	$\mu_2/\mu_1 = 1/3$
a/c	$K_I/\sigma_0 c^{1/2}$	$K_I/\sigma_0 c^{1/2}$
$\rightarrow \infty$	1.0794	0.8057
30	1.0856	0.8005
15	1.1037	0.7861
10	1.1317	0.7649
5	1.2507	0.6907
2	1.5812	0.5640
1.50	1.7046	0.5246
1.25	1.8023	0.4905
1.154	1.8678	0.4669
1.070	1.9846	0.4294
1.034	2.1172	0.3982
1.017	2.2315	0.3771

$$z = \frac{z_2 - z_1}{2}\,\xi + \frac{z_2 + z_1}{2}. \tag{22}$$

Equations (15) and (16) can now be written in the form

$$\int_{-1}^{1} \frac{b_n(\xi_0)}{\xi - \xi_0}\,d\xi_0 + \int_{-1}^{1} K_n(\xi, \xi_0) b_n(\xi_0)\,d\xi_0 = \frac{\pi(\kappa_2 + 1)}{\mu_2} F_n, \tag{23}$$

$$\int_{-1}^{1} \frac{b_t(\xi_0)}{\xi - \xi_0}\,d\xi_0 + \int_{-1}^{1} K_t(\xi, \xi_0) b_t(\xi_0)\,d\xi_0 = \frac{\pi(\kappa_2 + 1)}{\mu_2} F_t. \tag{24}$$

To find a unique solution to the integral equations, it is necessary to impose additional conditions such as the crack closure conditions

$$\int_{-1}^{1} b_n(\xi_0)\,d\xi_0 = 0 \tag{25}$$

$$\int_{-1}^{1} b_t(\xi_0)\,d\xi_0 = 0. \tag{26}$$

The unknown functions can be defined as follows:

$$b_n(\xi_0) = \frac{g_n(\xi_0)}{\sqrt{1 - \xi_0^2}} \tag{27}$$

Table 3 Stress intensity factors for a crack located in an elliptic inclusion, $m = -0.2$, $\theta = 0.0$ deg, $\kappa_1 = \kappa_2 = 1.8$, $\lambda = 90.0$ deg

	$\mu_2/\mu_1 = 3.0$	$\mu_2/\mu_1 = 1/3$
a/c	$K_I/\sigma_0 c^{1/2}$	$K_I/\sigma_0 c^{1/2}$
$\rightarrow \infty$	1.4000	0.5380
30	1.4000	0.5380
20	1.4015	0.5378
10	1.4062	0.5357
5	1.4249	0.5278
2	1.5624	0.4798
1.60	1.6654	0.4525
1.33	1.8151	0.4210
1.14	2.0734	0.3801
1.067	2.3414	0.3478
1.01	2.9259	0.2986

$$b_t(\xi_0) = \frac{g_t(\xi_0)}{\sqrt{1 - \xi_0^2}}, \tag{28}$$

which gives the square root singularity for a crack tip surrounding by a homogeneous medium. The system of singular integral equations can be solved by the method described by Gerasoulis (1982). The interval $[-1, 1]$ is divided into $2n$ equal parts with $2n$ collocation points and $2n + 1$ integration points. Piecewise quadratic polynomial representation of the singular and nonsingular parts of the integral equation is used to discretize the integral equations into a set of algebraic equations. The strength of the stress singularity at the crack tips are characterized by the stress intensity factors. They are related to the dislocations density functions as follows:

$$K_I(z_1) = \frac{2\mu_2}{1 + \kappa_2} \lim_{z \to z_1} [2(z_1 - z)]^{1/2} b_n(z) \tag{29}$$

$$K_I(z_2) = \frac{2\mu_2}{1 + \kappa_2} \lim_{z \to z_2} [2(z - z_2)]^{1/2} b_n(z) \tag{30}$$

$$K_{II}(z_1) = \frac{2\mu_2}{1 + \kappa_2} \lim_{z \to z_1} [2(z_1 - z)]^{1/2} b_t(z) \tag{31}$$

$$K_{II}(z_2) = \frac{2\mu_2}{1 + \kappa_2} \lim_{z \to z_2} [2(z - z_2)]^{1/2} b_t(z). \tag{32}$$

K_I and K_{II} are mode I and mode II stress intensity factors, respectively.

5 Results

Numerical results are given for the stress intensity factor defined by (29)–(32). Stress intensity factors for cracks inside elliptical inclusions, at different inclinations with different aspect ratios m, can be solved by changing the required parameters in the solution outlined above. The problem can also be solved for stress applied at different angles at infinity. In the following results cracks inside elliptical inclusions are studied extensively for various crack angles and for various values of m. The results for $m = 0$, crack inside a circular inclusion with uniaxial stresses applied at infinity, are shown in Table 6. To make a check the results for the circular inclusion are compared to the results presented by Erdogan and Gupta (1975) and they are shown in Table 7. The stress intensity factors are

Table 4 Stress intensity factors for a crack located in an elliptic inclusion, $m = 0.5$, $\theta = 30.0$ deg, $\kappa_1 = \kappa_2 = 1.8$, $\lambda = 90.0$ deg

	$\mu_2/\mu_1 = 3.0$		$\mu_2/\mu_1 = 1/3$	
a/d	$K_I/\sigma_0 c^{1/2}$	$K_{II}/\sigma_0 c^{1/2}$	$K_I/\sigma_0 c^{1/2}$	$K_{II}/\sigma_0 c^{1/2}$
$\rightarrow \infty$	0.7523	0.5666	0.6381	0.2903
8.660	0.7690	0.5735	0.6238	0.2856
4.330	0.8158	0.5909	0.5885	0.2750
2.887	0.8846	0.6118	0.5467	0.2642
2.165	0.9670	0.6308	0.5078	0.2563
1.732	1.0575	0.6467	0.4747	0.2514
1.443	1.1546	0.6611	0.4459	0.2483
1.237	1.2655	0.6802	0.4169	0.2451
1.083	1.4274	0.7617	0.3767	0.2306

Table 5 Stress intensity factors for a crack located in an elliptic inclusion, $m = 0.5$, $\theta = 0.0$ deg, $\kappa_1 = \kappa_2 = 1.8$, 15.0 deg $< \lambda <$ 150.0 deg

	$\mu_2/\mu_1 = 3.0$		$\mu_2/\mu_1 = 1/3$	
λ	$K_I/\sigma_0 c^{1/2}$	$K_{II}/\sigma_0 c^{1/2}$	$K_I/\sigma_0 c^{1/2}$	$K_{II}/\sigma_0 c^{1/2}$
15	0.1745	0.4162	0.0214	0.1195
30	0.4997	0.7209	0.1113	0.2070
45	0.9438	0.8324	0.2341	0.2390
60	1.3880	0.7209	0.3569	0.2070
90	1.8321	0.0000	0.4797	0.0000
120	1.3880	0.7209	0.3569	0.2070
150	0.4997	0.7209	0.1113	0.2070

Table 6 Stress intensity factors for crack located in a circular inclusion, $m = -0.0$, $\theta = 0.0$ deg, $\kappa_1 = \kappa_2 = 1.8$, $\lambda = 90.0$ deg

	$\mu_2/\mu_1 = 3.0$	$\mu_2/\mu_1 = 1/3$
a/c	$K_I/\sigma_0 c^{1/2}$	$K_I/\sigma_0 c^{1/2}$
$\rightarrow \infty$	1.2739	0.6098
20	1.2763	0.6085
10	1.2834	0.6046
5	1.3112	0.5898
4	1.3317	0.5796
2	1.4910	0.5144
1.25	1.8297	0.4279
1.11	2.0621	0.3894
1.05	2.3074	0.3140

Table 7 Stress intensity factors for a crack located in a circular inclusion, $m = 0.0$, $\theta = 0.0$ deg, $\kappa_1 = \kappa_2 = 1.8$, $\lambda = 90.0$ deg, comparison of results of Erdogan and Gupta (E&G) and Anlas and Santare (A&S)

	$\mu_2 = 3.0$		$\mu_2/\mu_1 = 1/3$	
a/c	*E.&G.*	*A.&S.*	*E.&G.*	*A.&S.*
10	1.283	1.283	0.6046	0.6046
4	1.332	1.332	0.5796	0.5796
2	1.491	1.491	0.5144	0.5144
1.33	1.752	1.753	0.4437	0.4435
1.11	2.062	2.062	0.3900	0.3894

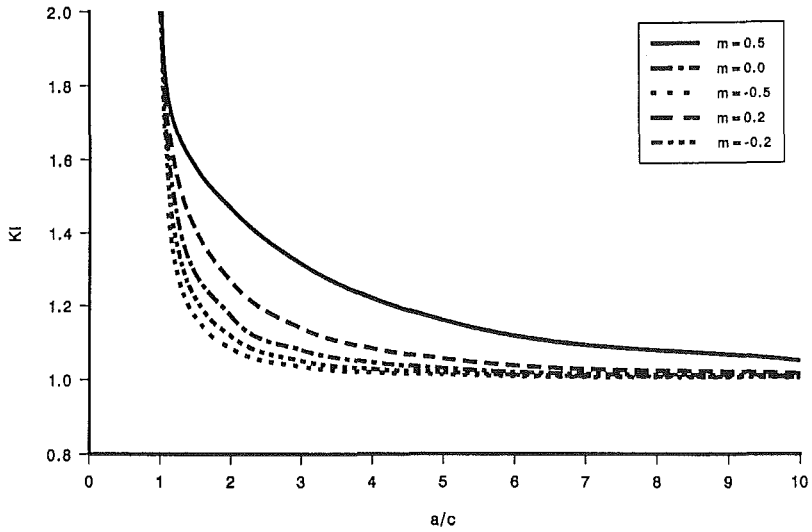

Fig. 3 Normalized stress intensity factor versus distance from interface, for different values of m, $\mu_2/\mu_1 = 3.0$, $\kappa_1 = \kappa_2 = 1.8$, $\lambda = 90.0$ deg

normalized with respect to $\sigma_0\sqrt{c}$, which is the stress intensity factor in a uniaxially stressed infinite plane containing a crack of length $2c$ perpendicular to the direction of loading.

In Table 1, mode I and mode II stress intensity factors are given for a crack oriented at 30 deg inside a circular inclusion, $m = 0.0$. Results for different crack lengths are tabulated for $\mu_2/\mu_1 = 3.0$, stiff inclusion and softer matrix, and $\mu_2/\mu_1 = 1/3$, soft inclusion and stiffer matrix. d is the distance from the origin to the elliptical boundary, when the crack angle, θ, $= 0$, $a = d$. In Table 2, a straight crack in a horizontal elliptic inclusion $m = 0.5$ is analyzed. The crack is perpendicular to external loading σ_0. Stress intensity factors for different crack lengths are given. The results show that, as the crack approaches the interface, for soft matrix, the stress intensity factor increases rapidly. For a soft inclusion they decrease as the crack approaches the interface.

Similar values are given for a vertical elliptical inclusion, $m = -0.2$, in Table 3. The crack is again perpendicular to the external loading. Stress intensity factors increase and decrease faster as the crack approaches the interface, compared to $m = 0.5$ case.

In Table 4, the results for a 30 deg inclined crack are given.

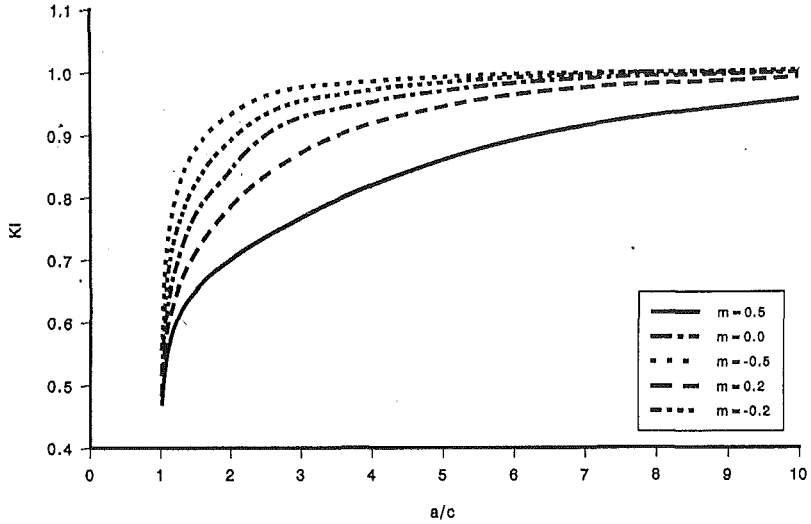

Fig. 4 Normalized stress intensity factor versus distance from interface, for different values of m, $\mu_2/\mu_1 = 1/3$, $\kappa_1 = \kappa_2 = 1.8$, $\lambda = 90.0$ deg

In this case, m is 0.5 and stress intensity factors for different crack lengths are tabulated.

The solution used in this problem allows the usage of different angles for loading. In Table 5, the results for an elliptic inclusion, $m = 0.5$, embedded in an infinite region loaded by a σ_0 at an angle λ, are given. Mode II stress intensity factor is symmetric w.r.t 45 deg as expected. The crack is straight and a/c ratio is 1.25.

In Figs. 3 and 4, the stress intensity factors are normalized with respect to the constant stress value inside the elliptical inclusion. The results are plotted for different crack lengths and different ellipses. Since the normalization has been done using the stresses inside the inclusion, when the crack is small, values of the stress intensity factors go to 1 as expected. These plots agree with those of Atkinson (1972), for the case of a circular inclusion.

Acknowledgments

The authors would like to gratefully acknowledge the support of the University of Delaware Center for Composite Materials University Industry Consortium.

References

Atkinson, C., 1972, "The Interaction Between a Crack and an Inclusion," *International Journal of Engineering Science*, Vol. 10, pp. 127–136.

Clegg, W. J., Horsfall, I., Mason, J. F., and Edwards, L., 1988, "The Tensile Deformation and Fracture of Al- "Saffil" Metal Matrix Composites," *Acta Metallurgica*, Vol. 36, No. 8, pp. 2151–2159.

Dundurs, J., and Mura, T., 1964, "Interaction Between an Edge Dislocation and a Circular Inclusion," *Journal of the Mechanics and Physics of Solids*, Vol. 12, pp. 177–189.

Dundurs, J., and Sendeckyj, G. P., 1965, "Edge Dislocation Inside a Circular Inclusion," *Journal of the Mechanics and Physics of Solids*, Vol. 13, pp. 141–147.

Erdogan, F., and Gupta, G. D., 1975, "The Inclusion Problem With a Crack Crossing the Boundary," *Int. Journal of Fracture*, Vol. 11, No. 1, pp. 13–27.

Erdogan, F., Gupta, G. D., and Ratwani, M., 1974, "Interaction Between a Circular Inclusion and an Arbitrarily Oriented Crack," ASME JOURNAL OF APPLIED MECHANICS, Vol. 41, pp. 1007–1013.

Gerasoulis, A., 1982, "The Use of Piecewise Quadratic Polynomials for the Solution of Singular Integral Equations of Cauchy Type," *Comp. and Maths. with Appls.*, Vol. 8, No. 1, pp. 15–22.

Hardiman, N. J., 1954, "Elliptic Elastic Inclusion in an Infinite Plate," *Quart. Journ. Mech. and Applied Math.*, Vol. VII, Pt. 2, pp. 226–230.

Mura, T., 1988, "Inclusion Problems," ASME *Applied Mechanics Reviews*, Vol. 41, No. 1, pp. 15–20.

Patton, E. M., and Santare, M. H., 1990, "The Effect of Rigid Elliptical Inclusion on a Straight Crack," *Int. Journal of Fracture*, Vol. 46, pp. 71–79.

Qaissaunee, M., 1992, "Elastic Elliptical Inclusion and Dislocation Interaction Problems," M.S. Thesis, University of Delaware, Newark, DE.

Stagni, L., and Lizzio, R., 1983, "Shape Effects in the Interaction Between an Edge Dislocation and an Elliptic Inclusion," *Journal of Applied Physics*, Vol. A30, pp. 217–221.

Santare, M. H., and Keer, L. M., 1986, "Interaction Between an Edge Dislocation and a Rigid Elliptical Inclusion," ASME JOURNAL OF APPLIED MECHANICS, Vol. 53, pp. 382–385.

Warren, W. E., 1983, "The Edge Dislocation Inside an Elliptical Inclusion," *Mechanics of Materials*, Vol. 2, pp. 319–330.

Warren, W. E., 1984, "Stress and Displacement Fields at the Tip of Craze Containing a Crack," *Polymer Engineering and Science*, Vol. 24, No. 10, pp. 814–819.

Wu, C. H., and Chen, Chao-Hsun, 1990, "A Crack in a Confocal Elliptical Inhomogeneity Embedded in an Infinite Medium," ASME JOURNAL OF APPLIED MECHANICS, Vol. 57, pp. 91–96.

Weichung Yeih
Associate Professor,
Department of River and
Harbor Engineering,
National Taiwan Ocean University,
Kee-Lung, Taiwan, R.O.C.

Tatsuhito Koya

Toshio Mura
Fellow ASME.

Department of Civil Engineering,
Northwestern University,
Evanston, IL 60208

An Inverse Problem in Elasticity With Partially Overprescribed Boundary Conditions, Part I: Theoretical Approach

A Cauchy problem in linear elasticity is considered. This problem is governed by a Fredholm integral equation of the first kind and cannot be solved directly. The regularization method, which has been originally employed by Gao and Mura (1989), is formulated from a different perspective in order to address some of the difficulties experienced in their formulation. The theoretical details are discussed in this paper. Numerical examples are treated to Part II.

Introduction

Inverse problems in science and engineering have been attracting more attention recently. Stanitz (1988) has studied the problem of designing a channel for arbitrarily prescribed velocity distribution. Sobieczky (1988) has investigated the problem of determining the profile of an airfoil from the given surface pressure distribution. Gao and Mura (1989) have used the residual surface displacements to determine the residual stress field around the damaged area. The latest developments in inverse problems in structural mechanics have been summarized by Kubo (1988).

In this paper, we investigate a linear elasticity inverse problem which is in the form of the Cauchy (initial value) problem. The problem is ill-posed since the solution's existence, uniqueness, and continuous dependence on the data are not necessarily guaranteed. Therefore, such problems must be solved indirectly by means of transformation like the regularization method.

First, we describe the type of problem in question along with the particular problem in which we are interested. Second, we examine the existence, uniqueness, and stability of solutions of such problems. Third, we briefly introduce the original formulation of the regularization method by Gao and Mura (1989). Fourth, we introduce our new one. Fifth, we give a simple demonstration of it. Finally, we conclude with remarks and discussions.

1 Problems

1.1 Forward (Well-Posed) Problem. Let us consider a well-posed boundary value problem first. For example, suppose as shown in Fig. 1, that the four edges of a thin rectangular plate are maintained at the following temperatures:

$$\begin{cases} \varphi(0, y) = 0, \\ \varphi(a, y) = 0 \\ \varphi(x, 0) = 0, \\ \varphi(x, b) = f(x). \end{cases} \tag{1}$$

The temperature is governed by the Laplace equation,

$$\nabla^2\varphi = \frac{\partial^2\varphi}{\partial x^2} + \frac{\partial^2\varphi}{\partial y^2} = 0, \tag{2}$$

for the steady-state problem.

The solution of this problem can be readily obtained as

$$\varphi(x, y) = \sum_{n=1}^{\infty} c_n \sin\frac{n\pi x}{a}\,\frac{\sinh(n\pi y/a)}{\sinh(n\pi b/a)}, \tag{3}$$

where

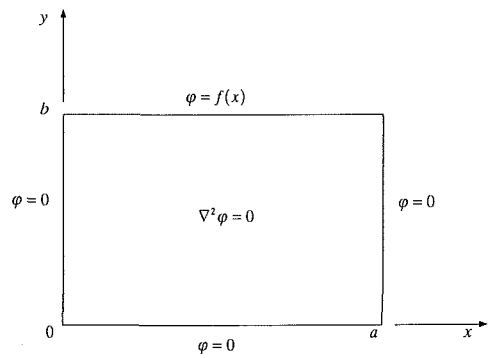

Fig. 1 Steady-state temperature distribution in a rectangular plate

Contributed by the Applied Mechanics Division of THE AMERICAN SOCIETY OF MECHANICAL ENGINEERS for publication in the JOURNAL OF APPLIED MECHANICS.

Discussion on this paper should be addressed to the Technical Editor, Professor Lewis T. Wheeler, Department of Mechanical Engineering, University of Houston, Houston, TX 77204-4792, and will be accepted until four months after final publication of the paper itself in the ASME JOURNAL OF APPLIED MECHANICS.

Manuscript received by the ASME Applied Mechanics Division, Mar. 22, 1991; final revision, Aug. 13, 1992. Associate Technical Editor: C. O. Horgan.

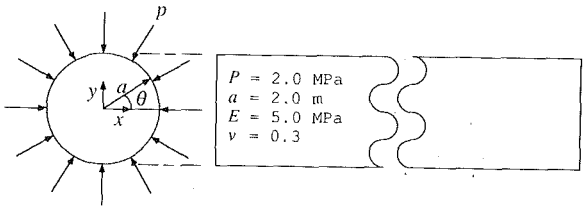

Fig. 2 A long cylinder under lateral compression

$$c_n = \frac{2}{a}\int_0^a f(x)\sin\frac{n\pi x}{a}dx, \tag{4}$$

assuming that the series is convergent.

1.2 Inverse (Ill-Posed) Problem. Now, instead of (1), suppose the following boundary conditions are prescribed:

$$\begin{cases} \varphi(x, b) = f(x) \\ \left.\dfrac{\partial\varphi(x, y)}{\partial y}\right|_{y=b} = g(x), \end{cases} \tag{5}$$

where

$$g(x) = \frac{\partial}{\partial y}\left[\sum_{n=1}^{\infty} c_n \sin\frac{n\pi x}{a}\frac{\sinh(n\pi y/a)}{\sinh(n\pi b/a)}\right]_{y=b}, \tag{6}$$

and the remaining boundaries are considered free (see Courant and Hilbert (1953)). We wish to know whether this problem is solvable, and if it is, whether the solution is unique and stable. If the solution indeed exists and is unique, (3) must be the solution and the boundary values along the free boundaries must be (1). A problem like (2) with (5) in which the boundary values are prescribed in the initial value problem manner is called a Cauchy problem (see Knops and Payne (1971)) which may be categorized as a type of inverse problem.

1.3 Forward (Well-Posed) Problems. Consider the problem of a long circular cylinder under lateral loading as shown in Fig. 2. Suppose that the lateral loads are given by

$$\begin{cases} p_x = p\cos(\theta) \\ p_y = p\sin(\theta) \end{cases} \tag{7}$$

for $0 \le \theta \le 2\pi$. The corresponding lateral displacements from the linear theory of isotropic elasticity are

$$\begin{cases} u_x = -\dfrac{1-\nu}{E} p\, a\cos(\theta) \\ u_y = -\dfrac{1-\nu}{E} p\, a\sin(\theta) \end{cases} \tag{8}$$

where E is Young's modulus and ν is Poisson's ratio.

1.4 Inverse Problem. Now, suppose that instead of (7), both the partial lateral displacements and loads are prescribed as

$$\begin{cases} p_x = p\cos(\theta) \\ p_y = p\sin(\theta) \\ u_x = -\dfrac{1-\nu}{E} p\, a\cos(\theta) \\ u_y = -\dfrac{1-\nu}{E} p\, a\sin(\theta) \end{cases} \tag{9}$$

along $0 \le \theta \le \pi$. We wish to know whether the displacements and the loads along $\pi \le \theta \le 2\pi$ can be uniquely characterized by assuming static equilibrium. If the characterization is possible, the solutions must be (7) and (8).

Inverse problems in elasticity date back as far as 1907 to Almansi (1907) (and a more recent study to Gao and Mura (1989)). They are not restricted to the above problems. For instance, Dulikravich has employed it in the so-called inverse design to design the optimum turbine blade from the given temperature and heat flux on the surface (Dulikravich (1988)). More rigorous mathematical treatment of the inverse problem has been done by many mathematicians (Tikhonov (1963), etc.).

2 Existence and Uniqueness of the Solution of the Inverse Problem

The fundamental requirements of the so-called well-posed problem have been established by Hadamard (1902), namely, existence, uniqueness, and continuous dependence on the given data. Therefore, any problem that violates even one of these conditions is called an ill-posed problem. Let us see how these conditions apply to the inverse problem.

2.1 Uniqueness. Before the theorem of existence, let us look first at the theorem of uniqueness. The uniqueness theorem for two-dimensional elasticity can be found in the book by Muskehelishvili (1963); a more general one, in Knops and Payne (1971). However, here we take a look at a simpler version by Gao and Mura (1989) instead. The assumption is that the system is in static equilibrium.

Lemma: Let Γ_1 and Γ_2 compose the entire boundary of an elastic body D. *If the boundary values along Γ_1 vanish identically, i.e., if the displacements and the tractions are identically equal to zero on Γ_1, then the displacements and stresses over the entire domain* D *are zero.*

Proof: Let u_i and σ_{ij} be the displacement and stress fields that give rise to the vanishing of the displacements and tractions along Γ_1. Similarly, let u_i^* and σ_{ij}^* be the displacements and stresses that cause the displacements along Γ_2 to vanish but not the tractions. The Betti-Maxwell reciprocal relation (see Jaswon and Symm (1977)) yields

$$\int_{\Gamma_1+\Gamma_2} \sigma_{ij}^* u_i n_j d\Gamma = \int_{\Gamma_1+\Gamma_2} \sigma_{ij} u_i^* n_j d\Gamma, \tag{10}$$

where n_j are the components of the normal vector along Γ_1 and Γ_2. According to the definitions of σ_{ij} and u_i^*, the right-hand side of (10) and the Γ_1 integration on the right-hand side vanish, so that (10) is reduced to

$$\int_{\Gamma_2} \sigma_{ij}^* u_i n_j d\Gamma = 0. \tag{11}$$

Equation (11) is valid for any arbitrary σ_{ij}^*, and so the displacements u_i must be identically zero along Γ_2. From this result, the divergence theorem implies that the displacement field vanishes identically over the entire domain which in turn means the stress field is identically zero.

The Fredholm alternative theorems (see Stakgold (1967)) states that the solution $\mathbf{x}$ of $\mathbf{Ax} = \mathbf{b}$ is unique if the homogeneous solution $\mathbf{x}_H$ of $\mathbf{Ax}_H = \mathbf{0}$ is nontrivial. By virtue of this theorem, the uniqueness theorem for two-dimensional elasticity is established.

2.2 Existence. According to Hadamard's definitions of the well-posedness, there is a class of inverse problem that does not have a solution at all. Here is an extreme case in linear elasticity. Suppose a set of displacements and tractions has been prescribed to Γ_1 and Γ_2 independently,

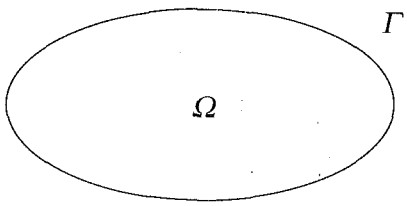

Fig. 3 A linear elastic body

$$\begin{cases} u_i = 0 \\ t_i = 0 \end{cases} \quad \text{on } \Gamma_1$$
$$\begin{cases} u_i = \bar{u}_i \neq 0 \\ t_i = \bar{t}_i \neq 0 \end{cases} \quad \text{on } \Gamma_2. \tag{12}$$

Clearly no linear elasticity solution exists satisfying (12) because of the lemma given in Section 2.1. Even though it is obvious at a glance that such a prescription is impossible, often the inverse solution has to rely on the values usually obtained from experimental measurements. Ideally, because the tractions are proportional to the normal derivatives of the displacements, we may be able to estimate roughly the compatibility of the data by

$$\begin{cases} t_i \propto \dfrac{-u_{i,x}\dot{y}(s) + u_{i,y}\dot{x}(s)}{\sqrt{\dot{x}^2(s) + \dot{y}^2(s)}} \\ \dfrac{du_i}{ds} = u_{i,x}\dot{x}(s) + u_{i,y}\dot{y}(s) \end{cases},$$

assuming the rectangular coordinates x and y are functions of the boundary parameter s.

2.3 Continuous Dependence on the Given Data (Stability). Consider the equation

$$\mathbf{Ax} = \mathbf{b}, \tag{13}$$

where $\mathbf{x}$ is the solution; $\mathbf{b}$, the given data; and $\mathbf{A}$ is a linear operator that may be a matrix, a differential operator, or integral operator. We introduce errors in the operator and the given data to observe the behavior of the solution

$$(\mathbf{A} + \delta\mathbf{A})\mathbf{x} = (\mathbf{b} + \delta\mathbf{b}). \tag{14}$$

These errors may have resulted from the experimental measurements. Bearing (13) in mind, (14) can be reduced to

$$\delta\mathbf{A}\mathbf{x} = \delta\mathbf{b}. \tag{15}$$

Then the solution becomes

$$\mathbf{x} = (\delta\mathbf{A})^{-1}\delta\mathbf{b}. \tag{16}$$

Equation (16) means that the inverse solution is extremely sensitive to the arbitrary errors introduced in the operator and the given data. For this reason, the inverse solution cannot be approached directly.

3 The Original Formulation of the Regularization Method

A brief summary of the original formulation of the regularization method employed by Gao and Mura is given. We leave the details to their paper (Gao and Mura (1989)). Our derivation is for a static two-dimensional linearly elastic homogeneous material Ω, bounded by the smooth boundary Γ, as shown in Fig. 3; therefore, some details may differ from those in their paper.

We start from Somigliana's integral equation (see Brebbia et al. (1984)) derived from the Betti-Maxwell reciprocal theorem,

$$\int_\Gamma T_{ij}(x, x')u_j(x)d\Gamma(x) + \frac{1}{2}u_i(x') = \int_\Gamma U_{ij}(x, x')t_j(x)d\Gamma(x), \tag{17}$$

where

$$U_{ij}(x, x') = \frac{-1}{4\pi(1-\nu)r}\left\{[(1-2\nu)\delta_{ij} + r_{,i}r_{,j}]\frac{\partial r}{\partial n} - (1-2\nu)(r_{,i}n_j - r_{,j}n_i)\right\}_{x_i - x_i'}$$

$$T_{ij}(x, x') = \frac{1}{8\pi(1-\nu)\mu}\{(3-4\nu)\ln(r)\delta_{ij} - r_{,i}r_{,j}\}$$

$$r = (r_i r_i)^{1/2}$$

$$r_i = r_{,i} = r_i/r$$

δ_{ij} = Kronecker delta

μ = shear modulus

ν = Poisson's ratio. (18)

Let us split the boundary Γ into two parts Γ_1 and Γ_2. Both displacements and tractions are prescribed along Γ_2, but Γ_1 remains as a free boundary (see Courant and Hilbert (1953)). Gao and Mura has written (17) as

$$\int_{\Gamma_1} T_{ij}(x, x')u_j(x)d\Gamma(x) - \int_{\Gamma_1} U_{ij}(x, x')t_j(x)d\Gamma(x) = b(x'), \tag{19}$$

where

$$b(x') = -\int_{\Gamma_2} T_{ij}(x, x')u_j(x)d\Gamma(x) - \frac{1}{2}u_i(x') + \int_{\Gamma_1} U_{ij}(x, x')t_j(x)d\Gamma(x). \tag{20}$$

Equation (19) is a Fredholm integral equation of the first kind (see Stakgold (1967)), and it cannot be solved as it is. Gao and Mura have applied the regularization method by Tikhonov (1963) derivable from the constrained minimization problem

$$\text{minimize} \sqrt{\int_{\Gamma_1} u_i^2(x)dx + \int_{\Gamma_1} t_i^2(x)dx} \tag{21}$$

subject to

$$\sqrt{\int_{\Gamma_2}\left[\int_{\Gamma_1} T_{ij}(x, x')u_j(x)d\Gamma(x) - \int_{\Gamma_1} U_{ij}(x, x')t_j(x)d\Gamma(x) - b(x')\right]^2 dx'} \leq \epsilon, \tag{22}$$

where ϵ is an arbitrary tolerance. The Euler equations for this problem are

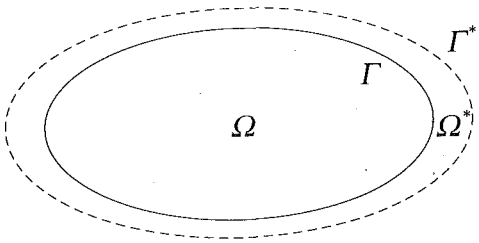

Note: $\Omega \subset \Omega^*$.

Fig. 4 A linear elastic body enclosed by the fictitious boundary

$$\begin{cases} \displaystyle\int_{\Gamma_1}\left[\int_{\Gamma_2} T_{ji}(\xi, x')T_{jk}(\eta, x')d\Gamma(x')\right]u_k(\eta)d\Gamma(\eta) \\ \quad \displaystyle -\int_{\Gamma_1}\left[\int_{\Gamma_2} T_{ji}(\xi, x')U_{jk}(\eta, x')d\Gamma(x')\right]u_k(\eta)d\Gamma(\eta) \\ \quad\quad + \alpha u_i(\xi) = \displaystyle\int_{\Gamma_2} T_{ji}(\xi, x')b_j(x')d\Gamma(x') \\ \displaystyle\int_{\Gamma_1}\left[\int_{\Gamma_2} U_{ji}(\xi, x')U_{jk}(\eta, x')d\Gamma(x')\right]t_k(\eta)d\Gamma(\eta) \\ \quad \displaystyle -\int_{\Gamma_1}\left[\int_{\Gamma_2} T_{ji}(\xi, x')U_{jk}(\eta, x')d\Gamma(x')\right]t_k(\eta)d\Gamma(\eta) \\ \quad\quad + \alpha t_i(\xi) = \displaystyle\int_{\Gamma_2} U_{ji}(\xi, x')b_j(x')d\Gamma(x') \end{cases} \tag{23}$$

where α is the reciprocal of the Lagrange multiplier. In general, (23) is solved numerically on computer.

The problem with (23) is that there are several double integrations involved, and the general consensus has that the implementation of multiple integrations on computer is discouraged unless it is absolutely necessary (see Press et al. (1986)). In addition, because T_{ij} and U_{ij} are singular kernels, extreme care must be taken to evaluate them. Moreover, because their singular natures have been convoluted in (23), implementing such multiple singular integrations costs CPU time and accuracy; and, therefore, is not recommended.

4 An Alternative Formulation of the Regularization Method

The numerical solution of Somigliana's integral Eq. (17) is called the solution of the direct boundary element (or integral) method (BEM). Naturally, there is an alternative method called the indirect BEM. The indirect BEM is based on either the simple or double layer potential theory (Kinoshita and Mura (1956)).

To put this method very simply, the displacement field u_i of a static linear elastic body, free of body forces, subjected to the external forces ϕ_i along its boundary Γ can be expressed as

$$u_i(x) = \int_\Gamma U_{ji}(x, x')\phi_j(x')d\Gamma(x'), \tag{24}$$

where U_{ij} is the Green's function (fundamental solution) tensor given in (18). By an application of Hooke's law and the traction-stress relation,

$$\begin{cases} \sigma_{ij} = C_{ijkl}u_{k,l} \\ t_i = \sigma_{ij}n_j \end{cases} \tag{25}$$

where C_{ijkl} are the material constants; n_j, the normal vectors, can be derived so that

$$t_i(x) = \int_\Gamma T_{ji}(x, x')\phi_j(x')d\Gamma(x'). \tag{26}$$

Suppose that the boundary Γ is enclosed by another boundary Γ^* and that the gap between the two boundaries is filled by the same material that composes the domain Ω as shown in Fig. 4, we can write the equations similar to (24) and (25) with Γ having been replaced by Γ^*. We can compute the corresponding forces (potentials) ϕ_j^* that take the values of u_i and t_i along Γ by

$$\begin{cases} u_i(x) = \displaystyle\int_{\Gamma^*} U_{ji}(x, x')\phi_j^*(x')d\Gamma(x') \\ t_i(x) = \displaystyle\int_{\Gamma^*} T_{ji}(x, x')\phi_j^*(x')d\Gamma(x') \end{cases}, \quad x \in \Gamma, \tag{27}$$

and once we have the forces, we can compute displacements and tractions at any point in the domain Ω^* by moving x in (27) to the desired position. This type of indirect boundary element method is called the fictitious (imaginary) boundary indirect method because of the presence of Γ^*. This indirect method effectively avoids singular integrations because x never coincides with x' in (27), but, on the other hand, the down side of this method may be that the judgement of the optimum location of Γ^* requires some experiences.

Let us formulate the regularization method based on the fictitious boundary indirect method. As before, we first set up the constrained problem

$$\text{minimize} \sqrt{\int_{\Gamma^*} [\phi_i^*(x)]^2 dx} \tag{28}$$

subject to

$$\sqrt{\int_{\Gamma_2}\left\{\left[\int_{\Gamma^*} U_{ji}(x, x')\phi_j^*(x')d\Gamma(x') - u_i(x)\right]^2 + \left[\int_{\Gamma^*} T_{ji}(x, x')\phi_j^*(x')d\Gamma(x') - t_i(x)\right]^2\right\}d\Gamma(x)} \le \epsilon, \tag{29}$$

where Γ_1, Γ_2, and ϵ are the same as the ones in the previous formulation. The Euler equation for this problem is

$$\int_{\Gamma^*}\left\{\int_{\Gamma_2} [U_{ik}(x, \xi)U_{jk}(x, \eta) + T_{ik}(x, \xi)T_{jk}(x, \eta)]d\Gamma(x)\right\} \times \phi_j^*(\eta)d\Gamma(\eta) + \alpha\phi_i^*(\xi) = \int_{\Gamma_2} [U_{ij}(x, \xi)u_j(x) + T_{ij}(x, \xi)t_j(x)]d\Gamma(x). \tag{30}$$

Note that even though there are still some multiple integrations in (30), we have effectively removed singular integrations. Numerically, (30) is much simpler to implement on computer than (23). After the forces ϕ_i^* are found, we can compute displacements and tractions at any point from (27) by moving x to the desired position.

5 A Simple Example

Although Part II of this paper shows more numerical discussions and results, here is a simple demonstration of (30)

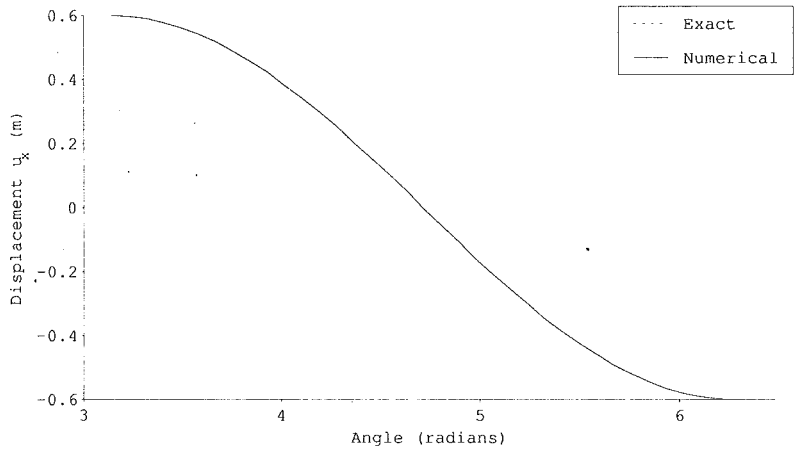

Fig. 5 *x*-displacements

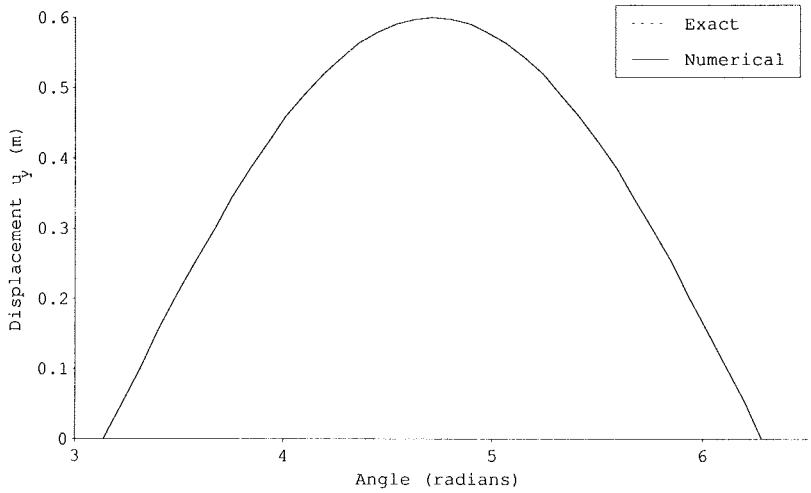

Fig. 6 *y*-displacements

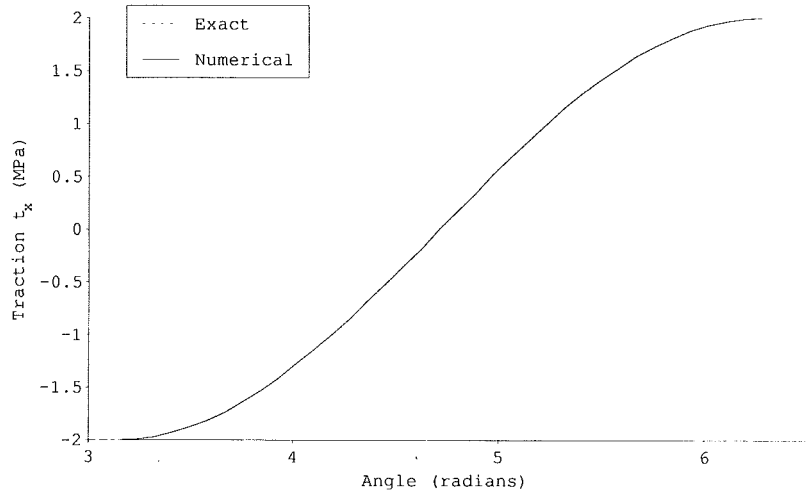

Fig. 7 *x*-tractions

using the inverse problem introduced in Section 1.4. This problem turns out to be very insensitive to the position of Γ^*; therefore, we simply show the results of this problem with the radius a, Young's modulus E, Poisson's ratio ν, and the pressure p having been set to 2m, 5 MPa, 0.25, and 2 MPa, respectively. Figures 5, 6, 7, and 8 respectively show how the computed u_x, u_y, t_x, and t_y, agree with the exact solutions (7) and (8). They are indeed in very good agreement.

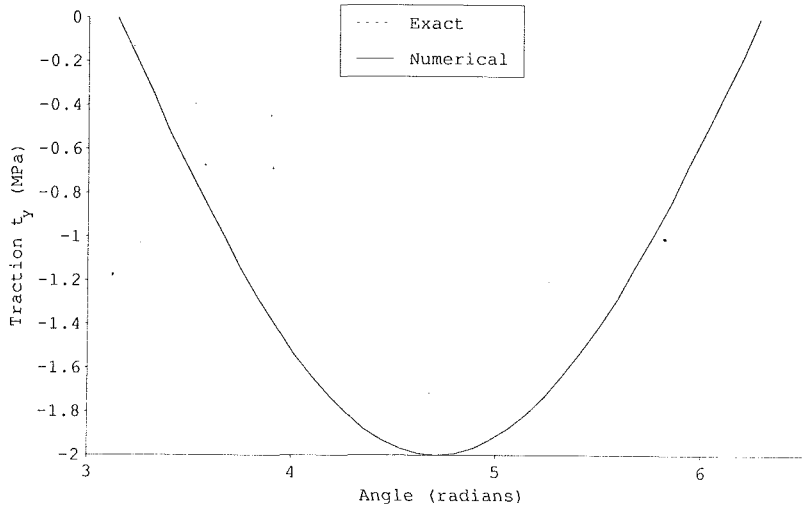

Fig. 8 *y*-tractions

6 Conclusions and Remarks

In this paper, the difficulties in solving inverse problems have been discussed. Nonexistence, nonuniqueness, and instabilities may occur. The inverse problem cannot be solved directly.

An alternative formulation of the regularization based on the fictitious boundary indirect method has been investigated. This regularization has effectively overcome the most difficult part of the regularization method based on the direct method—the singular integration. It has been applied to a linear elasticity problem and performed very well.

6 Acknowledgments

We would like to express gratitude to Professor Horgan, Associate Editor of the *Journal of Applied Mechanics*, for constructive advice during the rewriting period. We would also like to thank the reviewers for bringing some important literature to our attention, especially the work by Almansi. This research has been supported by U.S. Army Research Office under Grant No. DAAL03-89-K-0019.

References

Alamansi, E., 1907, "Un teorema sulle deformazioni elastiche dei solidi isotropi," *Atti R. Accad. Lincei Rend. Cl. Sci. Fis. Mat. Natur.* (Ser. 5), Vol. 16, pp. 865–867.

Brebbia, C. A., Telles, J. C. F., and Wrobel, L. C., 1984, *Boundary Element Techniques*, Springer-Verlag, New York.

Courant, R., and Hilbert, D., 1953, *Methods of Mathematical Physics*, Vol. 1, John Wiley and Sons, New York.

Dulikravich, G., 1988, "Inverse Design and Active Control Concepts in Strong Unsteady Heat Conduction," ASME *Appl. Mech. Rev.*, Vol. 41, pp. 270–277.

Gao, Z., and Mura, T., 1989, "Inversion of Residual Stresses From Surface Displacements," ASME JOURNAL OF APPLIED MECHANICS, Vol. 54, pp. 508–513.

Hadamard, I., 1902, *Sur les problemes aux derivees partielle et leur signification physique*, Bull. Univ. Princeton 13.

Jaswon, M. A., and Symm, G. T., 1977, *Ingetral Equation Methods in Potential Theory and Elastostatics*, Academic Press, New York.

Kinoshita, N., and Mura, T., 1956, "On the Boundary-Value Problem of Elasticity," *Res. Rep. Faculty of Engng.*, Meiji Univ., No. 8, pp. 1–7.

Knops, R. J., and Payne, L. E., 1971, *Uniqueness Theorems in Linear Elasticity*, Springer-Verlag, New York.

Kubo, S., 1988, "Inverse Problems Related to the Mechanics and Fracture of Solids and Structures," *JSME Int'l J.*, Vol. 31, pp. 157–166.

Muskhelishvili, N. I., 1963, *Some Basic Problems of the Mathematical Theory of Elasticity*, 3rd ed., P. Noordhoff, Ltd., Groningen, Holland.

Press, W. H., Brian, P. F., Teukolsky, S. A., and Vetterling, W. T., 1986, *Numerical Recipes*, Cambridge Univ. Press, Cambridge, U. K.

Sobieczky, H., 1988, "Research on Inverse Design and Optimization in Germany," ASME *Appl. Mech. Rev.*, Vol. 41, pp. 239–246.

Stakgold, I., 1967, *Mathematical Physics*, Vol. 1, Macmillan, New York.

Stanitz, H., 1988, "A Review of Certain Inverse Problem Methods for the Design of Ducts with 2- or 3-Dimensional Potential Flow," ASME *Appl. Mech. Rev.*, Vol. 41, pp. 217–238.

Tikhonov, A. N., 1963, "Solution of Incorrectly Formulated Problems and Regularization Method," *Doklady Akad. Nauk SSSR*, Vol. 151, No. 3, pp. 501–504.

Tatsuhito Koya
Department of Civil Engineering,
Northwestern University,
Evanston, IL 60208

Weichung Yeih
Assoc. Professor,
Department of River and
Harbor Engineering,
National Taiwan Ocean University,
Kee-Lung, Taiwan, R.O.C.

Toshio Mura
Department of Civil Engineering,
Northwestern University,
Evanston, IL 60208
Fellow ASME.

An Inverse Problem in Elasticity With Partially Overprescribed Boundary Conditions, Part II: Numerical Details

In Part I we examined an alternative formulation to the one employed by Gao and Mura (1989). In this paper, we look into numerical details to facilitate computer implementation. This implementation is quite general in that it works for both Gao and Mura and us (Koya and Mura (1992)).

Introduction

We have overcome the problem of evaluating convoluted singular integrations by means of basing the regularization method formulation on the fictitious boundary indirect method. However, this new formulation has not yet removed the other problem—multiple integrations. Implementing multiple integrations is not, in general, recommended (Press et al. (1986)), for the number of evaluations increases geometrically as the number of dimensions increases.

In this paper, we first take a look at the general procedure of solving integral equations numerically. We then incorporate the procedure into our regularization method formulation and solve a few example problems. Finally, we conclude with some remarks.

The General Procedure to Solve Integral Equations

Consider the integral equation

$$\int_0^1 x' x u(x)dx+\frac{1}{2}u(x')=\cos(\pi x'),\quad 0\le x'\le 1. \tag{1}$$

The exact solution is given by

$$u(x)=\frac{24x}{5\pi^2}+2\cos(\pi x), \tag{2}$$

and we would like to approximate (2) numerically at discrete points.

Here we employ the three-point Gauss-Legendre quadrature to evaluate the integral on the left-hand side of (1). The three-point Gauss-Legendre quadrature is given by (see Hildebrand (1987)),

$$\int_a^b f(x)dx\cong x_r\sum_{j=1}^{3} f(x_m+x_r\xi_j)w_j, \tag{3}$$

where

$$x_m=\frac{(b+a)}{2}$$

$$x_r=\frac{(b-a)}{2}, \tag{4}$$

$$\xi_{i=1,2,3}=\{-\sqrt{3/5},\quad 0,\quad \sqrt{3/5}\}$$

$$w_{i=1,2,3}=\{5/9,\quad 8/9,\quad 5/9\}$$

and therefore (1) becomes

$$\frac{1}{2}x'\sum_{j=1}^{3} x_j u(x_j)w_j+\frac{1}{2}u(x')=\cos(\pi x'), \tag{5}$$

where

$$x_j=\frac{1}{2}(1+\xi). \tag{6}$$

There are three unknowns—$u(x_1)$, $u(x_2)$, and $u(x_3)$—in (5). Instinctively, we would like to choose three points for x' so that there will be three equations,

$$\frac{1}{2}x_i'\sum_{j=1}^{3} x_j u(x_j)w_j+\frac{1}{2}u(x_i')=\cos(\pi x_i'),\quad i=1,2,3, \tag{7}$$

and we can solve (7) for the unknown us by simple inversion. The question is where to choose x_i'. The most obvious choice seems to be the same points as x_j. When these points are substituted into (7) and solved, we obtain

$$\begin{cases} u(x_1)=1.93053 \\ u(x_2)=0.242183, \\ u(x_3)=-1.44617 \end{cases} \tag{8}$$

Contributed by the Applied Mechanics Division of THE AMERICAN SOCIETY OF MECHANICAL ENGINEERS for publication in the ASME JOURNAL OF APPLIED MECHANICS.

Discussion on this paper should be addressed to the Technical Editor, Professor Lewis T. Wheeler, Department of Mechanical Engineering, University of Houston, Houston, TX 77204-4792, and will be accepted until four months after final publication of the paper itself in the ASME JOURNAL OF APPLIED MECHANICS.

Manuscript received by the ASME Applied Mechanics Division, Mar. 22, 1991; final revision, Aug. 13, 1992. Associate Technical Editor: C. O. Horgan.

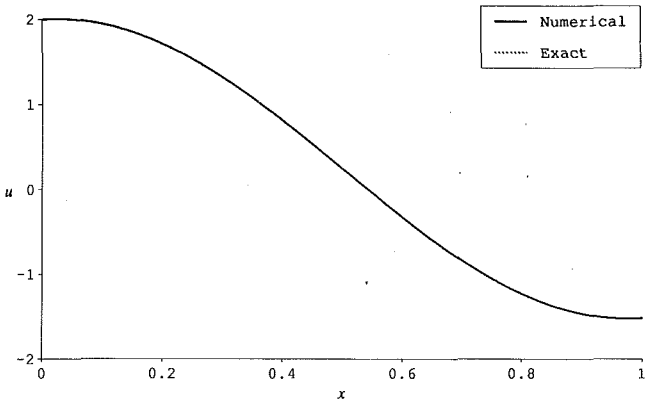

Fig. 1 Numerical and exact solutions of (1)

where

$$x_1 = \frac{1}{2} - \frac{\sqrt{3/5}}{2} \cong 0.112701665$$
$$x_2 = 0$$
$$x_3 = \frac{1}{2} + \frac{\sqrt{3/5}}{2} \cong 0.887298335 \tag{9}$$

which is in good agreement with the exact solution,

$$\begin{cases} u(x_1) = 1.93076 \\ u(x_2) = 0.243171 \\ u(x_3) = -1.44447. \end{cases} \tag{10}$$

It follows that as the order of the quadrature increases, the plot of the solution begins to look like the exact solution. Figure 1 shows the result of the 100th order quadrature and the exact solution. They almost match exactly. This solution method is called the Nystrom method (see Delves and Mohamed (1985)).

The Nystrom method allows us to replace the original integral equation into a system of simultaneous linear algebraic equations thereby treating the problem in terms of the linear algebra at which the computer truly excels.

Let us employ the Nystrom method in our formulation of the regularization method. From Part I, the original integral equations are

$$\begin{cases} u_i(x) = \displaystyle\int_{\Gamma^*} U_{ji}(x,x')\phi_j(x')d\Gamma(x') \\ t_i(x) = \displaystyle\int_{\Gamma^*} T_{ji}(x,x')\phi_j(x')d\Gamma(x'), \end{cases} \quad x \in \Gamma_1. \tag{11}$$

These are now converted into a system of simultaneous linear equations by means of the nth order quadrature,

$$\begin{cases} u_i(x_\alpha) = \displaystyle\sum_{\beta=1}^{n} U_{ji}(x_\alpha,x_\beta')\phi_j(x_\beta')w_\beta J(\xi_\beta) \\ t_i(x_\alpha) = \displaystyle\sum_{\beta=1}^{n} T_{ji}(x_\alpha,x_\beta')\phi_j(x_\beta')w_\beta J(\xi_\beta), \end{cases}$$
$$x \in \Gamma_1, \alpha = 1,2, \ldots ,m \tag{12}$$

where J is the Jacobian determinant which maps the natural coordinates ξ_β over to the global coordinates x_β' since most quadratures are defined in the natural coordinates. The type of quadrature used in (12) is not necessarily the Gauss-Legendre. It may be any suitable one which facilitates integration. In general, the selection is based on the type of kernel in question.

Notice that (12) forms an $m \times n$ system of simultaneous linear algebraic equations which may or may not be a square system. There is not much point in choosing n points for x to create a square system because unlike the previous example problem, the path of integration does not intersect x. Although we can form mechanically a square system, the coefficient matrix is usually singular and cannot be inverted.

Let us rewrite (12) as follows:

$$\begin{Bmatrix} \mathbf{u} \\ \mathbf{t} \end{Bmatrix} = \begin{bmatrix} \mathbf{U} \\ \mathbf{T} \end{bmatrix} \{\phi\}. \tag{13}$$

Now, the regularization formulation becomes

$$\text{minimize} \quad \sqrt{\phi^T\phi}$$

$$\text{subject to} \quad \sqrt{\left[\begin{Bmatrix} u \\ t \end{Bmatrix} - \begin{bmatrix} \mathbf{U} \\ \mathbf{T} \end{bmatrix} \{\phi\} \right]^T \left[\begin{Bmatrix} \mathbf{u} \\ \mathbf{t} \end{Bmatrix} - \begin{bmatrix} \mathbf{U} \\ \mathbf{T} \end{bmatrix} \{\phi\} \right]} \leq \epsilon. \tag{14}$$

Then the Euler equation for this constrained problem is

$$(\mathbf{U}^T\mathbf{U} + \mathbf{T}^T\mathbf{T} + \alpha\mathbf{I})\phi = \mathbf{U}^T\mathbf{u} + \mathbf{T}^T\mathbf{t}. \tag{15}$$

Notice the resemblance between (15) here and (30) in Part I; they are numerically equivalent. Moreover, there are no multiple integrations involved in (15). They have been replaced by matrix multiplications at which the computer excels. After the parameter ϕ has been computed with the appropriate value of α, we can proceed to calculate the displacements and tractions at any point by (13) with x having been moved to the desired position.

There still remains the problem of determining the appropriate value of α (Ribiére (1967) and Wahba (1977)). In general, there is no direct way to determine it; therefore, it must be done by iteration. Ideally, the solution should improve as the value of α approaches zero; consequently, it seems to be logical to set the initial value of α rather larger, and evaluate the inequality constraint in (14). If the test proves to be false, decrease the value of α and repeat the test. As to how much to decrease at each iteration is a difficult problem. Gao and Mura (1989) suggested the use of the bisection method, but to guess the initial two values of α may be difficult even though the convergence is absolute. In this paper, the secant method (see Hildebrand (1987)) is used because it requires only one initial guess, and the convergence, though conditional, is much faster than the bisection method. The procedure is as follows:

Step 1: Choose the initial α and the step length h. Set the iteration counter n to 1 and the maximum iteration count N to an arbitrary number.
Step 2: Evaluate the left-hand side of the inequality constraint in (14) at α and $\alpha + h$; and label them $f(\alpha)$ and $f(\alpha+h)$, respectively.
Step 3: Test the inequality (14) for both values.
Step 4: If either is true, stop.
Step 5: The next guess is given by $\alpha_{n+1} = \alpha_n - hf(\alpha)/[f(\alpha+h) - f(\alpha)]$.
Step 6: Increment n. If n is larger than N step, or else scale the step length h by half.
Step 7: Go to Step 2.

The function f in this case is the left-hand side of the inequality in (14).

So far we have examined integral equations with smooth paths of integration. However, when the paths take arbitrary and not necessarily smooth paths, we cannot expect to integrate numerically the entire path with sufficient accuracy. Moreover, as the size of the domain in question increases, its boundary increases accordingly, so does the order of quadrature. Because in reality we cannot afford to raise the order indefinitely just to keep up with the size of the domain, it is essential to economize without sacrificing accuracy.

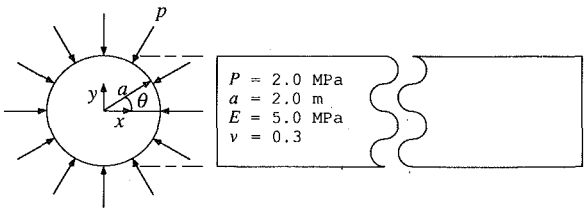

Fig. 2 A long cylinder under lateral compression

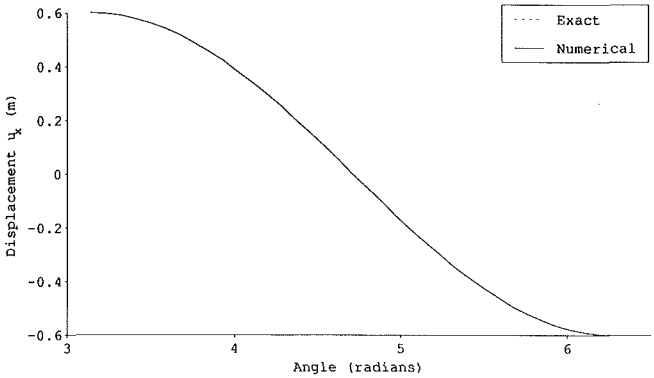

Fig. 3 *x* displacements

The simplest way to achieve this is to take advantage of the integration property

$$\int_{\Gamma} f(x)d\Gamma(x) = \sum_{i=1}^{N} \int_{\Gamma_i} f(x)d\Gamma(x), \tag{16}$$

where N is the number of smaller components of the total boundary Γ. Thus, we can subdivide into smaller boundaries for which lower order quadratures prove to be accurate enough. At the same time, discretization allows us to integrate any arbitrary path shape. There is no major difference between the discretized and continuous methods as long as the path is smooth enough. Furthermore, as the size of each subboundary decreases, the behavior of the solution along it may be approximated by a simpler function such as a constant, linear, or quadratic function. This "discretization" of the integral equation is the basis of the boundary element method.

In the next section, we examine the characteristics of the regularization method more closely by solving a couple of example problems. We would like to know whether this method always yields the solution we want.

Example Problem No. 1

As the first example, we repeat the problem discussed in Part I. As Fig. 2 shows, a long cylinder is under radial compression. The Cauchy data—displacements and tractions—along the upper half of the lateral surface, $0 \le \theta \le \pi$, is given and the lower surface, $\pi < \theta < 2\pi$, remains free. We would like to calculate the displacements and tractions along the lower surface.

We know the analytical solutions are

$$\begin{cases} p_x = 2\cos\theta \\ p_x = 2\sin\theta \\ u_x = -(14/25)\cos\theta \\ u_y = -(14/25)\sin\theta. \end{cases} \tag{17}$$

Figures 3, 4, 5, and 6 show the x and y displacements and the x and y tractions, respectively. They all agree excellently well.

Example Problem No. 2

Consider a square plate under uniaxial load as shown in Fig. 7. The Cauchy data—displacements and tractions—are prescribed along the right edge $x = 2.0$ of the plate, and the remaining boundaries are free. We would like to solve this Cauchy problem. The constant boundary element method is employed to discretize the original equation into the Nystrom form.

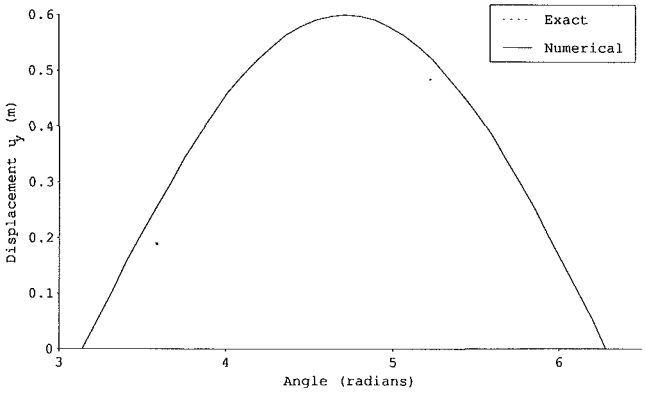

Fig. 4 *y* displacements

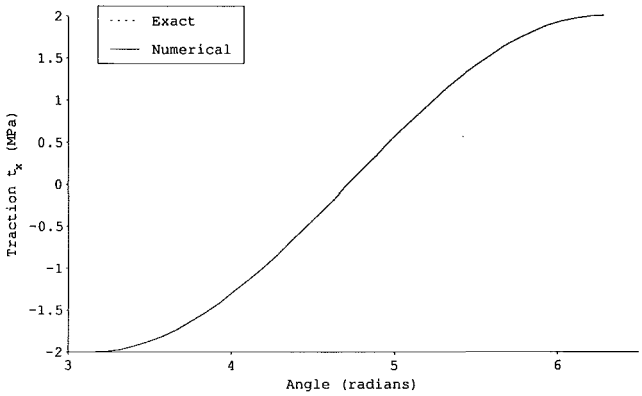

Fig. 5 *x* tractions

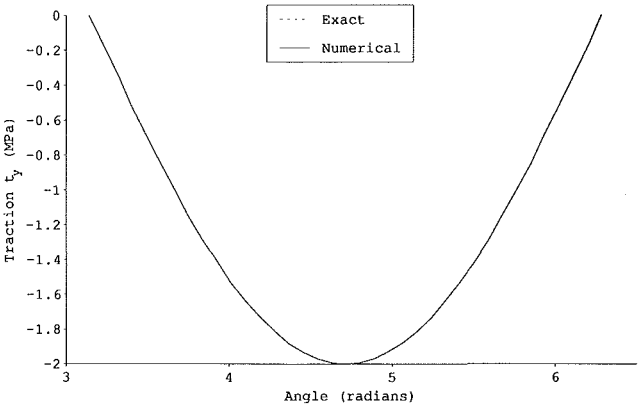

Fig. 6 *y* tractions

Unlike the previous problem, this problem poses some difficulties. Both displacements and tractions in the previous problem are smooth and continuous whereas the tractions in this problem are discontinuous at each corner. Because our formulation is based on the Euclidean L_2 norm which has a form of the quadratic function, it is uncertain as to how the regularized solution behaves in the neighborhood of these points.

Another concern is the applicability of the constant element discretization. We know the analytical solutions for the x and y displacements (m) are

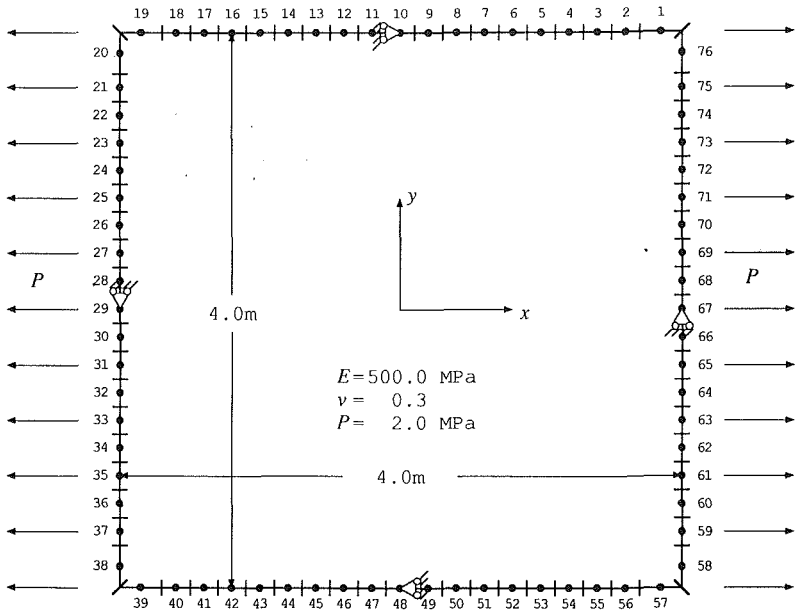

Fig. 7 A square plate under uniaxial load

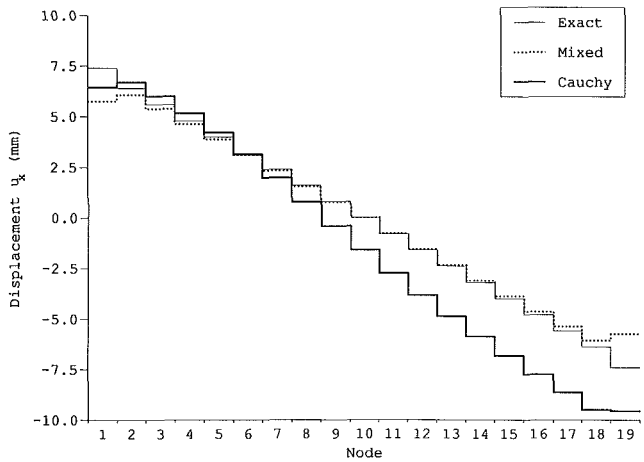

Fig. 8 *x* displacements based on the analytical data

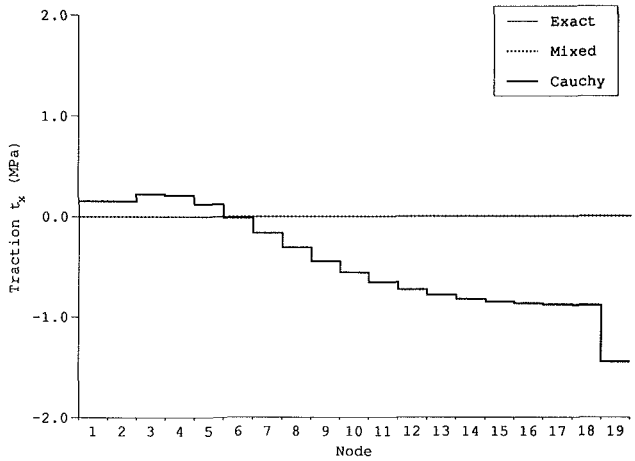

Fig. 10 *x* tractions based on the analytical data

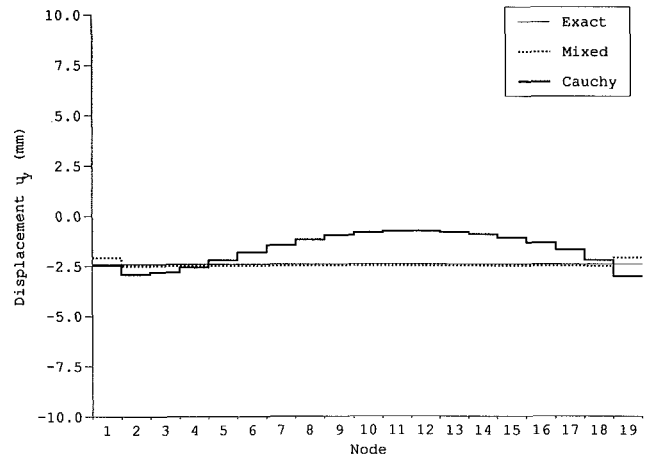

Fig. 9 *y* displacements based on the analytical data

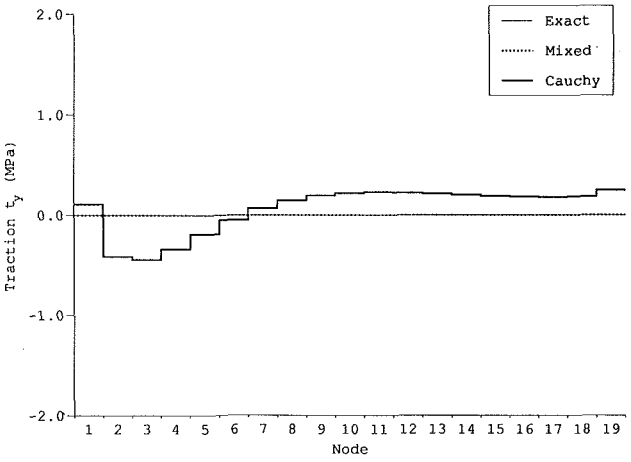

Fig. 11 *y* tractions based on the analytical data

$$\begin{cases} u_x = 0.004x \\ u_y = -0.0012y. \end{cases} \tag{18}$$

We are not certain whether the constant element approximation is suitable in this situation. Figures 8, 9, 10, and 11 show the results when the analytical values are given along $x = 2.0$. The errors in the displacements are still in the acceptable range, but those in the tractions are not. It seems that because the displacement is a continuous function, the regularization method works well; however, the traction may be either con-

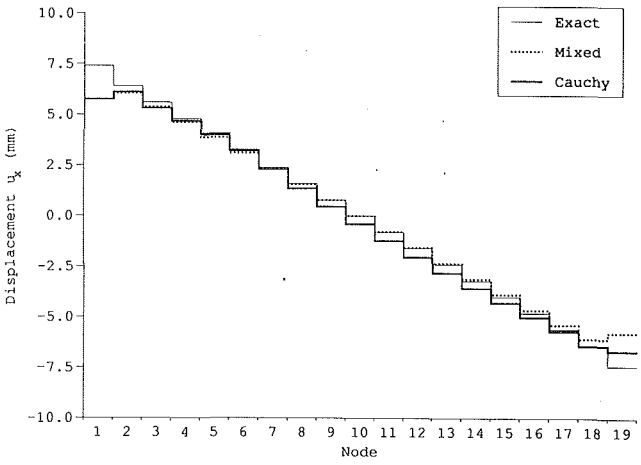

Fig. 12 *x* displacements based on the numerical data

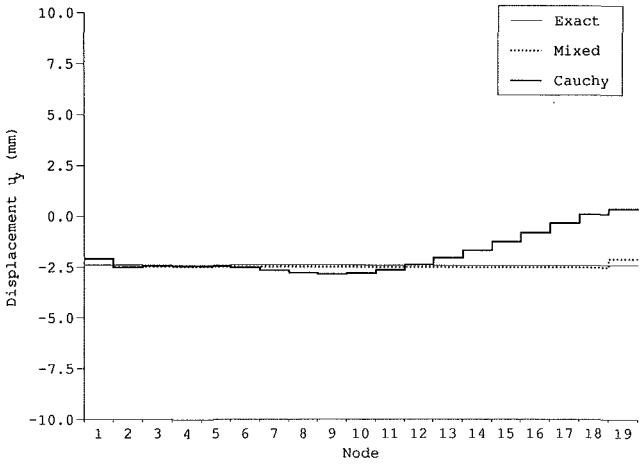

Fig. 13 *y* displacements based on the numerical data

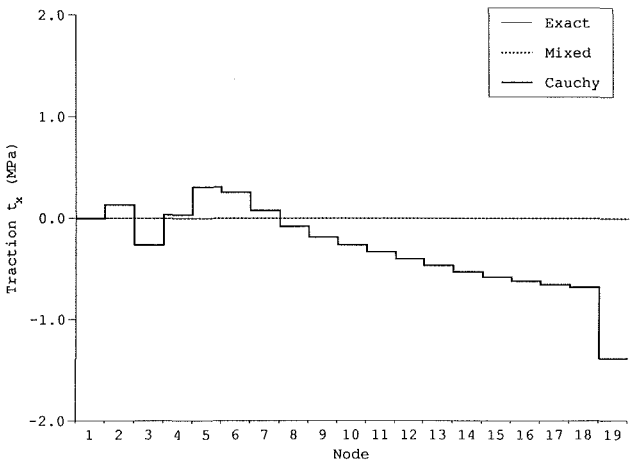

Fig. 14 *x* tractions based on the numerical data

tinuous or discontinuous so that the regularization cannot treat it reliably.

Furthermore, because the input data is the analytical solutions which are constant and linear, the constant element approximation is unable to fit the data completely. In other words, to the constant approximation these values are not the "exact" values. The values which can be approximated reliably by the constant element approximation are the "apparently" exact input data.

In order to show this behavior, we use the mixed boundary value problem solutions by the constant element approximation as the input data. In other words, for the *x* and *y* displacement input data, we use the numerical solutions. Figures 11, 12, 13, and 14 show the results. They are in better agreement.

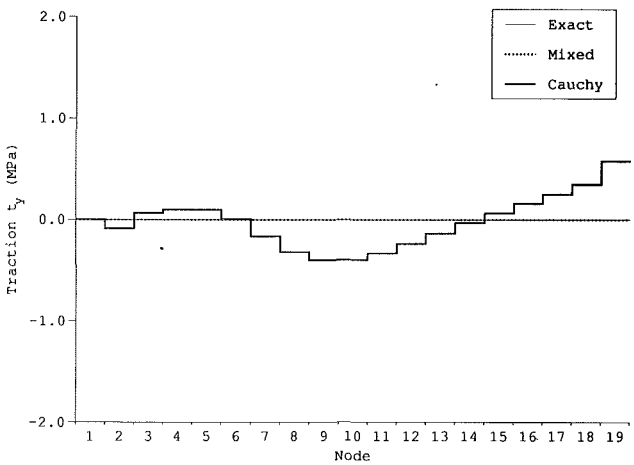

Fig. 15 *y* tractions based on the numerical data

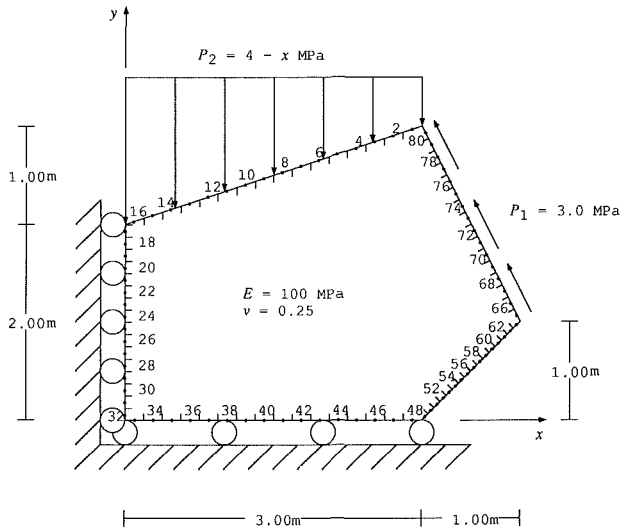

Fig. 16 More complicate boundary conditions

Example Problem No. 3

In this example, the geometry and the boundary conditions are slightly more complicated as shown in Fig. 16. This problem has been solved as the mixed boundary value problem first. Then these solutions have been used as the input data along the nodes #65 to #80, other boundaries are free. We would like to recover the remaining boundary conditions.

Figures 17, 18, 19, and 20 show the regularized solutions and the mixed boundary value solutions. They are in very good agreement. However, the traction solutions as shown in Figs. 15 and 16 are not as good as the displacement solutions due to the presence of discontinuities. Further studies are required to address the problem of discontinuity.

Conclusions

The numerical procedure based on the Nystrom method to solve the Cauchy (inverse) problem is discussed. As long as the input data is compatible, it can be solved with great accuracy. However, unlike the ordinary boundary value problem, the sensitivity of the solution to the input data is more pronounced. A very refined discretized model is required to solve

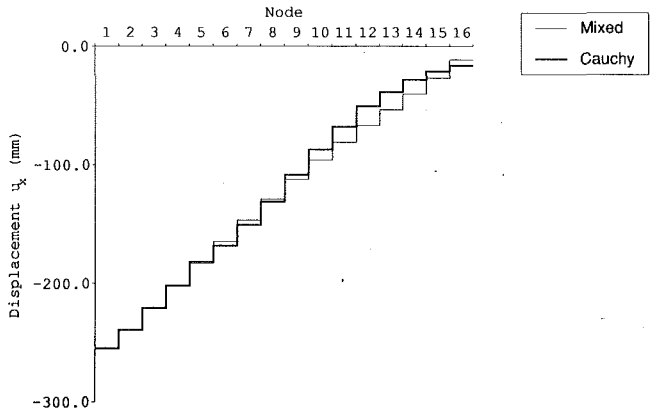

Fig. 17 *x* displacements

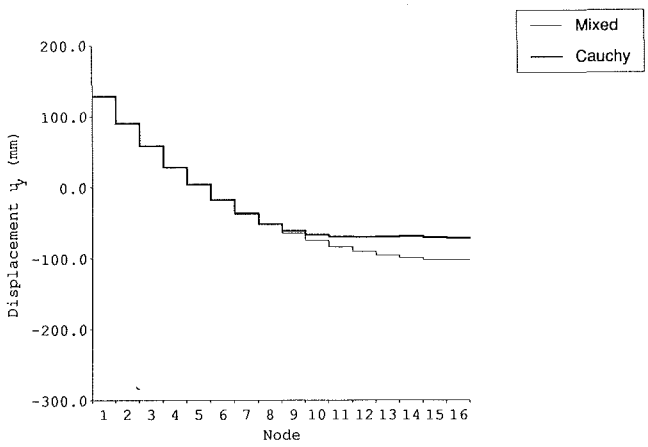

Fig. 18 *y* displacements

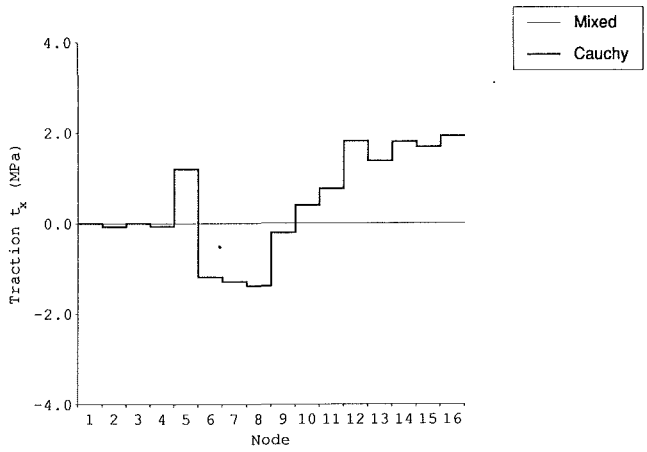

Fig. 19 *x* tractions

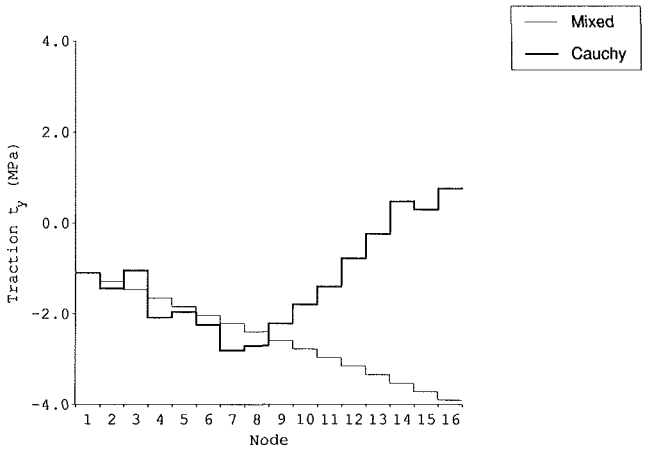

Fig. 20 *y* tractions

with sufficient accuracy. Moreover, a special procedure may be required to handle discontinuities in the solutions.

Acknowledgments

The authors wish to thank Professor Horgan, an Associate Editor of the *Journal of Applied Mechanics*, and the referees for their valuable suggestions. This research has been supported by U.S. Army Research Office under Grant No. DAAL03-K-0019.

References

Delves, L. M., and Mohamed, J. L., 1985, *Computational Methods for Integral Equations*, Cambridge Univ. Press, Cambridge, U.K.

Gao, Z., and Mura, T., 1989, "Inversion of Residual Stresses From Surface Displacements," ASME JOURNAL OF APPLIED MECHANICS, Vol. 54, pp. 508–513.

Hildebrand, F. B., 1987, *Introduction to Numerical Analysis*, Dover.

Koya, T., and Mura, T., 1991, "Boundary Element Method for Overprescribed Boundary-Value Problems," *Comp. Meth. in Appl. Mech. and Eng.*, submitted for publication.

Press, W. H., Brian, P. F., Tuekolsky, S. A., and Vetterling, W. T., 1986, *Numerical Recipes*, Cambridge Univ. Press, Cambridge, U.K.

Ribiére, G., 1967, "Regularisation d'opérateurs," *Rev. Franç. Inf. Rech. Opér.*, No. 1, pp. 57–79.

Wahba, G., 1977, "Practical Approximate Solutions to Linear Operator Equations When the Data are Noisy," *SIAM J. Numer. Anal.*, Vol. 14, pp. 651–667.

Singular Stress Field Near the Corner of Jointed Dissimilar Materials

Dai-heng Chen
Faculty of Computer Science
and Systems Engineering,
Kyushu Institute of Technology,
680-4 Kawazu, Iizuka, 820 Japan

Hironobu Nisitani
Faculty of Engineering,
Kyushu University,
6-10-1 Hakozaki, Fukuoka, 812 Japan

In this paper, the characteristics of the stress field near a corner of jointed dissimilar materials are studied as a plane problem. It is found that the order of singularity is dependent not only on the elastic constants of materials and the local geometry of corner, but also on the deformation mode. The dependence of the order of singularity was established for the case of mode I and the case of mode II. An explicit closed-form expression is given for the singular stress field at the close vicinity of the corner, in which the stress field is expressed as a sum of the symmetric state with a stress singularity of $1/r^{1-\lambda_1}$ *and the skew symmetric state with a stress singularity of* $1/r^{1-\lambda_2}$. *When both* λ_1 *and* λ_2 *are real the singular stress field around the point singularity is defined in terms of two constants* K_{I,λ_1}, K_{II,λ_2}, *as in the case of crack problems.*

Introduction

For a crack problem in a homogeneous plate, the singular stress field near the crack tip is expressed as

$$\sigma_{ij}=\frac{K_I}{\sqrt{r}}f_{ij}^{I}(\theta)+\frac{K_{II}}{\sqrt{r}}f_{ij}^{II}(\theta), \tag{1}$$

where r, θ are the components of polar coordinates with the origin of the coordinate system at the crack tip and the functions $f_{ij}^{I}(\theta)$ and $f_{ij}^{II}(\theta)$ correspond to the mode I and mode II deformations, respectively.

Since the order of the singularity (i.e., -0.5) and the explicit form of functions $f_{ij}^{I}(\theta)$ and $f_{ij}^{II}(\theta)$ in expression (1) are known, so based on the expression (1) the stress state at the crack tip is completely determined by the two parameters K_I and K_{II} (i.e., the stress intensity factors for mode I and mode II).

The study of stress singularities related to a wedge in plane elasticity was made by Williams (1952), Dempsey and Sinclair (1979, 1981), Bogy (1968, 1971), Bogy and Wang (1971), Hein and Erdogan (1971), and Theocaris (1974) et al. For the general case of N-material composite wedge, the dependence of the order of singularity on the elastic constants of materials and on the local geometry of the composite plate has been established already. However, few papers have been reported for the eigenfunction of displacement or stress (Bogy, 1970). In order to determine completely the local behavior of the displacement and the stress at the corner, the eigenfunctions corresponding to each eigenvalue are needed, simply as the functions $f_{ij}^{I}(\theta)$ and $f_{ij}^{II}(\theta)$ are needed in Eq. (1).

The present paper deals with the plane problem of a composite body consisting of two dissimilar isotropic, homogeneous and elastic wedges, perfectly bonded along both of their common interfaces, as shown in Fig. 1. The problem was studied by Bogy and Wang and an eigen equation for determining the order of the singularity in the stress field at the corner was given (Bogy and Wang, 1971), while the associate eigenfunction has not, to the best of our knowledge, been considered before. In this paper, an explicit closed-form expression, similar to Eq. (1), is established for the singular stress field at the corner. The stress field is expressed as a sum of a symmetric state and a skew-symmetric state. Both the eigenvalues and associated eigenfunctions are analyzed for the symmetric mode and the skew-symmetric mode, respectively. The stress field around the singular point is defined in terms of several constants similarly as in Eq. (1) for the crack problem.

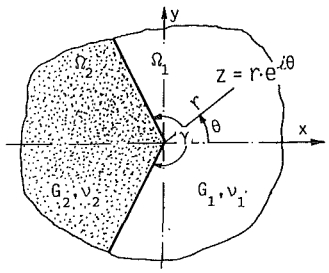

Fig. 1 Corner of two bonded wedges

Contributed by the Applied Mechanics Division of THE AMERICAN SOCIETY OF MECHANICAL ENGINEERS for publication in the ASME JOURNAL OF APPLIED MECHANICS.

Discussion on this paper should be addressed to the Technical Editor, Professor Lewis T. Wheeler, Department of Mechanical Engineering, University of Houston, Houston, TX 77204-4792, and will be accepted until four months after final publication of the paper itself in the ASME JOURNAL OF APPLIED MECHANICS.

Manuscript received by the ASME Applied Mechanics Division, June 26, 1991; final revision, June 4, 1992. Associate Technical Editor: X. Makenscoff.

Formulation

Consider a plane problem of two dissimilar wedges of angles γ and $2\pi-\gamma$, respectively, bonded perfectly at both of their interfaces (Fig. 1). The regions occupied by the two wedges are denoted by Ω_1 and Ω_2. The two wedges are made of different isotropic and homogeneous elastic materials. Denote the shear modulus and Poisson's ratios of the two materials by G_1, ν_1 and G_2, ν_2, respectively.

Take the vertex as the origin of coordinates and put the x-axis on the line which divides the region Ω_1 and Ω_2 equally. In each of the regions Ω_i $(i=1,2)$, displacements in the radial and circumferential directions, u_{r_i} and u_{θ_i}, stresses in the plane polar components, σ_{r_i}, σ_{θ_i} and $\tau_{r\theta_i}$, and resultant forces in the x and y-directions, P_{x_i} and P_{y_i} (resultant forces of the stresses, exerted upon the left-hand side region by the right-hand side across an arbitrary path leading to the moving point from a definite point) are expressed in terms of two complex potentials $\phi_i(z)$ and $\psi_i(z)$

$$2(u_{r_i}+iv_{\theta_i})=\frac{e^{-i\theta}}{G_i}\{\kappa_i\phi_i(z)-z\overline{\phi_i'(z)}-\overline{\psi_i(z)}\} \tag{2}$$

$$\sigma_{\theta_i}+\sigma_{r_i}=\mathrm{Re}[\phi_i'(z)],\ \sigma_{\theta_i}-\sigma_{r_i}+2i\tau_{r\theta_i}=2e^{2i\theta}\{\bar{z}\phi_i''(z)+\psi_i'(z)\} \tag{3}$$

$$-P_{y_i}+iP_{x_i}=\phi_i(z)+z\overline{\phi_i'(z)}+\overline{\psi_i(z)} \tag{4}$$

where

$$\kappa_i=\begin{cases}(3-\nu_i)/(1+\nu_i) & \text{(plane stress)}\\ (3-4\nu_i) & \text{(plane strain).}\end{cases}$$

In order to evaluate the singular behavior of stress at the corner tip we assume $\phi_i(z)$ and $\psi_i(z)$ to be of the following form, as Theocaris (1974) did.

$$\phi_i(z)=a_{1i}z^{\lambda}+a_{2i}\bar{z}^{\lambda},\ \psi_i(z)=b_{1i}z^{\lambda}+b_{2i}\bar{z}^{\lambda} \tag{5}$$

where the exponent λ and the coefficients a_{1i}, a_{2i}, b_{1i}, b_{2i} are in general complex.

On the interfaces at the vicinity of the vertex, the complex potentials $\phi_i(z)$ and $\psi_i(z)$ must satisfy the boundary conditions that the displacement and the traction are continuous at the interfaces as

$$\left.\begin{aligned}(-P_{y_1}+iP_{x_1})|_{\theta=\gamma/2}&=(-P_{y_2}+iP_{x_2})|_{\theta=\gamma/2}\\ (u_{r_1}+iv_{\theta_1})|_{\theta=\gamma/2}&=(u_{r_2}+iv_{\theta_2})|_{\theta=\gamma/2}\end{aligned}\right\} \tag{6}$$

and

$$\left.\begin{aligned}(-P_{y_1}+iP_{x_1})|_{\theta=-\gamma/2}&=(-P_{y_2}+iP_{x_2})|_{\theta=2\pi-\gamma/2}\\ (u_{r_1}+iv_{\theta_1})|_{\theta=-\gamma/2}&=(u_{r_2}+iv_{\theta_2})|_{\theta=2\pi-\gamma/2}.\end{aligned}\right\} \tag{7}$$

Although we can derive an eigen equation from Eqs. (6) and (7) for determining the eigenvalues, namely the order of the singular stress, as the others do. However, the equation would be complicated and it is too difficult to derive the eigenfunction in an explicit closed form. It can be overcome by noting that there exists a geometric symmetry in the given problem. This fact enables us to divide the elastic field considered here into a symmetric part and a skew-symmetric part, namely into a part due to the mode I deformation and a part due to the mode II deformation.

For the part due to the mode I deformation, we can use the following symmetric condition instead of Eq. (7):

$$P_{x_1}|_{\theta=0}=0,\ v_{\theta_1}|_{\theta=0}=0,\ P_{x_2}|_{\theta=\pi}=0,\ v_{\theta_2}|_{\theta=\pi}=0. \tag{8}$$

For the part due to mode II deformation, we can use the following skew-symmetric condition instead of Eq. (7):

$$P_{y_1}|_{\theta=0}=0,\ u_{r_1}|_{\theta=0}=0,\ P_{y_2}|_{\theta=\pi}=0,\ u_{r_2}|_{\theta=\pi}=0. \tag{9}$$

Eigen Equation

From Eqs. (6) and (8) and from Eqs. (6) and (9), we obtain two sets of eight linear equations, corresponding to the symmetric and the skew-symmetric deformations, respectively. The equations are homogeneous for the eight unknown coefficients a_{11}, $\bar{a}_{21}$, $\bar{b}_{21}$, b_{11}, a_{12}, $\bar{a}_{22}$, $\bar{b}_{22}$, b_{12}. The nonvanishing stresses correspond to nontrivial solutions of the set of eight equations, so λ is determined by the roots of the eigen equation derived by setting the determinant of the coefficient matrix equal to zero. After a little algebra the eigen equations are written as

$$\begin{aligned}D_1(\alpha,\beta,\gamma,\lambda)&=(\alpha-\beta)^2\lambda^2(1-\cos2\gamma)+2\lambda(\alpha-\beta)\sin\gamma\{\sin\lambda\gamma\\ &+\sin\lambda(2\pi-\gamma)\}+2\lambda(\alpha-\beta)\beta\sin\gamma\{\sin\lambda(2\pi-\gamma)-\sin\lambda\gamma\}\\ &+(1-\alpha^2)-(1-\beta^2)\cos2\lambda\pi+(\alpha^2-\beta^2)\cos\{2\lambda(\gamma-\pi)\}=0\end{aligned} \tag{10}$$

for the mode I deformation and as

$$\begin{aligned}D_2(\alpha,\beta,\gamma,\lambda)&=(\alpha-\beta)^2\lambda^2(1-\cos2\gamma)-2\lambda(\alpha-\beta)\sin\gamma\{\sin\lambda\gamma\\ &+\sin\lambda(2\pi-\gamma)\}-2\lambda(\alpha-\beta)\beta\sin\gamma\{\sin\lambda(2\pi-\gamma)-\sin\lambda\gamma\}\\ &+(1-\alpha^2)-(1-\beta^2)\cos2\lambda\pi+(\alpha^2-\beta^2)\cos\{2\lambda(\gamma-\pi)\}=0\end{aligned} \tag{11}$$

for the mode II deformation, where α and β are Dundurs' composite constants (Dundurs, 1967 and 1969), (Bogy, 1968) and are related to the elastic constants of each constituent by

$$\left.\begin{aligned}\alpha&=\frac{G_1(\kappa_2+1)-G_2(\kappa_1+1)}{G_1(\kappa_2+1)+G_2(\kappa_1+1)}\\ \beta&=\frac{G_1(\kappa_2-1)-G_2(\kappa_1-1)}{G_1(\kappa_2+1)+G_2(\kappa_1+1)}.\end{aligned}\right\} \tag{12}$$

One can verify that the product of $D_1(\alpha,\beta,\gamma,\lambda)$ and $D_2(\alpha,\beta,\gamma,\lambda)$ coincides with the eigen equation given by Bogy and Wang (1971).

$$\begin{aligned}&-4\times D_1(\alpha,\beta,\gamma,\lambda)\times D_2(\alpha,\beta,\gamma,\lambda)\\ &\qquad=\text{Eq. (19) in (Bogy and Wang, 1971).}\end{aligned} \tag{13}$$

Equation (13) means that the eigen equation in (Bogy and Wang, 1971) may be reduced to two factors; one factor determines the eigenvalues corresponding to the mode I deformation and another determines the eigenvalues corresponding to the mode II deformation.

We now proceed to solve the eigen equations (10) and (11). Bogy and Wang (1971) gave the numerical results for the order of the singularity in the stress field at the corner. However, they did not distinguish the eigenvalues corresponding to the two different modes and only showed the eigenvalues with the smallest real part. The eigenvalues corresponding to the mode I and the mode II are both needed for analyzing the singular stress field at the corner.

Denote the roots of Eqs. (10) and (11) by λ_1 and λ_2, respectively. Since only the singular stress fields are studied here, we only seek the roots λ_1 and λ_2 in the ranges as

$$0<\mathrm{Re}(\lambda_1)<1,\ 0<\mathrm{Re}(\lambda_2)<1. \tag{14}$$

Figures 2–4 show the values of λ_1 and λ_2 for any material combinations and for the vertex angle of $\gamma=210$ deg, 270 deg, 330 deg. The composite constants α and β are contained in the parallelograms in the (α,β) plane shown in Figs. 2–4, because under the restrictions

$$0\le\nu_1,\nu_2\le0.5,\ 0\le G_1,\ G_2\le\infty \tag{15}$$

all possible values of α and β defined by Eq. (12) are contained in the following range, as shown by Bogy (1971).

$$-1\le\alpha\le+1,\ (\alpha-1)/4\le\beta\le(\alpha+1)/4 \tag{16}$$

Figures 2–4 indicate that λ_1 (namely, the roots of Eq. (10) corresponding to the symmetric deformation) may be real or

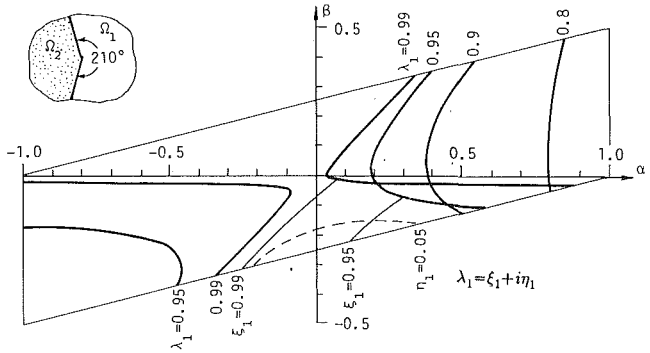

Fig. 2(*a*) λ_1 (corresponding to mode I deformation)

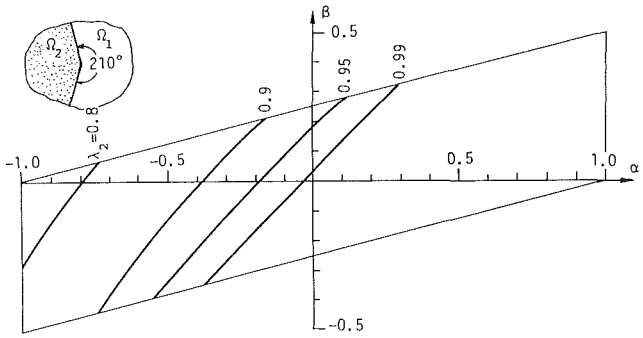

Fig. 2(*b*) λ_2 (corresponding to mode II deformation)

Fig. 2 λ_1 and λ_2 for $\rho = 210$ deg

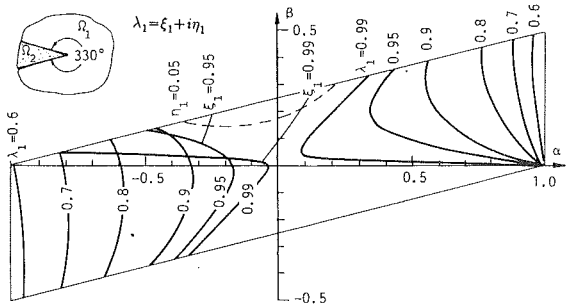

Fig. 4(*a*) λ_1 (corresponding to mode I deformation)

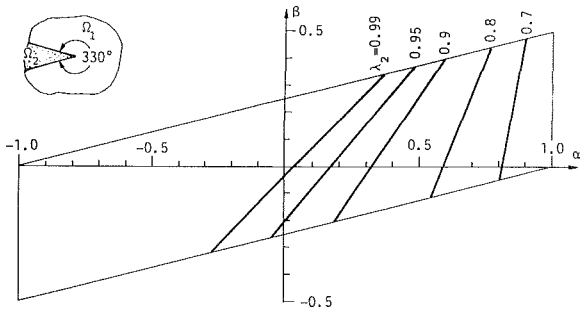

Fig. 4(*b*) λ_2 (corresponding to mode II deformation)

Fig. 4 λ_1 and λ_2 for $\rho = 330$ deg

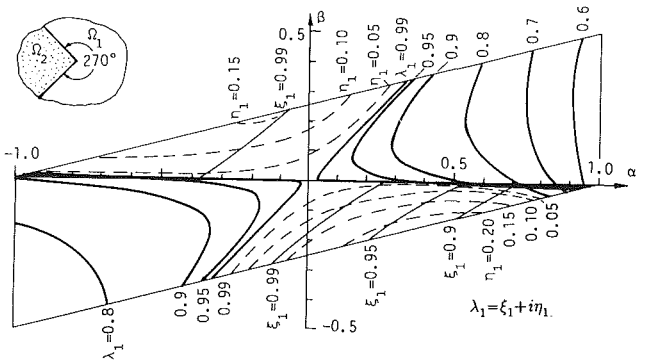

Fig. 3(*a*) λ_1 (corresponding to mode I deformation)

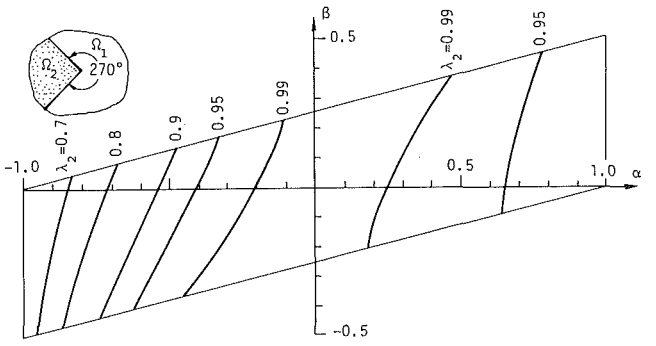

Fig. 3(*b*) λ_2 (corresponding to mode II deformation)

Fig. 3 λ_1 and λ_2 for $\rho = 270$ deg

complex, and the number of λ_1 may be more than one. However, in the range of α,β where

$$\beta(\alpha-\beta)>0. \tag{17}$$

λ_1 is real and the number is one. Equation (17) corresponds to

$$\frac{G_2}{G_1}>\frac{k_2-1}{k_1-1}\left(\text{if } \frac{G_2}{G_1}>1\right) \tag{18}$$

or

$$\frac{G_1}{G_2}>\frac{k_1-1}{k_2-1}\left(\text{if } \frac{G_1}{G_2}>1\right). \tag{19}$$

Figures 2–4 also show that the number of λ_2 is one at the most and it is always real. There exists a region of no singular stresses due to the mode II deformation, for example, for $\alpha>\beta$ when $\gamma=210$ deg and for $\alpha<\beta$ when $\gamma=330$ deg.

In Figs. 5 and 6 the values of λ_1, λ_2 for the materials of $\nu_1=\nu_2=0$ are plotted against the angle γ and the ratio G_2/G_1, respectively. These results indicate that there is no λ_1 or λ_2 less than 0.5. For the case of $\gamma=360$ deg and $G_2/G_1=0$ or $=\infty$, the singularity becomes the strongest: $\lambda_1=\lambda_2=0.5$. Figure 6 also shows, as a function of G_2/G_1, two distinct regions: the region of $\lambda_1>\lambda_2$ and the region of $\lambda_1<\lambda_2$.

In many studies about the singular stresses it is thought that only the eigenvalue $\lambda_{\min}$ with the smallest real part is necessary to be taken into account and so the singular stress field is assumed to be of the form

$$\sigma_{ij}\propto r^{\mathrm{Re}(\lambda_{\min})-1}. \tag{20}$$

However, it may be mistaken in some cases. Figure 7 shows one of the cases. In Fig. 7, a strip with a diamond-shaped inclusion is subjected to tension and the materials are such as $\lambda_1>\lambda_2$. So from Eq. (20) the singular stresses would be as $\sigma_{ij}\propto r^{\lambda_2-1}$, where λ_2 is the eigenvalue corresponding to the mode

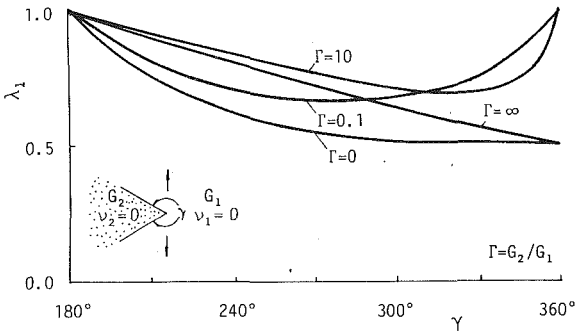

Fig. 5(*a*) λ_1 (corresponding to mode I deformation)

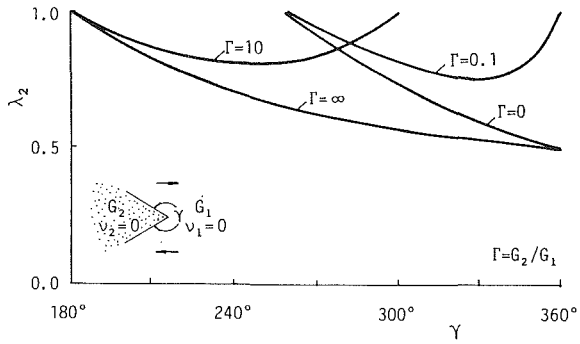

Fig. 5(*b*) λ_2 (corresponding to mode II deformation)

Fig. 5 Variation of λ_1 and λ_2 with vertex angle γ for $\nu_1=\nu_2=0$

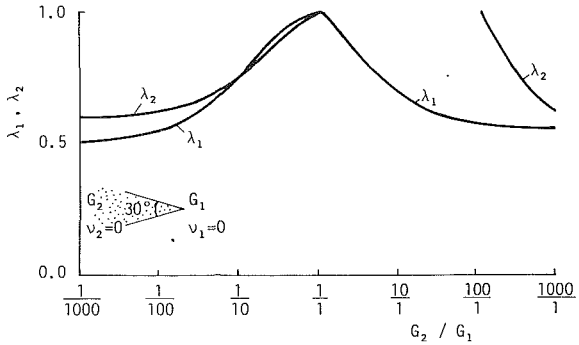

Fig. 6(*a*) $\gamma=330$ deg

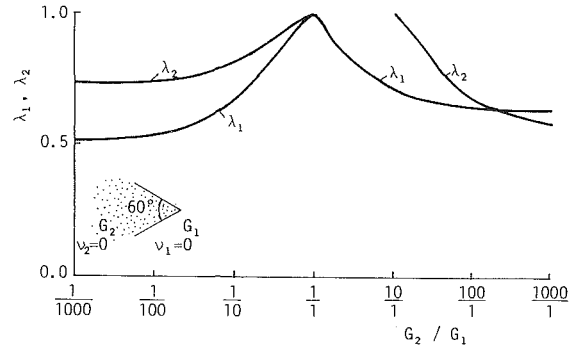

Fig. 6(*b*) $\gamma=300$ deg

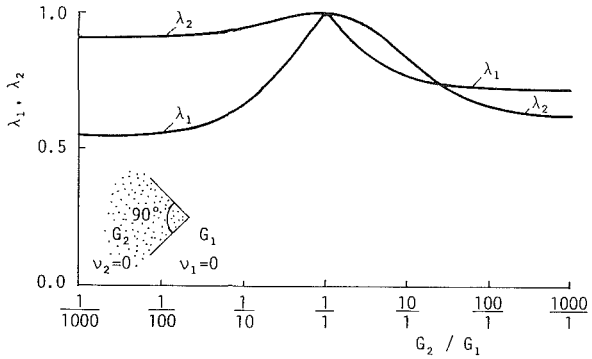

Fig. 6(*c*) $\gamma=270$ deg

Fig. 6 Variation of λ_1 and λ_2 with ratio G_2/G_1 for $\nu_1=\nu_2=0$

II deformation, but there is no mode II deformation in the given problem.

Eigenfunction

We now derive an explicit closed form for the eigenfunction. The eigenfunctions corresponding to each eigenvalue are determined straightforwardly. First, we consider the symmetric deformation.

Substituting the eigenvalue λ_1 into the coefficient matrix in the eight linear equations obtained from Eqs. (6) and (8) we obtain

$$a_{11}=\bar{a}_{21},\ b_{11}=\bar{b}_{21} \tag{21}$$

$$a_{12}e^{i\lambda_1\pi}=\bar{a}_{22}e^{-i\lambda_1\pi},\ b_{12}e^{i\lambda_1\pi}=\bar{b}_{22}e^{-i\lambda_1\pi} \tag{22}$$

and

$$\left.\begin{aligned}
\frac{a_{11}}{b_{11}}&=\frac{(\alpha-\beta)\sin\{\lambda_1(\gamma-\pi)\}}{\lambda_1(\alpha-\beta)\sin\{\gamma-\lambda_1(\gamma-\pi)\}+(1-\beta)\sin(\lambda_1\pi)}\\
\frac{a_{12}}{b_{12}}&=\frac{(\alpha-\beta)\sin\{\lambda_1(\gamma-\pi)\}}{\lambda_1(\alpha-\beta)\sin\{\gamma-\lambda_1(\gamma-\pi)\}+(1+\beta)\sin(\lambda_1\pi)}\\
\frac{a_{12}e^{i\lambda_1\pi}}{a_{11}}&=\frac{(1-\beta)\sin(\lambda_1\gamma)+(1-\alpha)\sin\{\lambda_1(\pi-\gamma)\}+\lambda_1(\alpha-\beta)\sin\gamma}{(1+\beta)\sin\{\lambda_1(2\pi-\gamma)\}+(1+\alpha)\sin\{\lambda_1(\gamma-\pi)\}+\lambda_1(\alpha-\beta)\sin\gamma}
\end{aligned}\right\}(23)$$

Since λ_1 is of order 1, the eight unknowns a_{11}, $\bar{a}_{21}$, $\bar{b}_{21}$, b_{11}, a_{12}, $\bar{a}_{22}$, $\bar{b}_{22}$, b_{12} are only related by seven Eqs. (21), (22), and (23). It means that we can arbitrarily choose one of the eight, for example, define a_{11} as

$$a_{11}=\frac{1}{2\sqrt{2\pi}}\sin\{\lambda_1(\gamma-\pi)\}\cdot\{K_{I,\lambda_1}+iK^*_{I,\lambda_1}\} \tag{24}$$

where K_{I,λ_1} and K^*_{I,λ_1} are real constants.

Substituting Eqs. (21)–(23) with the definition (24) into Eq. (5) we can derive the eigenfunction of stress and displacement without any difficulty. The size of the resulting expression is too large to print here. Therefore, we only indicate here that the singular stress around the point of singularity is determined by two real constants K_{I,λ_1}, K^*_{I,λ_1} and has the form as

$$
\begin{aligned}
\sigma_\theta = r^{p-1}[&(m_1K_{I,\lambda_1}+n_1K^*_{I,\lambda_1})\\
&\times\{\cos(q\ln r)\cosh[\theta q]\cos[(p-1)\theta]\\
&+\sin(q\ln r)\sinh[\theta q]\sin[(p-1)\theta]\}+(m_2K_{I,\lambda_1}\\
&+n_2K^*_{I,\lambda_1})\times\{\cos(q\ln r)\sinh[\theta q]\sin[(p-1)\theta]\\
&-\sin(q\ln r)\cosh[\theta q]\cos[(p-1)\theta]\}+(m_3K_{I,\lambda_1}+n_3K^*_{I,\lambda_1})\\
&\times\{\cos(q\ln r)\cosh[\theta q]\cos[(p+1)\theta]\\
&+\sin(q\ln r)\sinh[\theta q]\sin[(p+1)\theta]\}+(m_4K_{I,\lambda_1}+n_4K^*_{I,\lambda_1})\\
&\times\{\cos(q\ln r)\sinh[\theta q]\sin[(p+1)\theta]\\
&\qquad-\sin(q\ln r)\cosh[\theta q]\cos[(p+1)\theta]\}]\\
\tau_{r\theta} = r^{p-1}[&(m_5K_{I,\lambda_1}+n_5K^*_{I,\lambda_1})\\
&\times\{\cos(q\ln r)\cosh[\theta q]\sin[(p-1)\theta]\\
&-\sin(q\ln r)\sinh[\theta q]\cos[(p-1)\theta]\}+(m_6K_{I,\lambda_1}\\
&+n_6K^*_{I,\lambda_1})\times\{\cos(q\ln r)\sinh[\theta q]\cos[(p-1)\theta]\\
&+\sin(q\ln r)\cosh[\theta q]\sin[(p-1)\theta]\}+(m_7K_{I,\lambda_1}+n_7K^*_{I,\lambda_1})\\
&\times\{\cos(q\ln r)\cosh[\theta q]\sin[(p+1)\theta]\\
&-\sin(q\ln r)\sinh[\theta q]\cos[(p+1)\theta]\}+(m_8K_{I,\lambda_1}+n_8K^*_{I,\lambda_1})\\
&\times\{\cos(q\ln r)\sinh[\theta q]\cos[(p+1)\theta]\\
&\qquad+\sin(q\ln r)\cosh[\theta q]\sin[(p+1)\theta]\}]
\end{aligned}
\tag{25}
$$

for the material 1 $(-\gamma/2\le\theta\le\gamma/2)$ and as

$$
\begin{aligned}
\sigma_\theta = r^{p-1}[&m_9K_{I,\lambda_1}+n_9K^*_{I,\lambda_1})\\
&\times\{\cos(q\ln r)\cosh[q(\pi-\theta]\cos[(p-1)(\pi-\theta)]\\
&+\sin(q\ln r)\sinh[q(\pi-\theta)]\sin[(p-1)(\pi-\theta)\}\\
&\qquad+(m_{10}K_{I,\lambda_1}+n_{10}K^*_{I,\lambda_1})\\
&\times\{\cos(q\ln r)\sinh[q(\pi-\theta)]\sin[(p-1)(\pi-\theta)]\\
&-\sin(q\ln r)\cosh[q(\pi-\theta)]\cos[(p-1)(\pi-\theta)]\}\\
&\qquad+(m_{11}K_{I,\lambda_1}+n_{11}K^*_{I,\lambda_1})\\
&\times\{\cos(q\ln r)\cosh[q(\pi-\theta)]\cos[(p+1)(\pi-\theta)]\\
&+\sin(q\ln r)\sinh[q(\pi-\theta)]\sin[(p+1)(\pi-\theta)]\}\\
&\qquad+(m_{12}K_{I,\lambda_1}+n_{12}K^*_{I,\lambda_1})\\
&\times\{\cos(q\ln r)\sinh[q(\pi-\theta)]\sin[(p+1)(\pi-\theta)]\\
&\qquad-\sin(q\ln r)\cosh[q(\pi-\theta)]\cos[(p+1)(\pi-\theta)]\}\\
\tau_{r\theta} = r^{p-1}[&(m_{13}K_{I,\lambda_1}+n_{13}K^*_{I,\lambda_1})\\
&\times\{\cos(q\ln r)\cosh[q(\pi-\theta)]\sin[(p-1)(\pi-\theta)]\\
&+\sin(q\ln r)\sinh[q(\pi-\theta)]\cos[(p-1)(\pi-\theta)]\}\\
&\qquad+(m_{14}K_{I,\lambda_1}+n_{14}K^*_{I,\lambda_1}\\
&\times\cos(q\ln r)\sinh[q(\pi-\theta)]\cos[(p-1)(\pi-\theta)]\\
&-\sin(q\ln r)\cosh[q(\pi-\theta)]\sin[(p-1)(\pi-\theta)]\}\\
&\qquad+(m_{15}K_{I,\lambda_1}+n_{15}K^*_{I,\lambda_1})\\
&\times\{\cos(q\ln r)\cosh[q(\pi-\theta)]\sin[(p+1)(\pi-\theta)]\\
&+\sin(q\ln r)\sinh[q(\pi-\theta)]\cos[(p+1)(\pi-\theta)]\}\\
&\qquad+(m_{16}K_{I,\lambda_1}+n_{16}K^*_{I,\lambda_1})\\
&\times\{\cos(q\ln r)\sinh[q(\pi-\theta)]\cos[(p+1)(\pi-\theta)]\\
&\qquad-\sin(q\ln r)\cosh[q(\pi-\theta)]\sin[(p+1)(\pi-\theta)]\}]
\end{aligned}
\tag{26}
$$

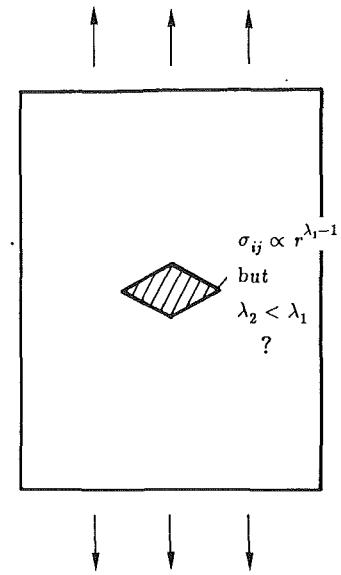

Fig. 7 Strip with a diamond-shaped inclusion under tension

for the material 2 $(\gamma/2\le\theta\le 2\pi-\gamma/2)$, where m_i, n_i $(i=1\sim16)$ are functions of α, β and γ alone.

Since $\overline{D_1(\alpha,\beta,\gamma,\lambda)}=D_1(\alpha,\beta,\gamma,\bar{\lambda})$, if λ is a zero of $D_1(\alpha,\beta,\gamma,\lambda)$ so is $\bar{\lambda}$. It is thought that the stress state around the point of singularity is expressed in terms of four real constants because both λ and $\bar{\lambda}$ are the eigenvalues (Hein and Erdogan, 1971). However, the eigenfunction corresponding to $\bar{\lambda}$ should be the same as the eigenfunction corresponding to λ, as can be understood by considering the form of function in expression (5). It means that the eigenvalue $\bar{\lambda}$ does not contribute to a new eigenfunction other than the eigenfunction corresponding to λ. That is, in the general case the stress state around the point of singularity is expressed in terms of two real constants.

When λ_1 is real, the associate eigenfunction becomes simple.

By making use of the relations (21), (22) and $\bar{\lambda}_1=\lambda_1$, the complex potential can be written as

$$\phi_1(z)=(a_{11}+\bar{a}_{11})z^{\lambda_1},\quad \psi_1(z)=(b_{11}+\bar{b}_{11})z^{\lambda_1} \tag{27}$$

for the region Ω_1 and as

$$
\begin{aligned}
\phi_2(z)&=(a_{12}e^{i\lambda_1\pi}+\bar{a}_{12}e^{-i\lambda_1\pi})e^{-i\lambda_1\pi}z^{\lambda_1},\\
\psi_2(z)&=(b_{12}e^{i\lambda_1\pi}+\bar{b}_{12}e^{-i\lambda_1\pi})e^{-i\lambda_1\pi}z^{\lambda_1}
\end{aligned}
\tag{28}
$$

for the region Ω_2.

The coefficients $a_{11}+\bar{a}_{11}$, $b_{11}+\bar{b}_{11}$, $a_{12}e^{i\lambda_1\pi}+\bar{a}_{12}e^{-i\lambda_1\pi}$ and $b_{12}e^{i\lambda_1\pi}+\bar{b}_{12}e^{-i\lambda_1\pi}$ in Eqs. (27), (28) are real and are given by the following expressions after use of Eqs. (23) and definition (24).

$$
\begin{aligned}
a_{11}+\bar{a}_{11}&=\frac{1}{\sqrt{2\pi}}\sin\{\lambda_1(\gamma-\pi)\}\cdot K_{I,\lambda_1}\\
b_{11}+\bar{b}_{11}&=\frac{1}{\sqrt{2\pi}(\alpha-\beta)}\\
&\times[\lambda_1(\alpha-\beta)\sin\{\gamma-\lambda_1(\gamma-\pi)\}+(1-\beta)\sin\lambda_1\pi]\cdot K_{I,\lambda_1}\\
a_{12}e^{i\lambda_1\pi}+\bar{a}_{12}e^{-i\lambda_1\pi}&=\frac{1}{\sqrt{2\pi}}\sin\{\lambda_1(\gamma-\pi)\}\cdot C_1\cdot K_{I,\lambda_1}\\
b_{12}e^{i\lambda_1\pi}+\bar{b}_{12}e^{-i\lambda_1\pi}&=\frac{1}{\sqrt{2\pi}(\alpha-\beta)}\\
&\times[\lambda_1(\alpha-\beta)\sin\{\gamma-\lambda_1(\gamma-\pi)\}+(1+\beta)\sin\lambda_1\pi]\cdot C_1\cdot K_{I,\lambda_1}
\end{aligned}
\tag{29}
$$

where

$$C_1=\frac{(1-\beta)\sin(\lambda_1\gamma)+(1-\alpha)\sin\{\lambda_1(\pi-\gamma)\}+\lambda_1(\alpha-\beta)\sin\gamma}{(1+\beta)\sin\{\lambda_1(2\pi-\gamma)\}+(1+\alpha)\sin\{\lambda_1(\gamma-\pi)\}+\lambda_1(\alpha-\beta)\sin\gamma}. \quad (30)$$

Equation (29) means that when λ_1 is real, the singular stress due to the mode I deformation is expressed in terms of one real constant K_{I,λ_1}.

In a similar way, for the part due to the mode II deformation we have

$$\left.\begin{array}{ll} a_{11}=-\bar{a}_{21}, & b_{11}=-\bar{b}_{21} \\ a_{12}e^{i\lambda_2 2\pi}=-\bar{a}_{22}e^{-i\lambda_2 2\pi}, & b_{12}e^{i\lambda_2 2\pi}=-\bar{b}_{22}e^{-i\lambda_2 2\pi}. \end{array}\right\} \quad (31)$$

Since λ_2 is always real it follows that the complex potentials become

$$\left.\begin{array}{l} \phi_1(z)=(a_{11}-\bar{a}_{11})z^{\lambda_2},\ \psi_1(z)=(b_{11}-\bar{b}_{11})z^{\lambda_2}\ (z\in\Omega_1) \\ \phi_2(z)=(a_{12}e^{i\lambda_2 2\pi}-\bar{a}_{12}e^{-i\lambda_2 2\pi})e^{-i\lambda_2 2\pi}z^{\lambda_2}, \\ \psi_2(z)=(b_{12}e^{i\lambda_2 2\pi}-\bar{b}_{12}e^{-i\lambda_2 2\pi})e^{-i\lambda_2 2\pi}z^{\lambda_2}\ (z\in\Omega_2). \end{array}\right\} \quad (32)$$

The coefficients $a_{11}-\bar{a}_{11}$, $b_{11}-\bar{b}_{11}$, $a_{12}e^{i\lambda_2 2\pi}-\bar{a}_{12}e^{-i\lambda_2 2\pi}$ and $b_{12}e^{i\lambda_2 2\pi}-\bar{b}_{12}e^{-i\lambda_2 2\pi}$ in Eqs. (32) are pure imaginary and are given by the following expressions as in the case of mode I deformation:

$$\left.\begin{array}{l} a_{11}-\bar{a}_{11}=\dfrac{-i}{\sqrt{2\pi}}\sin\{\lambda_2(\gamma-\pi)\}\cdot K_{II,\lambda_2} \\ b_{11}-\bar{b}_{11}=\dfrac{-i}{\sqrt{2\pi}(\alpha-\beta)}\times[\lambda_2(\alpha-\beta)\sin\{\gamma-\lambda_2(\gamma-\pi)\}-(1-\beta)\sin\lambda_2\pi]\cdot K_{II,\lambda_2} \\ a_{12}e^{i\lambda_2 2\pi}-\bar{a}_{12}e^{-i\lambda_2 2\pi}=\dfrac{-i}{\sqrt{2\pi}}\sin\{\lambda_2(\gamma-\pi)\}\cdot C_2\cdot K_{II,\lambda_2} \\ b_{12}e^{i\lambda_2 2\pi}-\bar{b}_{12}e^{-i\lambda_2 2\pi}=\dfrac{-i}{\sqrt{2\pi}(\alpha-\beta)}\times[\lambda_2(\alpha-\beta)\sin\{\gamma-\lambda_2(\gamma-\pi)\}-(1+\beta)\sin\lambda_2\pi]\cdot C_2\cdot K_{II,\lambda_2} \end{array}\right\} \quad (33)$$

where $K_{II\lambda_2}$ is a real constant and

$$C_2=\frac{(1-\beta)\sin(\lambda_2\gamma)+(1-\alpha)\sin\{\lambda_2(\pi-\gamma)\}-\lambda_2(\alpha-\beta)\sin\gamma}{(1+\beta)\sin\{\lambda_2(2\pi-\gamma)\}+(1+\alpha)\sin\{\lambda_2(\gamma-\pi)\}-\lambda_2(\alpha-\beta)\sin\gamma}. \quad (34)$$

The singular stress field is a sum of the stress field due to the symmetric deformation and the stress field due to the skew-symmetric deformation. When λ_1 is also real, an expression of the singular stress field is given by the following equation in the same form as Eq. (1).

$$\left.\begin{array}{l} \sigma_{r,i}=\dfrac{K_{I,\lambda_1}}{r^{1-\lambda_1}}f^I_{r,i}(\theta)+\dfrac{K_{II,\lambda_2}}{r^{1-\lambda_2}}f^{II}_{r,i}(\theta) \\ \sigma_{\theta,i}=\dfrac{K_{I,\lambda_1}}{r^{1-\lambda_1}}f^I_{\theta,i}(\theta)+\dfrac{K_{II,\lambda_2}}{r^{1-\lambda_2}}f^{II}_{\theta,i}(\theta) \quad (i=1,2) \\ \tau_{r\theta,i}=\dfrac{K_{I,\lambda_1}}{r^{1-\lambda_1}}f^I_{r\theta,i}(\theta)+\dfrac{K_{II,\lambda_2}}{r^{1-\lambda_2}}f^{II}_{r\theta,i}(\theta). \end{array}\right\} \quad (35)$$

where for material 1, $(-\gamma/2\le\theta\le\gamma/2)$:

$$f^I_{r,1}(\theta)=\frac{-\lambda_1}{\sqrt{2\pi}(\alpha-\beta)}[[\lambda_1(\alpha-\beta)\sin\{\gamma-\lambda_1(\gamma-\pi)\}+(1-\beta)\sin(\lambda_1\pi)]\times\cos\{(\lambda_1+1)\theta\}+[(\lambda_1-3)(\alpha-\beta)\sin\{\lambda_1(\gamma-\pi)\}]\times\cos\{(\lambda_1-1)\theta\}] \quad (36)$$

$$f^{II}_{r,1}(\theta)=\frac{-\lambda_2}{\sqrt{2\pi}(\alpha-\beta)}[[\lambda_2(\alpha-\beta)\sin\{\gamma-\lambda_2(\gamma-\pi)\}-(1-\beta)\sin(\lambda_2\pi)]\times\sin\{(\lambda_2+1)\theta\}+[(\lambda_2-3)(\alpha-\beta)\sin\{\lambda_2(\gamma-\pi)\}]\times\sin\{(\lambda_2-1)\theta\}] \quad (37)$$

$$f^I_{\theta,1}(\theta)=\frac{\lambda_1}{\sqrt{2\pi}(\alpha-\beta)}[[\lambda_1(\alpha-\beta)\sin\{\gamma-\lambda_1(\gamma-\pi)\}+(1-\beta)\sin(\lambda_1\pi)]\times\cos\{(\lambda_1+1)\theta\}+[(\lambda_1+1)(\alpha-\beta)\sin\{\lambda_1(\gamma-\pi)\}]\times\cos\{(\lambda_1-1)\theta\}] \quad (38)$$

$$f^{II}_{\theta,1}(\theta)=\frac{\lambda_2}{\sqrt{2\pi}(\alpha-\beta)}[[\lambda_2(\alpha-\beta)\sin\{\gamma-\lambda_2(\gamma-\pi)\}-(1-\beta)\sin(\lambda_2\pi)]\times\sin\{(\lambda_2+1)\theta\}+[(\lambda_2+1)(\alpha-\beta)\sin\{\lambda_2(\gamma-\pi)\}]\times\sin\{(\lambda_2-1)\theta\}] \quad (39)$$

$$f^I_{r\theta,1}(\theta)=\frac{\lambda_1}{\sqrt{2\pi}(\alpha-\beta)}[[\lambda_1(\alpha-\beta)\sin\{\gamma-\lambda_1(\gamma-\pi)\}+(1-\beta)\sin(\lambda_1\pi)]\times\sin\{(\lambda_1+1)\theta\}+[(\lambda_1-1)(\alpha-\beta)\sin\{\lambda_1(\gamma-\pi)\}]\times\sin\{(\lambda_1-1)\theta\}] \quad (40)$$

$$f^{II}_{r\theta,1}(\theta)=\frac{-\lambda_2}{\sqrt{2\pi}(\alpha-\beta)}[[\lambda_2(\alpha-\beta)\sin\{\gamma-\lambda_2(\gamma-\pi)\}-(1-\beta)\sin(\lambda_2\pi)]\times\cos\{(\lambda_2+1)\theta\}+[(\lambda_2-1)(\alpha-\beta)\sin\{\lambda_2(\gamma-\pi)\}]\times\cos\{(\lambda_2-1)\theta\}] \quad (41)$$

and for material 2, $(\gamma/2\le\theta\le 2\pi-\gamma/2)$:

$$f^I_{r,2}(\theta)=\frac{C_1\lambda_1}{\sqrt{2\pi}(\alpha-\beta)}[[\lambda_1(\alpha-\beta)\sin\{\gamma-\lambda_1(\gamma-\pi)\}+(1+\beta)\sin(\lambda_1\pi)]\times\cos\{(\lambda_1+1)(\pi-\theta)\}+[(\lambda_1-3)(\alpha-\beta)\sin\{\lambda_1(\gamma-\pi)\}]\times\cos\{(\lambda_1-1)(\pi-\theta)\}] \quad (42)$$

$$f^{II}_{r,2}(\theta)=\frac{-C_2\lambda_2}{\sqrt{2\pi}(\alpha-\beta)}[[\lambda_2(\alpha-\beta)\sin\{\gamma-\lambda_2(\gamma-\pi)\}-(1+\beta)\sin(\lambda_2\pi)]\times\sin\{(\lambda_2+1)(\pi-\theta)\}+[(\lambda_2-3)(\alpha-\beta)\sin\{\lambda_2(\gamma-\pi)\}]\times\sin\{(\lambda_2-1)(\pi-\theta)\}] \quad (43)$$

$$f^I_{\theta,2}(\theta)=\frac{-C_1\lambda_1}{\sqrt{2\pi}(\alpha-\beta)}[[\lambda_1(\alpha-\beta)\sin\{\gamma-\lambda_1(\gamma-\pi)\}+(1+\beta)\sin(\lambda_1\pi)]\times\cos\{(\lambda_1+1)(\pi-\theta)\}+[(\lambda_1+1)(\alpha-\beta)\sin\{\lambda_1(\gamma-\pi)\}]\times\cos\{(\lambda_1-1)(\pi-\theta)\}] \quad (44)$$

$$f^{II}_{\theta,2}(\theta)=\frac{C_2\lambda_2}{\sqrt{2\pi}(\alpha-\beta)}[[\lambda_2(\alpha-\beta)\sin\{\gamma-\lambda_2(\gamma-\pi)\}-(1+\beta)\sin(\lambda_2\pi)]\times\sin\{(\lambda_2+1)(\pi-\theta)\}+[(\lambda_2+1)(\alpha-\beta)\sin\{\lambda_2(\gamma-\pi)\}]\times\sin\{(\lambda_2-1)(\pi-\theta)\}] \quad (45)$$

$$f^I_{r\theta,2}(\theta)=\frac{C_1\lambda_1}{\sqrt{2\pi}(\alpha-\beta)}[[\lambda_1(\alpha-\beta)\sin\{\gamma-\lambda_1(\gamma-\pi)\}+(1+\beta)\sin(\lambda_1\pi)]\times\sin\{(\lambda_1+1)(\pi-\theta)\}+[(\lambda_1-1)(\alpha-\beta)\sin\{\lambda_1(\gamma-\pi)\}]\times\sin\{(\lambda_1-1)(\pi-\theta)\}] \quad (46)$$

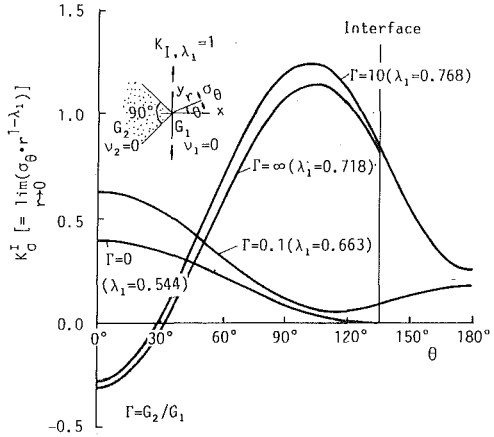

Fig. 8 Singular stress field σ_θ for $\gamma = 270$ deg and $K_{I,\lambda_1} = 1$

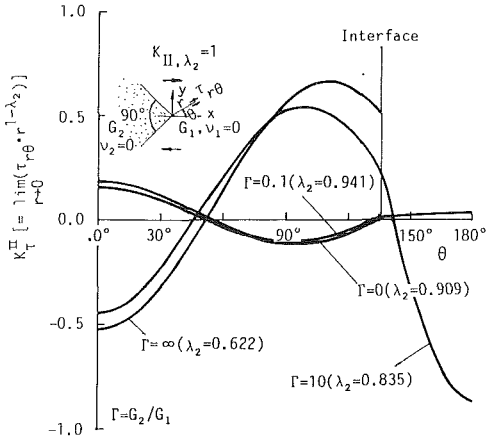

Fig. 9 Singular stress field $\tau_{r\theta}$ for $\gamma = 270$ deg and $K_{\pi,\lambda_2} = 1$

$$f^{II}_{r\theta,2}(\theta) = \frac{C_2\lambda_2}{\sqrt{2\pi}(\alpha-\beta)}\,[[\lambda_2(\alpha-\beta)\sin\{\gamma-\lambda_2(\gamma-\pi)\} - (1+\beta)\sin(\lambda_2\pi)]\times\cos\{(\lambda_2+1)(\pi-\theta)\} + [(\lambda_2-1)(\alpha-\beta)\sin\{\lambda_2(\gamma-\pi)\}]\times\cos\{(\lambda_2-1)(\pi-\theta)\}]. \quad (47)$$

In Eqs. (42)-(47) the constants C_1 and C_2 are defined by Eq. (30) and (34), respectively.

In Eq. (35) the stress field at the close vicinity of the corner is given as a sum of the symmetric state with a stress singularity of $1/r^{1-\lambda_1}$ and the skew-symmetric state with a stress singularity of $1/r^{1-\lambda_2}$, and is expressed in terms of two constants K_{I,λ_1} and K_{II,λ_2} as in the case of crack problem.

For $\gamma = 2\pi$ and $\alpha = 1$, the roots of eigen equations (10) and (11) become as $\lambda_1 = \lambda_2 = 0.5$ and Eq. (35) yields

$$\left.\begin{aligned}
\sigma_r &= \frac{K_{I,1/2}}{\sqrt{2\pi r}}\left\{\frac{5}{4}\cos\frac{\theta}{2}-\frac{1}{4}\cos\frac{3\theta}{2}\right\}+\frac{K_{II,1/2}}{\sqrt{2\pi r}}\left\{-\frac{5}{4}\sin\frac{\theta}{2}+\frac{3}{4}\sin\frac{3\theta}{2}\right\}\\
\sigma_\theta &= \frac{K_{I,1/2}}{\sqrt{2\pi r}}\left\{\frac{3}{4}\cos\frac{\theta}{2}+\frac{1}{4}\cos\frac{3\theta}{2}\right\}+\frac{K_{II,1/2}}{\sqrt{2\pi r}}\left\{-\frac{3}{4}\sin\frac{\theta}{2}-\frac{3}{4}\sin\frac{3\theta}{2}\right\}\\
\tau_{r\theta} &= \frac{K_{I,1/2}}{\sqrt{2\pi r}}\left\{\frac{1}{4}\sin\frac{\theta}{2}+\frac{1}{4}\sin\frac{3\theta}{2}\right\}+\frac{K_{II,1/2}}{\sqrt{2\pi r}}\left\{\frac{1}{4}\cos\frac{\theta}{2}+\frac{3}{4}\cos\frac{3\theta}{2}\right\}
\end{aligned}\right\} \quad (48)$$

which is in agreement with the concrete form of Eq. (1) for the crack problem in a homogeneous plate.

Figures 8 and 9 show the singular stress σ_θ and $\tau_{r\theta}$, as a function of θ, for $\gamma = 270$ and for $K_{I,\lambda_1} = 1$ and $K_{II,\lambda_2} = 1$, respectively. For $G_1 > G_2$ (G_1 corresponds to the material of the wedge with angle $\gamma > 180$ deg) one notes that the intensity of singular stress gets the maximum at $\theta = 0$ deg. However, for $G_1 < G_2$ the maximum does not occur at $\theta = 0$ deg.

References

Bogy, D. B., 1968, "Edge-bonded Dissimilar Orthogonal Elastic Wedge under Normal and Shear Loading," ASME JOURNAL OF APPLIED MECHANICS, Vol. 35, pp. 460-466.

Bogy, D. B., 1971, "On the Plane Elastostatic Problem of a Loaded Crack Terminating at a Material Interface," ASME JOURNAL OF APPLIED MECHANICS, Vol. 38, pp. 911-918.

Bogy, D. B., 1971, "Two Edge-Bonded Elastic Wedge of Different Materials and Wedge Angles Under Surface Traction," ASME JOURNAL OF APPLIED MECHANICS, Vol. 38, pp. 377-386.

Bogy, D. B., and Wang, K. C., 1971, "Stress Singularities at Interface Corners in Bonded Dissimilar Isotropic Elastic Materials," *Int. J. Solids Structures*, Vol. 7, pp. 993-1005.

Bogy, D. B., 1970, "On the Problem of Edge-Bonded Elastic Quarter-Planes Loaded at the Boundary," *Int. J. Solids Structures*, Vol. 6, pp. 1287-1313.

Dempsey, J. P., and Sinclair, G. B., 1979, "On the Stress Singularities in the Plane Elasticity of the Composite Wedge," *J. Elasticity*, Vol. 9, pp. 373-391.

Dempsey, J. P., and Sinclair, G. B., 1981, "On the Singular Behavior at the vertex of a Bi-Material Wedge," *J. Elasticity*, Vol. 11, pp. 317-327.

Dundurs, J., 1967, "Effect of Elastic Constants on Stress in a Composite under Plane Deformation," *J. Composite Materials*, Vol. 1, pp. 310-322.

Dundurs, J., 1969, discussion, 1969, ASME JOURNAL OF APPLIED MECHANICS, Vol. 36, pp. 650-652.

Hein, V. L., and Erdogan, F., 1971, "Stress Singularities in a Two-Material Wedge," *Int. J. Fracture Mech.*, Vol. 7, pp. 317-330.

Theocaris, P. S., 1974, "The Order of Singularity at a Multi-Wedge Corner of a Composite Plate," *Int. J. Enging. Sci.*, Vol. 12, pp. 107-120.

Williams, M. L., 1952, "Stress Singularities Resulting from Various Boundary Conditions in Angular Corners of Plates in Extension," ASME JOURNAL OF APPLIED MECHANICS, Vol. 19, pp. 526-528.

M. Grédiac
Mem. ASME

A. Vautrin

G. Verchery
Mem. ASME

Département Mécanique et Matériaux,
Ecole des Mines de Saint-Etienne,
42023 Saint-Etienne Cedex 2, France

A General Method for Data Averaging of Anisotropic Elastic Constants

Redundant experimental data are usually required to determine the best value for the whole set of compliances of an anisotropic laminate. A method is presented here to optimize the compliance tensor values using the five invariants of fourth-rank compliance tensors. A vectorial representation of those invariants is given. It provides a compact presentation of the data and reveals the experimental scatter. Experimental data obtained with bending tests on plates are used as an example to optimize the flexural compliance tensor of a laminate and to show the relevance of the method in practice.

1 Introduction

Several tests are required to assess the validity of a constitutive law of anisotropic composite materials. When a material is isotropic, the number of independent constants is only 2 within the framework of linear elasticity. For orthotropic plates, this number increases to 4. In the usual case of uncoupled multidirectional laminates, the independent stiffness or compliance components are as many as 12 (Tsai and Hahn, 1980): six in-plane and six flexural stiffnesses or compliances. Characterizing these 12 quantities is the challenge which must be faced before designing with composite materials; it will be all the more difficult because anisotropy induces particular parasitic effects (Pindera and Herakovich, 1982, for instance), which are to be taken into account through the use of suitable experimental tests and data treatments. For example, the in-plane compliance tensor of an anisotropic composite material can be obtained by several tensile tests performed in different directions, which lead to more quantities than coefficients to be identified. The unknown compliances are then optimized by means of these redundant data. However, conventional methods of analysis do not always take full advantage of the tensorial nature of these quantities.

In fact, the true goal is not really to assess and to optimize the compliances, but to optimize the fourth-rank compliance tensor itself, which is the mathematical tool describing the elastic behavior of the laminate. Rather than considering the compliances, which are extrinsic parameters for anisotropic materials, it is more relevant to use the invariants of the tensor which do not depend on the choice of axes and can therefore be regarded as intrinsic parameters. Hence, the rigorous procedure for optimization of compliance measurements presented here is performed by relevant operations on the whole set of compliance tensor invariants.

The polar representation of fourth-rank compliance tensors is first described. This representation is then used to define a norm and a deviation function involving the experimental data. Minimizing this function provides the optimized invariants. Finally, the method is used to average a set of experimental data.

2 Theoretical Analysis

2.1 Introduction. Only a few papers deal with the practical optimization of experimental anisotropic compliance data. In these, the tensorial nature of the Hooke's law relations of anisotropic materials is not strictly and completely taken into account. A first approach was given by Wu et al. (1973), but it can only be used for orthotropic materials. Vong and Verchery (1980) proposed a simple procedure based on the least squares method that does not require all the components of the tensor in each test configuration. In this latter case, the tensorial nature of the compliances only appears in their transformation equations and not in terms of invariants.

The method presented here is a rigorous approach of optimization through the use of the whole set of five invariants of the fourth-rank compliance tensors. It uses a polar representation of fourth-rank tensors, which clearly reveals the distance between experimental and optimized sets of data, and characterizes the type of anisotropy.

2.2 The Polar Representation of Fourth Rank Tensors. The theory of polar representation of tensors was developed and applied by Verchery and his co-workers, extending results for elasticity tensors obtained by Tsai in the 1960s and detailed by Tsai and Hahn (1980). The theory was presented by Verchery and Vong (1986). An English presentation of the essential points can be found in Kandil and Verchery (1989).

Contributed by the Applied Mechanics Division of THE AMERICAN SOCIETY OF MECHANICAL ENGINEERS for presentation at the First Joint ASCE-EMD, ASME-AMD, SES Meeting, Charlottesville, VA, June 6-9, 1993.

Discussion on this paper should be addressed to the Technical Editor, Professor Lewis T. Wheeler, Department of Mechanical Engineering, University of Houston, Houston, TX 77204-4792, and will be accepted until four months after final publication of the paper itself in the ASME JOURNAL OF APPLIED MECHANICS.

Manuscript received by the ASME Applied Mechanics Division, July 18, 1991; final revision, Oct. 23, 1992. Associate Technical Editor: W. N. Sharpe.

Paper No. 93-APM-26.

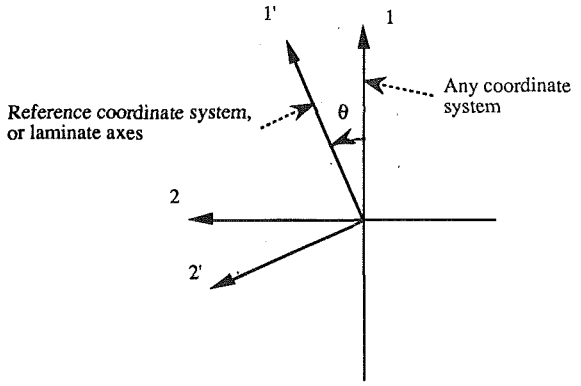

Fig. 1 Rotation of the coordinate system

The general constitutive equations for uncoupled laminates between the in-plane strain components ϵ^0, the curvatures k, the in-plane stress resultants N, and the moment components M can be written in the following form (Tsai and Hahn, 1980):

$$\begin{pmatrix} \mathbf{N} \\ \mathbf{M} \end{pmatrix} = \begin{pmatrix} \mathbf{A} & 0 \\ 0 & \mathbf{D} \end{pmatrix} \begin{pmatrix} \epsilon^0 \\ k \end{pmatrix}. \tag{1}$$

From an experimental point of view, the components of the two 3×3 stiffness matrices **A** and **D** are not directly measured. In fact, suitable tensile or bending tests provide their inverses which can be rewritten using the normalized form suggested by Tsai (1988): $h\mathbf{A}^{-1}$ and $h^3/12\ \mathbf{D}^{-1}$, h being the thickness of the laminate. Both of them are normalized compliance matrices denoted **S** in the following.

Because of the anisotropy of the laminates, compliances are tensor components and depend on the choice of axes. They can be expressed as a function of different invariant parameters and the angle θ depicted in Fig. 1 between the chosen axes and the frame of reference (Kandil and Verchery, 1989). Using the contracted notation with two subscripts (Tsai, 1988):

$$\begin{aligned}
S_{11} &= T_0 + 2T_1 + R_0\cos 4a_0 + 4R_1\cos 2a_1 \\
S_{22} &= T_0 + 2T_1 + R_0\cos 4a_0 - 4R_1\cos 2a_1 \\
S_{12} &= -T_0 + 2T_1 - R_0\cos 4a_0 \\
S_{66} &= 4(T_0 - R_0\cos 4a_0) \\
S_{16} &= 2(R_0\sin 4a_0 + 2R_1\sin 2a_1) \\
S_{26} &= 2(-R_0\sin 4a_0 + 2R_1\sin 2a_1)
\end{aligned} \tag{2}$$

T_0, T_1, R_0, and R_1 remain invariant under change of frame while a_0 and a_1 are changed into $a_0 + \theta$ and $a_1 + \theta$. T_0, T_1, R_0, R_1, and $a_0 - a_1$ are therefore the five independent invariants of a fourth-rank tensor of Hooke's law relations. They can be considered as intrinsic parameters that fully describe the tensor. A sixth parameter θ must be given in order to compute six compliances that are extrinsic, i.e., dependent on the coordinate system characterized by θ.

Intrinsic and extrinsic parameters must be clearly distinguished here. In the common case of isotropic materials, the compliances are intrinsic parameters and it is not relevant to consider other parameters. On the other hand, compliances of anisotropic materials are dependent on the choice of axes. Hence, they do not characterize the intrinsic nature of the material, whereas the five invariants fully define the type of material anisotropy. For instance, a square symmetry induces $R_1 = 0$, orthotropy is equivalent to $a_0 = a_1 + k\,45$ deg (where k is an integer) and isotropy to $R_0 = R_1 = 0$. As a result, one can detect whether a material is orthotropic and can easily find the orthotropy axes defined by angle a_1. By contrast, a set of six compliances expressed in axes different from the orthotropy directions does not allow this determination.

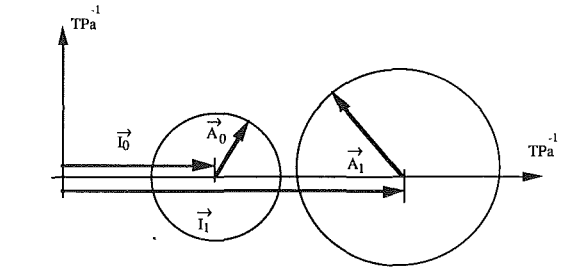

a- Vectors and generalized Mohr's circles

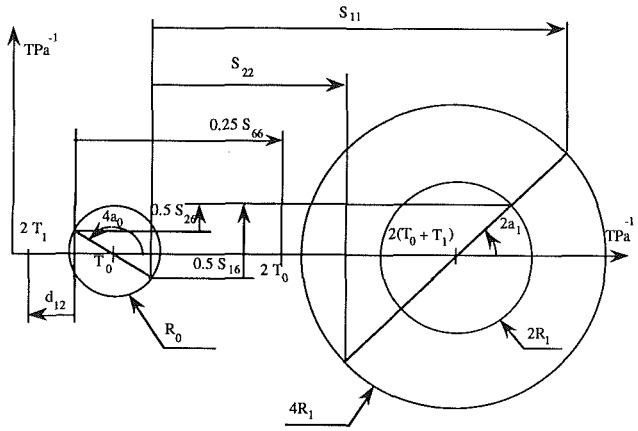

b- Generalized Mohr's circles

Fig. 2 Vectors and generalized Mohr's circles for the compliances

Equations (2) can easily be inverted to give the following quantities called "polar components":

$$\left.\begin{aligned} T_0 &= \frac{1}{8}(S_{11} + S_{22} - 2S_{12} + S_{66}) \\ T_1 &= \frac{1}{8}(S_{11} + S_{22} + 2S_{12}) \end{aligned}\right\} \text{ isotropic components}$$

$$\left.\begin{aligned} R_0 e^{4ia_0} &= \frac{1}{8}(S_{11} + S_{22} - 2S_{12} - S_{66} + 2i(S_{16} - S_{26})) \\ R_1 e^{2ia_1} &= \frac{1}{8}(S_{11} - S_{22} + i(S_{16} + S_{26})) \end{aligned}\right\}$$

anisotropic components. (3)

Two of them are real, and characterize the isotropic part of the constitutive law, the other two are complex and define the anisotropic part, which reduces to zero when the material is isotropic.

In the complex plane, the polar components can be fully and compactly represented by four vectors $\vec{I}_0$, $\vec{I}_1$, $\vec{A}_0$, and $\vec{A}_1$, defined by:

$$\vec{I}_0 \begin{pmatrix} T_0 \\ 0 \end{pmatrix} \qquad \vec{I}_1 \begin{pmatrix} 2(T_0 + T_1) \\ 0 \end{pmatrix} \quad \text{for the isotropic part}$$

$$\vec{A}_0 \begin{pmatrix} R_0\cos 4a_0 \\ R_0\sin 4a_0 \end{pmatrix} \quad \vec{A}_1 \begin{pmatrix} 4R_1\cos 2a_1 \\ 4R_1\sin 2a_1 \end{pmatrix} \quad \text{for the anisotropic part}$$

In a rotation of the axes through θ, $\vec{I}_0$, and $\vec{I}_1$ remain constant while $\vec{A}_0$ and $\vec{A}_1$ rotate through 4θ and 2θ, respectively. One can plot two circles with the tip of the two vectors $\vec{A}_0$ and $\vec{A}_1$ (Fig. 2(*a*)). They can be considered as Mohr's circles that generalize the familiar Mohr's circle of stress. In the present case, we have a second circle with an angular rotation four

times that of the coordinate axes. As for the stress components, the compliances are provided by graphical constructions plotted in Fig. 2(*b*)). These graphical interpretation of the compliances is directly related to Eqs. (2). Such generalized Mohr's circles are also used by other authors (Wu, Jerina, and Lavengood (1973), Tsai and Hahn (1980) for instance), but with different locations of the circle centers, because this choice is arbitrary.

2.3 Distance Between Two Tensors. Comparison of the elastic properties of two laminates is usually performed through a term-by-term comparison of the compliances or stiffnesses of both materials. However, this method cannot be considered as appropriate for anisotropic materials because those parameters depend on the choice of the coordinate system. For instance, some of the compliances $S_{\alpha\beta}$ of two different materials can be equal in a particular frame and different in another one. The approach suggested below does not depend on the coordinate system where the calculations are performed. It is proposed to reduce the comparison of two sets of six compliances referred to the same axes to a single scalar called distance. The characterization of the difference of two tensors will obviously allow a global comparison of any two materials.

From the four polar components defined above, it is easy to compute a distance between two tensors $\mathbf{S}$ and $\mathbf{S}'$. First, a norm $N(\mathbf{S})$ is defined as the square root of the sum of the squares of the norms of the four vectors:

$$N(\mathbf{S}) = [|\vec{I}_0|^2 + |\vec{I}_1|^2 + |\vec{A}_0|^2 + |\vec{A}_1|^2]^{1/2}. \quad (4)$$

The norm is therefore related to the lengths of the four vectors.

Introducing the polar components,

$$N(\mathbf{S}) = [(T_0)^2 + 4(T_0 + T_1)^2 + |R_0 e^{4ia_0}|^2 + 16|R_1 e^{2ia_1}|^2]^{1/2}. \quad (5)$$

The angular components have no influence, i.e., the norms are invariant under changes of the reference frame. $N(\mathbf{S})$ can therefore be considered as an intrinsic parameter characterizing $\mathbf{S}$.

Secondly, the distance between two tensors $\mathbf{S}$ and $\mathbf{S}'$ can be defined as the norm of the difference between the two tensors $\mathbf{S}$ and $\mathbf{S}'$. Obviously, $\mathbf{S}$ and $\mathbf{S}'$ components must be expressed in the same reference frame in order to define an intrinsic distance.

Introducing the polar components,

$$N(\mathbf{S}-\mathbf{S}') = [(T_0 - T_0')^2 + 4(T_0 + T_1 - T_0' - T_1')^2 + |R_0 e^{4ia_0} - R_0' e^{4ia_0'}|^2 + 16|R_1 e^{2ia_1} - R_1' e^{2ia_1'}|^2]^{1/2}. \quad (6)$$

Two tensors $\mathbf{S}$ and $\mathbf{S}'$ are equal if and only if $N(\mathbf{S} - \mathbf{S}')$ is equal to zero. In this case, the two sets of four vectors are the same. In the complex plane (Fig. 2), this means that the generalized Mohr's circles representing $\mathbf{S}$ and $\mathbf{S}'$ are the same and that the angular components a_0 and a_0' as well as a_1 and a_1' are equal.

One can define the relative deviation between two tensors as the ratio:

$$\epsilon = \frac{\mathbf{N}(\mathbf{S}-\mathbf{S}')}{\mathbf{N}(\mathbf{S})} \quad (7)$$

This nondimensional quantity is well suited to quantify the difference between the two tensors. In particular, if ϵ is small, the two tensors $\mathbf{S}$ and $\mathbf{S}'$ can be considered as close to one another and the two materials will therefore have approximately the same global mechanical response. This quantity can therefore be used to assess the global scatter of experimental results, $\mathbf{S}'$ being the tensor determined from a set of six experimental compliances in a particular coordinate system and $\mathbf{S}$ being the optimized tensor.

2.4 Optimization. Within the framework of data optimization, one can define a deviation function between an optimized tensor $\mathbf{S}^{\text{optimized}}$ and n tensors $\mathbf{S}^j$ ($j = 1 \ldots n$) called measured tensors, whose components are determined through mechanical tests carried out on coupons cut in the same laminate. The deviation function is the sum of the squares of the distances between the optimized tensor and the different measured tensors. As specified previously, all tensor components must be provided in the same frame to avoid any material rotation from one configuration to another. $\mathbf{S}^j$ must therefore be expressed in the reference frame rotated through θ^j from the coordinate system j where the experiments were performed. Each measured tensor expressed in frame j is defined by $\vec{I}_0^j$, $\vec{I}_1^j$, $\vec{A}_0^j$ and $\vec{A}_1^j$. In the reference frame, it is defined by $\vec{I}_0^j$, $\vec{I}_1^j$, $\vec{A}_0'^j$ and $\vec{A}_1'^j$. As specified above, $\vec{A}_0'^j$ and $\vec{A}_1'^j$ are rotated, respectively, through $-4\theta^j$ and $-2\theta^j$ from $\vec{A}_0^j$ and $\vec{A}_1^j$. The deviation function can be expressed as follows:

$$E = \sum_{j=1}^{n} [N(\mathbf{S}^{\text{optimized}} - \mathbf{S}^j)]^2 \quad (8)$$

In terms of vectors, the deviation function becomes

$$E = \sum_{j=1}^{n} [|\vec{I}_0 - \vec{I}_0^j|^2 + |\vec{I}_1 - \vec{I}_1^j|^2 + |\vec{A}_0 - \vec{A}_0'^j|^2 + |\vec{A}_1 - \vec{A}_1'^j|^2]. \quad (9)$$

All those sets of four vectors characterizing the same anisotropic laminate must be approximately the same after rotation of the tensor components through $-\theta^j$.

Using the polar components,

$$E = \sum_{j=1}^{n} [(T_0 - T_0^j)^2 + 4(T_0 + T_1 - T_0^j - T_1^j)^2 + |R_0 e^{4ia_0} - R_0^j e^{4i(a_0^j - \theta^j)}|^2 + 16|R_1 e^{2ia_1} - R_1^j e^{2i(a_1^j - \theta^j)}|^2]. \quad (10)$$

Each set of six components T_0^j, T_1^j, R_0^j, R_1^j, a_0^j, a_1^j is obtained through Eq. (3) from a set of six experimental compliances $S_{\alpha\beta}^j$ measured with appropriate mechanical tests in the axes j.

The best fit of n measurements can then be obtained by finding the minimum of E, which gives the optimized tensor defined by T_0, T_1, R_0, R_1, a_0 and a_1, i.e.,

$$\frac{\partial E}{\partial T_0} = \frac{\partial E}{\partial T_1} = \frac{\partial E}{\partial R_0} = \frac{\partial E}{\partial R_1} = \frac{\partial E}{\partial a_0} = \frac{\partial E}{\partial a_1} = 0 \quad (11)$$

Differentiation of Eq. (10) provides the optimized components.

$$T_0 = \frac{1}{n}\sum_{j=1}^{n} T_0^j \quad T_1 = \frac{1}{n}\sum_{j=1}^{n} T_1^j$$

$$R_0 = \frac{1}{n}\sum_{j=1}^{n} R_0^j \cos[4(a_0 - a_0^j + \theta^j)]$$

$$R_1 = \frac{1}{n}\sum_{j=1}^{n} R_1^j \cos[2(a_1 - a_1^j + \theta^j)]$$

$$tg(4a_0) = \left\{\sum_{j=1}^{n} R_0^j \sin[4(a_0^j - \theta^j)]\right\} \Big/ \left\{\sum_{j=1}^{n} R_0^j \cos[4(a_0^j - \theta^j)]\right\}$$

$$tg(2a_1) = \left\{\sum_{j=1}^{n} R_1^j \sin[2(a_1^j - \theta^j)]\right\} \Big/ \left\{\sum_{j=1}^{n} R_1^j \cos[2(a_1^j - \theta^j)]\right\}. \quad (12)$$

It can be noted that T_0 and T_1 are the direct averages of the corresponding experimental values. $\vec{I}_0$ and $\vec{I}_1$ are therefore directly the average of the corresponding experimental vectors $\vec{I}_0^j$ and $\vec{I}_1^j$, $j = 1 \ldots n$. On the other hand, R_0 and R_1 are, respectively, weighted by $\cos[4(a_0 - a_0^j + \theta^j)]$ and $\cos[2(a_1 -$

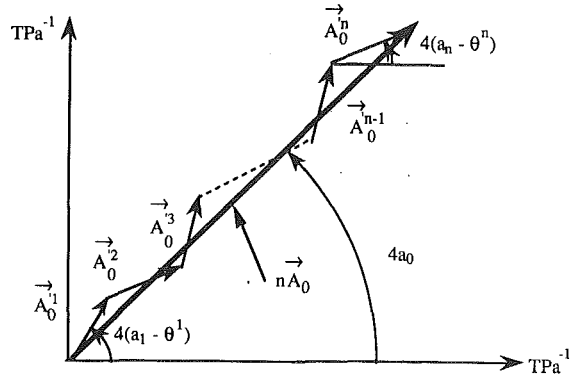

Fig. 3 Optimized vector $n\vec{A}_0$

$a_1^j + \theta^j)]$. This distinguishes the present treatment from that of Wu et al. (1973) who did not take into account the angles. In fact, the present procedure reduces to two averages of real numbers (the isotropic parts) and two averages of complex numbers (the anisotropic parts). Angular quantities are therefore involved in these two latter averages.

The average of the complex numbers is geometrically interpreted as an average of their associated vectors in the complex plane. This procedure is depicted in Fig. 3. The n vectors $\vec{A}_0'^j$ are plotted in sequence: the tip of one is joined to the tail of the other. The optimized vector $\vec{A}_0$ is the average of the n experimental vectors $\vec{A}_0'^j$. $\vec{A}_1$ is also obtained through a similar construction.

In conclusion, it can be written

$$\vec{I}_0 = \frac{1}{n}\sum_{j=1}^{n} \vec{I}_0^j \quad \vec{I}_1 = \frac{1}{n}\sum_{j=1}^{n} \vec{I}_1^j$$

$$\vec{A}_0 = \frac{1}{n}\sum_{j=1}^{n} \vec{A}_0'^j \quad \vec{A}_1 = \frac{1}{n}\sum_{j=1}^{n} \vec{A}_1'^j. \tag{13}$$

The two vectorial averages of $\vec{I}_0$ and $\vec{I}_1$ are obviously equivalent to two scalar averages of T_0 and T_1, as the imaginary part of the isotropic components in Eq. (3) is zero. Such a simplification cannot be performed for $\vec{A}_0$ and $\vec{A}_1$.

3 Application to the Averaging of Experimental Data

Bending tests have been carried out on a 16-ply $[0_2, 90_2]_{2S}$ symmetric glass/epoxy laminate. The experimental procedure is not described here. More details can be found in Grédiac and Vautrin (1990a) and (1990b). The tests were performed in different directions to measure the six flexural compliances in ten coordinate systems defined by the angle θ^j (j = 1 to 10). The increment from one configuration to another is -10 deg. The 0 direction coincides with the direction of the fibers of the external ply. Hence, the (0, 90) frame is expected to coincide with the orthotropy directions. Tables 1 and 2 respectively show the experimental values of the normalized flexural compliances of the plate specimen, and the invariants computed using Eq. (3).

It is apparent that a_0^j and a_1^j decreases as $-\theta^j$ increases. As expected, T_0^j, T_1^j, R_0^j, R_1^j remain approximately constant. The difference $a_0^j - a_1^j$ should be constant. However, it shows a large scatter due to the poor accuracy of a_1^j, the vector $\vec{I}_1^j$ being shorter than $\vec{I}_0^j$. Nevertheless, one can consider that the average value of this difference is realistic. The optimized components are shown in Table 3. The fifth invariant $a_0 - a_1$ is equal to -42.2 deg. Hence, the material can be regarded as "nearly orthotropic." This is due to the fact that $a_0 - a_1 = k\,45$ deg

Table 1 Experimental compliances

$-\theta^j$ deg.	S_{11} TPa^{-1}	S_{22} TPa^{-1}	S_{12} TPa^{-1}	S_{66} TPa^{-1}	S_{16} TPa^{-1}	S_{26} TPa^{-1}
0	32.4	50.4	-9.7	292.8	4.6	-5.1
10	36.7	58.0	-17.1	274.6	30.7	-30.0
20	52.6	70.3	-30.9	222.6	47.2	-42.6
30	71.7	79.9	-52.0	150.9	46.8	-28.0
40	84.5	91.5	-62.4	108.0	24.2	-8.9
50	85.2	86.9	-60.8	109.2	-7.5	23.6
60	88.4	72.0	-41.9	153.9	-33.5	44.4
70	65.1	57.4	-27.3	232.7	-42.9	45.7
80	65.7	37.6	-19.0	280.4	-35.4	29.8
90	50.4	31.1	-10.4	300.0	0.0	-11.9

Table 2 Invariants

$-\theta^j$ deg.	T_0^j TPa^{-1}	T_1^j TPa^{-1}	R_0^j TPa^{-1}	R_1^j TPa^{-1}	a_0^j deg.	a_1^j deg.	$a_0^j - a_1^j$ deg.
0	49.4	7.92	23.9	2.25	43.5	90.7	-47.1
10	50.4	7.58	23.8	2.66	35.0	89.1	-54.0
20	50.9	7.65	22.9	2.29	25.5	82.3	-57.2
30	50.8	5.94	23.1	2.73	13.9	52.0	-42.0
40	51.1	6.40	25.5	2.10	4.73	57.2	-52.5
50	50.4	6.32	24.3	2.02	-4.67	47.9	-52.6
60	49.7	9.56	22.5	2.46	-15.0	16.8	-31.8
70	51.2	8.48	23.2	1.04	-26.9	10.1	-37.0
80	52.7	8.17	23.8	3.59	-34.2	-5.63	-28.6
90	50.3	7.62	24.8	2.83	-46.7	-15.8	-30.9

Table 3 Optimized components

	T_0 TPa^{-1}	T_1 TPa^{-1}	R_0 TPa^{-1}	R_1 TPa^{-1}	a_0 deg.	a_1 deg.	$a_0 - a_1$ deg.
present method	50.7	7.57	23.8	2.22	44.5	87.1	-42.2
method of Wu et al.	50.7	7.57	23.8	2.35	n. p.	n. p.	n. p.

n. p. : not provided

(where k is an integer) is the relation characterizing orthotropic materials. The directions of orthotropy are given by a_1. In the present case, the "best" directions of orthotropy are rotated through 90 − 87.1 = 2.9 deg from the reference frame.

The experimental data are plotted in Figs. 4 and 5. Each set of six experimental results is illustrated by the four vectors $\vec{I}_0^j$, $\vec{I}_1^j$, $\vec{A}_0^j$, $\vec{A}_1^j$. For convenience, only $\vec{A}_0^j$ and $\vec{A}_1^j$ have been plotted in Fig. 4, but note that the origins of the vectors are not located at the same point because of the scatter in the length of $\vec{I}_0^j$, $\vec{I}_1^j$. The scatter of experimental results is clearly illustrated in this figure. Regularly orientated and constant-length vectors would show a very accurate experimental procedure. The left-hand set of vectors in Fig. 4 is more regular than the right-hand one. It is suggested that the main reason is the small value of R_1 (2.22 TPa^{-1}), which is therefore not identified with the same accuracy as R_0 (23.8 TPa^{-1}).

Figure 5 provides the four optimized vectors as well as the optimized Mohr's circles. The tips of the vectors $\vec{A}_0^j$ and $\vec{A}_1^j$ are plotted. One can see the good agreement between experimental data and optimized Mohr's circles.

The scatter between the experimental sets of vectors and the optimized ones is assessed using the relative deviation ϵ given by Eq. (7). Figure 6 provides ϵ as a function of the angle $-\theta^j$. The relative deviation remains less than ten percent, and the magnitude of ϵ can easily be related to Figs. 4 and 5. For instance, $\vec{A}_1^j$ at $\theta^j = -80$ deg is not really in agreement with

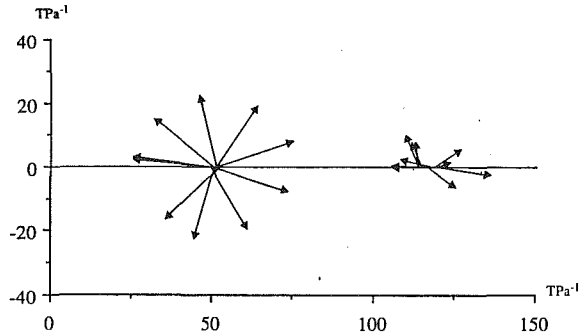

Fig. 4 Experimental vectors $\vec{A}_0^j$ and $\vec{A}_1^j$, $j = 1 \ldots 10$

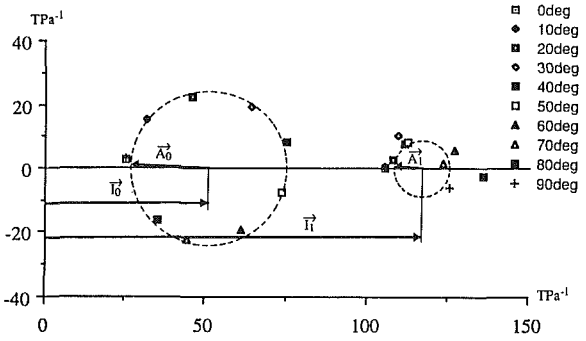

Fig. 5 Optimized vectors $\vec{I}_0$, $\vec{I}_1$, $\vec{A}_0$, $\vec{A}_1$ and generalized Mohr's circles

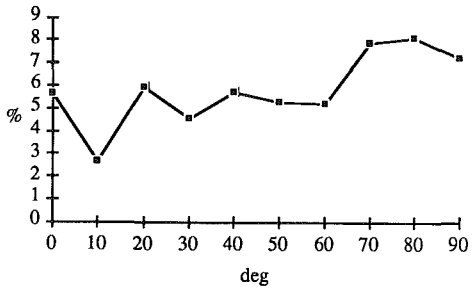

Fig. 6 Relative deviation of experimental data

the right-hand circle and one can observe that ϵ is highest for this angle. One could improve this procedure by selecting the most relevant experimental configurations that provide a low value of the relative deviation ϵ, and removing the experimental data characterized by a high value of ϵ (Babut and Brandt, 1977).

Optimized components computed using the present method and the method given by Wu et al. (1973) are compared in Table 3. As may be seen, this latter method provides a good assessment of the radii R_0 and R_1 even if the angular scatter is ignored. However, the angular components a_0 and a_1 cannot be computed. Finally, one can calculate the optimized compliances using Eq. (2). These values are provided in the reference frame (Table 4). The shear coupling compliances S_{16} and S_{26} are close to zero. Hence, it is verified that the plate is approximately orthotropic.

Table 4 Optimized compliances in the reference frame

S_{11} TPa^{-1}	S_{22} TPa^{-1}	S_{12} TPa^{-1}	S_{66} TPa^{-1}	S_{16} TPa^{-1}	S_{26} TPa^{-1}
33.2	50.9	-11.7	297.9	2.6	-0.7

4 Conclusion

In this paper, a rigorous process for averaging experimental compliances of composite materials has been presented. It is based on the use of the polar representation of fourth-rank compliance tensors and consists in minimizing a deviation function.

Strictly speaking, an anisotropic elastic law is completely characterized by five independent invariants that are here used to optimize the anisotropic elastic constitutive law. Because of their intrinsic nature, these quantities should certainly be more often used to represent and to characterize composite materials.

Acknowledgment

The Ministère de la Défense is gratefully acknowledged for the financial support provided for a part of this work (DRET grant 88/1208).

The authors would like to thank Dr. M. Phillips of the University of Bath (UK) for helpful comments on the final version of the present paper.

References

Babut, R., and Brandt, A. M., 1977, "Measurement of Internal Strains by Nine-Gauge Devices," *Strain*, N. 1, pp. 18–21.

Grédiac, M., and Vautrin, A., 1990a, "A New Method for Determination of Bending Rigidities of Thin Anisotropic Plates," ASME JOURNAL OF APPLIED MECHANICS, Vol. 57, pp. 964–968.

Grédiac, M., and Vautrin, A., 1990b, "Measurement of Laminate Elastic Parameters from Non-Uniform Strain Fields," *Mechanical Identification of Composites*, edited by A. Vautrin and H. Sol, eds., Elsevier Applied Sciences, pp. 91–98.

Kandil, N., and Verchery, G., 1989, "Some New Developments in the Design of Stacking Sequences of Laminates," *Proceedings of the 7th International Conference on Composite Materials* (ICCM 7), Vol. 3, pp. 358–363.

Pindera, M.-J., and Herakovich, C. T., 1982, "Shear Characterization of Unidirectional Composites with the Off-Axis Tension Test," *Experimental Mechanics*, Vol. 22, N. 1, pp. 103–112.

Tsai, S. W., and Hahn, H. T., 1980, *Introduction to Composite Materials*, Technomic Publishing Co., Westport, CT.

Tsai, S. W., 1988, *Composite Design*, 4th ed., Think Composites, Dayton, OH.

Vong, T. S., and Verchery, G., 1980, "Optimal Use of Redundant Measurements of Constrained Quantities. Application to Elastic Moduli of Anisotropic Composite Materials," *Proceedings of the 3rd International Conference on Composite Materials* (ICCM 3), Vol. 2, pp. 1783–1795.

Vong, T. S., and Verchery, G., 1986, "Graphical Aided Design of Stacking Sequences for Laminates," (in French with English summary), *Proceedings of the 5th French Conference on Composites Materials* (JNC 5), C. Bathias and D. Menkès, eds., Pluralis, Paris, pp. 267–280.

Wu, E. M., Jerina, K. L., and Lavengood, R. E., 1973, "Data Averaging of Anisotropic Composite Material Constants," *Analysis of Test Methods for High Modulus Fibers and Composites*, ASTM SPT 521, pp. 229–252.

Finite Deformation Constitutive Relations for Elastic-Plastic Fibrous Metal Matrix Composites

N. Fares
Civil Engineering Department,
Polytechnic University,
Brooklyn, NY 11201

G. J. Dvorak
Civil Engineering Department,
Rensselaer Polytechnic Institute,
Troy, NY 12180
Fellow ASME.

This paper presents a finite strain formulation of a plasticity theory of fibrous composite materials. An additive decomposition is adopted to describe the kinematics of large deformations; a lattice is defined by the current fiber direction. Elastic and plastic constitutive relations are developed from the proposition that distortions take place relative to the fiber direction. A numerical method is proposed for integrating the constitutive equations. Finally, an illustrative example of the formulation indicates that when axial loads along the fiber direction are comparable to the instantaneous shear stiffness, the finite deformation formulation is needed even with small strains.

Introduction

Elastic-plastic behavior of metal-matrix composites reinforced by continuous fibers has been investigated in many theoretical and experimental studies in recent years (Dvorak and Bahei-El-Din, 1979, 1982, 1987; Dvorak and Teply, 1985; Teply and Dvorak, 1988; Dvorak et al., 1988). These studies considered infinitesimal deformation formulations in view of the high stiffness and relatively low ductility of fibrous metal matrix composites as, for example, compared to ductile polycrystalline metals. However, due to the anisotropy of fibrous composites and the existence of preferential modes of low hardening plastic flow, a finite deformation formulation may be needed. This is due to the possible pronounced geometric hardening or softening that may occur with the reorientation of these modes under deformation-induced rotations. This is consistent with observations made in the literature concerning the need for finite deformation formulations in constitutive studies (Rice, 1970), finite element studies (McMeeking and Rice, 1974) and in localization studies (Rudnicki and Rice, 1975; Asaro and Rice, 1977; Rice, 1976). These observations are especially pertinent when strains are magnified by such stress concentrators as notches and cracks. For example, the Moire patterns of Post et al. (1988) show experimental evidence of large strains and the localization at and away from notch tips in boron-aluminum fibrous composite plates.

Finite deformation elastic-plastic constitutive relations have recently received considerable attention in the literature. Spencer (1984) and Fares and Dvorak (1989) studied the behavior of metal matrix fibrous composites. Christoffersen et al. (1981) and Nemat-Nasser (1983) studied plastic flow of granular and geomaterials. Hill and Rice (1972), Asaro and Rice (1977), and Pierce et al. (1982) considered the finite deformation of single crystals, while Lee (1969), Agah-Tehrani et al. (1987) and Lee and Agah-Tehrani (1988), Iwakuma and Nemat-Nasser (1984), among others, studied such deformations in polycrystalline metals. The single crystal studies were particularly influential in clarifying the structure of constitutive relations at finite deformations. Especially important was the concept of a lattice capable of rotating by an elastic spin which may be different from the spin derived from the antisymmetric part of the velocity gradient. The specific manner in which the lattice rotates effectively leads to a distinct constitutive relation (Asaro and Rice, 1977). In polycrystalline metals, this concept has led to a discussion of the constitutive specification of the plastic spin (Dafalias, 1984). The particular choice of lattice deformation has to be physically motivated by the microstructure (and experimentally verified) and cannot be fully determined by fundamental postulates such as the principle of material frame indifference (objectivity) or by conservation laws.

Fares and Dvorak (1989) considered a multiplicative decomposition (Lee, 1969) of the deformation gradient in formulating constitutive relations for fibrous metal matrix composites. The multiplicative decomposition facilitates the visualization of the deformation by introducing a relaxed, intermediate configuration represented by the plastic part of the deformation gradient. However, there are theoretical as well as practical reasons why an additive decomposition of the velocity gradient is preferred (Nemat-Nasser, 1981). Thus, we use an additive decomposition in the present formulation. We note, however, that both decompositions lead to approximately the same results when the elastic strains are small. As in the multiplicative decomposition, the choice of stress rates have to be carefully chosen (Dienes, 1979; Nagtegaal and deJong, 1982; Lee et al.,

Contributed by the Applied Mechanics Division of THE AMERICAN SOCIETY OF MECHANICAL ENGINEERS for publication in the ASME JOURNAL OF APPLIED MECHANICS.

Discussion on this paper should be addressed to the Technical Editor, Professor Lewis T. Wheeler, Department of Mechanical Engineering, University of Houston, Houston, TX 77204-4792, and will be accepted until four months after final publication of the paper itself in the ASME JOURNAL OF APPLIED MECHANICS.

Manuscript received by the ASME Applied Mechanics Division, Aug. 15, 1990; final revision, Apr. 23, 1992. Associate Technical Editor: L. M. Keer.

1983; Dafalias, 1983) but they follow from the physical assumptions.

The present work is concerned with the constitutive framework of finite elastic-plastic deformations of fibrous, metal matrix composites. A plane stress formulation is adopted which is appropriate to single or multiple (usually around 7) ply unidirectional materials. Laminated plate response may then be deduced from ply behavior and suitable lamination theories. The physical assumptions on which the constitutive framework is based is first discussed. These assumptions are motivated by analytical and experimental studies of the matrix-dominated mode (MDM) of plastic deformation of fibrous composites (Dvorak and Bahei-El-Din, 1987; Dvorak et al., 1988). We then describe the kinematics with emphasis on the fiber rotation and the elastic and plastic strain measures, the appropriate rates of field variables such as stress, and the specification of elastic and plastic constitutive relations. Next, we discuss the manner in which these constitutive relations may be integrated when given a deformation gradient history. We then present the elastic-plastic stiffness in a form suitable for implementation in a large deformation finite element program. Finally, we present some simulations under specific loading histories emphasizing the role of the finite deformation formulation in comparison with an infinitesimal deformation formulation.

Formulation

(i) Notation. In our discussions we will use the same fixed Cartesian frame to locate points in both the reference and deformed configurations. Vectors and tensors will be written in boldface letters and components of those will be written in normal type and indexed. The position vector to a material point in the reference and current configurations will be denoted by $\mathbf{X}$ and $\mathbf{x}$, respectively. We will also use the summation convention for repeated indices, comma notation for partial differentiation with respect to position, an overhead dot to denote a material time derivative, and a superscript "T" on a second-order tensor to mean a transpose.

(ii) Physical Assumptions. An additive decomposition of the velocity gradient will be adopted. Thus we have

$$\mathbf{L} = \mathbf{L}^e + \mathbf{L}^p. \tag{1}$$

Implicit in such a decomposition is that the elastic part of the velocity gradient contributes to an elastic constitutive relation. In particular, we will assume that the stress power formed between Cauchy stress and the elastic part of the velocity gradient contributes to an elastic potential. Thus a Green elastic or hyperelastic constitutive relation is assumed. Specifically,

$$\dot{W}(\mathbf{E}^e) = J^e \sigma\colon\ \mathbf{L}^e = J^e \sigma\colon\ \mathbf{D}^e = J^e \sigma_{ij} D^e_{ij} \tag{2}$$

$$\mathbf{E}^e = \frac{1}{2}\left(\mathbf{F}^{eT}\cdot\mathbf{F}^e - \mathbf{I}\right) \tag{3}$$

$$J^e = \det(\mathbf{F}^e) \tag{4}$$

$$\dot{\mathbf{F}}^e = \mathbf{L}^e\cdot\mathbf{F}^e \tag{5a}$$

$$\mathbf{F}^e|_{t=0} = \mathbf{I}. \tag{5b}$$

Equations (5) define an evolution equation from which $\mathbf{F}^e$ may be determined from $\mathbf{L}^e$. $\mathbf{F}^e$ coincides with the deformation gradient $\mathbf{F}$ if the material is purely elastic. We follow common terminology in referring to $\mathbf{F}^e$ as an elastic deformation gradient although it is understood that $\mathbf{F}^e$ is in general not the gradient of a vector field. Unlike the multiplicative decomposition, $\mathbf{F}^e$ is not to be associated with an intermediate relaxed configuration whereby an unloading of the material by $\mathbf{F}^e$ leads to a stress-free state. This is because the evolution of $\mathbf{F}^e$ is path dependent so that any finite unloading path may be accompanied by plastic flow.

There are two assumptions concerning the plastic deformation. The first is that plastic deformation does not deform the fibers in either shear or normal strain. This hypothesis is consistent with the matrix-dominated mode of plastic deformation. The work by Dvorak et al. (1988) provides extensive experimental support for the existence of this mode. The second assumption is that plastic deformation follows a flow rule, hence the rate of plastic deformation, relative to current configuration, is related to the rate of increase in stress. In addition to these physical assumptions, the elastic Green-Lagrange strain will be taken as a linear function of the second Piolla-Kirchoff stress based on the elastic deformation gradient, and kinematic hardening will be admitted in the plastic range.

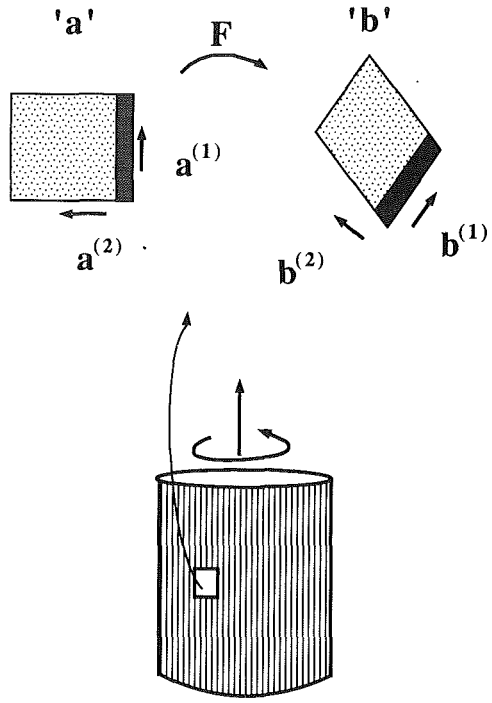

Fig. 1 The deformation gradient rotates the fiber direction $b^{(1)}$ with its associated normal $b^{(2)}$

(iii) Kinematics. Let the initial and current fiber directions and the vectors perpendicular (counterclockwise) to them be represented by $\mathbf{a}^{(1)}$, $\mathbf{b}^{(1)}$, $\mathbf{a}^{(2)}$, and $\mathbf{b}^{(2)}$, respectively (see Fig. 1). Note that due to the deformation, $\mathbf{b}^{(2)}$ may not be along the material element initially along $\mathbf{a}^{(2)}$. We will refer to the coordinate systems defined by ($\mathbf{a}^{(1)}$, $\mathbf{a}^{(2)}$) and ($\mathbf{b}^{(1)}$, $\mathbf{b}^{(2)}$) as the initial and current fiber coordinate systems, respectively. We will conveniently assume that the fixed Cartesian system chosen is aligned with the initial fiber coordinate system. If these two systems are unaligned, then all tensor relations given in the direct form remain valid and formulas for tensor components may be converted to the required Cartesian system by a simple rotation. The kinematical part of the spin of any material element currently along the unit direction $\mathbf{c}$ is given by

$$\mathbf{W}^c = \mathbf{W}^e + \mathbf{D}^e\cdot\mathbf{c}\otimes\mathbf{c} - \mathbf{c}\otimes\mathbf{c}\cdot\mathbf{D}^e \tag{6}$$

where $\otimes$ denotes a tensor product. Note that the elastic spin $\mathbf{W}^e$ and rate of deformation tensor $\mathbf{D}^e$ have been used in Eq. (6) in order to exclude the spin associated with plastic deformation. The total spin of the material element along the fiber direction coincides with the kinematical part of the spin due to the first physical assumption in the previous section. Thus,

$$\mathbf{W}^f = \mathbf{W}^e + \mathbf{D}^e\cdot\mathbf{b}^{(1)}\otimes\mathbf{b}^{(1)} - \mathbf{b}^{(1)}\otimes\mathbf{b}^{(1)}\cdot\mathbf{D}^e \tag{7a}$$

$$\mathbf{W}^f = \mathbf{W} + \mathbf{D}\cdot\mathbf{b}^{(1)}\otimes\mathbf{b}^{(1)} - \mathbf{b}^{(1)}\otimes\mathbf{b}^{(1)}\cdot\mathbf{D}. \tag{7b}$$

Therefore, by knowing the velocity gradient history, the rotation of the fiber may be kinematically determined without

resort to any further constitutive relations. The total fiber rotation $\mathbf{R}^f$ is obtained as

$$\dot{\mathbf{R}}^f = \mathbf{W}^f \cdot \mathbf{R}^f \tag{8a}$$

$$\mathbf{R}^f|_{t=0} = \mathbf{I} \tag{8b}$$

where $\mathbf{W}^f$ is calculated using Eq. (7). The initial and current fiber direction vectors are then related by

$$\mathbf{b}^{(i)} = \mathbf{R}^f \cdot \mathbf{a}^{(i)}, \tag{9}$$

where "i" is 1 or 2. In single crystal plasticity, the rotation of the lattice may not be obtained kinematically without resort to constitutive relations when there is more than one active slip mode. This is so because shearing across, as well as parallel to any given slip plane, may cause rotation of the material element and atomic realignment, but it does not affect the lattice orientation.

(iv) Stress and Stress Rate Measures. Plastic flow is assumed to occur relative to the current fiber direction, hence it is natural to consider the "driving forces" to be the Cauchy stress components relative to the current fiber coordinate system. Therefore, we define

$$\bar{\sigma} \equiv \mathbf{R}^{fT} \cdot \sigma \cdot \mathbf{R}^f \quad \Leftrightarrow \quad \bar{\sigma}_{ij} \equiv \mathbf{b}^{(i)} \cdot \sigma \cdot \mathbf{b}^{(j)} \tag{10}$$

$$\overset{\circ}{\bar{\sigma}} \equiv \mathbf{R}^f \cdot \sigma^o \cdot \mathbf{R}^{fT} \quad \Leftrightarrow \quad \overset{\circ}{\bar{\sigma}}_{ij} = \mathbf{b}^{(i)} \cdot \sigma^o \cdot \mathbf{b}^{(j)} \tag{11}$$

where σ is the Cauchy stress and σ^o will be referred to as the fiber stress rate of Cauchy's stress. Using Eqs. (8) and (10) we can show that

$$\sigma^o = \dot{\sigma} - \mathbf{W}^f \cdot \sigma + \sigma \cdot \mathbf{W}^f. \tag{12}$$

In addition, σ^o can be related to the Jaumann stress rate σ^∇ by

$$\sigma^\nabla = \sigma^o + \mathbf{P}:\mathbf{D} \tag{13}$$

$$P_{ijkl} = \sigma_{ip} b_p^{(1)} b_k^{(1)} \delta_{lj} - \sigma_{ik} b_l^{(1)} b_j^{(1)} + \sigma_{pj} b_l^{(1)} b_p^{(1)} \delta_{ik} - \sigma_{lj} b_i^{(1)} b_k^{(1)} \tag{14}$$

where δ_{ij} is the Kronecker delta, the "rs" components of $\mathbf{P}:\mathbf{D}$ are given by $P_{rskl} D_{kl}$, and $\mathbf{P}$ is a fourth-order tensor whose components with respect to the fixed Cartesian system are given by Eq. (14).

Elastic Constitutive Relations

As expressed in Eq. (2), we assume that the energy associated with the stress power formed using the elastic velocity gradient is conserved. Thus we obtain a hyperelastic constitutive relation based on the elastic deformation gradient defined by Eq. (5). This may be given as

$$\sigma^{PKe} = \frac{\partial W(\mathbf{E}^e)}{\partial \mathbf{E}^e} \tag{15a}$$

$$\sigma^{PKe} \equiv J^e \mathbf{F}^{e-1} \cdot \sigma \cdot \mathbf{F}^{e-T} \tag{15b}$$

where σ^{PKe} is the second Piolla-Kirchoff stress based on the elastic deformation gradient. This hyperelastic constitutive relation is path independent for any region in deformation space in which there is no plastic flow. A complete representation of $W(\mathbf{E}^e)$ for an anisotropic medium may be specified (Onat, 1990). However, an adequate realization of Eq. (15a) for small elastic strain but arbitrarily large rotation and plastic deformation may be given by

$$\sigma^{PKe} = \mathbf{K}:\mathbf{E}^e, \tag{16}$$

where $\mathbf{K}$ is a symmetric fourth-order tensor which does not depend on the elastic strain $\mathbf{E}^e$. σ^{PKe}, $\mathbf{E}^e$, and $\mathbf{K}$ are all defined with respect to a configuration pulled back from the current one by $\mathbf{F}^{e-1}$. In general, the components of $\mathbf{K}$ are not constant with respect to a fixed Cartesian coordinate system because the intermediate configuration may evolve as the deformation progresses. This is analogous to a change in the choice of the reference configuration in purely elastic constitutive frameworks. The configuration pulled back from the current one by $\mathbf{F}^{e-1}$ will be referred to as the intermediate configuration. If we now assume that the tensor $\mathbf{K}$ may at most take into account the orientation of the fibers in the intermediate configuration, then the components of $\mathbf{K}$ are constant. This follows from (7) which shows that there is no relative rotation of the fiber direction between the intermediate and the reference configuration. We now adopt a transversely isotropic elastic constitutive model for the unidirectional fibrous composite. In a Cartesian coordinate system having the X_1-direction along the fibers in the intermediate configuration, Eq. (16) may then be written as

$$\begin{bmatrix} \sigma_{11}^{PKe} \\ \sigma_{22}^{PKe} \\ \sigma_{12}^{PKe} \end{bmatrix} = \begin{bmatrix} c_\nu E_A & c_\nu \nu_A E_T & 0 \\ c_\nu \nu_A E_T & c_\nu E_T & 0 \\ 0 & 0 & 2G_A \end{bmatrix} \begin{bmatrix} E_{11}^e \\ E_{22}^e \\ E_{12}^e \end{bmatrix} \tag{17}$$

where E_A, E_T, G_A, and ν_A are constants and $c_\nu = 1/(1 - \nu_A^2 E_T / E_A)$. We also note that the coordinate system in which (17) is described does not rotate with the deformation. In numerical implementations the rate form of the elastic constitutive relation will be needed. Assuming that the elastic strains are small, this is given as

$$\sigma^{\Delta e} \approx \mathbf{K}:\mathbf{D}^e \tag{18a}$$

$$\sigma^{\Delta e} \equiv \dot{\sigma} + tr(\mathbf{D}^e)\sigma - \mathbf{L}^e \sigma - \sigma \cdot \mathbf{L}^{eT} \tag{18b}$$

where $\sigma^{\Delta e}$ is the Oldroyd stress rate based on the elastic velocity gradient. Therefore we note that when elastic strains are small and practical considerations require a hypoelastic constitutive relation, it is appropriate to use the Oldroyd rate of Cauchy stress rather than the commonly used Jaumann or corrotational rate. Even though the elastic strains are small, such a distinction may be important when low hardening conditions apply.

Plastic Constitutive Relations

(i) Yield Condition. We adopt a phenomenological but micromechanically motivated yield function of a fibrous layer in plane stress. This yield function is associated with the Matrix Dominated Mode (MDM) discussed by Dvorak and Bahei-El-Din (1987). Note that the normal stress component along the fiber direction (i.e., the axial stress) does not influence yielding. Using the components of the stress and backstress relative to the current fiber coordinate system, the yield function is defined by

$$\bar{f}(\bar{\sigma}_{ij} - \bar{\alpha}_{ij}) \equiv \begin{cases} \left(\dfrac{\bar{\sigma}_{12} - \bar{\alpha}_{12}}{\tau_0}\right)^2 + \left(\dfrac{\bar{\sigma}_{22} - \bar{\alpha}_{22}}{\tau_0} \pm 1\right)^2 - 1 & \text{if } q \le 1 \\ \left(\dfrac{\bar{\sigma}_{12} - \bar{\alpha}_{12}}{\tau_0}\right)^2 - 1 & \text{if } q > 1 \end{cases} \tag{19}$$

where $q = [(\bar{\sigma}_{12} - \bar{\alpha}_{12})/(\bar{\sigma}_{22} - \bar{\alpha}_{22})]$, and τ_0 is the initial yield strength of the material in shear. We note that although $\bar{\sigma}_{12}$ and $\bar{\sigma}_{21}$ are equal, they are to be considered as separate variables in Eq. (19). This distinction is related to the assumption of no plastic shearing across fibers and will be clarified in the discussion of the flow rule. The yield function defined in Eq. (19) allows for kinematic hardening and may be extended to allow for isotropic hardening. We note that the resolved stress and backstress components $\bar{\sigma}_{ij}$ and $\bar{\alpha}_{ij}$ are independent of the particular Cartesian coordinate system used or to superposed rotations and hence these components are objective scalars. Thus the yield function is an objective scalar function of the stress and backstress. The infinitesimal deformation formulation does not distinguish between the initial and current fiber coordinate systems and hence its direct application to finite deformations is not objective. Therefore, an important difference between the infinitesimal and finite deformation formulation is that the latter updates the current fiber coordinate

system using Eqs. (8) and (9). Using Eq. (10) and an equivalent one for the backstress α, we may rewrite the yield function as

$$\bar{f}(\bar{\sigma}_{ij}-\bar{\alpha}_{ij}) = \bar{f}(\mathbf{b}^{(i)T}\cdot(\sigma-\alpha)\cdot\mathbf{b}^{(j)}) = f(\sigma-\alpha). \tag{20}$$

Using the yield function defined by Eq. (20) and a plastic scalar loading variable λ to be used in the flow and hardening rules, the Kuhn-Tucker form of the yield condition for rate-independent plastic flow is given by

$$\begin{cases} \lambda \geq 0 \\ f \leq 0 \\ \lambda f = 0. \end{cases} \tag{21}$$

In this form, the yield condition has a form identical to that used in infinitesimal deformation formulations. However, the classical form of expressing the yield condition is different due to the fiber rotation and is given by

$$\begin{cases} \dfrac{\partial f}{\partial \sigma}:\sigma^o > 0 \text{ and } f=0 \Rightarrow \text{yielding occurs} \\ \dfrac{\partial f}{\partial \sigma}:\sigma^o \leq 0 \text{ and } f=0 \Rightarrow \text{neutral loading} \\ f<0 \Rightarrow \text{no yielding.} \end{cases} \tag{22}$$

The difference of conditions (22) with those of an infinitesimal deformation formulation is manifested in the use of σ^o instead of $\dot{\sigma}$. This difference is also necessary for the objectivity of the yield conditions (22).

(ii) Flow Rule. The plasticity velocity gradient is given by $\mathbf{L}^p$ and its components with respect to the current fiber coordinate system are given by

$$\dot{\bar{\gamma}} = \mathbf{R}^{fT}\cdot\mathbf{L}^p\cdot\mathbf{R}^f \Leftrightarrow \dot{\bar{\gamma}}_{ij} = \mathbf{b}^{(i)}\cdot\mathbf{L}^p\cdot\mathbf{b}^{(j)}. \tag{23}$$

The tensor $\dot{\bar{\gamma}}$ describes the plastic deformation relative to the fiber direction and must therefore be constitutively related to $\bar{\sigma}$ the stress components relative to the fiber direction using a flow rule. An associated flow rule (satisfying normality) is given by

$$\dot{\bar{\gamma}}_{ij} = \dot{\lambda}\frac{\partial \bar{f}}{\partial \bar{\sigma}_{ij}} \Leftrightarrow \mathbf{L}^p = \dot{\lambda}\frac{\partial f}{\partial \sigma}. \tag{24}$$

Note that $\dot{\bar{\gamma}}_{21}$ and $\dot{\bar{\gamma}}_{11}$ must be zero by the physical assumption of no plastic flow across fibers. This physical assumption is enforced by requiring $\bar{f}$ to be independent of $\bar{\sigma}_{21}$ and $\bar{\sigma}_{11}$ which, in Eq. (24), leads to $\dot{\bar{\gamma}}_{21}$ and $\dot{\bar{\gamma}}_{11}$ being zero. Note that similar to the single crystal studies, $\mathbf{L}^p$ and not $\mathbf{D}^p$ alone is constitutively prescribed in Eq. (24).

(iii) Hardening. We will only describe kinematic hardening although the present model can be easily extended to account for isotropic hardening if sufficient experimental data is available. The hardening is related to the evolution of the backstress α which can be given as

$$\dot{\bar{\alpha}}_{ij} = c\dot{\lambda}\bar{\nu}_{ij} \Leftrightarrow \alpha^o = c\dot{\lambda}\nu \tag{25}$$

where

$$\bar{\nu}_{ij} = h(\bar{\sigma}_{ij}-\bar{\alpha}_{ij}). \tag{26}$$

Equation (26) allows the direction of $\dot{\bar{\alpha}}_{ij}$ to vary along the yield surface and it is motivated by experimental evidence (Dvorak et al., 1988). For example, experiments suggest that when $q>1$ then $\dot{\bar{\alpha}}_{ij}$ follow Prager's rule

$$\nu = \frac{\partial f}{\partial \sigma} \Rightarrow \alpha^o = \frac{\dfrac{\partial f}{\partial \sigma}:\sigma^o}{\dfrac{\partial f}{\partial \sigma}:\dfrac{\partial f}{\partial \sigma}}\frac{\partial f}{\partial \sigma} \tag{27}$$

while when $q \leq 1$ Phillips hardening rule is more appropriate, i.e.,

$$\nu = \frac{\dfrac{\partial f}{\partial \sigma}:\dfrac{\partial f}{\partial \sigma}}{\dfrac{\partial f}{\partial \sigma}:\sigma^o}\sigma^o \Rightarrow \alpha^o = \sigma^o. \tag{28}$$

In Eqs. (27) and (28), the second result is implied by the consistency condition discussed below. In order to avoid a discontinuity in the specification of ν when $q=1$, we specify ν as

$$\nu = \begin{cases} \dfrac{\dfrac{\partial f}{\partial \sigma}:\dfrac{\partial f}{\partial \sigma}}{\dfrac{\partial f}{\partial \sigma}:\sigma^o}\sigma^o & \text{when } q \leq 1 \\ \dfrac{1}{|q|^m}\dfrac{\dfrac{\partial f}{\partial \sigma}:\dfrac{\partial f}{\partial \sigma}}{\dfrac{\partial f}{\partial \sigma}:\sigma^o}\sigma^o + \left(1-\dfrac{1}{|q|^m}\right)\dfrac{\partial f}{\partial \sigma} & \text{when } q \geq 1, \end{cases} \tag{29}$$

where m is a suitably large exponent and "m" is taken to be 6 in the simulations presented in a later section. We will assume that the hardening is linear so that c is a constant. A loading history-dependent c is more appropriate and can be accommodated by the use of further internal variables. For example, in two surface plasticity models (Dafalias and Popov, 1975; Krieg, 1975) the modulus c is a function of the plastic work and the distance between the yield surface and a second surface whose motion has to be described using additional internal variables. Such a specification of the modulus c in a manner consistent with experimental data is currently being developed for an infinitesimal deformation formulation and may be subsequently implemented in the finite deformation formulation. The yield function (19), yield condition (21), flow rule (24), and hardening rule (25) and (29) fully specify the finite deformation rate independent plastic constitutive relations. We conclude this section with an expression for the consistency condition required to maintain $\bar{f}=0$ during plastic yielding. It is given by

$$\frac{\partial \bar{f}}{\partial \bar{\sigma}_{ij}}\dot{\bar{\sigma}}_{ij} - \frac{\partial \bar{f}}{\partial \bar{\sigma}_{ij}}\dot{\bar{\alpha}}_{ij} = 0 \Leftrightarrow \frac{\partial f}{\partial \sigma}:\sigma^o - \frac{\partial f}{\partial \sigma}:\alpha^o = 0. \tag{30}$$

Integration of Constitutive Relations

In this section we will discuss a method of integrating the finite deformation constitutive relations when given a deformation gradient history. The method is an adaptation of the projection method of Ortiz and Simo (1986) to the present constitutive relation. In discussing this integration method, we will assume small elastic strains so that Eq. (18) applies. However, we will allow a more general form of the yield function of Eq. (19) and (20) in the form

$$\bar{f} = \bar{f}(\bar{\sigma}, \bar{\mathbf{q}}) \tag{31}$$

where $\bar{\mathbf{q}}$ is a vector containing internal state variables. For example, $\bar{\mathbf{q}}$ could be associated with the backstress $\bar{\alpha}$ as well as isotropic hardening parameters. The plastic constitutive relations also involve flow and hardening rules as in (24) and (25) in the general form

$$\mathbf{L}^p = \dot{\lambda}\mathbf{R}^f\cdot\bar{\mathbf{r}}(\bar{\sigma}, \bar{\mathbf{q}})\cdot\mathbf{R}^{fT} = \dot{\lambda}\mathbf{r}(\mathbf{R}^f, \bar{\sigma}, \bar{\mathbf{q}}) \tag{32}$$

$$\frac{d\bar{\mathbf{q}}}{d\lambda} = \bar{\mathbf{h}}(\bar{\sigma}, \bar{\mathbf{q}}). \tag{33}$$

The main idea of the integration method is as follows: The method starts with a specification of a deformation gradient increment. If the predicted stress σ based on the elastic constitutive relation at fixed internal state lies within the yield

Table 1 Stress update algorithm

(i) Kinematic update:

$$\mathbf{F}_n = \mathbf{F}_{n-1} + \Delta\mathbf{F}_n$$

$$\mathbf{b}_n^{(1)} = \mathbf{F}_n \cdot \mathbf{a}^{(1)} / \| \mathbf{F}_n \cdot \mathbf{a}^{(1)} \|$$

$$\mathbf{R}_n^f \text{ obtained from components of } \mathbf{b}_n^{(1)}$$

(ii) Elastic Predictor:

$$\mathbf{F}_n^{e0} = \mathbf{F}_{n-1}^e + \Delta\mathbf{F}_n$$

$$\bar{\sigma}_n^0 = \mathbf{R}_n^{fT} \cdot (\mathbf{K} : \mathbf{E}_n^{e0}) \cdot \mathbf{R}_n^f$$

$$\bar{\mathbf{q}}_n^0 = \bar{\mathbf{q}}_{n-1}$$

(iii) Check for Yielding: $\bar{f}_n^0 \le 0$?

YES: $\mathbf{F}_n^e = \mathbf{F}_n^{e0}$; $\bar{\sigma}_n = \bar{\sigma}_n^0$; $\bar{\mathbf{q}}_n = \bar{\mathbf{q}}_n^0$ EXIT

NO: $i = 0$

(iv) Plastic Correctors:

$$\frac{d\sigma_n^i}{d\lambda} = -\mathbf{K} : \mathbf{r}_{s\,n}^i + \mathrm{tr}(\mathbf{r}_n^i)\,\sigma_n^i - \mathbf{r}_n^i \cdot \sigma_n^i + \sigma_n^i \cdot \mathbf{r}_n^{T\,i}$$

$$\Delta\lambda_n^i = \frac{-\bar{f}_n^i}{(\partial \bar{f}_n^i/\partial\sigma) : (d\sigma_n^i/d\lambda) + (\partial \bar{f}_n^i/\partial\bar{\mathbf{q}}) \cdot \bar{\mathbf{h}}_n^i}$$

$$\bar{\mathbf{q}}_n^{i+1} = \bar{\mathbf{q}}_n^i + \Delta\lambda_n^i \bar{\mathbf{h}}_n^i$$

$$\Delta\mathbf{F}_n^{ei} = (\Delta\mathbf{F}_n \cdot \mathbf{F}_n^{-1} - \Delta\lambda_n^i \mathbf{r}_n^i) \cdot \mathbf{F}_n^{ei}$$

$$\mathbf{F}_n^{ei+1} = \mathbf{F}_n^{ei} + \Delta\mathbf{F}_n^{ei}$$

$$\bar{\sigma}_n^{i+1} = \mathbf{R}_n^{fT} \cdot (\mathbf{K} : \mathbf{E}_n^{ei+1}) \cdot \mathbf{R}_n^f$$

(v) Convergence Check: $|\bar{f}_n^{i+1}| \le$ TOLERANCE ?

YES: $\mathbf{F}_n^e = \mathbf{F}_n^{ei+1}$; $\bar{\sigma}_n = \bar{\sigma}_n^{i+1}$; $\bar{\mathbf{q}}_n = \bar{\mathbf{q}}_n^{i+1}$ EXIT

NO: $i \leftarrow i + 1$; GO TO (iv)

Table 2 Sample material properties

E_A (GPa)	E_T (GPa)	G_A (GPa)	ν_A	τ_0 (MPa)	c (GPa)
237	158.29	63.48	0.182	30.0	0.5 (fig 2a-c)

surface, then the increment is wholly elastic. If the predicted elastic state lies outside the yield surface, then plastic flow is allowed at a constant level of the total deformation gradient until consistency is restored. When plastic flow occurs, two critical results are required: The first is an expression for the evolution of stress with plastic flow at fixed total deformation gradient. The second is a good estimate of the increment in plastic loading variable $\Delta\lambda$ at the current deformation increment required to restore consistency. The first result is essential to the method, whereas the second has an important impact on efficiency. Using Eq. (18) and the additive decomposition (1), we may express the stress rate as

$$\dot{\sigma} = \mathbf{K}:(\mathbf{D} - \mathbf{D}^p) - tr(\mathbf{D} - \mathbf{D}^p)\sigma + (\mathbf{L} - \mathbf{L}^p)\cdot\sigma + \sigma\cdot(\mathbf{L}^T - \mathbf{L}^{pT}). \quad (34)$$

Using the flow rule (32) and noting that the velocity gradient does not evolve with λ, since the deformation gradient increment is held fixed at a given time increment, we obtain

$$\frac{d\sigma}{d\lambda} = -\mathbf{K}:\mathbf{r}_s + tr(\mathbf{r})\sigma - \mathbf{r}\cdot\sigma + \sigma\cdot\mathbf{r}^T \quad (35)$$

where $\mathbf{r}_s$ is the symmetric part of $\mathbf{r}$. The plastic loading parameter increment $\Delta\lambda$ at any current state is estimated by linearizing the yield condition around the current values of stress and internal variables and extrapolating to the consistent state at a fixed level of the total deformation gradient. Thus, an estimate of $\Delta\lambda$ is obtained as

$$\Delta\lambda \approx \frac{-\bar{f}}{\dfrac{\partial \bar{f}}{\partial\sigma} : \dfrac{d\sigma}{d\lambda} + \dfrac{\partial \bar{f}}{\partial \bar{\mathbf{q}}} \cdot \bar{\mathbf{h}}} \quad (36)$$

where $d\sigma/d\lambda$ is given by Eq. (35) and all functions on the right-hand side of Eq. (36) are evaluated at the current values of stress σ and internal state $\bar{\mathbf{q}}$. Having an estimate $\Delta\lambda$ from Eq. (36), the stress σ and state $\bar{\mathbf{q}}$ may be integrated as a coupled system of ordinary differential equations in λ using relations (33) and (35). If at the end of the increment $\Delta\lambda$, the yield condition is still violated, a new estimate of $\Delta\lambda$ based on the updated stress and internal state is calculated and the stress and internal state are further evolved. This process is repeated until consistency is restored to a certain tolerance. If the estimate $\Delta\lambda$ is accurate, only a few iterations are needed. The integration of the ordinary differential equations in λ of the stress and internal state may be conveniently accomplished using any explicit numerical integration scheme. Since only a few (typically one) increments of $\Delta\lambda$ are needed per deformation increment, a forward Euler formula may be used (Ortiz and Simo, 1986). A flowchart for the overall procedure is listed in Table 1.

Elastic-Plastic Stiffness

In this section we will outline the derivation of the "continuum" elastic-plastic stiffness for a specific pair of stress rate/deformation rate measure. This stiffness relates the Jaumann or corrotational stress rate to the rate of deformation, namely,

$$\sigma^{\nabla} = \mathbf{K}^{ep}:\mathbf{D}. \quad (37)$$

The stiffness $\mathbf{K}^{ep}$ is useful in some finite element implementations such as in the program ABAQUS. Using Eqs. (18), (13), and the flow rule (32), we may express the Jaumann and the fiber stress rates as

$$\sigma^{\nabla} = \mathbf{K}^{(1)}:\mathbf{D} + \dot{\lambda}\mathbf{K}^{(2)}:\mathbf{r} \quad (38)$$

$$\sigma^{o} = [\mathbf{K}^{(1)} - \mathbf{P}]:\mathbf{D} + \dot{\lambda}\mathbf{K}^{(2)}:\mathbf{r} \quad (39)$$

where

$$K^{(1)}_{ijkl} = K_{ijkl} - \sigma_{ij}\delta_{kl} + \sigma_{lj}\delta_{ik} + \sigma_{ik}\delta_{lj} \quad (40)$$

$$K^{(2)}_{ijkl} = -0.5K_{ijrs}(\delta_{rk}\delta_{sl} + \delta_{rl}\delta_{sk}) + \sigma_{ij}\delta_{kl} - \sigma_{lj}\delta_{ik} - \sigma_{il}\delta_{jk}. \quad (41)$$

Substituting Eq. (39) into the consistency condition (30) with generalized internal variables $\bar{\mathbf{q}}$ and solving for the plastic loading parameter rate $\dot{\lambda}$, we obtain

$$\dot{\lambda} = \mathbf{K}^{(3)}:\mathbf{D} \quad (42)$$

where

$$\mathbf{K}^{(3)} = -\left(\frac{1}{\dfrac{\partial f}{\partial\sigma}:\mathbf{K}^{(2)}:\mathbf{r} + \dfrac{\partial f}{\partial \bar{\mathbf{q}}}\cdot\bar{\mathbf{h}}}\right)\frac{\partial f}{\partial\sigma}:[\mathbf{K}^{(1)} - \mathbf{P}]. \quad (43)$$

Finally, substituting Eq. (42) into (38) we obtain the elastic-plastic stiffness as:

$$\mathbf{K}^{ep} = \mathbf{K}^{(1)} + [\mathbf{K}^{(2)}:\mathbf{r}] \otimes \mathbf{K}^{(3)}. \quad (44)$$

We note that the elastic-plastic stiffness $\mathbf{K}^{ep}$ is a function of $\mathbf{K}, \sigma, \bar{\mathbf{q}}, \mathbf{R}^f$ and whether elastic or elastoplastic deformation is involved. If the material is currently deforming purely elastically then the stiffness $\mathbf{K}^{ep}$ is given by $\mathbf{K}^{(1)}$. Note that the elastic-plastic stiffness does not directly involve $\mathbf{W}$, except implicitly when $\mathbf{R}^f$ is updated. We note that in general $K^{ep}_{rskl} \neq K^{ep}_{klrs}$. The components of $\mathbf{D}$ and $\mathbf{K}^{ep}$, with respect to a specific coordinate system, may be written as a column vector (i.e., $[D_{11}, D_{22}, 2\cdot D_{12}]^T$) and a 3×3, matrix respectively. This matrix representation of $\mathbf{K}^{ep}$ is in general nonsymmetric, but is in a form suitable for implementation in a large deformation finite element code which has an option for a nonsymmetric stiffness matrix (e.g., ABAQUS).

Example Problem

We will consider the deformation of a 0-deg ply tube specimen with the fibers being aligned with the cylinder axis. Due to boundary constraints, the material elements perpendicular

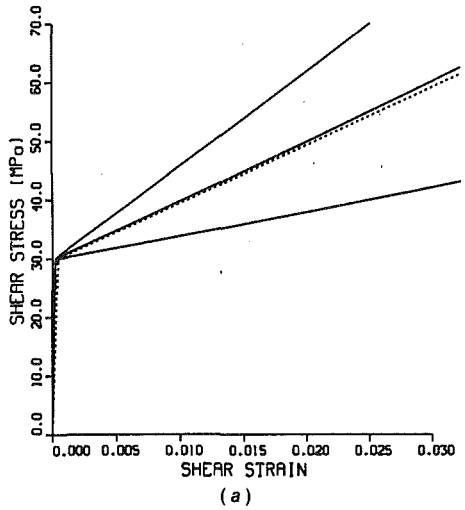

(a)

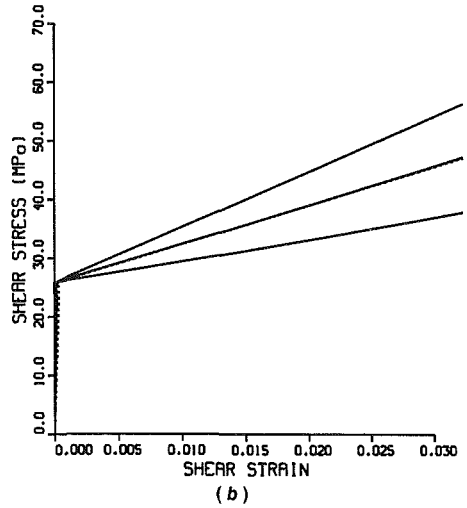

(b)

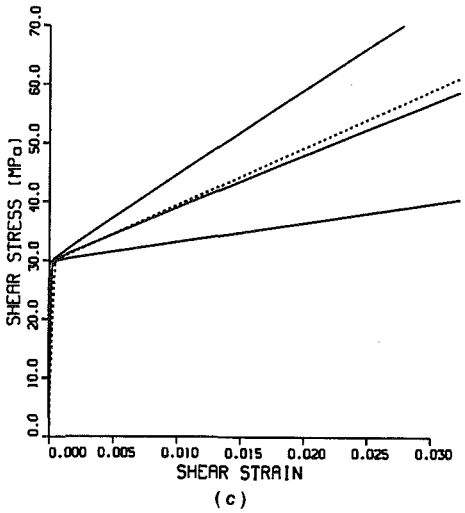

(c)

Fig. 2(*a–c*) The axial shear stress versus axial shear strain response of a 0-deg ply fibrous composite specimen under proportional transverse normal stress/axial shear stress and a fixed axial normal stress of either 0, −300, or 300 MPa (solid lines). Compression softens and tension stiffens the plastic response of a 0-deg ply fibrous composite tube specimen under shear. The dashed lines represents the calculated "small" strain predictions. The small strain predictions are not affected by the axial stress so, for the same case, they all have the same response. The proportionality constant during loading is 0.0, 1.0, and 1.73 for Figs. 2(*a*), 2(*b*), and 2(*c*), respectively. The plastic modulus *c* is 0.5 GPa.

to the cylinder axis are assumed not to rotate. The elastic response is assumed to be transversely anisotropic with constitutive model given by Eq. (17). For the plastic response, kinematic linear hardening is adopted with the evolution of the kinematic stress being defined by Eqs. (25) and (29). Finally, normality is assumed and Eq. (24) is used for the flow rule. The relevant material properties are given in Table 2. The elastic properties are representative of 6061 Al/B composites with a volume fraction of around 0.45. The plastic tangent modulus approximates the instantaneous plastic tangent modulus of 6061 Al/B at a volume fraction of 0.45 under a moderate strain of 1–2 percent. The chosen initial yield strength is slightly higher than that of 6061 Al/B at a volume fraction of 0.45 and is chosen to partially account for initial nonlinear plastic straining.

Three cases of proportional loading between the transverse normal stress and axial shear stress with a fixed axial load of either 0, −300 or 300 MPa are considered. The ratio of transverse normal to axial shear stress in the cases a, b, and c are 0.0, 1.0, and 1.73, respectively. Shear stress and strain are numerically obtained for cases a, b, and c, under the various conditions of fixed axial stress and are plotted in Fig. 2(*a–c*). The dashed lines in the figures are results obtained using a corresponding "small" strain formulation using the same material properties. The small strain predictions are not affected by the axial stress so, for the same case, they all have the same response and only one dashed line per case appears. The results show that axial tension stiffens, whereas axial compression softens the response of the specimen under shear loading with the given kinematic constraints. In contrast, the small strain shear response is not affected by superposed axial stresses. A simple rigid-plastic analysis of the same problem indicates that the instantaneous shear stiffness is approximately the sum of the material instantaneous stiffness without the axial load and the superposed axial stress. These results indicate a need for the finite deformation formulation when the applied loads in the fiber direction are comparable to the instantaneous shear stiffness. Due to the high stiffness and strength of fibrous composites when loaded in the direction of the fibers, such conditions may occur even at small to moderate strains.

Acknowledgments

This work was supported by the office of Naval Research. The authors are indebted to Profs. Yehia Bahei-El-Din, Dimitris Lagoudas, and David M. Parks for useful discussions.

References

Agah-Tehrani, A., Lee, E. H., Mallet, R. L., and Onat, E. T., 1987, "The Theory of Elastic-Plastic Deformation at Finite Strain with Induced Anisotropy Modelled as Combined Isotropy-Kinematic Hardening," *J. Mech. Phys. Solids*, Vol. 35, No. 5, p. 519.

Asaro, R. J., and Rice, J. R., 1977, "Strain Localization in Ductile Single Crystals," *J. Mech. Phys. Solids*, Vol. 25, p. 309.

Boyce, M. C., Parks, D. M., and Argon, A. S., 1988, "Large Inelastic Deformation of Glassy Polymers. Part I: Rate Dependent Constitutive Model," *Mech. of Materials*, Vol. 7, p. 15.

Boyce, M. C., Weber, G. G., and Parks, D. M., 1989, "On the Kinematics of Finite Strain Plasticity," submitted to *J. Mech. Phys. of Solids*.

Dafalias, Y. F., and Popov, E. P., 1975, "A Model of Nonlinearly Hardening Materials for Complex Loading," *Acta Mechanica*, Vol. 21, p. 173.

Dafalias, Y. F., 1983, "Corotational Rates for Kinematic Hardening at Large Plastic Deformations," ASME JOURNAL OF APPLIED MECHANICS, Vol. 50, p. 561.

Dafalias, Y. F., 1984, "The Plastic Spin Concept and a Simple Illustration of its Role in Finite Plastic Transformations," *Mech. of Materials*, Vol. 3, p. 223.

Dienes, J. K., 1979, "On the Analysis of Rotation and Stress Rate in Deforming Bodies," *Acta Mechanica*, Vol. 32, p. 217.

Dvorak, G. J., and Bahei-El-Din, Y. A., 1979, "Elastic-Plastic Behavior of Fibrous Composites," *J. Mech. Phys. Solids*, Vol. 27, p. 51.

Dvorak, G. J., and Bahei-El-Din, Y. A., 1982, "Plasticity Analysis of Fibrous Composites," ASME JOURNAL OF APPLIED MECHANICS, Vol. 49, p. 327.

Dvorak, G. J., and Bahei-El-Din, Y. A., 1987, "A Bimodal Plasticity Theory of Fibrous Composite Materials," *Acta Mechanica*, Vol. 69, p. 219.

Dvorak, G. J., Bahei-El-Din, Y. A., Macheret, Y., and Liu, C. H., 1988, "An Experimental Study of Elastic-Plastic Behavior of a Fibrous Boron-Aluminum Composite," *J. Mech. Phys. Solids*, Vol. 36, p. 655.

Dvorak, G. J., and Teply, J. L., 1985, "Periodic Hexagonal Array Models for Plasticity Analysis of Composite Materials," *Plasticity Today: Modelling, Methods and Applications*, (W. Olszak Memorial Volume), A. Sawczuk and V. Bianchi, eds., Elsevier, New York, p. 623.

Fares, N., and Dvorak, G. J., 1991, "Large Elastic-Plastic Deformations of Fibrous Metal Matrix Composites," *J. Mech. Phys. Solids*, Vol. 39, No. 6, pp. 725–744.

Hill, R., and Rice, J. R., 1972, "Constitutive Analysis of Elastic-Plastic Crystals at Arbitrary Strain," *J. Mech. Phys. Solids*, Vol. 20, p. 401.

Iwakuma, T., and Nemat-Nasser, S., 1984, "Finite Elastic-Plastic Deformation of Polycrystalline Metals," *Proc. R. Soc. Lond.*, Vol. A394, pp. 87–119.

Krieg, R. D., 1975, "A Practical Two-Surface Plasticity Theory," ASME JOURNAL OF APPLIED MECHANICS, Vol. 42, p. 641.

Lee, E. H., 1969, "Elastic-Plastic Deformation at Finite Strain," ASME JOURNAL OF APPLIED MECHANICS, Vol. 36, p. 1.

Lee, E. H., Mallet, R. L., and Wertheimer, T. B., 1983, "Stress Analysis for Anisotropic Hardening in Finite Deformation Plasticity," ASME JOURNAL OF APPLIED MECHANICS, Vol. 105, p. 554.

Lee, E. H., and Agah-Tehrani, A., 1988, "The Structure of Constitutive Equations for Finite Deformation of Elastic-Plastic Materials Involving Strain Induced Anisotropy with Applications," *Intl. J. for Num. Meth. in Eng.*, Vol. 25, p. 133.

Malvern, L. E., 1969, *Introduction to the Mechanics of a Continuous Medium*, Prentice-Hall, Englewood Cliffs, New Jersey.

McMeeking, R. M., and Rice, J. R., 1974, "Finite-Element Formulation for Problems of Large Elastic-Plastic Deformation," *Int. J. Solids Struct.*, Vol. 11, p. 601.

Mear, M. E., and Hutchinson, J. W., 1985, "Influence of Yield Surface Curvature on Flow Localization in Dilatant Plasticity," *Mechanics of Materials*, Vol. 4, p. 395.

Nagtegaal, J. C., and de Jong, J. E., 1982, "Some Aspects of Non-Isotropic Workhardening in Finite Strain Plasticity," *Proceedings of the Workshop on Plasticity of Metals at Finite Strain: Theory, Experiment and Computation*, E. H. Lee and R. L. Mallet, eds., Stanford University and RPI, p. 65.

Nemat-Nasser, S., 1982, "On Finite Deformation Elasto-Plasticity," *Int. J. Solids Structures*, Vol. 18, No. 10, pp. 857–872.

Nemat-Nasser, S., 1983, "On Finite Plastic Flow of Crystalline and Geomaterials," ASME JOURNAL OF APPLIED MECHANICS, Vol. 105, pp. 1114–1126.

Onat, E. T., 1982, *Recent Advances in Creep and Fracture of Engineering Materials and Structures*, Pineridge Press, Swansea, U.K., Chapter 5.

Onat, E. T., 1990, private communications.

Ortiz, M., and Simo, J. C., 1986, "An Analysis of a New Class of Integration Algorithms for Elastoplastic Constitutive Relations," *Intl. J. Num. Meth. Eng.*, Vol. 23, p. 353.

Pierce, D., Asaro, R. J., and Needleman A., 1982, "An Analysis of Nonuniform and Localized Deformation in Ductile Single Crystals," *Acta Metall.*, Vol. 30, p. 1087.

Post, D., Guo, Y., and Czarnek, R., 1988, "Deformation Analysis of Boron/Aluminum Specimens by Moire Interferometry," submitted to *J. Comp. Tech. Res.*

Rice, J. R., 1970, "A Note on the 'Small Strain' Formulation for Elastic-Plastic Problems," Tech. Rep. N00014-67-A-000318, Div. of Eng., Brown Univ., Providence, R. I.

Rice, J. R., 1977, "The Localization of Plastic Deformation," *Proceedings of the 14th International Congress of Theoretical and Applied Mechanics*, W. T. Koiter, ed., p. 207, North-Holland, Amsterdam.

Rudnicki, J. W., and Rice, J. R., 1975, "Conditions for the Localization of Deformation in Pressure-Sensitive Dilatant Materials," *J. Mech. Phys. Solids*, Vol. 23, p. 371.

Spencer, A. J. M., 1984, "Constitutive Theory for Strongly Anisotropic Solids," *Continuum Theory of the Mechanics of Fiber-Reinforced Composites*, A. J. M. Spencer, ed., Springer-Verlag, New York.

Teply, J. L., and Dvorak, G. J., 1988, "Bounds on Overall Instantaneous Properties of Elastic-Plastic Composites," *J. Mech. Phys. Solids*, Vol. 36, p. 29.

On the Anisotropic Elastic Inclusions in Plane Elastostatics

Chyanbin Hwu

Wen J. Yen

Institute of Aeronautics
and Astronautics,
National Cheng Kung University,
Tainan, Taiwan, 70101,
Republic of China

By combining the method of Stroh's formalism, the concept of perturbation, the technique of conformal mapping and the method of analytical continuation, a general analytical solution for the elliptical anisotropic elastic inclusions embedded in an infinite anisotropic matrix subjected to an arbitrary loading has been obtained in this paper. The inclusion as well as the matrix are of general anisotropic elastic materials which do not imply any material symmetry. The special cases when the inclusion is rigid or a hole are also studied. The arbitrary loadings include in-plane and antiplane loadings. The shapes of ellipses cover the lines or circles when the minor axis is taken to be zero or equal to the major axis. The solutions of the stresses and deformations in the entire domain are expressed in complex matrix notation. Simplified results are provided for the interfacial stresses along the inclusion boundary. Some interesting examples are solved explicitly, such as point forces or dislocations in the matrix and uniform loadings at infinity. Since the general solutions have not been found in the literature, comparison is made with some special cases of which the analytical solutions exist, which shows that our results are exact and universal.

1 Introduction

Determination of the stress fields induced by general elastic inclusions has aroused considerable interest for almost half a century. However, the analytical solutions presented in the literature are always restricted to some special loading conditions such as uniform loading or a concentrated couple (Chen, 1967; Yang and Chou, 1976; Hwu and Ting, 1989), special matrices such as isotropic matrix (Eshelby, 1957; Jaswon and Bhargave, 1961; Sendeckyi, 1970; Stagni, 1982), special inclusions such as rigid inclusions or holes (Santare and Keer, 1986; Hwu and Yen, 1991), special shapes such as lines or circles (Wang et al., 1985; Honein and Herrmann, 1990), or the uncoupling of in-plane and antiplane deformations. To the authors' knowledge, there is no general analytical solution for the elliptical anisotropic elastic inclusions imbedded in an infinite anisotropic matrix subjected to an arbitrary loading.

In this paper, the Stroh's formalism (Stroh, 1958; Hwu and Ting, 1989) for anisotropic elasticity combined with the method of analytical continuation (Muskhelishvili, 1954), which is similar to the one proposed by Suo (1990), is developed to solve the present problem. Moreover, the concept of perturbation given by Stagni (1982) is applied to formulate the general solutions. A transformation function which maps the ellipse onto a unit circle is introduced. However, a discontinuity problem occurs when the transformation is required to be single-valued and conformal in the entire domain including the matrix and inclusion. This is remedied by the way similar to those proposed by Stagni (1982) for isotropic materials, i.e., a restricted condition is introduced to force the continuity. The general loading conditions considered include the cases of point singularities such as point forces or dislocations. The analytical closed-form solutions presented in this paper are universal in the sense of materials (anisotropic elastic), loadings (arbitrary), and geometries (elliptic). The solutions for stresses and deformations in the entire domain are expressed in complex matrix notation. Simplified results are provided for the interfacial stresses along the inclusion boundary through the use of identities developed in the literature.

Some special and interesting examples are solved explicitly and are compared with existing analytical solutions such as point forces in the matrix (Hwu and Yen, 1991), uniform loadings at infinity (Hwu and Ting, 1989), and dislocations in the matrix (Dundurs and Mura, 1964; Stagni and Lizzio, 1983; Santare and Keer, 1986). Moreover, several new results about the anisotropic elastic inclusions are given. The cases of point singularities are important for practical application. The solutions of dislocations are frequently used as kernel functions of integral equations to consider the interactions between inclusions and cracks (Erdogan et al., 1974). The solutions of point forces can be employed as the fundamental solutions for the boundary element method (Ang and Clements, 1986; Hwu and Yen, 1991).

Contributed by the Applied Mechanics Division of THE AMERICAN SOCIETY OF MECHANICAL ENGINEERS for publication in the ASME JOURNAL OF APPLIED MECHANICS.

Discussion on this paper should be addressed to the Technical Editor, Professor Lewis T. Wheeler, Department of Mechanical Engineering, University of Houston, Houston, TX 77204-4792, and will be accepted until four months after final publication of the paper itself in the ASME JOURNAL OF APPLIED MECHANICS.

Manuscript received by the ASME Applied Mechanics Division, Mar. 14, 1991; final revision, Jan. 23, 1992. Associate Technical Editor: R. M. McMeeking.

2 Preliminary Formulations

2.1 General Solutions. The basic equations for two-dimensional anisotropic elasticity are the strain-displacement equations, the stress-strain laws, and the equations of equilibrium. To get solutions satisfying these equations there are two different formulations in the literature. One is the Lekhnitskii's approach (1968) which starts with the equilibrated stress functions then compatibility equations, the other is Stroh's formalism (1958) which starts with the displacements then equilibrium equations. The equivalency of these two formulations has been discussed in Suo (1990). In this paper, we follow Stroh's formalism due to its elegancy and simplicity. Using the notation employed in Hwu and Ting (1989), the general solutions for the displacements and stresses have been obtained as

$$\mathbf{u}=2\,\mathrm{Re}\left\{\sum_{\alpha=1}^{3}\mathbf{a}_\alpha f_\alpha(z_\alpha)\right\},\quad \boldsymbol{\phi}=2\,\mathrm{Re}\left\{\sum_{\alpha=1}^{3}\mathbf{b}_\alpha f_\alpha(z_\alpha)\right\},$$

$$\sigma_{i1}=-\phi_{i,2},\quad \sigma_{i2}=\phi_{i,1},\quad i=1,\,2,\,3,$$

$$z_\alpha=x_1+p_\alpha x_2. \tag{1}$$

(x_1, x_2) is a fixed rectangular coordinate system. Re denotes the real parts and a comma stands for differentiation. $\mathbf{u}$, σ_{ij}, and $\boldsymbol{\phi}$ represent, respectively, the displacements, stresses, and stress functions. p_α, $(\mathbf{a}_\alpha, \mathbf{b}_\alpha)$, $\alpha=1, 2, 3$, are the eigenvalues and eigenvectors of the materials. $f_\alpha(z_\alpha)$ are arbitrary functions with complex arguments z_α. Note that in Eq. (1), p_α are the eigenvalues whose imaginary parts are positive.

With similar reason as Suo (1990), that whether a function is analytic is not affected by different arguments $z_\alpha=x_1+p_\alpha x_2$, $\alpha=1, 2, 3$, another solution form appropriate for the method of analytic continuation is written as

$$\mathbf{u}=\mathbf{A}\mathbf{f}(z)+\overline{\mathbf{A}\mathbf{f}(z)},\quad \boldsymbol{\phi}=\mathbf{B}\mathbf{f}(z)+\overline{\mathbf{B}\mathbf{f}(z)}, \tag{2a}$$

where

$$\mathbf{A}=[\mathbf{a}_1,\,\mathbf{a}_2,\,\mathbf{a}_3],\quad \mathbf{B}=[\mathbf{b}_1,\,\mathbf{b}_2,\,\mathbf{b}_3],$$
$$\mathbf{f}(z)=[f_1(z)\;f_2(z)\;f_3(z)]^T. \tag{2b}$$

The superscript T denotes the transpose and the overbar represents the conjugate of a complex number. Note that the argument of each component function of $\mathbf{f}(z)$ is written as $z=x_1+px_2$ without referring to the associated eigenvalues p_α. Once the solution of $\mathbf{f}(z)$ is obtained for a given boundary value problem, a replacement of z_1, z_2, or z_3 should be made for each component function to calculate field quantities from (1).

2.2 Conformal Mapping. Consider an elliptical anisotropic inclusion imbedded in an infinite matrix. The contour of the interface is represented by $x_1=a\cos\psi$, $x_2=b\sin\psi$, where $2a$, $2b$ are the major and minor axes of the ellipse and ψ is a real parameter. It is known that the transformation function

$$z_\alpha=\frac{1}{2}\left\{(a-ibp_\alpha)\zeta_\alpha+(a+ibp_\alpha)\frac{1}{\zeta_\alpha}\right\} \tag{3}$$

will map the region outside the elliptic inclusion onto the exterior of a unit circle.

The roots of the equation, $dz_\alpha/d\zeta_\alpha=0$, are at

$$\zeta_\alpha^0=\pm\sqrt{\frac{a+ibp_\alpha}{a-ibp_\alpha}}=\pm\sqrt{m_\alpha}e^{i\theta_\alpha}, \tag{4}$$

where $\sqrt{m_\alpha}$ and θ_α denote, respectively, the modulus and argument of the critical points ζ_α^0. Since $\sqrt{m_\alpha}<1$, which can easily be proved if the imaginary part of p_α has been set to be positive, the transformation is single-valued and conformal outside the elliptic inclusion. However, the inside region is double-valued and nonconformal. Figure 1 shows the transformation among the z-plane, z_α-plane, and ζ_α-plane. It can be seen that there are two different ζ_α inside the unit circle corresponding to one z_α inside the elliptic inclusion. To have a one-to-one transformation, we designate the point nearest the unit circle to be the mapped point. For this choice, a discontinuity problem may happen when two originally continuous points $(z_\alpha)_1$ and $(z_\alpha)_2$ are mapped onto $(\zeta_\alpha)_1$ and $(\zeta_\alpha)_2$ shown in Fig. 1. Actually the points $(\zeta_\alpha)_1=\sqrt{m_\alpha}\sigma$ and $(\zeta_\alpha)_2=\sqrt{m_\alpha}e^{2i\theta_\alpha}/\sigma$ correspond to the same point in the z_α-plane, where $\sigma=e^{i\psi}$ denotes the points located on the unit circle. Hence, the transformation function (3) now maps the whole z_α-plane, cut along a slit, into the ζ_α-plane deprived of the circle of radius $\sqrt{m_\alpha}$. To remedy this discontinuity, i.e., eliminating the slit which does not exist in our problem, the following restriction should be satisfied:

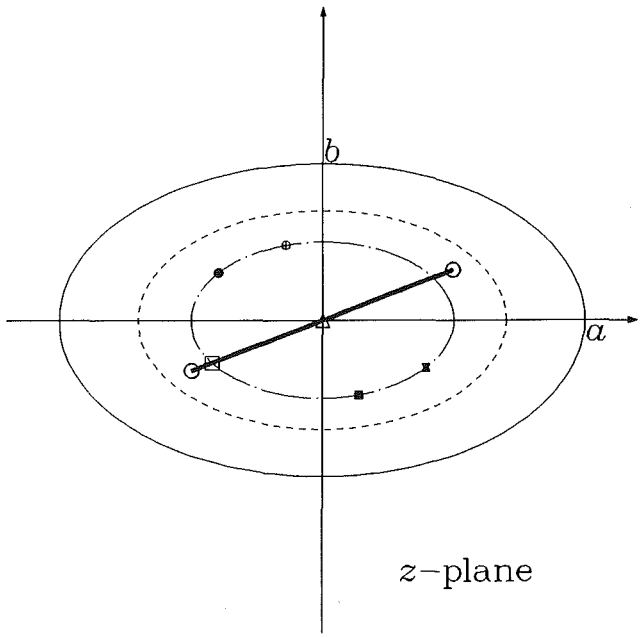

Fig. 1(*a*) z-plane ($b/a=0.6$, $p_\alpha=0.3+1.5i$)

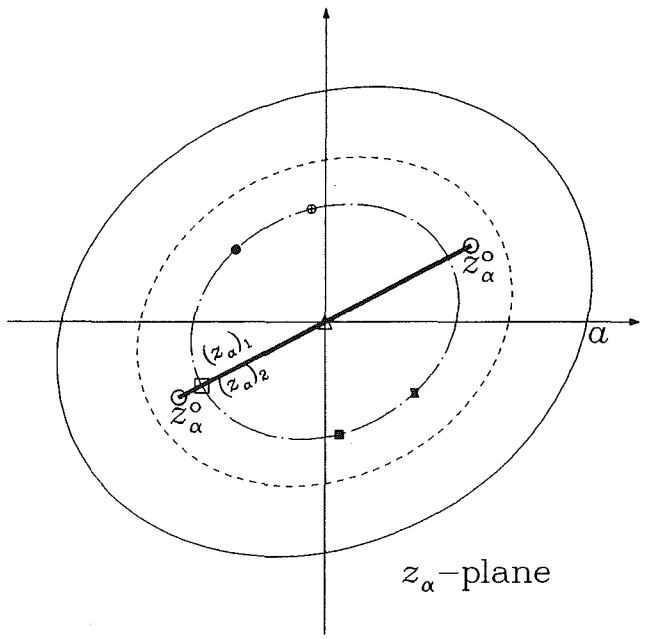

Fig. 1(*b*) z_α-plane ($b/a=0.6$, $p_\alpha=0.3+1.5i$)

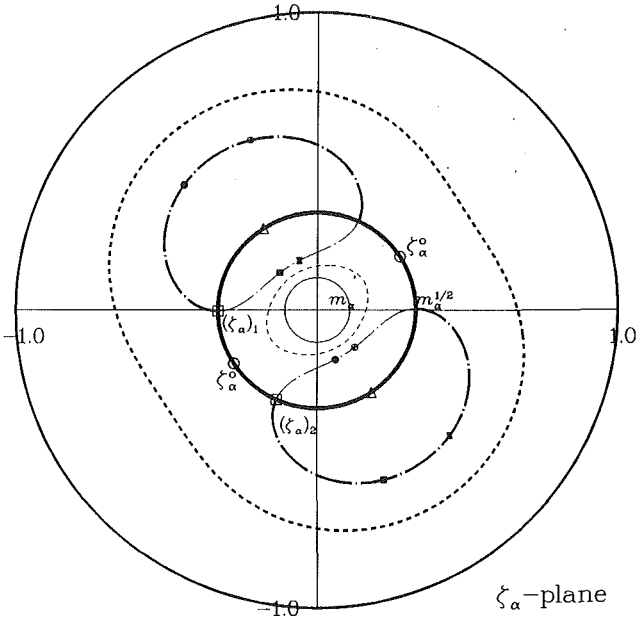

Fig. 1(*c*) ζ_α-plane ($b/a = 0.6$, $p_\alpha = 0.3 + 1.5i$)

$$f(\sqrt{m_\alpha}\sigma) = f(\sqrt{m_\alpha}e^{2i\theta_\alpha}/\sigma). \tag{5}$$

By applying the conformal mapping technique described above and the perturbation concept given in Stagni (1982), the general solutions for the inclusion problems can now be written in terms of the variables ζ_α, i.e.,

$$\left.\begin{aligned}\mathbf{u}_1 &= \mathbf{A}_1[\mathbf{f}_0(\zeta)+\mathbf{f}_1(\zeta)] + \overline{\mathbf{A}}_1[\overline{\mathbf{f}_0(\zeta)}+\overline{\mathbf{f}_1(\zeta)}]\\ \boldsymbol{\phi}_1 &= \mathbf{B}_1[\mathbf{f}_0(\zeta)+\mathbf{f}_1(\zeta)] + \overline{\mathbf{B}}_1[\overline{\mathbf{f}_0(\zeta)}+\overline{\mathbf{f}_1(\zeta)}]\end{aligned}\right\},\ \zeta\in S_1 \tag{6a}$$

and

$$\left.\begin{aligned}\mathbf{u}_2 &= \mathbf{A}_2\mathbf{f}_2(\zeta^*) + \overline{\mathbf{A}_2}\overline{\mathbf{f}_2(\zeta^*)}\\ \boldsymbol{\phi}_2 &= \mathbf{B}_2\mathbf{f}_2(\zeta^*) + \overline{\mathbf{B}_2}\overline{\mathbf{f}_2(\zeta^*)}\end{aligned}\right\},\quad \zeta^*\in S_2 \tag{6b}$$

where the subscripts 1 and 2 denote, respectively, the matrix and inclusion. ζ_α^* is the mapped point of $z_\alpha^* = x_1 + p_\alpha^* x_2$ where p_α^* is the material eigenvalue of the inclusion. $\mathbf{f}_0$ represents the function associated with the unperturbed elastic field which is related to the solutions of homogeneous media and is holomorphic in the entire domain except some singular points such as the points under concentrated forces or dislocations, and the points at zero or infinity. $\mathbf{f}_1$ (or $\mathbf{f}_2$) is the function corresponding to the perturbed field of matrix (or inclusion) and is holomorphic in region S_1 (or S_2) except some singular points. S_1 and S_2 denote, respectively, the regions occupied by the matrix and inclusion. Hence, in the ζ_α-plane, S_1 is the region outside the unit circle while S_2 is the region of the annular ring between the unit circle and the circle of radius $\sqrt{m_\alpha}$. Since $\mathbf{f}_2$ is holomorphic in the annular ring, it can be represented by Laurent's expansion,

$$\mathbf{f}_2(\zeta^*) = \sum_{k=-\infty}^{\infty} \mathbf{c}_k \zeta^{*k}. \tag{7a}$$

Satisfaction of (5) gives

$$\mathbf{c}_{-k} = \boldsymbol{\Gamma}_k^* \mathbf{c}_k,\quad \boldsymbol{\Gamma}_k^* = \ll \left(\frac{a+ibp_\alpha^*}{a-ibp_\alpha^*}\right)^k \gg, \tag{7b}$$

where the angular bracket stands for the diagonal matrix, i.e., $\ll f_\alpha \gg = \mathrm{diag}\{f_1\ f_2\ f_3\}$ which will be used throughout this paper.

Note that the general solutions of (2) and (6) require that each component of the column vector $\mathbf{f}$ have different argument z_α or ζ_α, $\alpha = 1, 2, 3$. Hence, Eq. (7*a*) has the implicit meaning that

$$\mathbf{f}_2(\zeta^*) = \sum_{k=-\infty}^{\infty} \{(c_k)_1\zeta_1^{*k},\ (c_k)_2\zeta_2^{*k},\ (c_k)_3\zeta_3^{*k}\}^T.$$

where $(c_k)_\alpha$, $\alpha = 1, 2, 3$, are the components of $\mathbf{c}_k$.

2.3 General Loading Conditions. For a given loading condition, $\mathbf{f}_0$ can be obtained immediately since it is related to the solutions of homogeneous media. However, it is not necessary to be exactly the same as the solutions of homogeneous media. The choices of $\mathbf{f}_0$ depend on the convenience in calculation. The final solutions for the stresses and deformations in the entire domain will not be influenced by the choices of $\mathbf{f}_0$. To have a better understanding about the choices, two special examples are discussed in the following.

(*a*) *A Dislocation* $\hat{\mathbf{b}}$ *or Point Force* $\hat{\mathbf{t}}$ *at* $z_\alpha = \hat{z}_\alpha$. Consider a dislocation line in the direction perpendicular to the x_1x_2 plane with Burger vector $\hat{\mathbf{b}}$, and a point force uniformly distributed along a line parallel to the x_3-axis with force per unit length $\hat{\mathbf{t}}$. Both singularities are at the point $(\hat{x}_1, \hat{x}_2)$. If $\mathbf{f}_0$ is chosen to represent exactly the solutions of homogeneous media, it may be written as (Suo, 1990; Hwu and Yen, 1991)

$$\mathbf{f}_0(\zeta) = \ll \log(z_\alpha - \hat{z}_\alpha) \gg \mathbf{q}, \tag{8a}$$

where

$$\mathbf{q} = \mathbf{B}^T\hat{\mathbf{b}}/2\pi i \quad \text{or} \quad \mathbf{q} = \mathbf{A}^T\hat{\mathbf{t}}/2\pi i. \tag{8b}$$

However, it is inconvenient in calculation when our general solution is expressed in terms of the variable ζ_α not z_α. An alternative choice for $\mathbf{f}_0$ is

$$\mathbf{f}_0(\zeta) = \ll \log(\zeta_\alpha - \hat{\zeta}_\alpha) \gg \mathbf{q}, \tag{9}$$

where $\mathbf{q}$ is the same as (8*b*). This expression is more convenient than the one given in (8*a*). Moreover, it also reflects the singularity characteristics of the original problems.

(*b*) *Uniform Loading Applied at Infinity.* The exact solution corresponding to the homogeneous media is (Ting, 1988)

$$\mathbf{f}_0(\zeta) = \ll z_\alpha \gg \mathbf{q} = \frac{1}{2}\ll a - ibp_\alpha \gg \ll \zeta_\alpha + \frac{a+ibp_\alpha}{a-ibp_\alpha}\zeta_\alpha^{-1} \gg \mathbf{q}, \tag{10a}$$

where

$$\mathbf{q} = \mathbf{A}^T\mathbf{t}_2^\infty + \mathbf{B}^T\boldsymbol{\epsilon}_1^\infty,\quad \mathbf{t}_2^\infty = \begin{Bmatrix}\sigma_{12}^\infty\\ \sigma_{22}^\infty\\ \sigma_{32}^\infty\end{Bmatrix},\quad \boldsymbol{\epsilon}_1^\infty = \begin{Bmatrix}\epsilon_{11}^\infty\\ \epsilon_{12}^\infty\\ 2\epsilon_{13}^\infty\end{Bmatrix}. \tag{10b}$$

σ_{ij}^∞, ϵ_{ij}^∞ are the constant stresses and strains induced by the uniform loading applied at infinity. An alternative choice may be provided by

$$\mathbf{f}_0(\zeta) = \ll \zeta_\alpha \gg \mathbf{q}_0,\quad \mathbf{q}_0 = \frac{1}{2}\ll a - ibp_\alpha \gg \mathbf{q}, \tag{11}$$

where $\mathbf{q}$ is the same as (10*b*). The infinity loading conditions are satisfied for both choices. The one given in (11) is not a solution for uniform stress distribution, which can be seen from the transformation function (3). However, in calculation, (11) is more convenient than (10*a*), because the singular points of (11) are at infinity while singularities occur at zero and infinity for (10*a*).

Based upon the above discussion, we know that if all the singular points of the physical domain z_α are considered to be located in the matrix, for different choices the complex function $\mathbf{f}_0$ associated with the general loading conditions may be expressed as follows:

(i) By Taylor's expansion,

$$\mathbf{f}_0(\zeta)=\sum_{k=0}^{\infty}\mathbf{e}_k\zeta^k,\quad \mathbf{e}_k=\frac{\mathbf{f}_0^{(k)}(0)}{k!}=\frac{1}{2\pi i}\int_C\frac{\mathbf{f}_0(\zeta)}{\zeta^{k+1}}d\zeta. \tag{12}$$

ζ belongs to a bounded region where $\mathbf{f}_0$ is holomorphic. The cases of $\mathbf{f}_0=\ll\log(\zeta_\alpha-\hat{\zeta}_\alpha)\gg\mathbf{q}$ and $\mathbf{f}_0=\ll\zeta_\alpha\gg\mathbf{q}_0$ belong to this category.

(ii) By Laurent's expansion,

$$\mathbf{f}_0(\zeta)=\sum_{k=-\infty}^{\infty}\mathbf{e}_k\zeta^k,\quad \mathbf{e}_{-k}=\mathbf{\Gamma}_k\mathbf{e}_k,\quad \mathbf{e}_k=\frac{1}{2\pi i}\int_C\frac{\mathbf{f}_0(\zeta)}{\zeta^{k+1}}d\zeta. \tag{13}$$

ζ belongs to an annular ring where $\mathbf{f}_0$ is holomorphic. The cases of $\mathbf{f}_0=\ll\log(z_\alpha-\hat{z}_\alpha)\gg\mathbf{q}$ and $\mathbf{f}_0=\ll z_\alpha\gg\mathbf{q}$ belong to this category.

For the case that all the singular points of the physical domain z_α are located in the inclusions, similar approaches as those described in Sections 2.2 and 2.3 can be applied.

3 Elastic Inclusions

If the inclusion and the matrix are assumed to be perfectly bonded along the interface, the displacements and surface tractions at the interface should be continuous. That is

$$\mathbf{u}_1=\mathbf{u}_2,\quad \boldsymbol{\phi}_1=\boldsymbol{\phi}_2,\quad \text{along the interface } \zeta=\sigma=e^{i\psi}, \tag{14}$$

where the second equation of (14) comes from the relation $\mathbf{t}=\partial\boldsymbol{\phi}/\partial s$ in which $\mathbf{t}$ is the surface traction and s is the arc length measured along the curved boundary. By using the general solution given in (6) and the expression given in (7), the traction continuity condition of (14) leads to

$$\mathbf{B}_1\mathbf{f}_1(\sigma)+\overline{\mathbf{B}}_1\overline{\mathbf{f}_0(\sigma)}-\sum_{k=1}^{\infty}\{\overline{\mathbf{B}}_2\bar{\mathbf{c}}_k+\mathbf{B}_2\mathbf{\Gamma}_k^*\mathbf{c}_k\}\sigma^{-k}$$

$$=-\overline{\mathbf{B}}_1\overline{\mathbf{f}_1(\sigma)}-\mathbf{B}_1\mathbf{f}_0(\sigma)+\sum_{k=1}^{\infty}\{\mathbf{B}_2\mathbf{c}_k+\overline{\mathbf{B}}_2\overline{\mathbf{\Gamma}}_k^*\bar{\mathbf{c}}_k\}\sigma^k. \tag{15}$$

One of the important properties of holomorphic functions used in the method of analytic continuation is that if $\mathbf{f}(\zeta)$ is holomorphic in S_1 (or S_2+S_0), then $\overline{\mathbf{f}(1/\bar{\zeta})}$ is holomorphic in S_2+S_0 (or S_1). Here, S_0 denotes the region inside the circle of radius $\sqrt{m_\alpha}$. From this property and Eq. (15), we may introduce a function which is holomorphic in the entire domain including the interface boundary, i.e.,

$$\theta(\zeta)=\begin{cases}\mathbf{B}_1\mathbf{f}_1(\zeta)+\overline{\mathbf{B}}_1\overline{\mathbf{f}_0(1/\bar{\zeta})})-\sum_{k=1}^{\infty}\{\overline{\mathbf{B}}_2\bar{\mathbf{c}}_k+\mathbf{B}_2\mathbf{\Gamma}_k^*\mathbf{c}_k\}\zeta^{-k}, & \zeta\in S_1\\ -\overline{\mathbf{B}}_1\overline{\mathbf{f}_1(1/\bar{\zeta})}-\mathbf{B}_1\mathbf{f}_0(\zeta)+\sum_{k=1}^{\infty}\{\mathbf{B}_2\mathbf{c}_k+\overline{\mathbf{B}}_2\overline{\mathbf{\Gamma}}_k^*\bar{\mathbf{c}}_k\}\zeta^k, & \zeta\in S_2+S_0\end{cases} \tag{16}$$

In the above, the singular points of $\mathbf{f}_0$ is assumed to be located in the matrix only, i.e., the case (i) given in (12). Since $\theta(\zeta)$ is now holomorphic and single-valued in the whole plane including the point at infinity, by Liouville's theorem we have $\theta(\zeta)\equiv$ constant. However, constant function $\mathbf{f}$ corresponds to rigid-body motion which may be neglected. Therefore, $\theta(\zeta)\equiv 0$. With this result, Eq. (16) leads to

$$\sum_{k=1}^{\infty}\{\overline{\mathbf{B}}_2\bar{\mathbf{c}}_k+\mathbf{B}_2\mathbf{\Gamma}_k^*\mathbf{c}_k\}\zeta^{-k}=\mathbf{B}_1\mathbf{f}_1(\zeta)+\mathbf{B}_1\mathbf{f}_0(1/\zeta),\quad \zeta\in S_1,$$

$$\sum_{k=1}^{\infty}\{\mathbf{B}_2\mathbf{c}_k+\overline{\mathbf{B}}_2\overline{\mathbf{\Gamma}}_k^*\bar{\mathbf{c}}_k\}\zeta^k=\overline{\mathbf{B}}_1\bar{\mathbf{f}}_1(1/\zeta)+\mathbf{B}_1\mathbf{f}_0(\zeta),\quad \zeta\in S_2+S_0. \tag{17}$$

Similarly, the continuity condition $\mathbf{u}_1=\mathbf{u}_2$ provides for

$$\sum_{k=1}^{\infty}\{\overline{\mathbf{A}}_2\bar{\mathbf{c}}_k+\mathbf{A}_2\mathbf{\Gamma}_k^*\mathbf{c}_k\}\zeta^{-k}=\mathbf{A}_1\mathbf{f}_1(\zeta)+\overline{\mathbf{A}}_1\bar{\mathbf{f}}_0(1/\zeta),\quad \zeta\in S_1,$$

$$\sum_{k=1}^{\infty}\{\mathbf{A}_2\mathbf{c}_k+\overline{\mathbf{A}}_2\overline{\mathbf{\Gamma}}_k^*\bar{\mathbf{c}}_k\}\zeta^k=\overline{\mathbf{A}}_1\bar{\mathbf{f}}_1(1/\zeta)+\mathbf{A}_1\mathbf{f}_0(\zeta),\quad \zeta\in S_2+S_0. \tag{18}$$

Cancellation of $\mathbf{f}_1(\zeta)$ between (17) and (18) leads to

$$\mathbf{f}_0(\zeta)=\sum_{k=1}^{\infty}i\mathbf{A}_1^T\{(\overline{\mathbf{M}}_1+\mathbf{M}_2)\mathbf{A}_2\mathbf{c}_k+(\overline{\mathbf{M}}_1-\overline{\mathbf{M}}_2)\overline{\mathbf{A}}_2\overline{\mathbf{\Gamma}}_k^*\bar{\mathbf{c}}_k\}\zeta^k \tag{19}$$

where $\mathbf{M}_k$ is the impedance matrix (Ingebrigtsen and Tonning, 1969) defined as

$$\mathbf{M}_k=-i\mathbf{B}_k\mathbf{A}_k^{-1}=\mathbf{H}_k^{-1}(\mathbf{I}+i\mathbf{S}_k)=(\mathbf{I}+i\mathbf{S}_k^T)^{-1}\mathbf{L}_k, \tag{20a}$$

where

$$\mathbf{S}_k=i(2\mathbf{A}_k\mathbf{B}_k^T-\mathbf{I}),$$
$$\mathbf{H}_k=2i\mathbf{A}_k\mathbf{A}_k^T,\ \mathbf{L}_k=-2i\mathbf{B}_k\mathbf{B}_k^T,\ k=1,2. \tag{20b}$$

The second and third equalities of (20a) have been given by Ting (1988) and $\mathbf{S}_k$, $\mathbf{H}_k$, $\mathbf{L}_k$ are real matrices which depend on the material constants. Moreover, $\mathbf{H}_k$ and $\mathbf{L}_k$ are positive definite if the strain energy is positive (Chadwick and Smith, 1977). Hence, the inverses of $\mathbf{H}_k$ and $\mathbf{L}_k$ exist. By substituting (12) into (19) and comparing the coefficients of corresponding terms, the unknown constants $\mathbf{c}_k$ are determined as

$$\mathbf{c}_k=\{\mathbf{G}_0-\overline{\mathbf{G}}_k\overline{\mathbf{G}}_0^{-1}\mathbf{G}_k\}^{-1}\{\mathbf{t}_k-\overline{\mathbf{G}}_k\overline{\mathbf{G}}_0^{-1}\bar{\mathbf{t}}_k\},\quad k=1,2,\cdots\infty \tag{21a}$$

where

$$\mathbf{G}_0=(\overline{\mathbf{M}}_1+\mathbf{M}_2)\mathbf{A}_2,\quad \mathbf{G}_k=(\mathbf{M}_1-\mathbf{M}_2)\mathbf{A}_2\mathbf{\Gamma}_k^*,$$
$$\mathbf{t}_k=-i\mathbf{A}_1^{-T}\mathbf{e}_k. \tag{21b}$$

Note that the solutions associated with $\mathbf{c}_o$ are ignored because the constant stress function does not produce stress, which represents a rigid-body motion. Having the solution of $\mathbf{c}_k$, function $\mathbf{f}_1(\zeta)$ can now be obtained from $(17)_1$ or $(18)_1$ with the understanding that the subscripts of ζ in (17) or (18) are dropped. Once the solution of $\mathbf{f}_1(\zeta)$ is obtained from $(17)_1$ or $(18)_1$, a replacement of ζ_1, ζ_2, or ζ_3 should be made for each component function. This calculation procedure will be applied throughout this paper. The whole field solution can then be found by using Eq. (6).

If one is interested in the interfacial stresses along the inclusion boundary, calculation may be performed by using the field solution of the matrix or inclusion. The stress components based upon the coordinate system $(\mathbf{n}, \mathbf{m})$ which are, respectively, the unit vectors tangent and normal to the interface boundary, are obtained as (Hwu and Ting, 1989)

$$\sigma_{mm}=\mathbf{m}^T(\theta)\boldsymbol{\phi}_{,n},\quad \sigma_{mn}=\mathbf{n}^T(\theta)\boldsymbol{\phi}_{,n},\quad \sigma_{m3}=(\boldsymbol{\phi}_{,n})_3,$$
$$\sigma_{nn}=-\mathbf{n}^T(\theta)\boldsymbol{\phi}_{,m},\quad \sigma_{nm}=-\mathbf{m}^T(\theta)\boldsymbol{\phi}_{,m}=\sigma_{mn},\quad \sigma_{n3}=-(\boldsymbol{\phi}_{,m})_3, \tag{22}$$

where the angle θ is directed counterclockwise from the positive x_1-axis to the direction of $\mathbf{n}$. The derivative of $\boldsymbol{\phi}$ along the interface, $\boldsymbol{\phi}_{,n}$, should be continuous across the interface since $\boldsymbol{\phi}_1=\boldsymbol{\phi}_2$ along the interface boundary. However, $\boldsymbol{\phi}_{,m}$ may be discontinuous. The evaluation of $\boldsymbol{\phi}_{,m}$ and $\boldsymbol{\phi}_{,n}$ can be performed by using chain rule as shown in Hwu and Yen (1991). If the field solution of the inclusion given in (6b) with $\mathbf{f}_2(\zeta^*)$ obtained in (7) and (21) is used, we have

$$\boldsymbol{\phi}_{2,m}=-\sum_{k=1}^{\infty}\frac{2k}{\rho}\mathrm{Im}\{\mathbf{B}_2\mathbf{P}^*(\theta)[e^{-ik\psi}\mathbf{\Gamma}_k^*-e^{ik\psi}\mathbf{I}]\mathbf{c}_k\},$$
$$\boldsymbol{\phi}_{1,n}=\boldsymbol{\phi}_{2,n}=\boldsymbol{\phi}_{,n}=-\sum_{k=1}^{\infty}\frac{2k}{\rho}\mathrm{Im}\{\mathbf{B}_2[e^{-ik\psi}\mathbf{\Gamma}_k^*-e^{ik\psi}\mathbf{I}]\mathbf{c}_k\}, \tag{23a}$$

where

$$\mathbf{P}^*(\theta) = \ll p_\alpha^*(\theta) \gg, \quad p_\alpha^*(\theta) = \frac{p_\alpha^* \cos\theta - \sin\theta}{p_\alpha^* \sin\theta + \cos\theta},$$
$$\rho = \sqrt{a^2 \sin^2\psi + b^2 \cos^2\psi}, \tag{23b}$$

and Im stands for the imaginary parts. Similarly, $\phi_{1,m}$ is obtained by applying the field solution of the matrix given in (6a), or by (Ting and Yan, 1991)

$$\begin{Bmatrix} \mathbf{u}_{1,m} \\ \phi_{1,m} \end{Bmatrix} = \mathbf{N}(\theta) \begin{Bmatrix} \mathbf{u}_{,n} \\ \phi_{,n} \end{Bmatrix}, \tag{24}$$

in which $\mathbf{u}_{,n}$ and $\phi_{,n}$ can be obtained by using the field solution of the inclusion or matrix since they are continuous across the interface. $\mathbf{N}(\theta)$ is the fundamental matrix of Stroh's formalism, and is a 6×6 real matrix composed of the material constants of the matrix.

We now consider the function $\mathbf{f}_0$ corresponding to the unperturbed elastic field is chosen to be the Case (ii) given in (13). By the method of analytic continuation shown previously for Case (i), one may find that the solution of $\mathbf{c}_k$ for this case has exactly the same expression as Eq. (21), and function $\mathbf{f}_1(\zeta)$ is obtained as

$$\mathbf{f}_1(\zeta) = -\sum_{k=1}^{\infty} \mathbf{B}_1^{-1} \{ \overline{\mathbf{B}}_1 \bar{\mathbf{e}}_k + \mathbf{B}_1 \boldsymbol{\Gamma}_k \mathbf{e}_k - \overline{\mathbf{B}}_2 \bar{\mathbf{c}}_k - \mathbf{B}_2 \boldsymbol{\Gamma}_k^* \mathbf{c}_k \} \zeta^{-k}, \tag{25a}$$

or

$$\mathbf{f}_1(\zeta) = -\sum_{k=1}^{\infty} \mathbf{A}_1^{-1} \{ \overline{\mathbf{A}}_1 \bar{\mathbf{e}}_k + \mathbf{A}_1 \boldsymbol{\Gamma}_k \mathbf{e}_k - \overline{\mathbf{A}}_2 \bar{\mathbf{c}}_k - \mathbf{A}_2 \boldsymbol{\Gamma}_k^* \mathbf{c}_k \} \zeta^{-k}. \tag{25b}$$

Notice again that $\mathbf{f}_k$, $k=0, 1, 2$, are required to have the form of $\{f_1(\zeta_1)\ f_2(\zeta_2)\ f_3(\zeta_3)\}_k^T$. The expressions for the interfacial stresses are also the same as in Case (i).

4 Holes and Rigid Inclusions

In this section, the subscripts 1 and 2 used to distinguish the matrix and inclusion are omitted for simplicity since only the matrix is considered for the problems containing holes or rigid inclusions.

4.1 Holes. When the inclusion is a traction-free hole, $\phi = \mathbf{0}$ along the hole boundary which leads to

$$\mathbf{B}\mathbf{f}(\sigma) + \overline{\mathbf{B}\mathbf{f}_0(\sigma)} = -\overline{\mathbf{B}\mathbf{f}(\sigma)} - \mathbf{B}\mathbf{f}_0(\sigma), \tag{26}$$

if $\mathbf{f}_0$ belongs to Case (i). By the method of analytic continuation we find that

$$\mathbf{f}(\zeta) = -\mathbf{B}^{-1}\overline{\mathbf{B}}\,\bar{\mathbf{f}}_0\left(\frac{1}{\zeta}\right). \tag{27}$$

By a way similar to those shown in (22)-(24), the hoop stress σ_{nn} along the hole boundary is obtained as $\sigma_{nn} = -\mathbf{n}^T(\theta)\phi_{,m}$, where

$$\phi_{,m} = -\frac{4}{\rho}\mathbf{N}_3(\theta)\mathbf{L}^{-1}\mathrm{Re}\{\sigma \mathbf{B}\mathbf{f}_0'(\sigma)\}, \tag{28a}$$

or

$$\phi_{,m} = -\frac{4}{\rho}\mathbf{N}_3(\theta)\mathbf{L}^{-1}\sum_{k=1}^{\infty}\mathrm{Re}\{ke^{ik\psi}\mathbf{B}\mathbf{e}_k\}, \tag{28b}$$

when $\mathbf{f}_0$ is expressed by the Taylor's expansion as (12). During the derivation of Eq. (28), one should be very careful about the $\mathbf{f}(\zeta)$ given in (27), whose argument of each component function should be replaced by ζ_1, ζ_2, and ζ_2, respectively. Moreover, the identities provided by Ting (1988) have been used, which are useful for the separation of a complex matrix into its real and imaginary parts.

If $\mathbf{f}_0$ belongs to Case (ii), similar approach can be applied and the results are

$$\mathbf{f}(\zeta) = -\mathbf{B}^{-1}\sum_{k=1}^{\infty}\{\overline{\mathbf{B}}\bar{\mathbf{e}}_k + \mathbf{B}\boldsymbol{\Gamma}_k\mathbf{e}_k\}\zeta^{-k}. \tag{29}$$

The expression for the hoop stress is the same as (28b).

4.2 Rigid Inclusions. Holes are extreme cases of elastic inclusions for which the inclusion is extraordinary soft relative to the matrix. The other extreme case is rigid inclusion which means that the inclusion is absolutely rigid and can not be deformed. However, a rigid-body rotation ω relative to the matrix may occur. Hence, the boundary conditions for the cases of rigid inclusions are

$$\mathbf{u} = \frac{\omega}{2}(\mathbf{k}\sigma + \bar{\mathbf{k}}\sigma^{-1}), \quad \mathbf{k} = \begin{Bmatrix} ib \\ a \\ 0 \end{Bmatrix}. \tag{30}$$

Substituting (6) into (30), we have

$$\mathbf{A}\mathbf{f}(\sigma) + \overline{\mathbf{A}\mathbf{f}_0(\sigma)} - \frac{\omega}{2}\mathbf{k}\sigma^{-1} = -\overline{\mathbf{A}\mathbf{f}(\sigma)} - \mathbf{A}\mathbf{f}_0(\sigma) + \frac{\omega}{2}\mathbf{k}\sigma \tag{31}$$

if $\mathbf{f}_0$ belongs to Case (i). By the method of analytic continuation, we find that

$$\mathbf{f}(\zeta) = -\mathbf{A}^{-1}\overline{\mathbf{A}}\,\bar{\mathbf{f}}_0\left(\frac{1}{\zeta}\right) + \frac{\omega}{2\zeta}\mathbf{A}^{-1}\bar{\mathbf{k}}. \tag{32}$$

To determine ω we use the condition that the total moment about the origin due to the traction $\mathbf{t}_m$ on the surface of rigid inclusion vanishes (Hwu and Ting, 1989) and the solutions given in (6a)$_2$ and (32). The result is

$$\omega = -\frac{2\int_0^{2\pi}\mathbf{y}^T\mathrm{Re}\{\mathbf{A}^{-T}\mathbf{f}_0'(e^{i\psi})\}d\psi}{\pi\,\mathrm{Im}\{\mathbf{k}^T\mathbf{B}\mathbf{A}^{-1}\bar{\mathbf{k}}\}}, \tag{33a}$$

where

$$\mathbf{y}^T = (-b\sin\psi \quad a\cos\psi \quad 0), \tag{33b}$$

and the prime ($'$) denotes differentiation with respect to its argument. Similar to the problems of elastic inclusions, the interfacial stresses can be determined by $\phi_{,m}$ and $\phi_{,n}$, which are

$$\phi_{,m} = -\frac{4}{\rho}\mathbf{N}_1^T(\theta)\mathbf{H}^{-1}\mathrm{Re}\{e^{i\psi}\mathbf{A}\mathbf{f}_0'(\sigma)\} + \frac{\omega}{\rho}\mathrm{Re}\{ie^{-i\psi}\mathbf{B}\mathbf{P}(\theta)\mathbf{A}^{-1}\bar{\mathbf{k}}\},$$
$$\phi_{,n} = -\frac{4}{\rho}\mathbf{H}^{-1}\mathrm{Re}\{e^{i\psi}\mathbf{A}\mathbf{f}_0'(\sigma)\} + \frac{\omega}{\rho}\mathrm{Re}\{ie^{-i\psi}\mathbf{B}\mathbf{A}^{-1}\bar{\mathbf{k}}\}, \tag{34a}$$

or

$$\phi_{,m} = -\frac{4}{\rho}\mathbf{N}_1^T(\theta)\mathbf{H}^{-1}\sum_{k=1}^{\infty}Re\{ke^{ik\psi}\mathbf{A}\mathbf{e}_k\} + \frac{\omega}{\rho}\mathrm{Re}\{ie^{-i\psi}\mathbf{B}\mathbf{P}(\theta)\mathbf{A}^{-1}\bar{\mathbf{k}}\},$$
$$\phi_{,n} = -\frac{4}{\rho}\mathbf{H}^{-1}\sum_{k=1}^{\infty}\mathrm{Re}\{ke^{ik\psi}\mathbf{A}\mathbf{e}_k\} + \frac{\omega}{\rho}\mathrm{Re}\{ie^{-i\psi}\mathbf{B}\mathbf{A}^{-1}\bar{\mathbf{k}}\}, \tag{34b}$$

in which the identities provided by Ting (1988) have been used. Similarly, if $\mathbf{f}_0$ belongs to Case (ii), we have

$$\mathbf{f}(\zeta) = -\mathbf{A}^{-1}\sum_{k=1}^{\infty}\{\overline{\mathbf{A}}\bar{\mathbf{e}}_k + \mathbf{A}\boldsymbol{\Gamma}_k\mathbf{e}_k\}\zeta^{-k} + \frac{\omega}{2\zeta}\mathbf{A}^{-1}\bar{\mathbf{k}}, \tag{35a}$$

and

$$\omega = \frac{-2\,\mathrm{Im}\{\mathbf{k}^T\overline{\mathbf{A}}^{-T}\bar{\mathbf{e}}_1\}}{\mathrm{Im}\{\mathbf{k}^T\mathbf{B}\mathbf{A}^{-1}\bar{\mathbf{k}}\}}. \tag{35b}$$

The expressions of the derivatives $\phi_{,m}$ and $\phi_{,n}$ are exactly the same as (34b).

5 Examples

5.1 Point Force in the Matrix. Consider an infinite anisotropic medium containing an elastic inclusion, subjected to a concentrated force applied on $(\hat{x}_1, \hat{x}_2)$ located in the matrix. The elasticity solution of this problem can be used as a Green's function for boundary element methods. For the case that the inclusion is replaced by a hole, the complex function $\mathbf{f}(\zeta)$ can be written explicitly by substituting (9) into (27) with the understanding that the subscript of ζ are dropped before the multiplication of matrices and a replacement of ζ_α should be made for each component function of $\mathbf{f}(\zeta)$ after the multiplication of matrices. The result is

$$\mathbf{f}(\zeta) = \sum_{k=1}^{3} \ll \log(\zeta_\alpha^{-1} - \bar{\hat{\zeta}}_k) \gg \mathbf{B}^{-1}\bar{\mathbf{B}}\mathbf{I}_k\bar{\mathbf{A}}^T\hat{\mathbf{t}}/2\pi i \qquad (36a)$$

where

$$\mathbf{I}_1 = \begin{bmatrix} 1 & 0 & 0 \\ 0 & 0 & 0 \\ 0 & 0 & 0 \end{bmatrix}, \quad \mathbf{I}_2 = \begin{bmatrix} 0 & 0 & 0 \\ 0 & 1 & 0 \\ 0 & 0 & 0 \end{bmatrix}, \quad \mathbf{I}_3 = \begin{bmatrix} 0 & 0 & 0 \\ 0 & 0 & 0 \\ 0 & 0 & 1 \end{bmatrix}. \qquad (36b)$$

This explicit expression is exactly the same as that shown in Hwu and Yen (1991). The derivative $\phi_{,m}$ shown in (28a) used to calculate the hoop stress can be reduced to

$$\phi_{,m} = \frac{2}{\pi\rho}\mathbf{N}_3(\theta)\mathbf{L}^{-1}\mathrm{Re}\{\mathbf{B} \ll ie^{i\psi}(e^{i\psi} - \bar{\hat{\zeta}}_\alpha)^{-1} \gg \mathbf{A}^T\}\hat{\mathbf{t}}. \qquad (37)$$

Similar to (36), the explicit solution of $\mathbf{f}(\zeta)$ given in (32) for the rigid inclusions subjected to a concentrated force applied on $(\hat{x}_1, \hat{x}_2)$ is obtained as

$$\mathbf{f}(\zeta) = \sum_{k=1}^{3} \ll \log(\zeta_\alpha^{-1} - \bar{\hat{\zeta}}_k) \gg \mathbf{A}^{-1}\bar{\mathbf{A}}\mathbf{I}_k\bar{\mathbf{A}}^T\hat{\mathbf{t}}/2\pi i + \frac{\omega}{2} \ll \zeta_\alpha^{-1} \gg \mathbf{A}^{-1}\bar{\mathbf{k}} \qquad (38)$$

where the relative rotation ω can be evaluated by (33) with $\mathbf{f}_0$ given in (9). With the aid of residue theorem, we obtain

$$\omega = \frac{\mathrm{Re}\{\bar{\mathbf{k}}^T\mathbf{A}^{-T} \ll \hat{\zeta}_\alpha^{-1} \gg \mathbf{A}^T\}\hat{\mathbf{t}}}{\pi\,\mathrm{Im}\{\mathbf{k}^T\mathbf{B}\mathbf{A}^{-1}\bar{\mathbf{k}}\}}. \qquad (39)$$

If the load is applied on the interface boundary, i.e., $\hat{\zeta}_\alpha = e^{i\hat{\psi}}$, we have

$$\omega = \frac{-\hat{x}_2\hat{t}_1 + \hat{x}_1\hat{t}_2}{\pi\,\mathrm{Im}\{\mathbf{k}^T\mathbf{B}\mathbf{A}^{-1}\bar{\mathbf{k}}\}} \qquad (40)$$

where $(\hat{x}_1, \hat{x}_2) = (a\cos\hat{\psi}, b\sin\hat{\psi})$ is the location of the applied force $\hat{\mathbf{t}} = (\hat{t}_1, \hat{t}_2, \hat{t}_3)$. This solution is equivalent to the one given by Ting and Yan (1991).

For general elastic inclusion, no analytical solution has been presented in the literature. To verify the present results, one may consider (1) the simplest condition that the matrix and inclusion are composed of the same material; and (2) the cases that the inclusions are very soft or hard, which can be checked by the results of holes or rigid inclusions. By setting $\mathbf{A}_1 = \mathbf{A}_2 = \mathbf{A}$, $\mathbf{M}_1 = \mathbf{M}_2 = \mathbf{M}$ in Eq. (21), and evaluating $\mathbf{e}_k$ from (9) and (12), one may obtain $\mathbf{c}_k$, $\mathbf{f}_1(\zeta)$ and $\mathbf{f}_2(\zeta)$ by (21), (17), and (7), respectively. The infinite series representations of $\mathbf{f}_1$ and $\mathbf{f}_2$ can then be shown to be a Taylor's expansion of logarithmic function. Combining the results, one may prove that $\mathbf{f}_0(\zeta) + \mathbf{f}_1(\zeta) = \mathbf{f}_2(\zeta) = \ll \log(z_\alpha - \hat{z}_\alpha) \gg \mathbf{q}$ which is the solution for a homogeneous medium under concentrated forces.

In the case that the inclusion is elastic, numerical calculation has been performed (Yen, 1991) and the results show that the solutions for holes or rigid inclusions are really approximated by very soft or hard inclusions. To see the effect of elliptic shape and the singular behavior near the crack tips or the tips of rigid line inclusions, a series of numerical data for the hoop stress have been plotted (Yen, 1991) by using Eqs. (23), (28), and (34). A nearly constant value of the hoop stress for $b \to 0$ has been observed when the inclusion is not a hole or rigid medium, which means that no singular behavior occurs for the general elastic inclusions. For elliptic holes or rigid inclusions, singular behavior occurs when $b \to 0$ which is expected for the cracks and rigid line inclusions.

5.2 Uniform Load at Infinity. In the case when the elastic inclusion in an infinite matrix is subjected to a uniform load at infinity, detail analysis has been given in Hwu and Ting (1989) by using the semi-inverse method, i.e., the function form of $\mathbf{f}(\zeta)$ is chosen before calculation. In this paper without any prior choices, general solutions of $\mathbf{f}(\zeta)$ are obtained for arbitrary loading conditions. In order to verify this solution, we reduce our results to uniform loading condition since it is the only analytical solution available for the general elastic inclusion problems. If the complex function $\mathbf{f}_0(\zeta)$ associated with the unperturbed elastic field is chosen as those shown in (10a), it belongs to the Case (ii). For hole problems, the function $\mathbf{f}(\zeta)$ corresponding to the perturbative field of matrix is then obtained from (29) with

$$\mathbf{e}_1 = \frac{1}{2} \ll a - ibp_\alpha \gg \mathbf{q}, \quad \mathbf{e}_k = \mathbf{0}, \quad k = 2, 3, \cdots \infty. \qquad (41)$$

The final simplified result is

$$\mathbf{f}(\zeta) = -\frac{1}{2} \ll \zeta_\alpha^{-1} \gg \mathbf{B}^{-1}(a\mathbf{t}_2^\infty - ib\mathbf{t}_1^\infty), \qquad (42)$$

which can be proved to be identical to those given in Hwu and Ting (1989).

As stated in Section 2.3, $\mathbf{f}_0$ can also be chosen as

$$\mathbf{f}_0(\zeta) = \ll \zeta_\alpha \gg \mathbf{q}_0, \quad \mathbf{q}_0 = \frac{1}{2} \ll a - ibp_\alpha \gg \mathbf{q}.$$

For this choice, function $\mathbf{f}(\zeta)$ should be found by using (27) instead of (29) since $\mathbf{f}_0(\zeta)$ now belongs to Case (i). By careful derivation, one can prove that the final results of $\mathbf{f}_0 + \mathbf{f}_1$ are the same for different choices of $\mathbf{f}_0$. A real form solution for the hoop stress along the hole boundary can be obtained by substituting (41) into (28b).

Similar to the hole problems, substitution of (41) into (35) provides the solutions for the rigid inclusions as

$$\mathbf{f}(\zeta) = -\frac{1}{2} \ll \zeta_\alpha^{-1} \gg \mathbf{A}^{-1}(a\,\boldsymbol{\epsilon}_1^\infty + ib\boldsymbol{\epsilon}_2^\infty + \omega\bar{\mathbf{k}}),$$

$$\omega = \frac{a^2(\mathbf{H}^{-1}\boldsymbol{\epsilon}_1^\infty)_2 - ab[(\mathbf{H}^{-1}\mathbf{S}\,\boldsymbol{\epsilon}_1^\infty)_1 + (\mathbf{H}^{-1}\mathbf{S}\,\boldsymbol{\epsilon}_2^\infty)_2] - b^2(\mathbf{H}^{-1}\boldsymbol{\epsilon}_2^\infty)_1}{a^2(\mathbf{H}^{-1})_{22} + 2ab(\mathbf{H}^{-1}\mathbf{S})_{21} + b^2(\mathbf{H}^{-1})_{11}}, \qquad (43)$$

which can be proved to be equivalent to the one given in Hwu and Ting (1989).

For the case of elastic inclusions, we first check the condition when the matrix and inclusion are composed of the same material. If $\mathbf{A}_1 = \mathbf{A}_2$, $\mathbf{B}_1 = \mathbf{B}_2$, $\mathbf{M}_1 = \mathbf{M}_2$, we have, by (21), (25), and (41), $\mathbf{f}_1(\zeta) = \mathbf{0}$. The zero perturbed solution means that there is no inclusion effect for the homogeneous medium which is expected, since the $\mathbf{f}_0$ chosen represents the exact solution of homogeneous medium subjected to uniform loading at infinity.

For general elastic inclusions, the functions $\mathbf{f}_1$ and $\mathbf{f}_2$ corresponding to the perturbed fields of matrix and inclusion are obtained from (21), (25), and (7) as

$$\mathbf{f}_1(\zeta) = -\ll \zeta_\alpha^{-1} \gg \mathbf{B}_1^{-1}\{\bar{\mathbf{B}}_1\bar{\mathbf{e}}_1 + \mathbf{B}_1\boldsymbol{\Gamma}_1\mathbf{e}_1 - \bar{\mathbf{B}}_2\bar{\mathbf{c}}_1 - \mathbf{B}_2\boldsymbol{\Gamma}_1^*\mathbf{c}_1\},$$

$$\mathbf{f}_2(\zeta) = \ll \frac{2z_\alpha^*}{a - ibp_\alpha^*} \gg \mathbf{c}_1, \qquad (44a)$$

where

$$\mathbf{c}_1 = -i\{\mathbf{G}_0 - \bar{\mathbf{G}}_1\bar{\mathbf{G}}_0^{-1}\mathbf{G}_1\}^{-1}\{\mathbf{A}_1^{-T}\mathbf{e}_1 + \bar{\mathbf{G}}_1\bar{\mathbf{G}}_0^{-1}\bar{\mathbf{A}}_1^{-T}\bar{\mathbf{e}}_1\}, \qquad (44b)$$

and

$$\mathbf{e}_1 = \frac{1}{2} \ll a - ibp_\alpha \gg (\mathbf{A}_1^T \mathbf{t}_2^\infty + \mathbf{B}_1^T \boldsymbol{\epsilon}_1^\infty). \tag{44c}$$

Note that $\mathbf{f}_2$ obtained in $(44a)_2$ represents a state of uniform stress which has been observed by Eshelby (1957). By numerical calculation (Yen, 1991), the solutions presented here have been proved to be identical to those given in the literature (Lekhnitskii, 1968; Hwu and Ting, 1989).

5.3 Interactions Between Dislocations and Inclusions. Interactions between dislocations and inclusions have been a topic of considerable research. Greater understanding of material defects can be gained through the solution of suitable elasticity problems. For the dislocation with Burgers vector $\hat{\mathbf{b}}$ located on $\hat{\mathbf{x}}$, the total stress field can be obtained in a straightforward manner from the known solution for a point force by using a certain analogy between dislocations and point forces. The only difference is that $\mathbf{q} = \mathbf{A}^T\hat{\mathbf{t}}/2\pi i$ is now replaced by $\mathbf{q} = \mathbf{B}^T\hat{\mathbf{b}}/2\pi i$.

The interactions are usually shown by the contour of the glide component of the image force (Hirth and Lothe, 1982). For the purpose of verification, comparison has been made for the case of isotropic materials. The results show that the analytical solutions presented in this paper are exactly the same as those given by Stagni and Lizzio (1983) for the holes interacted with dislocations, and by Santare and Keer (1986) for the interactions between rigid inclusions and dislocations. For the general cases that both the inclusions and matrices are elastically anisotropic, the detailed calculation and physical explanation can be found in (Yen and Hwu, 1993).

6 Conclusions

A general analytical solution for the elliptical anisotropic elastic inclusions embedded in an infinite anisotropic matrix subjected to an arbitrary loading has been obtained in this paper by combining the Stroh's formalism with the method of analytical continuation. The special cases when the elastic inclusion is replaced by a hole or a rigid inclusion are also studied. Some interesting and important examples such as point forces or dislocations in the matrix, and uniform loadings at infinity are solved explicitly.

Acknowledgments

The authors would like to thank the support by National Science Council, Republic of China, through Grant No. NSC 81-0401-E006-12.

References

Ang, W. T., and Clements, D. L., 1986, "A Boundary Element Method for Determining the Effect of Holes on the Stress Distribution Around a Crack," *Int. J. Num. Method in Eng.*, Vol. 23, pp. 1727–1737.

Chadwick, P., and Smith, G. D., 1977, "Foundations of the Theory of Surface Waves in Anisotropic Elastic Materials," *Adv. Appl. Mech.*, Vol. 17, pp. 303–376.

Chen, W. T., 1967, "On an Elliptic Elastic Inclusion in an Anisotropic Medium," *Q. Appl. Math.*, Vol. 20, pp. 307–313.

Dundurs, J., and Mura, T., 1964, "Interaction Between an Edge Dislocation and a Circular Inclusion," *J. Mech. Phys. Sol.*, Vol. 12, pp. 177–189.

Erdogan, F., Gupta, G. D., and Ratwani, M., 1974, "Interaction Between a Circular Inclusion and an Arbitrary Oriented Crack," ASME JOURNAL OF APPLIED MECHANICS, Vol. 41, pp. 382–385.

Eshelby, J. D., 1957, "The Determination of the Elastic Field of an Elliptic Inclusion, and Related Problems," *Proc. R. Soc.*, London, Vol. 241, pp. 376–396.

Hirth, J. P., and Lothe, J., 1982, *Theory of Dislocations*, McGraw-Hill, New York.

Honein, T., and Herrmann, G., 1990, "On Bonded Inclusions With Circular or Straight Boundaries in Plane Elastostatics," ASME JOURNAL OF APPLIED MECHANICS, Vol. 57, pp. 850–856.

Hwu, C., and Ting, T. C. T., 1989, "Two-Dimensional Problems of the Anisotropic Elastic Solid with an Elliptic Inclusion," *Q. J. Mech. Appl. Math.*, Vol. 42, pp. 553–572.

Hwu, C., and Yen, W. J., 1991, "Green's Function of Two-Dimensional Anisotropic Plates Containing an Elliptic Hole," *Int. J. Solid Structure*, Vol. 27, pp. 1705–1719.

Ingebrigtsen, K. A., and Tonning, A., 1969, "Elastic Surface Waves in Crystals," *Phys. Rev.*, Vol. 184, pp. 942–951.

Jaswon, M. A., and Bhargave, R. D., 1961, "Two-Dimensional Elastic Inclusion Problems," *Proceedings of the Cambridge Philosophical Society*, Vol. 57, pp. 669–680.

Lekhnitskii, S. G., 1968, *Anisotropic Plates*, Gordon and Breach.

Muskhelishvili, N. I., 1954, *Some Basic Problem of the Mathematical Theory of Elasticity*, Noordhoff Pub., Groningen.

Santare, M. H., and Keer, L. M., 1986, "Interaction Between an Edge Dislocation and a Rigid Elliptical Inclusion," ASME JOURNAL OF APPLIED MECHANICS, Vol. 53, pp. 382–385.

Sendeckyi, G. P., 1970, "Elastic Inclusion Problems in Plane Elastostatics," *Int. J. Solids Structures*, Vol. 6, pp. 1535–1543.

Stagni, L., 1982, "On the Elastic Field Perturbation by Inhomogeneous in Plane Elasticity," *ZAMP*, Vol. 33, pp. 313–325.

Stagni, L., and Lizzio, R., 1983, "Shape Effects in the Interaction Between an Edge Dislocation and an Elliptic Inhomogeneity," *Appl. Phys. A*, Vol. 30, pp. 217–221.

Stroh, A. N., 1958, "Dislocations and Cracks in Anisotropic Elasticity," *Phil. Mag.*, Vol. 7, pp. 625–646.

Suo, Z., 1990, "Singularities, Interfaces and Cracks in Dissimilar Anisotropic Media," *Proc. R. Soc. Lond.*, Vol. A427, pp. 331–358.

Ting, T. C. T., 1988, "Some Identities and the Structure of N_i in the Stroh Formalism of Anisotropic Elasticity," *Q. Appl. Math.*, Vol. 46, pp. 109–120.

Ting, T. C. T., and Yan, G., 1991, "The Anisotropic Elastic Solid With an Elliptic Hole or Rigid Inclusion," *Int. J. Solids Structures*, Vol. 27, pp. 1879–1894.

Wang, Z. Y., Zang, H. T., and Chou, Y. T., 1985, "Characteristics of the Elastic Field of Rigid Line Inhomogeneity," ASME JOURNAL OF APPLIED MECHANICS, Vol. 52, pp. 818–822.

Yang, H. C., and Chou, Y. T., 1976, "Generalized Plane Problems of Elastic Inclusions in Anisotropic Solids," ASME JOURNAL OF APPLIED MECHANICS, Vol. 43, pp. 424–430.

Yen, W. J., 1991, "Analysis of Anisotropic Bodies with Inclusions or Holes and its Applications to Composite Laminates," Ph.D. dissertation, National Cheng Kung University, Tainan, Taiwan, R.O.C.

Yen, W. J., and Hwu, C., 1993, "Interactions Between Dislocations and Anisotropic Elastic Elliptical Inclusions," ASME JOURNAL OF APPLIED MECHANICS, accepted for publication.

Frictionless Contact of Layered Half-Planes, Part I: Analysis

M.-J. Pindera
Assoc. Professor.

M. S. Lane
Research Assoc.,
Mem. ASME.

Civil Engineering and
Applied Mechanics Department,
University of Virginia,
Charlottesville, VA 22903

A method is presented for the solution of frictionless contact problems on multilayered half-planes consisting of an arbitrary number of isotropic, orthotropic, or monoclinic layers arranged in any sequence. A displacement formulation is employed and the resulting Navier equations that govern the distribution of displacements in the individual layers are solved using Fourier transforms. A local stiffness matrix in the transform domain is formulated for each layer which is then assembled into a global stiffness matrix for the entire multilayered half-plane by enforcing continuity conditions along the interfaces. Application of the mixed boundary condition on the top surface of the medium subjected to the force of the indenter results in an integral equation for the unknown pressure in the contact region. The integral possesses a divergent kernel which is decomposed into Cauchy type and regular parts using the asymptotic properties of the local stiffness matrix and the ensuing relation between Fourier and finite Hilbert transform of the contact pressure. For homogeneous half-planes, the kernel consists only of the Cauchy-type singularity which results in a closed-form solution for the contact stress. For multilayered half-planes, the solution of the resulting singular integral equation is obtained using a collocation technique based on the properties of orthogonal polynomials. Part I of this paper outlines the analytical development of the technique. In Part II a number of numerical examples is presented addressing the effect of off-axis plies on contact stress distribution and load versus contact length in layered composite half-planes.

Introduction

The solution to the frictionless contact problem of a rigid punch indenting an isotropic half-plane has been long known (Gladwell, 1980). The problem is typically formulated as a singular integral equation for the unknown normal stress distribution in the contact area using the constraint on the surface displacement due to the punch's profile. For homogeneous half-planes the solution to the singular integral equation is obtained in closed form for a parabolic or flat punch. For a parabolic punch, the normal stress distribution in the contact region is elliptical and the applied load varies parabolically with the contact length in direct proportion to the Young's modulus of the material. For transversely isotropic or orthotropic half-planes, the contact stress profile is also elliptical and the applied load is a quadratic function of the contact length (Conway, 1953; Chen, 1969). The dependence of the applied load on the elastic constants, however, is more complicated than for isotropic case and involves all the in-plane moduli. Similar results have been obtained for monoclinic half-planes within the framework of plane stress or plane strain (Chen, 1969; Conway, 1967). Recently, a closed-form solution to the contact problem of monoclinic half-planes within the framework of generalized plane deformation has been provided by the second author (Lane, 1991). The generalized plane deformation formulation allows us to model the response of composite materials with off-axis laminae.

Available solutions to layered media contact problems include Chen and Engel's (1972) solution for one and two layers bonded to a half-space based on an approximate treatment of the pressure distribution in the contact region, Ratwani and Erdogan's (1973) solution of an elastic strip supported by a half-plane indented by curved and flat rigid punches, Gupta and Walowit's (1974) Green's function solution for a layer bonded to a half-plane, and Shield and Bogy's (1988) solution to a flat punch contact problem of a layered half-plane using the transfer matrix approach. Only isotropic strips, layers, and half-planes were considered by the cited authors. The authors are not aware of an analytical solution to the contact problem of a multilayered half-plane consisting of orthotropic and monoclinic laminae. A summary of the different approaches for the contact problem of layered media has been given by Chen and Engel (1972) and most recently by Lane (1991).

The solution to the frictionless contact problem of a layered half-plane requires separation of the integral equation for the unknown pressure distribution in the contact region into singular and regular parts. The regular contribution to the integral

Contributed by the Applied Mechanics Division of THE AMERICAN SOCIETY OF MECHANICAL ENGINEERS for publication in the ASME JOURNAL OF APPLIED MECHANICS.

Discussion on this paper should be addressed to the Technical Editor, Professor Lewis T. Wheeler, Department of Mechanical Engineering, University of Houston, Houston, TX 77204-4792, and will be accepted until four months after final publication of the paper itself in the ASME JOURNAL OF APPLIED MECHANICS.

Manuscript received by the ASME Applied Mechanics Division, Feb. 5, 1991; final revision, Aug. 14, 1992. Associate Technical Editor: G. J. Dvorak.

equation results from the finite geometry effects (i.e., layer thickness) and typically requires numerical solution techniques. As discussed by Shield and Bogy (1988), this can be accomplished using the transfer matrix technique.

In this paper, we present an alternative method for solving the frictionless contact problem of arbitrarily layered half-planes that are indented by rigid punches with parabolic or flat profiles, and present results for half-planes laminated with differently oriented composite plies. The technique is based on the local/global flexibility matrix approach outlined by Bufler (1971) for isotropic layered media with constant elastic properties, that was later reformulated in terms of the local stiffness matrix by Rowe and Booker (1982) and applied to nonhomogeneous isotropic layered media. Chatterjee et al. (1982) and Chatterjee (1987) extended the method to anisotropic layered media for the interlaminar crack problem, and most recently Pindera (1991) gave an outline of the applications of the method to plane and axisymmetric problems in composite mechanics. The local/global stiffness matrix approach naturally facilitates decomposition of the integral equation for the contact stress distribution on the top surface of an arbitrarily laminated half-plane into singular and regular parts that, in turn, can be numerically solved using the collocation technique outlined by Erdogan (1969) and Erdogan and Gupta (1972). This decomposition uses the asymptotic properties of the local stiffness matrix and a relation between Fourier and finite Hilbert transforms of the contact pressure. Despite the fact that there is some similarity between the transfer matrix and the local/global stiffness matrix formulation of contact problems, the authors are of the opinion that the present approach offers a more natural way of separating the integral equation for the contact pressure into singular and regular parts.

Problem Formulation

We consider a laminated medium comprising a number of layers bonded to each other that, in turn, are bonded to a half-plane, Fig. 1. The assemblage is indented by a rigid punch of a parabolic profile. The individual layers and the half-plane can be isotropic (or transversely isotropic), orthotropic, or monoclinic. A local x-y-z coordinate system is placed in the center of each layer such that the x and y-axes lie in the plane of lamination and the z-axis is perpendicular to the lamination plane. The layered medium is infinite in the x-y plane and the loading is such that the problem is plane in the x-z coordinate system. For the bottom half-plane, the local coordinate system is placed at the bounding surface of the plane.

The stress-strain equations for a given layer are, in contracted notation,

$$\sigma_i = C_{ij}\epsilon_j \text{ for } i, j = 1, \ldots, 6. \tag{1}$$

Each type of layer, monoclinic, orthotropic, or isotropic, has a unique stiffness matrix **C**. Monoclinic materials have elastic symmetry about one plane. In this study, the plane of symmetry is orthogonal to the z-axis. The stiffness matrix for a monoclinic layer has 13 independent constants. Its structure for the specified plane of symmetry is

$$\begin{bmatrix} C_{11} & C_{12} & C_{13} & 0 & 0 & C_{16} \\ C_{12} & C_{22} & C_{23} & 0 & 0 & C_{26} \\ C_{13} & C_{23} & C_{33} & 0 & 0 & C_{36} \\ 0 & 0 & 0 & C_{44} & C_{45} & 0 \\ 0 & 0 & 0 & C_{45} & C_{55} & 0 \\ C_{16} & C_{26} & C_{36} & 0 & 0 & C_{66} \end{bmatrix}. \tag{2}$$

Orthotropic materials have elastic symmetry about three orthogonal axes. The stiffness matrix for an orthotropic layer has nine independent constants referred to the coordinate system coincident with the three axes of material symmetry. In this coordinate system, the coupling stiffness elements C_{16}, C_{26}, C_{36}, and C_{45} vanish in Eq. (2).

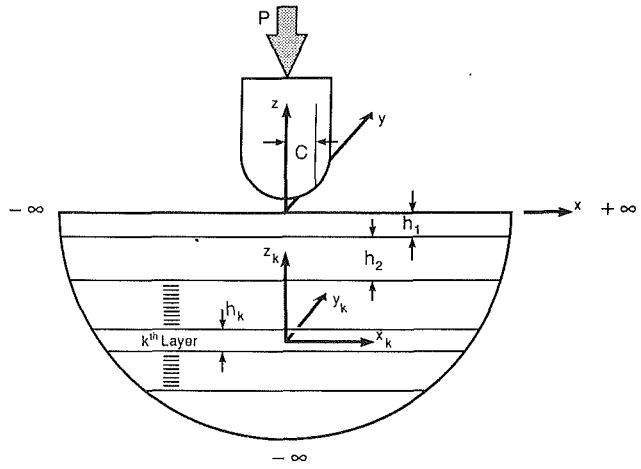

Fig. 1 Geometry of the layered half-plane

Unidirectional fiber-reinforced composite laminae are typically transversely isotropic, with one of the planes of material symmetry being isotropic. For example, if the y-z plane is isotropic, then $C_{13} = C_{12}$, $C_{33} = C_{22}$, $C_{66} = C_{55}$, and $C_{44} = 1/2(C_{22} - C_{23})$ in Eq. (2). There are only five independent elastic constants for transversely isotropic materials. A transversely isotropic material rotated through an angle about the z-axis behaves as a monoclinic material in the original coordinate system. As is well known, the stiffness matrix for an isotropic layer has only two independent constants, C_{11} and C_{12}, with $C_{44} = C_{55} = C_{66} = 1/2(C_{11} - C_{12})$.

In the present investigation, a displacement formulation will be employed. In this formulation, the equilibrium equations

$$\sigma_{ij,j} = 0 \tag{3}$$

are expressed in terms of displacements using the strain-displacement relations,

$$\epsilon_{ij} = \frac{1}{2}(u_{i,j} + u_{j,i}), \tag{4}$$

and the stress-strain equations, Eq. (1), in conjunction with the appropriate form of Eq. (2), depending on the ply material type. Due to the presence of monoclinic plies, generalized plane deformation formulation is employed with the displacement components given by

$$u = u(x, z),\ v = v(x, z),\ w = w(x, z). \tag{5}$$

Using the above assumption for the displacement field in each ply, the governing differential equations for a generic monoclinic ply become

$$\begin{aligned} &C_{11}u_{,xx} + C_{55}u_{,zz} + C_{16}v_{,xx} + C_{45}v_{,zz} + (C_{13} + C_{55})w_{,xz} = 0 \\ &C_{16}u_{,xx} + C_{45}u_{,zz} + C_{66}v_{,xx} + C_{44}v_{,zz} + (C_{36} + C_{45})w_{,xz} = 0 \\ &(C_{13} + C_{55})u_{,xz} + (C_{36} + C_{45})v_{,xz} + C_{55}w_{,xx} + C_{33}w_{,zz} = 0. \end{aligned} \tag{6}$$

We note that coupling exists between all the displacement components for a monoclinic layer. The above equations can be specialized for an orthotropic, transversely isotropic, or isotropic layer by noting that for these layers the stiffness matrix elements C_{16}, C_{36}, and C_{45} vanish. In this case, the out-of-plane displacement component $v(x, z)$ becomes uncoupled from the in-plane displacement components $u(x, z)$ and $w(x, z)$.

The solution of the equilibrium equations for each layer must satisfy the external surface mixed boundary conditions as well as the interfacial traction and displacement continuity conditions. The external surface mixed boundary conditions

ensure that the normal traction component σ_{zz} is zero outside the contact area $|x| > c$, while inside the contact area the vertical displacement $w(x, z)$ conforms to the profile of the punch. The condition on the vertical displacement is expressed in terms of the slope of the punch's profile to avoid logarithmic singularity at infinity. Thus the external surface mixed boundary conditions are given in the form

$$w_{1,x}(x, +h_1/2) = f(x) \text{ for } |x| < c \text{ and } \sigma_{zz} = 0 \text{ for } |x| > c \tag{7a}$$

$$\sigma_{xz} = \sigma_{yz} = 0 \text{ for } -\infty < x < +\infty. \tag{7b}$$

The continuity requirement for interfacial tractions and displacements in generalized plane deformation imposes six additional conditions at each interface. These conditions are

$$\begin{aligned} u_k(x, -h_k/2) &= u_{k+1}(x, h_{k+1}/2) \\ v_k(x, -h_k/2) &= v_{k+1}(x, h_{k+1}/2) \\ w_k(x, -h_k/2) &= w_{k+1}(x, h_{k+1}/2) \end{aligned} \tag{8a}$$

$$\begin{aligned} \sigma_{zz}^k(x, -h_k/2) &= \sigma_{zz}^{k+1}(x, h_{k+1}/2) \\ \sigma_{xz}^k(x, -h_k/2) &= \sigma_{xz}^{k+1}(x, h_{k+1}/2) \\ \sigma_{yz}^k(x, -h_k/2) &= \sigma_{yz}^{k+1}(x, h_{k+1}/2). \end{aligned} \tag{8b}$$

Method of Solution

The solution to Eqs. (6) subject to the boundary and continuity conditions specified by Eqs. (7) and (8) is facilitated through the use of Fourier transforms. Defining the displacement vector for the kth ply as $\mathbf{u}_k = (w_k, u_k, v_k)$, its Fourier transform $\bar{\mathbf{u}}_k(s, z)$ along with the inverse transform is given by

$$\begin{aligned} \bar{\mathbf{u}}_k(s, z) &= \frac{1}{\sqrt{2\pi}} \int_{-\infty}^{+\infty} \mathbf{u}_k(x, z) e^{isx} dx, \\ \mathbf{u}_k(x, z) &= \frac{1}{\sqrt{2\pi}} \int_{-\infty}^{+\infty} \bar{\mathbf{u}}_k(s, z) e^{-isx} ds. \end{aligned} \tag{9}$$

Application of the Fourier transform reduces the system of partial differential equations, Eqs. (6), to a system of ordinary differential equations in z with the transform variable s appearing as a parameter. For a monoclinic layer the transformed equilibrium equations are

$$\begin{aligned} &C_{55}\bar{u}_{,zz} - s^2 C_{11}\bar{u} + C_{45}\bar{v}_{,zz} - s^2 C_{16}\bar{v} - is(C_{13} + C_{55})\bar{w}_{,z} = 0 \\ &C_{45}\bar{u}_{,zz} - s^2 C_{16}\bar{u} + C_{44}\bar{v}_{,zz} - s^2 C_{66}\bar{v} - is(C_{36} + C_{45})\bar{w}_{,z} = 0 \\ &-is(C_{13} + C_{55})\bar{u}_{,z} - \text{is}(C_{36} + C_{45})\bar{v}_{,z} + C_{33}\bar{w}_{,zz} - s^2 C_{55}\bar{w} = 0. \end{aligned} \tag{10}$$

As indicated previously, the corresponding equations for orthotropic or transversely isotropic layers are obtained by setting C_{16}, C_{36}, and C_{45} to zero.

The solutions to the preceding equations are sought in the form $\bar{w}(s, z) = w_0 e^{s\lambda z}$, $\bar{u}(s, z) = u_0 e^{s\lambda z}$, and $\bar{v}(s, z) = v_0 e^{s\lambda z}$. If the thicknesses of the layers comprising the half-plane are finite, the exponential terms in the transform domain solutions are expressed in terms of hyperbolic functions to facilitate construction of the local stiffness matrix for a given layer. The solutions of Navier's equations in the transform domain for monoclinic, orthotropic (or transversely isotropic), and isotropic layers are presented as follows.

Monoclinic Layers:

$$\begin{aligned} \bar{u}(s, z) &= \sum_{j=1}^{3} [F_j(s)\cosh(s\lambda_j z) + G_j(s)\sinh(s\lambda_j z)] \\ \bar{v}(s, z) &= \sum_{j=1}^{3} [F_j(s)\cosh(s\lambda_j z) + G_j(s)\sinh(s\lambda_j z)] L_j(s) \\ \bar{w}(s, z) &= i \sum_{j=1}^{3} [G_j(s)\cosh(s\lambda_j z) + F_j(s)\sinh(s\lambda_j z)] R_j(s) \end{aligned} \tag{11}$$

Orthotropic Layers:

$$\begin{aligned} \bar{u}(s, z) &= \sum_{j=1}^{2} [F_j(s)\cosh(s\lambda_j z) + G_j(s)\sinh(s\lambda_j z)] \\ \bar{w}(s, z) &= i \sum_{j=1}^{2} [G_j(s)\cosh(s\lambda_j z) + F_j(s)\sinh(s\lambda_j z)] R_j(s) \\ \bar{v}(s, z) &= H_1(s)\cosh(s\lambda_3 z) + I_1(s)\sinh(s\lambda_3 z) \end{aligned} \tag{12}$$

Isotropic Layers in the x-z Plane:

$$\begin{aligned} \bar{u}(s, z) &= [F_1(s) + zF_2(s)]\cosh(sz) + [G_1(s) + zG_2(s)]\sinh(sz) \\ \bar{w}(s, z) &= i\left[\left(G_1(s) + \frac{R_1(s)}{s} F_2(s) + zG_2(s) \right) \cosh(sz) \right. \\ &\quad \left. + \left(F_1(s) + \frac{R_1(s)}{s} G_2(s) + zF_2(s) \right) \sinh(sz) \right] \\ \bar{v}(s, z) &= H_1(s)\cosh(sz) + I_1(s)\sinh(sz) \end{aligned} \tag{13}$$

In the above, λ_j's are the eigenvalues of the characteristic equation that ensures that Eqs. (11)–(13) satisfy Navier's equations (cf. Pagano, 1970, for explicit expressions), $F_j(s)$, $G_j(s)$, $H_1(s)$, $I_1(s)$, are the unknown Fourier coefficients, and $L_j(s)$, $R_j(s)$ are given in terms of the material properties of a given layer in the Appendix.

For homogeneous monoclinic, orthotropic, or transversely isotropic half-planes, the corresponding solutions are as follows.

Monoclinic Half-Plane:

$$\begin{aligned} \bar{u}(s, z) &= \sum_{j=1}^{3} F_j(s) e^{|s|\lambda_j z} \\ \bar{v}(s, z) &= \sum_{j=1}^{3} L_j(s) F_j(s) e^{|s|\lambda_j z} \\ \bar{w}(s, z) &= \text{sgn}(s) i \sum_{j=1}^{3} R_j(s) F_j(s) e^{|s|\lambda_j z} \end{aligned} \tag{14}$$

Orthotropic Half-Plane:

$$\begin{aligned} \bar{u}(s, z) &= \sum_{j=1}^{2} F_j(s) e^{|s|\lambda_j z} \\ \bar{w}(s, z) &= \text{sgn}(s) i \sum_{j=1}^{2} R_j(s) F_j(s) e^{|s|\lambda_j z} \\ \bar{v}(s, z) &= H_1(s) e^{|s|\lambda_3 z} \end{aligned} \tag{15}$$

Isotropic Half-Plane in the x-z Plane:

$$\begin{aligned} \bar{u}(s, z) &= [F_1(s) + zF_2(s)] e^{|s|z} \\ \bar{w}(s, z) &= \text{sgn}(s) i \left[F_1(s) + \frac{R_1(s)}{|s|} F_2(s) + zF_2(s) \right] e^{|s|z} \\ \bar{v}(s, z) &= H_1(s) e^{|s|z} \end{aligned} \tag{16}$$

The displacements given by Eqs. (11)–(16) are substituted back into the constitutive equations in order to determine interfacial tractions needed in applying the continuity conditions given by Eqs. (8) in the transform domain. For a monoclinic layer or half-plane, the continuous interfacial stresses given in terms of displacements in the transform domain are

$$\begin{aligned} \bar{\sigma}_{zz}(s, z) &= -isC_{13}\bar{u} + C_{33}\bar{w}_{,z} - isC_{36}\bar{v} \\ \bar{\sigma}_{xz}(s, z) &= C_{45}\bar{v}_{,z} + C_{55}(\bar{u}_{,z} - is\bar{w}) \\ \bar{\sigma}_{yz}(s, z) &= C_{44}\bar{v}_{,z} + C_{45}(\bar{u}_{,z} - is\bar{w}). \end{aligned} \tag{17}$$

For an orthotropic layer or half-plane, these stresses are given as follows:

$$\bar{\sigma}_{zz}(s, z) = -isC_{13}\bar{u} + C_{33}\bar{w}_{,z}$$
$$\bar{\sigma}_{xz}(s, z) = C_{55}(\bar{u}_{,z} - is\bar{w})$$
$$\bar{\sigma}_{yz}(s, z) = C_{44}\bar{v}_{,z}, \tag{18}$$

and for an isotropic layer or half-plane we have

$$\bar{\sigma}_{zz}(s, z) = -isC_{13}\bar{u} + C_{11}\bar{w}_{,z}$$
$$\bar{\sigma}_{xz}(s, z) = 1/2(C_{11} - C_{13})(\bar{u}_{,z} - is\bar{w})$$
$$\bar{\sigma}_{yz}(s, z) = 1/2(C_{11} - C_{13})\bar{v}_{,z}. \tag{19}$$

To determine the unknown Fourier coefficients $F_j(s)$, $G_j(s)$, $H_1(s)$, and $I_1(s)$ in the solutions for the displacements, interfacial continuity conditions in the transform domain are imposed and the external traction in the contact area is an unknown. The resulting system of simultaneous equations yields solutions for the unknown coefficients in terms of the single unknown normal contact stress distribution. Application of the remaining surface mixed boundary condition on the slope of the vertical displacement in the contact area yields an integral equation for the determination of the contact stress distribution.

Reduction of the Contact Problem to a Singular Integral Equation

In this section, the multilayered half-plane contact problem is reformulated using the local/global stiffness matrix approach. The local/global stiffness matrix approach eliminates the necessity of explicitly finding the unknown Fourier coefficients and directly leads to a singular integral equation for the unknown contact pressure which, as previously mentioned, is solvable by Erdogan's collocation technique.

The problem is reformulated in terms of interfacial displacements along the common interfaces separating the individual layers in place of the unknown Fourier coefficients. This is accomplished by formulating a local stiffness matrix for the kth layer that relates the traction components on top and bottom surfaces of the layer, $\bar{\sigma}_{zz}^{+}$, $\bar{\sigma}_{xz}^{+}$, $\bar{\sigma}_{yz}^{+}$ and $\bar{\sigma}_{zz}^{-}$, $\bar{\sigma}_{xz}^{-}$, $\bar{\sigma}_{yz}^{-}$ obtained from Eqs. (17)–(19), to the corresponding displacement components $\bar{u}^{+}$, $\bar{v}^{+}$, $\bar{w}^{+}$ and $\bar{u}^{-}$, $\bar{v}^{-}$, $\bar{w}^{-}$ obtained from Eqs. (11)–(13). For monoclinic layers we have

$$\begin{bmatrix} k_{11} & k_{12} & k_{13} & k_{14} & k_{15} & k_{16} \\ k_{12} & k_{22} & k_{23} & -k_{15} & k_{25} & k_{26} \\ k_{13} & k_{23} & k_{33} & -k_{16} & k_{26} & k_{36} \\ k_{14} & -k_{15} & -k_{16} & k_{11} & -k_{12} & -k_{13} \\ k_{15} & k_{25} & k_{26} & -k_{12} & k_{22} & k_{23} \\ k_{16} & k_{26} & k_{36} & -k_{13} & k_{23} & k_{33} \end{bmatrix} \begin{Bmatrix} \bar{w}^{+}/i \\ \bar{u}^{+} \\ \bar{v}^{+} \\ \bar{w}^{-}/i \\ \bar{u}^{-} \\ \bar{v}^{-} \end{Bmatrix} = \begin{Bmatrix} \bar{\sigma}_{zz}^{+}/is \\ \bar{\sigma}_{xz}^{+}/s \\ \bar{\sigma}_{yz}^{+}/s \\ -\bar{\sigma}_{zz}^{-}/is \\ -\bar{\sigma}_{xz}^{-}/s \\ -\bar{\sigma}_{yz}^{-}/s \end{Bmatrix}. \tag{20}$$

The above equation is expressed symbolically in the form

$$\begin{bmatrix} \mathbf{K}_{11}^{k} & \mathbf{K}_{12}^{k} \\ \mathbf{K}_{21}^{k} & \mathbf{K}_{22}^{k} \end{bmatrix} \begin{Bmatrix} \bar{\mathbf{U}}_k^{+} \\ \bar{\mathbf{U}}_k^{-} \end{Bmatrix} = \begin{Bmatrix} \bar{\mathbf{T}}_k^{+} \\ \bar{\mathbf{T}}_k^{-} \end{Bmatrix}. \tag{21}$$

In the case of orthotropic and transversely isotropic layers, the elements k_{13}, k_{23}, k_{16}, and k_{26} vanish since there is no coupling between the in-plane and out-of-plane displacements. The elements k_{ij} for monoclinic, orthotropic, and transversely isotropic layers in terms of the transform variable, material constants, and geometry of the layer are given in the Appendix.

An important feature of the transformed local stiffness matrix of a layer is its asymptotic behavior at large values of the transform variable. Examination of the local stiffness matrix reveals that as the transform variable s approaches positive or negative infinity, the coupling submatrices $\mathbf{K}_{12}^{k}$ and $\mathbf{K}_{21}^{k}$ in Eq. (21) vanish, yielding

$$\begin{Bmatrix} \bar{\mathbf{T}}_k^{+} \\ \bar{\mathbf{T}}_k^{-} \end{Bmatrix} = \begin{bmatrix} \mathbf{K}_{11}^{*k} & \mathbf{0} \\ \mathbf{0} & \mathbf{K}_{22}^{*k} \end{bmatrix} \begin{Bmatrix} \bar{\mathbf{U}}_k^{+} \\ \bar{\mathbf{U}}_k^{-} \end{Bmatrix}. \tag{22}$$

The elements k_{ij}^{*} of the asymptotic stiffness matrices $\mathbf{K}_{11}^{*k}$ and $\mathbf{K}_{22}^{*k}$, for monoclinic, orthotropic, and transversely isotropic layers are also given in the Appendix. They are functions of the material properties of the given layer but not functions of the transform variable s or geometry.

If, instead of a finite height layer, a homogeneous half-plane is considered, it can be shown, using Eqs. (14)–(16) and Eqs. (17)–(19), that the relationship between the tractions and displacements on the top surface of the half-plane is given by

$$\{\bar{\mathbf{T}}_n^{+}\} = [\mathbf{K}_{11}^{*n}]\{\bar{\mathbf{U}}_n^{+}\}. \tag{23}$$

We note that the elements of the local stiffness matrix for a homogeneous half-plane, $\mathbf{K}_{11}^{*n}$, are precisely the same as the corresponding elements of the asymptotic stiffness matrix given for a finite height layer in Eq. (22).

Imposition of continuity of displacements and tractions along the common interfaces together with the external boundary conditions (Eqs. (7)–(8)) gives rise to a system of equations in the unknown interfacial displacement components. The continuity of interfacial stresses is guaranteed by requiring that the resultant traction on the kth interface be zero,

$$\bar{\mathbf{T}}_k^{-} + \bar{\mathbf{T}}_{k+1}^{+} = \mathbf{0}, \quad k = 1, \ldots, n-1, \tag{24}$$

whereas the continuity of interfacial displacements is directly enforced by requiring the common interfacial displacements $\bar{\mathbf{U}}_k$ in the expressions for the tractions given by Eq. (21) to be

$$\bar{\mathbf{U}}_{k+1} = \bar{\mathbf{U}}_k^{-} = \bar{\mathbf{U}}_{k+1}^{+}, \quad k = 1, \ldots, n-1. \tag{25}$$

The system of equations is constructed by applying Eq. (24) to each interface, starting with the top surface where the boundary conditions are prescribed in terms of the unknown contact pressure, and using the common interfacial displacements defined by Eq. (25). In the case of layered medium of finite height, this process yields

$$\mathbf{K}_{11}^{1}\bar{\mathbf{U}}_1 + \mathbf{K}_{12}^{1}\bar{\mathbf{U}}_2 = \bar{\mathbf{T}}_1^{+} \qquad \text{for the top layer}$$
$$\mathbf{K}_{21}^{k}\bar{\mathbf{U}}_k + (\mathbf{K}_{22}^{k} + \mathbf{K}_{11}^{k+1})\bar{\mathbf{U}}_{k+1} + \mathbf{K}_{12}^{k+1}\bar{\mathbf{U}}_{k+2} = \mathbf{0}$$
$$\text{for the } k\text{th interface}$$
$$\mathbf{K}_{21}^{n}\bar{\mathbf{U}}_n + \mathbf{K}_{22}^{n}\bar{\mathbf{U}}_{n+1} = \bar{\mathbf{T}}_n^{-} \qquad \text{for the bottom layer} \tag{26}$$

where n is the number of layers. The above system of equations can be represented in the matrix form shown in (27). It is observed that the assembly of the global stiffness matrix for the entire layered medium is carried out by superposing local stiffness matrices of the individual layers along the main diagonal of the global matrix in an overlapping fashion.

$$\begin{bmatrix} \mathbf{K}_{11}^{1} & \mathbf{K}_{12}^{1} & 0 & \cdot & \cdot \\ \mathbf{K}_{21}^{1} & \mathbf{K}_{22}^{1} + \mathbf{K}_{11}^{2} & \mathbf{K}_{12}^{2} & \cdot & \cdot \\ 0 & \mathbf{K}_{21}^{2} & \mathbf{K}_{22}^{2} + \mathbf{K}_{11}^{3} & \cdot & \cdot \\ 0 & 0 & \mathbf{K}_{21}^{3} & \cdot & \cdot \\ 0 & 0 & 0 & \cdot & \mathbf{K}_{22}^{n} \end{bmatrix} \begin{Bmatrix} \bar{\mathbf{U}}_1 \\ \bar{\mathbf{U}}_2 \\ \cdot \\ \cdot \\ \bar{\mathbf{U}}_{n+1} \end{Bmatrix} = \begin{Bmatrix} \bar{\mathbf{T}}_1^{+} \\ 0 \\ \cdot \\ 0 \\ \bar{\mathbf{T}}_n^{-} \end{Bmatrix}. \tag{27}$$

If the bottom layer is a half-plane, $\bar{\mathbf{T}}_n^{-}$ in Eq. (27) is zero, the last submatrix in the global stiffness matrix of Eq. (27) is replaced by $\mathbf{K}_{22}^{n-1} + \mathbf{K}_{11}^{*n}$, and the last subvector of the global interfacial displacement vector is $\bar{\mathbf{U}}_n$.

By inverting the global stiffness matrix given in Eq. (27), the top surface displacements may be related to the top surface

tractions alone when the multilayered medium is a half-plane, i.e., when $\bar{\mathbf{T}}_n^-$ vanishes

$$\{\bar{\mathbf{U}}_1\} = [\mathbf{H}_{11}^1]\{\bar{\mathbf{T}}_1^+\}, \tag{28}$$

where $\mathbf{H}_{11}^1$ is the first 3 × 3 submatrix of the inverse of the global stiffness matrix. Defining the first element of the matrix $\mathbf{H}_{11}^1$ by $H_{11}(s)$, the transform of the normal displacement on the surface of the layered half-plane can be expressed in terms of the normal contact stress $\bar{\sigma}_{zz}^1$ in the absence of friction (i.e., $\sigma_{xz}^1 = \sigma_{yz}^1 = 0$),

$$\bar{w}_1 = H_{11}(s)\bar{\sigma}_{zz}^1(s)/s$$

$$\text{with } \bar{\sigma}_{zz}^1(s) = \bar{p}(s) = \frac{1}{\sqrt{2\pi}} \int_{-c}^{+c} p(x)e^{isx}dx.$$

Imposing the top surface mixed boundary condition on the slope of the normal displacement, $w_{1,x} = f(x)$ in the interval $-c < x < c$, an integral equation for the unknown contact stress distribution $p(x)$ is obtained in the form

$$w_{1,x} = \frac{-i}{\sqrt{2\pi}} \int_{-\infty}^{\infty} s\bar{w}_1 e^{-isx}ds = \frac{-i}{\sqrt{2\pi}} \int_{-\infty}^{\infty} H_{11}(s)\bar{p}(s)e^{-isx}ds. \tag{29}$$

The above is a singular integral equation because as s approaches $\pm\infty$, the kernel $H_{11}(s)$ does not vanish, making the integral unbounded. The limiting value of $H_{11}(s)$ for large s is readily identified by observing that the asymptotic behavior of the local stiffness matrix given by Eq. (22) ensures that in the limit as s approaches $\pm\infty$, the resulting global stiffness matrix has only diagonal elements, so that there is no coupling between top and bottom surfaces of each lamina of the layered half-plane for this limiting case. Consequently, for s approaching $\pm\infty$

$$\{\bar{\mathbf{U}}_1\} = \lim_{s\to\pm\infty} [\mathbf{H}_{11}^1]\{\bar{\mathbf{T}}_1^+\} = [\mathbf{K}_{11}^{*1}]^{-1}\{\bar{\mathbf{T}}_1^+\} \tag{30}$$

and so $\lim_{s\to\pm\infty} H_{11}(s) = \text{sgn}(s)H_{11}^*$, where $\text{sgn}(s)H_{11}^*$ is the first element of the inverse of the asymptotic stiffness matrix of the top layer. Thus, the first element of the inverse of the global stiffness matrix as s goes to $\pm\infty$ is just the first element of the asymptotic stiffness matrix of the top layer (or the corresponding half-plane). This result is used to separate the divergent integral in Eq. (29) into singular and regular parts by first rewriting it as

$$w_{1,x} = \frac{-i}{2\pi} \int_{-\infty}^{\infty} \text{sgn}(s)H_{11}^*\bar{p}(s)e^{-isx}ds - \frac{i}{2\pi} \int_{-\infty}^{\infty} (H_{11}(s) - \text{sgn}(s)H_{11}^*)\bar{p}(s)e^{-isx}ds. \tag{31}$$

In view of Eq. (30), a relation between the Fourier and finite Hilbert transforms of the contact pressure can be derived in the following form by considering $\lim_{z\to 0} w_{,x}(x, z)$ of the homogeneous half-plane problem (cf., Gladwell, 1980, p. 210),

$$\frac{1}{\sqrt{2\pi}} \int_{-\infty}^{\infty} -i\text{sgn}(s)\bar{p}(s)e^{-isx}ds = \frac{1}{\pi} \int_{-c}^{+c} \frac{p(x')}{x'-x}dx' \tag{32}$$

reducing the dominant part of the singular integral to an integral containing a Cauchy kernel

$$w_{1,x} = \frac{H_{11}^*}{\pi} \int_{-c}^{+c} \frac{p(x')}{x'-x}dx' - \frac{i}{2\pi} \int_{-\infty}^{\infty} \int_{-c}^{+c} H_{11}^0(s)p(x')e^{i(x'-x)s}dx'ds, \tag{33}$$

where $H_{11}^0(s) = H_{11}(s) - \text{sgn}(s)H_{11}^*$ is the regular kernel. Using the odd-even properties of the integrand, limits may be changed and the following form obtained:

$$w_{1,x} = \frac{H_{11}^*}{\pi} \int_{-c}^{+c} \frac{p(x')}{x'-x}dx' + \frac{1}{\pi} \int_0^{\infty} \int_{-c}^{+c} H_{11}^0(s)p(x')\sin(x'-x)sdx'ds. \tag{34}$$

A singular integral equation of the same form is given by Shield and Bogy (1988) for a layered isotropic half-plane indented by a flat punch using the transfer matrix approach and arguments based on the short wavelength limit of the Fourier transform of the Green's function for the considered problem. The present approach clearly reveals that the asymptotic relation between the transformed displacements and tractions on the surface of the layered half-plane is the same as that obtained for a homogeneous half-plane having the properties of the surface layer, naturally facilitating separation of the integral equation into singular and regular parts.

Solution of the Singular Integral Equation

Erdogan and Gupta (1969, 1972) have developed a numerical solution technique for singular integral equations such as Eq. (34) using orthogonal properties of Chebyshev polynomials in a Gaussian integration approach. To apply Erdogan and Gupta's solution technique, the interval $[-c, +c]$ is transformed to $[-1, +1]$ using $x = ct$. For the case where the unknown function is bounded on the interval $[-1, +1]$, as is the case for the rigid punch of a parabolic profile, the solution for the contact stress $p(t)$ is given by the product

$$p(t) = F(t)\sqrt{1+t^2} \text{ with } F(t) = \sum_0^p A_i U_i(t) \tag{35}$$

where $U_i(t)$ is the Chebyshev polynomial of the second kind and $\sqrt{1-t^2}$ is the weight function associated with the Chebyshev polynomial of the second kind.

Erdogan and Gupta's method results in a linear system of collocation equations where the function $F(t_k)$ is found at discrete points by matching discrete values of the integral equation's nonhomogeneous term. The system of collocation equations is given by

$$\sum_{k=1}^{n} \frac{1-t_k'^2}{n+1} F(t_k') \left[\frac{1}{t_k'-t_r} + \pi K_0(t_r, t_k')\right] = f(t_r) \tag{36}$$

for $k = 1, \ldots, n$ and $r = 1, \ldots, n+1$, with t_k' and t_r given by

$$t_k' = \cos\left(\pi \frac{k}{n+1}\right), \quad t_r = \cos\left(\pi \frac{2r-1}{2n+2}\right)$$

where, for a rounded indenter of radius R, the inhomogeneous term is

$$f(t) = \frac{w_{,x}}{H_{11}^*} = \frac{1}{H_{11}^*} \frac{ct}{R}$$

while the regular kernel is given by

$$K_0(t_r, t_k') = \frac{c}{\pi} \int_0^{\infty} \frac{H_{11}^0(s)}{H_{11}^*} \sin[c(t_k'-t_r)s]ds.$$

There are $n+1$ possible points to determine $F(t_k)$. Only n collocation points are required. For n even, the point $r = 1 + n/2$ is ignored. The function $F(t_k)$ obtained from the system of collocation equations is multiplied by the weight function to give the contact stress profile. In establishing the system of collocation equations, the regular kernel K_0 must be found by numerical integration for each combination of t_k' and t_r in the linear system.

Discussion and Closing Comments

The outlined method of solution for the contact problem of

an arbitrarily laminated half-plane is the first step in investigating the response of advanced composite materials under concentrated loading. The layered half-plane solution can be employed to study local distribution of stresses as a function of layer thickness, off-axis layer orientation, and degree of composite material's orthotropy for laminates for which global bending effects can be neglected.

It is possible to use this method to analyse a finite thickness, multilayered laminate of infinite extent in the longitudinal direction by modifying the formulation. Consider the possibility of support by resultant reactions P distributed over the distance ϵ centered at points $+x_0$ and $-x_0$ along the bottom surface of the terminal layer. In this case, the bottom traction $\overline{T}_n^-$ of Eq. (27) assumes the value of the Fourier transform of the expression for the concentrated reactions and $\overline{\mathbf{U}}_{n+1}$ is retained. Consideration of support tractions results in an additional term in the singular integral equation that has the form

$$\frac{P}{\pi}\int_0^\infty \frac{H_{1n-2}(s)}{H_{11}^*}\frac{\sin(\epsilon s/2)}{\epsilon s/2}\cos(x_0 s)\sin(xs)\,ds.$$

An iterative procedure may be applied to solve the modified singular integral equation. For a prescribed contact length, a value of P can be assumed and the singular integral equation solved. The resulting integrated contact traction is compared to the assumed reactions. This is repeated until $2P$ is found to equal $\int_{-c}^{+c} p(x)dx$.

In Part II of this paper, we present numerical results for layered half-spaces that address the effect of ply orientation, surface layer thickness, and the properties of supporting half-planes on the applied load versus contact length response and the resulting contact stress distribution. The contact problem of composite laminates of finite thickness using the outlined local/global stiffness matrix approach will be addressed in future investigations.

Acknowledgments

The authors thank the Civil Engineering Department and the Dean's Office at the University of Virginia for providing partial support in the course of this investigation. Comments offered by Prof. J. G. Simmonds of the Applied Mathematics Department at the University of Virginia in the course of preparation of this paper are particularly appreciated.

References

Bufler, H., 1971, "Theory of Elasticity of a Multilayered Medium," *J. Elasticity*, Vol. 1, pp. 125–143.

Chatterjee, S. N., 1987, "Three- and Two-Dimensional Stress Fields Near Delaminations in Laminated Composite Plates," *Int. J. Solids Structures*, Vol. 23, No. 11, pp. 1535–1549.

Chatterjee, S. N., Pindera, M.-J., Pipes, R. B., and Dick, B., 1982, "Composite Defect Significance," Naval Air Development Center Contracts Reports, NADC 81034-60, Warminster, PA, pp. 92–106.

Chen, C. T., 1969, "Stresses in Some Anisotropic Materials Due to Indentation and Sliding," *Int. J. Solids Structures*, Vol. 5, pp. 191–214.

Chen, W. T., and Engel, P. A., 1972, "Impact and Contact Stress Analysis in Multilayered Media," *Int. J. Solids Structures*, Vol. 8, pp. 1257–1281.

Conway, H. D., 1953, "Some Problems in Orthotropic Plane Stress," ASME JOURNAL OF APPLIED MECHANICS, Vol. 20, pp. 72–76.

Conway, H. D., 1967, "The Indentation of an Orthotropic Half Plane Having Inclined Principal Axes," ASME JOURNAL OF APPLIED MECHANICS, Vol. 34, pp. 1031–1032.

Erdogan, F., 1969, "Approximate Solutions of Systems of Singular Integral Equations," *SIAM J. Appl. Math.*, Vol. 17, pp. 1041–1059.

Erdogan, F., and Gupta, G., 1972, "On the Numerical Solution of Singular Integral Equations," *Quart. J. Applied Mathematics*, Jan., pp. 525–534.

Gladwell, G. M. L., 1980, *Contact Problems in the Classical Theory of Elasticity*, Sijthoff and Noordhoff, Alphen aan den Rijn, The Netherlands.

Gupta, P. K., and Walowit, J. A., 1974, "Contact Stresses Between an Elastic Cylinder and a Layered Elastic Solid," *J. Lubrication Technology*, Vol. 96, pp. 250–257.

Lane, M. S., 1991, "The Frictionless Contact Problem of Anisotropic Multilayered Media," Ph.D. dissertation, Civil Engineering Department, University of Virginia, Charlottesville, VA.

Pagano, N. J., 1970, "Influence of Shear Coupling in Cylindrical Bending of Anisotropic Laminates," *J. Composite Materials*, Vol. 4, pp. 330–343.

Pindera, M-J., 1991, "Local/Global Stiffness Matrix Formulation for Composite Materials and Structures," *Composites Engineering*, Vol. 1, No. 2, pp. 69–83.

Ratwani, M., and Erdogan, F., 1973, "On the Plane Contact Problem of a Frictionless Elastic Layer," *Int. J. Solids Structures*, Vol. 9, pp. 921–936.

Rowe, R. K., and Booker, J. R., 1982, "Finite Layer Analysis of Nonhomogeneous Soils," *ASCE J. Engineering Mechanics Division*, Vol. 108, No. EM1, pp. 115–132.

Shield, T. W., and Bogy, D. B., 1988, "Multiple Region Contact Solutions for a Flat Indenter on a Layered Elastic Half Space: Plane Strain Case," ASME JOURNAL OF APPLIED MECHANICS, Vol. 56, pp. 251–262.

APPENDIX

Elements of Local Stiffness Matrix

The elements of local stiffness matrices for monoclinic, orthotropic, and transversely isotropic layers in the Fourier transform domain for generalized plane deformation are given below as

Monoclinic Layers.

$$k_{11}(k_{14}) = A^{\pm}[P_1(L_3-L_2)+P_2(L_1-L_3)+P_3(L_2-L_1)]$$

$$k_{12}(k_{15}) = H^{\pm}(P_1L_2-P_2L_1)R_3+E^{\pm}(P_3L_1-P_1L_3)R_2 + F^{\pm}(P_2L_3-P_3L_2)R_1$$

$$k_{13}(k_{16}) = H^{\pm}(P_2-P_1)R_3+E^{\pm}(P_1-P_3)R_2+F^{\pm}(P_3-P_2)R_1$$

$$k_{22}(k_{25}) = B^{\pm}(T_2R_1-T_1R_2)L_3+C^{\pm}(T_1R_3-T_3R_1)L_2 + D^{\pm}(T_3R_2-T_2R_3)L_1$$

$$k_{23}(k_{26}) = B^{\pm}(T_1R_2-T_2R_1)+C^{\pm}(T_3R_1-T_1R_3) + D^{\pm}(T_2R_3-T_3R_2)$$

$$k_{33}(k_{36}) = B^{\pm}(R_2Q_1-R_1Q_2)+C^{\pm}(R_1Q_3-R_3Q_1) + D^{\pm}(R_3Q_2-R_2Q_3)$$

where the minus sign in the notation $A^{\pm}$, etc., refers to the elements k_{ij} in the parentheses, and

$$L_i=\frac{(C_{11}-C_{55}\lambda_i^2)(C_{36}+C_{45})-(C_{16}-C_{45}\lambda_i^2)(C_{13}+C_{55})}{(C_{45}\lambda_i^2-C_{16})(C_{36}+C_{45})-(C_{44}\lambda_i^2-C_{66})(C_{13}+C_{55})}$$

$$R_i= -\frac{(C_{45}\lambda_i^2-C_{16})(C_{45}\lambda_i^2-C_{16})-(C_{44}\lambda_i^2-C_{66})(C_{55}\lambda_i^2-C_{11})}{(C_{45}\lambda_i^2-C_{16})(C_{36}+C_{45})-(C_{44}\lambda_i^2-C_{66})(C_{13}+C_{55})}\frac{1}{\lambda_i}$$

$$P_i=-C_{13}+C_{33}\lambda_iR_i-C_{36}L_i,\quad Q_i=C_{44}\lambda_iL_i+C_{45}(\lambda_i+R_i),$$

$$T_i=C_{45}\lambda_iL_i+C_{55}(\lambda_i+R_i)$$

$$A^{\pm}=\frac{1}{2}\left(\pm\frac{c_1c_2c_3}{\Delta_1}+\frac{s_1s_2s_3}{\Delta_2}\right),\quad B^{\pm}=\frac{1}{2}\left(\frac{c_3s_1s_2}{\Delta_1}\pm\frac{c_1c_2s_3}{\Delta_2}\right),$$

$$C^{\pm}=\frac{1}{2}\left(\frac{c_2s_1s_3}{\Delta_1}\pm\frac{c_1c_3s_2}{\Delta_2}\right)\quad D^{\pm}=\frac{1}{2}\left(\frac{c_1s_2s_3}{\Delta_1}\pm\frac{c_2c_3s_1}{\Delta_2}\right),$$

$$E^{\pm}=\frac{1}{2}\left(\frac{c_1c_3s_2}{\Delta_1}\pm\frac{c_2s_1s_3}{\Delta_2}\right),\quad F^{\pm}=\frac{1}{2}\left(\frac{c_2c_3s_1}{\Delta_1}\pm\frac{c_1s_2s_3}{\Delta_2}\right)$$

$$H^{\pm}=\frac{1}{2}\left(\frac{c_1c_2s_3}{\Delta_1}\pm\frac{c_3s_1s_2}{\Delta_2}\right)$$

$c_i=\cosh(s\lambda_ih/2)$, $s_i=\sinh(s\lambda_ih/2)$, $h=$ ply thickness

$$\Delta_1=c_1c_2s_3(L_2-L_1)R_3+c_1c_3s_2(L_1-L_3)R_2+c_2c_3s_1(L_3-L_2)R_1$$

$$\Delta_2=c_3s_1s_2(L_2-L_1)R_3+c_2s_1s_3(L_1-L_3)R_2+c_1s_2s_3(L_3-L_2)R_1.$$

Orthotropic Layers.

$$k_{11}(k_{14}) = A^{\pm}(P_2-P_1)$$

$$k_{12}(k_{15}) = D^{\pm}P_1R_2-E^{\pm}P_2R_1$$

$$k_{22}(k_{25}) = B^{\pm}(T_1R_2-T_2R_1)$$

$$k_{33}(k_{36}) = C^{\pm}Q_3$$

where

$$R_i = -\frac{(C_{55}\lambda_i^2 - C_{11})}{(C_{13}+C_{55})\lambda_i}, \quad P_i = -C_{13} + C_{33}\lambda_i R_i,$$

$$Q_3 = C_{44}\lambda_3, \quad T_i = C_{55}(\lambda_i + R_i)$$

$$A_-^+ = \frac{1}{2}\left(\pm\frac{c_1c_2}{\Delta_1} + \frac{s_1s_2}{\Delta_2}\right), \quad B_-^+ = \frac{1}{2}\left(\frac{s_1s_2}{\Delta_1} \pm \frac{c_1c_2}{\Delta_2}\right),$$

$$C_-^+ = \frac{1}{2}\left(\frac{s_3}{c_3} \pm \frac{c_3}{s_3}\right)$$

$$D_-^+ = \frac{1}{2}\left(\frac{c_1s_2}{\Delta_1} \pm \frac{s_1c_2}{\Delta_2}\right), \quad E_-^+ = \frac{1}{2}\left(\frac{c_2s_1}{\Delta_1} \pm \frac{s_2c_1}{\Delta_2}\right)$$

$$\Delta_1 = c_1s_2R_2 - c_2s_1R_1, \quad \Delta_2 = c_2s_1R_2 - c_1s_2R_1.$$

Isotropic Layers.

$$k_{11}(k_{14}) = A_-^+P_2$$

$$k_{12}(k_{15}) = D_-^+P_1 - E_-^+P_2$$

$$k_{22}(k_{25}) = B_-^+(T_1R_1 - T_2)$$

$$k_{33}(k_{36}) = C_-^+Q_3$$

where

$$R_1 = -\frac{(3C_{33} - C_{12})}{(C_{11}+C_{12})}$$

$$P_1 = C_{11} - C_{12}, \quad P_2 = C_{11}(1+R_1), \quad T_1 = 2C_{55},$$

$$T_2 = C_{55}(1+R_1), \quad Q_3 = C_{44}$$

$$A_-^+ = \frac{1}{2}\left(\pm\frac{c_1^2}{\Delta_1} + \frac{s_1^2}{\Delta_2}\right)\frac{1}{s}, \quad B_-^+ = \frac{1}{2}\left(\frac{s_1^2}{\Delta_1} \pm \frac{c_1^2}{\Delta_2}\right)\frac{1}{s},$$

$$C_-^+ = \frac{1}{2}\left(\frac{s_1}{c_1} \pm \frac{c_1}{s_1}\right) \quad D_-^+ = \frac{1}{2}(1 \pm 1),$$

$$E_-^+ = \frac{1}{2}\left(\frac{c_1s_1}{\Delta_1} \pm \frac{c_1s_1}{\Delta_2}\right)\frac{1}{s} \quad \Delta_1 = \frac{h}{2}(c_1^2 - s_1^2) + \frac{R_1}{s}c_1s_1,$$

$$\Delta_2 = \frac{h}{2}(s_1^2 - c_1^2) + \frac{R_1}{s}c_1s_1.$$

The elements of asymptotic local stiffness matrices as $s \to \pm\infty$ for monoclinic, orthotropic, and transversely isotropic layers and the corresponding half-planes are given as follows.

Monoclinic Layers and Half-Planes.

$$\pm k_{11}^* = \pm\frac{1}{\Delta}[P_1(L_3 - L_2) + P_2(L_1 - L_3) + P_3(L_2 - L_1)]$$

$$k_{12}^* = \frac{1}{\Delta}[P_1(L_2R_3 - L_3R_2) - P_2(L_1R_3 - L_3R_1) + P_3(L_1R_2 - L_2R_1)]$$

$$k_{13}^* = \frac{1}{\Delta}[P_1(R_2 - R_3) + P_2(R_3 - R_1) + P_3(R_1 - R_2)]$$

$$\pm k_{22}^* = \pm\frac{1}{\Delta}[T_1(L_2R_3 - L_3R_2) - T_2(L_1R_3 - L_3R_1) + T_3(L_1R_2 - L_2R_1)]$$

$$\pm k_{23}^* = \pm\frac{1}{\Delta}[T_1(R_2 - R_3) + T_2(R_3 - R_1) + T_3(R_1 - R_2)]$$

$$\pm k_{33}^* = \pm\frac{1}{\Delta}[Q_1(R_2 - R_3) + Q_2(R_3 - R_1) + Q_3(R_1 - R_2)]$$

where

$$\Delta = (L_2R_3 - L_3R_2) - (L_1R_3 - L_3R_1) + (L_1R_2 - L_2R_1)$$

and the notation $\pm k_{ij}^*$ denotes limiting behavior of k_{ij} as s goes to $\pm\infty$.

Orthotropic Layers and Half-Planes.

$$\pm k_{11}^* = \pm\frac{P_2 - P_1}{R_2 - R_1}$$

$$k_{12}^* = \frac{R_2P_1 - R_1P_2}{R_2 - R_1}$$

$$\pm k_{22}^* = \pm\frac{R_2T_1 - R_1T_2}{R_2 - R_1}$$

$$\pm k_{33}^* = \pm Q_3$$

Isotropic Layers and Half-Planes.

$$\pm k_{11}^* = \pm C_{11}\frac{(1+R_1)}{R_1}$$

$$k_{12}^* = (C_{11} - C_{12}) - C_{11}\frac{(1+R_1)}{R_1}$$

$$\pm k_{22}^* = \pm C_{11}\frac{(1+R_1)}{R_1}$$

$$\pm k_{33}^* = \pm\frac{1}{2}(C_{11} - C_{12})$$

Frictionless Contact of Layered Half-Planes, Part II: Numerical Results

M.-J. Pindera
Assoc. Professor.

M. S. Lane
Research Associate,
Mem. ASME.

Civil Engineering and
Applied Mechanics Department,
University of Virginia,
Charlottesville, VA 22903

In Part I of this paper, analytical development of a method was presented for the solution of frictionless contact problems of multilayered half-planes consisting of an arbitrary number of isotropic, orthotropic, or monoclinic layers arranged in any sequence. The local/global stiffness matrix approach similar to the one proposed by Bufler (1971) was employed in formulating the surface mixed boundary condition for the unknown stress in the contact region. This approach naturally facilitates decomposition of the integral equation for the contact stress distribution on the top surface of an arbitrarily laminated half-plane into singular and regular parts that, in turn, can be solved using a numerical collocation technique. In Part II of this paper, a number of numerical examples is presented addressing the effect of off-axis plies on contact stress distribution and load versus contact length in layered half-planes laminated with unidirectionally reinforced composite plies. The results indicate that for the considered unidirectional composite, the load versus contact length response is significantly influenced by the orientation of the surface layer and the underlying half-plane, while the corresponding contact stress profiles are considerably less affected.

Introduction

Part I of this paper outlines the analytical development of a method for the solution of frictionless contact problems of multilayered half-planes consisting of an arbitrary number of isotropic, orthotropic, or monoclinic layers arranged in any sequence, indented by a rigid punch of parabolic profile. The problem is formulated in terms of displacements and the resulting Navier equations that govern the distribution of displacements in the individual layers are solved using Fourier transforms. A local stiffness matrix in the transform domain is formulated for each layer which is then assembled into a global stiffness matrix for the entire multilayered half-plane by enforcing continuity conditions along the interfaces. Application of the mixed boundary condition on the top surface of the medium subjected to the force of the indenter results in an integral equation for the unknown pressure in the contact region. The integral possesses a divergent kernel which is decomposed into Cauchy-type and regular parts using asymptotic properties of the local stiffness matrix and a relation between Fourier and finite Hilbert transform of the contact pressure. This results in the following singular integral equation for the unknown pressure distribution in the contact region (Eq. (34) of Part I),

$$w_{1,x}=\frac{H_{11}^{*}}{\pi}\int_{-c}^{+c}\frac{p(x')}{x'-x}\,dx' + \frac{1}{\pi}\int_{0}^{\infty}\int_{-c}^{+c}H_{11}^{0}(s)p(x')\sin(x'-x)s\,dx'\,ds. \quad (1)$$

In the above equation, H_{11}^{*} is the first element of the inverse of the Fourier transformed global stiffness matrix for the layered half-plane when the transform variable s approaches infinity (see Eq. (30) in Part 1), $H_{11}^{0}(s) = H_{11}(s) - \mathrm{sgn}(s)H_{11}^{*}$ is the regular kernel (where $H_{11}(s)$ is the first element of the inverse of the Fourier transformed global stiffness matrix), and $p(x)$ is the unknown pressure. For homogeneous half-planes, the kernel consists only of the Cauchy-type singularity ($H_{11}^{0}(s)$ vanishes), which results in a closed-form solution for the contact stress. For multilayered half-planes, the solution of the resulting singular integral equation is obtained using a collocation technique developed by Erdogan (1969) and Erdogan and Gupta (1972) which employs orthogonality properties of Chebyshev polynomials.

In Part II of the paper, we present numerical results for the contact problem of homogeneous and multilayered composite half-planes with different fiber orientations. The quantities of interest are the contact force and contact stress profile as a function of the contact length. Specifically, the effects of ply orientation, thickness, and stacking sequence on the aforementioned quantities are investigated.

Contributed by the Applied Mechanics Division of THE AMERICAN SOCIETY OF MECHANICAL ENGINEERS for publication in the ASME JOURNAL OF APPLIED MECHANICS.

Discussion on this paper should be addressed to the Technical Editor, Professor Lewis T. Wheeler, Department of Mechanical Engineering, University of Houston, Houston, TX 77204-4792, and will be accepted until four months after final publication of the paper itself in the ASME JOURNAL OF APPLIED MECHANICS.

Manuscript received by the ASME Applied Mechanics Division, Apr. 29, 1991; final revision, Aug. 14, 1992. Associate Technical Editor: G. J. Dvorak.

Numerical Solution Technique

The collocation technique outlined by Erdogan and Gupta reduces Eq. (1) to a system of algebraic equations for the unknown coefficients in the Chebyshev polynomial expansion of the unknown contact pressure (Eq. (36) in Part I of the paper). In the course of generating the algebraic system of equations, it is necessary to numerically evaluate the regular kernel $K_0(t_r, t_k')$

$$K_0(t_r, t_k') = \frac{c}{\pi} \int_0^\infty \frac{H_{11}^0(s)}{H_{11}^*} \sin[c(t_k' - t_r)s]ds \qquad (2)$$

for each combination of the collocation points t_r and t_k'. This is accomplished by first investigating the behavior of $H_{11}^0(s)/H_{11}^*$ in order to determine the value of $s = s_{max}$ at which the kernel becomes negligibly small. This depends on the geometry of the layered half-plane and, in particular, the thickness of the surface layer. The rate of decay of the function $H_{11}^0(s)/H_{11}^*$ decreases with decreasing surface layer thickness and can be quite slow for very thin layers. The numerical integration effort can thus be quite time consuming due to the periodic nature of the sinusoidal term appearing in the regular kernel.

The behavior of $H_{11}^0(s)/H_{11}^*$ was investigated for each layered half-plane configuration and the value of $s = s_{max}$ determined at which this function became very small. For instance, in the case of the [90 deg/±45 deg] layer sequence with 1.27 mm thick layers bonded to a 0 deg half-plane, the value of the function $H_{11}^0(s)/H_{11}^*$ decayed monotonically from -0.389 for very small s to -0.142×10^{-6} at $s_{max} = 200$. The regular integral was subsequently evaluated by dividing the interval $[0, s_{max}]$ into 16 subintervals that were mapped onto $[-1, +1]$ using appropriate transformation. The individual contributions were then evaluated using Gaussian quadrature with 64 integration stations in each subinterval and summed up. For the considered range of contact half lengths c, the outlined numerical integration scheme of Eq. (2) was found sufficiently accurate. Little difference was found between the results generated with 24 and 48 collocation points at which the pressure distribution was evaluated. As a final check of the accuracy of the integration scheme, the results presented by Gupta and Walowit (1974) for a thin isotropic layer bonded to an isotropic half-plane indented by a rigid punch were reproduced by the present technique with very good accuracy for the surface layer thickness of 1.27 mm and a range of different contact lengths (Pindera and Lane, 1991).

Numerical Results for the Composite Half-Planes

The investigated composite half-planes consist of unidirectionally reinforced plies with different fiber orientations bonded to a half-plane of the same material. The different fiber orientations are obtained by rotating each ply by an angle θ about the z-axis (see Fig. 1, Part I). The properties of the considered composite plies are given in Table 1. This composite is transversely isotropic when referred to its material principal coordinate system 1-2-3, with the 1-axis oriented along the fibers and coincident with the x-axis, the 2-axis coincident with the y-axis, and the 3-axis coincident with the z-axis. It is characterized by five independent stiffness elements and its stiffness matrix is given by

$$\begin{bmatrix} C_{11} & C_{12} & C_{12} & 0 & 0 & 0 \\ C_{12} & C_{22} & C_{23} & 0 & 0 & 0 \\ C_{12} & C_{23} & C_{22} & 0 & 0 & 0 \\ 0 & 0 & 0 & C_{44} & 0 & 0 \\ 0 & 0 & 0 & 0 & C_{66} & 0 \\ 0 & 0 & 0 & 0 & 0 & C_{66} \end{bmatrix} \qquad (3)$$

where $C_{44} = 1/2(C_{22} - C_{23})$.

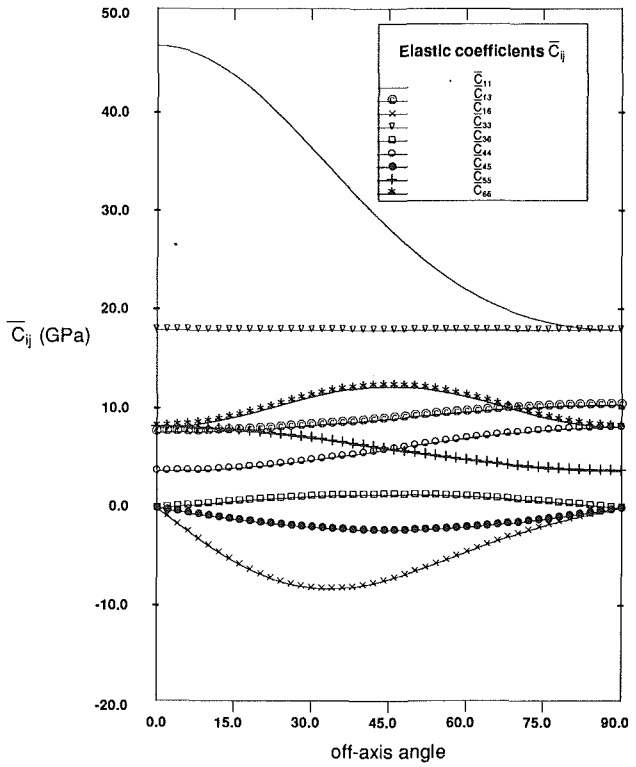

Fig. 1 Stiffness elements $\overline{C}_{ij}$ of unidirectionally reinforced plies and half-planes as a function of the rotation angle θ

Table 1 **Material properties of unidirectionally reinforced plies and half-planes**

Material property	
E_{11} (GPa)	42.74
E_{22} (GPa)	11.72
E_{33} (GPa)	11.72
ν_{12}	0.27
ν_{13}	0.27
ν_{23}	0.55
G_{12} (GPa)	8.238
G_{13} (GPa)	8.238
G_{23} (GPa)	3.778

When a given ply is rotated by an angle θ about the z-axis, the material principal coordinate system no longer coincides with the x-y-z coordinate system and the ply appears monoclinic when referred to the fixed coordinate system. The structure of its stiffness matrix in the x-y-z coordinate system is now

$$\begin{bmatrix} \overline{C}_{11} & \overline{C}_{12} & \overline{C}_{13} & 0 & 0 & \overline{C}_{16} \\ \overline{C}_{12} & \overline{C}_{22} & \overline{C}_{23} & 0 & 0 & \overline{C}_{26} \\ \overline{C}_{13} & \overline{C}_{23} & \overline{C}_{33} & 0 & 0 & \overline{C}_{36} \\ 0 & 0 & 0 & \overline{C}_{44} & \overline{C}_{45} & 0 \\ 0 & 0 & 0 & \overline{C}_{45} & \overline{C}_{55} & 0 \\ \overline{C}_{16} & \overline{C}_{26} & \overline{C}_{36} & 0 & 0 & \overline{C}_{66} \end{bmatrix}. \qquad (4)$$

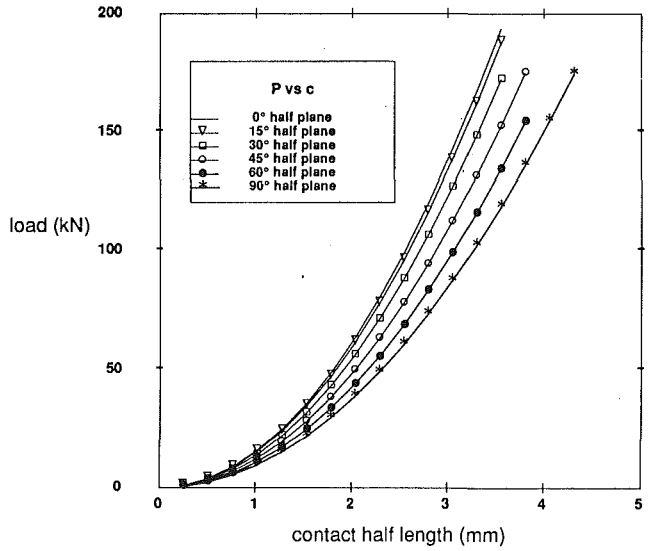

Fig. 2 Contact load as a function of half contact length for homogeneous half-planes with different fiber orientations

The barred stiffness elements $\overline{C}_{ij}$ are related to the unbarred stiffness elements C_{ij} by the familiar transformation equations. In the case of generalized plane deformation formulation, which must be used if off-axis plies are part of the layered half-plane, only nine of the stiffness elements $\overline{C}_{ij}$ appear in the governing Navier equations (Eq. (6) in Part I of this paper). For completeness, these are given below as follows:

$$\overline{C}_{11} = C_{11}\cos^4\theta + 2(C_{12} + 2C_{66})\cos^2\theta\sin^2\theta + C_{22}\sin^4\theta$$

$$\overline{C}_{13} = C_{12}\cos^2\theta + C_{23}\sin^2\theta$$

$$\overline{C}_{16} = [(C_{11} - C_{12} - 2C_{66})\cos^2\theta + (C_{12} - C_{22} + 2C_{66})\sin^2\theta]\cos\theta\sin\theta$$

$$\overline{C}_{33} = C_{33}$$

$$\overline{C}_{36} = (C_{13} - C_{23})\cos\theta\sin\theta$$

$$\overline{C}_{44} = C_{44}\cos^2\theta + C_{44}\sin^2\theta$$

$$\overline{C}_{45} = (C_{66} - C_{44})\cos\theta\sin\theta$$

$$\overline{C}_{55} = C_{44}\sin^2\theta + C_{44}\cos^2\theta$$

$$\overline{C}_{66} = (C_{11} - 2C_{12} + C_{22})\cos^2\theta\sin^2\theta + C_{66}(\cos^2\theta - \sin^2\theta)^2$$

where θ is the rotation angle about the z-axis measured from the x-axis in the x-y plane.

Figure 1 presents the nine stiffness elements $\overline{C}_{ij}$ as a function of the rotation angle. These stiffness elements can be related to the more commonly employed engineering constants. It is observed that the stiffness element $\overline{C}_{33}$, and thus the modulus E_{zz} in the direction of the applied force does not change with the off-axis angle. Further, even though the stiffness element $\overline{C}_{66}$ does change with the off-axis orientation, it can be shown that for this particular material the shear modulus G_{xy} remains practically constant. Any variation in the contact force and stress profile at a given contact length for differently oriented surface plies must therefore be attributable to variations in the inplane engineering moduli E_{xx}, G_{xz}, ν_{xz}, and the out-of-plane moduli G_{yz}, $\eta_{xy,x}$, $\eta_{xy,z}$ and $\mu_{yz,xz}$ that couple the in-plane displacements $u(x, z)$, $w(x, z)$ with the out-of-plane displacement $v(x, z)$.

The results for homogeneous composite half-planes with different fiber orientations are presented first, followed by the results for multilayered half-planes. Cases considered include layered half-planes with surface laminae of different orientations bonded to a half-plane with fiber direction coincident with the x-axis or a half-plane with fiber direction coincident with the y-axis, here called 0 deg and 90 deg half-planes, respectively. Also considered are the layer combinations [90 deg/ ± 45 deg] and [0 deg/ ±45 deg] bonded to 0 deg and 90 deg half-planes, respectively.

In generating the numerical results, the radius of the punch was fixed at 25.4 mm. For all the cases investigated, the layered half-plane consisted of three layers bonded to a homogeneous half-plane. Homogeneous half-plane cases were obtained by setting the properties of each layer equal to the properties of the supporting half-plane.

Homogeneous Half-Planes. In the case of homogeneous monoclinic (off-axis), orthotropic, transversely isotropic, or isotropic half-planes, the integral equation for the normal stress distribution in the contact area, Eq. (1) reduces to

$$w_{1,x} = \frac{H_{11}^*}{\pi}\int_{-c}^{+c}\frac{p(x')}{x'-x}\,dx'. \tag{5}$$

As is well known, the solution of Eq. (5) is obtained in closed form for isotropic and orthotropic half-planes, yielding an elliptical contact pressure profile and a parabolic load versus contact length response. By extension, the solution to the contact problem of a monoclinic half-plane for generalized plane deformation is also readily obtained in closed form.

Contact loads as a function of half contact length for homogeneous half-planes of different fiber orientations are shown in Fig. 2. The curves have been generated for half-planes with fiber orientations of 0 deg, 15 deg, 30 deg, 45 deg, 60 deg, and 90 deg. The results indicate that for a given contact length, the contact force is largest for the 0 deg half-plane and smallest for the 90 deg half-plane. The contact load response curves for the 0 deg and 90 deg half-planes form an envelope bounding the contact load versus contact length curves of the considered monoclinic half-planes (i.e., those with fiber direction at an angle θ from the x-axis in the x-y plane). For monoclinic half-planes, the contact force as a function of contact length diminishes in a monotonic fashion as fiber orientation increases from 15 deg to 60 deg. For small off-axis angles, the contact forces approach those of the 0 deg half-plane. For large off-axis angles, the contact forces approach those of the 90 deg half-plane.

Figure 3 shows the normalized contact stress σ_{zz} distribution for the considered half-planes when the half contact length is 2.54 mm. The same normalized profiles have been obtained for the entire range of contact lengths examined (see Fig. 2). As expected from the solution of Eq. (5), the curves are ellipses superposed on each other regardless of the off-axis orientation of the fibers and the contact length. Since the normalized pressure profiles shown in Fig. 3 have been generated using the aforementioned layered half-plane cross-section (consisting of three layers bonded to a homogeneous half-plane), the results presented in Fig. 3 provide an additional check on the solution technique. In fact, examination of the numerical values of the term $H_{11}^0(s)/H_{11}^*$ in the regular kernel in Eq. (2) indicates that they are practically zero when all the layers have the same properties as the supporting half-plane.

Monoclinic (Off-Axis) Lamina Supported by 90 Deg Half-Plane. Figure 4 shows contact force as a function of half contact length for laminae of different fiber orientations bonded to a 90 deg half-plane. The surface laminae have orientations of 0 deg, 30 deg, 45 deg, and 60 deg. The laminar thickness is 2.54 mm. The contact load curves for homogeneous 0 deg and 90 deg half-planes are included for comparison. It is observed that these curves form an envelope containing the curves for the half-planes having surface layer orientations of 0 deg, 30 deg, 45 deg, and 60 deg. For the half-plane with the 0 deg surface layer, the contact load versus contact length curve coincides with the homogeneous 0 deg half-plane curve for

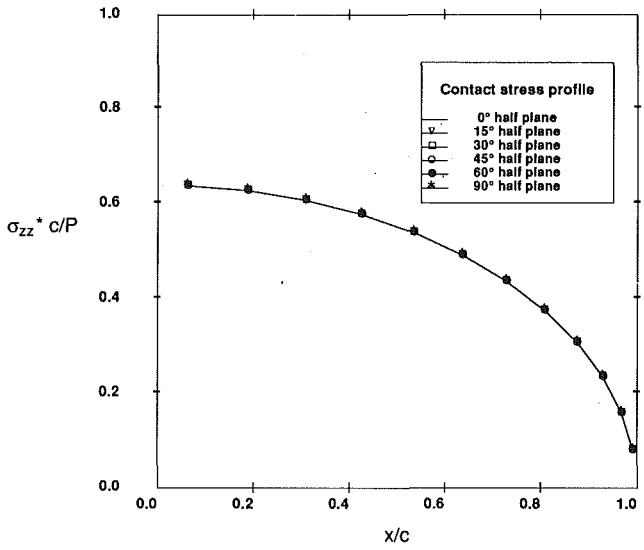

Fig. 3 Contact stress profiles for homogeneous half-planes with different fiber orientations

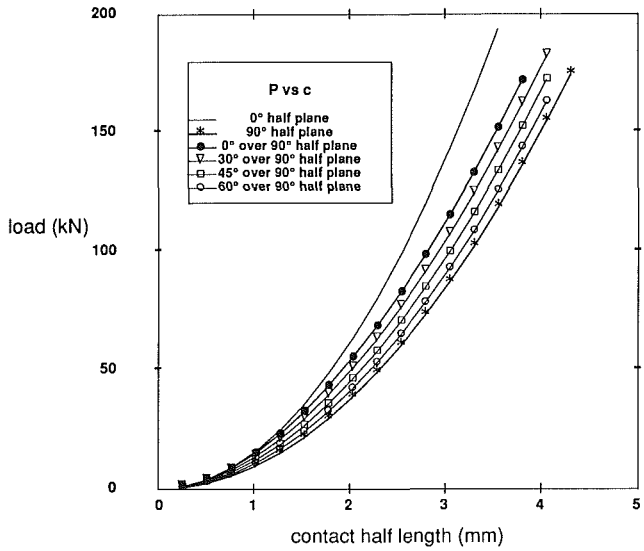

Fig. 4 Contact load as a function of half contact length for differently oriented laminae bonded to 90 deg half-plane

small contact lengths. As the contact length increases, the two curves deviate from each other, pointing to the influence of the underlying 90 deg half-plane. The response curves for the surface layers with off-axis orientations are bounded by the response curves of the half-plane with the 0 deg surface layer and the homogeneous 90 deg half-plane. These curves decrease monotonically with increasing off-axis orientations.

Figure 5 shows normalized contact stress profiles for each of the cases presented above when the half contact length is 3.81 mm. At this contact length, the parameter $\alpha = c/h$ is 1.5 when the surface layer is 2.54 mm thick, Fig. 5(*a*), and 3 when the surface layer is 1.27 mm thick, Fig. 5(*b*). In both cases, increasing the off-axis angle produces a stress profile which is closer to elliptical (i.e., homogeneous 90 half-plane profile). As expected, the half-plane with the thinner surface layer exhibits greater departures from elliptical stress profile for a given orientation at the considered contact length.

The effect of changing the thickness of the 0 deg surface layer also has been examined. Figure 6 shows the contact load

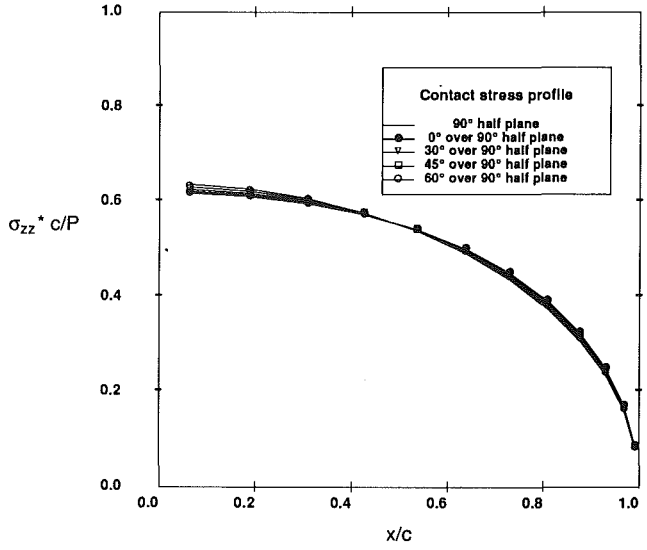

Fig. 5(*a*)

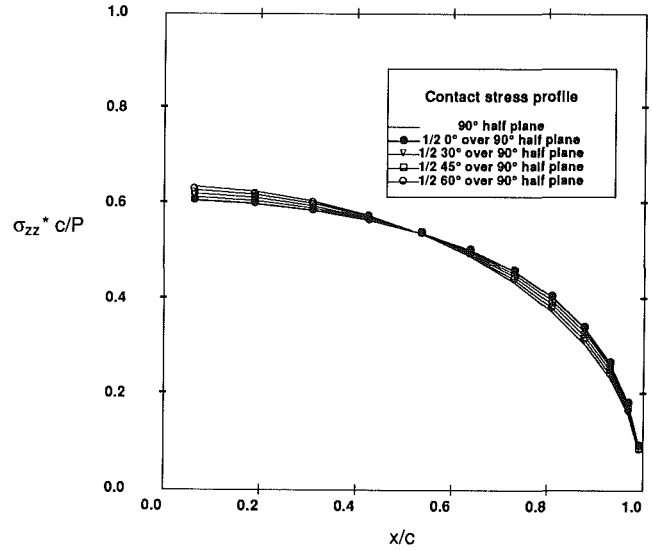

Fig. 5(*b*)

Fig. 5 Contact stress profiles for monoclinic laminae bonded to 90 deg half-plane for (*a*) $\alpha = 1.5$, and (*b*) $\alpha = 3.0$

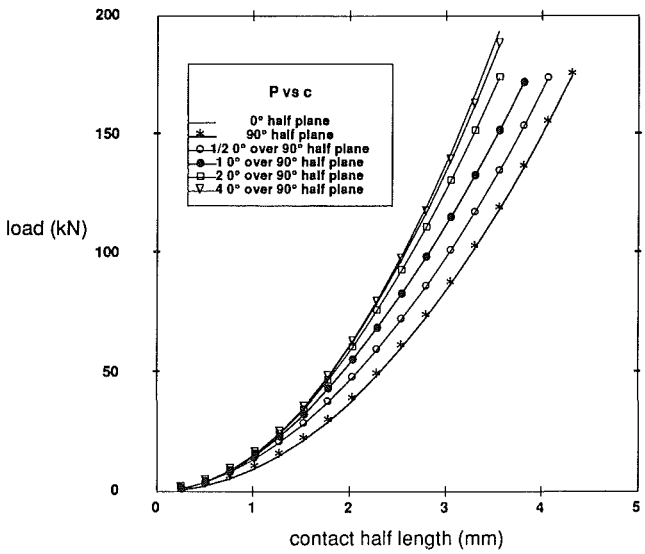

Fig. 6 The effect of surface layer thickness on contact load for 0 deg lamina bonded to 90 deg half-plane

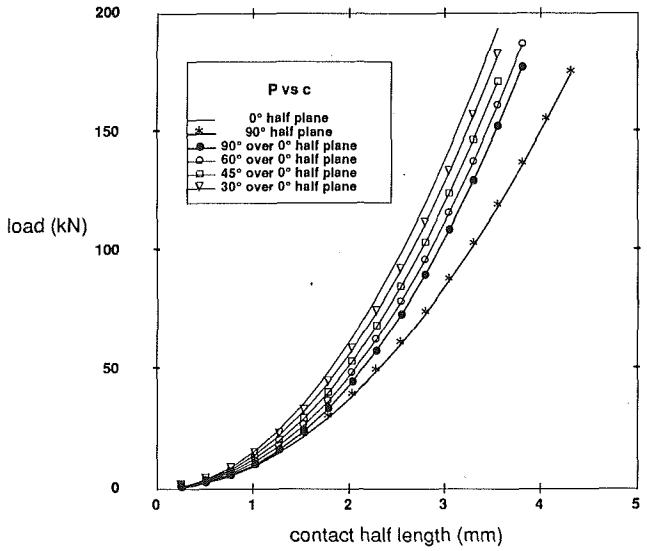

Fig. 7 Contact load as a function of half contact length for differently oriented laminae bonded to 0 deg half-plane

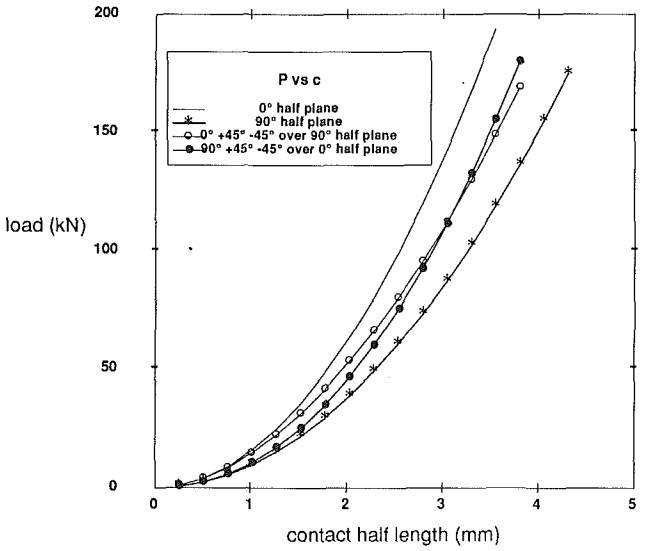

Fig. 8 Contact load as a function of half contact length for "quasi-isotropic" layered half-planes

versus half contact length response curves for half-planes with 0 deg surface layers 1.27, 2.54, 5.08, and 10.16 mm thick. These thicknesses are 1/2, 1, 2, and 4 times greater than the standard thickness of 2.54 mm employed in generating the response curves shown in Fig. 4. The contact load curves for homogeneous 0 deg and 90 deg half-planes are included for reference. The results presented in Fig. 6 indicate that the initial response of the half-plane is dominated by the surface layer. As the contact length increases, the response depends on the thickness of the surface layer and the contact length. As the surface layer thickness increases, the response of the layered half-plane tends to the response of the homogeneous 0 deg half-plane. For the half-plane with the surface layer of 1.27 mm, the response is dominated by the properties of the underlying 90 deg half-plane at larger contact lengths. Decreasing the thickness of the surface layer to 0.635 mm (not shown) brings the response curve still closer to that of the homogeneous 90 deg half-plane at longer contact lengths. The above results are commensurate with corresponding results obtained for isotropic surface layers bonded to isotropic half-planes.

Monoclinic (Off-Axis) Lamina Supported by 0 Deg Half-Plane. Contact loads and normalized contact stress profiles for layers of different fiber orientations bonded to a 0 deg half-plane also have been generated. Figure 7 shows the contact load as a function of half contact length for half-planes with surface layers having orientations of 30 deg, 45 deg, 60 deg, and 90 deg. The layer thickness is 2.54 mm. The contact load curves for homogeneous 0 deg and 90 deg half-planes are included as in the previous example. The results presented in Fig. 7 can be compared and contrasted with those of Fig. 4. In this case, the response of the investigated half-planes is also bounded by the response of the homogeneous 0 deg and 90 deg half-planes. Further, the response curves for the surface layers with off-axis orientations are bounded by the response curves of the half-plane with the 90 deg surface layer and the homogeneous 0 deg half-plane. These curves increase monotonically with decreasing off-axis orientations, producing responses that tend to approach the response of the homogeneous 0 deg half-plane. This is the reverse of the behavior shown in Fig. 4.

The normalized contact stress profiles (not shown) for the contact half length of 3.81 mm indicate that the half-plane with the 90 deg surface layer exhibits greatest departure from elliptical profile. In this case, the maximum value of the normalized profile in the center of the contact region is greater than the corresponding value for the elliptical profile, in contrast with the results shown in Fig. 5(*a*). Decreasing the thickness of the surface layer by half increases the departure from elliptical profile as in the preceding case illustrated in Fig. 5(*b*).

The effect of layer thickness on contact force for the case of a 90 deg layer bonded to a 0 deg half-plane was also investigated. The layer thicknesses were the same as in the previously discussed example. The results indicate behavior opposite to that shown in Fig. 6 and thus will not be discussed in more detail here.

Quasi-Isotropic Half-Planes. As the final example, contact load response curves and normalized contact stress profiles have been generated for the following configurations: [0 deg/ ±45 deg] layer sequence bonded to a 90 deg half-plane, and [90 deg/ ±45 deg] layer sequence bonded to a 0 deg half-plane. Symmetric laminates with these orientations are typically called "quasi-isotropic" in the composites literature. The thickness of the individual layers in these half-planes was 1.27 mm.

Figure 8 shows the contact load as a function of half contact length while the normalized contact stress profiles are shown in Fig. 9 for the contact length of 3.81 mm. Included in the figures are the results for homogeneous 0 deg and 90 deg half-planes. The results in Fig. 8 indicate that the initial contact load response of the two configurations is dominated by the surface layer. As the contact length increases, the response tends to be influenced by the properties of the underlying layers and the homogeneous half-planes. In fact, at a certain contact length, the response of the half-plane with the 90 deg surface layer becomes stiffer than that with the 0 deg surface layer. Similar trends are observed in Figs. 4 and 7. Interestingly, the response of the configuration with the 0 deg surface layer is very close to the response of the 90 deg half-plane with 0 deg surface layer shown in Fig. 4. The same applies to the configuration with the 90 deg surface layer and the corresponding 0 deg half-plane with the 90 deg surface layer shown in Fig. 7. Apparently, decreasing the thickness of the surface layer by half is offset by the inclusion of the two ±45 deg angle-ply layers. The results in Fig. 9 indicate that the configuration with the 0 deg surface layer produces lower contact stress profiles in the inner region and higher in the outer region than the elliptical profile of a homogeneous 0 deg or 90 deg half-plane. The contact stress profile of the configuration with the 90 deg surface layer exhibits opposite behavior. These trends are commensurate with the previously discussed response of 0

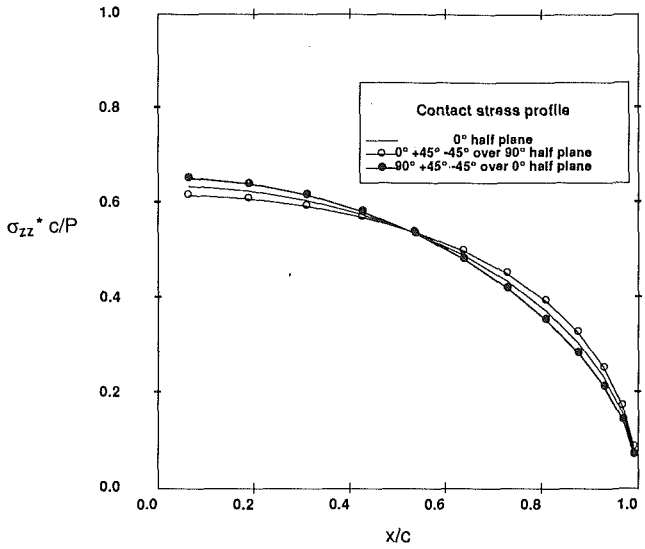

Fig. 9 Contact stress profiles for "quasi-isotropic" layered half-planes when α = 3.0

deg and 90 deg half-planes with 90 deg and 0 deg surface layers, respectively.

Discussion

The contact problem of layered half-planes with off-axis (monoclinic) plies introduces a number of additional parameters into the analysis in comparison with contact problems involving isotropic or even orthotropic layers. First of all, the presence of rotated plies introduces coupling between in-plane and out-of-plane displacement components which requires the use of generalized plane deformation analysis. This increases the number of elastic parameters (i.e., "constants") in the governing differential equations which influence the contact stress profile and the contact load as a function of the contact length. Equally important is the variation of the elastic parameters of a given ply with the off-axis or rotation angle. Finally, the geometry and configuration (stacking sequence) of the layered half-plane may be varied, producing a formidable analytical test matrix.

For this reason, the objective of Part II of the paper was to illustrate the applicability of the developed methodology outlined in Part I for a specific material system and what the authors believe to be fundamental half-plane configurations which illustrate the influence of the off-axis ply orientation on the quantities of interest. The authors are not aware of any investigations in which these effects have been addressed. Future investigations will be aimed at identifying the important parameters that govern the response of arbitrarily layered half-planes with isotropic, orthotropic, or monoclinic plies. The results presented in Parts I and II of the paper indicate that the developed technique can readily be employed to investigate the contact problem of such layered half-planes in an efficient manner.

Summary

The results presented in Part II of this paper indicate that the load versus contact length response curves are parabolic and the contact stress profiles elliptical for homogeneous composite half-planes regardless of off-axis orientation. For the composite material used in this study, homogeneous 0 deg half-planes generate the highest contact loads for a given contact length while 90 deg half-planes generate the lowest. Homogeneous monoclinic half-planes with small off-axis angles have contact loads approaching those of the 0 deg half-plane. As the off-axis angle increases, the contact loads diminish in a monotonic fashion, approaching the contact loads of the 90 deg half-plane. The monotonic decrease of the contact load at a given contact length with increasing off-axis orientation is accompanied by the decrease in the inplane moduli E_{xx} and G_{xz} and increase in the inplane Poisson's ratio ν_{xz}.

The contact load versus contact length response curves for the investigated layered half-planes are bounded by the response curves of homogeneous 0 deg and 90 deg half-planes. In the case of layered half-planes, the contact load depends on the orientation of the surface layer, relative size of the contact zone and the surface layer thickness, and the properties of the underlying half-plane. Monoclinic layers bonded to 90 deg half-plane generate loads tending to approach those of the 90 deg half-plane with increasing off-axis orientation. The reverse is true for monoclinic layers bonded to 0 deg half-plane. For contact lengths that are small relative to layer thickness, the contact force depends largely on the surface layer properties. For contact lengths that are large relative to layer thickness, the contact load is significantly influenced by the properties of the underlying half-plane.

The contact stress profiles for the layered half-planes exhibited departures from elliptical that depended on the off-axis orientation and the relative size of the contact zone and thickness of the surface layer. For the investigated cases, departures from elliptical profile were not dramatic. In general, 90 deg half-planes with 0 deg surface layers produced lower values of contact stress in the central region and higher in the outer region of the contact zone in comparison to the elliptical profile. Increasing the off-axis angle of the surface layer bonded to the 90 deg half-plane produced more elliptical profiles. The investigated half-planes with 90 deg surface layer bonded to the 0 deg half-plane produced stress profiles that were higher in the inner region of the contact zone and lower in the outer region in comparison to the elliptical profile. Decreasing the off-axis angle of the surface layer produced the same result as in the preceding case. The departure of the contact stress profile from elliptical increased with the relative size of the contact length to the surface layer thickness.

In summary, the results presented in this chapter indicate that while the load versus contact length response curves are considerably influenced by the surface layer orientation and the underlying half-plane, the corresponding contact stress profiles are not influenced as much for the considered unidirectional composite.

References

Bufler, H., 1971, "Theory of Elasticity of a Multilayered Medium," *J. Elasticity*, Vol. 1, pp. 125-143.

Erdogan, F., 1969, "Approximate Solutions of Systems of Singular Integral Equations," *SIAM J. Appl. Math.*, Vol. 17, pp. 1041-1059.

Erdogan, F., and Gupta, G., 1972, "On the Numerical Solution of Singular Integral Equations," *Quart. J. Applied Mathematics*, pp. 525-534.

Gupta, P. K., and Walowit, J. A., 1974, "Contact Stresses Between an Elastic Cylinder and a Layered Elastic Solid," *J. Lubrication Technology*, Vol. 96, pp. 250-257.

Pindera, M-J., and Lane, M. S., 1991, "Frictionless Contact of Layered Half Planes," *Recent Developments in Elasticity*, R. C. Batra and G. P. Mac Sithigh, eds., ASME AMD-Vol. 124, pp. 77-90.

Jen-San Chen[1]

D. M. Bogy
Mem. ASME

Computer Mechanics Laboratory,
Department of Mechanical Engineering,
University of California,
Berkeley, CA 94720

The Effects of a Space-Fixed Friction Force on the In-Plane Stress and Stability of Transverse Vibrations of a Spinning Disk

The membrane stress field in a spinning disk induced by a stationary circumferential friction force is first derived in the form of an infinite series. It is then shown, both by analysis and numerical computation, that this membrane stress field has no effect on the stability of transverse vibration of the spinning disk.

Introduction

The effects of various load parameters in the stationary point load system, such as friction force, transverse mass, damper, spring and their pitching counterparts, on the natural frequency and stability of a spinning disk are important to the design of high-density floppy disk drives. Ono et al. (1991) calculated the eigenvalues of the coupled system by the finite element method. Chen and Bogy (1992) derived the first-order derivatives of the eigenvalues with respect to various load parameters in the load system to obtain analytically a better understanding of the calculated results. In all these calculations and analytical derivations, however, the asymmetric membrane stress field induced by the friction force was neglected. It is known that the natural frequency and the stability of the system can be modified by changing the in-plane stresses (Mote, 1965), therefore, as suggested by a reviewer of Chen and Bogy (1992), the friction force of the load system may be important in this regard. Here we first derive the solution of the friction force-induced membrane stress field in the form of an infinite series, and then we obtain the derivative of the eigenvalues with respect to the friction force to determine its effect on the stability of transverse vibration. It is found that this derivative turns out to be zero and so the asymmetric membrane stress field has no effect on the eigenvalues of the system, at least to the first order. Furthermore, we incorporate this membrane stress field in the finite element program and confirm that its effect is negligible compared to the contribution from the transverse component of the same friction force associated with the slope change of the disk when it deflects. The results presented herein complement the previous two papers.

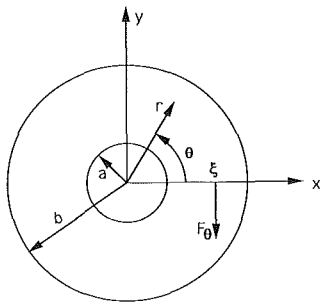

Fig. 1 Concentrated friction force in a disk

The Asymmetric Membrane Stress Field

Figure 1 shows a circular disk, which is clamped on the inner radius $r=a$ and free on the outer radius $r = b$, subjected to a concentrated force F_θ at point $(\xi, 0)$ in the negative y-direction, where $a < \xi < b$. To calculate the stress field in the disk due to F_θ we consider first the displacement and stress fields in an infinite domain due to the same force (Love, 1927), they are

$$u_r^{(1)} = \frac{F_\theta(1+\nu)}{8\pi hEG}\,[(3-\nu)G\log G\sin\theta + 2\xi(1+\nu)\sin\theta(\xi - r\cos\theta)]$$

$$u_\theta^{(1)} = \frac{F_\theta(1+\nu)}{8\pi hEG}\,\{(3-\nu)G\log G\cos\theta + (1+\nu)[H\cos\theta + r\sin^2\theta(r\cos\theta - \xi)]\}$$

$$\sigma_{rr}^{(1)} = \frac{F_\theta}{4\pi hG^2}\,\{r\sin^3\theta[(3+\nu)G - 2(1+\nu)H] - r\cos^2\theta\sin\theta[(1-\nu)G - 2(1+\nu)H] + \sin 2\theta(r\cos\theta - \xi)[(1-\nu)G + 2(1+\nu)r^2\sin^2\theta]\} \quad (1)$$

[1]Current address: Department of Mechanical Engineering, National Taiwan University, Taipei, Taiwan 107, Republic of China.

Contributed by the Applied Mechanics Division of THE AMERICAN SOCIETY OF MECHANICAL ENGINEERS for publication in the ASME JOURNAL OF APPLIED MECHANICS.

Discussion on this paper should be addressed to the Technical Editor, Professor Lewis T. Wheeler, Department of Mechanical Engineering, University of Houston, Houston, TX 77204-4792, and will be accepted until four months after final publication of the paper itself in the ASME JOURNAL OF APPLIED MECHANICS.

Manuscript received by the ASME Applied Mechanics Division, July 12, 1991; final revision, Aug. 14, 1992. Associate Technical Editor: F. Y. M. Wan.

$$\sigma_{r\theta}^{(1)}=\frac{F_\theta}{4\pi hG^2}\{(r\cos\theta-\xi)(\cos^2\theta-\sin^2\theta)]$$
$$\times[(1-\nu)G+2(1+\nu)r^2\sin^2\theta]+4r\sin^2\theta\cos\theta[G-(1+\nu)H]\} \quad (2)$$

$$\sigma_{\theta\theta}^{(1)}=\frac{F_\theta}{4\pi hG^2}\{r\cos^2\theta\sin\theta[(3+\nu)G-2(1+\nu)H]$$
$$-r\sin^3\theta[(1-\nu)G-2(1+\nu)H]$$
$$-\sin2\theta(r\cos\theta-\xi)[(1-\nu)G+2(1+\nu)r^2\sin^2\theta]\} \quad (3)$$

where

$$G=r^2+\xi^2-2r\xi\cos\theta, \quad H=r^2\cos^2\theta+\xi^2-2r\xi\cos\theta.$$

E, ν, and h are the Young's modulus, Poisson's ratio, and the thickness of the plate, respectively. It is noted that $\sigma_{r\theta}^{(1)}$ and $u_\theta^{(1)}$ are even functions of θ, while $\sigma_{rr}^{(1)}$ and $u_r^{(1)}$ are odd functions, and that these quantities are obtained from the two-dimensional generalized stress solution divided by thickness h to result in functions with units of displacement and stress. With use of these equations we can find the displacement distributions on $r = a$ and stress distributions on $r = b$ and expand them in Fourier series as follows:

$$Eu_r(r=a)=F_\theta\sum_{n=1}^{\infty}a_n\sin n\theta \quad (4)$$

$$Eu_\theta(r=a)=F_\theta\sum_{n=0}^{\infty}c_n\cos n\theta \quad (5)$$

$$\sigma_{rr}(r=b)=F_\theta\sum_{n=1}^{\infty}b_n\sin n\theta \quad (6)$$

$$\sigma_{r\theta}(r=b)=F_\theta\sum_{n=0}^{\infty}d_n\cos n\theta. \quad (7)$$

The coefficients in these expansions can be obtained easily by numerical integration. In general, these series converge very fast as long as ξ is not very close to a or b, and 20 terms are usually enough to obtain a satisfactory result. We now solve an auxiliary problem: Find the stress fields $\sigma_{rr}^{(2)}$, $\sigma_{r\theta}^{(2)}$, and $\sigma_{\theta\theta}^{(2)}$ in the annular disk with displacements on $r = a$ described by Eqs. (4) and (5), and tractions on $r = b$ described by Eqs. (6) and (7). Following a procedure similar to that described in Coker and Filon (1957), with some obvious modifications, the general expressions of the displacement and stress fields of this auxiliary problem can be obtained as

$$\frac{hEu_r^{(2)}}{F_\theta}=\left\{(1-3\nu)A_1r^2+\frac{(1+\nu)B_1}{r^2}\right.$$
$$\left.+\frac{1}{2}[\nu^2-1+(\nu+1)(\nu-3)\log r]C_1+D_1\right\}\sin\theta$$
$$+\sum_{n=2}^{\infty}\{[4-(1+\nu)(2+n)]A_nr^{n+1}+(1+\nu)nB_nr^{-n-1}$$
$$-(1+\nu)nC_nr^{n-1}+[4-(1+\nu)(2-n)]D_nr^{-n+1}\}\sin n\theta \quad (8)$$

$$\frac{hEu_\theta^{(2)}}{F_\theta}=-\frac{(1+\nu)C_0}{r}-D_0r-\left\{(5+\nu)r^2A_1+\frac{(1+\nu)B_1}{r^2}\right.$$
$$\left.+\left[1+\nu+\frac{1}{2}(1+\nu)(3-\nu)\log r\right]C_1+D_1\right\}\cos\theta$$
$$-\sum_{n=2}^{\infty}\{[4+(1+\nu)n]A_nr^{n+1}+(1+\nu)nB_nr^{-n-1}+(1+\nu)nC_nr^{n-1}$$
$$-[4-(1+\nu)n]D_nr^{-n+1}\}\cos n\theta \quad (9)$$

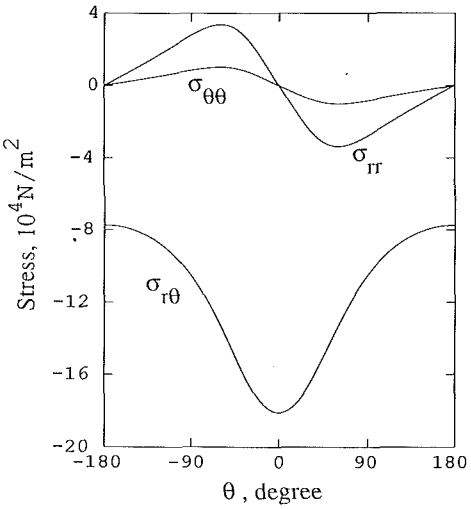

Fig. 2 Stress distributions on the inner radius for a conventional 3.5-in. floppy disk

$$\frac{h\sigma_{rr}^{(2)}}{F_\theta}=\left[2A_1r-\frac{2B_1}{r^3}-\frac{(3+\nu)C_1}{2r}\right]\sin\theta$$
$$-\sum_{n=2}^{\infty}[(n+1)(n-2)A_nr^n+n(n+1)B_nr^{-n-2}$$
$$+n(n-1)C_nr^{n-2}+(n-1)(n+2)D_nr^{-n}]\sin n\theta\} \quad (10)$$

$$\frac{h\sigma_{r\theta}^{(2)}}{F_\theta}=\frac{C_0}{r^2}-\left[2A_1r-\frac{2B_1}{r^3}+\frac{(1-\nu)C_1}{2r}\right]\cos\theta$$
$$-\sum_{n=2}^{\infty}[n(n+1)A_nr^n-n(n+1)B_nr^{-n-2}$$
$$+n(n-1)C_nr^{n-2}-n(n-1)D_nr^{-n}]\cos n\theta \quad (11)$$

$$\frac{h\sigma_{\theta\theta}^{(2)}}{F_\theta}=\left[6A_1r+\frac{2B_1}{r^3}+\frac{(1-\nu)C_1}{2r}\right]\sin\theta$$
$$+\sum_{n=2}^{\infty}[(n+1)(n+2)A_nr^n+n(n+1)B_nr^{-n-2}$$
$$+n(n-1)C_nr^{n-2}+(n-1)(n-2)D_nr^{-n}]\sin n\theta. \quad (12)$$

By comparing the coefficients of $\cos n\theta$ and $\sin n\theta$ between Eqs. (4)–(7) and (8)–(11), we can determine A_n, B_n, C_n, and D_n in terms of a_n, b_n, c_n, and d_n uniquely. The subtraction of the stress fields in Eqs. (10)–(12) from the stress fields in Eqs. (1)–(3) yields the desired solution for the membrane stresses in the clamped-free annular disk due to a circumferential load. Figure 2 shows the stress distributions on the inner radius when a = 16.5 mm, ξ = 48.75 mm, b = 65 mm, h = 0.078 mm, F_θ = 0.32 N, and ν = 0.3. These are typical parameters for a conventional 3.5-in. floppy disk. It is emphasized here that the resulting σ_{rr} and $\sigma_{\theta\theta}$ are odd functions of θ, while $\sigma_{r\theta}$ is an even function.

Effect of Friction Force on the Eigenvalues of the Spinning Disk

The equation of motion of a spinning disk subjected to a concentrated friction force in the circumferential direction, in terms of transverse displacement w and with respect to the stationary coordinate system (r, θ), is

$$(w_{,tt}+2\Omega w_{,t\theta}+\Omega^2w_{,\theta\theta})+\frac{D}{\rho h}\nabla^4w+L_1w+F_\theta L_2w$$
$$=-\frac{F_\theta}{\rho hr^2}w_{,\theta}\delta(r-\xi)\delta(\theta) \quad (13)$$

where Ω, h, and D are the rotational speed, thickness, and

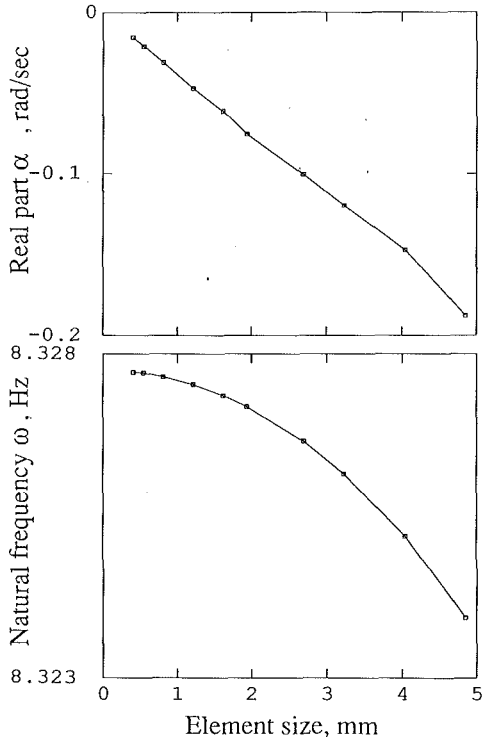

Fig. 3 Convergence of the natural frequency and the real part of an eigenvalue

flexural rigidity, respectively, of the disk. $\delta(:)$ is the Dirac delta function. L_1 is the membrane operator associated with the axisymmetrical stress due to centrifugal force, whose effect has been discussed in Chen and Bogy (1992). L_2 is the membrane operator associated with the asymmetrical stress due to the friction force,

$$L_2 = -\frac{1}{\rho r F_\theta}\left[\frac{\partial}{\partial r}\left(r\sigma_{rr}\frac{\partial}{\partial r}+\sigma_{r\theta}\frac{\partial}{\partial\theta}\right)+\frac{\partial}{\partial\theta}\left(\sigma_{r\theta}\frac{\partial}{\partial r}+\frac{1}{r}\sigma_{\theta\theta}\frac{\partial}{\partial\theta}\right)\right]$$

where σ_{rr}, $\sigma_{r\theta}$, and $\sigma_{\theta\theta}$ have been calculated in the preceding section. Since the membrane stress field is proportional to F_θ, the operator L_2 is independent of F_θ. To evaluate the effect of the friction force associated with the asymmetric stress on the eigenvalues $\lambda^0_{mn} = i\omega_{mn}$ of the freely spinning disk, we calculate the first-order derivative (see Chen and Bogy, 1992, for details of the method)

$$\frac{\partial\lambda^0_{mn}}{\partial F_\theta} = \frac{i\langle w^0_{mn}, L_2 w^0_{mn}\rangle}{4\pi(\omega_{mn}\pm n\Omega)\int_a^b R^2_{mn}(r)rdr}$$

where $w^0_{mn} = R_{mn}(r)e^{\pm in\theta}$ is the eigenfunction, with m nodal circles and n nodal diameters, of the freely spinning disk. The inner product in the numerator can be expressed as

$$\langle w^0_{mn}, L_2 w^0_{mn}\rangle = \frac{1}{\rho F_\theta}\int_a^b\int_{-\pi}^{\pi}\left[r\sigma_{rr}\frac{\partial\overline{w}^0_{mn}}{\partial r}\frac{\partial w^0_{mn}}{\partial r}+\frac{\sigma_{\theta\theta}}{r}\frac{\partial\overline{w}^0_{mn}}{\partial\theta}\frac{\partial w^0_{mn}}{\partial\theta}+\sigma_{r\theta}\left(\frac{\partial\overline{w}^0_{mn}}{\partial r}\frac{\partial w^0_{mn}}{\partial\theta}+\frac{\partial\overline{w}^0_{mn}}{\partial\theta}\frac{\partial w^0_{mn}}{\partial r}\right)\right]drd\theta$$

where the overbar represents complex conjugate. It is noted that the integration associated with $\sigma_{r\theta}$ always vanishes because the two terms in the parenthesis cancel, while the contributions from σ_{rr} and $\sigma_{\theta\theta}$ also vanish since they are odd functions of θ. So we can conclude that the membrane stress field induced by the friction force has no effect on the eigenvalues of the spinning disk, at least to the first order in the sense of a Taylor series expansion.

We next incorporate the asymmetric membrane stress field due to the friction force into the finite element program developed in Ono et al. (1991). In order to study the effect of this membrane stress field on the eigenvalues, we first consider the case when the right-hand side of Eq. (13) vanishes. Since there exists a singularity of order r^{-1} in the membrane stress field at point $(\xi, 0)$, it is expected to cause some problems in the convergence of the eigenvalue calculations. Figure 3 shows the relations between the element size in the radial direction and the imaginary (natural frequency ω) and real (stability parameter α) parts of the eigenvalue of the mode with one nodal diameter and zero nodal circle. The parameters used in the calculation are the same as those in Ono et al. (1991) and $\Omega = 100$ rpm. It is observed that as the element size approaches zero, the natural frequency converges to its correct value while the real part of the eigenvalue approaches zero almost linearly.

Additional eigenvalue calculations using Eq. (13) show that including or excluding the membrane effect L_2 alters the results by less than one percent. So, the significance of F_θ on the stability of the spinning disk-stationary load system is solely through the right-hand side of Eq. (13), and not through L_2 on the left-hand side.

Conclusions

We have shown both by analysis and numerical computation that the in-plane membrane stress field induced in a spinning disk by a stationary circumferential friction force has no effect, at least to the first order, on the stability of transverse vibration of the disk.

Acknowledgment

This work was supported by the Computer Mechanics Laboratory at the University of California at Berkeley.

References

Coker, E. G., and Filon, L. N. G., 1957, *A Treatise on Photo-Elasticity*, Cambridge University Press, London.

Chen, J.-S., and Bogy, D. B., 1992, "Effects of Load Parameters on the Natural Frequencies and Stability of a Flexible Spinning Disk with a Stationary Load System," ASME JOURNAL OF APPLIED MECHANICS, Vol. 59, pp. S230-S235.

Love, A. E. H., 1927, *A Treatise on the Mathematical Theory of Elasticity*, Cambridge University Press, London.

Mote, C. D., Jr., 1965, "Free Vibration of Initially Stressed Circular Disk," *ASME Journal of Engineering for Industry*, Vol. 87, pp. 258-264.

One, K., Chen, J.-S., and Bogy, D. B., 1991, "Stability Analysis for the Head-Disk Interface in a Flexible Disk Drive," ASME JOURNAL OF APPLIED MECHANICS, Vol. 58, pp. 1005-1014.

Response of Annular Plates to Circumferentially and Radially Moving Loads

G. N. Weisensel
Staff Engineer,
ADSTAR,
IBM Corporation,
Rochester, MN 55901
Mem. ASME

A. L. Schlack, Jr.
Professor,
Department of Engineering Mechanics,
University of Wisconsin,
Madison, WI 53706

The forced dynamic response of annular plates to circumferentially and radially moving concentrated transverse loads is investigated utilizing classical plate theory, with damping included, and solved in integral form. The boundary conditions are that the inner boundary of the plate is clamped and the outer boundary is free. An analytical expression in Fourier-Bessel series form is obtained for the forced deflection response to an arbitrarily moving concentrated load. This study includes radially moving loads and is a significant extension of the understanding of circular and annular plate dynamics. This understanding of radially moving loads is used to examine the nature of resonance conditions and corresponding critical values of the load parameters. The shapes of deflection modes of plate vibration are also presented. Damping and loading parameter sensitivities are studied in detail.

Introduction

The use of circular and annular plates in design and engineering of mechanical systems is very widespread and quite pervasive in certain industries. Particular applications of this type of mechanical component include turbines, saw blades, computer magnetic recording disks, grinding wheels, gears, phonograph records, and percussion musical instruments. The relative importance of these components in engineering necessitates a comprehensive understanding of their mechanical behavior. One critical facet of this behavior is the vibration response of circular and annular plates when used in mechanical system operation, particularly rotational operation.

This study examines the vibration response of an annular plate. A review of the literature briefly cites the history of the study of vibrations of circular and annular plates and a few of the primary studies of the free and forced vibrations of circular and annular plates. This foundation is heavily utilized in the analysis. The literature review focuses, however, on the vibrations of rotating circular and annular plates and on the response of plates to moving loads.

It must be noted that a difference exists between the problem of a rotating plate with a stationary or radially moving load and the problem of a stationary plate with a circumferentially moving load (Iwan and Stahl, 1973; Huang and Soedel, 1987). In the latter case, the complicating centrifugal effects of plate rotation are not encountered. Within certain ranges of rotational speed and excitation frequency, the differences between these two problems are not appreciable.

The general analysis and solution of this problem are developed utilizing classical plate theory. Therefore, it must also be recognized that for the response of rotating plates, both centrifugal and flexural effects are operative (Lamb and Southwell, 1921; Southwell, 1922) and the frequencies and modes of vibration will depend on the relative importance of these effects. Previous studies (Eversman and Dodson, 1969; Barasch and Chen, 1972) indicate, however, that the centrifugal membrane effects will be of the order of the bending effects only at very large rotational speeds for thin plates. It is common practice in both industry and the literature to neglect, when appropriate, the centrifugal effects due to rotation in analysis and design for many practical problems of interest. Further analytical research on the influence of centrifugal stiffening should be carried out.

Starting from the previous work cited in the literature review, the general analysis and solution of the problem of annular plates subject to arbitrary moving transverse loads is developed utilizing classical plate theory with damping included. Damping is included as a parameter, in the form of linear viscous damping, to provide further understanding of the nature of the solution.

The response of a plate to a general load $p(r, \theta, t)$ is first derived as an integral solution. Then any special case of surface loading can be studied as a special case of this general solution in Fourier-Bessel series form. As stated above, this problem has utility for studying the inverse problem of a rotating plate with an arbitrary moving load.

Specifically, the general analysis is applied to obtain an analytical solution for the case of an arbitrary circumferentially and radially moving load. This type of loading occurs in many of the applications mentioned above. Previous literature on circular and annular plate response to moving loads has dealt

Contributed by the Applied Mechanics Division of THE AMERICAN SOCIETY OF MECHANICAL ENGINEERS for publication in the ASME JOURNAL OF APPLIED MECHANICS.

Discussion on this paper should be addressed to the Technical Editor, Professor Lewis T. Wheeler, Department of Mechanical Engineering, University of Houston, Houston, TX 77204-4792, and will be accepted until four months after final publication of the paper itself in the ASME JOURNAL OF APPLIED MECHANICS.

Manuscript received by the ASME Applied Mechanics Division, Aug. 20, 1991; final revision, June 4, 1992. Associate Technical Editor: D. J. Inman.

only with circularly orbiting loads, i.e., loads at constant radial position. The general solution for the response of annular plates to arbitrary radially moving loads is then applied to the special case of a load with circumferential and harmonic radial motion. In addition to this detailed special case, the methods of analysis to obtain solutions for the more general cases of a concentrated load with arbitrary periodic radial motion and of an arbitrary periodically varying amplitude load are given.

The analytical expressions and resulting understanding of radially moving loads are used to examine the nature of resonance conditions and corresponding critical values of the load parameters. The shapes of deflection modes of plate vibration are also presented for several sets of input system parameters. These sets of parameters are used to determine damping and loading parameter sensitivities, which are studied in detail.

The study of circular and annular plate vibrations has a long history. Beginning with the first mathematical approach to the membrane theory of plates (Euler, 1766) and the observation of sand patterns on copper plates excited by a violin bow (Chladni, 1787, 1802; Waller, 1938, 1961), later work includes the classical thin plate formulation (Kirchhoff, 1850).

Vogel and Skinner (1965) derived the characteristic equation for all nine combinations of the classical boundary conditions associated with the transverse vibrations of uniform annular plates. A very thorough general analysis considering many different types of boundary conditions has been presented by McLeod and Bishop (1965).

Many more works on the free vibrations of plates are cited in the literature survey papers by Leissa (1977, 1978, 1981, 1987), Mote et al. (1978, 1982), D'Angelo et al. (1985), and Weisensel (1989).

The earliest study of a vibrating, rotating elastic plate appears to be by Lamb and Southwell (1921) who derived the linearized equations of transverse deflection and identified the respective contributions to the equations from bending stress and in-plane stress due to rotation. In that paper, and a subsequent one by Southwell (1922), they examined the frequencies and modes of free vibration for complete circular plates which were either very flexible or very stiff.

Mote (1970, 1977) investigated the stability of annular plates and plate/collar systems subjected to moving loads with harmonically varying amplitude. Benson and Bogy (1978) studied the deflection of a very flexible rotating annular plate due to a concentrated transverse load that is fixed in space.

Honda et al. (1985) have analyzed the steady-state response of stationary annular plates to concentrated harmonic forces moving in concentric circular paths at constant speed. The modal response is discussed in detail, with emphasis on the vibratory modes. The theoretical analysis described in that paper is useful for plates rotating at slow constant speeds. Weisensel and Schlack (1988, 1989, 1990) have very recently studied the natural frequencies and deflection profiles of rotating thin annular plates due to concentrated transverse loads of harmonically varying amplitude moving at constant angular speed relative to the plate surface. Their works treat both the case of constant radial position and the case of sudden changes in radial position. This work is similar in analysis to that cited above by Honda et al., but the conclusions derived are quite different.

The only text devoted entirely to the study of the vibration of elastic bodies due to moving loads is by Fryba (1972). This work definitely provides the most comprehensive treatment

Nomenclature

$A_{mn}(\bar{t})$, $B_{mn}(\bar{t})$ = coefficient functions in variation of parameters method

$a_{0,mn}$, $b_{0,mn}$ = coefficient constants

a_{mn}, b_{mn}, c_{mn}, d_{mn} = coefficient constants

a = outer radius of annular plate

b = inner radius of annular plate

$\bar{b} = b/a$ = ratio of inner radius to outer radius of annular plate

c_n, d_n = coefficient constants

$D = Eh^3/[12(1-\nu^2)]$ = flexural modulus of rigidity

E = modulus of elasticity

f_{mn} = undamped natural cyclic frequencies of plate

h = thickness of plate

$I_n(\cdot)$ = modified Bessel function of the first kind of integral order n

$J_n(\cdot)$ = Bessel function of the first kind of integral order n

$K_n(\cdot)$ = modified Bessel function of the second kind of integral order n

k = integer index

m = integer index, number of nodal circles

n = integer index, number of nodal diameters, integral order of Bessel function

N = sample size for arithmetic mean

$P(t)$ = amplitude of concentrated load

$\bar{P}(\bar{t})$ = dimensionless amplitude of concentrated load

P_0 = maximum amplitude of concentrated load

$\bar{P}_0$ = dimensionless maximum amplitude of concentrated load

$\bar{P}_{kc}$, $\bar{P}_{ks}$ = coefficients of Fourier series representation of general periodic amplitude variation

$p(r, \theta, t)$ = transverse load distribution (force per unit area)

$\bar{p}(\bar{r}, \bar{\theta}, \bar{t})$ = dimensionless transverse load distribution

$\bar{p}_0(\bar{r}, \bar{\theta}, \bar{t})$ = component of Fourier series representation of load with general periodic amplitude variation

$\bar{p}_{kc}(\bar{r}, \bar{\theta}, \bar{t})$, $\bar{p}_{ks}(\bar{r}, \bar{\theta}, \bar{t})$ = components of Fourier series representation of load with general periodic amplitude variation

q = integer index

Q_{mn} = radial characteristic function normalization constant

r = radial coordinate variable

r_0 = radial position constant

r_1 = radial motion amplitude

$\bar{r} = r/a$ = dimensionless radial coordinate variable

$\bar{r}_0 = r_0/a$ = dimensionless radial position constant

$\bar{r}_1 = r_1/a$ = dimensionless radial motion amplitude

$\bar{r}(\bar{t})$ = dimensionless radial motion function

$\bar{r}_{kc}$, $\bar{r}_{ks}$ = coefficients of Fourier series representation of general periodic radial motion function

$R_{mn}(\bar{r})$ = characteristic function in radial coordinate

available on this subject. An extensive bibliography is also included.

Significant background directly related to this problem is contained in the works by McLeod and Bishop (1965), Raske (1966), Raske and Schlack (1967), Mote (1970), and Fryba (1972). The current state of the art for this problem is represented in the works by Honda et al. and Weisensel and Schlack. These latter studies give a complete treatment of the response of circular and annular plates to circularly orbiting concentrated transverse loads.

Much of the work in the literature deals with natural and resonant frequencies of circular and annular plates with moving loads. Only a small portion further reports the influence of moving loads on mode shapes or studies system parameter sensitivities in detail. Benson and Bogy (1978) studied the deflection of very flexible rotating annular plates due to concentrated transverse loads that are fixed in space; first within the context of membrane theory, and then with bending stiffness included. Very nice graphical results are presented for various values of the stiffness parameter and load position.

Starting from this previous work the present study develops the general analysis and solution of the problem of annular plates subject to arbitrary moving transverse loads using classical plate theory. The current understanding of plate response to moving transverse loads is extended to include a component of motion in the radial direction in addition to a component of motion in the tangential direction. This achievement provides an understanding for cases of an arbitrary moving transverse load and can be used in any of the areas of practical application noted above.

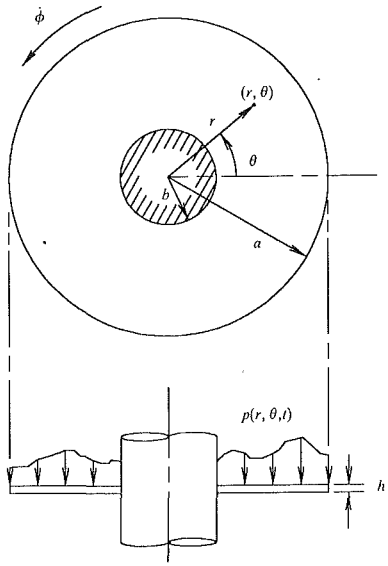

Fig. 1 Rotating thin annular plate with clamped inner boundary and free outer boundary subjected to arbitrary transverse load

Analysis

A homogeneous, isotropic, thin annular plate of uniform thickness is shown in Fig. 1. The plate is rigidly clamped at its inner boundary and free of support at its outer boundary.

Nomenclature (cont.)

t = time variable
$\bar{t} = t/\sqrt{\rho h a^4/D}$ = dimensionless time variable
$w(r, \theta, t)$ = transverse deflection of plate middle surface
$\overline{w}(\bar{r}, \bar{\theta}, \bar{t}) = w/a$ = dimensionless transverse deflection of plate middle surface
$\overline{w}_0(\bar{r}, \bar{\theta}, \bar{t})$ = component of Fourier series representation of deflection response
$\overline{w}_{kc}(\bar{r}, \bar{\theta}, \bar{t})$, $\overline{w}_{ks}(\bar{r}, \bar{\theta}, \bar{t})$ = components of Fourier series representation of deflection response
$\overline{w}_n(\bar{r}, \bar{\theta}, \bar{t})$ = fundamental solution of homogeneous equation of motion
$\overline{w}_{mn}(\bar{r}, \bar{\theta}, \bar{t})$ = characteristic function
$Y_n(\bullet)$ = Bessel function of the second kind of integral order n

Greek

α = arbitrary separation constant
α_{mn} = dimensionless frequency parameter (characteristic value)
β = oscillation frequency of radial motion of load
$\overline{\beta}$ = dimensionless oscillation frequency of radial motion of load
$\overline{\beta}_{k,mnq}$ = dimensionless critical oscillation frequency of radial motion of load
γ = equivalent viscous damping density of plate (damping constant per unit volume)
$\delta(\bullet)$ = Dirac delta generalized function
$\overline{\zeta}$ = dimensionless damping ratio
$\eta_{2,mn}$, $\eta_{3,mn}$, $\eta_{4,mn}$ = coefficient constants
θ = tangential coordinate variable
$\overline{\theta} = \theta/2\pi$ = dimensionless tangential coordinate variable
$\tilde{\theta}(\bar{t})$ = dimensionless tangential motion function
ν = Poisson's ratio
$\Pi(\bar{r}, \bar{\theta})$ = spatial distribution of loading function
ρ = mass density of plate (mass per unit volume)
$\bar{\tau}$ = dimensionless time integration variable
$\dot{\phi}$ = angular speed of plate rotation
$\dot{\bar{\phi}}$ = dimensionless angular speed of plate rotation
$\dot{\phi}_{k,mn}$, $\dot{\phi}_{k,mnq}$ = critical rotational speed of plate
$\dot{\bar{\phi}}_{k,mn}$, $\dot{\bar{\phi}}_{k,mnq}$ = dimensionless critical rotational speed of plate
Ω = undamped vibration circular frequency of plate
$\overline{\Omega}$ = dimensionless undamped vibration circular frequency of plate
Ω_{mn} = undamped natural circular frequencies of plate
$\overline{\Omega}_{mn}$ = dimensionless undamped natural circular frequencies of plate
ω = oscillation frequency of amplitude of concentrated transverse load
$\overline{\omega}$ = dimensionless oscillation frequency of amplitude of concentrated transverse load

The transverse surface load acting on the plate is taken in the general form $p(r, \theta, t)$, which can be used to represent all possible surface loadings that can be described as functions of position and time. According to classical plate theory, the governing partial differential equation of transverse motion for a damped plate subjected to a general transverse surface load is given by

$$D\nabla^4 w(r,\theta,t) + \rho h \frac{\partial^2 w(r,\theta,t)}{\partial t^2} + \gamma h \frac{\partial w(r,\theta,t)}{\partial t} = p(r,\theta,t) \quad (1)$$

where $\nabla^4 = \nabla^2\nabla^2$ is the biharmonic operator.

It is convenient for later analysis to render this governing equation dimensionless. For this purpose, introduce the following dimensionless quantities:

$$\bar{r} = r/a,\ \bar{\theta} = \theta/(2\pi),\ \bar{w} = w/a,\ \bar{b} = b/a,\ \bar{\zeta} = \gamma/(2\rho\Omega),$$
$$\bar{t} = t/\sqrt{\rho h a^4/D},\ \bar{p} = p/(D/a^3),\ \bar{\nabla}^2 = \frac{\partial^2}{\partial \bar{r}^2} + \frac{1}{\bar{r}}\frac{\partial}{\partial \bar{r}} + \frac{1}{4\pi^2\bar{r}^2}\frac{\partial^2}{\partial \bar{\theta}^2}. \quad (2)$$

Equation (1) can now be written in dimensionless form as

$$\bar{\nabla}^4 \bar{w}(\bar{r},\bar{\theta},\bar{t}) + \frac{\partial^2 \bar{w}(\bar{r},\bar{\theta},\bar{t})}{\partial \bar{t}^2} + \gamma a^2 \sqrt{\frac{h}{\rho D}} \frac{\partial \bar{w}(\bar{r},\bar{\theta},\bar{t})}{\partial \bar{t}} = \bar{p}(\bar{r},\bar{\theta},\bar{t}) \quad (3)$$

where $\bar{\nabla}^4 = \bar{\nabla}^2\bar{\nabla}^2$ is a dimensionless biharmonic operator. A fundamental set of solutions of the homogeneous governing partial differential equation of motion can be determined (by the method of separation of variables using Fourier-Bessel series techniques) as

$$\bar{w}_n(\bar{r},\bar{\theta},\bar{t}) = [J_n(\alpha\bar{r}) + \eta_{2,n}Y_n(\alpha\bar{r}) + \eta_{3,n}I_n(\alpha\bar{r}) + \eta_{4,n}K_n(\alpha\bar{r})](c_n \cos 2\pi n\bar{\theta} + d_n \sin 2\pi n\bar{\theta}) \times e^{-\bar{\zeta}\bar{\Omega}\bar{t}}\left(a_0 e^{i\sqrt{1-\bar{\zeta}^2}\bar{\Omega}\bar{t}} + b_0 e^{-i\sqrt{1-\bar{\zeta}^2}\bar{\Omega}\bar{t}}\right) \quad (4)$$

where $n = 0,1,2,\ldots$.

The boundary conditions for this problem are functions of the spatial variables only, thus they are time-independent boundary conditions. The classical boundary conditions at $\bar{r} = \bar{b}$, describing the fact that the deflection and slope are zero at the clamped inner boundary of the annular plate, are given in dimensionless form by

$$\bar{w} = 0, \quad \frac{\partial \bar{w}}{\partial \bar{r}} = 0. \quad (5)$$

The boundary conditions at $\bar{r} = 1$, describing the fact that the moment and resultant transverse shear are zero at the free outer boundary, are given by the so-called Kirchhoff boundary conditions

$$\frac{\partial^2 \bar{w}}{\partial \bar{r}^2} + \nu\left(\frac{1}{\bar{r}}\frac{\partial \bar{w}}{\partial \bar{r}} + \frac{1}{4\pi^2\bar{r}^2}\frac{\partial^2 \bar{w}}{\partial \bar{\theta}^2}\right) = 0,$$
$$\frac{\partial}{\partial \bar{r}}\left(\frac{\partial^2 \bar{w}}{\partial \bar{r}^2} + \frac{1}{\bar{r}}\frac{\partial \bar{w}}{\partial \bar{r}} + \frac{1}{4\pi^2\bar{r}^2}\frac{\partial^2 \bar{w}}{\partial \bar{\theta}^2}\right) + \frac{1-\nu}{4\pi^2\bar{r}^2}\frac{\partial^2}{\partial \bar{\theta}^2}\left(\frac{\partial \bar{w}}{\partial \bar{r}} - \frac{\bar{w}}{\bar{r}}\right) = 0. \quad (6)$$

The allowable values of the parameter α can be determined by satisfying the boundary conditions in (5)–(6) for the fundamental solution given in (4). This results in a family of characteristic equations, a different equation for each value of n. Thus, for each value of n, this equation will be satisfied only for certain values of the parameter α. These characteristic values, or eigenvalues, will be denoted α_{mn}.

Utilizing these eigenvalues, the dimensionless undamped natural frequencies of vibration of the plate are $\bar{\Omega}_{mn} = \alpha_{mn}^2$ where the undamped natural frequencies of vibration Ω_{mn} are related to $\bar{\Omega}_{mn}$ by $\bar{\Omega}_{mn} = \Omega_{mn}/\sqrt{D/(\rho h a^4)}$.

Since the partial differential equation (3) and boundary conditions (5)–(6) are linear, the general deflection equation for free vibration can, by superposition, be written as

$$\bar{w}(\bar{r},\bar{\theta},\bar{t}) = \sum_{m=1}^{\infty}\sum_{n=0}^{\infty}[J_n(\alpha_{mn}\bar{r}) + \eta_{2,mn}Y_n(\alpha_{mn}\bar{r}) + \eta_{3,mn}I_n(\alpha_{mn}\bar{r}) + \eta_{4,mn}K_n(\alpha_{mn}\bar{r})](c_n \cos 2\pi n\bar{\theta} + d_n \sin 2\pi n\bar{\theta}) \times e^{-\bar{\zeta}\bar{\Omega}_{mn}\bar{t}}\left(a_{0,mn}e^{i\sqrt{1-\bar{\zeta}^2}\bar{\Omega}_{mn}\bar{t}} + b_{0,mn}e^{-i\sqrt{1-\bar{\zeta}^2}\bar{\Omega}_{mn}\bar{t}}\right). \quad (7)$$

Since a fundamental set of solutions of the homogeneous partial differential equation is known, it is appropriate to use the method of variation of parameters to determine a particular solution to the corresponding nonhomogeneous partial differential equation of motion.

Using the Fourier-Bessel series representation for the plate transverse deflection given in (7), an appropriate solution for the forced response may be assumed in the form

$$\bar{w}(\bar{r},\bar{\theta},\bar{t}) = \sum_{m=1}^{\infty}\sum_{n=0}^{\infty} R_{mn}(\bar{r})[A_{mn}(\bar{t})\cos 2\pi n\bar{\theta} + B_{mn}(\bar{t})\sin 2\pi n\bar{\theta}] \quad (8)$$

where $R_{mn}(\bar{r}) = J_n(\alpha_{mn}\bar{r}) + \eta_{2,mn}Y_n(\alpha_{mn}\bar{r}) + \eta_{3,mn}I_n(\alpha_{mn}\bar{r}) + \eta_{4,mn}K_n(\alpha_{mn}\bar{r})$ and the coefficients $A_{mn}(\bar{t})$ and $B_{mn}(\bar{t})$ are now functions of time that must be determined through further analysis. These coefficient functions depend upon the physical plate parameters, the boundary conditions, and the loading function.

Using standard Fourier-Bessel series techniques, we obtain an ordinary differential equation for $A_{mn}(\bar{t})$ in the form

$$\ddot{A}_{mn}(\bar{t}) + \gamma a^2\sqrt{\frac{h}{\rho D}}\dot{A}_{mn}(\bar{t}) + \alpha_{mn}^4 A_{mn}(\bar{t}) = \frac{2}{Q_{mn}}\int_0^1\int_{\bar{b}}^1 R_{mn}(\bar{r})\cos 2\pi n\bar{\theta}\,\bar{p}(\bar{r},\bar{\theta},\bar{t})\bar{r}\,d\bar{r}\,d\bar{\theta} = \tilde{A}_{mn}(\bar{t}) \quad (9)$$

where $(\dot{\bullet})$ and $(\ddot{\bullet})$ represent ordinary derivatives with respect to $\bar{t}$.

The total solution of (9) for $A_{mn}(\bar{t})$ is

$$A_{mn}(\bar{t}) = \hat{A}_{mn}(\bar{t}) + A_{mn}^*(\bar{t}) \quad (10)$$

where the homogeneous solution $\hat{A}_{mn}(\bar{t})$ is given by

$$\hat{A}_{mn}(\bar{t}) = e^{-\bar{\zeta}\bar{\Omega}_{mn}\bar{t}}\left(a_{mn}e^{i\sqrt{1-\bar{\zeta}^2}\bar{\Omega}_{mn}\bar{t}} + b_{mn}e^{-i\sqrt{1-\bar{\zeta}^2}\bar{\Omega}_{mn}\bar{t}}\right). \quad (11)$$

The particular solution $A_{mn}^*(\bar{t})$ can be represented as a Duhamel convolution integral. For this purpose, note that the dimensionless Green's function for this problem is

$$G(\bar{t}) = \frac{1}{\sqrt{1-\bar{\zeta}^2}\bar{\Omega}_{mn}}e^{-\bar{\zeta}\bar{\Omega}_{mn}\bar{t}}\sin\sqrt{1-\bar{\zeta}^2}\bar{\Omega}_{mn}\bar{t}. \quad (12)$$

Using the appropriate Green's function (Moshaiov and Eareckson, 1988), $A_{mn}^*(\bar{t})$ can be given as

$$A_{mn}^*(\bar{t}) = \int_0^{\bar{t}}\tilde{A}_{mn}(\bar{\tau})G(\bar{t}-\bar{\tau})d\bar{\tau} = \frac{2}{Q_{mm}\sqrt{1-\bar{\zeta}^2}\bar{\Omega}_{mn}} \times \int_0^{\bar{t}}\left[\int_0^1\int_{\bar{b}}^1 R_{mn}(\bar{r})\cos 2\pi n\bar{\theta}\,\bar{p}(\bar{r},\bar{\theta},\bar{\tau})\bar{r}\,d\bar{r}\,d\bar{\theta}\right] \times e^{-\bar{\zeta}\bar{\Omega}_{mn}(\bar{t}-\bar{\tau})}\sin\sqrt{1-\bar{\zeta}^2}\bar{\Omega}_{mn}(\bar{t}-\bar{\tau})\,d\bar{\tau}. \quad (13)$$

In a completely analogous manner, an expression for $B_{mn}(\bar{t})$ can be obtained in the form

$$B_{mn}(\bar{t}) = \hat{B}_{mn}(\bar{t}) + B^*_{mn}(\bar{t}) \tag{14}$$

where the homogeneous solution $\hat{B}_{mn}(\bar{t})$ is given by

$$\hat{B}_{mn}(\bar{t}) = e^{-\bar{\zeta}\bar{\Omega}_{mn}\bar{t}}\left(c_{mn}e^{i\sqrt{1-\bar{\zeta}^2}\bar{\Omega}_{mn}\bar{t}} + d_{mn}e^{-i\sqrt{1-\bar{\zeta}^2}\bar{\Omega}_{mn}\bar{t}}\right) \tag{15}$$

and the particular solution $B^*_{mn}(\bar{t})$ is of the form

$$B^*_{mn}(\bar{t}) = \frac{2}{Q_{mn}\sqrt{1-\bar{\zeta}^2}\bar{\Omega}_{mn}} \cdot \times \int_0^{\bar{t}}\left[\int_0^1\int_{\bar{b}}^1 R_{mn}(\bar{r})\sin 2\pi n\bar{\theta}\bar{p}(\bar{r},\bar{\theta},\bar{\tau})\bar{r}d\bar{r}d\bar{\theta}\right] \times e^{-\bar{\zeta}\bar{\Omega}_{mn}(\bar{t}-\bar{\tau})}\sin\sqrt{1-\bar{\zeta}^2}\bar{\Omega}_{mn}(\bar{t}-\bar{\tau})d\bar{\tau}. \tag{16}$$

In (11) and (15), the constants a_{mn}, b_{mn}, c_{mn}, and d_{mn} must be determined from the initial conditions and represent a transient state of vibratory motion resulting from the initial conditions. The nature of the steady-state forced response of the rotating annular plate is contained entirely in the functions $A^*_{mn}(\bar{t})$ and $B^*_{mn}(\bar{t})$ which are defined by (13) and (16).

Substituting the expressions for the coefficient functions in (10)–(16) into (8), the general deflection solution for the forced response of a thin annular plate to an arbitrary transverse surface load $\bar{p}(\bar{r}, \bar{\theta}, \bar{t})$ is given in integral form by

$$\bar{w}(\bar{r},\bar{\theta},\bar{t}) = \sum_{m=1}^{\infty}\sum_{n=0}^{\infty} R_{mn}(\bar{r})e^{-\bar{\zeta}\bar{\Omega}_{mn}\bar{t}} \times \left\{\left\{a_{mn}e^{i\sqrt{1-\bar{\zeta}^2}\bar{\Omega}_{mn}\bar{t}} + b_{mn}e^{-i\sqrt{1-\bar{\zeta}^2}\bar{\Omega}_{mn}\bar{t}} + \frac{2}{Q_{mn}\sqrt{1-\bar{\zeta}^2}\bar{\Omega}_{mn}}\int_0^{\bar{t}}\left[\int_0^1\int_{\bar{b}}^1 R_{mn}(\bar{r})\cos 2\pi n\bar{\theta}\bar{p}(\bar{r},\bar{\theta},\bar{\tau})\bar{r}d\bar{r}d\bar{\theta}\right] \times e^{\bar{\zeta}\bar{\Omega}_{mn}\bar{\tau}}\sin\sqrt{1-\bar{\zeta}^2}\bar{\Omega}_{mn}(\bar{t}-\bar{\tau})d\bar{\tau}\right\}\cos 2\pi n\bar{\theta} + \left\{c_{mn}e^{i\sqrt{1-\bar{\zeta}^2}\bar{\Omega}_{mn}\bar{t}} + d_{mn}e^{-i\sqrt{1-\bar{\zeta}^2}\bar{\Omega}_{mn}\bar{t}} + \frac{2}{Q_{mn}\sqrt{1-\bar{\zeta}^2}\bar{\Omega}_{mn}}\int_0^{\bar{t}}\left[\int_0^1\int_{\bar{b}}^1 R_{mn}(\bar{r})\sin 2\pi n\bar{\theta}\bar{p}(\bar{r},\bar{\theta},\bar{\tau})\bar{r}d\bar{r}d\bar{\theta}\right] \times e^{\bar{\zeta}\bar{\Omega}_{mn}\bar{\tau}}\sin\sqrt{1-\bar{\zeta}^2}\bar{\Omega}_{mn}(\bar{t}-\bar{\tau})d\bar{\tau}\right\}\sin 2\pi n\bar{\theta}\right\}. \tag{17}$$

The general solution presented above can be integrated to determine the response of the annular plate for an arbitrary applied surface load $\bar{p}(\bar{r}, \bar{\theta}, \bar{t})$.

Concentrated Load With Arbitary Motion

Essentially no research has been published addressing the problem of circular or annular plate dynamics with radial load motion. Introducing a radial component in the motion of the load substantially complicates the deflection expression. The argument of the Bessel functions now becomes a function of time through the radial motion function. Thus, in general, the Bessel functions must remain inside the Duhamel convolution integral. The resulting integral expressions are extremely difficult to evaluate analytically. However, the general analysis developed above will now be applied to obtain the solution for the case of a concentrated transverse load with arbitrary tangential and radial motions and arbitrary amplitude variation.

A concentrated load with general motion and amplitude variation can be expressed as

$$\bar{p}(\bar{r},\bar{\theta},\bar{t}) = \bar{p}[\tilde{r}(\bar{t}),\tilde{\theta}(\bar{t}),\bar{t}] = \bar{P}(\bar{t})\frac{\delta[\bar{r}-\tilde{r}(\bar{t})]\delta[\bar{\theta}-\tilde{\theta}(\bar{t})]}{2\pi\bar{r}} \tag{18}$$

where $\bar{P} = P/(D/a)$.

Substituting the load function given by (18) into the general deflection solution and noting that the spatial integrals in (17) can be readily evaluated as

$$\int_0^1\int_{\bar{b}}^1 R_{mn}(\bar{r})\cos 2\pi n\bar{\theta}\bar{P}(\bar{\tau})\frac{\delta[\bar{r}-\tilde{r}(\bar{\tau})]\delta[\bar{\theta}-\tilde{\theta}(\bar{\tau})]}{2\pi\bar{r}}\bar{r}d\bar{r}d\bar{\theta} = \frac{\bar{P}(\bar{\tau})}{2\pi}\cos 2\pi n\tilde{\theta}(\bar{\tau})R_{mn}(\tilde{r}(\bar{\tau}))$$

$$\int_0^1\int_{\bar{b}}^1 R_{mn}(\bar{r})\sin 2\pi n\bar{\theta}\bar{P}(\bar{\tau})\frac{\delta[\bar{r}-\tilde{r}(\bar{\tau})]\delta[\bar{\theta}-\tilde{\theta}(\bar{\tau})]}{2\pi\bar{r}}\bar{r}d\bar{r}d\bar{\theta} = \frac{\bar{P}(\bar{\tau})}{2\pi}\sin 2\pi n\tilde{\theta}(\bar{\tau})R_{mn}(\tilde{r}(\bar{\tau})), \tag{19}$$

we obtain the following general expression for the deflection of a plate due to an arbitrarily moving concentrated load:

$$\bar{w}(\bar{r},\bar{\theta},\bar{t}) = \sum_{m=1}^{\infty}\sum_{n=0}^{\infty} R_{mn}(\bar{r})e^{-\bar{\zeta}\bar{\Omega}_{mn}\bar{t}} \times \left\{\left\{a_{mn}e^{i\sqrt{1-\bar{\zeta}^2}\bar{\Omega}_{mn}\bar{t}} + b_{mn}e^{-i\sqrt{1-\bar{\zeta}^2}\bar{\Omega}_{mn}\bar{t}} + \frac{2}{Q_{mn}\sqrt{1-\bar{\zeta}^2}\bar{\Omega}_{mn}}\int_0^{\bar{t}}\frac{\bar{P}(\bar{\tau})}{2\pi}\cos 2\pi n\tilde{\theta}(\bar{\tau})R_{mn}(\tilde{r}(\bar{\tau})) \times e^{\bar{\zeta}\bar{\Omega}_{mn}\bar{\tau}}\sin\sqrt{1-\bar{\zeta}^2}\bar{\Omega}_{mn}(\bar{t}-\bar{\tau})d\bar{\tau}\right\}\cos 2\pi n\bar{\theta} + \left\{c_{mn}e^{i\sqrt{1-\bar{\zeta}^2}\bar{\Omega}_{mn}\bar{t}} + d_{mn}e^{-i\sqrt{1-\bar{\zeta}^2}\bar{\Omega}_{mn}\bar{t}} + \frac{2}{Q_{mn}\sqrt{1-\bar{\zeta}^2}\bar{\Omega}_{mn}}\int_0^{\bar{t}}\frac{\bar{P}(\bar{\tau})}{2\pi}\sin 2\pi n\tilde{\theta}(\bar{\tau})R_{mn}(\tilde{r}(\bar{\tau})) \times e^{\bar{\zeta}\bar{\Omega}_{mn}\bar{\tau}}\sin\sqrt{1-\bar{\zeta}^2}\bar{\Omega}_{mn}(\bar{t}-\bar{\tau})d\bar{\tau}\right\}\sin 2\pi n\bar{\theta}\right\}. \tag{20}$$

To further evaluate the solution for arbitrary concentrated moving loads, the functional form of the load amplitude $\bar{P}(\bar{t})$, the tangential motion $\tilde{\theta}(\bar{t})$, and the radial motion $\tilde{r}(\bar{t})$ must be specified.

Concentrated Load With Harmonic Radial Motion

Analysis such as that above has been used in the literature to describe the special case of harmonically varying concentrated loads at constant radial position with constant-speed tangential motion (Mote, 1970; Honda, et al., 1985; Weisensel, 1988; Weisensel and Schlack, 1988, 1989, 1990). Such a load can be described as

$$\bar{p}(\bar{r},\bar{\theta},\bar{t}) = \bar{P}_0\cos\bar{\omega}\bar{t}\,\frac{\delta(\bar{r}-\bar{r}_0)\delta(\bar{\theta}-\dot{\bar{\phi}}\bar{t})}{2\pi\bar{r}} \tag{21}$$

where

$$\bar{P}_0 = P_0/(D/a), \quad \bar{\omega} = \omega/(\bar{t}/t), \quad \bar{r}_0 = r_0/a, \quad \dot{\bar{\phi}} = \dot{\phi}/(\bar{t}/t). \tag{22}$$

It is assumed that the angular position of the load at time $\bar{t} = 0$ is $\bar{\theta} = 0$ for convenience.

As an extension of the case of constant radial position,

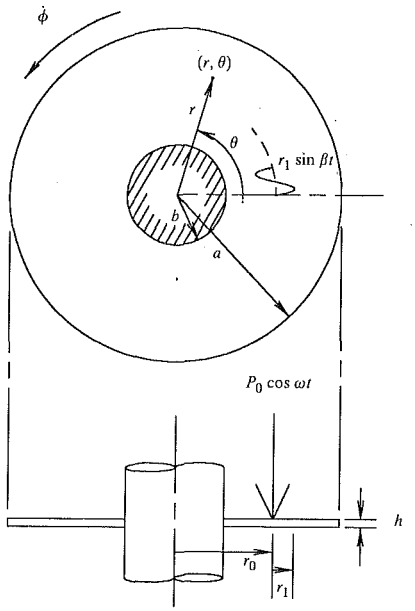

Fig. 2 Rotating thin annular plate with clamped inner boundary and free outer boundary subjected to harmonic concentrated transverse load with harmonic radial motion oscillation

another special case of interest and of much practical importance involves harmonic oscillatory motion of the radial position of the load as shown in Fig. 2. As mentioned previously, essentially no research has been published addressing the problem of circular or annular plate dynamics with radial load motion. The component of the load motion for harmonic oscillation in the radial direction with frequency β can be described as

$$\bar{r}(\bar{t}) = \bar{r}_0 + \bar{r}_1 \sin \bar{\beta}\bar{t} \tag{23}$$

where

$$\bar{r}_1 = r_1/a, \quad \bar{\beta} = \beta/(\bar{t}/t). \tag{24}$$

If the load amplitude function is harmonic as given in (21), the deflection response for this special case will be given in integral form by (20) as

$$\begin{aligned}
\bar{w}(\bar{r},\bar{\theta},\bar{t}) = \sum_{m=1}^{\infty}\sum_{n=0}^{\infty} R_{mn}(\bar{r}) e^{-\bar{\zeta}\bar{\Omega}_{mn}\bar{t}} \\
\times \Bigg\{ \Bigg\{ a_{mn} e^{i\sqrt{1-\bar{\zeta}^2}\bar{\Omega}_{mn}\bar{t}} + b_{mn} e^{-i\sqrt{1-\bar{\zeta}^2}\bar{\Omega}_{mn}\bar{t}} \\
+ \frac{2}{Q_{mn}\sqrt{1-\bar{\zeta}^2}\bar{\Omega}_{mn}} \int_0^{\bar{t}} \frac{\bar{P}_0 \cos \bar{\omega}\bar{\tau}}{2\pi} \cos 2\pi n \dot{\bar{\phi}} \bar{\tau} R_{mn}(\bar{r}_0 \\
+ \bar{r}_1 \sin \bar{\beta}\bar{\tau}) e^{\bar{\zeta}\bar{\Omega}_{mn}\bar{\tau}} \sin \sqrt{1-\bar{\zeta}^2}\bar{\Omega}_{mn}(\bar{t}-\bar{\tau}) d\bar{\tau} \Bigg\} \cos 2\pi n\bar{\theta} \\
+ \Bigg\{ c_{mn} e^{i\sqrt{1-\bar{\zeta}^2}\bar{\Omega}_{mn}\bar{t}} + d_{mn} e^{-i\sqrt{1-\bar{\zeta}^2}\bar{\Omega}_{mn}\bar{t}} \\
+ \frac{2}{Q_{mn}\sqrt{1-\bar{\zeta}^2}\bar{\Omega}_{mn}} \int_0^{\bar{t}} \frac{\bar{P}_0 \cos \bar{\omega}\bar{\tau}}{2\pi} \sin 2\pi n \dot{\bar{\phi}} \bar{\tau} R_{mn}(\bar{r}_0 \\
+ \bar{r}_1 \sin \bar{\beta}\bar{\tau}) e^{\bar{\zeta}\bar{\Omega}_{mn}\bar{\tau}} \sin \sqrt{1-\bar{\zeta}^2}\bar{\Omega}_{mn}(\bar{t}-\bar{\tau}) d\bar{\tau} \Bigg\} \sin 2\pi n\bar{\theta} \Bigg\}.
\end{aligned} \tag{25}$$

Note that $R_{mn}(\bar{r})$ is now an implicit function of time. Thus, it must remain inside the convolution integral.

It is readily apparent that to determine the explicit analytical solution for this special case, some extremely difficult integrals must be evaluated. The general approach used here is to expand the Bessel functions, trigonometric functions, logarithmic functions, and polynomial functions present in these integrands in appropriate finite and infinite series (Abramowitz, 1965; Spiegel, 1968). The deflection expression for the forced response of an annular plate to a harmonically varying concentrated transverse load with constant-speed tangential motion and harmonic radial motion can be written in the form

$$\begin{aligned}
\bar{w}(\bar{r},\bar{\theta},\bar{t}) = \sum_{m=1}^{\infty}\sum_{n=0}^{\infty} [J_n(\alpha_{mn}\bar{r}) + \eta_{2,mn} Y_n(\alpha_{mn}\bar{r}) \\
+ \eta_{3,mn} I_n(\alpha_{mn}\bar{r}) + \eta_{4,mn} K_n(\alpha_{mn}\bar{r})] \\
\times e^{-\bar{\zeta}\bar{\Omega}_{mn}\bar{t}} \Bigg[\Bigg[a_{mn} e^{if_1\bar{t}} + b_{mn} e^{-if_1\bar{t}} \\
+ \frac{\bar{P}_0}{\pi Q_{mn}\sqrt{1-\bar{\zeta}^2}\bar{\Omega}_{mn}} \Xi_1 \Bigg] \cos 2\pi n\bar{\theta} \\
+ \Bigg[c_{mn} e^{if_1\bar{t}} + d_{mn} e^{-if_1\bar{t}} + \frac{\bar{P}_0}{\pi Q_{mn}\sqrt{1-\bar{\zeta}^2}\bar{\Omega}_{mn}} \Xi_2 \Bigg] \sin 2\pi n\bar{\theta} \Bigg].
\end{aligned} \tag{27}$$

The definite integral functions Ξ_1 and Ξ_2 are evaluated in Weisensel (1988) for the general case of transient vibrations.

However, to understand the fundamental nature of the system response, it is sufficient to consider here only the steady-state response of this system. The steady-state deflection response is readily obtained from the general solution given in (27) by neglecting all the transient terms. The steady-state solution is also given explicitly in Weisensel (1988). These equations are the first known analytical solutions for the deflection of a circular or annular plate due to a transverse load with a nonconstant radial motion function. As such, this work represents a significant extension of the knowledge of plate dynamics as a result of moving loads.

Concentrated Load With General Periodic Radial Motion

The special cases of the forced dynamic response of a rotating thin annular plate to a moving concentrated load have been presented in the literature for constant radial position and herein for harmonically varying radial motion. These results can be extended beyond these cases to demonstrate the analysis for a load with general periodic radial motion by using Fourier decomposition to determine the individual harmonic components of the general periodic load radial motion.

Thus, the radial motion of the load used in (18) and defined in (22)–(24) can be viewed as simply the initial components of the infinite Fourier series expansion of the general periodic radial motion function,

$$\begin{aligned}
\bar{r}(\bar{t}) = \bar{r}_0 + \bar{r}_{1c} \cos \bar{\beta}\bar{t} + \bar{r}_{1s} \sin \bar{\beta}\bar{t} + \bar{r}_{2c} \cos 2\bar{\beta}\bar{t} + \bar{r}_{2s} \sin 2\bar{\beta}\bar{t} \\
+ \cdots = \bar{r}_0 + \sum_{k=1}^{\infty} \bar{r}_{kc} \cos k\bar{\beta}\bar{t} + \sum_{k=1}^{\infty} \bar{r}_{ks} \sin k\bar{\beta}\bar{t}.
\end{aligned} \tag{28}$$

The radial motion function given by (23) can be obtained from (28) by setting $\bar{r}_{1s} = \bar{r}_1$, $\bar{r}_{kc} = 0$ ($k = 1, 2, 3, \ldots$), $\bar{r}_{ks} = 0$ ($k = 2, 3, 4, \ldots$).

Thus, the general approach to determine the response to a load with general periodic radial motion begins with substituting (28) into (20). The critical step in this approach is to

evaluate integrals similar in form to those in (25), but with the argument of the characteristic function in the radial coordinate $R_{mn}(\bar{r})$ being the entire series given in (28),

$$\int_0^{\bar{t}} \cos \bar{\omega}\bar{\tau} \cos 2\pi n\dot{\bar{\phi}}\bar{\tau} R_{mn}\left[\bar{r}_0+\sum_{k=1}^{\infty}\bar{r}_{kc}\cos k\bar{\beta}\bar{\tau}+\sum_{k=1}^{\infty}\bar{r}_{ks}\sin k\bar{\beta}\bar{\tau}\right] e^{\bar{\xi}\bar{\Omega}_{mn}\bar{\tau}} \sin\sqrt{1-\bar{\xi}^2}\,\bar{\Omega}_{mn}(\bar{t}-\bar{\tau})\,d\bar{\tau}$$

$$= \int_0^{\bar{t}} e^{\bar{\xi}\bar{\Omega}_{mn}\bar{\tau}} \cos \bar{\omega}\bar{\tau} \cos 2\pi n\dot{\bar{\phi}}\bar{\tau} \sin\sqrt{1-\bar{\xi}^2}\,\bar{\Omega}_{mn}(\bar{t}-\bar{\tau})$$

$$\times\left[J_n\left[\alpha_{mn}\left[\bar{r}_0+\sum_{k=1}^{\infty}\bar{r}_{kc}\cos k\bar{\beta}\bar{\tau}+\sum_{k=1}^{\infty}\bar{r}_{ks}\sin k\bar{\beta}\bar{\tau}\right]\right]\right.$$

$$+\eta_{2,mn}Y_n\left[\alpha_{mn}\left[\bar{r}_0+\sum_{k=1}^{\infty}\bar{r}_{kc}\cos k\bar{\beta}\bar{\tau}+\sum_{k=1}^{\infty}\bar{r}_{ks}\sin k\bar{\beta}\bar{\tau}\right]\right]$$

$$+\eta_{3,mn}I_n\left[\alpha_{mn}\left[\bar{r}_0+\sum_{k=1}^{\infty}\bar{r}_{kc}\cos k\bar{\beta}\bar{\tau}+\sum_{k=1}^{\infty}\bar{r}_{ks}\sin k\bar{\beta}\bar{\tau}\right]\right]$$

$$\left.+\eta_{4,mn}K_n\left[\alpha_{mn}\left[\bar{r}_0+\sum_{k=1}^{\infty}\bar{r}_{kc}\cos k\bar{\beta}\bar{\tau}+\sum_{k=1}^{\infty}\bar{r}_{ks}\sin k\bar{\beta}\bar{\tau}\right]\right]\right]d\bar{\tau} \quad (29)$$

$$\int_0^{\bar{t}} \cos \bar{\omega}\bar{\tau} \sin 2\pi n\dot{\bar{\phi}}\bar{\tau} R_{mn}\left[\bar{r}_0+\sum_{k=1}^{\infty}\bar{r}_{kc}\cos k\bar{\beta}\bar{\tau}+\sum_{k=1}^{\infty}\bar{r}_{ks}\sin k\bar{\beta}\bar{\tau}\right] e^{\bar{\xi}\bar{\Omega}_{mn}\bar{\tau}} \sin\sqrt{1-\bar{\xi}^2}\,\bar{\Omega}_{mn}(\bar{t}-\bar{\tau})\,d\bar{\tau}$$

$$= \int_0^{\bar{t}} e^{\bar{\xi}\bar{\Omega}_{mn}\bar{\tau}} \cos \bar{\omega}\bar{\tau} \sin 2\pi n\dot{\bar{\phi}}\bar{\tau} \sin\sqrt{1-\bar{\xi}^2}\,\bar{\Omega}_{mn}(\bar{t}-\bar{\tau})$$

$$\times\left[J_n\left[\alpha_{mn}\left[\bar{r}_0+\sum_{k=1}^{\infty}\bar{r}_{kc}\cos k\bar{\beta}\bar{\tau}+\sum_{k=1}^{\infty}\bar{r}_{ks}\sin k\bar{\beta}\bar{\tau}\right]\right]\right.$$

$$+\eta_{2,mn}Y_n\left[\alpha_{mn}\left[\bar{r}_0+\sum_{k=1}^{\infty}\bar{r}_{kc}\cos k\bar{\beta}\bar{\tau}+\sum_{k=1}^{\infty}\bar{r}_{ks}\sin k\bar{\beta}\bar{\tau}\right]\right]$$

$$+\eta_{3,mn}I_n\left[\alpha_{mn}\left[\bar{r}_0+\sum_{k=1}^{\infty}\bar{r}_{kc}\cos k\bar{\beta}\bar{\tau}+\sum_{k=1}^{\infty}\bar{r}_{ks}\sin k\bar{\beta}\bar{\tau}\right]\right]$$

$$\left.+\eta_{4,mn}K_n\left[\alpha_{mn}\left[\bar{r}_0+\sum_{k=1}^{\infty}\bar{r}_{kc}\cos k\bar{\beta}\bar{\tau}+\sum_{k=1}^{\infty}\bar{r}_{ks}\sin k\bar{\beta}\bar{\tau}\right]\right]\right]d\bar{\tau}. \quad (30)$$

Admittedly, these integrals appear formidable. However, by carefully and consistently using the series representations of the Bessel functions and other functions, these integrals can be evaluated in terms of multiple infinite series. Then the corresponding analytical deflection expressions can be derived. This approach has special application to treating problems where the load radial motion function is analytically complicated or is the result of experimental measurements. In such cases, the load radial motion function may be adequately represented by just a few terms of its series expansion.

General Periodically Varying Load

The special case of the forced dynamic response of a rotating thin annular plate to a moving concentrated transverse load of harmonically varying amplitude (in time) has been discussed herein. This result can be extended beyond these cases to demonstrate the analysis for a load of general periodic amplitude variation by using Fourier decomposition to determine the individual harmonic components of the general periodically varying load amplitude. The responses to each of these components can then be superposed to obtain the response to a general periodic amplitude load. This approach has special application to correlating experimental measurements and analytical results.

Thus, the temporal harmonic amplitude variation of the load used in (18) and defined in (21) can be viewed as simply one component of the infinite Fourier series expansion of the general periodic amplitude variation,

$$\bar{P}(\bar{t}) = \bar{P}_0 + \bar{P}_{1c}\cos\bar{\omega}\bar{t} + \bar{P}_{1s}\sin\bar{\omega}\bar{t} + \bar{P}_{2c}\cos 2\bar{\omega}\bar{t} + \bar{P}_{2s}\sin 2\bar{\omega}\bar{t}$$

$$+ \cdots = \bar{P}_0 + \sum_{k=1}^{\infty}\bar{P}_{kc}\cos k\bar{\omega}\bar{t} + \sum_{k=1}^{\infty}\bar{P}_{ks}\sin k\bar{\omega}\bar{t}. \quad (31)$$

Each component amplitude $\bar{P}_{kc}$ or $\bar{P}_{ks}$ of a general load amplitude variation function may be determined in any of several ways. These include direct application of Fourier analysis for analytical functions, spectral analysis for empirical functions, or simply assuming that a load is comprised of only specific components. Once the component amplitudes are determined, they can be used to define component loading functions of the form

$$\begin{aligned}
\bar{p}_0(\bar{r},\bar{\theta},\bar{t}) &= \bar{P}_0\Pi(\bar{r},\bar{\theta})\\
\bar{p}_{1c}(\bar{r},\bar{\theta},\bar{t}) &= \bar{P}_{1c}\cos\bar{\omega}\bar{t}\,\Pi(\bar{r},\bar{\theta})\\
\bar{p}_{1s}(\bar{r},\bar{\theta},\bar{t}) &= \bar{P}_{1s}\sin\bar{\omega}\bar{t}\,\Pi(\bar{r},\bar{\theta})\\
\bar{p}_{2c}(\bar{r},\bar{\theta},\bar{t}) &= \bar{P}_{2c}\cos 2\bar{\omega}\bar{t}\,\Pi(\bar{r},\bar{\theta})\\
\bar{p}_{2s}(\bar{r},\bar{\theta},\bar{t}) &= \bar{P}_{2s}\sin 2\bar{\omega}\bar{t}\,\Pi(\bar{r},\bar{\theta})\\
&\vdots
\end{aligned} \quad (32)$$

where $\Pi(\bar{r},\bar{\theta})$ describes the spatial distribution of the loading function. The total periodic loading function can now be described as

$$\bar{p}(\bar{r},\bar{\theta},\bar{t}) = \bar{p}_0(\bar{r},\bar{\theta},\bar{t}) + \sum_{k=1}^{\infty}\bar{p}_{kc}(\bar{r},\bar{\theta},\bar{t}) + \sum_{k=1}^{\infty}\bar{p}_{ks}(\bar{r},\bar{\theta},\bar{t})$$

$$= \bar{P}_0\Pi(\bar{r},\bar{\theta}) + \sum_{k=1}^{\infty}\bar{P}_{kc}\cos k\bar{\omega}\bar{t}\,\Pi(\bar{r},\bar{\theta}) + \sum_{k=1}^{\infty}\bar{P}_{ks}\sin k\bar{\omega}\bar{t}\,\Pi(\bar{r},\bar{\theta})$$

$$= \left[\bar{P}_0 + \sum_{k=1}^{\infty}\bar{P}_{kc}\cos k\bar{\omega}\bar{t} + \sum_{k=1}^{\infty}\bar{P}_{ks}\sin k\bar{\omega}\bar{t}\right]\Pi(\bar{r},\bar{\theta})$$

$$= \bar{P}(\bar{t})\Pi(\bar{r},\bar{\theta}). \quad (33)$$

Each component loading function can be used as the nonhomogeneous term of a separate partial differential equation of motion of the form given in (1). Solving the equation of motion for each component loading function results in a set of general solutions of the form given in (7). These solutions can be denoted in a corresponding manner as $\bar{w}_0(\bar{r},\bar{\theta},\bar{t})$, $\bar{w}_{1c}(\bar{r},\bar{\theta},\bar{t})$, $\bar{w}_{1s}(\bar{r},\bar{\theta},\bar{t})$, $\bar{w}_{2c}(\bar{r},\bar{\theta},\bar{t})$, $\bar{w}_{2s}(\bar{r},\bar{\theta},\bar{t})$, ... Since the partial differential equation of motion and the boundary conditions are linear, the total deflection response to the total load given by (33) in just the superposition of the component deflection responses, i.e.,

Table 1 Eigenvalues and undamped natural frequencies of a thin annular plate with geometric and material parameters $\bar{b} = 0.5$, $\nu = 0.3$

m	n	$\bar{\Omega}_{mn}$	f_{mn} (Hz)
1	0	13.02426	362.16054
	1	13.28978	369.54389
	2	14.70381	408.86331
	3	18.56199	516.14615
	4	25.59582	711.73313
	5	35.73009	993.53304
2	0	85.03283	2364.47537
	1	86.70583	2410.99601
	2	91.73815	2550.92791
	3	100.16746	2785.31826
	4	112.04960	3115.72066
	5	127.44669	3543.86150
3	0	243.69404	6776.30723
	1	245.43582	6824.74022
	2	250.68249	6970.63238
	3	259.49153	7215.58200
	4	271.94106	7561.76145
	5	288.11390	8011.47341

$$\bar{w}(\bar{r},\bar{\theta},\bar{t}) = \bar{w}_0(\bar{r},\bar{\theta},\bar{t}) + \bar{w}_{1c}(\bar{r},\bar{\theta},\bar{t}) + \bar{w}_{1s}(\bar{r},\bar{\theta},\bar{t}) + \bar{w}_{2c}(\bar{r},\bar{\theta},\bar{t}) + \bar{w}_{2s}(\bar{r},\bar{\theta},\bar{t}) + \cdots = \bar{w}_0(\bar{r},\bar{\theta},\bar{t}) + \sum_{k=1}^{\infty} \bar{w}_{kc}(\bar{r},\bar{\theta},\bar{t}) + \sum_{k=1}^{\infty} \bar{w}_{ks}(\bar{r},\bar{\theta},\bar{t}). \quad (34)$$

Resonance Conditions and Critical Frequencies

The conditions for system dynamic deflection resonance occur when specific relationships exist between the system load parameters and the system natural frequencies. The lowest natural frequencies for the system studied are given in Table 1. For any particular special case of interest, the resonance conditions can be obtained by considering the expression for the motion as given by (27).

The resonance conditions are most clearly exhibited when damping is neglected. Thus, for a conservative system, the resonance conditions occur whenever any of the denominators in the steady-state deflection expression vanish. For example, for constant radial position, the resonance conditions can be stated as

$$\dot{\bar{\phi}}_{1,mn} = -\dot{\bar{\phi}}_{3,mn} = \frac{-\bar{\Omega}_{mn} + \bar{\omega}}{2\pi n}$$

$$\dot{\bar{\phi}}_{2,mn} = -\dot{\bar{\phi}}_{4,mn} = \frac{\bar{\Omega}_{mn} + \bar{\omega}}{2\pi n} \quad (35)$$

where $\dot{\bar{\phi}} = \dot{\phi}/(\bar{t}/t)$, $\bar{\Omega} = \Omega/(\bar{t}/t)$, $\bar{\omega} = \omega/(\bar{t}/t)$. Negative values of $\dot{\bar{\phi}}$ simply indicate plate rotation in the opposite direction. Also note that (35) is valid for $m = 1, 2, 3, \ldots$; $n = 1, 2, 3, \ldots$. Thus, there are no critical rotational speeds for the degenerate forms of the original resonance conditions when $n = 0$, corresponding to the axisymmetric component of the deflection response (Honda et al., 1985).

In addition to the resonance conditions given in (35), those for a load moving harmonically in the radial direction can be identified as

$$\dot{\bar{\phi}}_{1,mnq} = -\dot{\bar{\phi}}_{6,mnq} = \frac{-\bar{\Omega}_{mn} + \bar{\omega} - q\bar{\beta}}{2\pi n}$$

$$\dot{\bar{\phi}}_{2,mnq} = -\dot{\bar{\phi}}_{5,mnq} = \frac{-\bar{\Omega}_{mn} + \bar{\omega} + q\bar{\beta}}{2\pi n}$$

$$\dot{\bar{\phi}}_{3,mnq} = -\dot{\bar{\phi}}_{7,mnq} = \frac{\bar{\Omega}_{mn} + \bar{\omega} + q\bar{\beta}}{2\pi n}$$

$$\dot{\bar{\phi}}_{4,mnq} = -\dot{\bar{\phi}}_{8,mnq} = \frac{-\bar{\Omega}_{mn} + \bar{\omega} - q\bar{\beta}}{2\pi n} \quad (36)$$

where $\bar{\beta} = \beta/(\bar{t}/t)$.

Equations (36) define the critical rotational speeds of the plate, i.e., those rotational speeds that cause a resonance condition to be satisfied for the undamped annular plate system, for a specific load amplitude oscillation frequency $\bar{\omega}$ and a specific load radial motion oscillation frequency $\bar{\beta}$.

In the degenerate case of loads at constant radial position, i.e., $\bar{\beta} = 0$, (36) reduces to the resonance conditions given by (35). In the degenerate case of constant amplitude loads, i.e., $\bar{\omega} = 0$, (36) reduces to

$$\dot{\bar{\phi}}_{1,mnq} = -\dot{\bar{\phi}}_{3,mnq} = \frac{-\bar{\Omega}_{mn} - q\bar{\beta}}{2\pi n}$$

$$\dot{\bar{\phi}}_{2,mnq} = -\dot{\bar{\phi}}_{4,mnq} = \frac{-\bar{\Omega}_{mn} + q\bar{\beta}}{2\pi n}. \quad (37)$$

In the further degenerate case of constant amplitude loads at constant radial position, i.e., $\bar{\omega} = 0$ and $\bar{\beta} = 0$, (36) reduces to the widely known resonance conditions given by

$$\dot{\bar{\phi}}_{1,mnq} = \dot{\bar{\phi}}_{2,mnq} = \dot{\bar{\phi}}_{7,mnq} = \dot{\bar{\phi}}_{8,mnq} = \frac{-\bar{\Omega}_{mn}}{2\pi n}$$

$$\dot{\bar{\phi}}_{3,mnq} = \dot{\bar{\phi}}_{4,mnq} = \dot{\bar{\phi}}_{5,mnq} = \dot{\bar{\phi}}_{6,mnq} = \frac{\bar{\Omega}_{mn}}{2\pi n}. \quad (38)$$

In a similar manner, the original resonance conditions can be solved for the radial motion oscillation frequency as a function of the plate rotational speed and the load amplitude oscillation frequency,

$$\bar{\beta}_{2,mnq} = -\bar{\beta}_{1,mnq} = \frac{\bar{\Omega}_{mn} + 2\pi n\dot{\bar{\phi}} - \bar{\omega}}{q}$$

$$\bar{\beta}_{4,mnq} = -\bar{\beta}_{3,mnq} = \frac{\bar{\Omega}_{mn} - 2\pi n\dot{\bar{\phi}} + \bar{\omega}}{q}$$

$$\bar{\beta}_{5,mnq} = -\bar{\beta}_{6,mnq} = \frac{\bar{\Omega}_{mn} - 2\pi n\dot{\bar{\phi}} - \bar{\omega}}{q}$$

$$\bar{\beta}_{8,mnq} = -\bar{\beta}_{7,mnq} = \frac{\bar{\Omega}_{mn} + 2\pi n\dot{\bar{\phi}} + \bar{\omega}}{q}. \quad (39)$$

Equations (39) define the critical load radial motion oscillation frequencies, i.e., those frequencies of the load radial motion oscillation that cause a resonance condition to be satisfied for the undamped annular plate system for a specific load amplitude oscillation frequency $\bar{\omega}$ and a specific plate rotational speed $\dot{\bar{\phi}}$. It is important to note from (39) that

$$\bar{\beta}_{k,mnq} = \frac{\bar{\beta}_{k,mn1}}{q}. \quad (40)$$

However, note further that a relationship similar to (40) between $\dot{\bar{\phi}}$ and n cannot be derived from (35) because n is also an index of the natural frequencies $\bar{\Omega}_{mn}$, whereas q is not.

In the degenerate case of constant amplitude loads, i.e., $\bar{\omega} = 0$, (39) reduces to

$$\bar{\beta}_{2,mnq} = \bar{\beta}_{8,mnq} = \frac{\bar{\Omega}_{mn} + 2\pi n\dot{\bar{\phi}}}{q}$$

$$\bar{\beta}_{4,mnq} = \bar{\beta}_{5,mnq} = \frac{\bar{\Omega}_{mn} - 2\pi n\dot{\bar{\phi}}}{q}. \quad (41)$$

Table 2 Definition of parameter values and resulting maximum deflection magnitude values for particular sets of input system parameters that correspond to specific near-resonance conditions

Parameter Set No.	m	n	q	$\dot{\phi}$ (rad/s)	ω (rad/s)	β (rad/s)	r_1 (mm)	$\bar{\zeta}$	$\lvert\bar{w}\rvert$
1	1	1	--	370	0	0	0	0	0.72735
2								0.02	0.04625
3								0.05	0.02138
4	1	1	1	385	0	100	25	0	1.19204
5								0.02	0.02119
6								0.05	0.02918
7	1	1	1	401	0	200	25	0	1.44155
8								0.02	0.04253
9								0.05	0.01446
10	1	1	--	688	2000	0	0	0	1.14870
11								0.02	0.04383
12								0.05	0.02891
13	1	5	1	266	2000	100	25	0	0.05005
14								0.02	0.05120
15								0.05	0.03698
16	1	1	2	720	2000	200	25	0	0.90178
17								0.02	0.03696
18								0.05	0.01221

In the degenerate case of loads with no tangential (rotational) motion, i.e., $\dot{\bar{\phi}} = 0$, (39) reduces to

$$\bar{\beta}_{2,mnq} = \bar{\beta}_{5,mnq} = \frac{\bar{\Omega}_{mn} - \bar{\omega}}{q}$$

$$\bar{\beta}_{4,mnq} = \bar{\beta}_{8,mnq} = \frac{\bar{\Omega}_{mn} + \bar{\omega}}{q}. \tag{42}$$

In the further degenerate case of constant amplitude loads with no tangential (rotational) motion, i.e., $\bar{\omega} = 0$ and $\dot{\bar{\phi}} = 0$, (39) reduces to

$$\bar{\beta}_{1,mnq} = \bar{\beta}_{3,mnq} = \bar{\beta}_{6,mnq} = \bar{\beta}_{7,mnq} = \frac{-\bar{\Omega}_{mn}}{q}$$

$$\bar{\beta}_{2,mnq} = \bar{\beta}_{4,mnq} = \bar{\beta}_{5,mnq} = \bar{\beta}_{8,mnq} = \frac{\bar{\Omega}_{mn}}{q}. \tag{43}$$

Note from (41) and (43) that even constant amplitude loads can excite resonances of annular plates with radially oscillating loads. This is possible whether or not the plate is rotating. For design purposes, this type of loading must be thoroughly analyzed to ensure resonance is not a problem.

It should again be noted that if any of the above resonance conditions is satisfied, the expression for the dynamic deflection of the conservative system as given by the conservative degenerate form of (27) is indeterminate. The deflection expression at resonance can be determined from particular forms of (27) by using appropriate limiting procedures. However, for nonconservative systems ($\bar{\zeta} \neq 0$), the deflection expression given in (27) is valid and the deflection remains bounded for all parameter values.

This type of critical frequency information is very valuable and useful in the design of annular plate systems with the types of loading described.

Dynamic Deflections and Mode Shapes

The dynamic transverse deflection at any location on the surface of the plate and at any time can be computed using (27). The significance of the contribution of each individual mode to the total dynamic deflection decreases quite rapidly, especially for damped nonresonant conditions. Thus, based on the higher-frequency modes having negligible contributions in these cases, six modes were included in the dynamic deflection computation ($m = 1$, $n = 0, 1, 2, 3, 4, 5$). Precedent exists in the literature for using a small number of modes to approximate the total dynamic deflection. One common criterion is to only include modes that contribute more than one percent of the total deflection (Ramakrishnan and Kunukkasseril, 1974). Another is simply to include only the single mode that corresponds to the lowest values of the modal indices (Raske, 1966, 1983; Raske and Schlack, 1967; Laura et al., 1976).

For each set of input system parameters studied, several important quantities of interest were computed. These quantities were computed for each of the six modes included in the dynamic deflection. First, the mode shape was computed and the deflection values were analyzed to determine the maximum deflection magnitude (absolute value) for each mode shape. The mode shapes are used to gain insight into the nature of the dynamic response of the plate to a particular set of input system parameters. The deflection values for each of the six modes were summed to obtain the total dynamic deflection. The maximum total deflection magnitude values are used to compare different sets of input system parameters.

To demonstrate the nature and utility of the analytical results and the expressions for critical system frequency parameters, 18 particular sets of input system parameters are studied. These sets correspond to six near-resonance cases of the dynamic deflection at three levels of damping. The definition of these sets of input system parameters is given in Table 2, along with the resulting maximum deflection magnitude values. The influence of the system parameters on the dynamic deflections is readily apparent from this table.

As an example, when $m = 1$, $n = 1$, the resonance condition for the critical rotational speed $\dot{\bar{\phi}}_{2,mn}$ in (35) is satisfied for the degenerate case of a constant amplitude load ($\bar{\omega} = 0$) at constant radial position ($\bar{\beta} = 0$) when $\dot{\bar{\phi}}_{2,mn} = \dot{\bar{\phi}}_{2,11} = 2.12$ ($\dot{\phi}_{2,mn} = \dot{\phi}_{2,11} = 369.54$ rad/s $\cong$ 370 rad/s). These values correspond to parameter sets number 1, 2, and 3 in Table 2 for damping parameter values $\bar{\zeta} = 0$, 0.02, and 0.05, respectively (the values of $\bar{\zeta}$ are assumed to be approximately constant for each parameter set). The total dynamic deflection for parameter set 1 is $|\bar{w}| = 0.72735$. The prominent mode shapes, including the mode shape corresponding to the resonant condition, i.e., $m = 1$, $n = 1$, have maximum deflections of $|\bar{w}_{10}| = 0.00547$ and $|\bar{w}_{11}| = 0.65946$. The predominance of the selected mode for which the resonance condition was satisfied in the previous case is clearly evident. It must be noted that the maximum dynamic deflection magnitude for the undamped case near resonance admittedly exceeds the bounds of applicability of classical plate theory. Thus, the results for these undamped, near-resonance conditions must be viewed rather qualitatively.

Parameter sets number 13, 14, and 15 in Table 2 for damping

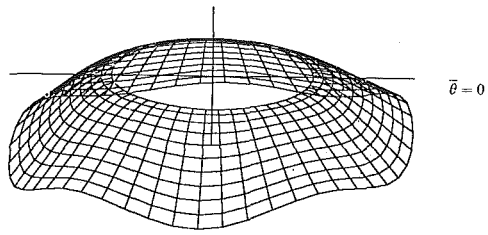

Fig. 3(*a*)

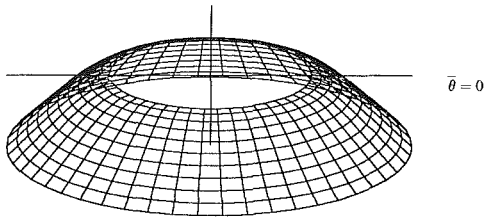

Fig. 3(*b*)

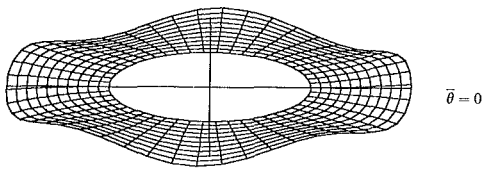

Fig. 3(*c*)

Fig. 3 Dynamic deflection of thin annular plate with clamped inner boundary and free outer boundary subjected to concentrated transverse load. Geometric, material, and loading parameters are: $b/a = 0.5$, $h/a = 0.01$, $\nu = 0.3$, $\sqrt{\rho h a^4/D} = 0.0057$ s, $\bar{\zeta} = 0$, $\bar{t} = 0$, $\bar{P}_0 = 0.011$, $\bar{r}_0 = 0.75$, $\bar{r}_1 = 0.25$, $\bar{\omega} = 11.45$, $\bar{\beta} = 0.57$, $\dot{\bar{\phi}} = 1.52$. (*a*) Total deflection. Maximum deflection $|\bar{w}| = 0.05005$. (*b*) Mode $m = 1$, $n = 0$. Maximum deflection $|\bar{w}_{10}| = 0.03724$. (*c*) Mode $m = 1$, $n = 5$. Maximum deflection $|\bar{w}_{15}| = 0.00533$.

parameter values $\bar{\zeta} = 0$, 0.02, and 0.05, respectively, correspond to the case of a load with amplitude oscillation frequency $\omega = 2000$ rad/s and load radial motion at an oscillation frequency $\beta = 100$ rad/s and a maximum oscillation amplitude $r_1 = 25$ mm. For $m = 1$, $n = 5$, $q = 1$, the resonance condition for the critical rotational speed $\dot{\phi}_{3,mnq}$ in (36) is satisfied for this degenerate case when $\dot{\bar{\phi}}_{3,mnq} = \dot{\bar{\phi}}_{3,151} = 152(\dot{\phi}_{3,mnq} = \dot{\phi}_{3,151} = 265.6$ rad/s $\cong 266$ rad/s). The total dynamic deflections for these parameter sets and the prominent mode shapes, including the mode shape corresponding to the resonant condition, i.e., $m = 1$, $n = 5$, are shown in Figs. 3(*a*)–(c). This particular set of input system parameters demonstrates that it is plausible that the higher modes may be excited to a significant degree, particularly when there is no damping. Notice from Figs. 3(*a*) and 3(*c*) that the influence of the $m = 1$, $n = 5$, mode is clearly evident in the total dynamic deflection. When damping is introduced, the influence of the resonant higher mode is no longer predominant. However, the magnitude of the $m = 1$, $n = 5$, mode is significantly greater than it is for the other resonance cases in which this higher mode is not specifically excited.

It must be noted at this point that the resonance conditions in (35) and (36) simply define relationships between the frequency parameters of the system, namely $\bar{\Omega}_{mn}$, $\bar{\omega}$, $\dot{\bar{\phi}}$, and $\bar{\beta}$. Thus, the perception of which parameter is responsible for a particular resonance condition being satisfied is, in general, not analytically meaningful. For example, the specific set of system frequency parameters defined as parameter set number 13 in Table 2 may be viewed as defining a critical rotational speed $\dot{\phi} = 266$ rad/s of a system that has a load amplitude oscillation frequency $\omega = 2000$ rad/s and a load radial motion oscillation frequency $\beta = 100$ rad/s. Alternatively, this set of system frequency parameters may be viewed as defining a critical load radial motion oscillation frequency $\beta = 100$ rad/s of a system that has a load amplitude oscillation frequency $\omega = 2000$ rad/s and a rotational speed $\dot{\phi} = 266$ rad/s. Which particular viewpoint is adopted in practice will depend upon the specific design and operating conditions of the system under consideration, along with any degenerate conditions. This understanding of the resonance conditions certainly applies to all the sets of input system parameters listed in Table 2.

Parameter Sensitivity

Special Cases of System Parameters. To investigate the sensitivity of plate dynamic deflections to the system parameters, especially the damping and loading parameters, 27 additional special cases of system parameters were examined. The definition of these nonresonance sets of input system parameters is given in Table 3, along with the resulting maximum deflection magnitude values. Again, the influence of the system parameters on the dynamic deflections is readily apparent from this table.

The dependent quantity for which system parameter sensitivities are desired is the maximum total deflection magnitude value $|\bar{w}|$. The selected system parameters for which the sensitivity of the maximum deflection magnitude value is studied include damping, load amplitude oscillation frequency, load radial motion oscillation frequency, and load radial motion oscillation amplitude. Whereas the sensitivity to rotational speed of the plate is not selected for further study, note from Table 3 that this parameter has been fixed at $\dot{\phi} = 300$ rad/s for these additional particular sets of the input system parameters.

Damping Sensitivity. To study the effect of system damping on the maximum total deflection magnitude value, three levels of this parameter were investigated, namely, $\bar{\zeta} = 0$, 0.02, and 0.05. The effect of damping was examined for both the near-resonance cases defined in Table 2 and the nonresonance cases defined in Table 3.

From Table 3, it can be seen that damping plays a significant role in determining the resulting maximum total deflection magnitude value for the nonresonance cases. Similarly, from Table 2, it can be seen that damping also plays a significant role in determining the resulting maximum total deflection magnitude value for the near-resonance cases. The average total deflection magnitude value for the nonresonance cases and the near-resonance cases for each value of the damping parameter is given in Table 4.

It is readily apparent from Table 4 that the average total deflection magnitude value decreases markedly as the damping parameter increases. As would be expected, this effect of damping is more pronounced for the near-resonance cases than for the nonresonance cases. This is because of the tendency of the deflection magnitude in the undamped near-resonance case to become unbounded, whereas in the nonresonance case the deflection magnitude is limited to a certain maximum steady-state value, even for an undamped system.

Another interesting influence of damping on the resulting deflection is the location of the maximum deflection magnitude value. Since damping (and also rotation) induces phase changes in the deflection expression, it is expected that the maximum deflection occurs in general at an angle away from the load location (Huang and Soedel, 1987a, 1987b). This effect can be clearly observed in the deflection shapes shown for the near-resonance parameter sets. For example, the location of the maximum deflection for the undamped case (parameter set 1) is at the load application point ($\bar{\theta} = 0$). This is quite significantly different from the location of the maximum deflection for the nonconservative case (parameter set 2, $\bar{\zeta} = 0.02$) which

Table 3 Definition of parameter values and resulting maximum deflection magnitude values for particular sets of input system parameters selected from a matrix of combinations of input system parameters

Parameter Set No.	$\dot{\phi}$ (rad/s)	ω (rad/s)	β (rad/s)	r_1 (mm)	$\bar{\zeta}$	$\lvert\bar{w}\rvert$
19	300	0	0	0	0	0.01120
20	300	0	100	10	0	0.01548
22			200			0.04251
24			300			0.11771
21	300	0	100	25	0	0.02606
23			200			0.05658
25			300			0.12075
26	300	200	0	0	0	0.01232
27	300	200	100	10	0	0.01864
29			200			0.02363
28	300	200	100	25	0	0.02619
30			200			0.05315
31	300	2000	0	0	0	0.02608
34	300	2000	100	10	0	0.03802
40			200			0.08713
37	300	2000	100	25	0	0.04927
43			200			0.10117
32	300	2000	0	0	0.02	0.02556
35	300	2000	100	10	0.02	0.03138
41			200			0.03329
38	300	2000	100	25	0.02	0.05079
44			200			0.02383
33	300	2000	0	0	0.05	0.02297
36	300	2000	100	10	0.05	0.02837
42			200			0.02630
39	300	2000	100	25	0.05	0.03762
45			200			0.01393

Table 4 Average total deflection magnitude value for cases of system input parameters for different values of the damping parameter

Case	$\bar{\zeta}$	N	$\lvert\bar{w}\rvert$	$\dfrac{\lvert\bar{w}\rvert}{\lvert\bar{w}\rvert_{\bar{\zeta}=0}}$
non-resonance	0	17	0.04858	1.0
	0.02	5	0.03297	0.68
	0.05	5	0.02584	0.53
near-resonance	0	6	0.91025	1.0
	0.02	6	0.04033	0.05
	0.05	6	0.02385	0.03

is rotated through a large angle away from the load application point. It has been shown previously that the shape of the resulting deflection profile of the plate is strongly dependent upon the speed of propagation of the load as well as the magnitude of the damping coefficient (Reismann, 1963). These damping sensitivity results confirm this prior finding.

Load Amplitude Oscillation Sensitivity. To study the effect of the amplitude oscillation frequency of the load on the maximum total deflection magnitude value, three levels of this parameter were investigated, namely, $\omega = 0$ rad/s, 200 rad/s, and 2000 rad/s. The effect of the load amplitude oscillation frequency was only examined for the nonresonance cases defined in Table 3. It is not particularly meaningful to examine the effect of the load amplitude oscillation frequency for the near-resonance cases since this parameter is not independent in these cases, but rather plays a role in defining the resonance.

The effect of the load amplitude oscillation frequency is relatively subtle in comparison with the other parameter sensitivities investigated. This is as expected over the ranges of nonresonance system configurations. Therefore, to look more closely at this parameter, the influence of the other parameters was eliminated by considering the effect of the load amplitude oscillation frequency for subsets of the results in which all other parameters were constant. These subsets can be easily examined if the entries in Table 3 are rearranged as in Table 5.

From Table 5, it can be seen that the load amplitude oscillation frequency has some effect on the maximum total deflection magnitude value for the nonresonance cases. For values of $\beta = 0$ rad/s and $\beta = 100$ rad/s, the influence of ω appears to be monotonic in that the maximum total deflection magnitude value increases as the load amplitude oscillation frequency increases. However, for values of $\beta = 200$ rad/s, the effect on the maximum total deflection magnitude value is not clear for low values of the load amplitude oscillation frequency. As the load amplitude oscillation frequency increases further, the relationship that exists for lower values of β seems to again emerge. More investigation is needed to explore the nature of this parameter interaction.

Table 5 Definition of parameter values and resulting maximum deflection magnitude values for nonresonance sets of input system parameters for different values of the load amplitude oscillation frequency

Parameter Set No.	$\dot{\phi}$ (rad/s)	ω (rad/s)	β (rad/s)	r_1 (mm)	$\bar{\zeta}$	$\lvert\bar{w}\rvert$
19	300	0	0	0	0	0.01120
26		200				0.01232
31		2000				0.02608
20	300	0	100	10	0	0.01548
27		200				0.01864
34		2000				0.03802
21	300	0	100	25	0	0.02606
28		200				0.02619
37		2000				0.04927
22	300	0	200	10	0	0.04251
29		200				0.02363
40		2000				0.08713
23	300	0	200	25	0	0.05658
30		200				0.05315
43		2000				0.10117

Table 6 Average total deflection magnitude value for nonresonance cases of system input parameters for different values of the load radial motion oscillation amplitude

r_1 (mm)	N	$\lvert\bar{w}\rvert$	$\dfrac{\lvert\bar{w}\rvert}{\lvert\bar{w}\rvert_{r_1=0}}$
0	5	0.01962	1.0
10	11	0.04424	2.25
25	11	0.05085	2.59

Load Radial Motion Oscillation Sensitivity. The sensitivity of the maximum total deflection magnitude value to the load radial motion oscillation is actually dependent upon two independent load parameters, namely, the load radial motion oscillation amplitude r_1 and the load radial motion oscillation frequency β. Each of these parameters will be examined separately as well as jointly.

In a coarse sense, the average total deflection magnitude value for the nonresonance cases for each value of the load radial motion oscillation amplitude can be examined in Table 6. This table indicates that the total deflection magnitude value is a strong function of the load radial motion oscillation amplitude, regardless of the value of the other parameters. This table further indicates that as the load radial motion oscillation amplitude increases, so does the resulting total deflection magnitude value of the plate.

Similarly, in a coarse sense, the average total deflection magnitude value for the nonresonance cases for each value of the load radial motion oscillation frequency can be examined in Table 7. This table indicates that the total deflection magnitude value is also a strong function of the load radial motion oscillation frequency, regardless of the value of the other parameters. This table further indicates that as the load radial motion oscillation frequency increases, so does the resulting total deflection magnitude value of the plate.

Table 7 Average total deflection magnitude value for nonresonance cases of system input parameters for different values of the load radial motion oscillation frequency

β (rad/s)	N	$\lvert\overline{w}\rvert$	$\dfrac{\lvert\overline{w}\rvert}{\lvert\overline{w}\rvert_{\beta=0}}$
0	5	0.01962	1.0
100	10	0.03218	1.64
200	10	0.04615	2.35
300	2	0.11923	6.07

Table 8 Definition of parameter values and resulting maximum deflection magnitude values for particular sets of input system parameters for different values of the load radial motion oscillation amplitude

Parameter Set No.	$\dot{\phi}$ (rad/s)	ω (rad/s)	β (rad/s)	r_1 (mm)	$\bar{\zeta}$	$\lvert\overline{w}\rvert$
19			0	0		0.01120
20			100	10		0.01548
21			100	25		0.02606
22	300	0	200	10	0	0.04251
23			200	25		0.05658
24			300	10		0.11771
25			300	25		0.12075
26			0	0		0.01232
27			100	10		0.01864
28	300	200	100	25	0	0.02619
29			200	10		0.02363
30			200	25		0.05315
31			0	0		0.02608
34			100	10		0.03802
37	300	2000	100	25	0	0.04927
40			200	10		0.08713
43			200	25		0.10117
32			0	0		0.02556
35			100	10		0.03138
38	300	2000	100	25	0.02	0.05079
41			200	10		0.03329
44			200	25		0.02383
33			0	0		0.02297
36			100	10		0.02837
39	300	2000	100	25	0.05	0.03762
42			200	10		0.02630
45			200	25		0.01393

A more subtle look at the joint effect or interaction of the load radial motion oscillation amplitude and the load radial motion oscillation frequency can be achieved by again eliminating the influence of the other parameters and considering the effect of these two parameters of interest for subsets of the results in which all other parameters were constant. These subsets can be more easily examined if the entries in Table 3 are rearranged as in Table 8 to highlight the effect of the load radial motion oscillation amplitude or as in Table 9 to highlight the effect of the load radial motion oscillation frequency.

From Tables 8 and 9, it appears that the influences of these two load radial motion parameters interact in such a way as to strengthen each other for most of the sets of input system parameters. This is particularly true when there is no damping. When damping is present, however, it appears that the interaction between these two load radial motion parameters is such that the maximum dynamic deflection magnitude value is reduced for cases where $\beta = 200$ rad/s. The fine details of this interaction would require more analysis using several sets of parameters at several more levels of each of these two parameters.

For further insight into the nature of the dynamic deflections resulting from the nonresonance sets of input system parameters, the total dynamic deflection shapes for each of the 27 sets are shown in Figs. 24–50, as well as others, of Weisensel (1988). By examining the entire plate deflected shape, the nature of the influence of the various system parameters is often much more clearly demonstrated.

Table 9 Definition of parameter values and resulting maximum deflection magnitude values for particular sets of input system parameters for different values of the load radial motion oscillation frequency

Parameter Set No.	$\dot{\phi}$ (rad/s)	ω (rad/s)	β (rad/s)	r_1 (mm)	$\bar{\zeta}$	$\lvert\overline{w}\rvert$
19			0	0		0.01120
20			100	10		0.01548
21			100	25		0.02606
22	300	0	200	10	0	0.04251
23			200	25		0.05658
24			300	10		0.11771
25			300	25		0.12075
26			0	0		0.01232
27			100	10		0.01864
28	300	200	100	25	0	0.02619
29			200	10		0.02363
30			200	25		0.05315
31					0	0.02608
32	300	2000	0	0	0.02	0.02556
33					0.05	0.02297
34					0	0.03802
35	300	2000	100	10	0.02	0.03138
36					0.05	0.02837
37					0	0.04927
38	300	2000	100	25	0.02	0.05079
39					0.05	0.03762
40					0	0.08713
41	300	2000	200	10	0.02	0.03329
42					0.05	0.02630
43					0	0.10117
44	300	2000	200	25	0.02	0.02383
45					0.05	0.01393

Summary

This work has practical use in any application that requires knowledge of the dynamic deflection (transient or steady state) due to loads with arbitrary circumferential and radial motion. The general analysis presented examines the vibration response of annular plates subject to arbitrary moving loads. The solution is developed using classical plate theory with damping included. The dynamic response of plates to general loads is first determined in the form of an integral solution. Then the solution for loads that move along the plate surface is determined as a special case of this general solution.

The general analysis is used to obtain the solution for the case of an arbitrary circumferentially and radially moving load. Previous literature in the area of circular and annular plate response to moving loads has dealt only with circularly orbiting loads, i.e., loads at constant radial position. This is one of the very few works addressing the problem of circular or annular plate dynamics with radial load motion. Thus, the current understanding of the response of circular and annular plates to moving transverse loads is extended to include a component of motion in the radial direction in addition to a component of motion in the tangential direction. In addition to the detailed special case, the methods of analysis to obtain the solutions for the more general cases of a concentrated load with arbitrary periodic radial motion and of an arbitrary periodically varying amplitude load are given.

The analytical results are used to demonstrate the nature and utility of the expression for the dynamic deflection. Resonance conditions are obtained from the deflection expression, and corresponding critical system parameter expressions are derived. The critical system parameter expressions indicate numerous critical system parameter values that satisfy the resonance conditions. Thus, this problem of moving loads, especially in the area of design, is much more complicated when radial load motion is present. This is one of the very few works addressing the problem of circular or annular plate dynamics with radial load motion.

Dynamic deflection shapes for numerous particular sets of input system parameters and maximum dynamic deflection magnitude values are presented. These results are used to compare various sets of system parameters. Parameter sensitivity of the maximum dynamic deflection magnitude value is also

examined for both near-resonance and nonresonance sets of input system parameters. The nature of the parameter sensitivities is discussed in detail. In particular, the importance of system damping is emphasized by the fact that physical systems with moving loads operate in the range of the critical parameter values without experiencing the large dynamic deflections indicated for the undamped sets of parameters.

References

Abramowitz, M., and Stegun, I. A., eds., 1965, *Handbook of Mathematical Functions*, Dover Publications, New York, pp. 355–494.

Barasch, S., and Chen, Y., 1972, "On the Vibration of a Rotating Disk," ASME JOURNAL OF APPLIED MECHANICS, Vol. 39, pp. 1143–1144.

Benson, R. C., and Bogy, D. B., 1978, "Deflection of a Very Flexible Spinning Disk Due to a Stationary Transverse Load," ASME JOURNAL OF APPLIED MECHANICS, Vol. 45, pp. 636–642.

Chladni, E. F. F., 1787, *Entdeckungen Uber die Theorie des Klanges*, Weidmann, Erben and Reich, Leipzig.

Chladni, E. F. F., 1802, *Die Akustik*, Breitkopf and Hartel, Leipzig.

D'Angelo, C., Alvarado, N. T., Wang, K. W., and Mote, C. D., 1985, "Current Research on Circular Saw and Band Saw Vibration and Stability," *Shock and Vibration Digest*, Vol. 17, pp. 11–23.

Euler, L., 1766, "De Motu Vibratorio Tympanorum," *Novi Commentarii Academiae Scientiarum Petropolitanae*, Vol. 10, pp. 243–260.

Eversman, W., and Dodson, R. O., 1969, "Free Vibration of a Centrally Clamped Spinning Circular Disk," *AIAA Journal*, Vol. 7, pp. 2010–2012.

Fryba, L., 1972, *Vibration of Solids and Structures Under Moving Loads*, Noordhoff International Publishing, Groningen, The Netherlands.

Honda, Y., Matsuhisa, H., and Sato, S., 1985, "Modal Response of a Disk to a Moving Concentrated Harmonic Force," *Journal of Sound and Vibration*, Vol. 102, pp. 457–472.

Huang, S. C., and Soedel, W., 1987, "Effects of Coriolis Acceleration on the Free and Forced In-Plane Vibrations of Rotating Rings on Elastic Foundation," *Journal of Sound and Vibration*, Vol. 115, pp. 253–274.

Huang, S. C., and Soedel, W., 1987, "Response of Rotating Rings to Harmonic and Periodic Loading and Comparison with the Inverted Problem," *Journal of Sound and Vibration*, Vol. 118, pp. 253–270.

Iwan, W. D., and Stahl, K. J., 1973, "The Response of an Elastic Disk with a Moving Mass System," ASME JOURNAL OF APPLIED MECHANICS, Vol. 40, pp. 445–451.

Kirchhoff, G. R., 1850, "Uber das Gleichgewicht und Bewegung einer Elastischen Scheibe," *Journal fur die Reine und Angenwandte Mathematik (Crelle)*, Vol. 40, pp. 51–88.

Kirchhoff, G. R., 1850, "Uber die Schwingungen einer Kreisformigen Elastischen Scheibe," *Annalen der Physik und Chemie (Poggendorf)*, Vol. 81, pp. 258–264.

Lamb, R., and Southwell, R. V., 1921, "The Vibrations of a Spinning Disk," *Proceedings of the Royal Society London*, Vol. A99, pp. 272–280.

Laura, P. A. A., Arias, A., and Luisoni, L. E., 1976, "Fundamental Frequency of Vibration of a Circular Plate Elastically Restrained Against Rotation and Carrying a Concentrated Mass," *Journal of Sound and Vibration*, Vol. 45, pp. 298–301.

Leissa, A. W., 1977, "Recent Research in Plate Vibrations: Classical Theory," *Shock and Vibration Digest*, Vol. 9, pp. 13–24.

Leissa, A. W., 1978, "Recent Research in Plate Vibrations, 1973–1976: Complicating Effects," *Shock and Vibration Digest*, Vol. 10, pp. 21–35.

Leissa, A. W., 1981, "Plate Vibration Research, 1976–1980: Classical Theory," *Shock and Vibration Digest*, Vol. 13, pp. 11–22.

Leissa, A. W., 1981, "Plate Vibration Research, 1976–1980: Complicating Effects," *Shock and Vibration Digest*, Vol. 13, pp. 19–36.

Leissa, A. W., 1987, "Recent Studies in Plate Vibrations: 1981–1985, Part I. Classical Theory," *Shock and Vibration Digest*, Vol. 19, pp. 11–18.

Leissa, A. W., 1987, "Recent Studies in Plate Vibrations: 1981–1985, Part II. Complicating Effects," *Shock and Vibration Digest*, Vol. 19, pp. 10–24.

McLeod, A. J., and Bishop, R. E. D., 1965, "The Forced Vibration of Circular Flat Plates," *Mechanical Engineering Science Monograph*, Vol. 1, pp. 1–33.

Moshaiov, A., and Eareckson, P. D., 1988, "Analysis of Axisymmetrically Loaded Annular Plates Using Green's Functions," *Computers and Structures*, Vol. 28, pp. 59–66.

Mote, C. D., 1970, "Stability of Circular Plates Subjected to Moving Loads," *Journal of The Franklin Institute*, Vol. 290, pp. 329–344.

Mote, C. D., 1977, "Moving-Load Stability of a Circular Plate on a Floating Central Collar," *Journal of the Acoustical Society of America*, Vol. 61, pp. 439–447.

Mote, C. D., and Szymani, R., 1978, "Circular Saw Vibration Research," *Shock and Vibration Digest*, Vol. 10, pp. 15–30.

Mote, C. D., Schajer, G. S., and Wu, W. Z., 1982, "Band Saw and Circular Saw Vibration and Stability," *Shock and Vibration Digest*, Vol. 14, pp. 19–25.

Ramakrishnan, R., and Kunukkasseril, V. X., 1974, "Asymmetric Response of Circular Plates," *Journal of Sound and Vibration*, Vol. 34, pp. 489–504.

Raske, T. F., 1966, "Dynamic Response of Elastic Bodies to Moving Point Loads," Ph.D.Thesis, University of Wisconsin, Madison, Wisconsin, pp. 1–93.

Raske, T. F., 1983, "Plate Response to a Circularly Orbiting Mass," *Journal of the Acoustical Society of America*, Vol. 73, pp. 688–691.

Raske, T. F., and Schlack, A. L., 1967, "Dynamic Response of Plates Due to Moving Loads," *Journal of the Acoustical Society of America*, Vol. 42, pp. 625–635.

Reismann, H., 1963, "Dynamic Response of an Elastic Plate Strip to a Moving Line Load," *AIAA Journal*, Vol. 1, pp. 354–360.

Southwell, R. V., 1922, "On the Free Transverse Vibrations of a Uniform Circular Disc Clamped at Its Centre: And on the Effects of Rotation," *Proceedings of the Royal Society London*, Vol. A101, pp. 133–153.

Spiegel, M. R., 1968, *Mathematical Handbook* (Schaum's Outline Series), McGraw-Hill, New York.

Vogel, S. M., and Skinner, D. W., 1965, "Natural Frequencies of Transversely Vibrating Uniform Annular Plates," ASME JOURNAL OF APPLIED MECHANICS, Vol. 32, pp. 926–931.

Waller, M. D., 1938, "Vibrations of Free Circular Plates. Part 1: Normal Modes," *Proceedings of the Physical Society of London*, Vol. 50, pp. 70–76.

Waller, M. D., 1938, "Vibrations of Free Circular Plates. Part 3: A Study of Chladni's Original Figures," *Proceedings of the Physical Society of London*, Vol. 50, pp. 83–86.

Waller, M. D., 1961, *Chladni Figures: A Study in Symmetry*, Bell, London, p. xviii.

Weisensel, G. N., 1988, "Response of Rotating Annular Plates to Arbitrary Radially Moving Loads," Ph.D. Thesis, University of Wisconsin, Madison, WI.

Weisensel, G. N., 1989, "Natural Frequency Information for Circular and Annular Plates," *Journal of Sound and Vibration*, Vol. 133, pp. 129–137.

Weisensel, G. N., and Schlack, A. L., 1988, "Forced Response of a Rotating Thin Annular Plate to a Moving Concentrated Transverse Load," *Proceedings of the 6th International Modal Analysis Conference*, Kissimmee, Florida, pp. 1643–1647.

Weisensel, G. N., and Schlack, A. L., 1989, "Forced Response of Rotating Thin Annular Plates to Moving Concentrated Transverse Loads with Sudden Changes in Radial Position," *Proceedings of the 7th International Modal Analysis Conference*, Las Vegas, Nevada, pp. 1199–1204.

Weisensel, G. N., and Schlack, A. L., 1990, "Annular Plate Response to Circumferentially Moving Loads with Sudden Radial Position Changes," *International Journal of Analytical and Experimental Modal Analysis*, Vol. 5, pp. 239–250.

Equations of Motion for Nonholonomic, Constrained Dynamical Systems via Gauss's Principle

R. E. Kalaba[1]
Professor of Economics,
Department of Eletrical Engineering
and Biomedical Engineering.

F. E. Udwadia[1]
Professor of Mechanical Engineering,
Civil Engineering and Decision Systems,
Mem. ASME.

University of Southern California,
Los Angeles, CA 90089-1453

In this paper we develop an analytical set of equations to describe the motion of discrete dynamical systems subjected to holonomic and/or nonholonomic Pfaffian equality constraints. These equations are obtained by using Gauss's Principle to recast the problem of the constrained motion of dynamical systems in the form of a quadratic programming problem. The closed-form solution to this programming problem then explicitly yields the equations that describe the time evolution of constrained linear and nonlinear mechanical systems. The direct approach used here does not require the use of any Lagrange multipliers, and the resulting equations are expressed in terms of two different classes of generalized inverses—the first class pertinent to the constraints, the second to the dynamics of the motion. These equations can be numerically solved using any of the standard numerical techniques for solving differential equations. A closed-form analytical expression for the constraint forces required for a given mechanical system to satisfy a specific set of nonholonomic constraints is also provided. An example dealing with the position tracking control of a nonlinear system shows the power of the analytical results and provides new insights into application areas such as robotics, and the control of structural and mechanical systems.

1 Introduction

D'Alembert's principle, which gives a complete conceptual solution to problems of classical mechanics, hinges upon the first-order virtual work done by the impressed (given) forces and that done by the forces of inertia (Lanczos, 1970). The former can often be expressed in terms of the variation of a potential energy function (Lanczos, 1970). By integrating with respect to time, the virtual work done by the forces of inertia can be transformed into a true variation (Rosenberg, 1972). Thus for holonomic systems, D'Alembert's principle can be reformulated as Hamilton's variational principle, which requires that a definite integral be stationary (Lanczos, 1970). The set of Lagrangian equations of motion that follow remain invariant under arbitrary, one-to-one point transformations.

It was in 1829 that Gauss (1829) gave an aesthetic and ingenious reinterpretation of D'Alembert's principle, changing it into a true minimum principle. This principle is applicable to systems with general constraints, including configuration constraints (Rosenberg, 1972). Gauss argued that the determination of the motion of an n-degree-of-freedom system in which positions and velocities were known, hinged on our ability to determine the accelerations under the given applied forces. He formulated the principle of "least constraint" for describing the motion of mechanical systems. This principle is closely analogous to his celebrated "method of least squares," a method he developed and applied to the adjustment of errors in measurements. Unlike Hamilton's principle, the principle of least constraint has the additional advantage of not requiring any integration in time. Hertz gave a geometrical interpretation of Gauss's principle for the special case when the impressed forces vanish (Hertz, 1917). He showed that in this case Gauss's "constraint" can be interpreted as the geodesic curvature of the configuration point in $3n$-dimensional space. Appell and Gibbs (see Pars, 1979) further extended the principle to apply to nonholonomic conditions and in cases where it may be advantageous to use kinematical variables (Lanczos, 1970). They used the idea of pseudo-coordinates (see, Pars 1979) which has, more recently, been again explored by Shan (1975)[2]. Synge (1926) has also provided an alternative set of equations of motion of nonholonomic systems in terms of the geometry

[1]The names of the authors are listed in alphabetical order.

Contributed by the Applied Mechanics Division of THE AMERICAN SOCIETY OF MECHANICAL ENGINEERS for publication in the ASME JOURNAL OF APPLIED MECHANICS.

Discussion on this paper should be addressed to the Technical Editor, Professor Leon M. Keer, The Technological Institute, Northwestern University, Evanston, IL 60208, and will be accepted until four months after final publication of the paper itself in the ASME JOURNAL OF APPLIED MECHANICS.

Manuscript received by the ASME Applied Mechanics Division, July 5, 1991; final revision, Oct. 30, 1991. Associate Technical Editor: R. L. Huston.

[2]The authors are thankful to an anonymous reviewer for pointing out this reference to them.

of the resultant trajectories. As such, his formulation is difficult to directly apply to engineering problems.

From a practical standpoint, however, the computational difficulties of directly solving a minimization problems at each instant of time to describe the motion of a mechanical system made Gauss's principle unattractive at the time. This caused mechanicians of the late 18th, 19th, and 20th centuries to expound on, and mainly utilize the methods of Jacobi and Hamilton in the solution of problems in mechanics. Modern day texts in classical mechanics usually concentrate on these two latter approaches (e.g., Arnold, 1980), often relegating Gauss's principle to the position of a theoretically insightful approach, yet practically speaking, an unusable novelty.

In this paper we show that with our improved understanding of generalized inverses of rank-deficient matrices, Gauss's principle may offer a new, direct and oftentimes simpler approach to handling complex problems in mechanical systems. This is true in particular where nonholonomic and rheonomic constraints may be present. *The key idea is that Gauss's Principle allows us to reformulate the equations of motion of constrained mechanical systems as a quadratic programming problem. In this paper we solve this quadratic programming problem, and thereby obtain a new set of explicit equations governing the motion of constrained, discrete dynamical systems.* In contrast with the hereto used standard approach, which requires the use of Lagrange multipliers (e.g., see Rosenberg, 1972) or an expanded set of coordinates (Appell, 1925), the new approach developed here does away with the need for Lagrange multipliers. Furthermore, these equations are valid for both holonomic and nonholonomic constraints thereby treating both these types of constraints with equal consideration, and ease. The paper thus presents a unified approach to the handling of equality constraints in the analytical mechanics of discrete systems. In addition, an explicit expression is provided for the determination of the forces-of-constraint required so that a discrete mechanical system satisfies a given set of nonholonomic constraints.

Wang and Huston (1989) have looked at the representation of the equations of motion for nonholonomic systems, more from a matrix algebra standpoint. They also obtain equations of motion which do not involve any Lagrange multipliers. The equations obtained in this paper are, in a sense, generalizations of their results because we present the results in terms of *nonspecific* generalized inverses which belong to certain classes. With the flexibility of choosing any generalized inverse from a given class of inverses, specific generalized inverses suitable for specific problem situations can often be found quickly and efficiently.

In Section 2 we present a simple, short derivation of Gauss's principle for nonholonomic systems. The constraints are taken to be in Pfaffian form. The exposition in this section, we belive, is not available in the current literature (e.g., in Whittaker (1917), Synge (1926) and Pars (1979)), and provides some new insights. In Section 3 we use the results obtained in Section 2 to provide an exact solution to the constrained quadratic minimization problem governing the motion of constrained, discrete mechanical systems. In Section 4 we obtain explicit expressions for the constraint forces needed to satisfy the imposed constraints. Explicit equations for systems subjected to nonholonomic constraints are also provided. Section 5 illustrates our results using three numerical examples. The first deals with nonholonomic constraints, the second with the nonlinear oscillations of a pendulum subjected to nonlinear constraints. The third deals with the determination of the forces of constraint that need to be imposed on an oscillatory system described by a coupled Duffing's oscillator so that a specified time-dependent trajectory (constraint) is followed in configuration space. This latter example shows the power of our new formulation to possible applications in the field of robotics and position-tracking control of mechanical systems.

2 Gauss's Principle

Consider a holonomic mechanical system with n-degrees-of-freedom whose generalized coordinates are $q_1, q_2, q_3, \ldots, q_n$. The Lagrange equations describing the motion of the system may be written as

$$\frac{d}{dt}\left(\frac{\partial T}{\partial \dot{q}_r}\right)-\frac{\partial T}{\partial q_r}=Q_r,\ r=1, 2, \ldots, n, \tag{1}$$

where T denotes the kinetic energy and Q_r is the generalized impressed force. The kinetic energy can be expressed as

$$T=\frac{1}{2}\sum_{i,\,j=1}^{n} a_{ij}\dot{q}_i\dot{q}_j+\sum_{i=1}^{n} b_i\dot{q}_i+c, \tag{2}$$

where, in general, the a_{ij} and b_i and c are functions of the generalized coordinates and time.

Assume now that the system is subjected to an additional $p(p < n)$ independent nonholonomic, Pfaffian constraints of the form

$$\sum_{r=1}^{n}\alpha_{kr}dq_r+\beta_{kt}dt=0,\ k=1, 2, \ldots, p \tag{3}$$

where α_{kr} and β_{kt} are functions of the generalized coordinates and time. We note that the constraints may be scleronomic or rheonomic, catastatic or a catastatic (Rosenberg, 1972). These p constraints may be thought of as imposing additional constraint forces, Q_i', on our system, thereby altering the set of Eqs. (1) to

$$\frac{d}{dt}\left(\frac{\partial T}{\partial \dot{q}_r}\right)-\frac{\partial T}{\partial q_r}=Q_r+Q_r',\ r=1, 2, \ldots, n. \tag{4}$$

Expanding the first term in Eq. (4) we get

$$\begin{aligned}\frac{d}{dt}\left(\frac{\partial T}{\partial \dot{q}_r}\right)&=\frac{d}{dt}\left\{\sum_{s=1}^{n}(a_{rs}\dot{q}_s+b_r)\right\}\\&=\sum_{s=1}^{n}a_{rs}\ddot{q}_s+\sum_{j,s=1}^{n}\frac{\partial a_{rs}}{\partial q_j}\dot{q}_j\dot{q}_s+\sum_{s=1}^{n}\frac{\partial a_{rs}}{\partial t}\dot{q}_s\\&\quad+\sum_{s=1}^{n}\frac{\partial b_r}{\partial t}+\sum_{j=1}^{n}\frac{\partial b_r}{\partial q_j}\dot{q}_j.\end{aligned} \tag{5}$$

Expanding the second term we similarly get

$$\frac{\partial T}{\partial q_r}=\frac{1}{2}\sum_{i,j=1}^{n}\frac{\partial a_{ij}}{\partial q_r}\dot{q}_i\dot{q}_j+\sum_{i=1}^{n}\frac{\partial b_i}{\partial q_r}\dot{q}_i+\frac{\partial c}{\partial q_r}. \tag{6}$$

Denoting $q:=[q_1\ q_2\ q_3\ \ldots\ q_n]^T$, and substituting expressions (5) and (6) in relation (4), we obtain Lagrange's equations as

$$A\ddot{q}+f(q,\ \dot{q},\ t)=Q+Q',\ q(0)=q_0,\ \dot{q}(0)=\dot{q}_0 \tag{7}$$

where the vector function f is in general a nonlinear function of its arguments and $Q:=[Q_1, Q_2, \ldots, Q_n]$. The vector Q' is similarly defined. The $n \times n$ matrix A is positive definite and symmetric, and is related to the inertial properties of the system (Rosenberg, 1972, pp. 202).

Given the generalized coordinates and the generalized velocities q_r and $\dot{q}_r$, let $\ddot{q}_r'$ be any kinematically admissible acceleration which satisfies the p nonholonomic constraints given by equation set (3). Thus, the set $(\ddot{q}_r', \dot{q}_r, q_r)$ satisfies the differential constraint equations

$$\begin{aligned}\sum_{r=1}^{n}\alpha_{kr}\ddot{q}_r'+\sum_{r=1}^{n}\sum_{s=1}^{n}\frac{\partial \alpha_{kr}}{\partial q_s}\dot{q}_s\dot{q}_r+\sum_{s=1}^{n}\frac{\partial \beta_{kt}}{\partial q_s}\dot{q}_s\\+\sum_{r=1}^{n}\frac{\partial \alpha_{kr}}{\partial t}\dot{q}_r+\frac{\partial \beta_{kt}}{\partial t}=0,\ k=1, 2, \ldots, p.\end{aligned} \tag{8a}$$

Furthermore, if $\ddot{q}_r$ are the actual generalized accelerations of the mechanical system satisfying both the Lagrange equa-

tions and the constraints (3), then the set $(\ddot{q}_r, \dot{q}_r, q_r)$ satisfies the set of equations

$$\sum_{r=1}^{n} \alpha_{kr}\ddot{q}_r + \sum_{r=1}^{n}\sum_{s=1}^{n} \frac{\partial \alpha_{kr}}{\partial q_s}\dot{q}_s\dot{q}_r + \sum_{s=1}^{n} \frac{\partial \beta_{kt}}{\partial q_s}\dot{q}_s + \sum_{r=1}^{n} \frac{\partial \alpha_{kr}}{\partial t}\dot{q}_r + \frac{\partial \beta_{kt}}{\partial t} = 0,\ k = 1, 2, \ldots, p. \quad (8b)$$

Subtracting the corresponding equations from the sets (8*a*) and (8*b*), we obtain

$$\sum_{r=1}^{n} \alpha_{kr}(\ddot{q}_r' - \ddot{q}_r) = 0,\ k = 1, 2, \ldots, p. \quad (9)$$

Thus,

$$\delta\ddot{q}_r = \ddot{q}_r' - \ddot{q}_r,\ r = 1, 2, \ldots, n, \quad (10)$$

are kinematically admissible instantaneous variations of the acceleration; i.e., virtual accelerations which are consistent with the nonholonomic constraints. Thus, by D'Alembert's principle, the total virtual work done by the forces of constraint, Q_r', under these virtual accelerations equals zero. This requires

$$\sum_{r=1}^{n} Q_r'\delta\ddot{q}_r = \sum_{r=1}^{n} Q_r'(\ddot{q}_r' - \ddot{q}_r) = [Q']^T(\ddot{q}' - \ddot{q}) = 0, \quad (11)$$

where in the last expression we have denoted $Q' = [Q_1', Q_2' Q_3' \ldots Q_n']^T$. Using Eq. (7), this in turn entails

$$[A\ddot{q} + f(q, \dot{q}, t) - Q]^T(\ddot{q}' - \ddot{q}) = 0. \quad (12)$$

This condition is equivalent to

$$[A\ddot{q}' + f(q, \dot{q}, t) - Q]^T A^{-1}[A\ddot{q}' + f(q, \dot{q}, t) - Q] = [A\ddot{q} + f(q, \dot{q}, t) - Q]^T A^{-1}[A\ddot{q} + f(q, \dot{q}, t) - Q] + (\ddot{q}_r' - \ddot{q}_r)^T A(\ddot{q}_r' - \ddot{q}_r). \quad (13)$$

Since A is positive definite, the second term on the right-hand side is always positive. Hence, we obtain the condition that the generalized accelerations, $\ddot{q}_r(t)$ of the constrained mechanical system are such as to minimize

$$\|J\{\ddot{q}(t) \mid \dot{q}(t), q(t)\}\|_2^2 := \|A^{-1/2}[A\ddot{q}(t) + f(q, \dot{q}, t) - Q]\|_2^2, \quad (14)$$

at each instant of time t, while satisfying the set of constraints (3). We note that both $\dot{q}_r(t)$ and $q(t)$ are known at time t.

We have thus reduced the problem of the determination of the evolution of a mechanical system subjected to given forces to that of solving a constrained quadratic minimization problem at each instant of time. We note that while the expression J in (14) may be nonlinear in terms of the generalized coordinates and velocities, it is always linear in the unknown accelerations.

We point out here that were we to have chosen rectangular coordinates (x_i, y_i, z_i), $i = 1, 2, \ldots, n$, for the $3n$ degrees-of-freedom of a discrete system of n masses m_i, $i = 1, 2, \ldots, n$ then expression (14) would reduce to

$$\sum_{r=1}^{r=n} \left[m_r\left\{\ddot{x}_r - \frac{X_r}{m_r}\right\}^2 + m_r\left\{\ddot{y}_r - \frac{Y_r}{m_r}\right\}^2 + m_r\left\{\ddot{z}_r - \frac{Z_r}{m_r}\right\}^2 \right], \quad (15)$$

where X_r, Y_r, Z_r, refer to the x, y, z-components of the impressed forces on mass m_r. This expression was first ennuciated in words by Gauss (1829) who called it the "constraint," thereby ennuciating the "principle of minimum constraint" (Whittaker, 1917). It was further elaborated on by Hertz (1917) and many others.

Since the forces of constraint Q' satisfy Eq. (7), the minimization in (14) can also be expressed as

$$\underset{\ddot{q}}{\text{Minimize}}\{\|A^{-1/2}Q'\|_2^2\}. \quad (16)$$

Thus, we see that for the mechanical system to satisfy a given set of constraints at each instant of time, Gauss's principle requires that at each instant the *norm of the constraint forces Q' weighted with respect to $A^{-1/2}$* be minimized—hence the name, the principle of minimum constraint. In addition, the p constraint equations need to be satisfied. We show in the next section how this minimization can be carried out explicitly and also the explicit expression that can be written down for the constraint forces.

3 Solution of the Constrained Quadratic Minimization Problem

Using Gauss's Principle, we have thus reduced problems in mechanics to finding the accelerations $\ddot{q}_r(t)$ at each instant, t, given $q(t)$ and $\dot{q}(t)$, so that we require to

$$\underset{\ddot{q}}{\text{Minimize}}\{\|A^{-1/2}[A\ddot{q}(t) + f(q, \dot{q}, t) - Q]\|_2^2\}, \quad (17)$$

while satisfying the constraints (8*b*). These constraints are again linear in the accelerations and can be written in matrix form as

$$D\ddot{q}(t) = g\{\dot{q}(t), q(t), t\} \quad (18)$$

where we have denoted by D the $p \times n$ matrix $[\alpha]_{ij}$ and by g the vector containing the remainder of the terms in Eq. (8*b*). The right-hand side of Eq. (18) is known. For convenience, we shall now drop reference to the independent variable t, remembering that Eqs. (17) and (18) need to be satisfied at each instant of time. The solution of the consistent set of Eqs. (18) is obtained as (Rao and Mitra, 1972)

$$\ddot{q} = D^- g + (I - D^- D)h \quad (19)$$

where the $n \times p$ matrix D^- is any generalized inverse (g-inverse) of D which satisfies the relation

$$DD^-D = D. \quad (20)$$

The vector h is arbitrary. Substituting relation (19) into relation (17), we obtain

$$\underset{h}{\text{Min}}\ \|Hh - z\|_2^2 \quad (21)$$

where

$$H = A^{1/2}(I - D^- D) := A^{1/2}\hat{H}, \quad (22)$$

and

$$z = -\{A^{1/2}D^- g + A^{-1/2}(f - Q)\}. \quad (23)$$

For brevity, we have dropped the arguments of the vector function f. We next obtain the solution, h, of the least squares problem (21) as (Rao and Mitra, 1972),

$$h = H_{ls}^- z + (I - H_{ls}^- H)w, \quad (24)$$

where the matrix H_{ls}^- is the generalized "least-squares" inverse defined as satisfying the relations

$$(HH_{ls}^- H) = H, \quad (25)$$

and

$$[HH_{ls}^-]^T = HH_{ls}^-. \quad (26)$$

The vector w is again an arbitrary vector.

Using expression (24) in (19), we thus obtain the explicit solution to the constrained minimization problem given by Eqs. (17) and (18) as

$$\ddot{q} = D^- g + (I - D^- D)\{H_{ls}^- z + (I - H_{ls}^- H)w\} \quad (27a)$$

$$= D^- g + (I - D^- D)H_{ls}^- z + (I - D^- D)w - (I - D^- D)H_{ls}^- Hw. \quad (27b)$$

We now express the matrix H, as in Eq. (22), by $A^{1/2}\hat{H}$. The least squares g-inverse, H_{ls}^-, can now be expressed as

$$H_{ls}^- := \hat{H}_{ls}^- A^{-1/2} = (I - D^- D)_{ls}^- A^{-1/2}, \quad (28)$$

where

$$\hat{H}\hat{H}_{ls}^{-}\hat{H}=\hat{H}, \text{ and } [\hat{H}\hat{H}_{ls}^{-}]^{T}A=A[\hat{H}\hat{H}_{ls}^{-}]. \quad (29)$$

Relations (29) follow from the definition of H in Eq. (22) and that of H_{ls}^{-} in relations (25) and (26). Using relation (28) in (27*b*), we observe that the last two terms on the right-hand side cancel out, yielding

$$\ddot{q}=D^{-}g+(I-D^{-}D)H_{ls}^{-}z \quad (30a)$$

$$=D^{-}g-(I-D^{-}D)(I-D^{-}D)_{ls}^{-}\{D^{-}g+A^{-1}(f-Q)\}. \quad (30b)$$

We have thus obtained *explicit expressions for the accelerations at time t for the constrained motion*, given the generalized coordinates and velocities.

Heuristically speaking, the inverse, D^{-}, comes about (and is related to) to the constraints on the mechanical system, while the inverse, H_{ls}^{-}, comes about (and is related to) the motion of the dynamical system. These two inverses employed in expression (30*a*) are in general *different in nature* from each other (Rao and Mitra, 1972). The matrix D^{-} refers to *any* g-inverse of D (i.e., satisfying relation (20)), while the matrix H_{ls}^{-} refers to *any* "least-squares g-inverse" of H (satisfying relations (25) *and* (26)). From a practical standpoint, the flexibility of choosing *any* g-inverse belonging to the requisite classes stated above is a useful advantage in obtaining the equations of motion of complex dynamical systems, for, depending on the situation at hand, certain g-inverses are easier to determine than others.

For example, a possible candidate for H_{ls}^{-} might be $[H^{T}H]^{-}H^{T}$. Another might be the often-used Moore-Penrose (MP) inverse. However, the MP inverse is an element of both the set of g-inverses and the set of least squares g-inverses, and is a useful candidate because of the several computer codes available for its ready determination. The MP inverse can thus be used for both D^{-} and H_{ls}^{-} in Eq. (30*a*).

Even if the matrix D has rank $p_1 < p$, we are assured (Lawson and Hanson, 1974) that the accelerations thus obtained are unique because the matrix A is of rank n. However, when $p_1 < p$, the equation set (18) may not be consistent (Dahlquist and Bjorck, 1974) for all right-hand sides g. When the rank of D is p, a unique solution to the constrained minimization problem exists for all g.

4 Explicit Form of Constrained Equations of Motion and the Constraint Forces

We have obtained in Eq. (30) an explicit expression for the generalized accelerations at time t, given the generalized coordinates and the velocities. Using this, we can therefore express the constrained equations of motion, valid at any time, t, for a general system in first-order form, as

$$\frac{d}{dt}\begin{bmatrix} q \\ \dot{q} \end{bmatrix}=\begin{bmatrix} \dot{q} \\ D^{-}g+(I-D^{-}D)H_{ls}^{-}z \end{bmatrix}, \text{ with } q(0)=q_o,\ \dot{q}(0)=\dot{q}_o. \quad (31)$$

The quantity z is defined in Eq. (23). We note this explicit set of equations for the system include the effects of the Pfaffian constraints. They can therefore be thought of as the new equivalent equations of motion; they constitute a generalization of the equations found in Wang and Huston (1989).

The equation set (31), which in general will be nonlinear, can now be numerically solved using any of the standard numerical integration schemes, such as the fourth-order Runge-Kutta method, or other methods like the predictor corrector methods. The right-hand side of Eq. (31) guarantees that the accelerations satisfy both the constraints and Gauss's Principle simultaneously at each instant of time.

Furthermore, comparing Eqs. (7) and (30*a*), the forces of constraint can also be explicitly written as

$$Q'=(I-AXA^{-1})[f(q,\dot{q},t)-Q]+A(I-X)D^{-}g, \quad (32)$$

where we have denoted by the matrix X the quantity $(I-D^{-}D)H_{ls}^{-}A^{1/2}$. Often the constraints require that the system follows a given trajectory in configuration space. The constraint forces can then be thought of as the control forces necessary to cause the system to follow this particular trajectory.

The satisfaction of the constraint equations *at each instant of time* for the mechanical system entails the development of constraint forces which, *at each instant of time*, satisfy Eq. (16); the constraint forces Q', by Guass's Principle, must therefore minimize $\|A^{-1/2}Q'\|^2$. We note the the constraint forces acting at any instant, thus require for their determination nothing other than the displacement and velocity information at that instant, along with information about the constraints, *at that specific instant*. These forces of constrain can hence be determined at each time instant as the system's dynamics evolve. This makes the approach useful in real-time control, especially when the complete constrained trajectory is not known a priori. Thus, use of relation (32) may be made in the determination of real-time control required for tracking a given trajectory.

Equation (32) also shows that, in general, the control force vector, Q', is dependent on q, $\dot{q}$, and t, and therefore constitutes *closed-loop control*. We note that the elements of matrices D and A depend on the coordinates q_i and time. Similarly, elements of the vector g depend on q_i, $\dot{q}_i$ and time. In certain special situations the elements of D, A, and g may depend solely on time; then, the second term on the right-hand side of Eq. (32) is not dependent on q_i, and $\dot{q}_i$ and may be thought of as the *feed-forward* component of the total control force which is required to generate the constrained motion. Thus, in this special case, the control force may be thought of as being composed of a feedback control force (the first term of Eq. (32)) and a feed-forward control force.

5 Numerical Examples

In this section we consider three examples, the last two of which are numerical. The first deals with the constrained motion of a particle free of any "given" forces, where the constraint is nonholonomic. The second deals with the large amplitude motion of a planar pendulum. The pendulum bob is provided with two degrees-of-freedom and a constraint relation is provided on the length of the pendulum. We first constrain the length of the pendulum to be a constant. We use this example as a base line to check our results with the direct use of Runge-Kutta integration where the angle coordinate is used to preserve the length constraint. We next consider a more general, nonlinear constraint on the length of the pendulum. The third example is related to the problem of controlling a dynamical system (e.g., a machine tool) so that it follows a given trajectory. Here we show the ease with which the feedback tracking control force can be obtained using Eq. (31). In all the computations, a variable-step Runge-Kutta integration scheme is used with a local error tolerance of 10^{-10}. The Moore-Penrose inverse is used for each of the generalized inverses in Eqs. (31) and (32).

(1) Consider the motion of a particle of unit mass, free of any "given" forces, moving in three-dimensional euclidean space ($q_1 = x$, $q_2 = y$, $q_3 = z$). Let the particle be subjected to the nonholonomic, catastatic constraint

$$\dot{y}=z\dot{x}. \quad (36)$$

At time $t = 0$, the initial conditions of the particle are compatible with this constraint. We want to find the equations of motion for the particle for $t \geq 0$.

The system has two degrees-of-freedom; yet, the nonholonomic nature of the constraint requires three coordinates for a specification of the system's configuration. This example is taken from Rosenberg (1972, p. 204). Since there are no "given"

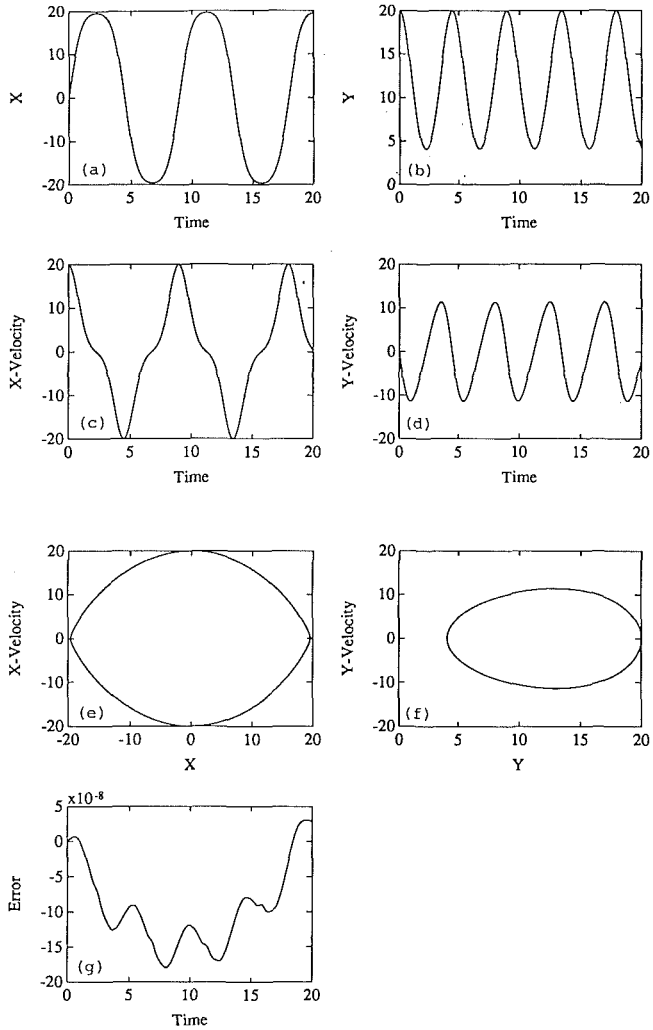

Fig. 1 Response of a pendulum of constant length to large amplitude motions using the new constrained equations of motion

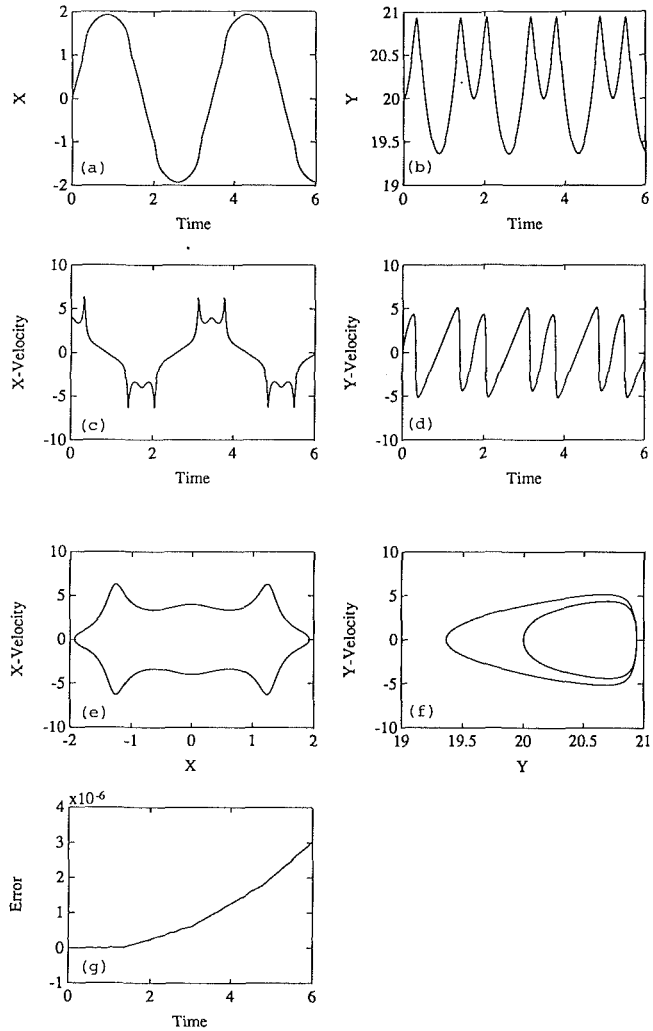

Fig. 2 Response of a pendulum with nonlinear constraints with $\mu = -0.1$ and $a = 4.0$

forces, $Q = f = 0$. The matrix $D = [-z\ 1\ 0]$ here, and the matrix $D^- = \{1/(1+z^2)\}[-z\ 1\ 0]^T$. The matrix A and the vector g are scalars equal to unity and $\dot{z}\dot{x}$, respectively. The vectors f and Q are zero, and the MP inverse of $(I - D^-D)$, obtained by using full rank factorization, is given by

$$(I-D^-D)^+ = \begin{bmatrix} \frac{1}{(1+z^2)} & \frac{z}{(1+z^2)} & 0 \\ \frac{z}{(1+z^2)} & \frac{z^2}{(1+z^2)} & 0 \\ 0 & 0 & 1 \end{bmatrix}. \tag{37}$$

Using Eq. (29), we obtain explicitly the constrained equations of motion as

$$\begin{bmatrix} \ddot{x} \\ \ddot{y} \\ \ddot{z} \end{bmatrix} = \frac{\dot{z}x}{(1+z^2)} \begin{bmatrix} -z \\ 1 \\ 0 \end{bmatrix} \tag{38}$$

which are, of course, the same as Rosenberg's result.

(2) Using rectangular axes in an inertial frame of reference, we can express the motion of the pendulum bob in the x and y-directions (y taken downwards) as

$$m\ddot{x} = 0,\ m\ddot{y} = g;\ x(0) = \dot{y}(0) = 0,\ \dot{x}(0) = a,\ y(0) = L, \tag{33}$$

along with the constraint given by

$$x^2 + y^2 = L^2\{1 - \mu\sin(x^2)\}. \tag{34}$$

The value of m is taken to be unity, that of L was chosen to be 20 units, and that of g to be 4π. Figures 1(a-d) show the results obtained by using Eq. (31), for $a = 20$ units, with $\mu = 0$. The fourth-order Runge-Kutta scheme (RK) was used. The oscillations are in the nonlinear range; the maximum angle made by the pendulum bob with the vertical during the oscillation being about 80 degrees. These results are the same (to within the error tolerance) as those obtained using the direct Runge-Kutta (RK) integration taking the angle of rotation (about the vertical) of the pendulum bob as the generalized coordinate. Figures 1(e) and 1(f) show the phase plots in the x-$\dot{x}$ and the y-$\dot{y}$ planes. Figure 1(g) shows the extent to which the constraint is satisfied during the numerical computations. Here, the error is defined as the difference between the left-hand side and the right-hand side of Eq. (34), a quantity which should theoretically be zero.

Figures 2(a-d) show the response of the system when $a = 4$ and $\mu = -0.1$. We again integrate Eqs. (31) using the fourth-order RK method. Figures 2(e) and 2(f) show the phase plots. As before, Fig. 2(g) shows the error in satisfying the constraint.

Figure 3 shows the phase trajectories of the same system starting with different initial velocities, $a = 0.5$, 1, 2, and 4.

(3) The third example deals with a coupled, damped Duffing's oscillator described by the equations

$$m_1\ddot{x}_1 + k_1(x_1 - x_2) + c_1(\dot{x}_1 - \dot{x}_2) + \bar{k}_1(x_1 - x_2)^3 = 0 \tag{35a}$$

$$m_2\ddot{x}_2 + k_2x_2 - k_1(x_1 - x_2) + c_2\dot{x}_2 - c_1(\dot{x}_1 - \dot{x}_2) + \bar{k}_2x_2^3 - \bar{k}_1(x_1 - x_2)^3 = 0, \tag{35b}$$

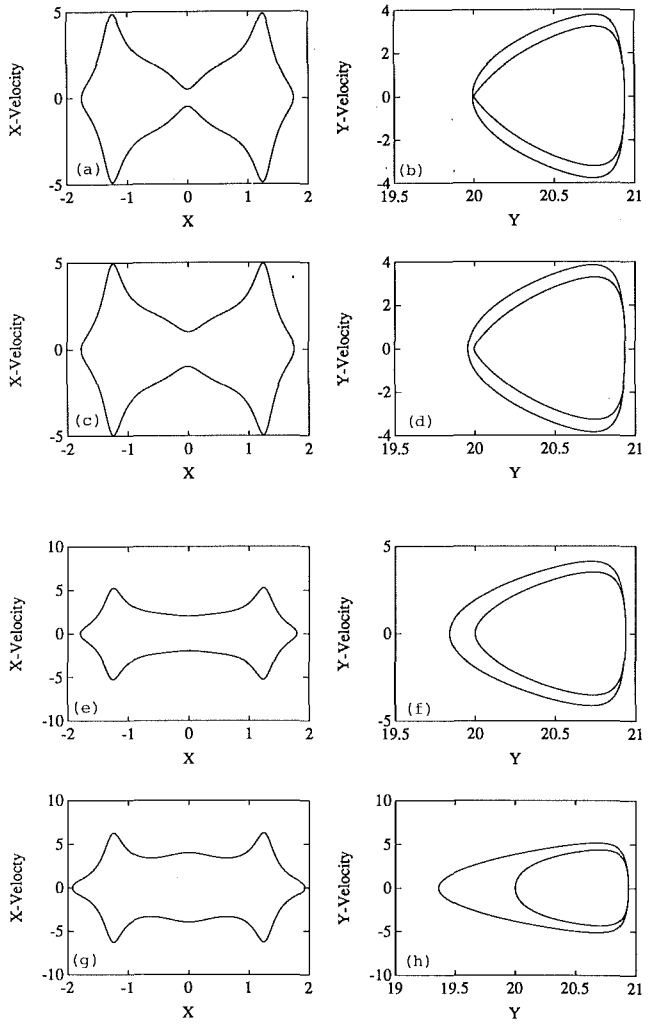

Fig. 3 The phase plots for $\mu = -0.1$. Figs. 3(*a*) and 3(*b*) show the response for $a = 0.5$; Figs. 3(*c*) and 3(*d*) show the response for $a = 1.0$; Figs. 3(*e*) and 3(*f*) show the response for $a = 2$; and, Figs. 3(*g*) and 3(*h*) show the response for $a = 4.0$

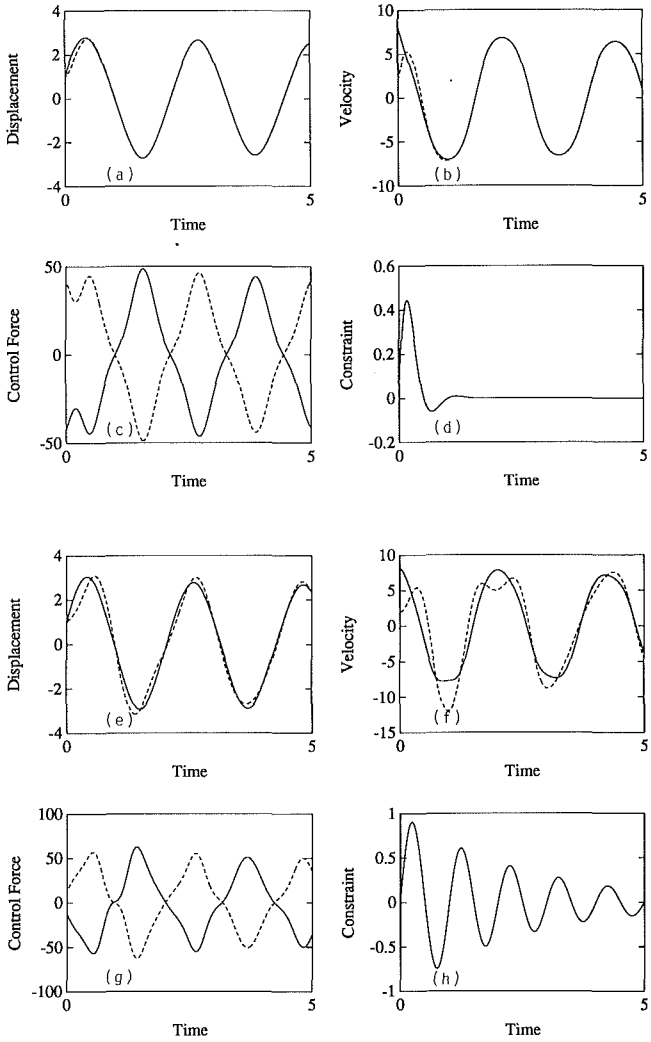

Fig. 4 Figures 4(*a*) and 4(*b*) shows the constrained response of the coupled Duffing's Oscillator, with $\alpha = 4.0$; Fig. 4(*c*) shows the two components of the control force needed to have the system follow this constrained trajectory; Fig. 4(*d*) shows $[x_1(t) - x_2(t)]$. Figures 4(*e–h*) show similar results when the constraint is enforced with $\alpha = 0.4$.

with

$$x_1(0) = a,\ x_2(0) = b,\ \dot{x}_1(0) = c, \text{ and } \dot{x}_1(0) = d.$$

We aim to determine the tracking control forces required so that the relative displacements of the masses are constrained to follow the exponentially decaying sinusoidal trajectory given by

$$x_1(t) - x_2(t) = Ae^{-\alpha t}\sin(\omega t). \tag{35c}$$

The parameters describing the system and its constraints are

$$m_1 = 2,\ m_2 = 1,\ k_1 = 10,\ k_2 = 12,\ \bar{k}_1 = 1,\ \bar{k}_2 = 2,\ c_1 = 0.1,\ c_2 = 0.15,\ A = 1,\ \omega = 2\pi.$$

The initial conditions are taken to be $a = 1$, $b = 1$, and $d = 2$. We note that the initial conditions must satisfy the constraints and hence the parameter c is determined from d and Eq. (35*c*). Figures 4(*a*) and 4(*b*) show the time histories of the displacement and velocity, obtained by integrating Eq. (31), when the parameter α equals 4 in Eq. (35*c*). The solid lines show quantities relevant to the "1" coordinate (i.e., to mass m_1), and the dashed lines show quantities relevant to the "2" coordinate (i.e., to mass m_2). Figure 4(*c*) shows the control forces (f_1 and f_2), calculated using Eq. (32), required to be applied to masses m_1 and m_2, respectively, to track this trajectory appropriately in configuration space. Figure 4(*d*) shows the computed value of $[x_1(t) - x_2(t)]$. We find (see, Fig. 5(*a*)) that the constraint is tracked to within an error (i.e., LHS-RHS of Eq. 35(*c*)) of 10^{-9}, a number consistent with the local error tolerance level of 10^{-10} used for the RK integration. Figures 4(*e–h*) show similar results when the value of α in Eq. (35*c*) is now taken to be 0.4. All other parameter values are left unchanged. As before, the solid lines show quantities relevant to the "1" coordinate and the dashed lines show quantities relevant to the "2" coordinate. The error in tracking this trajectory is shown in Fig. 5(*b*), and is again found to be of the order of 10^{-9}.

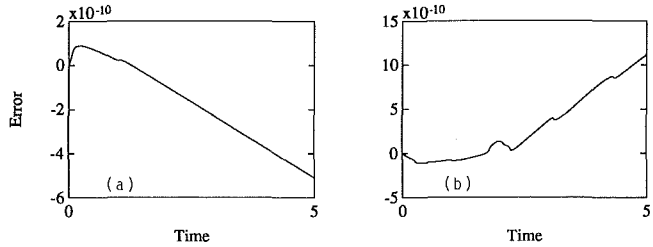

Fig. 5 (*a*) position tracking error for $\alpha = 4$; (*b*) position tracking error for $\alpha = 0.4$

6 Conclusions and Discussion

This paper deals with discrete, dynamical systems which are

subjected to Pfaffian, holonomic, and nonholonomic constraints. By using Gauss's Principle of Least Constraint, we have recast the Lagrange equations which describe the constrained motion of such a system in the form of a quadratic programming problem. In this paper we present an explicit analytical solution to this constrained quadratic minimization problem and thereby obtain an exact and explicit set of equations that describe the constrained motion of discrete, mechanical systems subjected to Pfaffian constraints. These equations can be numerically integrated using standard numerical techniques like the Runge-Kutta and Predictor-Corrector methods.

We summarize our finding as follows:

1 We have used Gauss's Principle to obtain a new conceptualization of the equations of motion of a constrained, discrete dynamic system. The equations of motion that we develop, *directly* yield the time evolution of the system; we do away with the need to use any Lagrange multipliers. Thus Gauss's principle, though largely neglected by the mechanicians of this century, is shown to yield significant insights into the dynamics of constrained systems.

2 Besides its aesthetic appeal, the method proposed herein has special advantages when working with nonintegrable constraints. In fact it does away with the somewhat unnecessary categorization of Pfaffian constraints into: (a) holonomic and nonholonomic constraints and (b) rheonomic and scleronomic constraints—the approach being able to handle all these types of equality constraints with equal ease. The equations developed here can be used in situations where the derivation of the equations of motion (using Lagrange multipliers) for constrained systems may become cumbersome and/or difficult to implement computationally. The approach thus provides a conceptual and practical simplicity in the formulation of the equations of motion of complex mechanical systems, because the constraints can be explicitly handled as additional equations whose effect can be directly incorporated in the equations of motion. The flexibility that this formulation affords in the specific choices of the generalized inverses D^- and H_{ls}^-, is an added feature which is new, and particularly helpful from a practical standpoint. Response sensitivity studies related to altering the constraints can thus be easily carried out.

3 Even for systems, where it may be possible to eliminate certain variables directly from the equations of motion, the method provides a direct and more aesthetic approach by not favoring any particular subset of coordinates over any other.

4 The explicit expressions obtained for the constraint forces may be used to advantage when dealing with the determination of control forces required to control a system so that it follows a certain trajectory in configuration space, or more generally, satisfies a given set of Pfaffian constraints. Such problems arise in many areas of application, like position tracking of machine tools (Tomizuka, 1987) and robotic manipulator control (Seraji, 1987).

Furthermore, we obtain the additional insight from Gauss's Principle that for the system to satisfy the constraint equations *at each instant* of time, a *specific* quadratic function of the constraint forces, namely, $Q'^T A^{-1} Q'$, must be minimized at each instant of time. This sheds light on the reason why least-squares formulations of the tracking control problem have often *not* led to proper trajectory tracking when minimizing the integrals of general quadratic functions of the control forces.

5 The three examples considered here illustrate that the approach may be useful in answering the two commonly occurring problems in particle mechanics (Rosenberg, 1972): (a) finding the response of mechanical systems subjected to general types of time-dependent, Pfaffian equality constraints and (b) finding the control forces required to be imposed on a system, in real-time, so that it satisfies a given set of holonomic or nonholonomic Pfaffian constraints. Our third example shows that by using the new set of dynamical equations obtained herein, the accuracy with which the system is led to follow a constrained trajectory can indeed be high.

References

Appell, P., 1925, *Sur une forme generale des equations de la dynamique*, Memorial des Sciences Mathem, Paris, Gauthier-Villars.

Arnold, V. I., 1980, *Mathematical Methods of Classical Mechanics*, Springer-Verlag, New York.

Dahlquist, G., and Bjorck, A., 1974, *Numerical Methods*, Prentice-Hall, Englewood Cliffs, N.J.

Hertz, H., 1917, *Principles of Mechanics*, Macmillan, London.

Gauss, C., 1829, "Uber ein neues allgemeines Grundgesetz der Mechanik," *Journal fur Reine und Angewandte Mathematik*, pp. 232–235.

Lanczos, C., 1970, *The Variational Principles of Mechanics*, Dover Publications, New York.

Lawson, C., and Hanson, R., 1974, *Solving Least Squares Problems*, Prentice-Hall, Englewood Cliffs, N.J.

Pars, L. A., 1979, *A Treatise on Analytical Dynamics*, Ox Bow Press, Connecticut.

Rao, C., and Mitra, S., 1972, *Generalized Inverse of Matrices and Its Applications*, John Wiley and Sons, New York.

Rosenberg, R., 1972, *Analytical Dynamics of Discrete Systems*, Plenum Press.

Seraji, H., 1987, "Design of Feedforward Controllers for Multi-variable Plants," *International Journal of Control*, Vol. 46, pp. 1633–1651.

Shan, D., 1975, "Canonical Equations for Mechanical Systems With Second-Order Linear Nonholonomic Constraints," *Prikladnaya Mekhanika*, Vol. 11, No. 2, pp. 58–67.

Synge, J. L., 1926, "On the Geometry of Dynamics," *Proceedings of the Royal Society, London*, Vol. A226, pp. 31–106.

Tomizuka, M., 1987, "Zero Phase Error Tracking Algorithm for Digital Control," ASME *Journal of Dynamic Systems, Measurement and Control*, Vol. 109, pp. 65–68.

Wang, J. T., and Huston, R. L., 1989, "A Comparison of Analysis Methods of Redundant Multibody Systems," *Mechanics Research Communications*, Vol. 16, pp. 175–182.

Whittaker, E., 1917, *A Treatise on the Analytical Dynamics of Particles and Rigid Bodies*, Cambridge, Univ. Press, Cambridge, U.K.

Jumps to Resonance: Long Chaotic Transients, Unpredictable Outcome, and the Probability of Restabilization

M. S. Soliman[1]
Department of Civil Engineering,
University College London,
London, WC1E 6BT, U.K.

For nonlinear oscillators with the ability to escape from a potential well, jumps to resonance from a fold can result in qualitatively different types of response. They may be safe *where the system* always *restabilizes onto a oscillation within the well;* unsafe *where the system* always *escapes out of the well; or* indeterminate *where the outcome is unpredictable. In the indeterminate case, long chaotic transients may persist before the system decides to which long-term behavior it will settle upon. We determine at which control parameters indeterminate jumps occur. We also examine how the transients scale as well as the probability of restabilization after the bifurcation.*

1 Introduction

The periodically driven motions of a mass in a potential field, with one or more minima, have often been used to model the nonlinear oscillations of a wide class of mechanical and electrical dynamical systems. The single well problem has been used to model the nonlinear rolling motions of a ship (Thompson, 1989; Soliman and Thompson, 1989); the Duffing two-well potential has been used to describe the motions of a column loaded beyond its buckled state (Holmes and Whitley, 1983; Moon and Li, 1985; Holmes and Moon, 1983); and multiple wells have been used to model the motions of a pendulum which is of importance in the study of Josephson junctions and charge density plasmas (Huberman and Crutchfield, 1979).

Through analytical investigations, numerical simulations and experimental observations, all of these systems have exhibited a wide range of complex nonlinear phenomena; multiple co-existing attractors, quasi-periodic, subharmonic and chaotic oscillations, cross-well motions, discontinuous jumps, and hysteresis phenomena as well as other bifurcational behavior. Basins of attraction, associated with each attractor, and the boundaries that separate them also undergo changes.

Recent studies have shown that for such nonlinear oscillators with the ability to escape from a potential well, qualitatively different types of response can occur after a jump to resonance at a *fold* or a *saddle-node bifurcation* (Soliman and Thompson, 1991; Thompson and Soliman, 1991).

In this paper we consider the various types of jumps, their associated transient behavior, and the nature of the long-term response that can occur for a typical softening sinusoidally forced damped mechanical oscillator with a cubic potential, $V = 1/2x^2 - 1/3x^3$. This particular potential is the universal form always encountered just before a mechanical oscillator loses its stability at a fold catastrophe; this being the only typical mode of instability that can be generically encountered by a gradient system under the variation of a single control parameter (Virgin, 1986).

We hence consider the equation of motion

$$\ddot{x}+\beta\dot{x}+x-x^2=F\sin(\omega t) \quad \dot{x}\equiv y \tag{1}$$

where x is the dependent variable and a dot denotes differentiation with respect to time t. The positive coefficient, β, represents the magnitude of damping, and the oscillator is driven by the sinusoidal force of magnitude F and circular frequency ω. We fix throughout on $\beta = 0.1$, and focus attention on driving phase $\varphi = 180$ deg, so that $t_0 = \pi/\omega$. We pay particular attention to jumps *to* resonance, which from a practical point of view have important implications since they can result in large amplitude oscillations that may be dangerous or even catastrophic.

In Section 2 we look at *safe determinate* jumps to resonance. We show that under the slow variation of a control parameter, a small stable oscillation can become a large amplitude oscillation which remains *within* the well (Fig. 1, Case (i)). This bifurcation is not catastrophic in the sense that the system *always* restabilizes onto the bounded oscillation. Long, almost periodic transients can persist until the system settles onto the large amplitude oscillation.

In Section 3, we consider *indeterminate* jumps to resonance. Here, jumps can result in a long-term oscillation that remains

[1]Current address: Department of Mechanical Engineering, Queen Mary and Westfield College, University of London, Mile End Road, London E1 4NS, U.K.

Contributed by the Applied Mechanics Division of THE AMERICAN SOCIETY OF MECHANICAL ENGINEERS for publication in the ASME JOURNAL OF APPLIED MECHANICS.

Discussion on this paper should be addressed to the Technical Editor, Professor Lewis T. Wheeler, Department of Mechanical Engineering, University of Houston, Houston, TX 77204-4792, and will be accepted until four months after final publication of the paper itself in the ASME JOURNAL OF APPLIED MECHANICS.

Manuscript received by the ASME Applied Mechanics Division, July 18, 1991; final revision, Jan. 7, 1992. Associate Technical Editor: P. D. Spanos.

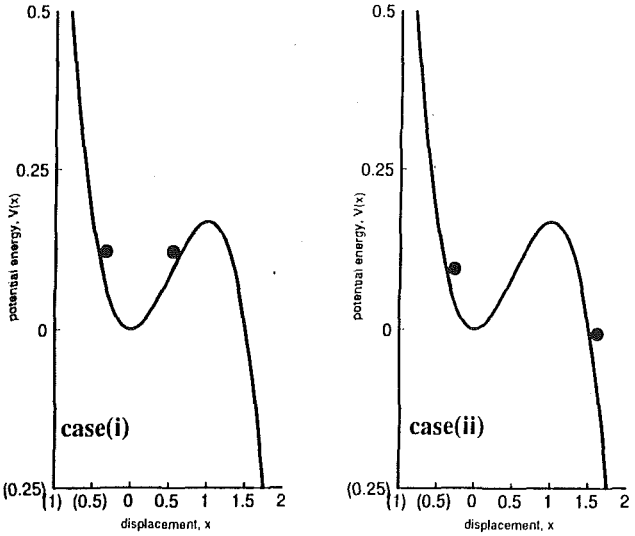

Fig. 1 For the anharmonic potential, $V(x) = 1/2x^2 - 1/3x^3$, a jump to resonance at a fold can result in qualitatively different types of response. After some initial transient, the system may either restabilize to a large amplitude oscillation *within* the well (Case (i)) or may "escape" to a remote attractor *outside* the well (Case (ii)).

bounded *or* can result in motions that explode and escape over the hilltop and out of the well to the remote attractor at infinity, with $x \to \infty$ as $t \to \infty$ (Fig. 1, Case (ii)). In the physical sense escape can be regarded as failure of the system: in the case of the ship problem this would mean capsize; in the case of the buckled beam problem it would mean snap-through. For these indeterminate jumps we may not predict the final outcome, whether it be safe or unsafe, but long chaotic transients can occur until the system finally settles down.

In Section 4 we consider *unsafe* jumps to resonance. Here, under small parameter changes the system *always* escapes out of the well.

By establishing the events which render a system indeterminate, we determine, in the (F, ω) control space the critical control parameter values which put bounds on the type of jump that occur. For control parameters in which indeterminate jumps occur, we examine the probability of restabilization, and how such a measure may be useful when defining the robustness of a system that is liable to such bifurcations.

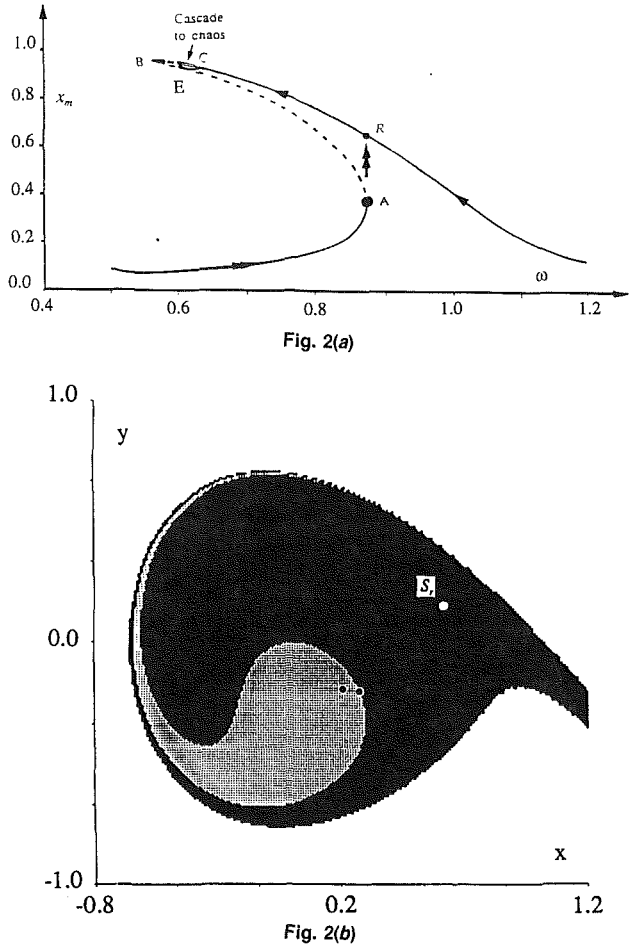

Fig. 2 (*a*) Resonance response curve, where a *safe* jump to resonance from fold *A* occurs. Here, under small parameter changes, the system *always* restabilizes at *R*. (*b*) Attractor-basin phase portrait at $\beta = 0.1$, $F = 0.0562$, $\omega = 0.873$ just prior to the jump at *A*. The saddle-node pair, D_r and S_n (whose basin of attraction is shaded in grey dots), are indicated by black dots within white circles. The large amplitude oscillation, S_n is indicated by a white circle, whose basin of attraction is shaded in black. White denotes the unsafe (escaping) basin of attraction for the attractor at infinity. Here it can clearly be seen why the forthcoming bifurcation will result in the system settling onto S_r.

2 Safe Determinate Jumps: Predictable Transients and Outcome

In order to illustrate the jump phenomena it is useful to plot the steady-state resonance response diagrams showing how x_m, the maximum value of $x(t)$, varies with ω at different F levels. Figure 2(*a*) shows such a diagram which clearly delineates the softening hysteresis phenomena; here a fourth-order Runge-Kutta numerical algorithm was used to integrate Eq. (1).

If the system is started at a relatively high frequency, and then one *slowly* decreases the excitation frequency there is an increase in amplitude along the resonant part of the response curve, S_r. The smooth variation of amplitude and frequency continues until point C; near the peak of the response curve. Here there is a flip bifurcation where the $n = 1$ oscillation loses its stability and becomes an $n = 2$ subharmonic oscillation. There is then an infinite period-doubling cascade which eventually results in a chaotic attractor, which is then destroyed in a crisis (Grebogi et al., 1983, 1987). The system may then restabilize or escape out of the well (Stewart and Ueda, 1991). There is also an opposing cascade and a jump *from* resonance at fold point B, which always restabilizes onto the nonresonant attractor (Soliman and Thompson, 1991).

Conversely, by slowly increasing the frequency from a relatively small value, one suddenly encounters a jump *to* resonance from fold A. Here the system which was originally oscillating with a small amplitude (lying on the nonresonant branch, S_n) settles on to a large resonant amplitude oscillation, R.

Between fold points A and B there is the well-known region of resonant hysteresis. Here the two stable steady-state oscillations are separated by an unstable saddle solution, D_r. To which of the stable co-existing attractors the system will approach depends upon the initial conditions. In the space of the starting conditions $(x_0, \dot{x}_0)$ at $t = 0$, there will be domains or basins of attraction such that motions originating in the basin of S_n will lead, after the decay of transients, to S_n, while initial conditions in the basin of S_r will lead to S_r. Although physically unrealizable, the unstable saddle solution D_r plays an important role in the basin organization; the stable manifold, $W^s(D_r)$, of D_r determines the boundary between the two co-existing stable attractors. Furthermore it is the stable manifold, $W^s(D_h)$, of the hilltop saddle cycle D_h (which originates from the unstable equilibrium $\{F = y = 0, x = 1\}$) that determines the boundary between the *safe* starts (all initial conditions generating orbits that remain bounded) and *unsafe* starts that tend to $x \to \infty$ as $t \to \infty$.

Figure 2(*b*) shows the basin organization, in the Poincaré section, just prior to the jump to resonance at A. Here 200 × 200 initial conditions were chosen in the form of a grid and integrations were continued until the system either stabilized onto one of the bounded attractors, or escaped out of the well. Here it can clearly be seen that when the saddle-node annihiliation of $S_n - D_r$ occurs, the system will restabilize onto the resonance attractor S_r as it is located in the interior of the safe basin well away from the smooth escape boundary, giving a totally determinate jump to S_r which is preserved under conditions of small external noise or small but finite incrementation of a control parameter.

Long transient behavior is observed after the saddle-node bifurcation as is seen in Fig. 3(*a*). Here the system is set on the saddle node and then given a small increment $\Delta F = F - F^A$. There is no significance whether we chose to cross the saddle-node boundary by an increment of F or by an increment of ω, or indeed by any other parameter. Here long, almost periodic transients occur which mimic the behavior of the destroyed saddle node until the orbit settles onto the steady-state large amplitude oscillation. Moreover, it would be not only the initial conditions of the former saddle node that would exhibit this type of behavior, but *all* the initial conditions which constituted its basin prior to its destruction that would generate orbits with long transient behavior; they would rapidly approach the remnant of the destroyed attractor, remain there for some time, and then be expelled towards the resonant attractor (Van Damme and Valkeering, 1987).

In our studies we have considered the transient length τ of a given initial condition as the time to reach a given attractor. This would be a combination of the trapping time spent in the vicinity of the destroyed saddle node, the intermediate transient, and thereafter the time taken to reach the chosen attractor to within a specified criterion. Figure 3(*b*) shows that the "time" taken to reach the resonant attractor for several increments of ΔF. It can be seen that τ approximately scales with the system parameter such that

$$\tau \propto (\mu - \mu^*)^{-\gamma},$$

where μ^* is the critical parameter and γ is the critical exponent. For relatively small values of ΔF, we find $\gamma = 0.49$ which corresponds very closely to the analytical predictions ($\gamma = 0.50$) and numerical results of Van Damme and Valkeeing (1987) concerning the scaling of transients in the *local* neighborhood of a fold bifurcation for the two-dimensional quadratic map. This suggests that for very small changes in the incremental bifurcation parameter, the criterion for steady-state oscillations would not adversely effect the value of the critical exponent although it may have a significant effect on the constant of proportionality.

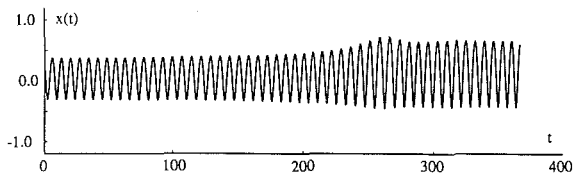

Fig. 3(*a*)

3 Indeterminate Jumps: Unpredictable Chaotic Transients and Unpredictable Outcome

As parameters are varied both qualitative and quantitative changes occur not only to attractors (and their corresponding resonance responses), but as a result of global bifurcations their basins of attractions also undergo metamorphoses. It has been shown that at critical parameter values, a homoclinic tangling of the stable and unstable manifolds of the hilltop saddle cycle, D_h, can generate a fractal escape boundary (McDonald et al., 1985; Moon and Li, 1985; Thompson and Soliman, 1990). A further increase in a parameter can result in the unstable manifold of the resonant saddle D_r which leads towards the resonant attractor, becoming heteroclinically tangled with the stable manifold of D_h. Under these conditions a jump to resonance at fold A becomes essentially indeterminate because the saddle node lies on the fractal escape boundary with an infinite number of escaping fingers having accumulated on to it (Soliman and Thompson, 1992a). If ω were increased slowly at an infinitesimal rate, the system would find itself at A, sitting precisely on the escape boundary. It would therefore experience an infinite chaotic transient as its Poincaré point maps along the stable manifold of D_h leading to the unstable oscillation of the hilltop saddle cycle. After the saddle node

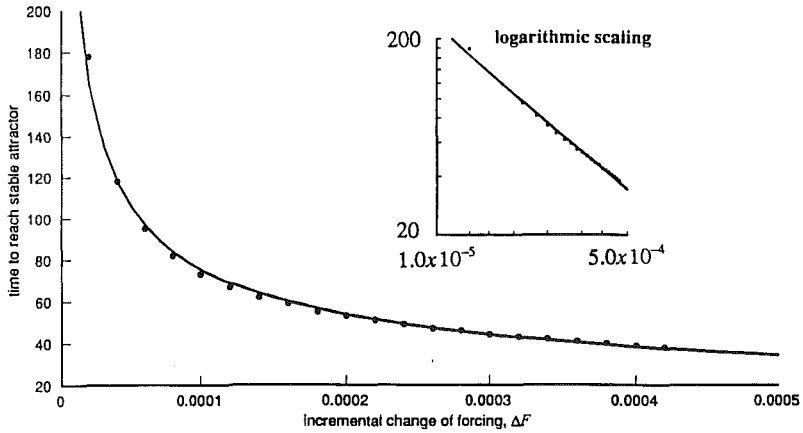

Fig. 3(*b*)

Fig. 3 (*a*) A typical time history illustrating the long transients that occur just after the bifurcation. Here $\omega = 0.873$, $F = 0.0569$, $\Delta F = F - F^A = 0.0002$, $x(0) = 0.243$, $y(0) = -0.209$. (*b*) Long transients beyond the saddle node bifurcation occur. Scaling of the transients gives $\tau = k(F - F^A)^{-\gamma}$, where τ is the time to reach the attractor and γ is the critical exponent. Here $k = 0.826$, $\gamma = 0.49$. In this figure, the time to reach the attractor is measured in the number of forcing cycles.

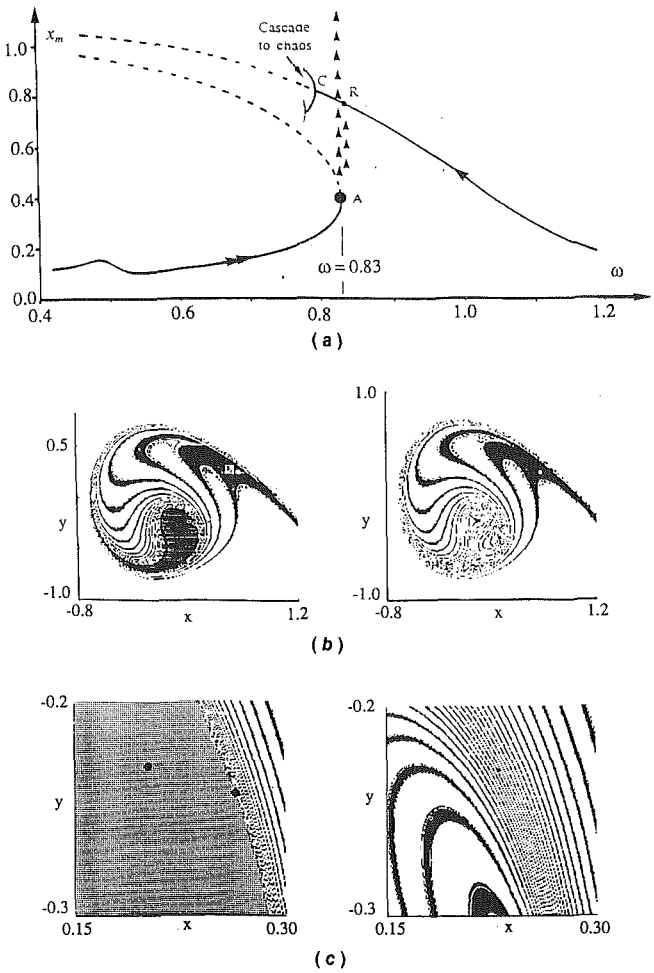

Fig. 4 (*a*) Here an *indeterminate* jump to resonance from fold *A* occurs. Under small parameter changes, the system *may* restabilize at *R* (or indeed any other existing attractor within the well), or may escape to infinity. (*b*) Attractor-basin phase portraits at $\beta = 0.1$, $\omega = 0.83$ just before ($F = 0.0800$) and after ($F = 0.0805$) the jump at *A*. The saddle-node pair, D_r and S_n, are indicated by black dots within white circles. The large amplitude oscillation, S_n is indicated by a white circle. (*c*) Blow-up in the region of phase space close to the saddle and node just before and after the bifurcation. The large solid circles represent the saddle-node pair, and the small solid circle denotes the position of the destroyed saddle node.

annihilation, the basins that were accumulated onto the stable manifold of D_r will rearrange themselves and "sweep" through and fill the region of phase space previously occupied by the nonresonant basin (Enschenzi et al., 1989). The value of the bifurcational increment ΔF, will determine to which basin the initial conditions of the saddle node will preside. However, in any real situation, due to the inherent uncertainties in the specification in the parameter values, long-term predictability will be lost and hence the jump will become indeterminate. This behavior is clearly seen in Fig. 4. The system will experience a long chaotic transient leading either to the stable resonant attractor (or indeed any other attractor present within the well), or escape over the hilltop with $x \to \infty$ as $t \to \infty$. Figure 5(*a*) shows three possible outcomes under three slightly different increments of ΔF. The first time history shows the jump settling onto a $n = 3$ subharmonic oscillation; the second trace, from the same starting conditions but at a slightly different F, leads to the attractor at infinity; and the final trace shows the system settling onto the stable $n = 1$ resonant attractor S_r. In all three time histories initially long, almost periodic transient behavior occurs; this is as a result of the coexisting basins being highly intertwined in the vicinity of the saddle node; points mapping from one finger to the next will remain there for long periods until the system converges to its final outcome. Indeed the highly intertwined basin structure will result in fingers folding back upon on one another where longer thinner fingers wrap around the shorter fatter fingers, will result in unpredictability in *both* outcome and transient length which is clearly seen in Fig. 5(*b*). Here it can be seen that the transients are not typically scaled; an increase in ΔF does not necessarily imply a decrease of transient length. However, if one was to consider separately those transients that were qualitatively and quantitatively similar (i.e., those that lead to the same type of attractor; and neglect trials that initialized on relatively thin (fat) fingers that obviously generated "exceptionally" long (short) transient times) a general scaling trend may be estimated.

4 Unsafe Determinate Jumps: Predictable Transients and Outcome

At a higher forcing level, several qualitative differences in the response curves occur as can be seen in Fig. 6. First, there is the growth of the superharmonic at about half the linearized natural frequency, but more importantly is the fact that the

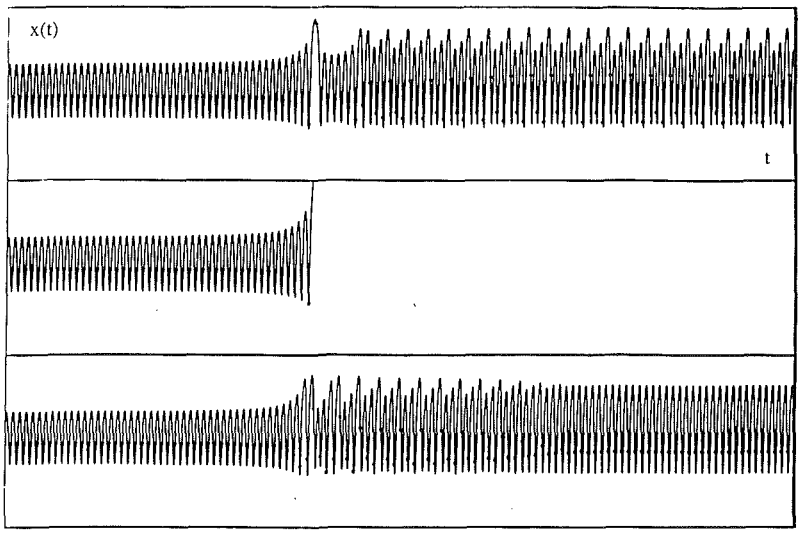

Fig. 5(*a*)

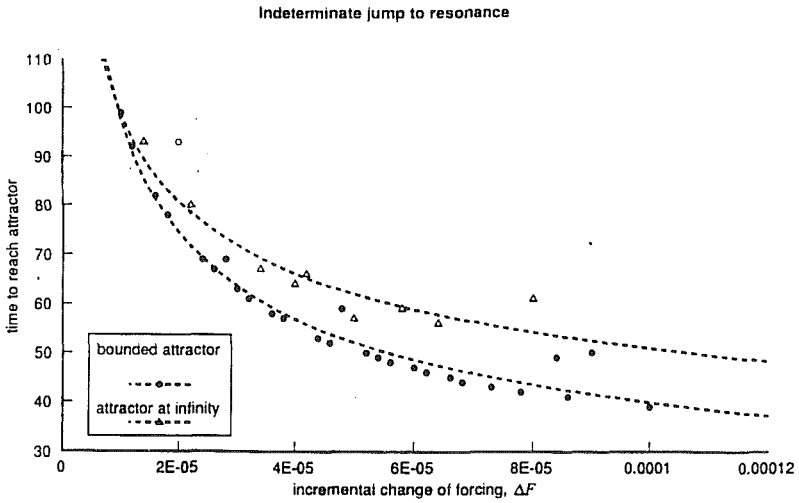

Fig. 5(*b*)

Fig. 5 (*a*) Indeterminate chaotic transients under a small forcing increment. Three possible outcomes from values of F just beyond the indeterminate tangled saddle-node bifurcation at $F \approx 0.08$, $\omega = 0.83$, $\beta = 0.1$. Trace (a) at $F = 0.080068$ restabilizes on an $n = 3$ attractor. Trace (b) at $F = 0.080069$ escapes to infinity. Trace (c) at $F = 0.008070$ restabilizes on the resonant $n = 1$ attractor. Poincaré points are marked at phase $\phi = 0$. Window is $-1.2 < x < 1.2$, $0 < t < 900$. All runs start from $x(0) = -0.04166$, $y(0) = 0.3119$. (*b*) Scaling of the transients beyond the saddle-node bifurcation becomes arbitrary; circles represent bifurcation realizations that escaped; triangles represent bifurcation realizations that restabilized. The dominant trend for the escaping trails is estimated, with $\gamma = 0.52$.

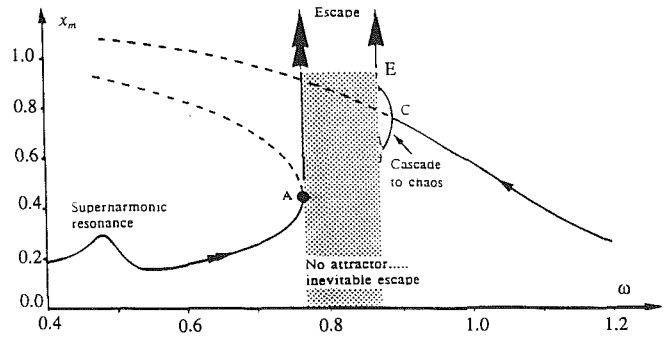

Fig. 6(*a*)

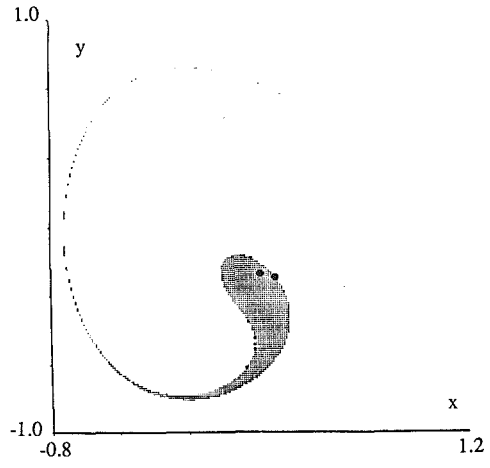

Fig. 6(*b*)

Fig. 6 As in Fig. 2 but here the jump is *unsafe* at $F = 0.1211$. All small changes in parameters will result in escape.

forcing frequency at E is greater than that at A. This leaves a regime where there is no attractor within the well and hence an inevitable jump to escape under both decreasing frequency, after the crisis of the chaotic attractor, and under increasing frequency from fold A. Figure 6(*b*) showing the basins of attraction just before the jump at fold A clarifies this situation. A typical time history just beyond the jump at A is shown in Fig. 7(*a*). The behavior observed here is similar to that seen for the safe jump but here rather than restabilizing onto the bounded attractor, the system *always* escapes out of the well. This situation may thus be deemed to be unsafe *but* determinate. The transients can be long but are determinate with respect to their scaling properties as seen in Fig. 7(*b*).

5 Critical Frequencies and the Probability of Restabilization

In most mechanical systems, sudden jumps to resonance are undesirable. It is thus important to know, over a wide range of operating parameters, whether jumps exist and if they do whether they are safe, unsafe, determinate, or indeterminate. However, as in all dynamical systems there are uncertainties in the specification of the initial conditions and the parameter values, it is useful to know the probability of restabilization, as it would give a measure of the relative robustness of a system liable to experience these types of bifurcations. By determining critical control parameters which place limits on the type of jumps that occur, and analyzing the probability of restabilization, systems may be designed accordingly such that dangerous frequencies may be avoided or indeed the level of damping level may be prescribed such this type of resonant behavior is suppressed (Soliman and Thompson, 1992b).

Figure 8 show the bifurcation diagram in (F, ω) control space at $\beta = 0.1$. Here, we are mainly concerned with the region around the primary resonance. Lines A and B are saddle-node folds corresponding to jumps to and from resonance. They meet at a cusp point P, which limits the hysteresis domain.

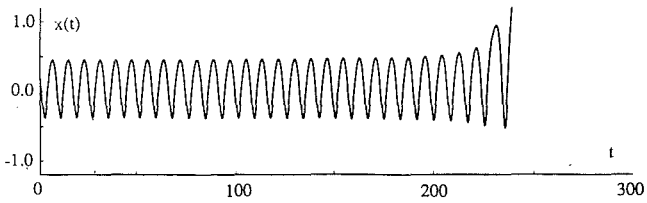

Fig. 7(a)

Unsafe and determinate jump to resonance

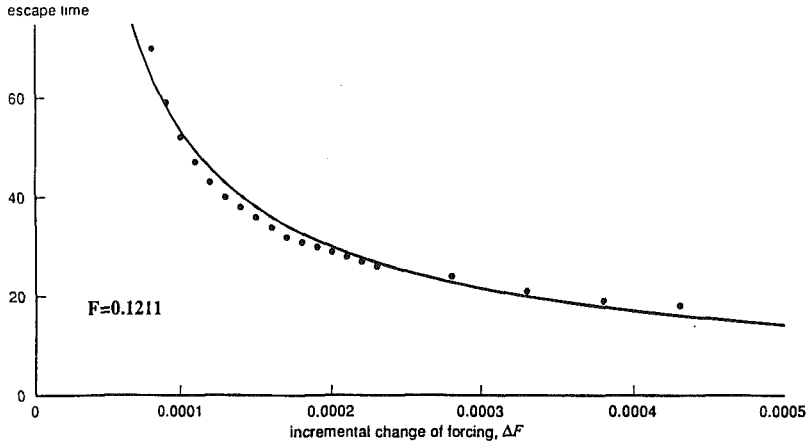

Fig. 7(b)

Fig. 7 As in Fig. 3 but here the jump is *unsafe* at $F = 0.1211$. All small changes in parameters will result in escape.

For forcing levels below P, there are no jumps to resonance. Line C is the first period-doubling flip bifurcation at which the resonance harmonic attractor period doubles to a stable subharmonic of order 2. There is an infinite cascade of these flip bifurcations leading to a chaotic attractor which finally loses its stability at a crisis at E. Line E meets fold line A in a codimension-two bifurcation at Q (Stewart et al., 1991). Line M is the locus of the homoclinic tangency between the stable and unstable manifolds of the hilltop saddle; $W^s(D_h)$ and $W^u(D_h)$. Line H is the heteroclinic tangency between the stable manifold of the hilltop saddle, $W^s(D_h)$, and the unstable manifold of the resonant saddle, $W^u(D_r)$; this bifurcation will generate an indeterminate jump to resonance at the saddle node A.

There are several important parameter values that concern the jump to resonance from fold A. The first critical control parameters, (F^P, ω^P) are those at the cusp point P. For this particular softening system, for frequencies above ω^P or forcing levels below F^P, no jump to resonance occurs. The second critical frequency is (F^T, ω^T) corresponding to the intersection of line H with line A where there is a simultaneous simple saddle-node bifurcation and a heteroclinic tangency between $W^s(D_h)$ and $W^u(D_r)$. This is the smallest forcing is required to cause an indeterminate jump to resonance; an infinite number of fingers of the escaping basin line up along the unstable manifold, $W^u(D_r)$, and simultaneously the saddle-node annihilation occurs. Figure 9 shows the manifold organization close to these parameter values. These manifolds were located numerically using a technique similar to that described by Alexander (1989). This involves mapping backwards in time from a ladder of starts along the ingoing eigenvectors of (D_h) to determine $W^s(D_h)$, and forwards in time along the outgoing eigenvectors to determine $W^u(D_h)$. The Poincaré sections employed are at phase $\phi = 180$ deg. The final critical control parameter is at (F^Q, ω^Q). This corresponds to where line E intersects line A. Just below this forcing level, the jump to resonance is indeterminate; here the outcome is to any available attractor present (including possibly a chaotic attractor) or escape. Just above this forcing level there are no available attractors to jump to, and hence a purely deterministic but unsafe jump occurs.

We may estimate the probability of restabilization at various frequency values along the fold line A, by various realizations of the bifurcation. Figure 10 shows the results in which we have considered an array of different increments of ΔF; here the probability of restabilization was defined as the ratio of those trials which restabilized onto a bounded solution within the potential well, to the total number tested. It can be seen that for frequencies above ω^T all the jumps lead to restabilization. Below ω^T gradually less and less restabilize until about ω^Q in which all the trails escape. In order to understand this behavior we have to consider the organization of the co-existing basins at the saddle-node bifurcation, namely those accumulating on the saddle node. We may say that the degree of erosion of the safe (recipient) basin by the escaping fingers (Soliman and Thompson, 1992a) will determine the probability of restabilization. For low forcing levels, the recipient basin is not highly eroded such that there is a high probability of restabilization. At intermediate forcing levels this erosion will be more developed such that there is a reasonable chance of restabilization (Fig. 10). For bifurcations occurring at forcing levels just below F^Q, where the resonant attractor is chaotic, the safe basin is very small indeed. This is shown in Fig. 11, which when compared to the basins of attraction at the lower forcing values (e.g., see Fig. 4), clearly illustrate a high degree of basin erosion and thus very small chance of restabilization. Indeed it has been shown that even the resonant steady-state attractor lying within these small highly fractal basins is very sensitive to any external noise excitation (Gwinn and Westervelt; 1986; Soliman and Thompson, 1990).

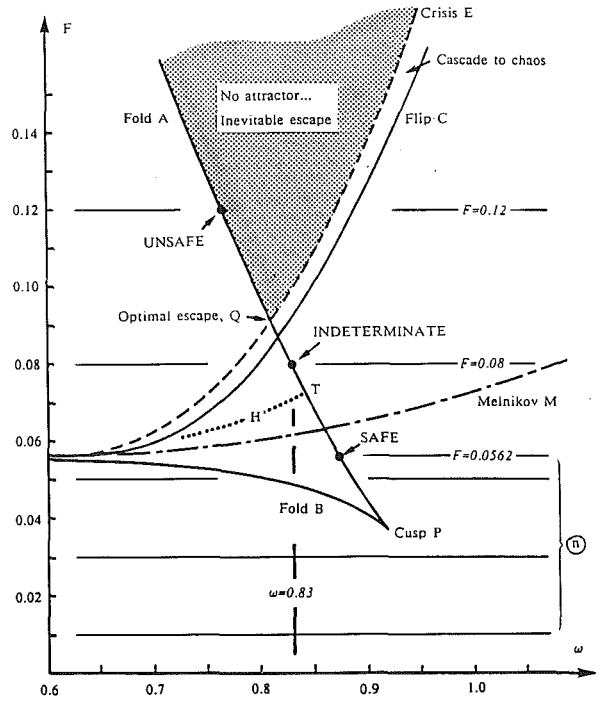

Fig. 8 Bifurcation diagram in the (F, ω) control space at $\beta = 0.1$, showing safe, indeterminate, and unsafe jumps from fold *A*. The marked *F* levels correspond to the earlier figures. Point *T*, where the arc *H* of the hetroclinic tangency meets arc *A* of the saddle-node bifurcation, is the boundary between safe and indeterminate jumps. Point *Q*, where the arc *E* of the crisis line meets arc *A*, is the boundary between indeterminate jumps and unsafe jumps.

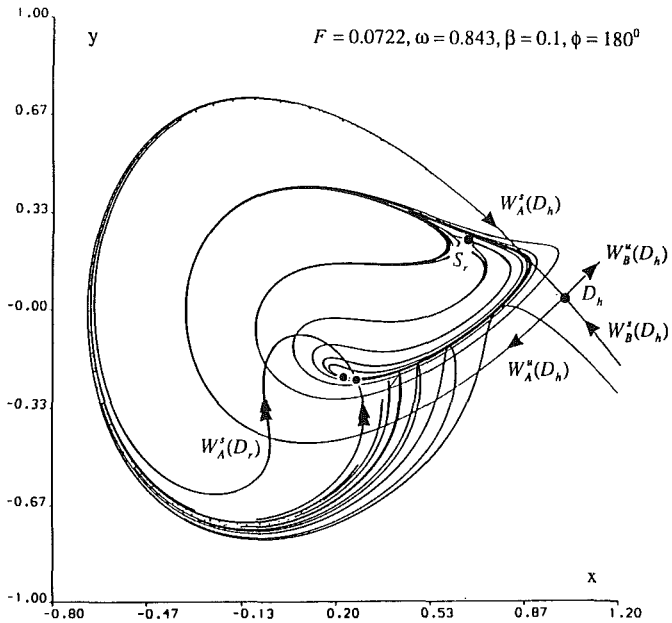

Fig. 9 Fixed points and invariant manifolds at $\beta = 0.1$, $F = 0.0722$, $\omega = 0.843$ close to the optimal escape point at point *T*. This occurs when the saddle-node annihilation occurs *simultaneously* with the hetroclinic event between $W^u_B(D_r)$ and $W^s_A(D_h)$.

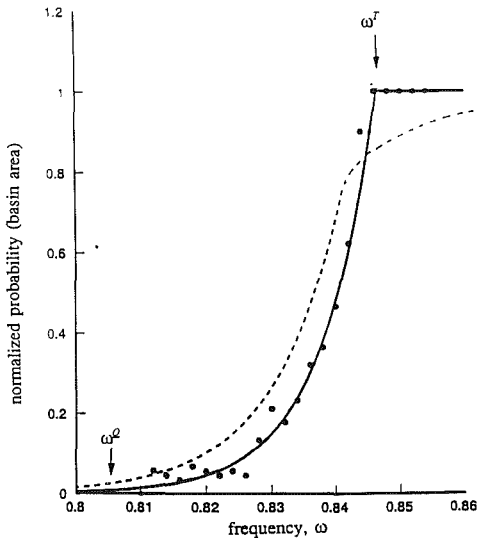

Fig. 10 Estimation of the probability of restabilization from fold *A* in the region between $\omega^T \approx 0.843$ and $\omega^Q \approx 0.805$. Here 50 different increments, ΔF, were chosen from $\Delta F = 0.00001$ to $\Delta F = 0.0005$ and the probability of restabilization was found. The dashed line represents the safe basin area at the saddle-node bifurcation. As the basin becomes eroded, the probability of restabilization decreases.

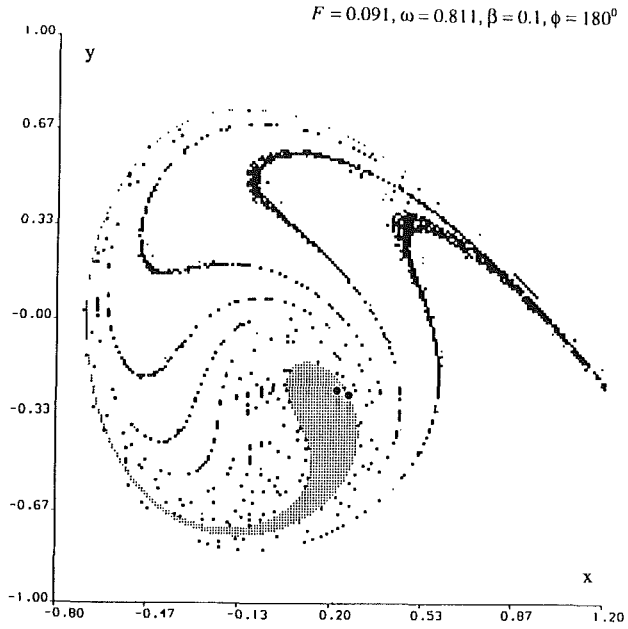

Fig. 11 Fixed points and basins of attraction at $\beta = 0.1$, $F = 0.091$, $\omega = 0.811$ close to the optimal point *Q*. Here the jump to resonance may result in escape or restabilization to any attractor within the well, possibly a chaotic attractor. As can be seen, the recipient safe basin is highly eroded leaving little chance of restabilization.

6 Conclusions

In summary, critical parameters may be determined that put bounds on the type of jump to resonance that occurs for a system with the ability to escape from a potential well. For determinate jumps, the final steady-state response was insensitive to how the bifurcation was realized. Here although the step in the bifurcation parameter determined the transient length, the outcome was always quantitatively and qualitatively the same (i.e., either the system always restabilized or always escaped). However, for indeterminate jumps to resonance, the outcome as well as the transient length was extremely sensitive to how the bifurcation was realized. As in all dynamical systems there are inherent uncertainties in the specification of the initial conditions and parameters this bifurcation was deemed to be unpredictable. By estimating the probability of restabilization after the bifurcation, we may assess the integrity of a physical system that is suspect to this type of resonant behavior.

Acknowledgment

The author would like to thank Prof. J. M. T. Thompson for useful discussions and also the Science and Engineering Research Council of the United Kingdom which have made this work possible. The author would also like to acknowledge that part of this work was carried out while at the University College of London.

References

Alexander, N. A., 1989, "Productional of Computational Portraits of Bounded Invariant Manifolds," *Journal of Sound and Vibration*, Vol. 135, pp. 63–77.

Eschenazi, E., Solari, H. G., and Gilmore, R., 1989, "Basins of Attraction in Driven Dynamical Systems," *Physical Review*, Vol. A39, pp. 2609–2627.

Grebogi, C., Ott, E., and Yorke, J. A., 1983, "Crises, Sudden Changes in Chaotic Attractors and Transients to Chaos," *Physica*, Vol. 7D, pp. 181–191.

Grebogi, C., Ott, E., Romerias, F., and Yorke, J. A., 1987, "Critical Exponents for Crisis-Induced Intermittency," *Physical Review*, Vol. A36, pp. 5365–5380.

Gwinn, E. G., and Westervelt, R. M., 1986, "Fractal Basin Boundaries and Intermittency in the Driven Damped Pendulum," *Physical Review*, Vol. A, pp. 4143–4155.

Huberman, B. A., and Crutchfield, J. P., 1979, "Chaotic States of Anharmonic Systems in Periodic Fields," *Physical Review Letters*, Vol. 43, pp. 1743–1746.

Holmes, P. J., and Moon, F. C., 1983, "Strange Attractors and Chaos in Nonlinear Mechanics," ASME JOURNAL OF APPLIED MECHANICS, Vol. 50, pp. 1021–1032.

Holmes, P. J., and Whitley, D. C., 1983, "On the Attracting Set for Duffing's Equation. II. A Geometrical Model for Moderate Force and Damping," *Physica*, Vol. 7D, pp. 111–123.

McDonald, S. W., Grebogi, C., Ott, E., and Yorke, J. A., 1985, "Fractal Basin Boundaries," *Physica*, Vol. 17D, pp. 125–153.

Moon, F. C., and Li, G. X., 1985, "Fractal Basin Boundaries and Homoclinic Orbits for Periodic Motions in a Two Well Potential," *Physical Review*, Vol. A55, pp. 1439–1442.

Soliman, M. S., and Thompson, J. M. T., 1989, "Integrity Measures Quantifying the Erosion of Smooth and Fractal Basins of Attraction," *Journal of Sound and Vibration*, Vol. 135, pp. 453–475.

Soliman, M. S., and Thompson, J. M. T., 1990, "Stochastic Penetration of Smooth and Fractal Basins of Attraction," *Dynamics and Stability of Systems*, Vol. 5, pp. 281–298.

Soliman, M. S., and Thompson, J. M. T., 1991, "Basin Organization Prior to a Tangled Saddle-Node Bifurcation," *Bifurcation and Chaos*, Vol. 1, pp. 107–118.

Soliman, M. S., and Thompson, J. M. T., 1992a, "Global Dynamics Underlying Sharp Basin Erosion in Nonlinear Driven Oscillators," *Physical Review A*, Vol. 45, pp. 3425–3431.

Soliman, M. S., and Thompson, J. M. T., 1992b, "The Effect of Damping on the Steady-state and Basin Bifurcation Patterns of a Nonlinear Mechanical Oscillator," *Bifurcation and Chaos*, Vol. 2, pp. 81–91.

Stewart, H. B., and Ueda, Y., 1991, "Catastrophes with Indeterminate Outcome," *Proc. Roy. Soc. Lond.*, Vol. A432, pp. 113–123.

Stewart, H. B., Thompson, J. M. T., Lansbury, A. N., and Ueda, Y., 1991, "Generic Patterns of Bifurcations Governing the Escape from a Potential Well," *Bifurcation and Chaos*, Vol. 1, pp. 265–267.

Thompson, J. M. T., 1989, "Chaotic Phenomena Triggering the Escape from a Potential Well," *Proc. Roy. Soc. London*, Vol. A421, pp. 195–225.

Thompson, J. M. T., and Soliman, M. S., 1990, "Fractal Control Boundaries of Driven Oscillators and Their Relevance to Safe Engineering Design," *Proc. Roy. Soc. Lond.*, Vol. A428, pp. 1–13.

Thompson, J. M. T., and Soliman, M. S., 1991, "Indeterminate Jumps to Resonance from a Tangled Saddle-node Bifurcation," *Proc. Roy. Soc. Lond.*, Vol. A432, pp. 101–111.

Van Damme, R., and Valkeerng, P., 1987, "Transient Periodic Behaviour Related to a Saddle-node Bifurcation," *Journal Phys. A: Math. Gen.*, Vol. 20, pp. 4161–4171.

Virgin, L. N., 1986, "Parametric Studies of the Dynamic Evolution through a Fold," *Journal of Sound and Vibration*, Vol. 110, pp. 99–109.

S. T. Ariaratnam
Professor.

Wei-Chau Xie
Asst. Professor.
Assoc. Mem. ASME.

Solid Mechanics Division,
Faculty of Engineering,
University of Waterloo,
Waterloo, Ontario N2L 3G1,
Canada

Lyapunov Exponents and Stochastic Stability of Two-Dimensional Parametrically Excited Random Systems

The variation of the largest Lyapunov exponent for two-dimensional parametrically excited stochastic systems is studied by a method of linear transformation. The sensitivity to random disturbance of systems undergoing bifurcation is investigated. Two commonly occurring examples in structural dynamics are considered, where the random fluctuation appears in the stiffness term or the damping term. The boundaries of almost-sure stochastic stability are determined by the vanishing of the largest Lyapunov exponent of the linearized system. The validity of the approximate results is checked by numerical simulation.

1 Introduction

Investigations of the dynamic stability of elastic systems, such as slender columns and thin plates under axial loading, or buildings, bridges, and aircraft structures under wind loading frequently lead to the study of the dynamical behavior of the solutions of a parameterized family of nonlinear differential equations of the form

$$\dot{\mathbf{x}} = \mathbf{f}(\mathbf{x}, \gamma_0), \quad \mathbf{x} = (x_1\ x_2\ \cdots\ x_n)^T \in \mathbf{R}^n, \quad \mathbf{f}(\mathbf{0}, \gamma_0) = \mathbf{0}, \tag{1}$$

where $\mathbf{f}$ is an n-vector of nonlinear functions of $\mathbf{x}$, and γ_0 is a scalar parameter characterizing the loading condition.

In many practical situations, the loading may be subjected to fluctuations of a stochastic nature. The loading parameter becomes $\gamma = \gamma_0 + \sigma\xi(t)$, where $\xi(t)$ is a zero mean, ergodic random process and σ a parameter characterizing the intensity of random load fluctuation. The governing equation of motion is then modified to the form

$$\dot{\mathbf{x}} = \mathbf{f}(\mathbf{x}, \gamma_0, \sigma\xi(t)), \quad \mathbf{f}(\mathbf{0}, \gamma_0, \sigma\xi(t)) = \mathbf{0}. \tag{2}$$

In order to study the almost-sure stability of the trivial solution of the system (2), it is necessary to determine the largest Lyapunov exponent of the linearized equation

$$\dot{\mathbf{x}} = D_{\mathbf{x}}\mathbf{f}(\mathbf{x}, \gamma_0, \sigma\xi(t))|_{\mathbf{x}=\mathbf{0}}\mathbf{x}. \tag{3}$$

The trivial solution $\mathbf{x} = \mathbf{0}$ is stable or unstable with probability 1 (w.p.1) according to whether the largest Lyapunov exponent is negative or positive. Thus, the vanishing of the largest Lyapunov exponent gives the boundary of stochastic stability w.p.1.

It is also of interest to study the sensitivity to random disturbances of systems undergoing bifurcations. In particular, it is important to know to what extent such perturbations influence the nature and "direction" of the bifurcation when a system is on the verge undergoing a bifurcation. The problems examined in this paper deal with two commonly occurring examples in structural dynamics, namely pitchfork bifurcation and Hopf bifurcation. For both examples, the Lyapunov exponents are evaluated, both analytically and by simulation, from which the almost-sure stability boundaries and the shift in the bifurcation point can be determined.

2 Stochastic Perturbation in Stiffness Parameter

The typical system considered is described by a nondimensionalized equation of motion of the form

$$\ddot{q} + 2\beta\dot{q} - [\gamma_0 + \sigma\xi(t)]q + \alpha q^3 = 0, \quad \alpha, \beta > 0 \tag{4}$$

where γ_0 is the stiffness parameter and $\xi(t)$ is a unit white Gaussian noise process. In the absence of stochastic perturbation, the system undergoes pitchfork bifurcation when γ_0 changes from a negative to a positive value.

Examples of system (4) are found in many applications in mechanics, especially in problems of dynamical stability of elastic systems. In particular, the transverse vibrations of columns and flat plates under axial loading or end displacement are governed by equations of the form (4). The question is: In what direction is the bifurcation point shifted and by what amount as a result of small random fluctuations to the applied axial load or displacement?

In order to study the stochastic stability of the trivial solution $\mathbf{q} = \mathbf{0}$, the variation of the largest Lyapunov exponent λ_q of the linearized system

$$\ddot{q} + 2\beta\dot{q} - [\gamma_0 + \sigma\xi(t)]q = 0 \tag{5}$$

has to be determined.

Contributed by the Applied Mechanics Division of THE AMERICAN SOCIETY OF MECHANICAL ENGINEERS for publication in the ASME JOURNAL OF APPLIED MECHANICS.

Discussion on this paper should be addressed to the Technical Editor, Professor Lewis T. Wheeler, Department of Mechanical Engineering, University of Houston, Houston, TX 77204-4792, and will be accepted until four months after final publication of the paper itself in the ASME JOURNAL OF APPLIED MECHANICS.

Manuscript received by the ASME Applied Mechanics Division, May 3, 1991; final revision, Mar. 30, 1992. Associate Technical Editor: D. J. Inman.

2.1 Lyapunov Exponent by Linear Transformation. The linearized system (5) can be replaced by a pair of Itô stochastic differential equations:

$$dq_1 = q_2 dt,$$
$$dq_2 = -(2\beta q_2 - \gamma_0 q_1)dt + \sigma q_1 dW. \tag{6}$$

Now polar coordinates (a, ϕ) are introduced via

$$q_1 = a\cos\phi, \quad q_2 = a\sin\phi, \tag{7}$$

so that if one defines a pth norm $P = a^p$, a new pair of Itô equations for P and ϕ can be found by applying Itô's lemma:

$$dP = pPf(\phi)dt - pP\sigma\sin\phi\cos\phi\, dW,$$
$$d\phi = -F(\phi)dt - \sigma\cos^2\phi\, dW, \tag{8}$$

where

$$f(\phi) = (1+\gamma_0)\sin\phi\cos\phi - 2\beta\sin^2\phi + \frac{1}{2}\sigma^2[\cos^4\phi + (p-1)\sin^2\phi\cos^2\phi],$$

$$F(\phi) = 1 - (1+\gamma_0)\cos^2\phi + 2\beta\sin\phi\cos\phi + \sigma^2\sin\phi\cos^3\phi.$$

Following Wedig (1988), a linear stochastic transformation is then applied through

$$S = T(\phi)P, \quad P = T^{-1}(\phi)S, \tag{9}$$

where the new norm process S and the scalar function $T(\phi)$ are defined on the stationary phase process ϕ in the range $-\pi/2 \le \phi < \pi/2$. The Itô equation for S is given by

$$dS = \left\{\frac{1}{2}\sigma^2\cos^4\phi\, T_{\phi\phi} + [p\sigma^2\sin\phi\cos^3\phi - F(\phi)]T_\phi + pf(\phi)T\right\} \times P\, dt - \sigma\cos\phi[\cos\phi\, T_\phi + p\sin\phi T]P\, dW. \tag{10}$$

For bounded and nonsingular transformation $T(\phi)$, both processes P and S are expected to have the same stability behavior. Therefore, $T(\phi)$ is chosen so that the drift term of the Itô differential Eq. (10) is independent of the phase process ϕ, so that

$$dS = \Lambda S\, dt + \sigma S g(\phi) dW. \tag{11}$$

Such a transformation T is governed by the following equation:

$$\frac{1}{2}\sigma^2\cos^4\phi T_{\phi\phi} - [1 - (1+\gamma_0)\cos^2\phi + 2\beta\sin\phi\cos\phi + \sigma^2(1-p)\sin\phi\cos^3\phi]T_\phi + \frac{1}{2}p[(p-1)\sigma^2\sin^2\phi\cos^2\phi + \sigma^2\cos^4\phi + 2(1+\gamma_0)\sin\phi\cos\phi - 4\beta\sin^4\phi]T = \Lambda T, \tag{12}$$

which defines an eigenvalue problem for a second-order differential operator with T as the unknown eigenfunction and Λ the associated eigenvalue. The eigenvalue Λ is seen, from (11), to be the Lyapunov exponent of the pth moment. The Lyapunov exponent λ_q of system (16) is related to Λ through the relation (Kozin and Sugimoto, 1977; Molchanov, 1978; Arnold, 1988)

$$\lambda_q = \lim_{p\to 0}\frac{\Lambda}{p}. \tag{13}$$

It now remains to solve the eigenvalue problem (12). Since the coefficients in Eq. (12) are periodic with period π, consider a series expansion of the linear transformation $T(\phi)$ in the form

$$T(\phi) = u_0 + \sum_{k=1}^{\infty}(C_{2k}u_k + S_{2k}v_k), \tag{14}$$

where the notations $C_{2k} = \cos 2k\phi$, $S_{2k} = \sin 2k\phi$ have been used. Substituting from (13) in Eq. (12) results in

$$-n^2\sigma_2(3+4C_2+C_4)\left[\sum_{k=1}^{\infty}(C_{2k}u_k + S_{2k}v_k)\right] + 2n\left\{\frac{(1-\gamma_0)}{2} + [\beta + \sigma_2(1-p)]S_2 - \frac{(1+\gamma_0)}{2}C_2 + \frac{\sigma_2}{2}(1-p)C_4\right\} \times \left[\sum_{k=1}^{\infty}(C_{2k}u_k + S_{2k}v_k)\right] + \left\{\frac{p}{2}\left[\frac{\sigma_2}{2}(p+2) - 2\beta\right] + \frac{p}{2}(1+\gamma_0)S_2 + p(\sigma_2+\beta)C_2 + \frac{p\sigma_2}{4}(2-p)C_4\right\} \times \left[u_0 + \sum_{k=1}^{\infty}(C_{2k}u_k + S_{2k}v_k)\right] = \Lambda\left[u_0 + \sum_{k=1}^{\infty}(C_{2k}u_k + S_{2k}v_k)\right], \quad n = 0, 1, 2, \cdots, \tag{15}$$

where $\sigma_2 = \sigma^2/4$.

Equating the coefficients of like trigonometric terms $\sin 2n\phi$, $\cos 2n\phi$, $n = 0, 1, 2, \cdots$ leads to a system of infinitely many homogeneous linear equations for the unknowns u_0, u_n, v_n, $n \in \mathbf{Z}^+$. The existence of nontrivial solution requires that the determinant of the coefficient matrix be equal to zero, from which the eigenvalue Λ can be obtained in principle. In practice, only a finite number of terms is considered to obtain an approximate value for the eigenvalue Λ.

First-Order Approximation. If only the terms u_0, u_1, v_1 are considered in Eq. (14), the determinant of the coefficient matrix obtained from (15) is of the form

$$\Delta^{(1)} = \begin{vmatrix} a-\Lambda & \frac{1}{2}(p+2)(\beta-\sigma_2) & \frac{1}{4}(p+2)(1+\gamma_0) \\ p(\beta+\sigma_2) & a-(\Lambda+3\sigma_2) & -1+\gamma_0 \\ \frac{1}{2}p(1+\gamma_0) & 1-\gamma_0 & a-(\Lambda+3\sigma_2) \end{vmatrix} = 0, \tag{16}$$

where $a = p[(1/4)\sigma_2(p+2) - \beta]$. Expanding $\Delta^{(1)}$ in powers of σ and neglecting terms of order $O(\sigma^4)$ yields

$$\Delta^{(1)} = -\Lambda^3 + 3(a-2\sigma_2)\Lambda^2 - [(1-\gamma_0)^2 - \frac{1}{8}p(p+2)(1+\gamma_0)^2]\Lambda + p\left\{\frac{\sigma_2}{2}(p+2)(1-\gamma_0^2) - \frac{1}{8}(p+2)(1+\gamma_0)^2(a-3\sigma_2) + (1-\gamma_0)^2\left[\frac{\sigma_2}{4}(p+2) - \beta\right]\right\}.$$

The largest Lyapunov exponent is then obtained as

$$\lambda_q = \lim_{p\to 0}\frac{\Lambda}{p} = \lim_{p\to 0}\frac{\frac{\sigma_2}{2}(p+2)(1-\gamma_0^2) - \frac{1}{8}(p+2)(1+\gamma_0)^2(a-3\sigma_2) + (1-\gamma_0)^2\left[\frac{\sigma_2}{4}(p+2) - \beta\right]}{(1-\gamma_0)^2 - \frac{1}{8}p(p+2)(1+\gamma_0)^2} = -\beta + \frac{8+(1+\gamma_0)^2}{16(1-\gamma_0)^2}\sigma^2, \quad (\sigma\to 0). \tag{17}$$

Wedig (1988) considered the case of finite values of $\gamma_0 < 0$. By setting $\gamma_0 = -1$, one obtains $\lambda = -\beta + \sigma^2/8$, which is the same as that obtained by Wedig (1988).

Second Order Approximation. If five terms u_0, u_1, v_1, u_2, v_2 are considered in Eq. (14), the determinant of the 5×5 coefficient matrix is found to be

$$\Delta^{(2)} = \begin{vmatrix} a-\Lambda & (p+2)(\beta-\sigma_2)/2 & (p+2)(1+\gamma_0)/4 & -(p+2)(p+4)\sigma_2/8 & 0 \\ p(\beta+\sigma_2) & a-(\Lambda+3\sigma_2) & -1+\gamma_0 & (p+4)(\beta-3\sigma_2)/2 & (p+4)(1+\gamma_0)/4 \\ p(1+\gamma_0)/2 & 1-\gamma_0 & a-(\Lambda+3\sigma_2) & -(p+4)(1+\gamma_0)/4 & (p+4)(\beta-3\sigma_2)/2 \\ -p(p-2)\sigma_2/4 & (p-2)(\beta+3\sigma_2)/2 & -(p-2)(1+\gamma_0)/4 & a-(\Lambda+12\sigma_2) & -2(1-\gamma_0) \\ 0 & (p-2)(1+\gamma_0)/4 & (p-2)(\beta+3\sigma_2)/2 & 2(1-\gamma_0) & a-(\Lambda+12\sigma_2) \end{vmatrix} = 0 \quad (18)$$

where $a = p[(1/4)\sigma_2(p+2) - \beta]$.

After some lengthy calculations, the largest Lyapunov exponent is obtained as

$$\lambda_q = -\beta + \frac{\sigma^2}{16} \frac{32(93 - 44\gamma_0 + 142\gamma_0^2 + 20\gamma_0^3 - 3\gamma_0^4) + 12(659 + 126\gamma_0 - 21\gamma_0^2)\sigma^4 + 27\sigma^8}{16(9 - 60\gamma_0 + 118\gamma_0^2 - 60\gamma_0^3 + 9\gamma_0^4) + 24(91 - 64\gamma_0 + 13\gamma_0^2)\sigma^4 + 81\sigma^8}, \quad (\sigma \to 0). \quad (19)$$

The method presented here for obtaining the largest Lyapunov exponent λ is straightforward. The accuracy of the result can be increased by considering more terms in the series expansion (14). However, the amount of calculation increases drastically with increase in the number of terms considered. Equation (19) is again valid only for finite value of γ_0.

2.2 Lyapunov Exponent for Small Values of γ_0. It may be noted that when the stiffness and the damping coefficients γ_0 and β are both zero, the largest Lyapunov exponent has been obtained as $\lambda_q = 0.28931\sigma^{2/3}$ by Ariaratnam and Xie (1990), which implies that for γ_0 in the vicinity of 0, λ_q varies as $\sigma^{2/3}$. Therefore, Eqs. (17) and (19) become increasingly invalid when $\gamma_0 \to 0$, since λ_q varies as the square of σ rather than as $\sigma^{2/3}$. This case is of particular importance in studies of stochastic perturbation of systems in the vicinity of a point of pitchfork bifurcation.

The results of Eq. (19) cannot be used directly for small values of γ_0. In order to use them, a preliminary scaling of the governing equations has to be made. It will be shown that the shift in the bifurcation point is of the order $\sigma^{2/3}$ rather than σ^2 as in the case when the stiffness is *finite*.

Applying the transformation $q = xe^{-\beta t}$ to Eq. (5), one has $\lambda_q = -\beta + \lambda_x$, and

$$\dot{x}_1 = x_2,$$
$$\dot{x}_2 = -\gamma x_1 - \sigma x_1 \xi(t),$$

where $\gamma = -\gamma_0 - \beta^2$. Introducing the scaling $x_1 = y_1$, $x_2 = \sigma^{\alpha_1} y_2$, $\gamma = \sigma^{\alpha_2}\hat{\gamma}$, these equations become

$$\dot{y}_1 = \sigma^{\alpha_1} y_2,$$
$$\dot{y}_2 = -\sigma^{\alpha_2 - \alpha_1}\hat{\gamma} y_1 - \sigma^{1-\alpha_1} y_1 \xi(t),$$

and $\lambda_x = \lambda_y$. For the right sides of both equations to have comparable influence, α_1, α_2 must be chosen so that

$$\sigma^{\alpha_1} = \sigma^{\alpha_2 - \alpha_1} = \epsilon, \quad \sigma^{1-\alpha_1} = \epsilon^{1/2}, \quad 0 < \epsilon \ll 1,$$

which implies that $\alpha_1 = 2/3$, $\alpha_2 = 4/3$, and these equations may now be written as

$$dy_1 = \epsilon y_2 \, dt,$$
$$dy_2 = -\epsilon\hat{\gamma} y_1 \, dt - \epsilon^{1/2} y_1 \, dW,$$

where $\epsilon = \sigma^{2/3}$.

Using the results obtained in (17) and (19), the Lyapunov exponent for system (5) is then found to be

$$\lambda_q = -\beta + \frac{8 + (1-\hat{\gamma})^2}{16(1+\hat{\gamma})^2}\sigma^{2/3} \quad (20a)$$

as the first-order approximation, and

$$\lambda_q = -\beta + \frac{1}{16}\frac{10911 - 104\hat{\gamma} + 4292\hat{\gamma}^2 - 640\hat{\gamma}^3 - 96\hat{\gamma}^4}{2409 + 2496\hat{\gamma} + 2200\hat{\gamma}^2 + 960\hat{\gamma}^3 + 144\hat{\gamma}^4}\sigma^{2/3} \quad (20b)$$

as the second-order approximation, or, after expanding in powers of $\hat{\gamma}$,

$$\lambda_q = -\beta + 0.28308\,\sigma^{2/3}[1.0 - 1.04564\hat{\gamma} + 0.56352\hat{\gamma}^2 + O(\hat{\gamma}^3)],$$

where $\hat{\gamma} = -(\gamma_0 + \beta^2)/\sigma^{4/3}$. In the case of the nilpotent system, i.e., when $\beta = 0$ and $\gamma_0 = 0$, Eq. (20*a*) gives $\lambda_q = 0.28308\,\sigma^{2/3}$, which is consistent with the exact result $0.28931\,\sigma^{2/3}$ obtained by Ariaratnam and Xie (1990).

The validity of the approximate results (20) is checked by a digital simulation. It is seen that the first-order approximation (20*a*) does not give the correct result for small values of γ_0, while the second-order approximation (20*b*) agrees well with that obtained from digital simulation (Fig. 1).

2.3 Lyapunov Exponent for Finite Values of Stiffness. Consider the linearized system (5)

$$\ddot{q} + 2\beta\dot{q} - [\gamma_0 + \sigma\xi(t)]q = 0,$$

when the value of stiffness $-\gamma_0$ is positive and finite. By time scaling $\tau = (-\gamma_0)^{1/2}t$, it can be simplified to

$$q'' + 2\bar{\beta}q' + [1 + \bar{\sigma}\eta(\tau)]q = 0, \quad (21)$$

where $\bar{\beta} = \beta(-\gamma_0)^{-1/2}$, $\bar{\sigma} = \sigma(-\gamma_0)^{-3/4}$, $\eta(\tau)$ is a unit Gaussian white noise process, and a prime denotes differentiation with respect to τ. The Lyapunov exponent $\bar{\lambda}_q$ of system (21) is related to that of (5), λ_q, by

$$\lambda_q = (-\gamma_0)^{1/2}\bar{\lambda}_q. \quad (22)$$

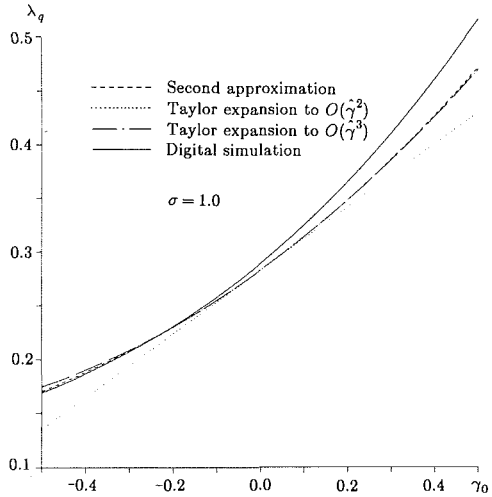

Fig. 1 Largest Lyapunov exponent for $\ddot{q} - [\gamma_0 + \sigma\xi(t)]q = 0$

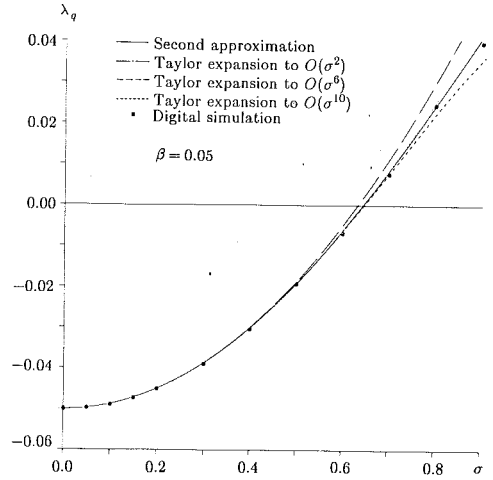

Fig. 2(*a*) Largest Lyapunov exponent for $\ddot{q} + 2\beta q + [1 + \sigma\xi(t)]q = 0$

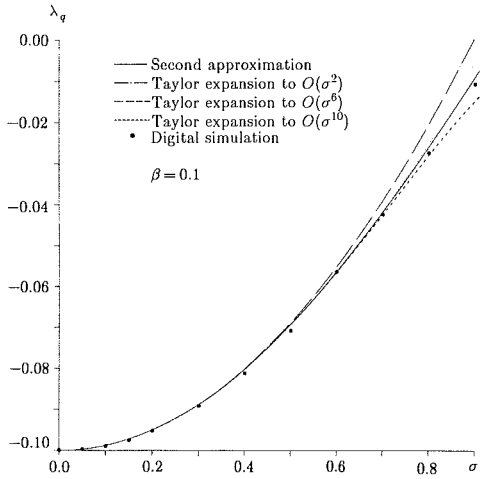

Fig. 2(*b*) Largest Lyapunov exponent for $\ddot{q} + 2\beta q + [1 + \sigma\xi(t)]q = 0$

Suppose the damping constant is small and $\beta \ll (-\gamma_0)^{1/2}$, then all the first approximation methods yield the same expression for the largest Lyapunov exponent for system (21) (see, e.g., Pardoux and Wihstutz, 1988; Ariaratnam and Xie, 1989)

$$\bar{\lambda}_q = -\bar{\beta} + \frac{1}{8}\bar{\sigma}^2. \tag{23}$$

For system (21), the method of stochastic averaging (Stratonovich, 1963; Khas'minskii, 1966) is applicable and can be employed to evaluate the largest Lyapunov exponent, which also gives Eq. (23). This result was first obtained in this manner by Stratonovich and Romanovskii (1958).

The largest Lyapunov exponent of system (5) in the first approximation is then obtained from (22) and (23) as

$$\lambda_q = -\beta + \frac{1}{8}\frac{\sigma^2}{(-\gamma_0)}. \tag{24}$$

For a second-order approximation, Eq. (19) is employed, by setting $\gamma_0 = -1$, to yield

$$\bar{\lambda}_q = -\bar{\beta} + \frac{8192 + 6144\bar{\sigma}^4 + 27\bar{\sigma}^8}{4096 + 4032\bar{\sigma}^4 + 81\bar{\sigma}^8}\frac{\bar{\sigma}^2}{16}, \tag{25}$$

or, after expanding in powers of $\bar{\sigma}$,

$$\bar{\lambda}_q = -\bar{\beta} + \frac{1}{8}\bar{\sigma}^2 - \frac{15}{512}\bar{\sigma}^6 + \frac{1755}{65536}\bar{\sigma}^{10} + O(\bar{\sigma}^{14}). \tag{26}$$

By using the relation (22), the largest Lyapunov exponent of system (5) is obtained as

$$\lambda_q = -\beta + \frac{1}{8}\frac{\sigma^2}{(-\gamma_0)} - \frac{15}{512}\frac{\sigma^6}{(-\gamma_0)^4} + \frac{1755}{65536}\frac{\sigma^{10}}{(-\gamma_0)^7} + O(\sigma^{14}). \tag{27}$$

Pardoux and Wihstutz (1988) also showed that the largest Lyapunov exponent of system (5) was of the form

$$\lambda_q = -\beta + \frac{1}{8}\frac{\sigma^2}{(-\gamma_0)} + O(\sigma^6),$$

but did not calculate the coefficient of σ^6 explicitly.

The correctness of the approximate results for λ_q is checked by computer simulation, with typical plots shown in Figs. 2(*a*) and (*b*) for $\gamma_0 = -1$, $\beta = 0.05$ and $\beta = 0.1$, respectively. It is observed that the second-order approximation (25) agrees with the result obtained by simulation extremely well, while the Taylor series expansion (26) also gives good agreement. Equation (24) is seen to be a valid first-order asymptotic approximation.

By examining the results (20) obtained for the nearly nilpotent system, one may conclude that when γ_0 is in the vicinity of 0, namely when the natural frequency of the system is vanishingly small, the largest Lyapunov exponent grows in the form $\sigma^{2/3}$ when the system is perturbed by stochastic disturbance. The second approximation by linear transformation agrees well with digital simulation, while the first approximation is found to be invalid. On the other hand, when γ_0 is negative and finite, it can always be scaled to -1 by suitable time scaling, and the largest Lyapunov exponent grows according to σ^2. In this case, all the first-order approximate methods yield the same result for the largest Lyapunov exponent, which is seen to be a valid first-order asymptotic approximation, while the second-order approximation gives very good agreement with that obtained by digital simulation even for larger values of σ.

3 Stochastic Perturbation in Damping Coefficient

A typical system perturbed parametrically in the damping term by a stochastic process may be described by the differential equation

$$\ddot{x} + [2\beta + \sigma\xi(t)]\dot{x} + x = f(x, \dot{x}, \sigma\xi(t)), \tag{28}$$

where $\xi(t)$ is a Gaussian broad-band random process and $f(x, \dot{x}, \sigma\xi(t))$ a nonlinear function. The equation of motion for many problems of wind-induced vibration is of the form (28). For example, the vibration of transmission cables, slender bridges, and tall buildings under the action of turbulent wind loads is governed by Eq. (28) (Blevins, 1977; Simiu and Scanlan, 1978) with

$$f(x, \dot{x}, \xi(t)) = \sum_{k=1}^{n} [A_{2k+1} + \alpha_{2k+1}\sigma\xi(t)]\dot{x}^{2k+1}, \tag{29}$$

where A_{2k+1}, α_{2k+1}, $k = 1, 2, \cdots, n$, are deterministic constants.

3.1 Lyapunov Exponent by the Method of Linear Transformation. In this section, the method of linear transformation introduced in Section 2.1 is employed to evaluate the largest Lyapunov exponent of the linearized system

$$\ddot{x} + [2\beta + \sigma\xi(t)]\dot{x} + x = 0, \tag{30}$$

where $\xi(t)$ is approximated by "physical" white noise. Equation (30) can be written in the form of the Stratonovich stochastic differential equations

$$\begin{aligned} d^*x_1 &= x_2 dt, \\ d^*x_2 &= -(x_1 + 2\beta x_2)dt - \sigma x_2 dW, \end{aligned} \tag{31}$$

where $d^*(\cdot)$ denotes the differential in the Stratonovich sense (Stratonovich, 1966) and $W(t)$ is the unit Wiener process. The equivalent Itô equations are

$$dx_1 = x_2 dt,$$
$$dx_2 = -\left[x_1 - \left(\frac{1}{2}\sigma^2 - 2\beta\right)x_2\right]dt - \sigma x_2 dW. \quad (32)$$

As in Section 2.1, one introduces polar coordinates (a, ϕ) defined by (7). The Itô differential equations for the angle ϕ and the pth norm $P = a^p$ are found to be

$$dP = pPf(\phi)dt - pP\sigma\sin^2\phi\, dW,$$
$$d\phi = -F(\phi)dt - \sigma\sin\phi\cos\phi\, dW, \quad (33)$$

where

$$f(\phi) = (-2\beta + \sigma^2)\sin^2\phi + \frac{1}{2}(p-2)\sigma^2\sin^4\phi,$$
$$F(\phi) = 1 + \left(2\beta - \frac{1}{2}\sigma^2\right)\sin\phi\cos\phi - \sigma^2\sin^3\phi\cos\phi.$$

The linear transformation $S = T(\phi)P$, $-(1/2)\pi \le \phi \le (1/2)\pi$, is then applied to yield the Itô differential equation for S,

$$dS = \left\{\frac{1}{2}\sigma^2\sin^2\phi\cos^2\phi\, T_{\phi\phi} + [p\sigma^2\sin^3\phi\cos\phi - F(\phi)]T_\phi + pf(\phi)T\right\}P\,dt - \sigma\sin\phi(\cos\phi\, T_\phi + p\sin\phi\, T)P\,dW. \quad (34)$$

Function $T(\phi)$ is chosen so that the drift term of (34) is independent of ϕ, namely,

$$dS = \Lambda S\,dt + \sigma S g(\phi)dW. \quad (35)$$

From Eqs. (34) and (35), it is found that $T(\phi)$ is the eigenfunction of the following second-order eigenvalue problem

$$\frac{1}{2}\sigma^2\sin^2\phi\cos^2\phi T_{\phi\phi} - \left[1 + \left(2\beta - \frac{1}{2}\sigma^2\right)\sin\phi\cos\phi - (p+1)\sigma^2\sin^3\phi\cos\phi\right]T_\phi + p\left[(-2\beta+\sigma^2)\sin^2\phi + \frac{1}{2}(p-2)\sigma^2\sin^4\phi\right]T = \Lambda T, \quad (36)$$

where Λ is the associated eigenvalue.

Following the procedure as described in Section 2.1, one seeks the eigenfunction $T(\phi)$ in the form of series expansion (13). Since in system (30) the stiffness is finite and is normalized to unity, the observation from the last section shows that the first-order approximation gives a satisfactory approximation result for the Lyapunov exponent. Therefore, one considers only

$$T(\phi) = u_0 + u_1\cos 2\phi + v_1\sin 2\phi. \quad (37)$$

Substituting from (37) in Eq. (36) and equating the coefficient of like terms 1, $\sin 2\phi$, $\cos 2\phi$ while neglecting higher order terms yield

$$\begin{bmatrix} a-\Lambda & \left(1+\frac{1}{2}p\right)\beta - \left(2+p+\frac{1}{2}p^2\right)\sigma_2 & 0 \\ p(\beta - p\sigma_2) & a + \left(\frac{5}{8}p - \frac{1}{4}\right)\sigma_2 - \Lambda & -2 \\ 0 & 2 & a - \left(\frac{5}{8}p + \frac{7}{4}\right)\sigma_2 - \Lambda \end{bmatrix}\begin{Bmatrix} u_0 \\ u_1 \\ v_1 \end{Bmatrix} = 0, \quad (38)$$

where $a = p(-\beta + (1/2)\sigma_2(3/4)p\sigma_2)$, $\sigma_2 = (1/4)\sigma^2$.

For Eq. (38) to have a nonzero solution, it is necessary that the determinant of the coefficient matrix vanishes, which gives

$$-\Lambda^3 + (3a + 2\sigma_2)\Lambda^2 + \left\{p(\beta - p\sigma_2)\left[\left(1+\frac{1}{2}p\right)\beta - \left(2+p+\frac{1}{2}p^2\right)\sigma_2\right] - 2a(a-\sigma_2) - b\right\}\Lambda + a\left\{b - p(\beta - p\sigma_2)\left[\left(1+\frac{1}{2}p\right)\beta - \left(2+p+\frac{1}{2}p^2\right)\sigma_2\right]\left[a - \left(\frac{5}{8}p+\frac{7}{4}\right)\sigma_2\right]\right\} = 0, \quad (39)$$

where

$$b = \left[a + \left(\frac{5}{8}p - \frac{1}{4}\right)\sigma_2\right]\left[a - \left(\frac{5}{8}p + \frac{7}{4}\right)\sigma_2\right] + 4.$$

The cubic Eq. (39) can be solved to yield the largest Lyapunov exponent for system (30). After neglecting higher order terms, the result is

$$\lambda = \lim_{p\to 0}\frac{\Lambda}{p} = -\beta + \frac{1}{2}\sigma_2 = -\beta + \frac{1}{8}\sigma^2, \quad (40)$$

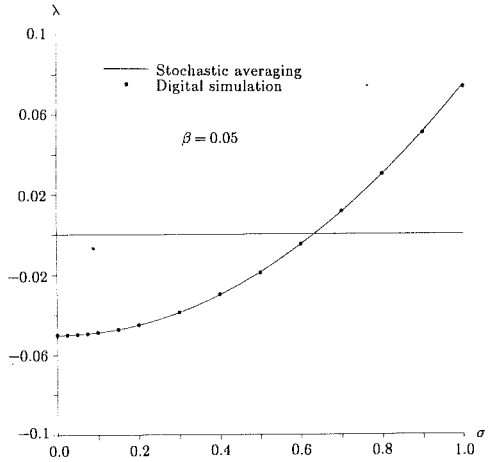

Fig. 3(*a*) Largest Lyapunov exponent for $\ddot{x} + [2\beta + \sigma\xi(t)]\dot{x} + x = 0$

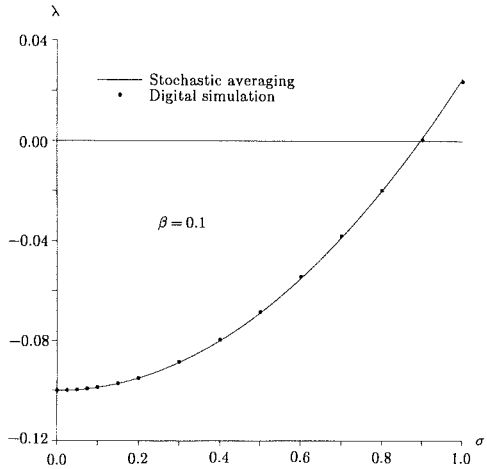

Fig. 3(*b*) Largest Lyapunov exponent for $\ddot{x} + [2\beta + \sigma\xi(t)]\dot{x} + x = 0$

which is the same as that obtained by other approximate methods such as asymptotic expansion of integrals and stochastic averaging (Ariaratnam and Xie, 1989). The almost-sure stability region is found to be $\sigma^2 \leq 8\beta$.

The validity of the approximate result (40) is checked by a digital simulation with typical plots shown in Figs. 3(a) and 3(b). It can be seen that the first-order approximation (40) agrees well with numerical simulation, especially for small values of the damping coefficient β. This is to be expected, since for system (30), the natural frequency of the system or the coefficient of x is finite and can be normalized to unity. This observation is consistent with that seen in Section 2. Hence, it is not necessary to obtain the second-order approximation.

4 Conclusion

The Lyapunov exponents of two-dimensional parametrically excited stochastic systems have been investigated. The sensitivity to random disturbance of systems undergoing bifurcations has been studied. Two commonly occurring examples in structural dynamics, namely pitchfork bifurcation and Hopf bifurcation, were considered. The almost-sure stability conditions were obtained by setting the largest Lyapunov exponent of the system to zero. The validity of the asymptotic results has been checked by digital computer simulation.

Acknowledgment

This research was supported by the Natural Sciences and Engineering Research Council of Canada through grant A-1815.

References

Ariaratnam, S. T., and Xie, Wei-Chau, 1989, "Lyapunov Exponents and Stochastic Bifurcations," *Proceedings of IUTAM Symposium on Nonlinear Dynamic Engineering Systems*, Stuttgart, W. Germany, Aug. 21–25, W. Schiehlen, ed., Springer-Verlag, Berlin, pp. 1–8.

Ariaratnam, S. T., and Xie, Wei-Chau, 1990, "Lyapunov Exponent and Rotation Number of a Two-Dimensional Nilpotent Stochastic System," *Dynamics and Stability of Systems*, Vol. 5, No. 1, pp. 1–9.

Arnold, L., 1984, "A Formula Connecting Sample and Moment Stability of Linear Stochastic Systems," *SIAM Journal of Applied Mathematics*, Vol. 44, pp. 793–802.

Blevins, R. D., 1977, *Flow-Induced Vibration*, Van Nostrand Reinhold Co., New York.

Khas'minskii, R. Z., 1966, "A Limit Theorem for the Solutions of Differential Equations with Random Right-Hand Sides," *Theory of Probability and Its Applications*, Vol. 11, pp. 390–406 (English translation).

Kozin, F., and Sugimoto, S., 1977, "Relations Between Sample and Moment Stability for Linear Stochastic Differential Equations," *Proceedings of the Conference on Stochastic Differential Equations and Applications*, Park City, UT, J. David Mason, ed., Academic Press, New York.

Molchanov, S. A., 1978, "The Structure of Eigenfunctions of One-Dimensional Unordered Structures," *Math USSR Izvestija*, Vol. 12, pp. 69–101 (in Russian).

Pardoux, E., and Wihstutz, V., 1988, "Lyapunov Exponent and Rotation Number of Two-Dimensional Linear Stochastic Systems with Small Diffusion," *SIAM Journal of Applied Mathematics*, Vol. 48, No. 2, pp. 442–457.

Simiu, E., and Scanlan, R. H., 1978, *Wind Effects on Structures: An Introduction to Wind Engineering*, John Wiley and Sons, New York.

Stratonovich, R. L., and Romanovskii, Yu. M., 1958, "Parametric Effect of a Random Force on Linear and Non-Linear Oscillatory Systems," *Nauchnye doklady vysshei shkoly fiziko-mat. nauk.*, Vol. 3, reprinted in *Non-Linear Transformations of Stochastic Processes*, P. I. Kuznetsov, R. L. Stratonovich, and V. I. Tikhonov, eds., Pergamon Press, pp. 322–326 (English translation).

Stratonovich, R. L., 1963, *Topics in the Theory of Random Noise*, Vol. 1, Gordon and Breach, New York (English translation).

Stratonovich, R. L., 1966, "A New Representation for Stochastic Integrals and Equations," *SIAM Journal on Control*, Vol. 4, pp. 362–371.

Wedig, W., 1988, "Lyapunov Exponents of Stochastic Systems and Related Bifurcation Problems," *Stochastic Structural Dynamics—Progress in Theory and Applications*, S. T. Ariaratnam, G. I. Schuëller, and I. Elishakoff, eds., Elsevier, New York, pp. 315–327.

Convex Models of Uncertainty in Radial Pulse Buckling of Shells

Y. Ben-Haim
Faculty of Mechanical Engineering,
Technion—Israel Institute of Technology,
Haifa 32000, Israel
Assoc. Mem. ASME

The buckling of shells subject to radial impulse loading has been studied by many investigators, and it is well known that the severity of the buckling response is greatly amplified by initial geometrical imperfections in the shell shape. Traditionally, these imperfections have been modeled stochastically. In this study convex models provide a convenient alternative to probabilistic representation of uncertainty. Convex models are well suited to the limitations of the available information on the nature of the geometrical uncertainties. An ellipsoidal convex model is employed and the maximum pulse response is evaluated. The ellipsoidal convex model is based on three types of information concerning the initial geometrical uncertainty of the shell: (1) which mode shapes contribute to the imperfections, (2) bounds on the relative amplitudes of these modes, and (3) the magnitude of the maximum initial deviation of the shell from its nominal shape. The convex model analysis yields reasonable results in comparison with a probabilistic analysis due to Lindberg (1992a,b). We also consider localized imperfections of the shell. Results with a localized envelope-bound convex model indicate that very small regions of localized geometrical imperfections result in buckling damage which is a substantial fraction of the damage resulting from full circumferential initial imperfection.

1 Introduction

In a series of two papers Lindberg (1992a,b) applies convex models to the representation of geometrical uncertainty in radial pulse buckling of shells. He skillfully demonstrates both the usefulness and the limitations of this method of handling uncertainty. In the present paper some extensions of the convex models employed by Lindberg are proposed and their application to radial pulse buckling is examined.

The uniform bound convex model constrains the initial geometrical imperfection of the shell shape between an upper bound, $+\hat{\delta}$, and a lower bound, $-\hat{\delta}$. This convex model of uncertainty was used by Lindberg (1992a) in analysis of radial pulse buckling, in the analysis of static axial buckling of shells by Ben-Haim and Elishakoff, (1989) and in other applications (Ben-Haim and Elishakoff, 1990). The imperfection parameter $\hat{\delta}$ promises to be a useful quality control parameter during or after manufacture of the shell. However, as Lindberg (1992a) very convincingly demonstrates, the uniform bound convex model is rather conservative in comparison with probabilistic models.

The conservatism of the uniform bound model is explained as arising from the contribution of extraneous modes and excessive amplitudes to the imperfection shape. To overcome this limitation Lindberg (1992b) employs an ellipsoidal convex model defined in the space of Fourier coefficients. In this convex model the Fourier coefficients of a selected range of mode numbers are constrained to fall in an ellipsoid (see Ben-Haim and Elishakoff, 1990, for further discussion of this convex model). The shape of this ellipsoid can be based on measured Fourier spectra of imperfections (see measurements by Kirkpatrick and Holmes, 1989). Determination of the size of the ellipsoid remains an open question, which is discussed in this paper. Our approach is to relate the size parameter of the ellipsoid to the maximum initial deflection of the shell. By fixing the size of the ellipsoid in terms of the initial shell deflection, we are able to relate the maximum response after impulse loading to this convenient and practical quality control parameter.

The formalism of multimode buckling is summarized in Section 2 and the convex models employed are briefly discussed in Section 3. In Section 4, the size of ellipsoid is related to the maximum deflection parameter $\hat{\delta}$ of the uniform bound model. In this way the attractive quality control features of the uniform bound model are transferred to the more realistic ellipsoidal model. Then, in Section 5, the ellipsoidal model is extended to include the possibility that the nominal imperfection of the shell shape deviates from zero. In Section 6 a different convex model is discussed, which allows one to study spatial localization of the imperfections.

2 Multimode Buckling

We will follow the notation of Lindberg (1992b) in describing the buckling response of a thin shell to a radial pressure im-

Contributed by the Applied Mechanics Division of THE AMERICAN SOCIETY OF MECHANICAL ENGINEERS for publication in the ASME JOURNAL OF APPLIED MECHANICS.

Discussion on this paper should be addressed to the Technical Editor, Professor Lewis T. Wheeler, Department of Mechanical Engineering, University of Houston, Houston, TX 77204-4792, and will be accepted until four months after final publication of the paper itself in the ASME JOURNAL OF APPLIED MECHANICS.

Manuscript received by the ASME Applied Mechanics Division, Sept. 10, 1991; final revision, Feb. 25, 1992. Associate Technical Editor: R. M. Bowen.

pulse. This method of solution of pulsed buckling phenomena was derived by Abrahamson and Goodier (1962) and is extensively discussed in Lindberg and Florence (1987). Linear deflection equations are obtained by treating the material as perfectly plastic, by relating the initial geometrical imperfections to the initial radial velocity of the shell, and by considering only short times after application of the load.

The initial deviation of the shell from its nominal shape, as a function of azimuthal position θ, is described by a truncated Fourier series as

$$\delta(\theta)=\sum_{n=2}^{N}(a_n\cos n\theta+b_n\sin n\theta)=D^T\varphi(\theta) \tag{1}$$

where D is the vector of Fourier coefficients

$$D^T=(a_2,\ a_3,\ \ldots,\ a_N,\ b_2,\ b_3,\ \ldots,\ b_N) \tag{2}$$

and

$$\varphi(\theta)^T=(\cos 2\theta,\ \cos 3\theta,\ ,\ \ldots,\ \cos N\theta,\ \sin 2\theta,\ \sin 3\theta,\ \ldots,\ \sin N\theta). \tag{3}$$

The flexural deformation of the shell at normalized time τ after the impulse loading and at azimuthal position θ is

$$u(\theta,\tau)=\sum_{n=2}^{N}[a_nG_n(\tau)\cos n\theta+b_nG_n(\tau)\sin n\theta]=D^T\phi(\theta,\tau) \tag{4}$$

where

$$\phi(\theta,\tau)^T=(G_2(\tau)\cos 2\theta,\ G_3(\tau)\cos 3\theta,\ \ldots,\ G_N(\tau)\cos N\theta,\ G_2(\tau)\sin 2\theta,\ G_3(\tau)\sin 3\theta,\ \ldots,\ G_N(\tau)\sin N\theta). \tag{5}$$

The amplification function is

$$G_n(\tau)=\frac{1}{\eta^2-1}\left[1-\begin{matrix}\cosh\\ \cos\end{matrix}\ p_n\tau\right]\quad\begin{matrix}\eta<1\\ \eta>1\end{matrix} \tag{6}$$

where

$$\eta=n/s,\quad p_n=\sqrt{|[\eta^2-(1/s^2)][1-\eta^2]|},\quad \tau=\frac{s^2c_p\alpha}{a}\,t \tag{7}$$

and

$$\alpha=\frac{h}{a\sqrt{12}},\quad s^2=\frac{\sigma_y}{E_h\alpha^2},\quad c_p=\sqrt{\frac{E_h}{\rho}} \tag{8}$$

where h is the wall thickness, a is the shell radius, σ_y is the yield stress, E_h is the strain-hardening modulus, and ρ is the density. The amplification function for $\eta=1$ is $G_n(\tau)=\tau^2/2$.

3 Convex Models

A convex model is a set of functions. Each function represents a possible realization of an uncertain, spatially varying quantity. Convex models are used here to represent the spatial uncertainty of the initial imperfection profile, $\delta(\theta)$. Following are six different convex models for describing uncertainty in the initial radial deflection $\delta(\theta)$ of the shell.

The *uniform bound convex model*:

$$R_{\mathrm{UB}}=\{\delta(\theta):|\delta(\theta)|\le\hat{\delta}\}. \tag{9}$$

This is the simplest model, easy to apply and attractive because very little information is needed for its implementation and because the single parameter $\hat{\delta}$ is useful as a quality control variable.

The *envelope bound convex model* is a variation on the uniform bound model. In its most general form the initial imperfection is constrained to vary within a specified envelope:

$$R_{\mathrm{EB}}=\{\delta(\theta):\ \ \delta_1(\theta)\le\delta(\theta)\le\delta_2(\theta)\} \tag{10}$$

where $\delta_1(\theta)$ and $\delta_2(\theta)$ are specified functions.

A common application of this type of convex model is for representation of localized imperfections. (See Ben-Haim (1990) for a typical application.) For example, if the imperfection is uniformly bounded in the angular range from θ_1 to θ_2 and zero outside of this region, then the envelope functions $\delta_1(\theta)$ and $\delta_2(\theta)$ are chosen as

$$\delta_n(\theta)=\begin{cases}0, & \theta\notin[\theta_1,\ \theta_2]\\ (-1)^n\hat{\delta}, & \theta\in[\theta_1,\ \theta_2]\end{cases},\quad n=1,\ 2. \tag{11}$$

The resulting special case of the envelope bound convex model is called a *localized uniform bound convex model*, and is denoted R_{LUB}. This model would be useful for representing initial imperfections in the localized loading experiments reported by Kirkpatrick and Holmes (1989) or the localized imperfections in the constrained shells studied by Li and Kyriakides (1991). Localized imperfections will be discussed further in Section 6.

The *band limited uniform bound convex model* is a different modification of the uniform bound model. The imperfection function is uniformly bounded but limited to a specific range of mode shapes,

$$R_{\mathrm{BLUB}}=\left\{\delta(\theta):\ \ \delta(\theta)=\sum_{n=N_0}^{N_1}[a_n\cos n\theta+b_n\sin n\theta],\quad |\delta(\theta)|\le\hat{\delta}\right\}. \tag{12}$$

The motivation for this modification of the uniform bound model is that the band limitation eliminates the unrealistic high-mode numbers from the initial imperfections. The pertinent mode numbers N_0 and N_1 can be obtained from studies such as Kirkpatrick and Holmes (1989). However, this model is difficult to handle both numerically and analytically. The ellipsoidal models are much more convenient.

The *ellipsoidal convex model*:

$$R_{\mathrm{ELP}}=\{D:\ \ D^TW\,D\le\kappa^2\}, \tag{13}$$

where D is the vector of Fourier coefficients of the initial deflection, defined in Eq. (2).

Lindberg (1992b) uses two different choices of the matrix W, which is square and of dimension $2(N-1)$ and determines the shape of the bounding ellipsoid. In the absence of specific knowledge of the variation of the Fourier coefficients, W equals the identity matrix

$$W=I. \tag{14}$$

Alternatively, one may choose W to be diagonal, where the inverse of each diagonal element approximates the square of the variation of the corresponding Fourier coefficient.

Again, following the notation of Lindberg (1992b), the variation of the Fourier amplitudes measured by Kirkpatrick and Holmes (1989) can be approximated by the function

$$f_p(n)=\begin{cases}1 & \text{for } n<n_c\\ (n_c/n)^p & \text{for } n\ge n_c\end{cases}. \tag{15}$$

The constant p is typically between 1 and 2. Then W is chosen as

$$W=\mathrm{diag}\{f_p^{-2}(2),\ f_p^{-2}(3),\ \ldots,\ f_p^{-2}(N),\ f_p^{-2}(2),\ f_p^{-2}(3),\ \ldots,\ f_p^{-2}(N)\}. \tag{16}$$

An important problem raised by Lindberg (1992b) is determination of the size parameter κ. In Section 4 we will determine κ, after having chosen W, so that the maximum initial deflection equals the quantity $\hat{\delta}$ as it is defined in the uniform bound model. The parameter $\hat{\delta}$ is of considerable practical value, as Lindberg (1992a) emphasizes and as discussed in Section 1.

The *shifted ellipsoidal convex model*:

$$R_{\mathrm{SELP}}=\{D:\ \ (D-h)^TW(D-h)\le\kappa^2\}. \tag{17}$$

The motivation for this convex model is that the Fourier

coefficients D of the initial deflection may have a nominal value, h, different from zero. In fact, one could interpret the imperfection data discussed by Kirkpatrick and Holmes (1989) as representing nominal or typical values of the Fourier coefficients, rather than the typical spread of these coefficients. Kirkpatrick and Holmes in fact may have this in mind when they write: "The imperfection data banks show that imperfections have characteristic distributions that include decreasing modal amplitudes with increasing mode number." (1989, p. 1076).

One could thus choose the vector h in Eq. (17) as

$$h^T = (f_p(2), f_p(3), \ldots, f_p(N), f_p(2), f_p(3), \ldots, f_p(N)). \tag{18}$$

Again, κ can be related to $\hat{\delta}$, as for the regular ellipsoidal model. Results with this model will be presented in Section 5.

4 Ratio of Peaks Based on the Ellipsoidal Model

Let us consider the ellipsoidal model defined in Eq. (13). We will choose W as either the identity matrix or the diagonal matrix obtained from the function $f_p(n)$. Then our tasks will be

1 choose κ so that the greatest initial deflection of any profile in R_{ELP} equals $\hat{\delta}$.
2 evaluate the ratio of the maximum pulse response (Eq. (4)) to $\hat{\delta}$. This dimensionless ratio expresses the degree to which the initial imperfections are amplified in response to the pulse loading. This "ratio of peaks" will be compared with the probabilistic ratio of peaks from Lindberg (1992a).

The initial deflection is $\delta(\theta) = D^T\varphi(\theta)$ as in Eq. (1). We wish to choose κ, the size of the initial imperfection ellipsoid, so that the greatest initial deflection of any profile equals $\hat{\delta}$. Thus, we choose κ so as to satisfy

$$\hat{\delta} = \max_{\theta} \max_{D \epsilon R_{\text{ELP}}} D^T\varphi(\theta). \tag{19}$$

We begin by seeking $\max_{D\epsilon R_{\text{ELP}}} D^T\varphi(\theta)$. We are looking for the maximum of a linear function, $D^T\varphi(\theta)$, on the convex set R_{ELP}. The maximum occurs on the boundary, so this is an elementary optimization. Using the method of Lagrange multipliers[1] one finds

$$\max_{D \epsilon R_{\text{ELP}}} D^T\varphi(\theta) = \kappa\sqrt{\varphi(\theta)^T W^{-1}\varphi(\theta)}. \tag{20}$$

Now choose κ to satisfy Eq. (19):

$$\kappa = \frac{\hat{\delta}}{\max_\theta \sqrt{\varphi(\theta)^T W^{-1}\varphi(\theta)}}. \tag{21}$$

Having now derived an expression for the size of the ellipsoid of initial imperfection profiles, we can proceed to evaluate the ratio of peaks. The shell deformation at position θ and time τ is $u(\theta, \tau) = D^T\phi(\theta, \tau)$, as in Eq. (4). The greatest deflection in response to a radial impulse is the maximum of $u(\theta, \tau)$ on the set R_{ELP} of allowed initial imperfection profiles

$$u_{\max}(\theta, \tau) = \max_{D \epsilon R_{\text{ELP}}} D^T\phi(\theta, \tau). \tag{22}$$

This is the maximum of a linear function, $D^T\phi(\theta, \tau)$, on a convex set, R_{ELP}, and thus occurs on the boundary of the set. The method of Lagrange multipliers again provides an immediate solution:

$$u_{\max}(\theta, \tau) = \kappa\sqrt{\phi(\theta, \tau)^T W^{-1}\phi(\theta, \tau)} \tag{23}$$

which is precisely what Lindberg (1992a, Eq. (22)) obtained.

Let us assume that W is diagonal and that the first $N-1$ and last $N-1$ elements along the diagonal are the same. That is

$$W_{nn} = W_{N-1+n,N-1+n},\ n = 1, \ldots, N-1. \tag{24}$$

This condition holds for both Eq. (14) and Eq. (16). Then, using Eq. (21) in Eq. (23), the dependence on θ vanishes and one finds the maximum response related to the maximum initial deflection as

$$u_{\max}(\tau) = \hat{\delta}\sqrt{\frac{\sum_{n=2}^{N} G_n^2(\tau)/W_{n-1,n-1}}{\sum_{n=2}^{N} 1/W_{n-1,n-1}}}. \tag{25}$$

This relation indicates that the maximum pulse deflection is a weighted average of the amplification functions, $G_n^2(\tau)$. The average is weighted by the terms $1/W_{nn}$. The specific choice of W determines the relative contribution of the various modes to the predicted maximum response. Furthermore, the variation of $u_{\max}$ with N, the greatest mode number, depends strongly on the choice of W, as we will see.

The ratio of peaks is defined as the ratio of the maximum pulse response to the maximum initial deflection. The convex model ratio of peaks for the two choices of W, Eqs. (14) and (16) are, respectively,

$$\frac{u_{\max}}{\hat{\delta}} = \sqrt{\frac{1}{N-1}\sum_{n=2}^{N} G_n^2(\tau)} \tag{26}$$

and

$$\frac{u_{\max}}{\hat{\delta}} = \sqrt{\frac{\sum_{n=2}^{N} G_n^2(\tau) f_p^2(n)}{\sum_{n=2}^{N} f_p^2(n)}}. \tag{27}$$

A prominent difference between these two predictions of $u_{\max}/\hat{\delta}$ is that Eq. (26) weights the amplification function uniformly throughout the range of mode numbers from 2 to N, while Eq. (27) weights the first n_c+1 modes equally and the remaining modes are apportioned a weight which decreases as $(n_c/n)^{2p}$. If N is not too large, we should thus expect Eq. (26) to predict larger values of $u_{\max}/\hat{\delta}$ than Eq. (27), because the latter model will depress the modes for which G_n^2 is large. On the other hand, as the number of modes becomes very large, the right-hand side of Eq. (26) converges to zero, while the right-hand side of Eq. (27) will converge to a fixed positive value (if $p > 1/2$).

Table 1 shows results of numerical evaluation of Eqs. (26) and (27), for various values of the greatest mode number, N, and for $p=1$ an $p=2$ in the function $f_p(n)$. The third and fourth columns show the value of $u_{\max}/\hat{\delta}$, which is the convex model version of the ratio of peaks. The probabilistic ratio of peaks at three standard deviations from the mean is 12.027 (for $p=1$) or 6.631 (for $p=2$), as presented in Table 2 of Lindberg (1992a). These probabilistic results by Lindberg are based on Monte Carlo generation of shell populations with random imperfections. The Fourier coefficients of the initial imperfections in Lindberg's work are assumed to be normally distributed with zero mean and standard deviations which vary with the mode number. Columns five and six of Table 1 here show the ratio of the convex to the probabilistic ratio of peaks.

[1]Such optimizations occur frequently in applying convex models. Examples can be found on pp. 139–140 and elsewhere in Ben-Haim and Elishakoff (1990).

Table 1 Comparison of convex and probabilistic ratio of peaks based on the ellipsoidal convex model; $s=20$, $\tau=6$, $n_c=5$

N	p	$u_{max}/\hat{\delta}$ $(W=I)$	$u_{max}/\hat{\delta}$ $(W=\{f_p\})$	Conv/Prb $(W=I)$	Conv/Prb $(W=\{f_p\})$
10	1	3.6771	2.5658	0.306	0.213
	2	3.6771	1.7679	0.555	0.267
12	1	5.7791	3.6345	0.481	0.302
	2	5.7791	2.1816	0.872	0.329
15	1	9.6465	5.4234	0.802	0.451
	2	9.6465	2.7550	1.455	0.415
17	1	12.002	6.4500	0.998	0.536
	2	12.002	3.0329	1.810	0.457
20	1	13.721	7.2606	1.141	0.604
	2	13.721	3.2253	2.069	0.486
22	1	13.561	7.3525	1.128	0.611
	2	13.561	3.2492	2.045	0.490
25	1	12.739	7.3026	1.059	0.607
	2	12.739	3.2495	1.921	0.490
30	1	11.600	7.2282	0.964	0.601
	2	11.600	3.2481	1.749	0.490
40	1	10.006	7.1357	0.832	0.593
	2	10.006	3.2468	1.509	0.490
50	1	8.9285	7.0814	0.742	0.589
	2	8.9285	3.2463	1.346	0.490
75	1	7.2659	7.0103	0.604	0.583
	2	7.2659	3.2460	1.096	0.490
100	1	6.2819	6.9754	0.522	0.580
	2	6.2819	3.2459	0.947	0.490
150	1	5.1206	6.9408	0.426	0.577
	2	5.1206	3.2459	0.772	0.490
200	1	4.4309	6.9237	0.368	0.576
	2	4.4309	3.2458	0.668	0.489

Table 2 Comparison of convex and probabilistic ratio of peaks based on the ellipsoidal convex model; $s=20$, $\tau=6$, $N=200$

n_c	p	$u_{max}/\hat{\delta}$ $(W=\{f_p\})$	Conv/Prb $(W=\{f_p\})$
2	1	5.0236	0.418
	2	1.0584	0.160
5	1	6.9237	0.576
	2	3.2458	0.490
8	1	8.4852	0.706
	2	6.0186	0.908

The most striking aspect of the results in Table 1 is that the convex model ratio of peaks is generally less than the probabilistic value. This means that the convex model is generally *less* conservative than the probabilistic model. This is in strong contrast to the uniform bound model studied by Lindberg (1992a). The explanation is that the ellipsoidal model strongly constrains the initial deflections, even though the size of the ellipsoid is such that the magnitude of the largest initial deflection equals $\hat{\delta}$, as in the uniform bound model.

The second point of interest in Table 1 is the dependence of the comparison on the number of modes included in the convex model. As expected, the convex model for $W=I$ predicts greater ratio of peaks than the model in which W is based on $f_p(n)$. Furthermore, the former model varies much more strongly with N. The range of N values of real interest is probably for N no less than about 50, since these modes are all excited in the buckling process. On the other hand, $N>200$ is an unrealistic model since these very high modes are not involved.

The results for the ellipsoidal model with W based on $f_p(n)$ are fairly sensitive to the choice of the cutoff mode number, n_c, above which $f_p(n)\leq 1$. This is illustrated in Table 2. The convex model ratio of peaks increases with n_c. This is because the large values of the amplification function are less strongly damped when n_c is large.

5 Ratio of Peaks Based on the Shifted Ellipsoidal Model

Now we consider the shifted ellipsoidal convex model, Eq. (17). First we choose the size parameter κ to cause the greatest initial deflection to equal $\hat{\delta}$. Then we present the maximum deflection in response to radial impulse loading and evaluate the ratio-of-peaks.

The maximum initial deflection at angle θ is

$$\hat{u}_{init}(\theta)=\max_{D\in R_{SELP}} D^T\varphi(\theta) \tag{28}$$

This maximum is found with the usual Lagrange technique. Since we are optimizing a linear function on a convex set, one maximizes $D^T\varphi(\theta)$ subject to the equality constraint $(D-h)^T W(D-h)=\kappa^2$. If W is diagonal and satisfies the symmetry condition of Eq. (24), then one obtains

$$\hat{u}_{init}(\theta)=h^T\varphi(\theta)+\kappa\sqrt{\sum_{n=1}^{N-1}1/W_{nn}}. \tag{29}$$

Now the size parameter, κ, is chosen so that $\hat{\delta}$ equals the greatest value which $\hat{u}_{init}(\theta)$ obtains for any value of θ. That is, we choose κ to satisfy

$$\hat{\delta}=\max_{\theta}\hat{u}_{init}(\theta) \tag{30}$$

which results in

$$\kappa=\frac{\hat{\delta}-\max_\theta h^T\varphi(\theta)}{\sqrt{\sum_{n=2}^{N}1/W_{n-1,n-1}}}. \tag{31}$$

The maximum pulse response is found by means of the usual Lagrange optimization technique. One maximizes $D^T\phi(\theta,\tau)$ subject to the constraint $(D-h)^T W(D-h)=\kappa^2$. If W is diagonal and satisfies the symmetry condition of Eq. (24), then one obtains

$$u_{max}(\theta,\tau)=h^T\phi(\theta,\tau)+\kappa\sqrt{\sum_{n=2}^{N}G_n^2(\tau)/W_{n-1,n-1}}. \tag{32}$$

Employing the value of κ from Eq. (31), and maximizing on θ, the greatest pulse response at time τ becomes

$$u_{max}(\tau)=\max_\theta h^T\phi(\theta,\tau)+\left(\hat{\delta}-\max_\theta h^T\varphi(\theta)\right)\sqrt{\frac{\sum_{n=2}^{N}G_n^2(\tau)/W_{n-1,n-1}}{\sum_{n=2}^{N}1/W_{n-1,n-1}}} \tag{33}$$

Before discussing this relation, let us recall that h is the vector of Fourier coefficients of the nominal initial imperfection profile. Thus, $h^T\varphi(\theta)$ is the deflection at angle θ of the nominal initial imperfection, and $\max_\theta h^T\varphi(\theta)$ is the greatest deflection of the nominal initial imperfection profile. Similarly, $h^T\phi(\theta,\tau)$ is the pulse response of the nominal imperfection, and $\max_\theta h^T\phi(\theta,\tau)$ is the greatest response at time τ of the nominal initial imperfection. The maximum of $h^T\phi(\theta,\tau)$ and $h^T\varphi(\theta)$ do not necessarily occur at the same angle.

Comparing the ellipsoidal and shifted ellipsoidal expressions for the maximum pulse response, Eqs. (25) and (33), we see that Eq. (33) reduces to Eq. (25) if $h=0$. This is expected since R_{SELP} reduces to R_{ELP} if $h=0$. Also, both relations involve a weighted average of the amplification functions, where the diagonal elements of W^{-1} are the weighting terms. Thus, both expressions involve similar sensitivity to the choice of N and

Table 3 Comparison of convex and probabilistic ratio of peaks based on the shifted ellipsoidal convex model

p	N	$\hat{\delta}$	$u_{max}/\hat{\delta}$, $(W=I)$	$u_{max}/\hat{\delta}$, $(W=\{f_p\})$	Conv/Prb $(W=I)$	Conv/Prb $(W=\{f_p\})$
1	20	142.1242	3.7748	3.7748	0.314	0.314
		299.8731	9.0073	5.6086	0.749	0.466
		536.4965	11.0865	6.3372	0.922	0.527
2	20	132.1510	1.8263	1.8263	0.275	0.275
		175.8291	4.7812	2.1738	0.721	0.328
		241.3462	7.2081	2.4593	1.087	0.371
1	50	145.3221	3.8417	3.8417	0.319	0.319
		310.5071	6.5478	5.5652	0.544	0.463
		558.2845	7.6044	6.2381	0.632	0.519
2	50	132.8226	1.8340	1.8340	0.277	0.277
		177.1302	3.6086	2.1873	0.544	0.330
		243.5916	5.0601	2.4762	0.763	0.373
1	100	145.4310	3.8400	3.8400	0.319	0.319
		310.6381	5.1387	5.5075	0.427	0.458
		558.4488	5.6460	6.1589	0.469	0.512
2	100	132.8160	1.8341	1.8341	0.277	0.277
		177.1281	2.9468	2.1873	0.444	0.330
		243.5961	3.8568	2.4761	0.582	0.373
1	200	143.7866	3.8836	3.8836	0.323	0.323
		309.6362	4.1767	5.5120	0.347	0.458
		558.4106	4.2899	6.1409	0.357	0.511
2	200	132.7646	1.8348	1.8348	0.277	0.277
		177.0967	2.4847	2.1880	0.375	0.330
		243.5949	3.0159	2.4768	0.455	0.374

W. However, numerical evaluation will show that the shifted ellipsoidal model is less conservative than the regular ($h=0$) ellipsoidal model. This is related to the fact that the term involving the amplification functions is multiplied by $\hat{\delta}-\max_\theta h^T\varphi(\theta)$ in Eq. (33) and by $\hat{\delta}$ in Eq. (25). Furthermore, the shifted ellipsoid relation is not homogeneous in $\hat{\delta}$ and therefore does not allow evaluation of $u_{max}/\hat{\delta}$ without first explicitly choosing a value for $\hat{\delta}$.

Table 3 presents results of the numerical evaluation of the Eq. (33). The vector h of Fourier coefficients of the nominal initial deflection is given in Eq. (18). The first column shows the value of p used in the function $f_p(n)$, the second column is the value of the greatest mode number, N. The third column is the value of $\hat{\delta}$. Three different values of $\hat{\delta}$ are used. The first equals $\max_\theta h^T\varphi(\theta)$, which is the greatest deflection of the nominal initial imperfection profile. The third value of $\hat{\delta}$ equals $\max_\theta h^T\phi(\theta)$, which is the greatest pulse response deflection of the nominal initial profile. The second value of $\hat{\delta}$ is intermediate between the first and the third. The fourth and fifth columns show the convex model ratio of peaks $u_{max}/\hat{\delta}$, for W given by Eqs. (14) and (16), respectively. The sixth and seventh columns show the ratio of the fourth and fifth columns to the corresponding probabilistic ratio of peaks value from Lindberg (1992a). The probabilistic ratio of peaks values used are 12.027 for $p=1$ and 6.631 $p=2$, respectively. The other parameter values are $s=20$, $\tau=6$ and $n_c=5$. Comparing Tables 1 and 3 one sees that the shifted ellipsoid model is even less conservative than the regular ellipsoid model.

6 Ratio of Peaks Based on the Localized Uniform Bound Model

Let us consider uncertain initial imperfections which are limited to a certain angular range of the shell. The envelope bound convex model R_{EB} is suitable for representing this sort of uncertainty in the initial deformation profile. We will consider also the special case of the localized uniform bound model, R_{LUB}.

We will evaluate the maximum pulse response as the initial imperfection varies on the convex model. The pulse response at angle θ is, from Lindberg (1992a, Eq. (14)),

$$u(\theta,\tau)=\int_0^{2\pi}\delta(\xi)S(\xi,\theta,\tau)d\xi \tag{34}$$

Table 4 Ratio of peaks based on the localized uniform bound convex model

θ_2 (deg)	θ (deg)	$u_{max}(\theta,\tau)/\hat{\delta}$
1.00000	0.50000	1.37809
3.00000	1.50000	4.00272
5.00000	2.50000	6.25326
7.00000	3.50000	7.94303
10.00000	5.00000	9.20630
15.00000	7.50000	10.56260
20:00000	10.00000	14.58738
30.00000	15.00000	21.90472
50.00000	25.00000	27.38136
120.00000	60.00000	31.15329
360.00000	180.00000	31.77872

where

$$S(\xi,\theta,\tau)=\frac{1}{\pi}\sum_{n=2}^{N}G_n(\tau)\cos\, n(\theta-\xi). \tag{35}$$

The maximum response for $\delta(\xi)\epsilon R_{EB}$ is obtained when $\delta(\xi)$ switches back and forth between the envelope functions $\delta_1(\xi)$ and $\delta_2(\xi)$ as $S(\xi,\theta,\tau)$ changes sign. To represent this maximum, define the following sets of points: $\Xi_+(\theta)$ is the set of points in the interval $[0, 2\pi]$ for which the sensitivity function $S(\xi,\theta,\tau)$ is non-negative. Similarly, $\Xi_-(\theta)$ is the set of points for which $S(\xi,\theta,\tau)$ is negative.

$$\Xi_+(\theta)=\{\xi\epsilon[0,2\pi]:\ S(\xi,\theta,\tau)\geq 0\} \tag{36}$$

$$\Xi_-(\theta)=\{\xi\epsilon[0,2\pi]:\ S(\xi,\theta,\tau)<0\} \tag{37}$$

The maximum response at angle θ becomes

$$u_{max}(\theta,\tau)=\max_{\delta\epsilon R_{EB}}u(\theta,\tau)=\int_{\Xi_+(\theta)}\delta_2(\xi)S(\xi,\theta,\tau)d\xi+\int_{\Xi_-(\theta)}\delta_1(\xi)S(\xi,\theta,\tau)d\xi. \tag{38}$$

In particular, for the localized uniform bound model, R_{LUB}, where $\delta_n(\xi)$ is rectangular as in Eq. (11), the maximum response is

$$u_{max}(\theta,\tau)=\hat{\delta}\int_{\theta_1}^{\theta_2}|S(\xi,\theta,\tau)|d\xi. \tag{39}$$

It is evident that $u_{max}(\theta,\tau)$ reaches a maximum for $\theta=(\theta_1+\theta_2)/2$, and diminishes rapidly as θ moves out of the interval $[\theta_1,\theta_2]$.

Equation (39) has been evaluated for $\theta=(\theta_1+\theta_2)/2$, with $\theta_1=0$ and for various values of θ_2. Results appear in Table 4, for $s=20$, $\tau=6$ and $N=50$. When $\theta_2=360$ deg, one gets the value of the uniform bound ratio of peaks found in Lindberg (1992a, Table 1). This value is very nearly attained for $\theta_2=120$ deg, due to the fact that $S(\xi,\theta,\tau)$ becomes quite small for $|\xi-\theta|>120$ deg.

Furthermore, Table 4 indicates to what extent localization of the imperfection reduces the severity of the response. It is noteworthy, for instance, that when the imperfection is restricted to a 15-deg sector ($\theta_2=15$) the ratio of peaks is 10.6, which is about 1/3 of the value of 31.8 when $\theta_2=360$. Similarly, an imperfection subtending only five degrees produces a ratio of peaks of 6.3 which is fully 20 percent of the value for the 360-deg imperfection. Very localized imperfections can produce such substantial damage because the sensitivity function $S(\xi,\theta,\tau)$ is strongly peaked at $\xi=\theta$.

7 Conclusions

The following conclusions can be drawn from this discussion.

(1) We have demonstrated the use of a variety of convex models for representing uncertainty in the initial shell shape.

Each convex model is suited to a different type and extent of prior knowledge about the shell imperfections. Convex models provide a useful alternative to probabilistic description of uncertainty when sufficient information is unavailable for reliably realizing a probability density function.

(2) The ellipsoidal convex models of imperfection uncertainty, R_{ELP} and R_{SELP}, when compared with a probabilistic analysis, seem more realistic than the uniform bound convex model. The radial tolerance of the shell, $\hat{\delta}$, which is a potentially useful parameter for quality control in the manufacture of thin shells, has been incorporated into the ellipsoidal models.

(3) For $W=I$ and $N=50$ the ellipsoidal convex model, R_{ELP}, (Table 1) and the probabilistic model at three standard deviations predict approximately the same values of the ratio of peaks damage parameter.

(4) For W based on $f_p(n)$ and $N=50$ the ellipsoidal model R_{ELP} is more conservative than the probabilistic model by about a factor of 2.

(5) The shifted ellipsoidal model, R_{SELP}, (Table 3) is less conservative than the regular ellipsoidal model, R_{ELP}, (Table 1) by about a factor of 2. That is, the predicted ratio of peaks is less with R_{SELP} than with R_{ELP}.

(6) Localized imperfections are very effective in producing damage after pulsed radial loading (Table 4). For example, an imperfection subtending only five degrees of the shell circumference produces a maximum ratio of peaks which is 20 percent of the value obtained from imperfections subtending the full circumference.

References

Abrahamson, G. R., and Goodier, J. N., 1962, "Dynamic Plastic Flow Buckling of a Cylindrical Shell from Uniform Radial Impulse," 4th U.S. National Congress of Applied Mechanics, Berkeley, CA, pp. 939–950.

Ben-Haim, Y., 1990, "Detecting Unknown Lateral Forces on a Bar by Vibration Measurement," *Journal of Sound and Vibration*, Vol. 140, pp. 13–29.

Ben-Haim, Y., and Elishakoff, I., 1989, "Non-Probabilistic Models of Uncertainty in the Nonlinear Buckling of Shells With General Imperfections: Theoretical Estimates of the Knockdown Factor," ASME JOURNAL OF APPLIED MECHANICS, Vol. 56, pp. 403–410.

Ben-Haim, Y., and Elishakoff, I., 1990, *Convex Models of Uncertainty in Applied Mechanics*, Elsevier, New York.

Kirkpatrick, S. W., and Holmes, B. S., 1989, "Effect of Initial Imperfections on Dynamic Buckling of Shells," *ASCE Journal of Engineering Mechanics*, Vol. 115, pp. 1075–1093.

Li, F. S., and Kyriakides, S., 1991, "On the Propagation Pressure of Buckles in Cylindrical Confined Shells," ASME JOURNAL OF APPLIED MECHANICS, Vol. 57, pp. 1091–1094.

Lindberg, H. E., and Florence, A. L., 1987, *Dynamic Pulse Buckling*, Martinus Nijhoff Publishers, Dordrecht, The Netherlands, Kluwer Academic Publishers, U.S. and Canada distributer, Hingham, MA.

Lindberg, H. E., 1992a, "An Evaluation of Convex Modeling for Multimode Dynamic Buckling," ASME JOURNAL OF APPLIED MECHANICS, Vol. 59, pp. 929–936.

Lindberg, H. E., 1992b, "Convex Models for Uncertain Imperfection Control in Multimode Dynamic Buckling," ASME JOURNAL OF APPLIED MECHANICS, Vol. 59, pp. 937–945.

M. Di Paola
Dipartimento di Ingegneria
Strutturale e Geotecnica, DISEG,
Università di Palermo,
Viale delle Science,
90128 Palermo, Italy

Representation of Strongly Stationary Stochastic Processes

A generalization of the orthogonality conditions for a stochastic process to represent strongly stationary processes up to a fixed order is presented. The particular case of non-normal delta correlated processes, and the probabilistic characterization of linear systems subjected to strongly stationary stochastic processes are also discussed.

1 Introduction

Engineering systems, such as civil or mechanical structures, can be subjected to excitations adequately modeled as stochastic processes. In these circumstances the response of such systems is a stochastic process too, and has to be characterized in a probabilistic sense. The probabilistic description of a stochastic process is provided by the finite m-dimensional distributions ($m = 1, 2, \ldots, \infty$) or equivalently by the correlations of order m (see, e.g., Lin, 1977; Stratanovich, 1963).

If the finite m-dimensional distributions are invariant under time shifts, then the process is said to be strongly stationary of order m. If this property is satisfied only for $m = 2$ then the process is a weakly stationary one and the mean is constant while the second-order correlation depends only on the difference between the two instants. For normal (i.e., Gaussian) processes, the weak stationarity guarantees the strong stationarity because all the correlations of order greater than two are exactly zero.

The spectral representation of a zero mean weakly stationary stochastic process is the Fourier transform of an increment of a generating stochastic process having orthogonal increments (Priestley, 1965).

For normal processes this representation is sufficient for the complete characterization of stationary processes. In some problems, however, the input is affected by significant non-normality, such is the case, for example, of nonlinear drag forces which are exerted on structures subjected to wind or ocean waves (Morison et al., 1950; Soize, 1978). The response of systems subjected to such inputs is non-normal too, and the probabilistic description of both input and output processes can be obtained by means of higher order correlations. In these circumstances the representation of the stationary stochastic processes is not sufficient for the complete characterization of these processes, because the classical orthogonality condition only guarantees the weak stationarity. Usually (Lutes, 1986; Lutes and Hu, 1986; Grigoriu, 1986) the definition of strongly stationary processes is made through the properties of the correlation of higher order without first defining the generating process and this complicates the subsequent analysis. Here the explicit representation of the strongly stationary stochastic process is presented and consists of introducing generalized orthogonality conditions on the generating process of the spectral representation in order to account for the features of the higher order correlations of the process.

The particular case of a strongly stationary, delta correlated process and the probabilistic description of a linear system subjected to a strongly stationary (non-normal) process are also discussed.

Throughout the paper the Kronecker algebra is repeatedly employed because of its simplicity in extending the probabilistic analysis to vectors of stochastic processes. Readers unfamiliar with this algebra are referred to Graham (1981) and Ma (1987).

2 Preliminary Concepts

In this section some preliminary concepts are briefly reviewed for clarity and for introducing appropriate notation.

Let $\mathbf{X}(t)$ be an n-vector of real stochastic processes. At a fixed time t_0 the vector $\mathbf{X}(t_0)$ constitutes a vector of random variables and its probabilistic description can be made by means of the joint probability density function $p_{\mathbf{X}}(\mathbf{x}; t_0)$ or equivalently by means of its Fourier transform, that is,

$$M_{\mathbf{X}}(\vartheta; t_0) = \int_{-\infty}^{\infty} \ldots \int_{-\infty}^{\infty} \exp(-i\vartheta^T\mathbf{x}) \, p_{\mathbf{X}}(\mathbf{x}; t_0) dx_1 dx_2 \ldots dx_n \quad (1)$$

where $i = \sqrt{-1}$ is the imaginary unit, ϑ is an n-vector of real parameters, the apex T denotes transpose, x_j is the jth component of the vector $\mathbf{x}$, and $M_{\mathbf{X}}(\vartheta; t_0)$ is the so-called characteristic function. The latter can be expressed as

$$M_{\mathbf{X}}(\vartheta; t_0) = \sum_{r=0}^{\infty} \frac{(-i)^r}{r!} \vartheta^{[r]^T} \mathbf{m}_r[\mathbf{X}; t_0] = \exp \sum_{r=1}^{\infty} \frac{(-i)^r}{r!} \vartheta^{[r]^T} \mathbf{k}_r[\mathbf{X}; t_0] \quad (2)$$

where the exponent in the square brackets denotes tensor or Kronecker power. Specifically,

Contributed by the Applied Mechanics Division of THE AMERICAN SOCIETY OF MECHANICAL ENGINEERS for publication in the ASME JOURNAL OF APPLIED MECHANICS.

Discussion on this paper should be addressed to the Technical Editor, Professor Lewis T. Wheeler, Department of Mechanical Engineering, University of Houston, Houston, TX 77204-4792, and will be accepted until four months after final publication of the paper itself in the ASME JOURNAL OF APPLIED MECHANICS.

Manuscript received by the ASME Applied Mechanics Division, Mar. 12, 1990; final revision, May 7, 1991. Associate Technical Editor: P. D. Spanos.

$$\vartheta^{[r]} = \frac{\vartheta \otimes \vartheta \otimes \ldots \otimes \vartheta}{r\text{-fold}}. \tag{3}$$

In this equation the symbol $\otimes$ denotes tensor or Kronecker product (Graham, 1981; Ma, 1987), see also the Appendix, so that $\vartheta^{[r]}$ is a vector of order n^r. In Eq. (2) $\mathbf{m}_r[\mathbf{X};\ t_0]$ and $\mathbf{k}_r[\mathbf{X};\ t_0]$ are the moments and the cumulants of order r, respectively. They are given by the equations

$$\mathbf{m}_r[\mathbf{X};\ t_0] = E[\mathbf{X}^{[r]}(t_0)] = \int_{-\infty}^{\infty} \frac{n}{\text{fold}} \int_{-\infty}^{\infty} x^{[r]} p_{\mathbf{X}}(\mathbf{x};\ t_0)$$

$$\times dx_1 \ldots dx_n = \frac{1}{(-i)^r} \left[\nabla_{\vartheta}^{[r]} M_{\mathbf{X}}(\vartheta;\ t_0) \right]_{\vartheta = 0} \tag{4}$$

$$\mathbf{k}_r[\mathbf{X};\ t_0] = \frac{1}{(-i)^r} \left[\nabla_{\vartheta}^{[r]} \ln M_{\mathbf{X}}(\vartheta;\ t_0) \right]_{\vartheta = 0} \tag{5}$$

where $E[\bullet]$ represents stochastic average and ∇_{ϑ} is the differential vector defined by

$$\nabla_{\vartheta}^{T} = \left[\frac{\partial}{\partial \vartheta_1} \frac{\partial}{\partial \vartheta_2} \ldots \ldots \frac{\partial}{\partial \vartheta_n} \right]. \tag{6}$$

Comparing Eqs. (1) and (2) one can conclude that the probabilistic description of the stochastic vector process $\mathbf{X}(t)$ at a fixed time t_0 can be obtained by the knowledge of the probability density function, or by the characteristic function, or equivalently by the moments or the cumulants of all orders of the vector process $\mathbf{X}(t)$.

Choose arbitrarily $s + 1$ time instants, namely $t_0, t_1, \ldots, t_s$, the related vectors $\mathbf{X}(t_0), \mathbf{X}(t_1), \ldots, \mathbf{X}(t_s)$ constitute a family of vectors of random variables. Therefore its probabilistic description can be made by means or the joint probability density functions

$$p_{\overline{\mathbf{X}}_s}(\overline{\mathbf{x}}_s;\ t_s) = P_{\mathbf{X}_0},\ \mathbf{x}_1,\ \ldots,\ \mathbf{x}_s$$

$$(\mathbf{x}_0; t_0,\ \mathbf{x}_1;\ t_1,\ \ldots,\ \mathbf{x}_s;\ t_s)\ (s = 1,2,\ldots) \tag{7}$$

where

$$\overline{\mathbf{X}}_s^T = [\mathbf{X}^T(t_0)\mathbf{X}^T(t_1) \ldots \mathbf{X}^T(t_s)] = [\mathbf{X}_0^T \mathbf{X}_1^T \ldots \ldots \mathbf{X}_s^T]$$

$$\mathbf{t}_s^T = [t_0\ t_1 \ldots\ t_s] \tag{8}$$

the corresponding characteristic function is given in the form

$$\mathbf{M}_{\overline{\mathbf{X}}_s}(\overline{\vartheta}_s;\ \mathbf{t}_s)$$

$$= \int_{-\infty}^{\infty} \ldots \int_{-\infty}^{\infty} \exp(-i\overline{\vartheta}_s^T \overline{\mathbf{x}}_s) p_{\overline{\mathbf{X}}_s}(\overline{\mathbf{x}}_s;\ \mathbf{t}_s) dx_{01} dx_{02} \ldots dx_{sn} \tag{9}$$

where x_{ij} is the jth component of the vector $\mathbf{x}_i$ and $\overline{\vartheta}_s$ is the $n(s + 1)$ vector of real parameters given as

$$\overline{\vartheta}_s^T = \left[\vartheta_0^T \vartheta_1^T \ldots \ldots \ldots \vartheta_s^T \right]. \tag{10}$$

The characteristic function $M_{\overline{\mathbf{X}}}(\overline{\vartheta}_s;\ \mathbf{t}_s)$ can be expressed in terms of moments and cumulants in the form

$$M_{\overline{\mathbf{X}}_s}(\overline{\vartheta}_s;\ \mathbf{t}_s) = \sum_{r=0}^{\infty} \frac{(-i)^r}{r!} \overline{\vartheta}_s^{[r]T} \mathbf{m}_r[\overline{\mathbf{X}}_s;\ \mathbf{t}_s]$$

$$= \exp \sum_{r=1}^{\infty} \frac{(-i)^r}{r!} \overline{\vartheta}_s^{[r]T} \mathbf{k}_r[\overline{\mathbf{X}}_s;\ \mathbf{t}_s] \tag{11}$$

where the moments $\mathbf{m}_r[\overline{\mathbf{X}}_s;\ \mathbf{t}_s]$ and cumulants $\mathbf{k}_r[\overline{\mathbf{X}}_s;\ \mathbf{t}_s]$, both of order $[n(s + 1)]^r$, are given as

$$\mathbf{m}_r[\overline{\mathbf{X}}_s;\ \mathbf{t}_s] = \frac{1}{(-i)^r} \left[\nabla_{\overline{\vartheta}_s}^{[r]} M_{\overline{\mathbf{X}}_s}(\overline{\vartheta}_s;\ \mathbf{t}_s) \right]_{\overline{\vartheta}_s = 0} = E[\overline{\mathbf{X}}_s^{[r]}] \tag{12}$$

$$\mathbf{k}_r[\overline{\mathbf{X}}_s;\ \mathbf{t}_s] = \frac{1}{(-i)^r} \left[\nabla_{\overline{\vartheta}_s}^{[r]} \ln M_{\overline{\mathbf{X}}_s}(\overline{\vartheta}_s;\ \mathbf{t}_s) \right]_{\overline{\vartheta}_s = 0} \tag{13}$$

and the differential vector $\nabla_{\overline{\vartheta}_s}$ is given in the form

$$\nabla_{\overline{\vartheta}^s}^{T} = \left[\nabla_{\vartheta_0}^{T}\ \nabla_{\vartheta_1}^{T} \ldots \ldots \nabla_{\vartheta_s}^{T} \right]. \tag{14}$$

In some circumstances it is of interest to address the issue of incomplete representation of the moments, that is with vector $E_{\mathbf{x}}^{(s+1)}(\mathbf{t}_s)$ given in the form

$$\mathbf{E}_{\mathbf{X}}^{(s+1)}(\mathbf{t}_s) = E[\mathbf{X}_0 \otimes \mathbf{X}_1 \otimes \ldots \ldots \otimes \mathbf{X}_s] \tag{15}$$

the vector $E_{\mathbf{x}}^{(s+1)}(\mathbf{t}_s)$ (order n^{s+1}) will be called "average at multiple times" and can be obtained by the characteristic function in the form

$$\mathbf{E}_{\mathbf{X}}^{(s+1)}(\mathbf{t}_s)$$

$$= \frac{1}{(-i)^s} \left[\nabla_{\vartheta_0} \otimes \nabla_{\vartheta_1} \otimes \ldots \ldots \otimes \nabla_{\vartheta_s} \otimes M_{\overline{\mathbf{X}}_s}(\overline{\vartheta}_s;\ \mathbf{t}_s) \right]_{\overline{\vartheta}_s = \mathbf{0}}. \tag{16}$$

It will be stressed that the various components of this vector are contained in the vector $\mathbf{m}_{s+1}[\overline{\mathbf{X}}_s;\ \mathbf{t}_s]$. The counterpart of $\mathbf{E}_{\mathbf{x}}^{(s+1)}(\mathbf{t}_s)$ in terms of cumulants is, following the nomenclature introduced by Stratanovich (1963), the "correlation at multiple times" or simply "correlation" vector $\mathbf{R}_{\mathbf{x}}^{(s+1)}(t_s)$, that is

$$\mathbf{R}_{\mathbf{X}}^{(s+1)}(\mathbf{t}_s)$$

$$= \frac{1}{(-i)^s} \left[\nabla_{\vartheta_0} \otimes \nabla_{\vartheta_1} \otimes \ldots \otimes \nabla_{\vartheta_s} \otimes \ln M_{\overline{\mathbf{X}}_s}(\overline{\vartheta}_s;\ \mathbf{t}_s) \right]_{\overline{\vartheta}_s = \mathbf{0}}. \tag{17}$$

The various components of $\mathbf{R}_{\mathbf{x}}^{(s+1)}(\mathbf{t}_s)$ are contained in the vector $\mathbf{k}_{s+1}[\overline{\mathbf{X}}_s;\ \mathbf{t}_s]$. A suitable choice of the time instants t_0, $t_1, \ldots, t_s$ in Eqs. (15) and (17) allows the complete construction of the moments and cumulants vectors $\mathbf{m}_{s+1}[\overline{\mathbf{X}}_s;\ \mathbf{t}_s]$ and $\mathbf{k}_{s+1}[\overline{\mathbf{X}}_s;\ \mathbf{t}_s]$, respectively. Putting $t_0 = t_1 = \ldots = t_s$ in Eqs. (16) and (17) we obtain $\mathbf{m}_{s+1}[\mathbf{X};\ t_0]$ and $\mathbf{k}_{s+1}[\mathbf{X};\ t_0]$. As a conclusion the averages at multiple times and correlations of any order completely characterize the stochastic vector process $\mathbf{X}(t)$. For zero mean processes the correlations and the averages at multiple times coincide up to the third order.

A process is strongly stationary up to $(s + 1)$th order of the correlations at multiple times depend not on $t_0, t_1, \ldots, t_s$ taken separately but on the differences $\tau_j = t_j - t_0$, i.e., on the vector $\tau_s^T = [\tau_1\ \tau_2 \ldots \tau_s]$ (having s components), that is

$$\mathbf{R}_{\mathbf{X}}^{(s+1)}(\mathbf{t}_s) = \mathbf{R}_{\mathbf{X}}^{(s+1)}(\tau_s) \quad \forall \mathbf{t}_s. \tag{18}$$

In this case both the average at multiple times and the probability density function depend on the vector τ_s instead of the vector $\mathbf{t}_s$. If this property is satisfied for a fixed value of $s + 1$ it is also satisfied for all orders less than $s + 1$. Moreover, if $s = \infty$, then the process $\mathbf{X}(t)$ is called strictly stationary; if the property is satisfied for $s = 1$, then the process is called weakly stationary. If the process is normal, then distinction between weak and strongly stationarity is not necessary because all correlations of order greater than two are exactly zero, so that a weakly stationary normal process is strictly stationary too. In all other cases a strongly stationary process is also weakly stationary but not vice versa.

3 Representation of Stationary Process

An explicit spectral representation of a weakly stationary zero-mean real n-vector process $\mathbf{X}(t)$, (see, e.g, Priestley, 1965) is given as

$$\mathbf{X}(t) = \int_{-\infty}^{\infty} exp(-i\omega t) d\mathbf{Z}(\omega) \tag{19}$$

where $d\mathbf{Z}(\omega)$ is a zero mean complex stochastic vector process belonging to the family of orthogonal increments stochastic processes, that is

$$E\left[d\mathbf{Z}^*(\omega_0) d\mathbf{Z}(\omega_1)^T \right] = \Delta(\omega_1 - \omega_0) d\Phi_{\mathbf{X}}^{(2)}(\omega_0, \omega_1) \tag{20}$$

where the star means complex conjugate, $\Delta(\cdot)$ is the Kronecker delta ($\Delta(\omega_1 - \omega_0) = 1$ if $\omega_0 = \omega_1$, $\Delta(\omega_1 - \omega_0) = 0$ otherwise), $\Phi_{\mathbf{X}}^{(2)}(\omega_0, \omega_1)$ is an $n \times n$ deterministic matrix. If $\omega_0 = \omega_1$, then Eq. (20) gives the covariance matrix of the process $d\mathbf{Z}(\omega)$ and $d\Phi_{\mathbf{X}}^{(2)}(\omega_0, \omega_0)$ is a Hermitian matrix. Equation (20) can be rewritten in the other form

$$E[d\mathbf{Z}^*(\omega_0) \otimes d\mathbf{Z}(\omega_1)] = \Delta(\omega_1 - \omega_0) d\Psi_{\mathbf{X}}^{(2)}(\omega_1, \omega_0) \tag{21}$$

where the n^2 vector $d\Psi_{\mathbf{X}}^{(2)}(\omega_0, \omega_1)$ is the vectorized form of the matrix $d\Phi_{\mathbf{X}}^{(2)}(\omega_0, \omega_0)$ namely

$$\mathrm{Vec}\left[d\Phi_{\mathbf{X}}^{(2)}(\omega_0, \omega_1) \right] = d\Psi_{\mathbf{X}}^{(2)}(\omega_0, \omega_1) \tag{22}$$

where Vec[•] is a vector column formed by all the columns of the matrix in parenthesis written one below another.

The definition given in Eq. (21) is not well framed in the context outlined in the above section in which the probabilistic description of stochastic processes is made by the correlation. Therefore, the orthogonality condition expressed in this form is not easily extendible in order to represent a strongly stationary process, for this reason it is preferable to write Eq. (21) in terms of second correlation $\mathbf{R}_{dz}^{(2)}$. Because the stochastic vector process $\mathbf{X}(t)$ is real, then the process $\mathbf{Z}(\omega)$ has an even real part and an odd imaginary part, and it can be easily seen that Eq. (21) can be rewritten in the form involving the second correlation of $d\mathbf{Z}(\omega)$ as follows:

$$\mathbf{R}_{dz}^{(2)}(\omega_1) = E[d\mathbf{Z}(\omega_0) \otimes d\mathbf{Z}(\omega_1)]$$

$$= \Delta(\omega_0 + \omega_1) d\Psi_{\mathbf{X}}^{(2)}(-\omega_0, \omega_1) \tag{23}$$

in which $\omega_s^T = [\omega_0\ \omega_1\ \ldots\ \omega_s]$.

It is interesting to note that putting $\omega_0 = \omega_1$ in Eq. (23), the second correlation of $d\mathbf{Z}(\omega)$ does not coincide with the vectorized form of the covariance matrix. For example for a complex scalar process $dZ(\omega)$ the covariance $E[dZ^*(\omega_0) dZ(\omega_0)]$ is a real positive function, representing the measure of the process $dZ(\omega)$, while the second correlation $R_{dz}^{(2)}(\omega_0, \omega_0)$ remains a complex function.

Starting from the characterization of the vector process $d\mathbf{Z}(\omega)$ one can proceed to characterize the process $\mathbf{X}(t)$ given in Eq. (19). The second correlation of the vector process $\mathbf{X}(t)$ is given as

$$\mathbf{R}_{\mathbf{X}}^{(2)}(t_1) = E[\mathbf{X}(t_0) \otimes \mathbf{X}(t_1)]$$

$$= \int_{-\infty}^{\infty} \int_{-\infty}^{\infty} \exp(-i\omega_0 t_0 - i\omega_1 t_1) \mathbf{R}_{dz}^{(2)}(\omega_1). \tag{24}$$

Putting Eq. (23) in (24) we obtain

$$R_{\mathbf{X}}^{(2)}(t_1) = \int_{-\infty}^{\infty} \int_{-\infty}^{\infty} exp(-i\omega_0 t_0 - i\omega_1 t_1) \Delta$$

$$\times (\omega_0 + \omega_1) d\Psi_{\mathbf{X}}^{(2)}(-\omega_0, \omega_1) \tag{25}$$

and using the main property of the Kronecker delta function, Eq. (25) can be rewritten in the form

$$R_{\mathbf{X}}^{(2)}(t_1) = \mathbf{R}_{\mathbf{X}}^{(2)}(\tau_1) = \int_{-\infty}^{\infty} \exp(-i\omega_1 \tau_1) d\Psi_{\mathbf{X}}^{(2)}(\omega_1, \omega_1). \tag{26}$$

This equation shows that the second-order correlation depends on the time difference τ_1 and not on t_0 and t_1 taken separately, so that the orthogonality condition (23) guarantees the weak stationarity of the vector process $\mathbf{X}(t)$.

If $\Psi_{\mathbf{X}}^{(2)}(\omega, \omega)$ is differentiable then we can write

$$d\Psi_{\mathbf{X}}^{(2)}(\omega, \omega) = \mathbf{S}_{\mathbf{X}}^{(2)}(\omega) d\omega \tag{27}$$

where $\mathbf{S}_{\mathbf{x}}^{(2)}(\omega)$ is the vectorized form of the Hermitian Power Spectral Density function (PSD) matrix $\mathbf{G}_{\mathbf{X}}^{(2)}(\omega)$ of the process $X(t)$, i.e.,

$$\mathbf{S}_{\mathbf{X}}^{(2)}(\omega) = \mathrm{Vec}(\mathbf{G}_{\mathbf{X}}^{(2)}(\omega)). \tag{28}$$

By inserting Eq. (27) in Eq. (24), we obtain

$$\mathbf{R}_{\mathbf{X}}^{(2)}(\tau) = \int_{-\infty}^{\infty} \exp(-i\omega\tau) \mathbf{S}_{\mathbf{X}}^{(2)}(\omega) d\omega \tag{29}$$

or the inverse relationship

$$\mathbf{S}_{\mathbf{X}}^{(2)}(\omega) = \frac{1}{2\pi} \int_{-\infty}^{\infty} \exp(i\omega\tau) \mathbf{R}_{\mathbf{X}}^{(2)}(\tau) d\tau \tag{30}$$

that shows that the correlation vector is the Fourier transform of the PSD vector and vice versa.

If the vector process is normal then all the correlations of order greater than two are exactly zeros and the second correlation vector or the PSD vector fully characterizes the stochastic vector process $\mathbf{X}(t)$. If the vector $\mathbf{X}(t)$ is non-normal, then the probabilistic characterization of the vector $\mathbf{X}(t)$ has to be made by correlations of order higher than two. Using the representation given in Eq. (19), the probabilistic characterization of the process $\mathbf{X}(t)$ requires the probabilistic characterization of the generating process $d\mathbf{Z}(\omega)$ by means of correlations of higher order.

If $\mathbf{X}(t)$ is strongly stationary up to $(s + 1)$th order, then other orthogonality conditions in the generating process $\mathbf{Z}(\omega)$ have to be attached; we refer to these as "generalized orthogonality conditions." For a strong stationary process vector up to $(s + 1)$th order, the extension of equation (23) leads to

$$\mathbf{R}_{dz}^{(s+1)}(\omega_s) = \Delta(\omega_0 + \omega_1 + \ldots + \omega_s)$$

$$\times d\Psi_{\mathbf{X}}^{(s+1)}(-\omega_0, \omega_1, \ldots, \omega_s). \tag{31}$$

In this way the $(s + 1)$th correlation vector of $\mathbf{X}(t)$ is obtained in the form

$$\mathbf{R}_{\mathbf{X}}^{(s+1)}(\mathbf{t}_s) = \int_{-\infty}^{\infty} \frac{s+1}{\text{fold}} \int_{-\infty}^{\infty} \exp\left(-i \sum_{j=0}^{s} \omega_j t_j \right)$$

$$\times \Delta(\omega_0 + \omega_1 + \ldots + \omega_s) d\Psi_{\mathbf{X}}^{(s+1)}(-\omega_0, \omega_1, \ldots, \omega_s), \tag{32}$$

and using the main property of the Kronecker delta, we obtain

$$\mathbf{R}_{\mathbf{X}}^{(s+1)}(\mathbf{t}_s) = \mathbf{R}_{\mathbf{X}}^{(s+1)}(\tau_s) = \int_{-\infty}^{\infty} \frac{s}{\text{fold}} \int_{-\infty}^{\infty} \exp\left(-i \sum_{j=1}^{s} \omega_j \tau_j \right)$$

$$\times d\Psi_{\mathbf{X}}^{(s+1)}(\omega_1 + \omega_2 + \ldots + \omega_s, \omega_1, \omega_2, \ldots, \omega_s). \tag{33}$$

That shows that the $(s + 1)$th correlation vector depends on the vector τ_s containing the time differences $\tau_j = t_j - t_0$, and not on $t_0, t_1, \ldots, t_s$ taken separately, so that the generalized orthogonality conditions (31) guarantee the strong stationarity of the process $\mathbf{X}(t)$ up to $(s + 1)$th order.

If $d\Psi_{\mathbf{X}}^{(s+1)}(\omega_1 + \omega_2 + \ldots + \omega_s, \omega_1, \omega_2, \ldots, \omega_s)$ is differentiable then we can write

$$d\Psi_{\mathbf{X}}^{(s+1)}(\omega_1 + \omega_2 + \ldots + \omega_s, \omega_1, \omega_2, \ldots, \omega_s)$$

$$= \mathbf{S}_{\mathbf{X}}^{(s+1)}(\Omega_s) d\omega_1 d\omega_2 \ldots d\omega_s \tag{34}$$

in which $\Omega_s^T = [\omega_1, \omega_2, \ldots, \omega_s]$ and $\mathbf{S}_{\mathbf{x}}^{(s+1)}(\Omega_s)$ is the generalized PSD vector (order n^{s+1}). By inserting Eq. (34) in (33) we obtain

$$\mathbf{R}_{\mathbf{X}}^{(s+1)}(\tau_s)=\int_{-\infty}^{\infty}\frac{s}{\text{fold}}\int_{-\infty}^{\infty}\exp\left(-i\sum_{j=1}^{s}\omega_j\tau_j\right)\mathbf{S}_{\mathbf{X}}^{(s+1)}(\Omega_s)d\omega_1 d\omega_2\ldots d\omega_s \quad (35)$$

and the inverse relationship

$$\mathbf{S}_{\mathbf{X}}^{(s+1)}(\Omega_s)=\frac{1}{(2\pi)^s}\int_{-\infty}^{\infty}\frac{s}{\text{fold}}\int_{-\infty}^{\infty}\exp\left(i\sum_{j=1}^{s}\omega_j\tau_j\right)\times\mathbf{R}_{\mathbf{X}}^{(s+1)}(\tau_s)d\tau_1 d\tau_2\ldots d\tau_s \quad (36)$$

that shows that the correlation vector of an $(s+1)$th order strongly stationary vector process is the sth Fourier transform of the generalized PSD and vice versa. Equations (35) and (36) are the generalization of Eqs. (29) and (30) to the case of strongly stationary processes.

As a conclusion a stochastic vector process $\mathbf{X}(t)$ given in the form (19) in which the process $d\mathbf{Z}(\omega)$ has an $(s+1)$th order correlation vector expressed by Eq. (31) is an $(s+1)$th order strongly stationary process, the correlation or equivalently its Fourier transform, i.e., the corresponding generalized PSD vectors describing the statistical properties of $\mathbf{X}(t)$ up to $(s+1)$th order. If all the correlations of order greater than $s+1$ are negligible then the complete characterization of $\mathbf{X}(t)$, from a probabilistic point of view, is ensured by the correlations or the generalized PSD up of to order $s+1$, and the vector process $\mathbf{X}(t)$ is strictly stationary.

4 Strongly Stationary Delta Correlated Processes

It has been recognized (Grigoriu, 1986; Horsthemke and Lefever, 1984), that a white noise stationary vector process $\mathbf{W}(t)$ can be obtained by the equation

$$\mathbf{W}(t)=\frac{d}{dt}\mathbf{L}(t) \quad (37)$$

in which $\mathbf{L}(t)$ is a process with stationary orthogonal increments and $\mathbf{W}(t)$ is a Lévy white noise. Strictly speaking, this definition is invalid in the ordinary differential calculus because $\mathbf{L}(t)$ is not differentiable everywhere. However, it can be considered rigorous in the framework of the generalized theory of stochastic differential calculus (Itô 1969). Usually the method for representing non-normal white noise is based on assumptions regarding the form of the higher-order correlation function of the white noise (Stratanovich, 1963; Lutes and Hu, 1986). Here the generalized orthogonality conditions ensuring the stationarity of the process is used in order to define $(s+1)$th order strongly stationary white noise vector process. Let $\mathbf{W}(t)$ given in the form

$$\mathbf{W}(t)=\int_{-\infty}^{\infty}\exp(-i\omega t)d\mathbf{Z}(\omega) \quad (38)$$

where $\mathbf{Z}(\omega)$ is a vector process having generalized orthogonal increments up to $(s+1)$th order

$$\mathbf{R}_{d\mathbf{Z}}^{(s+1)}(\omega_s)=\Delta(\omega_0+\omega_1+\ldots+\omega_s)d\Psi_{\mathbf{W}}^{(s+1}\times(-\omega_0,\omega_1,\ldots,\omega_s) \quad (39)$$

in which

$$d\Psi_{\mathbf{W}}^{(s+1)}(\omega_1+\omega_2+\ldots+\omega_s,\omega_1,\omega_2,\ldots,\omega_s)=\mathbf{S}_{\mathbf{W}}^{(s+1)}d\omega_1 d\omega_2\ldots d\omega_s \quad (40)$$

$\mathbf{S}_{\mathbf{W}}^{(s+1)}$ being the constant PSD vector, that is a measure of the strength of the white noise process. In this way the $(s+1)$th correlation vector of $\mathbf{W}(t)$ is simply given in the form

$$\mathbf{R}_{\mathbf{W}}^{(s+1)}(\tau_s)=\mathbf{S}_{\mathbf{W}}^{(s+1)}\int_{-\infty}^{\infty}\frac{s}{\text{fold}}\int_{-\infty}^{\infty}\times\exp\left(-i\sum_{j=1}^{s}\omega_j\tau_j\right)d\omega_1 d\omega_2\ldots d\omega_s$$
$$=(2\pi)^s\mathbf{S}_{\mathbf{W}}^{(s+1)}\delta(\tau_1)\delta(\tau_2)\ldots\delta(\tau_s), \quad (41)$$

i.e., the correlation of order $s+1$ of the vector $\mathbf{W}(t)$ given in the form (38), having the generalized orthogonality conditions (39) and constant PSD, is given as the product of Dirac's delta functions. Random processes having correlation given in Eq. (41) following Stratanovich (1963), are the so-called delta correlated processes. Recently, Lutes and Hu (1986) called them white and Grigoriu (1987) showed that such delta correlated processes coincide up to fourth order with the Poisson white noise.

The corresponding correlation of an increment of $\mathbf{L}(t)$ admits the $(s+1)$th correlation in the form

$$\mathbf{R}_{d\mathbf{L}}^{(s+1)}(\mathbf{t}_s)=(2\pi)^s\mathbf{S}_{\mathbf{W}}^{(s+1)}\delta(\tau_1)\delta(\tau_2)\ldots\delta(\tau_s)dt_0 dt_1\ldots dt_s \quad (42)$$

that is the vector process $d\mathbf{L}$ has stationary orthogonal increments.

Putting $t_0=t_1=\ldots=t_s=t$ in Eq. (41) we obtain

$$\mathbf{R}_{d\mathbf{L}}^{(s+1)}(t,t,\ldots,t)=\mathbf{k}_{s+1}[d\mathbf{L};t]=(2\pi)^s\mathbf{S}_{\mathbf{W}}^{(s+1)}dt. \quad (43)$$

This equation shows that all the cumulant vectors up to $s+1$ order of the process $d\mathbf{L}$ are of order dt. If $\mathbf{W}(t)$ is a Gaussian white noise process, then $\mathbf{L}(t)$ coincides with a Wiener process and all the cumulants of order greater than two are exactly zero, i.e., the Wiener process is of order $dt^{1/2}$. If $\mathbf{W}(t)$ is a non-normal process, the order of an increment $d\mathbf{L}$ cannot a priori be established depending of the strength $\mathbf{S}_{\mathbf{W}}^{(s+1)}$. As a conclusion, a delta correlated non-normal stochastic process is strongly stationary if the generating process $\mathbf{Z}(\omega)$ satisfies Eq. (39) in which the generalized PSD vector is constant, i.e., $\mathbf{Z}(\omega)$ belongs to the class of processes with generalized orthogonal increments, the strong stationarity requiring information regarding the strengths $\mathbf{S}_{\mathbf{W}}^{(s+1)}$ of the white noise vector process.

5 Input-Output Relationships

In this section the probabilistic characterization of the response of a linear dynamic system subjected to a strong stationary process is discussed.

Let $\mathbf{X}(t)$ be a vector solution of an n-dimensional linear dynamical system subjected to the strongly stationary up to $(s+1)$th order vector process $\mathbf{F}(t)$ then the steady-state response can be adequately represented in the Duhamel integral form

$$\mathbf{X}(t)=\int_{-\infty}^{t}\mathbf{H}(t-\bar{t})\mathbf{F}(\bar{t})d\bar{t}, \quad (44)$$

$\mathbf{H}(t)$ being the impulse response function matrix. Because $\mathbf{F}(t)$ is stationary and the system operates from $t=-\infty$ then $\mathbf{X}(t)$ is also a stationary process. In particular, if $\mathbf{F}(t)$ is normal, then $\mathbf{X}(t)$ is also normal and the second correlation vector completely defines the response process from a probabilistic point of view. On the other hand, because $\mathbf{F}(t)$ as a stationary process admits a representation given in the form

$$\mathbf{F}(t)=\int_{-\infty}^{\infty}\exp(-i\omega t)d\mathbf{Z}_{\mathbf{F}}(\omega), \quad (45)$$

where $\mathbf{Z}_{\mathbf{F}}(\omega)$ is an orthogonal increments vector process given in the form (21), then the corresponding vector response is given as

$$\mathbf{X}(t)=\int_{-\infty}^{\infty}\left[\int_{-\infty}^{t}\exp(-i\omega\bar{t})\mathbf{H}(t-\bar{t})d\bar{t}\right]d\mathbf{Z}_{\mathbf{F}}(\omega). \quad (46)$$

After some easy manipulation, $\mathbf{X}(t)$ is written in the form

$$\mathbf{X}(t) = \int_{-\infty}^{\infty} \exp(-i\omega t)\mathbf{H}^*(\omega)d\mathbf{Z}_\mathbf{F}(\omega) \quad (47)$$

where $\mathbf{H}(\omega)$ is the Fourier transform of $\mathbf{H}(t)$, i.e.,

$$\mathbf{H}(\omega) = \int_0^{\infty} \exp(-i\omega t)\mathbf{H}(t)dt. \quad (48)$$

Equation (47) is the representation of $\mathbf{X}(t)$ in which the generating process is now $\mathbf{H}^*(\omega)d\mathbf{Z}_\mathbf{F}(\omega)$, such a process is orthogonal since

$$E\left[(\mathbf{H}^*(\omega_0)d\mathbf{Z}_\mathbf{F}(\omega_0))\otimes(\mathbf{H}^*(\omega_1)d\mathbf{Z}_\mathbf{F}(\omega_1))\right]$$
$$= [\mathbf{H}^*(\omega_0)\otimes\mathbf{H}^*(\omega_1)]E[d\mathbf{Z}_\mathbf{F}(\omega_0)\otimes d\mathbf{Z}_\mathbf{F}(\omega_1)]$$
$$= \Delta(\omega_0+\omega_1)[\mathbf{H}^*(\omega_0)\otimes\mathbf{H}^*(\omega_1)]d\Psi_\mathbf{F}^{(2)}(-\omega_0,\omega_1). \quad (49)$$

Comparing Eq. (49) and Eq. (23), one can state that the new generating process $\mathbf{H}^*(\omega)d\mathbf{Z}_\mathbf{F}(\omega)$ is a weakly stationary process.

The correlation vector of the output $\mathbf{X}(t)$ is given as

$$\mathbf{R}_\mathbf{X}^{(2)}(\tau_1) = E[\mathbf{X}(t_0)\otimes\mathbf{X}(t_1)]$$
$$= \int_{-\infty}^{\infty} \exp(-i\omega_1\tau_1)[\mathbf{H}(\omega_1)\otimes\mathbf{H}^*(\omega_1)]d\Psi_\mathbf{F}^{(2)}(\omega_1,\omega_1). \quad (50)$$

That shows that the correlation vector of the response process $\mathbf{X}(t)$ is weakly stationary, depending only on the difference $t_1 - t_0 = \tau_1$. If $\Psi_\mathbf{F}^{(2)}$ is differentiable then equation (50) leads to

$$\mathbf{R}_\mathbf{X}^{(2)}(\tau_1) = \int_{-\infty}^{\infty} \exp(-i\omega_1\tau_1)[\mathbf{H}(\omega_1)\otimes\mathbf{H}^*(\omega_1)]\mathbf{S}_\mathbf{F}^{(2)}(\omega_1)d\omega_1 \quad (51)$$

that is the vectorized form of the well-known expression for the correlation matrix.

If $\mathbf{F}(t)$ is a non-normal strongly stationary process up to $(s + 1)$th order then the response vector process $\mathbf{X}(t)$ is non-normal too and the probabilistic description of this vector process has to be made by correlations of higher order. In particular, the correlation of orders $s + 1$ of the vector $\mathbf{X}(t)$ is given in the form

$$\mathbf{R}_\mathbf{X}^{(s+1)}(\mathbf{t}_s) = \int_{-\infty}^{\infty} \frac{s+1}{\text{fold}} \int_{-\infty}^{\infty} \exp\left(-i\sum_{j=0}^{s}\omega_j t_j\right)$$
$$\times[\mathbf{H}^*(\omega_0)\otimes\mathbf{H}^*(\omega_1)\otimes\ \ldots\ \otimes\mathbf{H}^*(\omega_s)]\mathbf{R}_{d\mathbf{Z}_\mathbf{F}}^{(s+1)}(\omega_s). \quad (52)$$

Inserting Eq. (31) in Eq. (52) we obtain

$$\mathbf{R}_\mathbf{X}^{(s+1)}(\mathbf{t}_s) = \mathbf{R}_\mathbf{X}^{(s+1)}(\mathbf{t}_s) = \int_{-\infty}^{\infty} \frac{s}{\text{fold}} \int_{-\infty}^{\infty} \exp\left(-i\sum_{j=1}^{s}\omega_j\tau_j\right)$$
$$\hat{\mathbf{H}}(\Omega_s)d\Psi_\mathbf{F}^{(s+1)}(\omega_1+\omega_2+\ldots+\omega_s,\omega_1,\omega_2,\ \ldots,\ \omega_s) \quad (53)$$

where

$$\hat{\mathbf{H}}(\Omega_s) = \mathbf{H}\left(\sum_{j=1}^{s}\omega_j\right)\otimes\mathbf{H}^*(\omega_1)\otimes\mathbf{H}^*(\omega_2)\otimes\ \ldots\ \otimes\mathbf{H}^*(\omega_s). \quad (54)$$

Equation (53) shows that if the input vector process is stationary up to $(s + 1)$th order then the response vector process is also stationary of the same order. If $\Psi_\mathbf{F}^{(s+1)}$ is differentiable then we can write

$$\mathbf{R}_\mathbf{X}^{(s+1)}(\tau_s) = \int_{-\infty}^{\infty} \frac{s}{\text{fold}} \int_{-\infty}^{\infty}$$
$$\times\exp\left(-i\sum_{j=1}^{s}\omega_j\tau_j\right)\hat{\mathbf{H}}(\Omega_s)\mathbf{S}_\mathbf{F}^{(s+1)}(\Omega_s)d\omega_1 d\omega_2\ \ldots\ d\omega_s. \quad (55)$$

Letting $\tau_1 = \ldots = \tau_s = 0$, Eq. (55) gives the cumulants of the response vector process, that is

$$\mathbf{R}_\mathbf{X}^{(s+1)}(0) = \mathbf{k}_{s+1}[\mathbf{X};\ t]$$
$$= \int_{-\infty}^{\infty} \frac{s}{\text{fold}} \int_{-\infty}^{\infty} \hat{\mathbf{H}}(\Omega_s)\mathbf{S}_\mathbf{F}^{(s+1)}(\Omega_s)d\omega_1 d\omega_2\ \ldots\ d\omega_s. \quad (56)$$

If $\mathbf{F}(t)$ is delta correlated up to $(s + 1)$th order, then Eq. (55) becomes

$$\mathbf{R}_\mathbf{X}^{(s+1)}(\tau_s) = \left[\int_{-\infty}^{\infty} \frac{s}{\text{fold}} \int_{-\infty}^{\infty} \exp\left(-i\sum_{j=1}^{s}\omega_j\tau_j\right)\right.$$
$$\left.\hat{\mathbf{H}}(\Omega_s)d\omega_1 d\omega_2\ \ldots\ d\omega_s\right]\mathbf{S}_\mathbf{F}^{(s+1)}. \quad (57)$$

An analogous expression to that given by Eq. (57) has been obtained by Lutes (1986) for a single oscillator excited by a strongly delta-correlated stationary process.

6 Conclusions

The spectral representation of a weakly stationary process by using the Fourier transform of a complex stochastic generating process having orthogonal increments is often used in stochastic analysis. In order to ensure the strong stationarity other orthogonality conditions on the generating process have to be attached, here these conditions have been referred to as the "generalized orthogonality conditions", which accounts for the higher correlations of the given process.

The extension of the generalized orthogonality conditions has been done by using the Kronecker algebra and interpreting the classical orthogonality condition by means of the covariance matrix of the stochastic vector of generating process, in the form involving the second correlation vector of the generating process.

It is shown that the second correlation evaluated at zero and the variance are quite different concepts for complex processes. The former being the second term of the Taylor expansion of the characteristic function while the latter represents the measure of the process. A consistent definition of the orthogonality condition has been found by transferring the usual orthogonality condition of the complex generating process in terms of correlation. Then the generalization of the orthogonality conditions in order to represent strongly stationary processes is quite straightforward.

The particular case of non-normal strongly stationary delta correlated processes has been also examined showing that in this case all the cumulants up to a fixed order of an increment of the vector process $\mathbf{L}(t)$ whose formal derivative is the Lévy white noise process are infinitesimal of first order.

The probabilistic characterization of the response of a linear system subjected to a strongly stationary process has also been discussed, extending results available in the literature for a single-degree-of-freedom linear system to multi-degree-of-freedom systems.

References

Graham, A., 1981, *Kronecker Products and Matrix Calculus with Applications*, Ellis Horwood, England.

Grigoriu, M., 1986, "Response of Linear Systems to Quadratic Gaussian Excitation," *ASCE Journal of Engineering Mechanics*, Vol. 112, No. 6, pp. 523–535.

Grigoriu, M., 1987, "White Noise Process," *ASCE Journal of Engineering Mechanics*, Vol. 113, No. 5, pp. 757–765.

Horsthemke, W., and Lefever, R., 1984, *Noise-induced Transition: Theory and Applications in Physics, Chemistry and Biology*, Springer-Verlag, New York.

Ito, K., 1969, *Stochastic Processes* (Lecture notes series No. 16), Aarhus University, Aarhus, Denmark.

Lin, Y. K., 1967, *Probabilistic Theory of Structural Dynamics*, Kruger, New York.

Lutes, L. D., 1986, "Cumulants of Stochastic Response for Linear Systems," *ASCE Journal of Engineering Mechanics*, Vol. 112, No. 10, pp. 1062-1075.

Lutes, L. D., and Hu, S. J., 1986, "Non-normal Stochastic Response of Linear Systems," *ASCE Journal of Engineering Mechanics*, Vol. 112, No. 2, pp. 127-141.

Ma, F., 1987, "Extension of Second Moment Analysis to Vector Valued and Matrix-Valued Functions," *Int. J. Nonlinear Mech.*, Vol. 22, pp. 251-260.

Morison, J. R., O'Brien, M. P., Johnson, J. W., and Shaaf, S. A., 1950, "The Force Exerted by Surface Waves on Piles," *Petroleum Transactions*, AIME, p. 189.

Priestley, M. B., 1965, "Evolutionary Spectra and Non-Stationary Processes," *J. Royal Statistical Soc.*, Vol. 827, pp. 204-288.

Soize, C., 1978, "Gust Loading Factors with Nonlinear Pressure Terms," *J. Engrg. Struct. Div., ASCE*, Vol. 104, No. ST6, pp. 991-1007.

Stratonovich, R. L., 1963, *Topics in the Theory of Random Noise*, Vol. 1, Gordon and Breach Science Publishers, New York.

APPENDIX

In this Appendix some elements of the Kronecker algebra are reported.

Let $\mathbf{A}$ and $\mathbf{B}$ two matrices of order $m \times n$ and $p \times q$, respectively, then the Kronecker product of the two matrices denoted as $\mathbf{A} \otimes \mathbf{B}$ is a matrix $\mathbf{C}$ of order $(m\ p) \times (n\ q)$ given as

$$\mathbf{C} = \mathbf{A} \otimes \mathbf{B} = \begin{bmatrix} a_{11}\mathbf{B} & a_{12}\mathbf{B} & a_{1n}\mathbf{B} \\ \dots & \dots & \dots \\ a_{m1}\mathbf{B} & a_{m2}\mathbf{B} & a_{mn}\mathbf{B} \end{bmatrix}. \tag{A1}$$

The following properties hold

$$\mathbf{A} \otimes (\mathbf{B} \otimes \mathbf{C}) = (\mathbf{A} \otimes \mathbf{B}) \otimes \mathbf{C} \tag{A2}$$

$$\mathbf{A} \otimes (\mathbf{B} + \mathbf{C}) = \mathbf{A} \otimes \mathbf{B} + \mathbf{A} \otimes \mathbf{C} \tag{A3}$$

$$(\mathbf{A} \otimes \mathbf{B})^T = \mathbf{A}^T \otimes \mathbf{B}^T \tag{A4}$$

$$(\mathbf{A} \otimes \mathbf{B})^{-1} = \mathbf{A}^{-1} \otimes \mathbf{B}^{-1} \tag{A5}$$

$$(\mathbf{A} \otimes \mathbf{B})(\mathbf{C} \otimes \mathbf{D}) = (\mathbf{A}\ \mathbf{C}) \otimes (\mathbf{B}\ \mathbf{D}), \tag{A6}$$

provided the various quantities exist.

On the Approximate Solution of Nonclassically Damped Linear Systems

J. H. Hwang
Postdoctoral Fellow.

F. Ma
Associate Professor of Applied Mechanics, Mem. ASME.

Department of Mechanical Engineering, University of California, Berkeley, CA 94720

A common procedure in the solution of a nonclassically damped linear system is to neglect the off-diagonal elements of the associated modal damping matrix. For a large-scale system, substantial reduction in computational effort is achieved by this method of decoupling the system. In the present paper, the error introduced by disregarding the off-diagonal elements is evaluated, and a quadrature formula for the approximation error is derived. A tight error bound is then obtained. In addition, an effective scheme to improve the accuracy of the approximate solution is outlined.

1 Introduction

The method of modal superposition is a very powerful technique for evaluating the response of a linear dynamic system. A linear system is said to have classical normal modes if the system possesses a complete set of real orthonormal eigenvectors. In general, an undamped dynamic system always possesses classical normal modes. When dissipative forces are present, the system may or may not possess classical normal modes. If it does, the system is said to be classically damped. Caughey and O'Kelly (1965) established a necessary and sufficient condition for the existence of classical normal modes in a damped linear system. If classical normal modes exist, the differential equations of motion become decoupled when expressed in modal coordinates which are real. Otherwise, the system is said to be nonclassically damped. In reality, nonclassical damping comes from drastic variations of energy absorption rates of the materials in different parts of the structure. Typical examples of nonclassically damped systems are a nuclear reactor containment vessel founded on soft soil subjected to earthquake motion (Clough and Mojtahedi, 1976), and a base-isolated structure in the same environment (Tsai and Kelly, 1988).

When dissipative forces are nonclassical, it is generally difficult to analyze the system dynamics, owing to the complex nature of the eigensolutions. Foss (1958) and Vigneron (1986) proposed a state-space approach which takes into account the orthogonality relations between the complex eigenvectors of a nonclassically damped system. The key to the utility of the eigensolutions is of course orthogonality, which allows decoupling of the governing equations. One disadvantage of such exact methods is that they require significant numerical effort to determine the eigensolutions. The effort required is evidently intensified by the fact that the eigensolutions of a nonclassically damped system are complex. From the analysts' viewpoint, another disadvantage is the lack of physical insight afforded by methods which are intrinsically numerical in nature. Several authors have studied nonclassically damped linear systems by approximate techniques. For instance, Cronin (1976) obtained an approximate solution for a nonclassically damped system under harmonic excitation by perturbation techniques. Using the frequency domain approach, Hasselman (1976) proposed a criterion for determining whether the equations of motion might be considered practically decoupled if nonclassical damping exists. A similar criterion was also suggested by Warburton and Soni (1977). Chung and Lee (1986) applied perturbation techniques to obtain the eigensolutions of damped systems with weakly nonclassical damping. Prater and Singh (1986), and Nair and Singh (1986) developed several indices to determine quantitatively the extent of nonclassical damping in discrete vibratory systems. Nicholson (1987) gave upper bounds for the response of nonclassically damped systems under impulsive loads and step loads. Bellos and Inman (1990) studied the frequency response of nonproportionally damped linear systems.

In analyzing a nonclassically damped system, one common approximation is to neglect those damping terms which are nonclassical and retain the classical ones. This approach is termed the method of decoupling approximation. For large-scale systems, the computational effort at adopting decoupling approximation is at least an order of magnitude smaller than the method of complex modes. The solution of the decoupled equations would be close to the exact solution of the coupled equations if the nonclassical damping terms are sufficiently small. A discussion on this topic was given, for example, by Meirovitch (1967), Thomson et al. (1974), and Cronin (1976). Solution of a damped linear system by decoupling approximation is often convenient and practical. An attempt to evaluate the error of approximation, introduced by neglecting the nonclassical damping terms, was recently reported by Shahruz

Contributed by the Applied Mechanics Division of THE AMERICAN SOCIETY OF MECHANICAL ENGINEERS for publication in the ASME JOURNAL OF APPLIED MECHANICS.

Discussion on this paper should be addressed to the Technical Editor, Professor Lewis T. Wheeler, Department of Mechanical Engineering, University of Houston, Houston, TX 77204-4792, and will be accepted until four months after final publication of the paper itself in the ASME JOURNAL OF APPLIED MECHANICS.

Manuscript received by the ASME Applied Mechanics Division, Jan. 16, 1991; final revision, Jan. 22, 1992. Associate Technical Editor: P. D. Spanos.

and Ma (1988). It is claimed that the error bounds obtained in their paper are the tightest in a certain functional form for arbitrary external excitation. Ma and Hwang (1989) have attempted to generalize these error bounds in other functional forms.

The purpose of this paper is to derive a quadrature formula for the error due to decoupling approximation. While still assuming that the excitation is arbitrary, a new error bound, which is generally tighter than the previous ones given by Shahruz and Ma (1988), is obtained. An iterative scheme to improve the accuracy of the approximate solution is also proposed. The organization of the paper is as follows: In Section 2, a formulation of the problem is given. It is shown in Section 3 that the approximation error can be decomposed into an infinite series, with each term being the solution of the decoupled system. The series is then summed exactly in the Laplace domain, from which an error bound is obtained. An approach to improve the accuracy of the approximate solution is outlined in Section 4. This approach, inspired by the summation of the error series due to decoupling approximation, was discussed earlier by Ma and Hwang (1989). An example in Section 5 illustrates the theoretical developments pursued in this paper. In Section 6 a summary of findings is provided.

2 The Neglect of Off-Diagonal Elements

Consider the equation of motion of a discrete linear system under external excitation

$$M\ddot{x}+C\dot{x}+Kx=f(t), \quad x(0)=x_0,\ \dot{x}(0)=\dot{x}_0, \quad t\geq 0, \tag{1}$$

where the mass matrix M, the damping matrix C, and the stiffness matrix K are of order $n \times n$. The displacement vector $x(t)$ and external excitation $f(t)$ are n-dimensional vectors. For passive systems, the matrices M, C, and K are symmetric and positive definite. These assumptions are not arbitrary, but in fact have solid footing in the theory of Lagrangian dynamics. Symmetry of M results naturally from the transformation from Cartesian to generalized coordinates for a scleronomic system, and the positive definiteness requirement is a property of kinetic energy. Symmetry of K results from linearization of the potential energy function about an equilibrium point, and the form of the Rayleigh dissipation function ensures symmetry of C.

Let U denote the $n \times n$ modal matrix corresponding to the system (1). The modal matrix is a nonsingular matrix whose columns are the eigenvectors of the generalized symmetric eigenvalue problem

$$K u^{(i)}=\omega_i^2 M u^{(i)}, \tag{2}$$

where $\omega_i^2 > 0$ and $u^{(i)}$, $i = 1, \ldots, n$, are the eigenvalues and the corresponding eigenvectors, respectively. The modal matrix is usually orthonormalized according to $U^TMU=I_n$, where U^T denotes the transpose of U, and I_n is the identity matrix of order n. In addition, $U^TKU = \text{diag}\,(\omega_1^2, \ldots, \omega_n^2) = \Omega$. By the linear transformation $x(t) = Uq(t)$, Eq. (1) can be written in the normalized form

$$\ddot{q}+D\,\dot{q}+\Omega q=g(t), \quad q(0)=U^TMx_0, \quad \dot{q}(0)=U^TM\dot{x}_0, \quad t\geq 0, \tag{3}$$

where $g(t) = U^Tf(t)$, and $q(t)$ is the n-dimensional vector of normal coordinates. The symmetric matrix $D = U^TCU$ is called the modal damping matrix. If D is diagonal, the system (1) is said to be classically damped. In the event that the damping matrix C is a linear combination of the mass and the stiffness matrices, then D is diagonal. This is a sufficient condition for D to be diagonal, and was originally given by Lord Rayleigh (1945). The necessary and sufficient condition under which system (1) is classically damped has been given by Caughey and O'Kelly (1965). When D is diagonal, system (3) is a set of n decoupled second-order differential equations, which can be solved for $q(t)$ conveniently. Then, the solution of (1) is obtained from $x(t) = Uq(t)$, for all $t \geq 0$.

Write the modal damping matrix in the form

$$D=\Lambda+R \tag{4}$$

where $\Lambda = \text{diag}\,(2\zeta_1\omega_1, \ldots, 2\zeta_n\omega_n)$ is a matrix composed of the diagonal elements of D, and $R = [d_{ij}]$ is a symmetric $n \times n$ matrix with zero diagonal elements, and whose off-diagonal elements coincide with those of D. Note that by the positive definiteness of C, $\zeta_i > 0$ for $i = 1, \ldots, n$. Neglect the matrix R in Eq. (3), and denote the solution of the decoupling approximation by $q_a(t)$. Thus,

$$\ddot{q}_a+\Lambda\,\dot{q}_a+\Omega\,q_a=g(t), \quad t\geq 0, \tag{5}$$

where $q_a(0) = q(0)$, and $\dot{q}(0) = \dot{q}(0)$. Define the n-dimensional vector of error due to decoupling approximation by

$$e=q-q_a. \tag{6}$$

Subtracting Eq. (5) and (3), we obtain

$$\ddot{e}+\Lambda\dot{e}+\Omega e+R\dot{q}=0, \quad t\geq 0, \tag{7}$$

with $e(0) = \dot{e}(0) = 0$. The above expression implies that the error $e(t)$ can be regarded as the image of $q(t)$ under a certain linear operator $\overline{H}$, so that

$$e(t)=\overline{H}(q(t)). \tag{8}$$

In the following, we shall use the L_∞ norm of a vector, defined by $\|h(p)\| = \max_{1\leq i\leq n} |h_i(p)|$ for any vector $h(p) = [h_1(p), \ldots, h_n(p)]^T$. The parameter p can be real or complex. If p is real and non-negative, we put $p = t$, and define $\|h(t)\| = \max_{1\leq i\leq n} \sup_{t\geq 0} |h_i(t)|$. It will always be clear from the context which of these norms is used. As shown by Shahruz and Ma (1988), Eq. (7) can be manipulated to give an error bound of the form

$$\|e\|\leq m\|q\|. \tag{9}$$

The smallest value of m that satisfies the above inequality is given by

$$m=\|\overline{H}\|=\max_{1\leq i\leq n}\frac{2\sigma_i}{\omega_i}\cdot\frac{\exp(V(\zeta_i))}{1-\exp(W(\zeta_i))}, \tag{10}$$

where ζ_i is the damping ratio defined earlier, and

$$V(\zeta_i)=-\frac{\zeta_i}{(1-\zeta_i^2)^{1/2}}\tan^{-1}\frac{(1-\zeta_i^2)^{1/2}}{\zeta_i}, \tag{11}$$

$$W(\zeta_i)=-\frac{\pi\zeta_i}{(1-\zeta_i^2)^{1/2}}. \tag{12}$$

The quantity σ_i is the row sum of the absolute values of the off-diagonal elements of the modal damping matrix D,

$$\sigma_i=\sum_{\substack{j=1\\ j\neq i}}^{n}|d_{ij}|. \tag{13}$$

Several variants of the error bound have also been given by Shahruz and Ma (1988). Although the above error bound is the tightest of the form (9), the error bound is still relatively large for many applications. This is perhaps due to the fact that a functional form of the type (9) does not take into account the excitation $f(t)$. In the next section, we shall incorporate the driving force $f(t)$ into the analysis to derive a tighter error bound.

3 Analysis of Error

It will be shown that the error due to decoupling approximation can be decomposed into an infinite series, which may then be summed exactly in the Laplace domain. Based upon this exact sum, the error bound of the last section will be sharpened. In order to do that, it is necessary to take into consideration the external excitation, and to cast the new error

bound in a functional form that is different from (9). Recall that $e = q - q_a$. If q_a is used in place of q in Eq. (7), we have

$$\ddot{e} + (\Lambda + R)\dot{e} + \Omega e = -R\ddot{q}_a, \quad t \geq 0, \tag{14}$$

where $e(0) = \dot{e}(0) = 0$. This equation has the same form as (3), with e and $-R\ddot{q}_a$ replacing q and $g(t)$, respectively. At this stage, invoke the decoupling approximation on (14), and denote the solution of the resulting equation by u_0. Then

$$\ddot{u}_0 + \Lambda\, \ddot{u}_0 + \Omega\, u_0 = -R\ddot{q}_a, \quad t \geq 0, \tag{15}$$

with the same initial conditions as Eq. (14). Subtracting Eq. (15) from (14), and denoting the corresponding error vector by

$$e_1 = e - u_0, \tag{16}$$

we have

$$\ddot{e}_1 + \Lambda\, \dot{e}_1 + \Omega\, e_1 + R\dot{e} = 0, \quad e_1(0) = \dot{e}_1(0) = 0, \quad t \geq 0. \tag{17}$$

Substituting e from (16),

$$\ddot{e}_1 + (\Lambda + R)\dot{e}_1 + \Omega\, e_1 = -R\ddot{u}_0, \quad e_1(0) = \dot{e}_1(0) = 0, \quad t \geq 0. \tag{18}$$

If the decoupling approximation is invoked again on the above equation, with the resulting solution denoted by u_1, then

$$\ddot{u}_1 + \Lambda\, \dot{u}_1 + \Omega\, u_1 = -R\ddot{u}_0, \quad u_1(0) = \dot{u}_1(0) = 0, \quad t \geq 0, \tag{19}$$

which has the same form as (15). Define the error of this approximation by

$$e_2 = e_1 - u_1. \tag{20}$$

It can be easily shown that

$$\ddot{e}_2 + (\Lambda + R)\dot{e}_2 + \Omega\, e_2 = -R\ddot{u}_1, \quad e_2(0) = \dot{e}_2(0) = 0, \quad t \geq 0, \tag{21}$$

and

$$e_2 = e - u_0 - u_1. \tag{22}$$

Thus, the error vector e_2 and the error vector e are related through terms u_0, u_1, obtained by successive application of decoupling approximation. By induction, the following scheme can be defined: for every integer $k \geq 1$,

$$e_k = e_{k-1} - u_{k-1}, \quad e_0 = e \tag{23}$$

$$\ddot{u}_k + \Lambda\, \dot{u}_k + \Omega\, u_k = -R\dot{u}_{k-1}, \quad u_k(0) = \dot{u}_k(0) = 0, \quad t \geq 0, \tag{24}$$

$$\ddot{e}_k + (\Lambda + R)\dot{e}_k + \Omega\, e_k = -R\dot{u}_{k-1}, \quad e_k(0) = \dot{e}_k(0), \quad t \geq 0, \tag{25}$$

where u_0 is given by Eq. (15). From (23), it is easy to see that

$$e - \lim_{k \to \infty} e_k = \sum_{k=1}^{\infty} (e_{k-1} - e_k) = \sum_{k=1}^{\infty} u_{k-1}. \tag{26}$$

For each k, u_k is the solution of a decoupled system that can be solved very readily. In the Appendix it is shown that the vector e_k tends to zero as k increases without bound. The total error e due to the decoupling approximation of system (3) can therefore be expressed as

$$e = q - q_a = \sum_{k=0}^{\infty} u_k. \tag{27}$$

It is possible to sum the above series exactly in the Laplace domain. Applying the Laplace transform to Eqs. (5), (15), and (24), and taking into account the initial conditions, we obtain

$$\hat{q}_a(s) = (I_n s^2 + \Lambda s + \Omega)^{-1}\hat{g}(s) + (I_n s^2 + \Lambda s + \Omega)^{-1}[(sI_n + \Lambda)q(0) + \dot{q}(0)], \tag{28}$$

$$\hat{u}_0(s) = -(I_n s^2 + \Lambda s + \Omega)^{-1} sR\hat{q}_a(s) + (I_n s^2 + \Lambda s + \Omega)^{-1} Rq(0), \tag{29}$$

$$\hat{u}_k(s) = -(I_n s^2 + \Lambda s + \Omega)^{-1} sR u_{k-1}(s), \quad k \geq 1, \tag{30}$$

where $\hat{q}_a(s)$, $\hat{g}(s)$, $\hat{u}_0(s)$, and $\hat{u}_k(s)$ are, respectively, the Laplace transforms of $q_a(t)$, $g(t)$, $u_0(t)$, and $u_k(t)$, and I_n is the identity matrix. Define two linear operators $\hat{H}(s)$ and $\hat{F}(s)$ by

$$\hat{H}(s) = -s(I_n s^2 + \Lambda s + \Omega)^{-1} R, \tag{31}$$

$$\hat{F}(s) = (I_n s^2 + \Lambda s + \Omega)^{-1}. \tag{32}$$

Note that these $n \times n$ matrix functions depend only upon the parameters of system (3). In addition, $\hat{H}(s) = -s\hat{F}(s)R$. The ith row of $\hat{H}(s)$ is

$$\frac{-s}{s^2 + 2\zeta_i\omega_i s + \omega_i^2}\,[d_{i1}, \ldots, d_{i,i-1}, 0, d_{i,i+1}, \ldots, d_{in}], \tag{33}$$

and the ith row of $\hat{F}(s)$, on the other hand, is

$$\frac{1}{s^2 + 2\zeta_i\omega_i s + \omega_i^2}\,[0, \ldots, 1, \ldots, 0], \tag{34}$$

where d_{ij} is the ijth element of R. In terms of $\hat{H}(s)$ and $\hat{F}(s)$, we have

$$\hat{q}_a(s) = \hat{F}(s)\hat{g}(s) + \hat{F}(s)[(sI_n + \Lambda)q(0) + \dot{q}(0)], \tag{35}$$

$$\hat{u}_0(s) = \hat{H}(s)\hat{q}_a(s) + \hat{F}(s)Rq(0), \tag{36}$$

$$\hat{u}_k(s) = \hat{H}(s)u_{k-1}(s), \quad k \geq 1. \tag{37}$$

Combining the last two equations

$$\hat{u}_k(s) = [\hat{H}(s)]^{k+1}\,\hat{q}_a(s) + [\hat{H}(s)]^k\,\hat{F}(s)Rq(0), \quad k \geq 0, \tag{38}$$

it follows that

$$\hat{e}(s) = \sum_{k=0}^{\infty} \hat{u}_k(s) = \hat{H}(s)[I_n - \hat{H}(s)]^{-1}\hat{q}_a(s) + [I_n - \hat{H}(s)]^{-1}\hat{F}(s)Rq(0). \tag{39}$$

From Eq. (35) we obtain

$$\hat{e}(s) = \hat{H}(s)[I_n - \hat{H}(s)]^{-1}\hat{F}(s)\hat{g}(s) + \hat{H}(s)[I_n - \hat{H}(s)]^{-1}\hat{F}(s)[(sI_n + \Lambda)q(0) + \dot{q}(0)] + [I_n - \hat{H}(s)]^{-1}\hat{F}(s)Rq(0). \tag{40}$$

Thus, the error due to decoupling approximation has been summed exactly in the Laplace domain. This may also be regarded as a quadrature solution of the error function $e(t)$, which can be obtained by taking the inverse Laplace transform. The right-hand side of Eq. (40) depends only on the parameters of system (3), the external excitation, and initial conditions. The convergence of this expression is always satisfied if the modal damping matrix D is diagonally dominant. Expression (40) can also be derived by other methods. The method adopted here lends itself to an iterative approach, which will be expounded in the next section.

In many applications, the maximum error is attained in the steady state. In order to derive a new error bound, it is necessary to compute the norm of $\|\hat{e}(s)\|$ in the steady state. Since the steady-state response does not depend on initial conditions, it can be assumed that $q(0) = \dot{q}(0) = 0$. Taking norms on both sides of Eq. (40) we have

$$\|\hat{e}(s)\| \leq \frac{\|\hat{H}(s)\|}{1 - \|\hat{H}(s)\|}\,\|\hat{F}(s)\|\,\|\hat{g}(s)\|, \tag{41}$$

where the L_∞ induced norm of the matrices $\hat{H}(s)$ and $\hat{F}(s)$ is the maximum row sum of absolute values, defined by

$$\|\hat{H}(s)\| = \max_{1 \leq i \leq n} \left| \frac{s\sigma_i}{s^2 + 2\zeta_i\omega_i s + \omega_i^2} \right|, \tag{42}$$

$$\|\hat{F}(s)\| = \max_{1 \leq j \leq n} \left| \frac{1}{s^2 + 2\zeta_j\omega_j s + \omega_j^2} \right|, \tag{43}$$

with σ_i given by expression (13). Suppose the maximum row sum is attained when $i = l$ in Eq. (42), and when $j = m$ in (43). Then inequality (41) can be manipulated into the form

$$\|\hat{e}(s)\| \le \left| \frac{\alpha_1 s+\alpha_2}{s^2+2\eta_l\omega_l s+\omega_l^2} - \frac{\alpha_1 s+(\omega_m^2/\omega_l^2)\alpha_2}{s^2+2\zeta_m\omega_m s+\omega_m^2} \right| \|\hat{g}(s)\|, \quad (44)$$

where

$$\eta_l = \frac{2\zeta_l\omega_l - \sigma_l}{2\omega_l}, \quad (45)$$

and α_1 and α_2 are constants given by

$$\alpha_1 = \frac{\sigma_l(\omega_m^2-\omega_l^2)}{(\omega_l^2-\omega_m^2)^2+4\omega_l^2\omega_m^2(\eta_l^2+\zeta_m^2)-4\eta_l\omega_l\zeta_m\omega_m(\omega_l^2+\omega_m^2)}, \quad (46)$$

$$\alpha_2 = \frac{-2\sigma_l\omega_l^2(\eta_l\omega_l-\zeta_m\omega_m)}{(\omega_l^2-\omega_m^2)^2+4\omega_l^2\omega_m^2(\eta_l^2+\zeta_m^2)-4\eta_l\omega_l\zeta_m\omega_m(\omega_l^2+\omega_m^2)}. \quad (47)$$

It follows from Eq. (44) that

$$\|\hat{e}(s)\| \le \max_{1\le k\le n} \left| \frac{\alpha_1 s+\alpha_2}{s^2+2\eta_l\omega_l s+\omega_l^2}\hat{g}_k(s) - \frac{\alpha_1 s+(\omega_m^2/\omega_l^2)\alpha_2}{s^2+2\zeta_m\omega_m s+\omega_m^2}\hat{g}_k(s) \right|, \quad (48)$$

where an inequality of the type $||a|-|b|| \le |a-b|$ has been used, and $\hat{g}(s) = [\hat{g}_1(s), \ldots, \hat{g}_n(s)]^T$. Note that the coefficients of $\hat{g}_k(s)$ are only ratios of simple polynomials. Clearly, the above error bound can be recast in the form

$$\|e(t)\| \le \|b(t)\|, \quad (49)$$

by inverse Laplace transform, with $b(t)$ determined by the two terms on the right-hand side of inequality (48). The procedure to compute the error bound (49) is much simpler than it appears. Given an excitation vector $g(t)$, Laplace transform is first applied to obtain $\hat{g}(s)$. Ratios of simple polynomials are then multiplied to $\hat{g}(s)$, as shown in inequality (48). Taking the inverse Laplace transform of the products leads to the new error bound (49). The new error bound (49) is generally much sharper than that given by (9) and (10), as will be illustrated in Section 5. The new error bound is not of the functional form (9), and it involves the external excitation. If the approximate solution q_a is first computed, then the error bound defines a neighborhood about q_a in which the actual solution q lies.

As an example, in the computation of the new error bound, consider a system subjected to harmonic excitation, with $g(t) = A \sin\omega t[1, \ldots, 1]^T$. In this case,

$$\|\hat{g}(s)\| = \frac{A\omega}{s^2+\omega^2}. \quad (50)$$

Expression (44) becomes

$$\|\hat{e}(s)\| \le \left| \frac{\alpha_1 s+\alpha_2}{s^2+2\eta_l\omega_l s+\omega_l^2} - \frac{\alpha_1 s+(\omega_m^2/\omega_l^2)\alpha_2}{s^2+2\zeta_m\omega_m s+\omega_m^2} \right| \left| \frac{A\ \omega}{s^2+\omega^2} \right|. \quad (51)$$

Therefore, the error bound (49) is

$$\|e(t)\| \le \sup_{t\ge 0} |C\cos(\omega t) + D\sin(\omega t)|, \quad (52)$$

where

$$C = \frac{-A\omega[\alpha_1(\omega^2-\omega_l^2)+2\alpha_2\eta_l\omega_l] + A\omega\left[\alpha_1(\omega^2-\omega_m^2)+2\alpha_2\frac{\omega_m^2}{\omega_l^2}\zeta_m\omega_m\right]}{(\omega_l^2-\omega^2)^2+4\eta_l^2\omega_l^2\omega^2}, \quad (53)$$

$$D = \frac{A[2\alpha_1\eta_l\omega_l\omega^2+\alpha_2(\omega_l^2-\omega^2)] - A\left[2\alpha_1\zeta_m\omega_m\omega^2+\alpha_2\frac{\omega_m^2}{\omega_l^2}(\omega_m^2-\omega^2)\right]}{(\omega_l^2-\omega^2)^2+4\eta_l^2\omega_l^2\omega^2}. \quad (54)$$

As another example, let $g(s) = u(t)[1, \ldots, 1]^T$, where $u(t)$ is the unit step function. Hence, $\|\hat{g}(s)\| = |1/s|$. Inequality (44) can now be written as

$$\|\hat{e}(s)\| \le \left| \frac{\alpha_1 s+\alpha_2}{s^2+2\eta_l\omega_l s+\omega_l^2} - \frac{\alpha_1 s+(\omega_j^2/\omega_l^2)\alpha_2}{s^2+2\zeta_m\omega_m s+\omega_m^2} \right| \left| \frac{1}{s} \right|. \quad (55)$$

The error bound (49), valid for $\zeta_m > 0$ and $\eta_l > 0$, is

$$\|e(t)\| \le \sup_{t\ge 0} \left| \frac{\alpha_1}{\omega_l(1-\eta_l)^{1/2}} e^{-\eta_l\omega_l t} \left[\sin(\omega_l(1-\eta_l)^{\frac{1}{2}}t + \frac{\alpha_2}{\alpha_1\omega_l}\sin(\omega_l(1-\eta_l)^{\frac{1}{2}}t-\phi_l) \right] - \frac{\alpha_1}{\omega_m(1-\zeta_m)^{1/2}} e^{-\zeta_m\omega_m t} \times \left[\sin(\omega_m(1-\zeta_m)^{\frac{1}{2}}t) + \frac{\alpha_2}{\alpha_1\omega_m}\sin(\omega_m(1-\zeta_m)^{\frac{1}{2}}t-\phi_m) \right] \right|, \quad (56)$$

for which

$$\phi_l = -\tan^{-1}\frac{(1-\eta_l^2)^{1/2}}{\eta_l}, \quad (57)$$

$$\phi_m = -\tan^{-1}\frac{(1-\zeta_m^2)^{1/2}}{\zeta_m}. \quad (58)$$

Other types of excitation may be considered with the same readiness. In fact, a table of error bounds corresponding to excitation of various forms has been compiled.

Similar results apply in the analysis of frequency response. For example, the ratio of $\|e(j\omega)\|$ to $\|\hat{g}(j\omega)\|$ is bounded in such way that

$$\frac{\|\hat{e}(j\omega)\|}{\|\hat{g}(j\omega)\|} \le \left| \frac{j\alpha_1\omega+\alpha_2}{\omega_l^2-\omega^2+j\,2\eta_l\omega_l\omega} - \frac{j\alpha_1\omega+(\omega_m^2/\omega_l^2)\alpha_2}{\omega_m^2-\omega^2+j\,2\zeta_m\omega_m\omega} \right|, \quad (59)$$

where $j = \sqrt{-1}$, and ω is the frequency of external excitation.

4 Improving the Accuracy of Approximate Solution

In this section, we shall present an iterative approach to the approximate solution of nonclassically damped systems. We collect Eqs. (5), (15), and (24) together in the following system:

$$\ddot{q}_a + \Lambda\,\dot{q}_a + \Omega\,q_a = g(t), \quad q_a(0)=q(0), \quad \dot{q}_a(0)=\dot{q}(0), \quad t\ge 0, \quad (60)$$

$$\ddot{u}_0 + \Lambda\,\dot{u}_0 + \Omega\,u_0 = -R\,\dot{q}_a, \quad u_0(0)=\dot{u}_0(0)=0, \quad t\ge 0, \quad (61)$$

$$\ddot{u}_k + \Lambda\,\dot{u}_k + \Omega\,u_k = -R\,\dot{u}_{k-1}, \quad u_k(0)=\dot{u}_k(0)=0, \quad t\ge 0, \quad k\ge 1. \quad (62)$$

The above system can be solved iteratively. Solution of (60) yields q_a, which defines the inhomogeneous part of (61). Solution of (61) yields u_0, which serves as input to (62). The solution of (62) generates u_k for $k \ge 1$. Moreover, each of the above equations represents a decoupled system, the solution of which can be found very readily. From Eq. (27),

$$q = q_a + \sum_{k=0}^{\infty} u_k(t). \quad (63)$$

Hence, the exact solution q of system (3) can also be obtained by the above iterative procedure. The starting point of the iteration is q_a, the solution obtained by neglecting the off-

diagonal elements of the modal damping matrix. Once q_a is determined, u_0, and subsequently u_k, $k \geq 1$, can be computed iteratively. Each iteration simply involves the solution of a decoupled equation.

It is proposed that the first few terms of the infinite series in (63) can be used as an approximate solution of the non-classically damped linear system (3). This is indeed an effective procedure, as the accuracy of the approximate solution is generally very high. For a specified degree of tolerance, we can always estimate the smallest number N of terms needed to achieve that degree of accuracy. To see this, assume again that $q(0) = \dot{q}(0) = 0$. Applying the Laplace transform to Eqs. (61) and (62), we have

$$\hat{u}_0(s) = \hat{H}(s)\hat{q}_a(s), \tag{64}$$

$$\hat{u}_k(s) = \hat{H}(s)\hat{u}_{k-1}(s), \quad k \geq 1, \tag{65}$$

where $\hat{H}(s)$ has been defined in Eq. (31). It follows that

$$u_0(t) = \int_0^t H(t-\tau)\, q_a(\tau)\, d\tau, \tag{66}$$

$$u_k(t) = \int_0^t H(t-\tau)\, u_{k-1}(\tau)\, d\tau, \; k \geq 1, \tag{67}$$

where $H(t)$ is the inverse Laplace transform of $\hat{H}(s)$. Define a linear operator $\overline{H}$ by

$$\overline{H}(h(t)) = (H^* h)(t) = \int_0^t H(t-\tau)\, h(\tau)\, d\tau, \tag{68}$$

so that $\overline{H}$ represents the convolution of the functions $H(t)$ and $h(t)$. In this case, Eqs. (66) and (67) can be rewritten as

$$u_0(t) = \overline{H}(q_a(t)), \; t \geq 0, \tag{69}$$

$$u_k(t) = \overline{H}(u_{k-1}(t)), \; t \geq 0. \tag{70}$$

Hence,

$$\|u_0\| \leq \|\overline{H}\|\, \|q_a\|, \tag{71}$$

$$\|u_k\| \leq \|\overline{H}\|\, \|u_{k-1}\|, \; k \geq 1. \tag{72}$$

Combining the last two equations,

$$\|u_k\| \leq \|\overline{H}\|^{k+1} \|q_a\|. \tag{73}$$

As it turns out, the linear operator $\overline{H}$ has been used by Shahruz and Ma (1988), and $\|\overline{H}\|$ is given exactly by expression (10). The operator norm $\|\overline{H}\|$ is induced by the vector norm $\|h(t)\| = \max_{1 \leq i \leq n} \sup_{t \geq 0} |h_i(t)|$, and is different from the operator norm used in Section 3. If we solve (60), (61), and the first m equations of (62), then an approximate solution q^* is furnished by

$$q^* = q_a + u_0 + \ldots + u_m. \tag{74}$$

The error e of the above approximate solution is

$$e = q - q^* = \sum_{k=m+1}^{\infty} u_k. \tag{75}$$

Using the triangle inequality and (73), we have

$$\|e\| \leq \sum_{k=m+1}^{\infty} \|u_k\| \leq \frac{\|\overline{H}\|^{m+2}}{1 - \|\overline{H}\|} \|q_a\|. \tag{76}$$

If an error tolerance is specified by $\|e\| \leq \epsilon\, \|q_a\|$, we obtain

$$N = m + 2 \geq \left| \frac{\ln(\epsilon(1 - \|\overline{H}\|))}{\ln \|\overline{H}\|} \right|, \tag{77}$$

where N is the number of equations to be solved to meet the specified error tolerance. For example, when $\|\overline{H}\| = 0.2$, and $\epsilon = 0.05$ or five percent, then $m = 0$. That means $N = 2$. In other words, the true solution q lies within a band centered at $q^* = q_a + u_0$, with $0.05\, \|q_a\|$ as the half-width. In general, we need only solve a small number of decoupled equations to achieve a high degree of accuracy. For a large-scale system, substantial reduction in computational effort results in utilizing this iterative scheme of solution. The above iterative scheme was first proposed by Ma and Hwang (1989); however, Udwadia and Esfandiari (1990) have also recently discussed an iterative method of similar kind.

5 Example

In this section, an example is given to illustrate possible applications of the results obtained so far. A low-order system is employed for convenience. Consider a system whose normalized equation is

$$\begin{bmatrix} 1 & 0 \\ 0 & 1 \end{bmatrix} \begin{bmatrix} \ddot{q}_1 \\ \ddot{q}_2 \end{bmatrix} + \begin{bmatrix} 1.559 & -0.2 \\ -0.2 & 1.6 \end{bmatrix} \begin{bmatrix} \dot{q}_1 \\ \dot{q}_2 \end{bmatrix} + \begin{bmatrix} 3.8 & 0 \\ 0 & 4 \end{bmatrix} \begin{bmatrix} q_1 \\ q_2 \end{bmatrix} = \begin{bmatrix} 1 \\ 1 \end{bmatrix} g(t). \tag{78}$$

It is easy to see that $\omega_1 = 1.9493$, $\omega_2 = 2$, and $\zeta_1 = \zeta_2 = 0.4$. An approximate solution of system (78) is obtained by solving the following decoupled equation:

$$\begin{bmatrix} 1 & 0 \\ 0 & 1 \end{bmatrix} \begin{bmatrix} \ddot{q}_{a1} \\ \ddot{q}_{a2} \end{bmatrix} + \begin{bmatrix} 1.559 & 0 \\ 0 & 1.6 \end{bmatrix} \begin{bmatrix} \dot{q}_{a1} \\ \dot{q}_{a2} \end{bmatrix} + \begin{bmatrix} 3.8 & 0 \\ 0 & 4 \end{bmatrix} \begin{bmatrix} \dot{q}_{a1} \\ \dot{q}_{a2} \end{bmatrix} = \begin{bmatrix} 1 \\ 1 \end{bmatrix} g(t). \tag{79}$$

Case (i). $g(t) = \sin(2t)$. The steady-state solution of (79) is

$$q_s(t) = \begin{bmatrix} -(0.320)\sin(2t + 1.506) \\ -(0.313)\sin(2t - 1.571) \end{bmatrix}. \tag{80}$$

For the system (79), $\|q_a\| = \|q_s\| = 0.32$. For illustration we shall focus on the first normal coordinate $q_1(t)$. The exact solution $q_1(t)$, the solution $q_{a1}(t)$ by decoupling approximation, and the approximate solution $q_1^*(t)$ obtained by iteration are all plotted in Fig. 1. To compute $q_1^*(t)$ it is specified that $\epsilon = 0.05$, so that the error tolerance becomes $\|e\| \leq \epsilon\, \|q_a\| = 0.016$. Using Eq. (10), we find that $\|\overline{H}\| = 0.166$. From formula (77), $N = 2$. Therefore, $q_1^*(t) = q_{a1}(t) + u_{01}(t)$ is sufficient to meet the given error tolerance. It should be noted that $q_1^*(t)$ is remarkably close to the exact solution $q_1(t)$.

According to Shahruz and Ma (1988), the tightest error bound of the functional form (9) is given by $\|e\| \leq (0.166)$

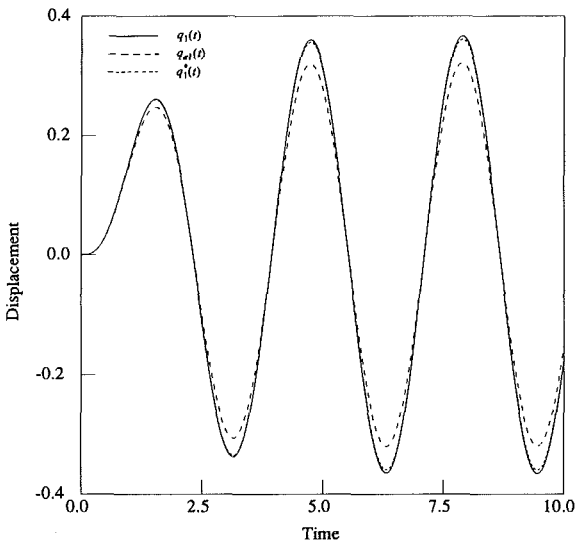

Fig. 1 Exact and approximate solutions for sinusoidal excitation

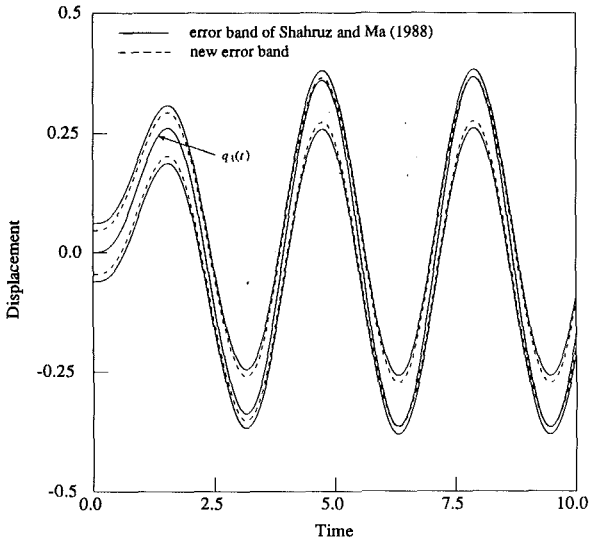

Fig. 2 Comparison of error bands for sinusoidal excitation

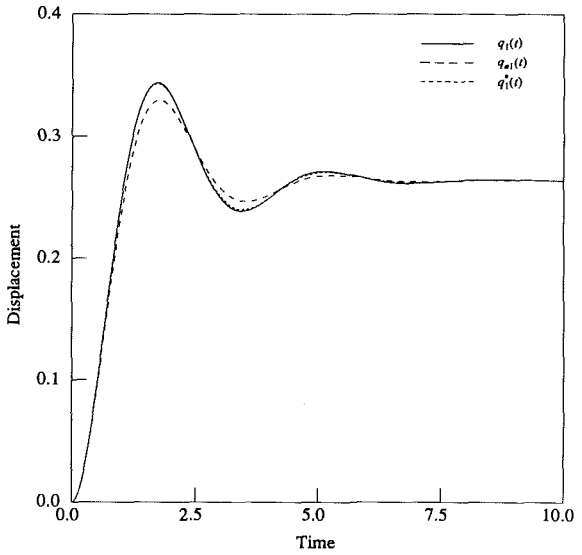

Fig. 3 Exact and approximate solutions for unit step excitation

$\|q\| = 0.061$. This error bound is plotted as solid lines in Fig. 2. The new error bound (52) leads to $\|e\| \leq 0.046$, which is clearly sharper than the tightest error bound of the form (9). The new error bound is plotted as dashed lines in Fig. 2, where the exact solution $q_1(t)$ is also shown. Since the exact solution almost meets the new error bound, the new error bound is indeed quite close to the maximum exact error in the steady state.

Case (ii). $g(t) = u(t)$. When the excitation is the unit step function, the steady-state solution of (79) is

$$q_s(t) = \begin{bmatrix} 0.263 \\ 0.250 \end{bmatrix}, \tag{81}$$

and $\|q_a\| = \|q_s\| = 0.263$. The exact solution $q_1(t)$, the solution $q_{a1}(t)$ by decoupling approximation, and the approximate solution $q_1^*(t) = q_{a1}(t) + u_{01}(t)$, are all plotted in Fig. 3. The tightest possible error bound of the form (9) is given by $\|e\| \leq (0.166)\ \|q\| = 0.0436$, where $\|q\|$ is the exact solution. The new error bound (56) yields $\|e\| \leq 0.020$, which is sharper than the previous bound. The error bound of Shahruz and Ma (1988) and the new error bound are plotted in Fig. 4. Extensive numerical calculations have been performed by the authors,

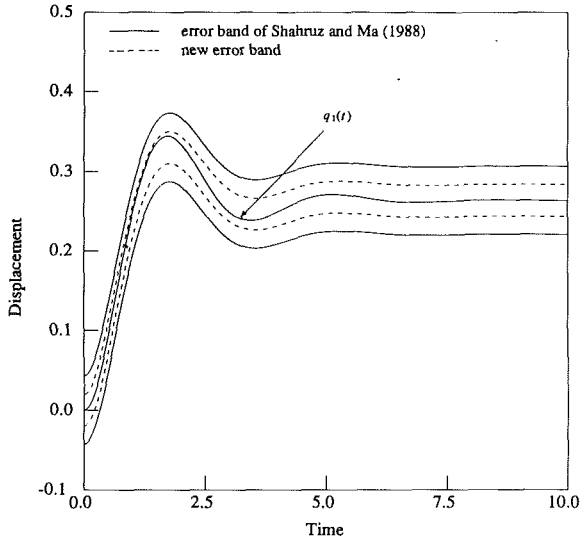

Fig. 4 Comparison of error bands for unit step excitation

and all calculations have yielded the same qualitative conclusion that the new error bound is generally much sharper than that previously given by Shahruz and Ma (1988).

6 Conclusions

The normal coordinates of a nonclassically damped system are coupled by the nonzero off-diagonal elements of the associated modal damping matrix. One common procedure in the solution of such a system is to neglect the off-diagonal elements of the modal damping matrix. For a large-scale system, substantial reduction in computational effort is achieved by this method of decoupling the system. In the present paper, the extent of approximation introduced by disregarding the off-diagonal elements is evaluated, and a tight error bound has been derived. The exact approximation error has been decomposed into an infinite series, and an iterative scheme to improve the accuracy of the approximate solution has been outlined. The major results, summarized in the following, are applicable to any linear system with nonclassical damping elements.

(1) It has been shown that the error due to decoupling approximation can be decomposed into an infinite series, which can then be summed exactly in the Laplace domain. The exact sum is given by expression (40), which may be regarded as a quadrature solution of the error function.

(2) When the external excitation is taken into account, a new error bound (48) has been derived. This new error bound is generally sharper than that provided by expression (9). The error bound defines a neighborhood about the approximate solution q_a in which the exact solution q of the original system lies.

(3) An effective procedure to improve the accuracy of solution by decoupling approximation has been proposed. This involves the solution of systems (60), (61), and the first few equations of (62). By solving a small number of additional decoupled equations in an iterative fashion, the accuracy of the approximate solution of a nonclassically damped system can be greatly enhanced.

The above statements are valid for any type of external excitation. An example has been employed to illustrate the theoretical developments pursued in this paper.

Acknowledgment

This research has been supported in part by the National Science Foundation under Grant No. MSS-8657619 and by the

Alexander von Humboldt Foundation. Opinions, findings, and conclusions expressed in this paper are those of the authors and do not necessarily reflect the views of the National Science Foundation.

References

Bellos, J., and Inman, D. J., 1990, "Frequency Response of Nonproportionally Damped, Lumped Parameter, Linear Dynamic Systems," ASME *Journal of Vibration and Acoustics*, Vol. 112, pp. 194–201.

Caughey, T. K., and O'Kelly, M. E. J., 1965, "Classical Normal Modes in Damped Linear Dynamic Systems," ASME JOURNAL OF APPLIED MECHANICS, Vol. 32, pp. 583–588.

Chung, K. R., and Lee, C. W., 1986, "Dynamic Reanalysis of Weakly Nonproportionally Damped Systems," *J. Sound and Vibration*, Vol. 111, pp. 37–50.

Clough, R. W., and Mojtahedi, S., 1976, "Earthquake Response Analysis Considering Non-Proportional Damping," *Earthq. Engng. Struct. Dyn.*, Vol. 4, pp. 489–496.

Cronin, D. L., 1976, "Approximation for Determining Harmonically Excited Response of Nonclassically Damped Systems," ASME *Journal of Engineering for Industry*, Vol. 98, pp. 43–47.

Foss, K. A., 1958, "Coordinates which Uncouple the Equations of Motion of Damped Linear Dynamic Systems," ASME JOURNAL OF APPLIED MECHANICS, Vol. 25, pp. 361–364.

Hasselman, T. K., 1976, "Modal Coupling in Lightly Damped Structures," *AIAA J.*, Vol. 14, pp. 1627–1628.

Ma, F., and Hwang, J. H., 1989, "On Decoupling the Equations of Motion of Nonclassically Damped Systems," ASME Paper 89-GT-123.

Meirovitch, L., 1967, *Analytical Methods in Vibrations*, Macmillan, New York.

Nair, S. S., and Singh, R., 1986, "Examination of the Validity of Proportional Damping Approximations with Two Further Numerical Indices," *J. Sound and Vibration*, Vol. 104, pp. 348–350.

Nicholson, D. W., 1987, "Response Bounds for Nonclassically Damped Mechanical Systems Under Transient Loads," ASME JOURNAL OF APPLIED MECHANICS, Vol. 54, pp. 430–433.

Prater, Jr., G., and Singh, R., 1986, "Quantification of the Extent of Non-Proportional Viscous Damping in Discrete Vibratory Systems," *J. Sound and Vibration*, Vol. 104, pp. 109–125.

Lord Rayleigh, 1945, *The Theory of Sound*, Vol. 1, Dover, New York.

Shahruz, S. M., and Ma, F., 1988, "Approximate Decoupling of the Equations of Motion of Linear Underdamped Systems," ASME JOURNAL OF APPLIED MECHANICS, Vol. 55, pp. 716–720.

Thomson, W. T., Calkin, T., and Caravani, P., 1974, "A Numerical Study of Damping," *Earthq. Engng. Struct. Dyn.*, Vol. 3, pp. 97–103.

Tsai, H.-C., and Kelly, J. M., 1988, "Non-classical Damping in Dynamics Analysis of Base-Isolated Structures with Internal Equipment," *Earthq. Engng. Struct. Dyn.*, Vol. 16, pp. 29–43.

Vigneron, F. R., 1986, "A Natural Modes Model and Modal Identities for Damped Linear Structures," ASME JOURNAL OF APPLIED MECHANICS, Vol. 53, pp. 33–38.

Udwadia, F. E., and Esfandiari, R. S., 1990, "Nonclassically Damped Dynamic Systems: An Iterative Approach," ASME JOURNAL OF APPLIED MECHANICS, Vol. 57, pp. 423–433.

Warburton, G. B., and Soni, S. R., 1977, "Errors in Response Calculations for Non-Classically Damped Structures," *Earthq. Engng. Struct. Dyn.*, Vol. 5, pp. 365–376.

APPENDIX

It will be shown that both vectors e_k and u_k tend to zero as k increases without bound. Taking norms in Eq. (38), we have

$$\|\hat{u}_k(s)\| \le \|\hat{H}(s)\|^{k+1}\|q_a(s)\| + \|\hat{H}(s)\|^k\|\hat{F}(s)Rq(0)\|. \quad \text{(A1)}$$

It has been assumed that $\|\hat{H}(s)\| < 1$. This assumption is certainly valid if the modal damping matrix D is diagonally dominant. From the above equation, it is clear that $\lim_{k\to\infty} \|\hat{u}_k\| = 0$. It follows that $\lim_{k\to\infty} \hat{u}_k = 0$, implying

$$\lim_{k\to\infty} u_k = u_\infty = 0. \quad \text{(A2)}$$

Let $k \to \infty$ in Eq. (25). Then

$$\ddot{e}_\infty + (\Lambda + R)\dot{e}_\infty + \Omega e_\infty = -R\dot{u}_\infty = 0. \quad \text{(A3)}$$

Since $e_\infty(0) = \dot{e}_\infty(0) = 0$, it follows from the uniqueness of the solution of the differential Eq. (A3) that

$$\lim_{k\to\infty} e_k = e_\infty = 0. \quad \text{(A4)}$$

This completes the demonstration.

G. W. Hunt
Department of Civil Engineering,
Imperial College,
London University,
London SW7 2BU, U.K.

E. L. Neto[1]
Instituto Technologico de Aeronautica,
12225 San Jose dos Campos-SP,
Sao Paulo, Brazil

Maxwell Critical Loads for Axially Loaded Cylindrical Shells

It is proposed that the classical Maxwell criterion for instability of gradient systems has significance as a lower bound on the appearance of localized as opposed to repeated periodic buckling. The hypothesis is tested against experiments, for the classic nonlinear problem of diamond-pattern buckling in the long thin axially loaded cylindrical shell. Excellent correlation is achieved.

1 Introduction

The response of an elastic structure in the post-buckling range is often directly represented by one or more fourth-order nonlinear differential equations. With time rather than a spatial dimension as the independent variable, these would relate to the special class of nonlinear dynamical system, known as Hamiltonian or energy preserving, most often associated with celestial mechanics: the spatial differential equation is of course independent of the choice of positive direction, while the general non-Hamiltonian dynamical system has a time domain that is irreversible, to take account of energy loss via damping.

For long structures, where the response may localize over a portion of the length, a time-like interpretation of the spatial dimension has great appeal. In particular, the conservative nature of the Hamiltonian suggests an energy interchange, over the spatial dimension, of "local" potential energy V, with a spatial form of "kinetic" energy T. Statical equilibrium, for which $T = 0$, corresponds to the periodic (constant amplitude) response, while "dynamical" equilibrium, with $T \neq 0$, allows for fluctuation in amplitude along the length, opening the way for modulation and localization of the buckle pattern in an exchange of energy between V and T. The response is then analogous to movement on a potential surface, which is the same as the periodic potential and contains all the inherent nonlinearities.

With the focus exclusively on localized responses, it is then possible to predict maximum amplitudes directly from energy considerations. For problems like the axially loaded cylindrical shell, which first destabilize and then restabilize in the post-buckling range, such amplitudes are apparently only attainable for loads greater than the classical Maxwell critical load, where the energy levels on the unbuckled fundamental path and restabilized post-buckled path are equal. The Maxwell load should thus represent a lower bound on the appearance of localized responses.

To check the validity of this conjecture requires solution well into the post-buckling range. The underlying theory is presently developed only in an asymptotic context (Hunt and Wadee, 1991), and we might expect some drift from the exact result as deflexions increase. We have therefore chosen, as a first check on this new theory, to compare with the careful experiments of Yamaki (1984) on the axially loaded cylindrical shell. Agreement with the minimum experimental load, and the corresponding wavelengths, is found to be excellent.

2 Lagrangian Formulation

Let us consider the well-known form of an unstable symmetric point of bifurcation, shown at the left of Fig. 1. This might represent the equilibrium response of a single-degree-of-freedom system, or perhaps a continuous system buckling periodically into a discrete post-buckling mode of amplitude A_i, such as a strut on an elastic foundation (Thompson and Hunt, 1973). In each case, evolution of the potential energy $V(A_i, P)$ under variation of the single control (loading) parameter P is as shown; equilibrium corresponds to stationary states of V, giving the single equation $\partial V/\partial A_i = 0$.

For a single-degree-of-freedom system the stationary state (a) is the only post-buckling solution available. Periodic buckling, however, can give way to a modulated (b) or a fully-localized (c) form, such that amplitude A_i varies along the length of the structure as seen at the top right of Fig. 1. It might then be postulated that the system is behaving as a point mass sliding frictionlessly in a potential well, as shown at the bottom right, with the varying amplitude expressed as $A_i(X)$, where X is a distance measure replacing time t in a Lagrangian formulation. Potential energy remains the same as for periodic responses but there is a new kinetic energy contribution T, which can be written

$$T(\dot{A}_i) = \frac{1}{2} T_{ii} \dot{A}_i^2, \tag{1}$$

the dot denoting differentiation with respect to X. Motion is then described by the Lagrange equation

$$\frac{d}{dX}\left(\frac{\partial \mathcal{L}}{\partial \dot{A}_i}\right) - \frac{\partial \mathcal{L}}{\partial A_i} = 0, \tag{2}$$

[1]Present address: Department of Civil Engineering, Imperial College, London University, London SW7 2BU, U.K.

Contributed by the Applied Mechanics Division of THE AMERICAN SOCIETY OF MECHANICAL ENGINEERS for publication in the ASME JOURNAL OF APPLIED MECHANICS.

Discussion on this paper should be addressed to the Technical Editor, Professor Lewis T. Wheeler, Department of Mechanical Engineering, University of Houston, Houston, TX 77204-4792, and will be accepted until four months after final publication of the paper itself in the ASME JOURNAL OF APPLIED MECHANICS.

Manuscript received by the ASME Applied Mechanics Division, May 30, 1991; final revision, Aug. 13, 1992. Associate Technical Editor: M. E. Fourney.

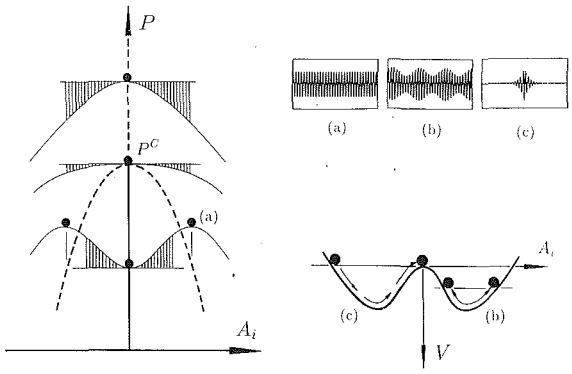

Fig. 1 The rolling ball analogy, as applied to: (*a*) periodic, (*b*) modulated, and (*c*) localized responses

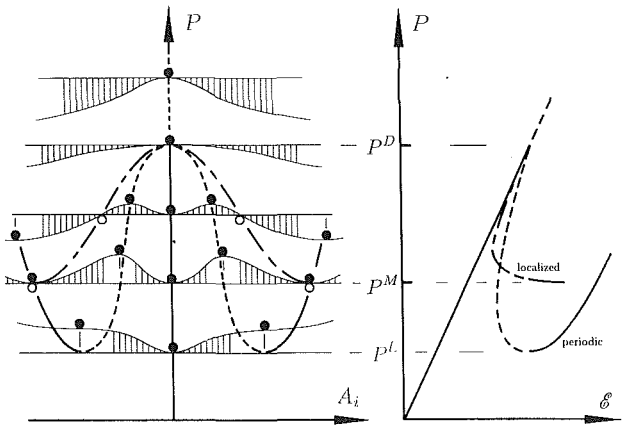

Fig. 2 No localization below Maxwell critical load, P^M, where fundamental and (periodic) post-buckled states have equal energy

where the Lagrangian $\mathcal{L}(\dot{A}_i, A_i, P) = T(\dot{A}_i) - V(A_i, P)$. We note that, as motion is described in an inverted potential well in Fig. 1, we would expect the coefficient T_{ii} to be negative.

The hypothesis has some attractive features, notably that the potential energy carries all the nonlinearities of the problem, and is obtainable from a periodic formulation. It can be developed analytically, and readily extends to more than one degree-of-freedom, the new kinetic energy function T being obtained either from the underlying differential equation (Hunt et al., 1989) or from an initial potential energy functional via the calculus of variations (Hunt and Wadee, 1991). There is, however, often an asymptotic flavor to such analysis; the adopted spatial measure X is related to the true spatial dimension x by

$$X = sx, \tag{3}$$

for instance, where s is a perturbation parameter measuring progress outwards from the critical point C. This has led X to be referred to as *slow space*, and the analysis to be termed *double scale* (Lange and Newell, 1971; Potier-Ferry, 1983; Hunt et al., 1989; Hunt and Lucena Neto, 1991).

The Maxwell criterion discussed below takes s some way into the post-buckling regime, and extra validation of any asymptotically based approach is thus desirable. For a strut on a nonlinear foundation, numerical runs of the full underlying fourth-order nonlinear differential equation provide useful checks (Hunt and Wadee, 1991), but for the diamond-buckling of cylindrical shells, such an approach is impossibly complex. The careful experiments of Yamaki (1984), however, provide a most useful basis for comparison.

3 Localized Buckling and Zero Energy

To trace the correct amplitude variation for a localized response, specific conditions need to be met. The response must take infinite "time" X to reach, or move away from, the maximum of $-V$ that corresponds to the flat fundamental state $A_i = 0$. This is achieved by "release," with zero kinetic energy, from the point on the V-surface with the same V-level as the maximum, as shown in the left-hand well of the bottom right diagram of Fig. 1; the full variation of the upper right is of course traced by starting and finishing at the maximum.

Thus, for localized buckling, alternative states of *zero potential energy* (the same V-level as the flat fundamental state) take on a new significance (Toland, 1986). This contrasts with the more familiar variational view, really only useful for periodic responses, where equilibrium depends only on the first variation, $\partial V/\partial A_i$, of potential energy, never on its absolute value.

4 Maxwell Criterion

It is often the case that a buckling problem has a post-buckling path which is initially unstable and falling with respect to load P, as seen in Fig. 1, but then restabilizes and rises again from some lower load. Such a situation is shown in Fig. 2, where we suppose that a periodic form of buckling is initiated at a critical delay bifurcation load P^D, giving an unstable path which restabilizes at the lower post-buckling load P^L. The potential energy surface then evolves under changing P as shown; we see that, for $P^L < P < P^D$, there is a total of five equilibrium states, three stable and two unstable, all being depicted by closed circles. An assumed load P to end-shortening $\mathcal{E}$ form is shown at the right.

Zero energy states corresponding to maximum amplitude at the center of localization are shown as open circles in Fig. 2. We see that, somewhere in the range $P^L < P < P^D$, there must be a specific load P^M below which no zero energy post-buckling state exists. Interestingly, this coincides with the classical *Maxwell critical load* for periodic responses, which marks, under increasing P, the point of interchange of the *global* minimum of V from the fundamental, to the stable post-buckling, state (Zeeman, 1977). The Maxwell critical load for a periodic response thus represents a lower bound on the possible appearance of a localized form of the same buckle pattern.

5 Periodic Analysis of Cylindrical Shells

It is clear from experiments on long, thin, axially loaded cylindrical shells (Sendelbeck et al., 1967; Yamaki, 1984), that the well-known diamond-pattern buckling appears in a localized, rather than a periodic, form along the length. In a recent paper (Hunt and Lucena Neto, 1991), double-scale analysis is used to generate a theoretical amplitude variation that seems to compare well with experiment. The analysis has a strong asymptotic flavor, however, and the thoroughly unstable nature of the response means that comparisons are conducted a considerable way into the post-buckling range. The concept of Maxwell critical load as a lower bound for localized responses provides a useful independent check against experiments; it has the advantage of being defined with respect to periodic behavior, and is thus amenable to standard modeling techniques such as the Rayleigh-Ritz method.

Such techniques have been used before (Madsen and Hoff, 1965; Hunt et al., 1986), but with interest focussed on the minimum post-buckling load P^L not the Maxwell load P^M. In the modern context, because of the large deflexions and consequent large number of contributing modes, analysis is most conveniently conducted using algebraic manipulation software, such as the standard package Mathematica (Wolfram, 1988), which has the advantage of avoiding roundoff error.

Moderately large deflexions of a thin axially compressed

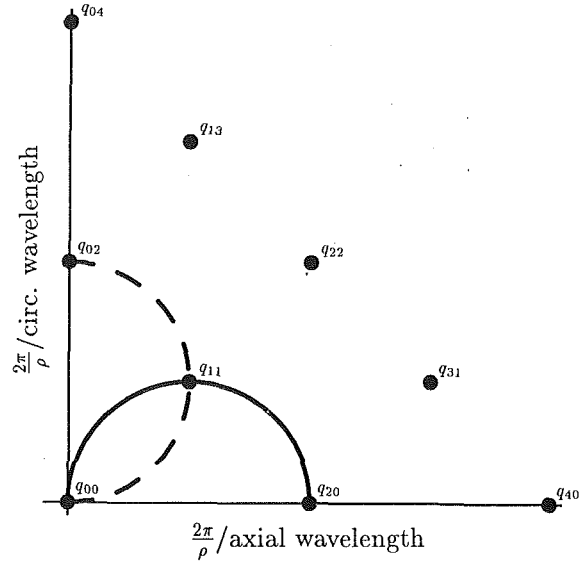

Fig. 3 The first modes of Eq. (6), for $\beta = 1$, in relation to the Koiter circle

Table 1 Comparisons of minimum load level, corresponding β, and corresponding maximum inward (positive) and outward (negative) displacements

	n	Present analysis	Yamaki's results	
			Experimental	Theoretical
P^M/P^D	12	0.27	–	0.29
	11	0.24	0.24	0.26
	10	0.21	0.21	0.22
	9	0.18	0.17	0.17
	8	0.16	0.14	0.12
β	12	1.48	–	–
	11	1.49	1.43	1.54
	10	1.51	–	–
	9	1.56	–	–
	8	1.60	1.37*	1.42*
w/t	12	8.3, -3.7	–	6.0, -2.8
	11	10.0, -4.4	7.7, -3.3	7.7, -3.6
	10	12.2, -5.5	10.6, -4.6	10.2, -5.0
	9	15.1, -6.8	13.0, -5.9	13.0, -6.3
	8	19.3, -8.7	16.5, -7.7	16.3, -7.7

* not at minimum load.

cylindrical shell are assumed to be governed by the von Kármán-Donnell equations

$$k^2\nabla^4 w+\lambda\frac{\partial^2 w}{\partial x^2}-\rho\frac{\partial^2\phi}{\partial x^2}=\frac{\partial^2 w}{\partial x^2}\frac{\partial^2\phi}{\partial y^2}+\frac{\partial^2 w}{\partial y^2}\frac{\partial^2\phi}{\partial x^2}-2\frac{\partial^2 w}{\partial x\partial y}\frac{\partial^2\phi}{\partial x\partial y} \tag{4}$$

$$\nabla^4\phi+\rho\frac{\partial^2 w}{\partial x^2}=\left(\frac{\partial^2 w}{\partial x\partial y}\right)^2-\frac{\partial^2 w}{\partial x^2}\frac{\partial^2 w}{\partial y^2}, \tag{5}$$

where x and y are axial and circumferential coordinates; ∇^4 denotes the two-dimensional biharmonic operator; w is inwards displacement; $k^2 = t^2/12(1-\nu^2)$; $\lambda = P/Et$; ρ and t are the shell curvature and thickness; P is axial load per unit length; E is Young's modulus and ν is Poisson's ratio; and ϕ is a stress function related to the in-plane stress resultant deviations from the uniform membrane state (Hunt and Lucena Neto, 1991). The first is an equilibrium, and the second a compatibility equation.

For a Rayleigh-Ritz formulation employing a kinematically admissible displacement field, the second equation must be satisfied completely. Noting the linearity in ϕ, we can start with an assumed w,

$$w=\sum_{i=0}^{\infty}\sum_{j=0}^{\infty} q_{ij}\cos i\gamma x\cos j\beta\gamma y,\quad i+j=\text{even} \tag{6}$$

and write down the corresponding ϕ in standard manner (Cowell, 1986). The first equation is not solved completely; rather the assumed form for w, with its corresponding ϕ, is substituted into an energy formulation (Hunt et al., 1986). All of the above processes can be performed exactly within Mathematica.

The assumed form for w comprises a uniform post-buckling dilation q_{00}, which is determined from consideration of continuity of circumferential displacement together with a set of mutually orthogonal buckling modes. Here, β is the mode-aspect ratio (axial/circumferential wavelength); $\gamma = \rho n/\beta$ is a scaling factor; and n is the number of whole circumferential waves for the "seed" mode of amplitude q_{11}.

The nonlinearity in w in the compatibility equation and consequent extended form for ϕ introduces a cascade of relevant buckling modes via the phenomenon of mode interaction (Hunt et al., 1986). A typical set of modes for $\beta = 1$ ($n = 1/2\sqrt{\rho k}$), in the wavelength related space due to Koiter (1945), is shown in Fig. 3; the first eight periodic modes, together with q_{00}, are given, with the next significant row of seven lying on a straight line between q_{06} and q_{60}.

Nonlinear equilibrium equations are solved using a Newton-Raphson scheme. Minimization is also carried out with respect to the mode aspect ratio β. Thus, with the sole input of the circumferential wave number n, the minimum-energy axial wavelength and combination of assumed modes is found for any post-buckled state.

6 Comparison With Experiments

To compare with the experiments of Yamaki (1984), calculations are carried out for a shell with the following properties:

$$\rho=0.01\ \text{mm}^{-1},\quad t=0.247\ \text{mm},\quad \nu=0.3,$$

and for circumferential wave numbers $n = 8$, 9, 10, 11, and 12. Results with 16 terms retained in Eq. (6), i.e., terms satisfying $i+j=0$, $i+j=2$, $i+j=4$ and $i+j=6$, are summarized in Table 1.

Yamaki's experiments were carefully carried out for clamped cylindrical shells with different lengths; only results from the longest one ($L = 160.9$ mm) will be considered. Figures 4(*a*) and 4(*b*) show, respectively, recorded relations between load and end-shortening displacement and load and maximum inwards (positive) and outwards (negative) deflexions. The post-buckling configuration observed spontaneously is of asymmetric type with two tiers of staggered buckles, as seen in contour line representations in Figs. 4(*c*) and 4(*d*) for $n = 11$ and $n = 8$, respectively; here solid and dotted lines correspond to inwards and outwards deflexions. In the same reference, a theoretical post-buckling analysis is performed by applying the Galerkin procedure to Eq. (4), after Eq. (5) has been satisfied completely, with w assumed as a trigonometric series which satisfies the clamped end conditions; this gives an excellent reproduction of the observed diamond pattern.

In the present analysis the periodic post-buckling curve, shown schematically at right in Fig. 2, is calculated for each assumed value of n; the Maxwell critical load is then picked up by checking the energy level in this state against that of the fundamental path. Table 1 shows our results together with those taken directly from the plots of Yamaki (1984) (see Figs. 4(*a*) and 4(*b*)).

It became clear during the analysis that, as might be expected from the relative deflexions involved, the lower the wave num-

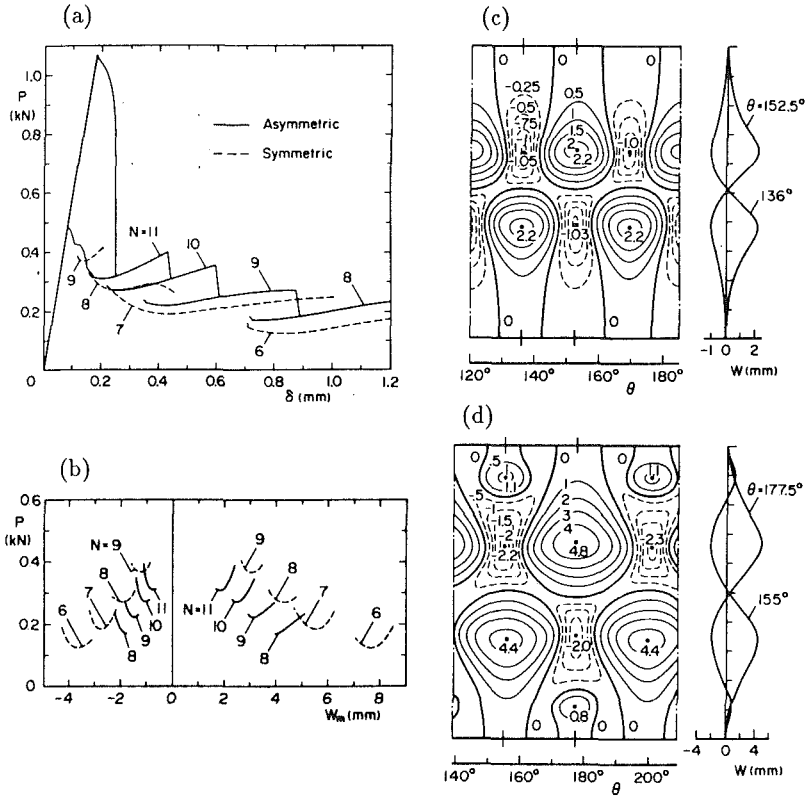

Fig. 4 Experimental results for a long cylinder (after Yamaki, 1984)

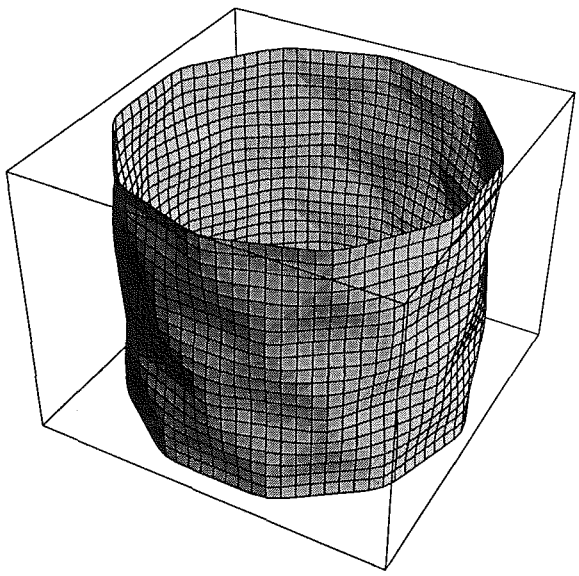

Fig. 5 Periodic buckled surface corresponding to Maxwell critical load for $n = 10$, where $\beta_{opt} = 1.51$

ber n, the more terms are required in Eq. (6) for satisfactory convergence. With the chosen 16 terms, modal interactions at cubic and quartic energy levels are extensive, and the microcomputer used for the study was working close to its limit. In Table 1 we find that the Maxwell critical load creeps slightly above the experimental minimum load for $n \leq 9$ and we attribute this to a lack of complete convergence. Otherwise, agreement between the theoretical Maxwell load and the experimental minimum load is apparently very good.

But perhaps the clearest evidence for the importance of the periodic Maxwell load comes from a wavelength comparison, as evidenced by the mode aspect ratio β of Table 1. Yamaki's account of the experiments unfortunately gives no indication of axial wavelength at the minimum load level, apart from for $n = 11$, which is contour-mapped close to this state (see Fig. 4(c); note that Fig. 4(d) for $n = 8$ is clearly not at a minimum state). It is noticeable from our periodic runs that in the restabilizing region, while the load may only change fractionally, there is a simultaneous quite rapid change in the optimum (minimum-energy) value of β. For $n = 11$, for instance, $P^L/P^D = 0.22$ and $\beta_{opt} = 2.05$, but at the slightly higher Maxwell load of $P^M/P^D = 0.24$, $\beta_{opt} = 1.49$. The latter, but not the former, compares well with the experimental value of $\beta = 1.43$, taken directly from Fig. 4(c).

Finally, Fig. 5 shows a computer-drawn image of the periodic deflected shape, built from the 16 harmonic functions of Eq. (6) at the Maxwell load for $n = 10$. Displacement comparisons are also carried out in Table 1, but it must be remembered that localized values would be less than their periodic counterparts, since the deflexion pattern must damp down along the length. There is also a further trend in this comparison, in that if convergence is incomplete, peak values should be yet further reduced; the corners of the diamond pattern, where the peaks occur, would appear more rounded than they should be. Combine these two effects, and the deflexion comparisons of Table 1 are much as expected.

7 Concluding Remarks

The paper introduces a new criterion for localized buckling, based on the potential energy of an associated periodic form; it is suggested that the minimum localized post-buckling load coincides with the classical Maxwell critical load for periodic responses. Since periodic solutions of von Kármán-Donnell equations based on energy methods are well known, results are obtained simply by adding $V = 0$ to the condition $\partial V/\partial q_{ij} = 0$ in the restabilized post-buckling state.

In essence, the new approach is quite different in concept from other mode-fitting procedures; it remains independent of end conditions, for instance, on the assumption that if the shell is long enough, boundaries have little or no effect on a localized form. This contrasts with the Galerkin procedure of Yamaki (1984) in which, to compare with experiments, clamped end conditions are fed into a model of finite length. It is noted by Yamaki that convergence erodes as length increases; apart from problems associated with too short a cylinder there are no such length limitations in the new approach.

The comparisons show excellent agreement between the Maxwell critical load and the minimum load from experiments; in spite of the limited available results for the mode aspect ratio β, agreement is again most encouraging. For small values of circumferential wave number n, it is noted that more terms must be retained in Eq. (6) for satisfactory convergence.

We are at present unable to compare with experiments other than at the Maxwell critical load since the "kinetic" energy component, T, remains undefined; its description is certainly possible (Hunt and Wadee, 1991) but is left for future work.

References

Cowell, R. G., 1986, "Looping Post-Buckling Paths of an Axially-Loaded Elastic Cylindrical Shell," *Dyn. Stab. Systems*, Vol. 1, No. 2, pp. 115–123.

Hunt, G. W., Bolt, H. M., and Thompson, J. M. T., 1989, "Structural Localization Phenomena and the Dynamical Phase-Space Analogy," *Proc. Royal Soc. Lond.*, Vol. A425, pp. 245–267.

Hunt, G. W., and Lucena Neto, E., 1991, "Localized Buckling in Long Axially-Loaded Cylindrical Shells," *J. Mech. Phys. Solids*, Vol. 39, No. 7, pp. 881–894.

Hunt, G. W., and Wadee, M. K., 1991, "Comparative Lagrangian Formulations for Localized Buckling," *Proc. Royal Soc. Lond.*, Vol. A434, pp. 485–502.

Hunt, G. W., Williams, K. A. J., and Cowell, R. G., 1986, "Hidden Symmetry Concepts in the Elastic Buckling of Axially-Loaded Cylinders," *Int. J. Solids Structures*, Vol. 22, No. 12, pp. 1501–1515.

Koiter, W. T., 1945, "On the Stability of Elastic Equilibrium," dissertation, Delft, The Netherlands (English Translation: Tech. Report AFFDL-TR-70-25, Air Force Flight Dyn. Lab., 1970).

Lange, C. G., and Newell, A. C., 1971, "The Post-Buckling Problem for Thin Elastic Shells," *SIAM J. Appl. Math.*, Vol. 21, No. 4, pp. 605–629.

Madsen, W. A., and Hoff, N. J., 1965, "The Snap-Through and Postbuckling Equilibrium Behavior of Circular Cylindrical Shells under Axial Load," Report SUDAAR No. 227, Dept. of Aeronautics and Astronautics, Stanford University.

Potier-Ferry, M., 1983, "Amplitude Modulation, Phase Modulation and Localization of Buckle Patterns," *Collapse: The Buckling of Structures in Theory and Practice*, J. M. T. Thompson and G. W. Hunt, eds., Cambridge University Press, pp. 149–159.

Sendelbeck, R. L., Carlson, R. L., and Hoff, N. J., 1967, "An Experimental Study of the Effect of Length on the Buckle Pattern of Axially Compressed Circular Cylindrical Shells," Report SUDAAR No. 318, Dept. of Aeronautics and Astronautics, Stanford University.

Thompson, J. M. T., and Hunt, G. W., 1973, *A General Theory of Elastic Stability*, John Wiley, London.

Toland, J. F., 1986, "Existence of Symmetric Homoclinic Orbits for Systems of Euler-Lagrange Equations," *Amer. Math. Soc., Proc. Symp. Pure Math.*, Vol. 45, Part 2, pp. 447–459.

Wolfram, S., 1988, *Mathematica: A System for Doing Mathematics by Computer*, Addison-Wesley, Redwood City, CA.

Yamaki, N., 1984, *Elastic Stability of Circular Cylindrical Shells*, Elsevier, Amsterdam.

Zeeman, E. C., 1977, *Catastrophe Theory: Selected Papers, 1972–1977*, Addison-Wesley, Reading, MA.

A Similar Flow Between Two Rotating Disks in the Presence of a Magnetic Field

R. Usha

S. Vasudevan

Department of Mathematics,
College of Engineering,
Anna University,
Madras, 600 025 India

A similarity solution is obtained for a flow between two rotating parallel disks which, at time t^* *are spaced a distance* $H(1 - \alpha t^*)^{1/2}$ *apart and a magnetic field proportional to* $B_0(1 - \alpha t^*)^{-1/2}$ *is applied perpendicular to the disks. Approximate analytic solutions are given and a numerical solution to the resulting nonlinear ordinary differential equations is presented. The effects of magnetic forces on the velocity profiles, the normal forces and the torques which the fluid exerts on the disks are studied. It is observed that by increasing the magnetic force a considerable increase in the load can be achieved. Also, the torques are more sensitive to changes in the squeeze Reynolds number than to changes in the rotation Reynolds number.*

1 Introduction

A similarity solution has been obtained for a flow between two parallel disks which, at time t^*, are spaced a distance $H(1 - \alpha t^*)^{1/2}$ apart, and a magnetic field proportional to $B_0(1 - \alpha t^*)^{-1/2}$ is applied perpendicular to the disks by Hamza (1989), where H denotes a representative length and B_0 denotes a representative magnetic field. The effects of the magnetic forces on the velocity profiles, and on the normal forces which the fluid exerts on the disks, are considered, and it has been found that by increasing the magnetic force, a considerable increase in the load could be achieved. Hamza and MacDonald (1984) have obtained a similarity solution to the motion of a viscous incompressible fluid contained between two parallel disks, which at time t^* are spaced a distance $H(1 - \alpha t^*)^{1/2}$ apart, and are rotating with angular velocities proportional to $\Omega_1(1 - \alpha t^*)^{-1}$ by reducing the governing Navier-Stokes' equations to a set of ordinary differential equations. Here α^{-1} denotes representative time and Ω_1 denotes a representative angular velocity. They have examined the way in which the normal forces are modified by the rotation of the disks and the torque is modified by the normal motion of the disks by presenting approximate solutions for a range of values of the three linearly independent parameters that influence the fluid motion.

The effect of magnetic field on such flows have received considerable attention due to the important role they play in many industrial applications. Many studies of the problem have been motivated by the increased use of liquid metal lubricants in high-temperature bearings. The theoretical and experimental investigations into the magnetohydrodynamic effects in lubrication that have been reported include Hughes and Elco (1962), Kuzma, Maki, and Donnelley (1964), Krieger, Day, and Hughes (1967), Kamiyama (1969), and Hamza (1988). In this paper we examine the motion of a viscous, incompressible fluid contained between two parallel disks, which at time t^* are spaced a distance $H(1 - \alpha t^*)^{1/2}$ apart and are rotating with angular velocities proportional to $\Omega_1(1 - \alpha t^*)^{-1}$. Also a magnetic field proportional to $B_0(1 - \alpha t^*)^{-1/2}$ is applied perpendicular to the disks and thus the paper considered here is a unified presentation of the effects of rotation, squeezing, and magnetic field on fluid between two parallel disks. Approximate analytic solutions are given and a numerical solution to the resulting nonlinear ordinary differential equations is presented for a range of values of the squeeze Reynolds number $R_e^S = \alpha H^2/2\nu$, the rotation Reynolds number $R_e^R = \Omega_1 H^2/\nu$, and the Hartmann Number $M^2 = \sigma B_0^2/\mu$ (σ denotes electrical conductivity and μ denotes viscosity) which influence the motion. The effect of the magnetic forces on the velocity profiles, on the normal force which the fluid exerts on the disks, and on the torque which the fluid exerts on the disks are considered.

2 Mathematical Formulation

We consider an axisymmetric, incompressible flow between two parallel infinite disks which rotate in their own planes and are spaced a distance $h(t^*)$ apart where t^* denotes time. A magnetic field $B(t^*)$ is applied perpendicular to the two disks kept at $z^* = 0$ and $z^* = h(t^*)$, $h(o) = H$, and the upper disk is moving with velocity $h'(t^*)$ towards the lower disk. The disks rotate in their own planes with angular velocities proportional to $\Omega_1(1 - \alpha t^*)^{-1}$ and $\Omega_2(1 - \alpha t^*)^{-1}$. We select cylindrical polar coordinates (r^*, θ^*, z^*) and denote by u^*, v^*,

Contributed by the Applied Mechanics Division of THE AMERICAN SOCIETY OF MECHANICAL ENGINEERS for publication in the ASME JOURNAL OF APPLIED MECHANICS.

Discussion on this paper should be addressed to the Technical Editor, Professor Lewis T. Wheeler, Department of Mechanical Engineering, University of Houston, Houston, TX 77204-4792, and will be accepted until four months after final publication of the paper itself in the ASME JOURNAL OF APPLIED MECHANICS.

Manuscript received by the ASME Applied Mechanics Division, June 11, 1991; final revision, Feb. 17, 1992. Associate Technical Editor: K. R. Sreenivasan.

w^* the velocity components in the radial (r^*), the tangential (θ^*), and the axial (z^*) directions. The equations of continuity and momentum governing the motion are

$$\frac{1}{r^*}\frac{\partial(u^*r^*)}{\partial r^*}+\frac{\partial w^*}{\partial z^*}=0 \tag{1}$$

$$u_t^*+u^*u_r^*+w^*u_z^*-\frac{v^{*2}}{r^*}=-\frac{1}{\rho}p_r^* + \nu\left[u_r^*{}_r^*+\frac{1}{r^*}u_r^*+u_z^*{}_z^*-\frac{u^*}{r^{*2}}\right]+\frac{1}{\rho}J_\theta B_a \tag{2}$$

$$v_t^*+u^*v_r^*+w^*v_z^*+\frac{u^*v^*}{r^*} = \nu\left[v_r^*{}_r^*+\frac{1}{r^*}v_r^*+v_z^*{}_z^*-\frac{v^*}{r^{*2}}\right]-\frac{1}{\rho}J_rB_a \tag{3}$$

$$w_t^*+u^*w_r^*+w^*w_z^* = -\frac{1}{\rho}p_z^*+\nu\left[w_r^*{}_r^*+\frac{1}{r^*}w_r^*+w_z^*{}_z^*\right] \tag{4}$$

where B_a, p, (E_r, E_θ, E_z), (J_r, J_θ, J_z) are the applied magnetic field, the pressure at a point, the electric field, and the current density with

$$J_r=(E_r+v^*B_a)$$

$$J_\theta=-\sigma u^*B_a.$$

On the assumption that

$$u^*=\frac{\alpha r^*}{2(1-\alpha t^*)}f'(y),\quad v^*=\frac{r^*\Omega_1}{(1-\alpha t^*)}g(y)$$

$$w^*=-\frac{\alpha H}{\sqrt{1-\alpha t^*}}f(y),\quad B_a=\frac{B_0}{\sqrt{1-\alpha t^*}}$$

$$y=\frac{z^*}{H\sqrt{(1-\alpha t^*)}},\ r=r^*,\ t=t^*,$$

the equation of continuity (1) is satisfied and the equations of motion reduce to

$$f''''=R_e^S[yf'''+3f''-2ff'''-\frac{8\Omega_1^2}{\alpha^2}gg']+M^2f'' \tag{6}$$

$$g''=R_e^S[yg'+2g+2gf'-2fg']-M^2E^*+M^2g \tag{7}$$

where $\Omega_1/\alpha = R_e^R/2R_e^S$ and $E^* = \int_0^1 g(y)dy$ and $f(y)$, $g(y)$ are unknown functions to be determined. The boundary conditions are

$$f(0)=0,\quad f'(0)=0,\quad g(0)=1$$

$$f(1)=1/2,\quad f'(1)=0,\quad g(1)=\frac{\Omega_2}{\Omega_1}=s. \tag{8}$$

In the limiting case when $M^2/R_e^S \to 0$ and $R_e^R = 0$, Eqs. (6) and (7) and the boundary conditions (8) reduce to the equations which govern the unsteady flow between two disks at a distance $h(t^*) = H\sqrt{1-\alpha t^*}$ apart and moving towards or away from each other with relative velocity $h'(t^*)$. This case was studied by Wang (1976) and Ishizawa (1966). In the case when $M = 0$, they reduce to equations which govern the motion of a viscous incompressible fluid contained between two parallel disks spaced a distance $H\sqrt{1-\alpha t^*}$ apart and are rotating with angular velocities proportional to $\Omega_1(1-\alpha t^*)^{-1}$ that were examined by Hamza and MacDonald (1984). In the limiting case $R_e^R = 0$, the equations yield a similarity solution obtained by Hamza (1989) for a flow between two parallel disks which at time t^* are spaced a distance $H\sqrt{1-\alpha t^*}$ apart and a magnetic field proportional to $B_0(1-\alpha t^*)^{1/2}$ is applied perpendicular to the disk.

The Normal Force. On integrating the equations of motion, the fluid pressure is obtained as

$$p^*(r, y, t)=p(t)+\frac{\rho\alpha^2r^2}{8(1-\alpha t^*)^2}\left[\frac{f'''_{(o)}}{R_e^S}+\frac{4\Omega_1^2}{\alpha^2}\right]+\frac{\rho\alpha^2H^2}{8(1-\alpha t^*)}, \tag{9}$$

where $p(t)$ is an arbitrary function of time. If the disks are assumed to be of finite radius "a" and of negligible thickness, the normal force or load W^* which the fluid exerts on the disk is

$$W^*=2\pi\int_0^a r[p^*(r, 1, t)-p_o^*(a, 1, t)]dr = -\frac{\pi\mu\alpha a^4}{8H^2(1-\alpha t)^2}\left[f'''_{(o)}+4R_e^S\frac{\Omega_1^2}{\alpha^2}\right]$$

or

$$W=-\frac{1}{6R_e^S}\left[f'''_{(o)}+4R_e^S\frac{\Omega_1^2}{\alpha^2}\right] \tag{10}$$

where

$$W=\frac{8W^*(1-\alpha t)^2}{3\pi\rho\alpha^2a^4}.$$

The Torques Exerted on the Disks. When $\sqrt{\nu t} \ll a$, the torque T_U^*, which the fluid exerts on the upper disk, is given by

$$T_U^*=\int_0^a 2\pi r^2\mu\left.\frac{\partial_u}{\partial_z}\right|_{z=H\sqrt{1-\alpha t}}dr = \frac{\pi\mu a^4\Omega_1}{2H(1-\alpha t)^{3/2}}g'(1) \tag{11}$$

or

$$T_U=g'(1)\ \text{where}\ T_U=\frac{2H(1-\alpha t)^{3/2}}{\pi\mu a^4\Omega_1}T_U^*. \tag{12}$$

For the lower disk, the corresponding result is $T_L = g'(o)$.

3 Approximate Analytic Solution

We describe approximate analytical results which can be obtained for $R_e^S = 0(1)$, $R_e^R = 0(1)$ and $M = 0(1)$, when $M = O(R_e^S)$ and $R_e^R = O(R_e^S)$ and also when $M = O(R_e^S)$ and $R_e^R = O(R_e^S)^{1/2}$. The functions f and g for $R_e^S = 0(1)$ may be expanded in the form

$$f=f_0+R_e^Sf_1+0(R_e^S)^2 \tag{13}$$

$$g=g_0+R_e^Sg_1+0(R_e^S)^2. \tag{14}$$

Case (i). For $R_e^S = o(1)$, $R_e^R = O(R_e^S)$ and $M = O(R_e^S)$, f_0, g_0, f_1 and g_1 satisfy the equations

$$f_0''''=0$$

$$f_1''''=yf_0'''+3f_0''-2f_0f_0''''-2\frac{R_e^R}{R_e^S}g_0g_0'+\frac{M^2}{R_e^S}f_0''$$

$$g_0''=0$$

$$g_1''=yg_0'+2g_0f_0'-2f_0g_0'-\frac{M^2}{R_e^S}E_0^*+\frac{M^2}{R_e^S}g_0.$$

We obtain

$$f_0(y)=y^2(3/2-y)$$

$$g_0(y)=1-(1-s)y$$

$$f_1(y)=\frac{y^2(1-y)^2}{280}\left[19-40y+6y^2-4y^3+\frac{70}{3}(1-s)\left(\frac{R_e^R}{R_e^S}\right)^2-\frac{14}{3}(1-s)^2\left(\frac{R_e^R}{R_e^S}\right)^2(2+y)+\frac{7M^2}{R_e^S}(1-2y)\right]$$

$$g_1(y)=\frac{y(1-y)}{20}\left[-(11s+19)+(1-11s)y+(11-s)y^2-4(1-s)y^3+\frac{10}{3}\frac{M^2}{R_e^S}\{(1-s)y-(s+2)+3E_0^*\}\right]$$

where the parameter $s(=\Omega_2/\Omega_1)$ may, by symmetry, be taken to lie in the interval $-1 \le s \le 1$.

The Load W is given by

$$W=\frac{1}{R_e^S}\left[1+\frac{R_e^S}{6}\left\{\frac{117}{70}-\left(\frac{R_e^R}{R_e^S}\right)^2\left[\frac{3}{10}(1-s)^2-s\right]+\frac{3}{5}\frac{M^2}{R_e^S}\right\}+O(R_e^S)^2\right].$$

The torques exerted by the fluid at the disks are

$$T_U=-1+s+\frac{R_e^S}{20}\left[\{19s+11\}+\frac{10}{3}\frac{M^2}{R_e^S}(2s+1)-\frac{10M^2}{R_e^S}E_0^*+O(R_e^S)^2\right]$$

$$T_L=-1+s-\frac{R_e^S}{20}\left[\{11s+19\}+\frac{10}{3}\frac{M^2}{R_e^S}(s+2)-\frac{10}{3}\frac{M^2}{R_e^S}E_0^*+O(R_e^S)^2\right].$$

Case (ii). For $R_e^S = o(1)$, $R_e^R = O(R_e^S)^{1/2}$ and $M = O(R_e^S)$, the equations satisfied by f_0, g_0, f_1 and g_1 are

$$f_0'''' = -2\frac{(R_e^R)^2}{R_e^S}g_0g_0'$$

$$f_1'''' = yf_0'''' + 3f_0'' - 2f_0f_0'''' - 2\frac{(R_e^R)^2}{R_e^S}(g_0g_1' + g_0'g_1) + \frac{M^2}{R_e^S}f_0''$$

$$g_0'' = 0$$

$$g_1'' = 2g_0 + yg_0' + 2g_0f_0' - 2f_0g_0' - \frac{M^2}{R_e^S}E_0^* + \frac{M^2}{R_e^S}g_0.$$

We obtain

$$f_0=y^2\left(\frac{3}{2}-y\right)+\frac{1}{60}\frac{(R_e^R)^2}{R_e^S}(1-s)y^2(1-y)^2[5-(2+y)(1-s)]$$

$$g_0=1-(1-s)y.$$

The expressions for f_1 and g_1, which are more lengthy than in Case (i), will not be quoted here. The results for W, T_U, and T_L are

$$W=\frac{1}{R_e^S}\left[1-\frac{1}{60}\frac{(R_e^R)^2}{R_e^S}(3s^2+4s+3)+\frac{R_e^S}{420}\times\left\{117+\frac{1}{45}\frac{(R_e^R)^2}{R_e^S}(521s^2+983s+521)+\frac{1}{10{,}800}\left(\frac{(R_e^R)^2}{R_e^S}\right)^2\times(579s^4-16s^3-10966s^2-16s+579)+42\frac{M^2}{R_e^S}\right\}+O(R_e^S)^2\right]$$

$$T_U=-1+s+\frac{R_e^S}{20}\left\{19s+11+\frac{1}{315}\times\frac{(R_e^R)^2}{R_e^S}(27s^3-11s^2-24s+8)+\frac{10}{3}\frac{M^2}{R_e^S}(2s+1)-10\frac{M^2}{R_e^S}E_0^*\right\}+O(R_e^S)^2\right]$$

$$T_L=-1+s+\frac{R_e^S}{20}\left\{-11s-19-\frac{1}{315}\frac{(R_e^R)^2}{R_e^S}(8s^3-24s^2-11s+27)-\frac{10}{3}\frac{M^2}{R_e^S}(s+2)+\frac{10}{3}\frac{M^2}{R_e^S}E_0^*\right\}+O(R_e^S)^2\right].$$

4 Numerical Solution

To test the accuracy of the perturbation solution and to obtain reliable information on the nature of the flow for values of R_e^S, R_e^R, and M which are not small, a numerical solution of the governing equations is necessary. For wide ranges of the three parameters, the two-point boundary value problem, expressed by Eqs. (6), (7), and (8), has been integrated by using the Runga-Kutta Gill method where the initial estimates for the unknown boundary conditions at $y = 0$ were determined by shooting methods. The calculations were performed for values of R_e^S, R_e^R and M in the ranges $0.01 \le R_e^S \le 1.0$, $0.02 \le R_e^R \le 5.0$ and $0 \le M \le 4$.

5 Results and Discussion

We present and discuss the case where a thin film of fluid is squeezed between two parallel rotating disks in the presence of an axial magnetic field. In the following we shall be concerned with the combined effects of magnetic forces, rotation

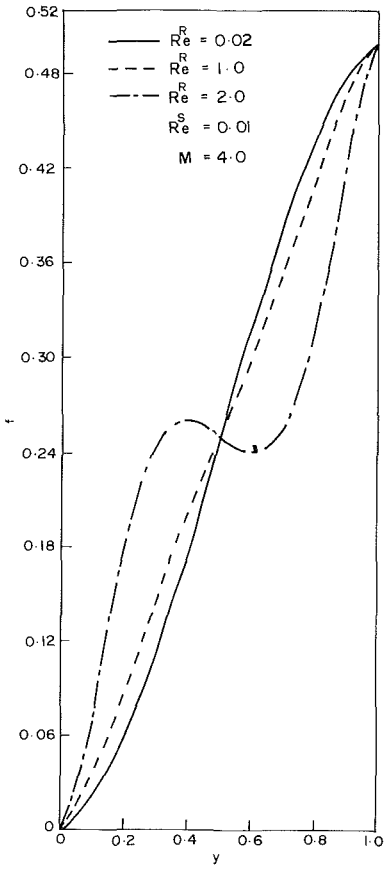

Fig. 1(*a*)

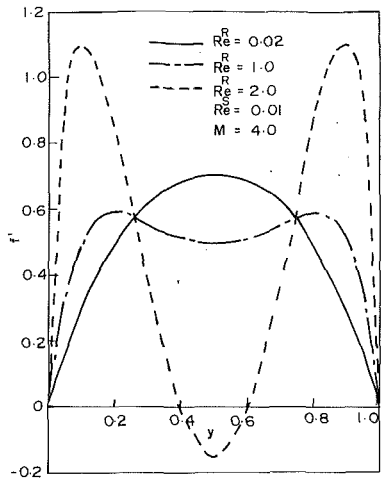

Fig. 1(*b*)

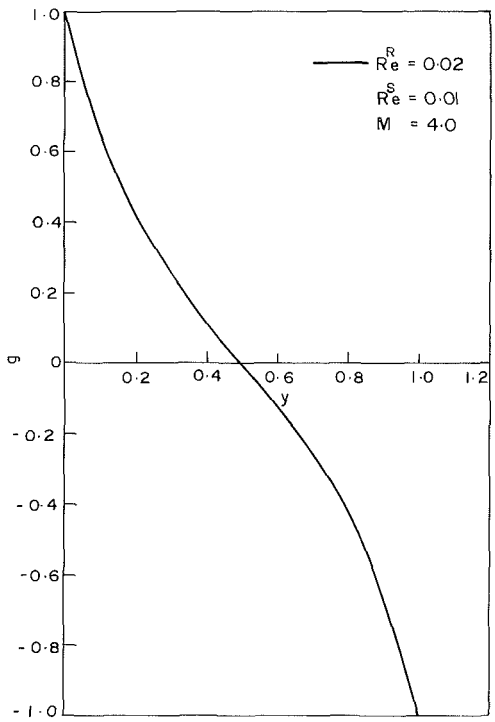

Fig. 1(*c*)

Fig. 1 Variation of dimensionless functions *f*, *f'*, and *g* with R_e^R when $s = -1.0$

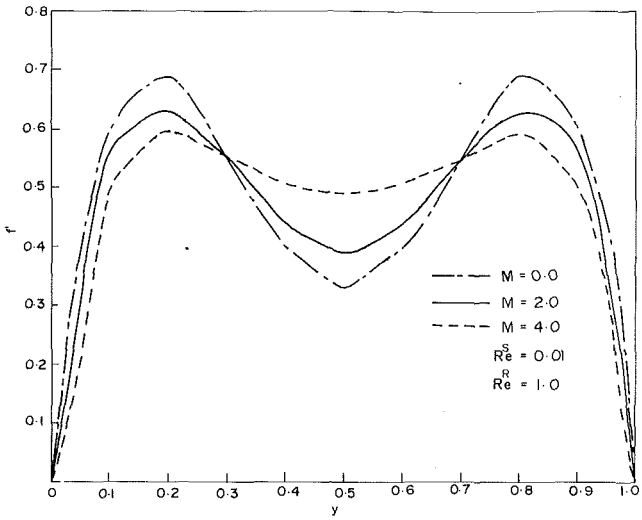

Fig. 2(*a*)

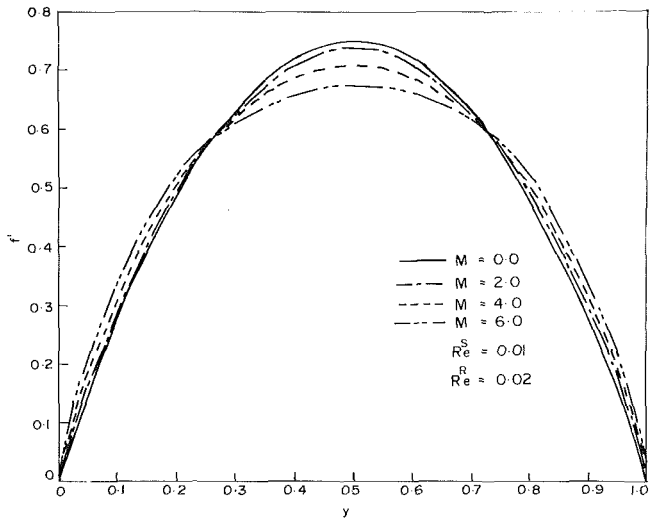

Fig. 2(*b*)

Fig. 2 Variation of dimensionless function *f'* with *M* when $s = -1.0$

and squeezing on the velocity profiles, the normal force (load) which the fluid exerts on the upper disk, and the torques which the fluid exerts on each disk.

The Velocity Field. The dimensionless functions f, f' and g which give components of velocity, are approximately given by the zeroth-order perturbation results since $R_e^S = o(1)$ when $M = O(R_e^S)$ and $R_e^R = O(R_e^S)$, i.e., by

$$f(y) = y^2(3/2 - y)$$

$$f'(y) = 3y(1-y)$$

$$g(y) = 1 - (1-s)y.$$

Thus, we have the usual parabolic distribution in the radial direction. The azimuthal velocity component adjusts linearly from the value unity at $y = 0$ to the value s at $y = 1$.

Figure 1 displays the dimensionless functions f, f', and g which describe the velocity components u, v, and w when $M = 4.0$ with $s = -1.0$ for a range of values of R_e^R. The numerical results indicate that the radial velocity is directed inwards towards the axis in the vicinity of the midplane $y = 1/2$. This inwardly directed flow is evident in the radial flow when $R_e^R = 1.0$ and $R_e^R = 2.0$. The corresponding graphs for the nonmagnetic case when $M = 0$ with $s = -1.0$ for a range of values of R_e^R have been displayed by Hamza and MacDonald (1984). It is observed that despite remarkable changes in both f and f' as R_e^R varies, g, to a good order of approximation, remains linear in the nonmagnetic case. However, this is not so when the magnetic field is present and it is evident from the graph of g in Fig. 1. Also, appreciable change in the value of f', due to the presence of the magnetic field, is more evident for $R_e^R = 2.0$ from Fig. 1.

With an increase in M, with R_e^R and R_e^S fixed, there is a slight increase in the radial velocity profile near the disks and a slight decrease in the region of the mid-plane $y = 1/2$. This increase (decrease) becomes more pronounced with increase in M, and the radial velocity profiles in the interior region become more

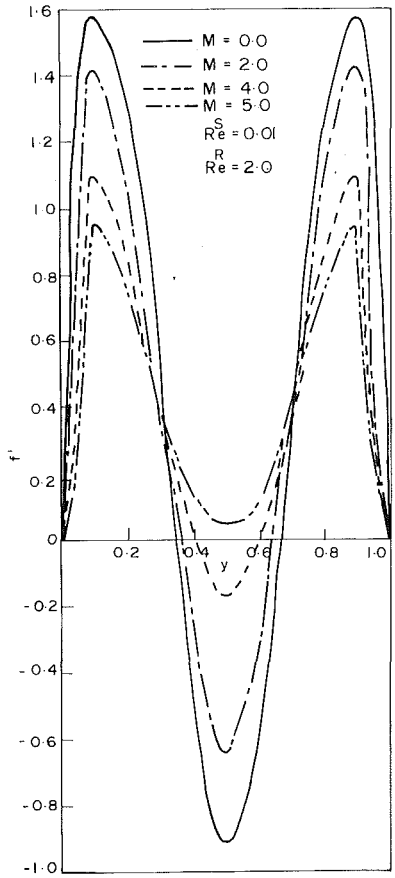

Fig. 3 Variation of dimensionless function f' with M when $s = -1.0$

flat—features which are common to values $R_e^S = 0.01$ and $R_e^R = 0.02$ when $s = -1.0$ with M ranging from 0 to 6, is seen in Fig. 2. Regions of inward radial flow are evident near $y = 1/2$ when $R_e^R = 1.0$ and 2.0 for $R_e^S = 0.01$ and $s = -1.0$ as seen from Figs. 2-3 for $M = 0.0$ to 4.0.

The Load. Of particular interest is the response of the load to changes in the squeeze Reynolds number, the rotation Reynolds number, and the Hartmann number. When a magnetic field is absent, the load exerted on the upper disk is large and positive and decreases with increase of squeeze Reynolds number when $R_e^R = 0.02$ and $s = -1.0$ and 0.5 as is evident from Fig. 4. By applying a perpendicular magnetic field, the results of this indicate that a remarkable increase in the load can be obtained. Figure 5 shows for values of $R_e^S = 0.01$, 0.1, and 1.0, the way in which W varies with M when $R_e^R = 1.0$. The results indicate that the load increases with increase of magnetic field. Figure 6 shows the way in which W varies with M for values of $s = -1.0$ and 0.5 when $R_e^R = 2.0$. It is observed that at this value of R_e^R, when $s = 0.5$, W increases with increase in R_e^S for a fixed value of M.

Figures 7 and 8 show for values of $M = 4.0$, the variation of W with R_e^R when $s = 0.0$. and 1.0. It is clear that for fixed R_e^S, W decreases with increase of R_e^R and this decrease is more rapid when $s = 1.0$ than when $s = 0.0$, -1.0 or 0.5. From Figs. 7 and 8 and from the corresponding graphs of the re-

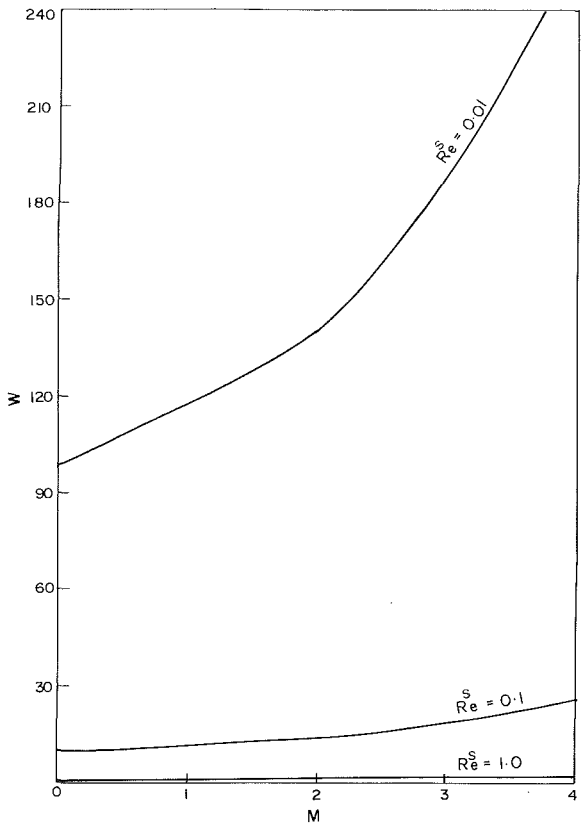

Fig. 4(*a*)

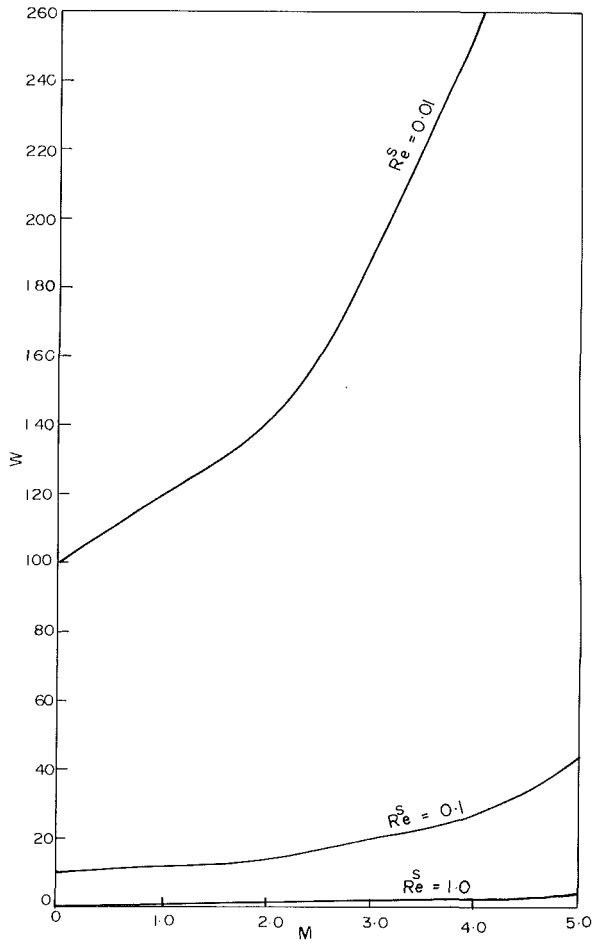

Fig. 4(*b*)

Fig. 4 Response of load to changes in M when $R_e^R = 0.02$ and $s = 0.5$ and -1.0

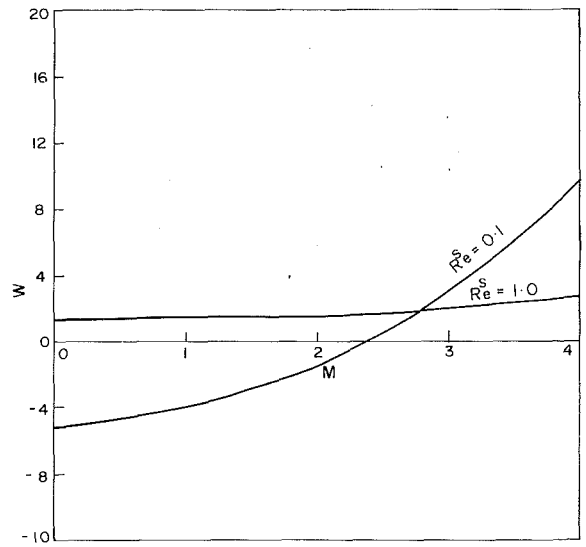

Fig. 5(*a*)

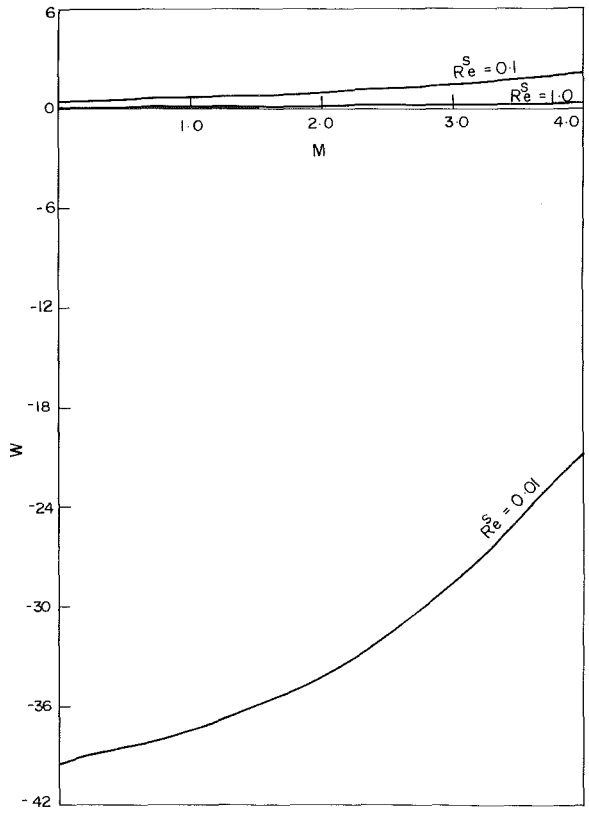

Fig. 5(*b*)

Fig. 5 Response of load to changes in M when $R_e^R = 1.0$ and $s = 1.0$ and 0.0

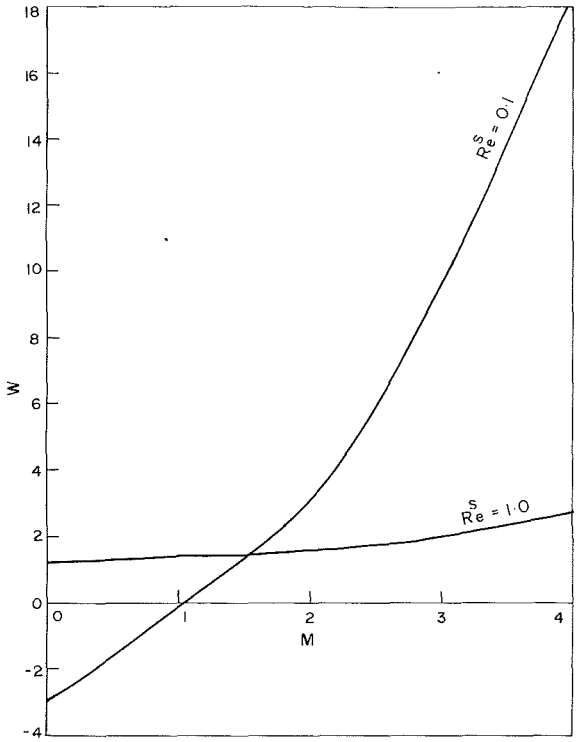

Fig. 6(*a*)

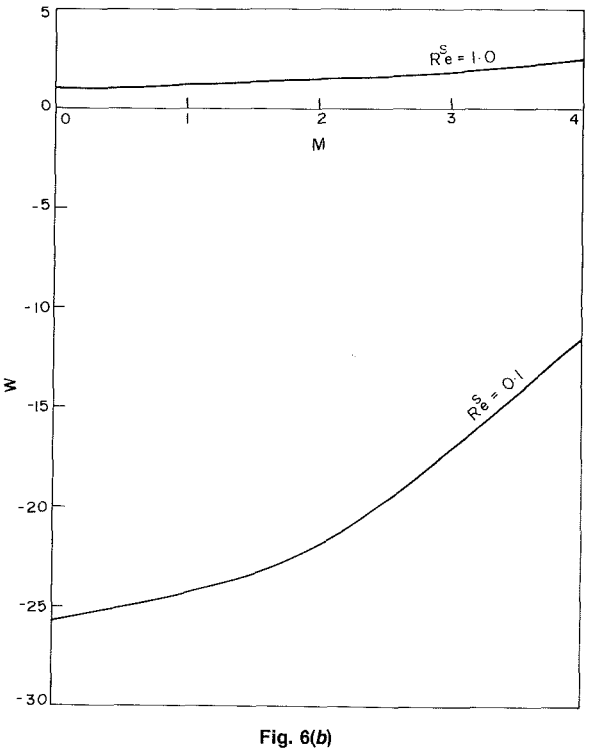

Fig. 6(*b*)

Fig. 6 Response of load to changes in M when $R_e^R = 2.0$ and $s = -1.0$ and 0.5

sponse of normal force to changes in the rotation Reynolds number R_e^R for the nonmagnetic case with fixed R_e^S when $s = 0.0, +1.0, -1.0$, given by Hamza and MacDonald (1984), we observe that the load increases with increase of the magnetic field M for a fixed value of R_e^S.

The increase of the load-carrying capacity with increase of the magnetic field is of significant interest in situations like high-temperature bearings, where use of liquid metal lubricants is unavoidable. This helps in achieving an improvement in the lubrication characteristic of the liquid-metal lubricants.

The Torques. When the disks rotate with same angular velocities (i.e., $s = 1.0$), the magnitude of the torque which the fluid exerts on each disk is given by

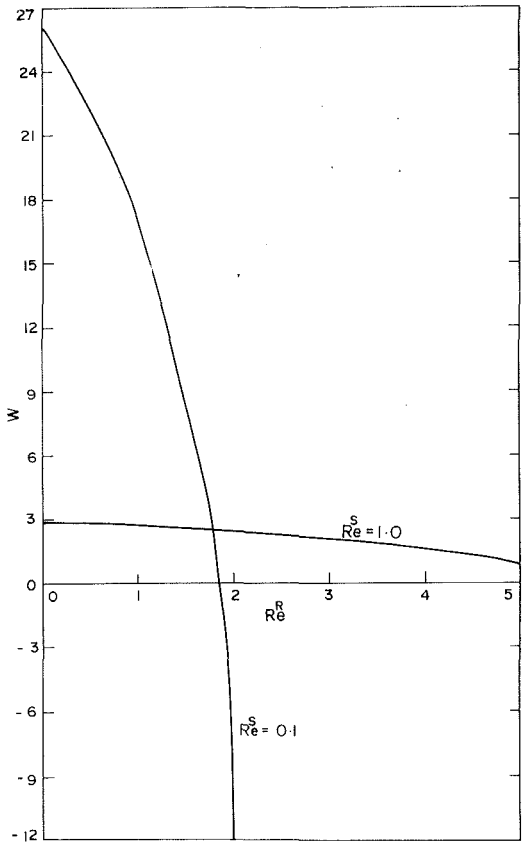

Fig. 7(*a*)

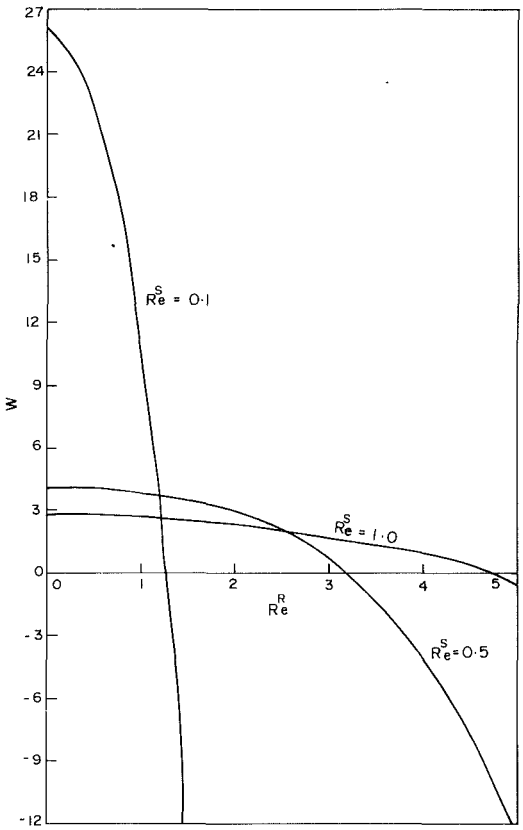

Fig. 8(*a*)

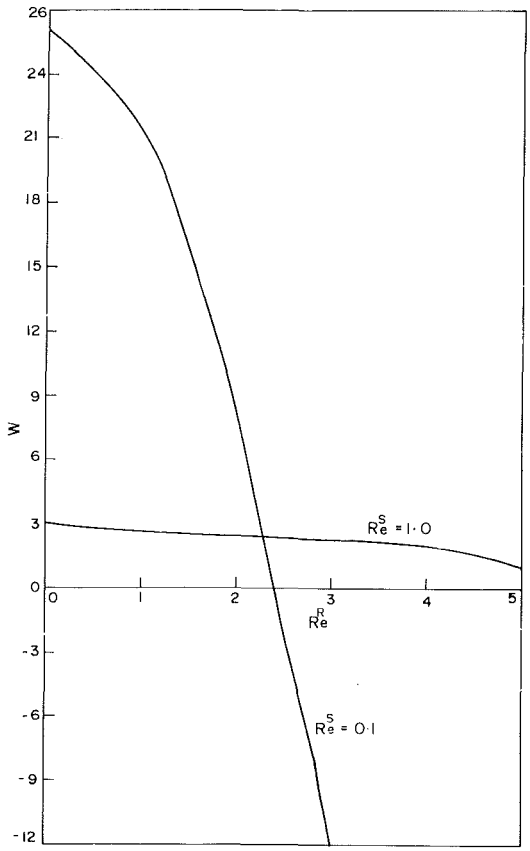

Fig. 7(*b*)

Fig. 7 Response of load to changes in R_e^R when $M = 4.0$ and $s = 1.0$ and 0.0

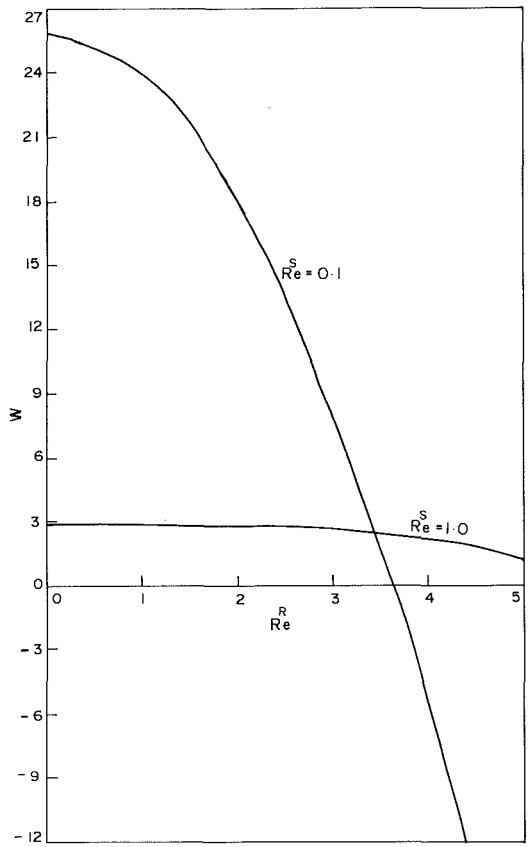

Fig. 8(*b*)

Fig. 8 Response of load to changes in R_e^R when $M = 4.0$ and $s = 0.5$ and -1.0

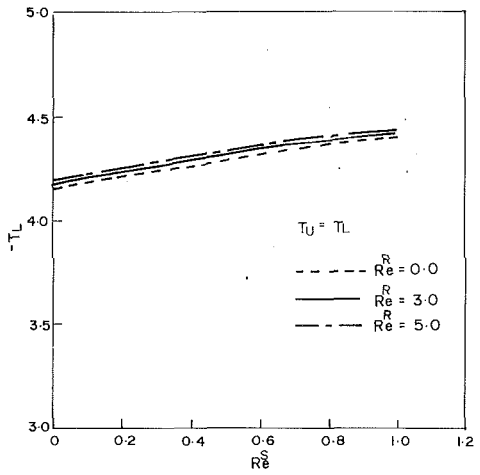

Fig. 9(*a*)

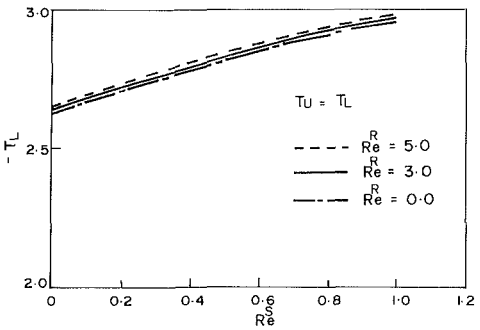

Fig. 9(*b*)

Fig. 9 Response of torque on the upper and lower disks to changes in R_e^S when $s = -1.0$ and $M = 4.0$ and 2.0

$$T_U = -T_L = \frac{3\pi a^4 \Omega_1 \mu}{4H(1-\alpha t)^{3/2}} R_e^S + O(R_e^S)^2.$$

Hence, as $R_e^S \to 0$, the torques which act on the disks tend to zero. But when $R_e^S \neq 0$ and $s = 1.0$, the angular velocities of the disks, and hence the rate of diffusion of angular momentum, are time dependent. Therefore solid-body rotation is not possible.

When $(R_e^R/R_e^S) \gg 1$, the torques which the fluid exerts on the rotating disks are of greater interest than the normal forces. Figure 9 shows for values of $s = -1.0$ the way in which $-T_L$ varies with R_e^S, when $R_e^R = 0.0$, 3.0, and 5.0 for $M = 4.0$ and 2.0. It is apparent from the figures that the torques are more sensitive to changes in R_e^S than to changes in R_e^R.

References

Hamza, E. A., and MacDonald, D. A., 1984, "A Similar Flow Between Two Rotating Disks," *Quarterly of Applied Mathematics*, Vol. 41, pp. 495–511.

Hamza, E. A., 1989, "A Similar Flow Between Two Disks in the Presence of a Magnetic Field," ASME JOURNAL OF APPLIED MECHANICS, Vol. 56, pp. 218–221.

Hamza, E. A., 1988, "The Magnetohydrodynamic Squeeze Film," ASME *Journal of Tribology*, Vol. 110, No. 2, pp. 375–377.

Hughes, W. F., and Elco, R. A., 1962, "Magnetohydrodynamic Lubrication Flow Between Parallel Rotating Disks," *J. Fluid Mech.*, Vol. 13, pp. 21–32.

Ishizawa, S. A., 1966, "The Unsteady Laminar Flow Between Two Parallel Disks with Arbitrarily Varying Gap Width," *Bull. of the JSME*, Vol. 9, pp. 533–550.

Kamiyama, S., 1969, "Inertia Effects in MHD Hydrostatic Thrust Bearing," ASME *Journal of Lubrication Technology*, Vol. 91, No. 4, pp. 589–596.

Krieger, R. J., and Day, H. J., and Hughes, W. F., 1967, "The MHD Hydrostatics Thrust Bearings—Theory and Experiments," *Journal of Lubrication Technology*, Vol. 89, pp. 307–313.

Kuzma, D. C., Maki, E. R., and Donnelly, R. J., 1964, "The Magnetohydrodynamic Squeeze Film," *J. Fluid Mech.*, Vol. 19, pp. 395–400.

Wang, C. Y., 1976, "The Squeezing of a Fluid Between Two Plates," ASME JOURNAL OF APPLIED MECHANICS, Vol. 98, pp. 579–582.

Free-Edge Stress Intensity Factor for a Bonded Ductile Layer Subjected to Shear

E. D. Reedy, Jr.
Sandia National Laboratories,
Albuquerque, NM 87185
Mem. ASME

The stress state found in a thin, power-law hardening ductile layer bonded between a pair of rigid adherends and subjected to a shear loading is investigated. Within the context of a work-hardening plasticity theory, a stress singularity of type Kr^{δ} *(*$\delta < 0$*) exists at the point where the interface between one of the rigid adherends and the ductile layer intersects the stress-free edge. The intensity of this singularity (i.e.,* K*) has been calculated for a plane strain condition using a technique that combines results of an asymptotic analysis of the stress singularity with those of a detailed finite element analysis. A dead-soft aluminum layer is considered first with emphasis placed on an assessment of the region dominated by the plastic stress singularity. Results for a fully plastic layer with negligible elastic strains are presented next. The relation defining the fully plastic, free-edge stress intensity factor for a shear loading depends only on a characteristic shear stress, layer thickness, and the layer's hardening exponent.*

Introduction

Within the context of both elasticity and work-hardening plasticity theory, a stress singularity of type Kr^{δ} ($\delta < 0$) can exist at an interface corner (i.e., the point where an interface between bonded materials intersects a stress-free edge, Fig. 1(*a*)). For example, see Williams (1952) and Bogy (1968) for linear elasticity solutions and Lau et al. (1987, 1988) and Duva (1989) for work-hardening plasticity solutions. Most previous work has been aimed at determining the strength of this stress singularity (i.e., δ). In recent work, the relation defining the elastic, free-edge stress intensity factor K_f for a thin linear elastic layer bonded to rigid adherends and subjected to either a tensile or shear loading has been fully determined for a plane strain condition (Reedy, 1990, 1991). Specifically, for a shear loading

$$K_f = \sigma^* h^{1-\lambda} A_s(\nu) \tag{1}$$

where σ^* is the nominal shear stress found at the center of the layer, $2h$ is layer thickness, $\lambda - 1$ is the order of the stress singularity, and $A_s(\nu)$ is a function defined for a shear loading. $A_s(\nu)$ and $\lambda - 1$ are functions of Poisson's ratio only, and their values are plotted in Fig. 2. Note that K_f is defined so that $\sigma_\theta(r, 0) = K_f r^{\lambda - 1}$ where $\sigma_\theta(r, 0)$ is the stress normal to the interface (see Fig. 1(*b*)).

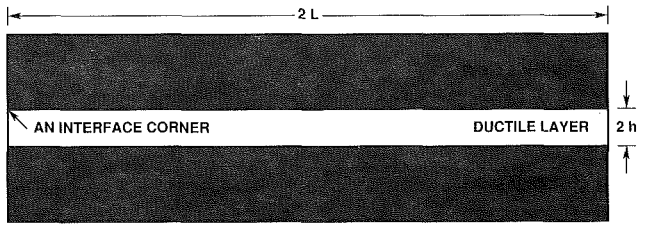

Fig. 1(*a*) The plastic, free-edge stress intensity factor K_f^p is determined for a ductile layer bonded to rigid adherends

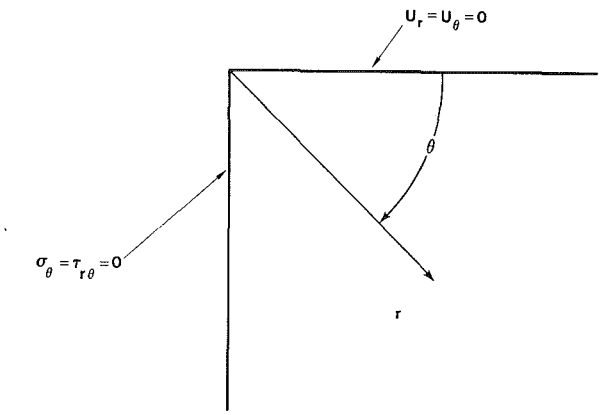

Fig. 1(*b*) Boundary conditions used in the interface corner singularity analysis of a power-law hardening quarter-plane bonded to a rigid layer. Note: stress-free edge at $\theta = -\pi/2$.

Contributed by the Applied Mechanics Division of THE AMERICAN SOCIETY OF MECHANICAL ENGINEERS for publication in the ASME JOURNAL OF APPLIED MECHANICS.

Discussion on this paper should be addressed to the Technical Editor, Professor Lewis T. Wheeler, Department of Mechanical Engineering, University of Houston, Houston, TX 77204-4792, and will be accepted until four months after final publication of the paper itself in the ASME JOURNAL OF APPLIED MECHANICS.

Manuscript received by the ASME Applied Mechanics Division, Nov. 15, 1990; final revision, Mar. 25, 1992. Associate Technical Editor: M. E. Fourney.

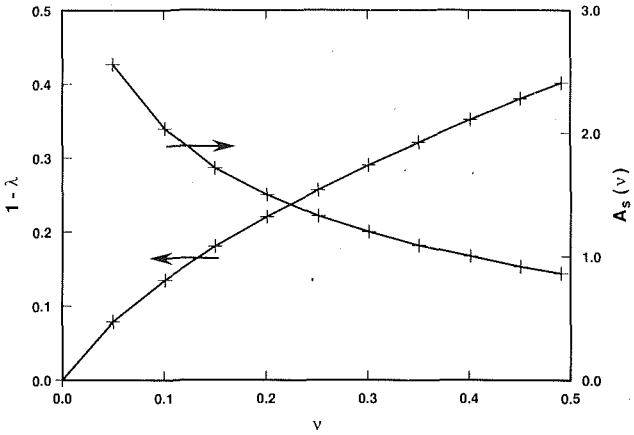

Fig. 2 Calculated dependence of the quantity $1 - \lambda$ and the function $A_s(\nu)$ on Poisson's ratio ν. Note $K_f = \sigma^* h^{1-\lambda} A_s(\nu)$ for a linear elastic layer subjected to shear.

Since the intensity of the stress singularity (i.e., K) characterizes the magnitude of the stress state in the region where the interface and stress-free edge intersect, this parameter may, under suitable conditions, characterize flaw nucleation, the initial growth of small preexisting flaws, or other aspects of the failure process. Several experimental studies have investigated the use of a linear elastic, interface corner stress intensity factor to predict the failure of relatively brittle bonded materials, and these studies lend some support to its use (Gradin, 1982; Groth, 1988; Hattori et al., 1988). The failure of bonded elastic-to-plastically deformable materials is also of technological interest with application to glass or ceramic-to-metal seals, soldered microelectronic components, and metal matrix composites. For example, the failure of a thin ductile adhesive layer used to bond to ceramic adherends together has been the subject of recent studies (Evans et al., 1986; Cao et al., 1988, and Dalgleish et al., 1988).

Reported as follows are the results of an analysis of the interface corner stress state found in a thin, power-law hardening ductile layer bonded between a pair of rigid adherends and subjected to a shear loading. In particular, the intensity of the interface corner singularity, referred to here as the plastic, free-edge stress intensity factor K_f^p, has been calculated for a plane strain condition using a technique that combines results of an asymptotic analysis of the stress singularity with those of a detailed finite element analysis. This study examines the effect of material, geometric, and load parameters on the value of K_f^p.

Asymptotic Solution for Region Near Interface Corner

The present analysis determines the order of the dominant, interface corner stress singularity of type r^δ ($\delta < 0$) for bonded ductile and rigid quarter planes, and also the spatial variation of stresses and displacements in the region dominated by the stress singularity. Both Lau et al. (1987, 1988) and Duva (1989) have analyzed related problems. The method of analysis used here is similar to that carried out by Hutchinson (1968) in his asymptotic analysis of crack-tip stress fields in a strain-hardening material (i.e., the HRR singularity field); only boundary conditions and angular domain differ.

Figure 1(*b*) shows the problem analyzed. As indicated, a single elastic-plastic quarter-plane is considered, and a polar coordinate system is centered at the interface corner. The presence of the bonded, rigid quarter-plane is specified by interface boundary conditions. The four homogeneous boundary conditions applied to the edges that form the interface corner are

$$U_r(r, 0) = U_\theta(r, 0) = \sigma_\theta(r, -\pi/2) = \sigma_{r\theta}(r, -\pi/2) = 0. \quad (2)$$

The layer's tensile elastic-plastic behavior is represented by the Ramberg-Osgood relation

$$\epsilon = (\sigma_y/E)\{\sigma/\sigma_y + \alpha(\sigma/\sigma_y)^n\} \quad (3)$$

where E is Young's modulus, α is a material constant, σ_y is yield strength, and n is the hardening exponent. The layer's response to multi-axial stress states is based upon a J_2-deformation theory of plasticity generalization of Eq. (3). A deformation theory of plasticity is physically reasonable only under conditions of monotonic, proportional loading. It is assumed, as it is in the HRR crack-tip singularity analysis, that this condition is approximately satisfied. In the singularity analysis, consideration is limited to the region in the immediate neighborhood of the interface corner. In this region, the elastic strains are negligible compared to plastic strains, so only the nonlinear, power-law term of Eq. (3) enters into the analysis.

The differential equation governing the stress state at the interface corner can be formulated in a straightforward manner using the nonlinear, plane strain J_2-deformation theory constitutive relations, linear strain-displacement relations, and a stress function of the form

$$\phi = r^{s+1}\hat{\phi}(\theta), \quad -\pi/2 \le \theta \le 0, \quad r > 0. \quad (4)$$

Note, this stress function is used to investigate a stress singularity of type r^{s-1} ($s < 1$). Solutions with $(1 - 1/n) < s < 1$ are of interest since they produce unbounded stresses and vanishing displacements as the interface corner is approached.

The governing homogeneous, forth-order, nonlinear differential equation for $\hat{\phi}(\theta)$ will not be listed here since it is similar to that used in the well-known HRR crack-tip singularity analysis (Hutchinson, 1968). The boundary conditions for the interface corner singularity problem (Eq. (2)) take the following form when expressed in terms of $\hat{\phi}$.

$$\ddot{\hat{\phi}}(0) = (s^2 - 1)\hat{\phi}(0) \quad (5a)$$

$$\dddot{\hat{\phi}}(0) = (s(4n(1-s) + s - 4) - 1)\dot{\hat{\phi}}(0) \quad (5b)$$

$$\hat{\phi}(-\pi/2) = 0 \quad (5c)$$

$$\dot{\hat{\phi}}(-\pi/2) = 0 \quad (5d)$$

Note that in the above $(\cdot) = \partial/\partial\theta$.

The governing homogeneous differential equation and homogeneous boundary conditions define an eigenvalue problem in s. This type of problem can be solved for a specified hardening exponent n using a shooting method. In essence, this method adjusts the values of s and $\dot{\hat{\phi}}(0)$ until the boundary conditions at $\theta = -\pi/2$ are satisfied (note that the condition $\hat{\phi}(0) = 1$ can be arbitrarily applied in this eigenvalue analysis). A fourth-order Runge-Kutta method was used to integrate the differential equation, and a Newton's method was used to update the values of s and $\dot{\hat{\phi}}(0)$. MACSYMA (1989), a symbolic algebra program, was used to develop the governing differential equation, and also to implement the shooting method for solving the governing equation.

The solution for $n = 1$ corresponds to an incompressible, linear elastic material. A solution for this case can be determined using an alternate approach (Reedy, 1991), and it has been verified that the present method reproduces that solution. A parameter tracking scheme was used to determine the initial guess for s and $\dot{\hat{\phi}}$ for the n of interest using calculated values for smaller values of n. Using this approach, results for hardening exponents ranging from 1 to 13 have been attained with no difficulty (calculations for higher values of n were not attempted).

The calculated order of the interface corner stress singularity $(s - 1)$ is plotted in Fig. 3 as a function of hardening exponent. This plot indicates that the strength of the singularity decreases rapidly with increasing hardening exponent; the value at $n = 1$ is -0.41, while at $n = 5$ the value is -0.15. For a specified

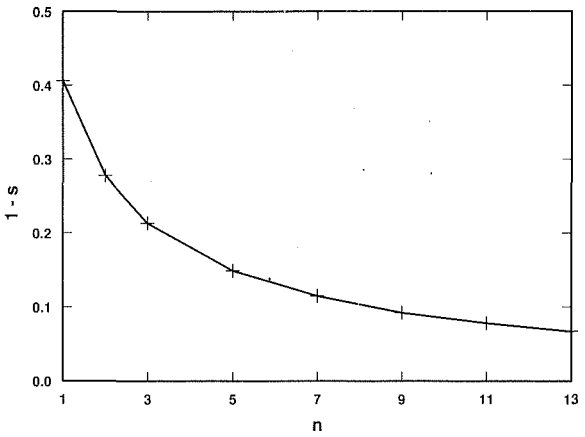

Fig. 3 Order of the interface corner stress singularity $-(1 - s)$ as a function of hardening exponent for a power-law hardening quarter plane bonded to a rigid layer

value of n and the corresponding value of s, the solution for stresses and displacements near the interface corner can be determined to within a single constant, the intensity of the singularity, using the calculated values of ϕ and its derivatives.

The stress intensity factor is defined here so that

$$\sigma_\theta(r, 0) = K_f^p r^{s-1} \tag{6}$$

$\sigma_\theta(r, 0)$ is the stress component normal to the interface, and K_f^p is called the plastic, free-edge stress intensity factor. If it proved convenient, a strain intensity factor could also be defined. In the region dominated by the stress singularity, displacement, and stress quantities are then given by

$$U_r = (\alpha\sigma_y/E)\,(K_f^p/\sigma_y)^n r^{n(s-1)+1}\hat{U}_r(\theta) \tag{7a}$$

$$U_\theta = (\alpha\sigma_y/E)\,(K_f^p/\sigma_y)^n r^{n(s-1)+1}\hat{U}_\theta(\theta) \tag{7b}$$

$$\sigma_r = K_f^p r^{s-1}\hat{\sigma}_r(\theta) \tag{8a}$$

$$\sigma_\theta = K_f^p r^{s-1}\hat{\sigma}_\theta(\theta) \tag{8b}$$

$$\sigma_{r\theta} = K_f^p r^{s-1}\hat{\sigma}_{r\theta}(\theta) \tag{8c}$$

$$\sigma_e = K_f^p r^{s-1}\hat{\sigma}_e(\theta) \tag{8d}$$

$$\sigma_m = K_f^p r^{s-1}\hat{\sigma}_m(\theta) \tag{8e}$$

where σ_e is effective stress and σ_m is mean stress. The functions $\hat{U}_r(\theta)$, $\hat{U}_\theta(\theta)$, $\hat{\sigma}_r(\theta)$, $\hat{\sigma}_\theta(\theta)$, $\hat{\sigma}_{r\theta}(\theta)$, $\hat{\sigma}_e(\theta)$, and $\hat{\sigma}_m(\theta)$ are fully determined by the asymptotic analysis. Although a complete tabular listing of function values is not presented here, Table 1 does list values of $s - 1$, $\hat{U}_r(-\pi/2)$, $\hat{U}_\theta(-\pi/2)$, $\hat{\sigma}_\theta(0)$, and $\hat{\sigma}_{r\theta}(0)$ as a function of the hardening exponent n. Note that $\hat{U}_r(-\pi/2)$ and $\hat{U}_\theta(-\pi/2)$ are used to define displacements along the stress-free edge, while $\hat{\sigma}_\theta(0)$, and $\hat{\sigma}_{r\theta}(0)$ are used to define interfacial stresses.

Finite Element Solution for the Intensity of the Stress Singularity

Plane strain finite element calculations were carried out for an idealized configuration that models a thin layer bonded between rigid adherends. The layer has thickness $2h$, and length $2L$. All calculations were carried out for an applied shear loading. As shown in Fig. 4, the applied shear loading was enforced by displacing the layer's lower edge relative to the fixed upper edge. One quarter of the layer was modeled with boundary conditions consistent with a skew symmetric loading, and $L = 2.5$ mm. Most calculations were performed for $h = 0.125$ mm ($L/h = 20$). Preliminary calculations showed that the stress state at the center of the layer is uniform for this L/h ratio, and consequently the results are appropriate for all L/h values of 20 or greater. Figure 4 shows a typical finite element mesh. The object of a calculation is to determine the

Table 1 Quantities used to define displacements along the stress-free edge and stresses along the interface of a plastically deforming quarter-plane bonded to a rigid layer in the region of the interface corner

n	$s - 1$	$\hat{U}_r(-\pi/2)$	$\hat{U}_\theta(-\pi/2)$	$\hat{\sigma}_\theta(0)$	$\hat{\sigma}_{r\theta}(0)$
1	−0.4054	1.2720	2.5222	1.000	0.5042
2	−0.2759	0.9646	1.8943	1.000	0.4871
3	−0.2126	0.6872	1.3622	1.000	0.4739
5	−0.1475	0.3318	0.6767	1.000	0.4563
7	−0.1135	0.1568	0.3288	1.000	0.4452
9	−0.0924	0.0735	0.1579	1.000	0.4375
11	−0.0779	0.0343	0.0753	1.000	0.4318
13	−0.0674	0.0160	0.0357	1.000	0.4274

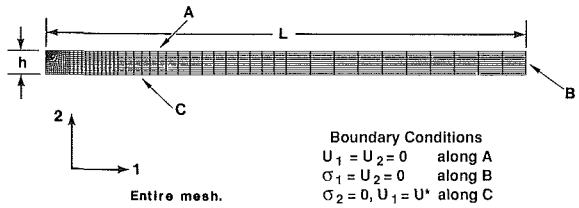

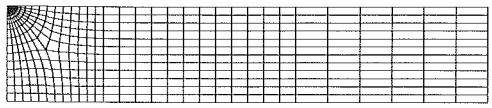

Detail of mesh near free edge.

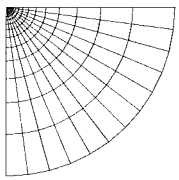

Detail of mesh near interface corner. There are 24 element rings.

Fig. 4 Typical finite element mesh used in analysis

value of the free-edge stress intensity factor K_f^p, and for this reason the mesh is highly refined in the region of the interface corner. There are 24 rings of elements surrounding the interface corner with radial nodal positions at $r = 0, 0.033, 0.067, 0.100, (10^{0.125i})/10$ μm, where $i = 1, 2, \ldots, 21$. The finite element calculations were performed with the ABAQUS code (1989) using 4-node bilinear elements. The mesh shown in Fig. 4 contains 876 elements and has 1930 degrees-of-freedom.

As discussed in the previous section, the tangential displacement along the stress-free edge in the region dominated by the stress singularity is given by Eq. 7(a), and a plot of $\log(U_r)$ versus $\log(r)$ will be a straight line with slope $n(s - 1) + 1$. The logarithm of the free-edge tangential displacements calculated by the finite element method does indeed vary in an essentially linear manner with the logarithm of distance from the interface corner for $0.1 \le r \le 1.0$ μm for hardening exponents of 3 to 13 (Fig. 5, each curve is defined by displacement values computed at 9 nodal points). The values of s determined from the slopes of the lines in Fig. 5 are within 1.0 percent of the value determined by the singularity analysis. The value of K_f^p was determined from computed free-edge displacements by a linear least square fit of

$$(U_r/\{(\alpha/E\sigma_y^{n-1})\hat{U}_r(-\pi/2)r^{n(s-1)+1}\})^{1/n} = C_1 + C_2 r \tag{9}$$

where C_1 and C_2 are constants ($C_1 = K_f^p$), the value of s and $\hat{U}_r(-\pi/2)$ are known for a given value of the hardening exponent (see Table 1), and $0.1 \le r \le 1.0$ μm.

The deformation generated by a shear loading is sketched

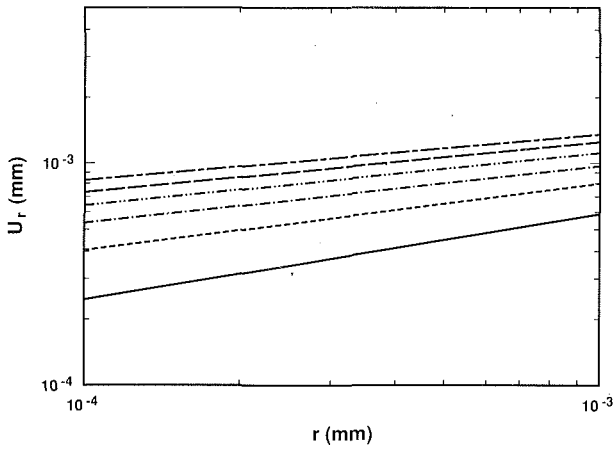

Fig. 5 Displacement U_r along the stress-free edge for $\gamma^* = 0.10$. From the lower to upper curve $n = 3, 5, 7, 9, 11$, and 13.

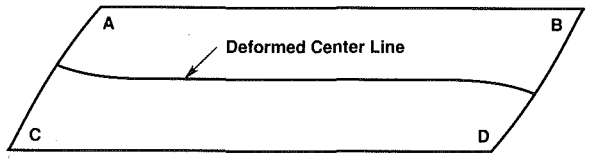

Fig. 6 Deformed shape of a ductile layer subjected to a positive a shear loading

in Fig. 6. The calculated magnitude of K_f^p is the same at points A, B, C, and D; however, K_f^p is positive at points B and C, and negative at points A and D.

Results for a Soft Aluminum Adhesive Layer

Results for a thin, soft aluminum layer are presented first ($h = 0.125$ mm, E = 69 GPa, $\nu = 0.33$, $n = 5$, $\alpha = 0.5$, $\tau_y = 11.5$ MPa). This particular analysis can be considered to model stiff adherends (e.g., alumina) bonded together with a dead soft aluminum adhesive layer.

Calculated values of K_f^p are listed in Table 2 and plotted in Fig. 7 as a function of γ^*, the shear strain in the center of the layer. Note that $\gamma^* = U^*/h$, where U^* is the applied edge displacement defined in Fig. 4. Values of K_f^p are presented for $\gamma^* = 0.001$ to 0.100. These results are for a layer that is fully yielded ($\gamma^*/\gamma_y = 2$ to 225, where $\gamma_y = \tau_y/G$). As anticipated, Fig. 7 shows that K_f^p increases in a power-law-like manner. According to Ilyushin's theorem (see Hutchinson, 1979, p. 59), the solution to a boundary value problem with a single, monotonically increasing displacement parameter λ, will have strains that increase linearly with λ, and stresses that increase as $\lambda^{1/n}$ when the material obeys a power-law hardening, $J2$-deformation theory of plasticity (i.e., the linear term in Eq. (3) is neglected). In the problem considered here, the applied edge displacement is a monotonically increasing displacement parameter. As the layer approaches a fully plastic condition (elastic strains are negligible), the ratio of K_f^p, a stress-like quantity, to σ^*, the shear stress in the center of the layer, should approach a constant value. Table 2 shows this to be the case.

The ability of K_f^p to characterize interface corner failure processes is currently unknown. Clearly, to be of any potential use the stress state characterized by K_f^p must dominate a sufficiently large region around the interface corner. One approach for characterizing the region dominated by the stress singularity is to compare the angular dependence of stress quantities as determined by the finite element analysis to that determined from analytic considerations. Figures 8(*a*) and 8(*b*) plot such results for effective and mean stress, respectively. Close to the interface corner, at a radial distance of 1.2 μm (0.01 h) or less, the calculated angular dependence is in excellent agreement with that determined analytically for an interface corner singularity. This verifies the accuracy of the finite element calculation, and also indicates that the asymptotic analysis did actually identify the dominate singularity. At a radial distance of 37 μm (0.3 h), the calculated effective and mean stress begin to show a substantial deviation from that expected when the singularity dominates. Figures 9(*a*) and 9(*b*) compare the interfacial stresses $\sigma_{r\theta}$ and σ_θ calculated by the finite element method with the one-term, singular asymptotic expressions over a distance h (125 μm). These results suggest that interfacial normal stress is closely approximated by the one-term singular expression to a distance of roughly 0.25 h (30 μm), while agreement between asymptotic and calculated interfacial shear stress is only fair at comparable distances. Finally note, when $\gamma^* = 0.01$, the calculated effective plastic strain is less than 0.10 when distance from the interface corner exceeds 0.01 h (1 μm).

Table 2 Calculated values of the plastic, free-edge stress intensity factor K_f^p as a function of applied load ($n = 5$, $h = 0.125$ mm)

γ^*	σ^* (MPa)	$\lvert K_f^p \rvert$ (MPa-mm$^{0.1475}$)	$\frac{\lvert K_f^p \rvert}{\sigma^* h^{0.1475}}$
0.001	13.20	18.16	1.870
0.002	16.22	21.66	1.815
0.003	17.99	23.82	1.799
0.004	19.28	25.42	1.792
0.005	20.30	26.71	1.788
0.010	23.67	31.00	1.780
0.019	27.05	35.34	1.775
0.033	30.38	39.65	1.774
0.041	31.84	41.54	1.773
0.050	33.08	43.15	1.773
0.100	38.13	49.71	1.772

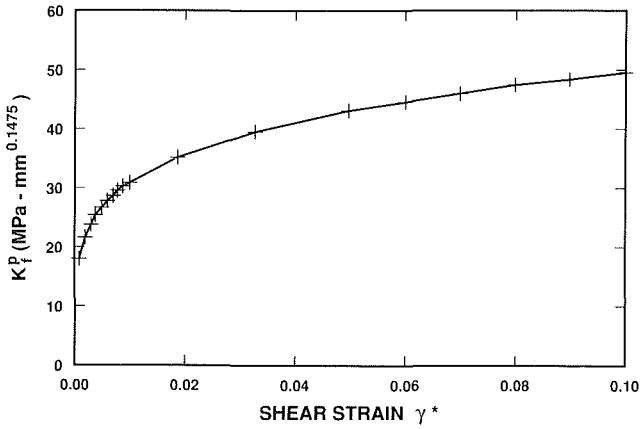

Fig. 7 Calculated plastic, free-edge stress intensity factor K_f^p as a function of nominal applied shear strain ($n = 5$, $h = 0.125$ mm)

Fully Plastic Solutions

The relation for the plastic, free-edge stress intensity factor for a semi-infinite layer (i.e., $L/h > 20$) subjected to shear and at load levels such that elastic strains are negligible is taken to be of the form

$$K_f^{fp} = \sigma^* h^{1-s} B_s(n) \tag{10}$$

where K_f^{fp} is the fully plastic, free-edge stress intensity factor, σ^* is the nominal shear stress in the interior of the layer, $2h$ is layer thickness, $s - 1$ is the order of the stress singularity, and $B_s(n)$ is a function defined for shear loading. Note, $B_s(n)$

Table 3 Calculated values of the fully plastic, free-edge stress intensity factor K_f^{fp} for various material and geometric parameters

CASE	$2h$ (mm)	α	E (GPa)	τ_y (MPa)	n	σ^* (MPa)	$\lvert K_f^{fp} \rvert$ (Mpa-mm^{1-s})
1	0.250	0.5	69.0	11.5	3	84.0	82.1
2	0.250	0.5	69.0	11.5	5	38.1	49.7
3	0.250	0.5	69.0	11.5	7	27.1	41.2
4	0.250	0.5	69.0	11.5	9	22.4	37.5
5	0.250	0.5	69.0	11.5	11	19.9	35.5
6	0.250	0.5	69.0	11.5	13	18.3	34.3
7	0.250	0.1	100.0	5.0	5	29.0	37.9
8	0.125	0.5	69.0	11.5	5	38.1	45.0

Note: $\gamma^* = 0.10$ in all cases; $\gamma_y = ((3\tau_y)/E)$; and $\sigma^* = \tau_y(\gamma^*/(\alpha\gamma_y))^{1/n}$ when fully plastic

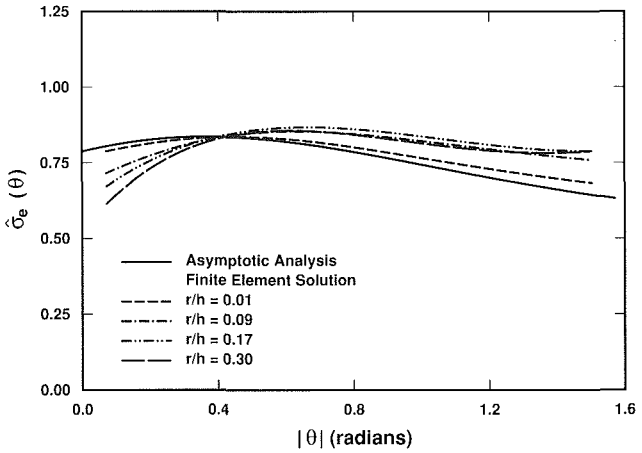

Fig. 8(*a*) Variation of effective stress with angular position for $\gamma^* = 0.01$. Note: $\hat{\sigma}_e(\theta) = \sigma_e/(K_f^p r^{s-1})$.

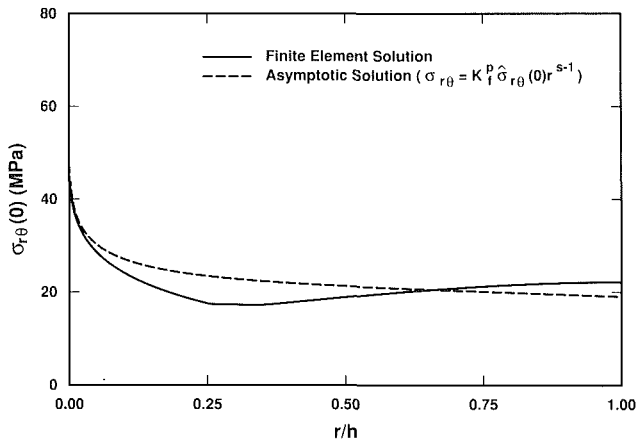

Fig. 9(*a*) Comparison of finite element and asymptotic interfacial shear stress for $\gamma^* = 0.01$

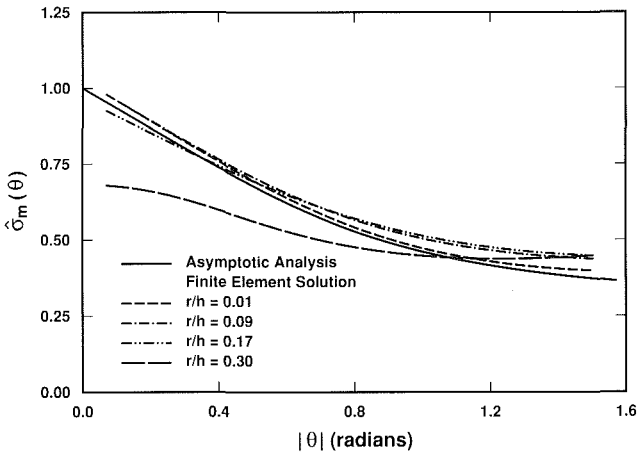

Fig. 8(*b*) Variation of mean stress with angular position for $\gamma^* = 0.01$. Note: $\hat{\sigma}_m(\theta) = \sigma_m/(K_f^p r^{s-1})$.

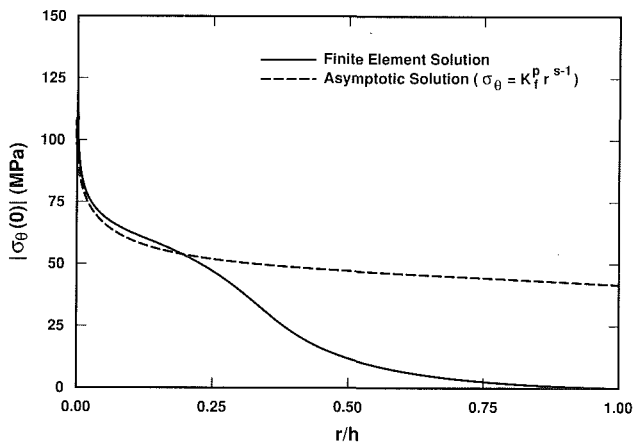

Fig. 9(*b*) Comparison of finite element and asymptotic interfacial normal stress for $\gamma^* = 0.01$

and $s - 1$ depend only on hardening exponent n. As discussed above, Ilyushin's theorem indicates that K_f^p varies as σ^* when the layer is fully plastic, consequently, B_s will not depend on a load-like parameter. Furthermore, B_s is independent of the material parameters α and τ_y since the stress solution for a specified σ^* does not depend on these parameters when the layer is fully plastic.

Table 3 lists calculated values of K_f^{fp} for eight different plane strain calculations. Cases 1 thru 6 examine the effect of varying the layer's hardening exponent. Case 7 changes yield strength, Young's modulus, and Ramberg-Osgood parameter α. Case 8 reduces layer thickness by 50 percent. Tabulated results are for a shear loading where the nominal shear strain γ^* at the center of the layer is 0.10.

Finally, note that the value of K_f^{fp} for different values of hardening exponent are not directly comparable since the order of the singularity is also a function of hardening exponent. Also note that the dimensions of K_f^{fp} in Table 3 are MPa-mm^{1-s}.

The calculated values of K_f^{fp} listed in Table 3 confirm Eq. (10). First consider the calculated results for layers with the identical hardening exponent, but with different Young's modulus and yield strength (Cases 2 and 7). As expected, the ratio of the calculated K_f^{fp}'s equals the ratio of their characteristic

Table 4 Quantities used to define the fully plastic, free-edge stress intensity factor K_f^{fp}

n	$1 - s$	$B_s(n)$
3	0.2126	1.52
5	0.1475	1.77
7	0.1135	1.92
9	0.0924	2.02
11	0.0779	2.10
13	0.0674	2.16

shear stresses. This confirms that the function B_s does not depend on layer yield strength. As indicated by Eq. (10), K_f^{fp} is expected to vary with layer thickness as h^{1-s} when the hardening exponent and σ^* are held fixed. For example, when the hardening exponent equals 5, a 50 percent reduction in layer thickness should cause a $0.5^{0.1475} = 0.903$ reduction in K_f^{fp}. This is confirmed by comparing Cases 2 and 8. Cases 1 thru 6 define the dependence of K_f^{fp} on the hardening exponent. These values have been used to define the function $B_s(n)$ in Eq. (10) (see Table 4).

Finally note that with proper interpretation, the fully plastic results presented here can be applied to steady, power-law creep by identifying strain with strain rate.

Acknowledgment

This work was performed at Sandia National Laboratories and was supported by U.S. Department of Energy under Contract DE-AC04-76DP00789.

References

ABAQUS Version 4.8, 1989, Hibbitt, Karlsson, and Sorensen, Providence, RI.

Bogy, D. B., 1968, "Edge-Bonded Dissimilar Orthogonal Elastic Wedges Under Normal and Shear Loading," ASME JOURNAL OF APPLIED MECHANICS, Vol. 35, pp. 460–466.

Cao, H. C., Thouless, M. D., and Evans, A. G., 1988, "Residual Stresses and Cracking in Brittle Solids Bonded with a Thin Ductile Layer," *Acta Metallurgica*, Vol. 36, pp. 2037–2046.

Dalgleish, B. J., Lu, M. C., and Evans, A. G., 1988, "The Strength of Ceramics Bonded with Metals," *Acta Metallurgica*, Vol. 36, pp. 2029–2035.

Duva, J. M., 1989, "The Singularity at the Apex of a Rigid Wedge after Partial Separation," ASME JOURNAL OF APPLIED MECHANICS, Vol. 56, pp. 977–979.

Evans, A. G., Lu, M. C., Schmauder, S., and Ruhle, M., 1986, "Some Aspects of the Mechanical Strength of Ceramic/Metal Bonded Systems," *Acta Metallurgica*, Vol. 34, pp. 1643–1655.

Gradin, P. A., 1982, "A Fracture Criterion for Edge-Bonded Bimaterial Bodies," *Journal of Composite Materials*, Vol. 16, pp. 448–456.

Groth, H. L., 1988, "Stress Singularities and Fracture at Interface Corners in Bonded Joints," *International Journal of Adhesion and Adhesives*, Vol. 8, pp. 107–113.

Hattori, T., Sakata, S., and Watanabe, T., 1988, "A Stress Singularity Parameter Approach for Evaluating Adhesive and Fretting Strength," *Advances in Adhesively Bonded Joints*, S. Mall et al., ed., ASME New York, MD-Vol. 6, pp. 43–50.

Hutchinson, J. W., 1968, "Singular Behaviour at the End of a Tensile Crack in a Hardening Material," *Journal of the Mechanics and Physics of Solids*, Vol. 16, pp. 13–31.

Hutchinson, J. W., 1979, *Nonlinear Fracture Mechanics*, The Technical University of Denmark, Lyngby, Denmark.

Lau, C. W., and Rahman, A., 1987, "Interfacial Mechanics of Seals," *Technology of Glass, Ceramic, or Glass-Ceramic to Metal Sealing*, W. E. Moddeman et al., ed., ASME New York, MD-Vol. 4, pp. 89–98.

Lau, C. W., and Delale, F., 1988, "Interfacial Stress Singularities at Free Edge of Hybrid Metal Matrix Composites," ASME *Journal of Engineering Materials and Technology*, Vol. 110, pp. 41–47.

MACSYMA Version 412.61, 1988, Symbolics, Inc., Burlington, MA.

Reedy, Jr., E. D., 1990, "Intensity of the Stress Singularity at the Interface Corner between a Bonded Elastic and Rigid Layer," *Engineering Fracture Mechanics*, Vol. 36, pp. 575–583.

Reedy, Jr., E. D., 1991, "Intensity of the Stress Singularity at the Interface Corner of a Bonded Elastic Layer Subjected to Shear," *Engineering Fracture Mechanics*, Vol. 38, pp. 273–281.

Williams, M. L., 1952, "Stress Singularities Resulting from Various Boundary Conditions in Angular Corners of Plates in Extension," ASME JOURNAL OF APPLIED MECHANICS, Vol. 74, pp. 526–528.

Fluid Flow and Heat Transfer in the Crescent-Shaped Lumen Catheter

M. A. Ebadian[1]
Fellow ASME.

H. Y. Zhang[2]

Department of Mechanical Engineering,
Florida International University,
Miami, FL 33199

This paper presents a numerical investigation of fluid flow, frequency response in the fully developed region, and convective heat transfer in the entrance region of the crescent-shaped lumen catheter. The catheter is commonly used in the biomedical field to clinically diagnose heart disease and also to treat vessel blockage in surgery. The catheter is subjected to a constant wall temperature. The solution to discretization of the momentum and energy equations is obtained by using the numerically generated boundary fitted coordinate system. According to this method, the complex domain in the physical plane is transformed into a regular square domain in the computational plane. The control volume-based finite difference method is then used to discretize the transformed governing equations. Results for the thermal entry region flow, frequency response, and heat transfer are presented in graphical form. The representative curves illustrating variations of the flow rate, frequency response, damping coefficient, bulk temperature, and the Nusselt numbers with pertinent parameters in the entire thermal entry region are plotted. The optimized catheter design for diagnostic use in the medical industry is also presented graphically.

Introduction

The Dual Lumen Pressure Monitoring (DLPM) catheter is commonly used to diagnose heart disease in the clinic and also to treat vessel blockage in surgery (cf. Pepine et al., 1989; Intaglietta, 1987). A pressure measurement system used in clinical catheterization for a left heart study is shown in Fig. 1. A catheter is attached via Luer connectors to a manifold that in turn is connected to a contrast medium (ionic diatrizoate) and pressure transducer. The transducer may be attached directly to the manifold or via extension pressure tubing, as illustrated. The active element of the pressure transducer is a resistive bridge deposited on, or attached to, the diaphragm and connected, via isolation amplifiers, to the recording system. This system is usually treated as a second-order instrument in biomedical engineering. For this instrument, designers assume laminar flow in a circular tube, having the parabolic velocity profile characteristic of steady flow (cf. Doebelin, 1990). Traditionally, the catheter is built with circular lumens. Both lumens are commonly used to measure pressure within the bloodstream. In measuring valvular gradients, the catheter is positioned across the aortic valve in such a way that the distal end of the catheter exposes the larger lumen to the blood within the ventricles, thus allowing measurement of ventricular pressure. The smaller lumen is exposed to the blood contained within the aorta allowing it to measure aortic pressure. In addition, since the temperature of the fluid to be injected is different than the blood temperature, thermodilution techniques have been extensively studied for almost 40 years. In this case, the indicator is "cold" and its "concentration" is on temperature. Distinct fluctuations in pulmonary arterial temperature related to cardiac and respiratory cycling result in a fluctuating thermal baseline. In some critically ill patients,

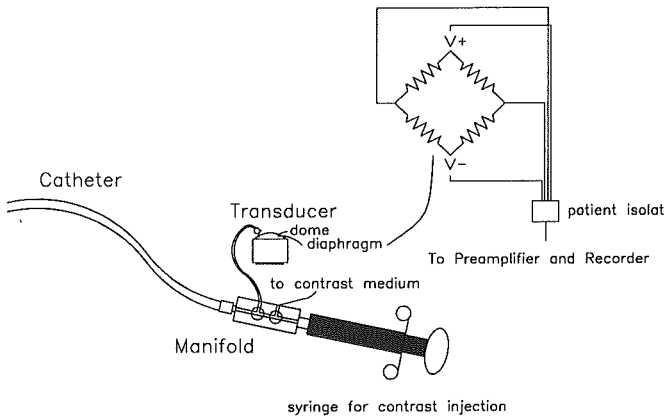

Fig. 1 Typical pressure measurement system used in clinical catheterization

[1]To whom correspondence should be addressed.
[2]Graduate student.

Contributed by the Applied Mechanics Division of THE AMERICAN SOCIETY OF MECHANICAL ENGINEERS for publication in the ASME JOURNAL OF APPLIED MECHANICS.

Discussion on this paper should be addressed to the Technical Editor, Professor Lewis T. Wheeler, Department of Mechanical Engineering, University of Houston, Houston, TX 77204-4792, and will be accepted until four months after final publication of the paper itself in the ASME JOURNAL OF APPLIED MECHANICS.

Manuscript received by the ASME Applied Mechanics Division, Feb. 21, 1992; final revision, Apr. 22, 1992. Associate Technical Editor: T. R. Akylas.

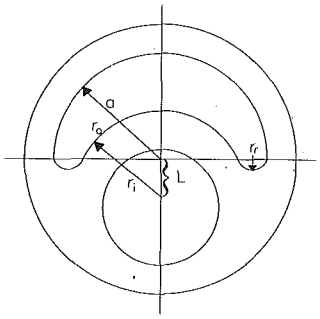

Fig. 2 Lumen cross-section and characteristic length

these fluctuations approach the magnitude of the temperature change that follows a "cold" injection (cf. Brathwaite and Bradley, 1968; Weisel et al., 1975). Although electronic averaging provides a more stable baseline, iced rather than room temperature injection must be used in patients to provide a sufficient signal-to-noise ratio. Thus, knowledge of temperature distribution in thermodilution cardiac output is very important. It is therefore important to numerically investigate the thermal properties of the catheter.

The problem with this design is that when one tries to measure pressure through the smaller lumen, damping of the signal occurs. Obviously, this creates a problem since an ideal catheter design would have both lumens providing adequate flow characteristics in independent, but equivalent, frequency response systems. In order to solve this problem and still be able to keep other characteristics of the catheter unchanged, it is proposed that the cross-sectional geometry of the smaller lumen be replaced with a crescent-shaped geometry, thus increasing the cross-sectional area of this lumen. Although this crescent-shaped lumen geometry has provided excellent frequency response and thermal properties, the medical industry strongly believes that the cross-sectional area of the lumen can be optimized to have the same flow as well as the frequency response characteristics of the larger lumen. Being able to approximate numerically the optimum lumen cross-sectional area is the problem. Most of the available mathematical models do not take into consideration anything other than circular geometries. Therefore, these models are not able to calculate the flow rate and the frequency response of the crescent-shaped design. In fact, inspection of a literature survey by Shah and London (1978), Kakac et al. (1987), Eckert et al. (1989), Martynenko (1988), Eckert et al. (1990), and Pepine et al. (1989) indicates that no work has been cited in this area of study. At present, one must be able to predict the flow rate and frequency response of catheters that have irregular lumen geometries. This must be accomplished through computer simulation since bench testing of these irregular designs is not practical due to the high cost involved in extrusion tooling. Therefore, the problem examined here is concerned with convective heat transfer in the entrance region of the catheter, Fig. 2. A uniform wall temperature boundary condition is considered. Additionally, the fully developed flow is considered to be laminar and the physical properties are also assumed to be constant (cf. Doebelin, 1990). The developing temperature in these ducts is determined by solving the three-dimensional energy equation by applying the control volume-based finite difference method. The boundary fitted coordinate system (BFCS) by Thompson et al. (1974, 1977, 1982) is used to transform the crescent-shaped physical lumen to the regular geometry of a rectangular tube. Thus, one can use regular geometric methods to investigate the process of the crescent-shaped lumen fluid flow. Those finite difference expressions at and adjacent to the boundary may then be applied using grid points only on the intersections of coordinate lines without the need for any interpolation between points of the grid, Fig. 3. Avoiding interpolation is particularly important for boundaries with strong curvature or slope discontinuities, both of which are common in physical applications. Likewise, interpolation between grid points not coincident with the boundaries is particularly inaccurate with differential systems that produce large gradients in the vicinity of the boundaries. As a result, the character of the solution may be significantly altered in such cases. In many differential systems, the boundary conditions are the dominant influence on the character of the solution, and the use of grid points not coincident with the boundaries thus places the most inaccurate difference representations in precisely the region of the greatest sensitivity. Generation of a curvilinear coordinate system with coordinate lines coincident with all boundaries is

Nomenclature

a = characteristic length, $a = r_o$
A = cross-sectional area (m^2)
A_o/A_i = frequency response
c_p = specific heat (kJ kg^{-1} k^{-1})
D_h = hydraulic diameter (m)
e = dimensionless center distance of the lumen, Eq. (24)
e_c = dimensionless center distance of inner and outer arcs, L/r_o
f = skin friction factor, $-\dfrac{D_h(dp/dz)}{1/2\rho\bar{u}^2}$
h = heat-transfer coefficient (Wm^{-2} K^{-1})
J = Jacobian matrix of transformation, Eq. (22)
k = thermal conductivity (Wm^{-1} K^{-1})
$\dot{m}$ = mass flow rate (kg s^{-1})
Nu = Nusselt number, hD_h/k
p = pressure (N m^{-2})
Pr = Prandtl number, ν/α_T
R_i = dimensionless inner arc radius, r_i/a
R_o = dimensionless outer arc radius, r_o/a
R_r = dimensionless round corner radius, r_r/a
Re = Reynolds number, $\bar{u}D_h/\nu$
T = temperature (K)
T_i = inlet temperature (K)
T_w = circumferential duct wall temperature (K)
u = velocity (m s^{-1})
$\bar{u}$ = mean velocity (m s^{-1})
u^* = dimensionless velocity, $-\dfrac{\mu u}{D_h^2(dp/dz)}$
U = dimensionless mean velocity
x, y = transversal coordinates (m)
X, Y = dimensionless transversal coordinates, x/a, y/a
z = axial coordinate (m)
Z = dimensionless axial coordinate, $\dfrac{z}{D_h\mathrm{RePr}}$

Greek Symbols

α_T = thermal diffusivity (m^2 s^{-1})
α = coefficient, Eq. (15)
β = coefficient, Eq. (16)
γ = coefficient, Eq. (17)
δ = dimensionless round corner of the lumen, Eq. (25)
ζ = damping coefficient
θ = dimensionless temperature $(T_w - T)/(T_w - T_i)$
θ_b = dimensionless bulk temperature $(T_w - T_b)/(T_w - T_i)$
μ = dynamic viscosity (N s m^{-2})
ν = kinematic viscosity (m^2 s^{-1})
ρ = density (kg m^{-3})
Ψ = coefficient, Eq. (19)
ξ, η = transversal coordinates in the computational plane

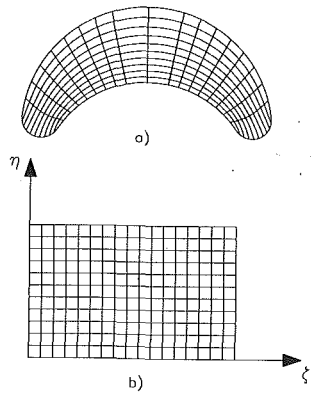

Fig. 3 Grid configuration: (*a*) the physical plane, (*b*) the computational domain

thus an essential part of a numerical solution. A BFCS is generated by solving a set of partial differential equations, which may be of the hyperbolic, parabolic, or elliptic type. We have used elliptic equations with Dirichlet-type boundary conditions requiring simplification of the physical coordinates for the end points of the curvilinear coordinate lines in the physical domain. The crescent-shaped cross-section is used in the transducer/tubing system. The results presented are in terms of isotherms, variations of the bulk temperature, and the Nusselt number in the entire thermal region of the crescent-shaped lumen catheter for various values of the dimensionless center distance of lumen, e, and the dimensionless round corner of lumen, δ. Also, in order to have the same flow rate in each lumen, the crescent-shaped lumen catheter is optimized based on some specific features of the biomedical equipment making different shaped lumens match each other, and the Nusselt number is graphically presented against the δ values. It is believed that the availability to the medical field of such an analytical/numerical solution is essential for a better designed catheter.

Basic Equations

Consideration is given to laminar flow in a catheter having a crescent-shaped cross-section geometry, as shown in Fig. 2. The physical attributes are concerned with fully developed velocity and developing temperature, where thermal properties are assumed constant. Neglecting the axial diffusion term in the energy equation, the governing equations in terms of dimensionless variables are expressed as

Momentum Equation.

$$\frac{\partial^2 u^*}{\partial Y^2}+\frac{\partial^2 u^*}{\partial X^2}+1=0 \tag{1}$$

Energy Equation.

$$U\frac{\partial\theta}{\partial Z}=\frac{\partial^2\theta}{\partial Y^2}+\frac{\partial^2\theta}{\partial X^2}, \tag{2}$$

where, in the above equations,

$$u^*=\frac{\mu u}{D_h^2(-dp/dz)}, \quad Y=\frac{y}{a}, \quad X=\frac{x}{a},$$

$$U=\frac{1}{2}(f\mathrm{Re})u^*, \quad U=\frac{u}{\bar{u}}, \quad \theta=\frac{T-T_w}{T_e-T_w},$$

$$Z=\frac{z}{D_h\mathrm{Pe}}, \quad \mathrm{Re}=\frac{\bar{u}D_h}{\nu}, \quad \mathrm{Pe}=\mathrm{RePr}. \tag{3}$$

In the above equations, u^* represents the dimensionless velocity and is taken from the solution of the momentum Eq. (1); θ is the dimensionless temperature; D_h is the hydraulic diameter of the crescent-shaped lumen catheter; and X, Y, and Z represent the two dimensionless transversal coordinates and one dimensionless axial coordinate, respectively. Equations (1) and (2) are also subjected to the following boundary conditions:

$$u^*=0, \quad \theta=0$$

on the wall of the cresent-shaped lumen catheter (4)

$$\frac{\partial u^*}{\partial X}=0, \quad \frac{\partial\theta}{\partial X}=0 \quad \text{on the symmetrical line} \tag{5}$$

and

$$u^*=1, \quad \theta=1, \quad Z=0 \tag{6}$$

Parameters of Interest

The characteristics of fluid flow and heat transfer in the catheter can be represented by the product of the friction factor and the Reynolds number, the dimensionless bulk temperature, and the Nusselt number.

$$f\mathrm{Re}=\frac{2D_h^2}{\mu\bar{u}}\left(-\frac{dp}{dz}\right) \tag{7}$$

$$\theta_b(Z)=\int_A U\theta dA\Big/\int_A U dA \tag{8}$$

Accordingly, considering the energy balance in a control volume of length, ΔZ, the local Nusselt number may be computed as follows:

$$\mathrm{Nu}_{Z,T}=-\frac{1}{4\theta_b}\left[\frac{D_h^2}{a^2}\right]\frac{d\theta_b}{dZ}. \tag{9}$$

Likewise, with a length of ΔZ, the mean Nusselt number is given by the relation

$$\mathrm{Nu}_{m,T}=-\frac{1}{\Delta Z}\ln\theta_{bZ}, \tag{10}$$

where Z designates the length of the catheter.

Solution Procedure

The difficulty with the complex nature of the quasi-crescent lumen catheter may be circumvented by a numerically generated coordinate system. The basic idea of the boundary fixed coordinate system (BFCS) is to have a coordinate system such that the body contour coincides with the coordinate lines. One of the methods often used to accomplish this goal was suggested by Thompson et al. (1974). The transformation between the physical coordinates (X, Y) and the boundary fitted coordinates (ξ, η) is achieved by solving two Poisson equations, namely,

$$\frac{\partial^2\xi}{\partial X^2}+\frac{\partial^2\xi}{\partial Y^2}=P, \tag{11}$$

$$\frac{\partial^2\eta}{\partial X^2}+\frac{\partial^2\eta}{\partial Y^2}=Q, \tag{12}$$

where P and Q are nonhomogeneous terms, or contracting functions, for the grid distribution in the computational domain. Alternatively, it should be remarked that by using Eqs. (11) and (12), a problem arises about the proper algebraic representation of the irregular boundaries in the physical domain. Thompson et al. (1974) inverted Eqs. (11) and (12) into the transformed domain (ξ, η), where the boundary is easier to specify. At the same time, using the method proposed by Thomas and Middlecoff (1982) for selecting P and Q, Eqs. (11) and (12) are inverted into

$$\alpha\left[\frac{\partial^2 X}{\partial\xi^2}+\phi\frac{\partial X}{\partial\xi}\right]-2\beta\frac{\partial^2 X}{\partial\xi\partial\eta}+\gamma\left[\frac{\partial^2 X}{\partial\eta^2}+\Psi\frac{\partial X}{\partial\eta}\right]=0 \tag{13}$$

Table 1 Grid independence test for the fully developed flow

δ	e = 0.10				e = 0.19				e = 0.40			
	31x21		41x21		31x21		41x21		31x21		41x21	
	fRe	$Nu_{z,T}$	fRe	$Nu_{z,T}$	fRe	$Nu_{z,T}$	fRe	$Nu_{z,T}$	fRe	$Nu_{z,T}$	fRe	$Nu_{z,T}$
0.0001	55.063	2.189	55.095	2.196	56.664	2.430	56.682	2.437	58.752	2.844	58.762	2.851
0.001	55.129	2.191	55.168	2.198	56.715	2.432	56.732	2.439	58.777	2.845	58.787	2.853
0.01	55.732	2.216	55.771	2.223	57.189	2.453	57.208	2.460	59.063	2.860	59.081	2.867
0.1	61.287	2.461	61.339	2.468	61.550	2.660	61.577	2.667	61.657	2.999	61.672	3.006
0.2	66.435	2.740	66.484	2.747	65.553	2.894	65.581	2.901	63.949	3.150	63.965	3.157
0.3	70.497	3.031	70.538	3.037	68.651	3.134	68.682	3.139	65.644	3.297	65.667	3.303
0.4	73.473	3.334	73.523	3.339	70.851	3.377	70.894	3.381	66.788	3.437	66.834	3.441
0.5	75.384	3.644	75.462	3.646	72.181	3.618	72.258	3.618	67.434	3.564	67.497	3.566
0.6	76.264	3.948	76.392	3.946	72.061	3.836	72.527	3.837	67.627	3.672	67.727	3.671
0.7	76.109	4.216	76.316	4.209	72.350	4.013	72.555	4.007	67.392	3.750	67.537	3.747
0.8	73.904	4.391	74.424	4.387	70.398	4.105	70.942	4.105	66.695	3.788	66.853	3.783
0.9	71.075	4.338	71.673	4.336	68.744	4.037	69.127	4.023	65.136	3.786	65.271	3.771
0.99875	63.140	3.669	63.383	3.664	63.815	3.658	63.929	3.656	63.679	3.663	63.887	3.658

and

$$\alpha\left[\frac{\partial^2 Y}{\partial \xi^2}+\phi\frac{\partial Y}{\partial \xi}\right]-2\beta\frac{\partial^2 Y}{\partial \xi\partial\eta}+\gamma\left[\frac{\partial^2 Y}{\partial \eta^2}+\Psi\frac{\partial Y}{\partial \eta}\right]=0, \quad (14)$$

where

$$\alpha=\left[\frac{\partial X}{\partial \eta}\right]^2+\left[\frac{\partial Y}{\partial \eta}\right]^2 \quad (15)$$

$$\beta=\frac{\partial X}{\partial \xi}\frac{\partial X}{\partial \eta}+\frac{\partial Y}{\partial \xi}\frac{\partial Y}{\partial \eta} \quad (16)$$

$$\gamma=\left[\frac{\partial X}{\partial \xi}\right]^2+\left[\frac{\partial Y}{\partial \xi}\right]^2 \quad (17)$$

$$\phi=-\frac{\left[\frac{\partial X}{\partial \xi}\frac{\partial^2 X}{\partial \xi^2}+\frac{\partial Y}{\partial \xi}\frac{\partial^2 Y}{\partial \xi^2}\right]}{\left[\frac{\partial X}{\partial \xi}\right]^2+\left[\frac{\partial Y}{\partial \xi}\right]^2} \quad (18)$$

$$\Psi=-\frac{\left[\frac{\partial Y}{\partial \eta}\frac{\partial^2 Y}{\partial \eta^2}+\frac{\partial X}{\partial \eta}\frac{\partial^2 X}{\partial \eta^2}\right]}{\left[\frac{\partial X}{\partial \eta}\right]^2+\left[\frac{\partial Y}{\partial \eta}\right]^2} \quad (19)$$

under the conditions of the given grid distribution on the boundaries. The resulting grid construction is shown in Fig. 3 for the case studied in this paper.

Finite Difference Solution

Equations (1) and (2) can be transformed as follows:

$$\frac{\partial}{\partial \xi}\left\{\frac{1}{J}\left[\alpha\frac{\partial u^*}{\partial \xi}-\beta\frac{\partial u^*}{\partial \eta}\right]\right\}+\frac{\partial}{\partial \eta}\left\{\frac{1}{J}\left[\gamma\frac{\partial u^*}{\partial \eta}-\beta\frac{\partial u^*}{\partial \xi}\right]\right\}+J=0 \quad (20)$$

and

$$JU\frac{\partial \theta}{\partial Z}=\frac{\partial}{\partial \xi}\left\{\frac{1}{J}\left[\alpha\frac{\partial \theta}{\partial \xi}-\beta\frac{\partial \theta}{\partial \eta}\right]\right\}+\frac{\partial}{\partial \eta}\left\{\frac{1}{J}\left[\gamma\frac{\partial \theta}{\partial \eta}-\beta\frac{\partial \theta}{\partial \xi}\right]\right\}, \quad (21)$$

where

$$J=\frac{\partial X}{\partial \xi}\frac{\partial Y}{\partial \eta}-\frac{\partial X}{\partial \eta}\frac{\partial Y}{\partial \xi}. \quad (22)$$

Invoking a control volume-based finite difference procedure, the partial differential equations are reduced to a standard system of algebraic equations. The energy equation is then solved by a marching technique. The cross-derivative terms appearing in the above equations are treated as source terms. The presence of those terms necessitates the adoption of a marching procedure in conjunction with an iterative approach for calculation of the fully developed velocity field, u^*, and the developing temperature field, θ, at each axial position, Z. The convergence criterion chosen for each dependent variable is given by the inequality,

$$\frac{\|F_{i,j}^{k+1}-F_{i,j}^{k}\|_\infty}{\|F_{i,j}^{k+1}\|_\infty}\le 10^{-4}, \quad (23)$$

where F refers to the dependent variables, u^* and θ, respectively; k stands for the kth iteration, and $\|\bullet\|_\infty$ is the infinite norm. When the convergence temperature field is satisfied, the bulk temperature and the local Nusselt number are tabulated from Eqs. (8) and (9).

To ensure the accuracy of the results presented, numerical tests were performed for the catheter to determine the effects of the grid size. The tabular results are given in Table 1. Comparison of these results indicates that for the case studied, the grid size has no effect on the results. Therefore, the results that are illustrated in the figures are based on a grid size of 31×21. The axial marching step size of $\Delta z=0.00025$ is used in all the computations.

Optimization Procedure

The biomedical engineer requires an optimized design of the lumen catheter for diagnostic use in the hospital. The lumen geometry configuration will be optimized by certain constraints of some specific features of the biomedical equipment, making different shaped lumens match each other. This paper investigates all possibilities from a scientific point of view. At this point, the optimization procedure is a problem with no constraints. During a cardiac catheterization procedure, several different catheters are used. Since the contrast medium flowing

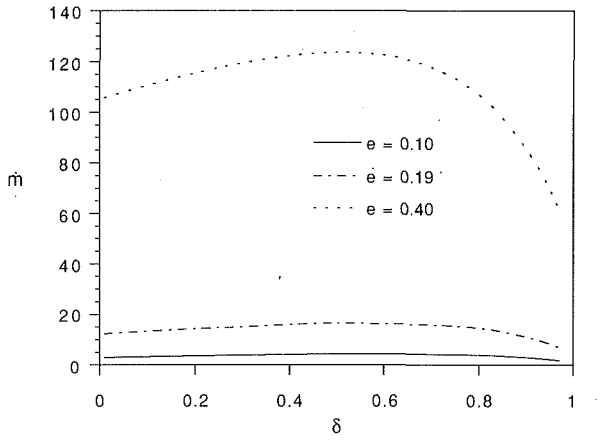

Fig. 4 Variation of the flow rate

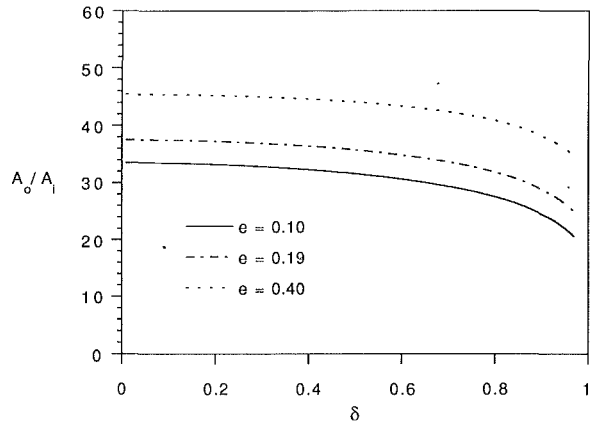

a) resonant

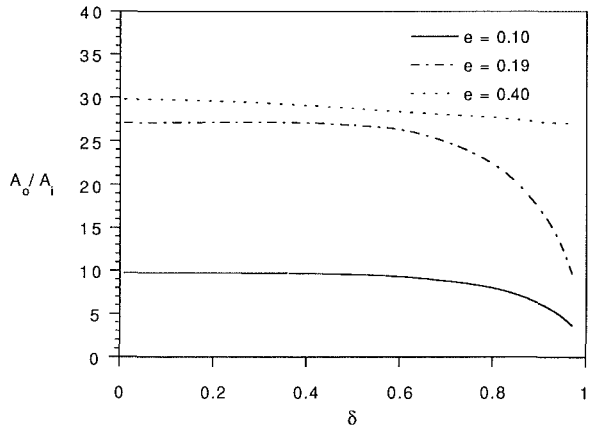

b) flat

Fig. 5 Variation of the frequency response: (*a*) resonant, (*b*) flat

within the catheter must be heated, it is important for the engineer to find heat transfer and flow parameters of the quasi-crescent lumen according to the regular geometry lumen that is matched with it.

Two geometric parameters are defined for expressing lumen geometry changes. These are

$$e=\frac{e_c-(R_o-R_i)}{2R_i} \tag{24}$$

and

$$\delta=\frac{R_r}{[R_o-(R_i-e_c)]/2} \tag{25}$$

where, in the above equations, e and δ represent the dimensionless center distance and the dimensionless round corner of the lumen, respectively. Thus, the objective function in terms of e and δ may be written as

$$\mathrm{Nu}_{z,T}=\mathrm{Nu}(e,\delta). \tag{26}$$

The function, Nu, is explored by the changes, e and δ. The $\mathrm{Nu}_{z,T}$ function curve is found and plotted and one can easily see the heat transfer characteristics from the graph.

Results

In this paper of primary importance are the results of the calculations of flow rate, frequency response, and damping coefficient of the fully developed velocity field, the bulk temperature distribution, $\theta_b(z)$, the local Nusselt number, $\mathrm{Nu}_{z,T}$, and optimization of the geometry parameters in the thermal entrance region of the crescent-shaped lumen catheter. The effects of three major parameters, namely the axial distance, Z; the dimensionless center distance of lumen, e; and the dimensionless round corner of the lumen, δ, are discussed in this section. In addition, the study of grid independence for the numerical solution has been executed by choosing different combinations of grid sizes and marching steps. This is shown in Table 1. The solution is terminated when the asymptotic solution is achieved.

The crescent lumen in the dual lumen catheter has excellent features when compared with the double circle lumen. The crescent lumen provides more diversity than the circle lumen, if the main circle lumen is fixed. When the designer wants to obtain, as accurately as possible, the frequency response of the small lumen without any change in the catheter diameter and any alteration to the main circle lumen, the main advantage is obvious. It is a well-known fact that the maximum flow area is very limited due to the small circle lumen. This is because the small circle lumen diameter is severely limited by the main circle lumen and the catheter diameter. Therefore, the flow rate and frequency response improvements are limited. However, the crescent lumen can break these limits and can provide a larger flow rate. Therefore, the following section is devoted to the enhancement of flow rate and frequency response.

Figure 4 illustrates the variation of the flow rate with respect to the dimensionless round corner of the lumen, δ, for different values of the dimensionless center distance of the lumen, e. It is observed that the flow rate is enhanced as e increases. This is due mainly to the large flow area, which causes a greater flow rate. It is also noted that the flow rate achieves an optimum value. In addition, the flow rate is not proportional to the area, because when the round corner is sharp, it will provide more resistance force. At the same time, when the round corner is less acute, the resistance force is smaller, which causes the flow rate to increase. However, at the same time, the flow rate decreases until $\delta=0.5\sim0.6$, after which the effect of the flow area is dominant. Finally, the flow rate decreases as the round corner radius enlarges.

Figure 5 illustrates that the frequency response increases as e increases and δ decreases. The flow area is dominated by the effect of the frequency response because more fluid is in the catheter, thus causing the elastance to be higher.

Figure 6 shows the variation of the damping coefficient with respect to the dimensionless round corner of the lumen. Inspection of this figure reveals that the damping coefficient of the crescent lumen decreases as parameter e increases. It also illustrates that when the crescent lumen flow area is wider the damping coefficient is lower. Also, one can find that the damping coefficient will not vary when δ is less than 0.8, and changes

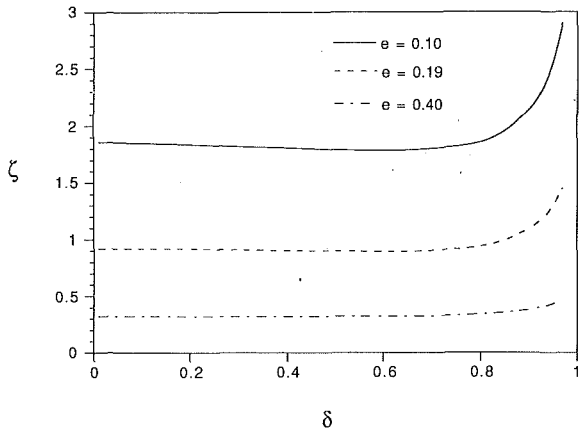

Fig. 6 Variation of the damping coefficient

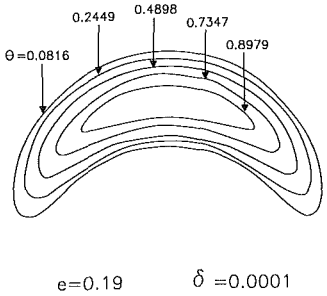

Fig. 7 Isotherms for $\delta = 0.0001$ and $e = 0.19$

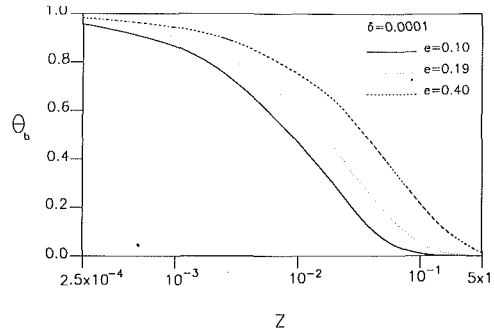

Fig. 8 Effect of e on the bulk temperature

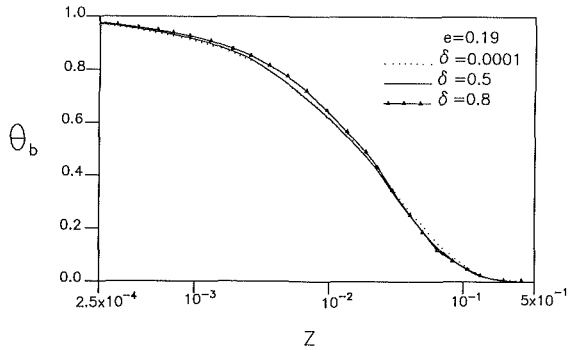

Fig. 9 Effect of δ on the bulk temperature

sharply as δ rises higher than 0.8. When the δ value is small, the lumen round corner is sharp, meaning more resistance, but also has more fluid and will produce more elastance to compensate. Effects of resistance and elastance decline when δ is smaller than 0.8. When δ is greater than 0.8, resistance dominates the effect because the flow area is too small to provide enough to compensate with elastance.

Figure 7 represents the isotherms for a dimensionless center distance of $e = 0.19$ and a round corner of $\delta = 0.0001$. Inspection of this figure indicates that the temperature reaches a maximum value at the center of the medium and gradually decreases and reaches a minimum value, 0, at the inner section of the catheter. This corresponds with the boundary conditions specified by Eqs. (4) and (5).

Figures 8 and 9 represent variations of the bulk temperature for different δ and e parameters. Specifically, Fig. 8 represents the bulk temperature distribution versus the dimensionless axial coordinate of the catheter for $\delta = 0.0001$, with $e = 0.10$, 0.19, and 0.40. Inspection of these curves reveals that the bulk temperature is not strongly invariant with e at the entrance region of the catheter. However, as the medium passes through the catheter, the bulk temperature is dependent on the value of e. This should be obvious since more surface area is now available.

Figure 9 represents variations of the bulk temperature with the dimensionless axial coordinate for $e = 0.19$, with $\delta = 0.0001$, 0.5, and 0.8. Inspection of the curves in this figure indicates that the bulk temperature is dependent on the variations of the dimensionless round corners of the catheter. Comparison of Figs. 8 and 9 clearly reveals that the bulk temperature can be increased only by increasing the dimensionless center distance of the lumen, and is independent of the variations of the dimensionless round corners of the catheter.

Figures 10 and 11 represent variations of the local Nusselt number for different e and δ parameters. Specifically, Fig. 10 represents variations of the local Nusselt number against the

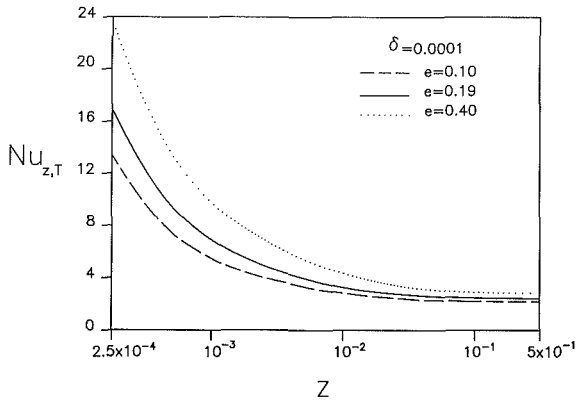

Fig. 10 Effect of e on the local Nusselt number

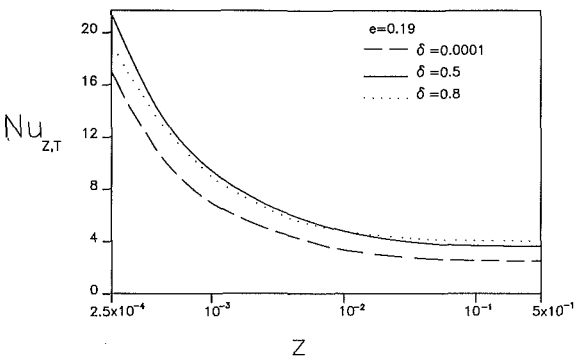

Fig. 11 Effect of δ on the local Nusselt number

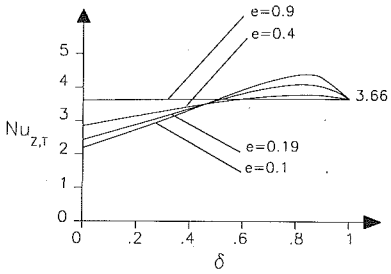

Fig. 12 Optimization of the lumen catheter

dimensionless axial coordinate for $\delta = 0.0001$, with various values of $e = 0.1$, 0.19, 0.4. Inspection of the curves in this figure clearly illustrates that the local Nusselt number increases dramatically at the entrance region of the catheter as the center distance of the lumen increases. This behavior is entirely different from that observed in Figs. 8 and 9. This is due mainly to the definition of the diameter. However, this variation decreases gradually until it reaches the asymptotic value of 3.66 at the end of the catheter.

Figure 11 illustrates variations of the local Nusselt number with the dimensionless axial coordinate for $e = 0.19$, with $\delta = 0.0001$, 0.5, and 0.8. The explanation for Fig. 10 is also valid here. However, comparison of Fig. 10 with Fig. 11 reveals that the Nusselt number is strongly influenced by e, not δ. This conclusion is consistent with the one already mentioned in Figs. 8 and 9.

Finally, Fig. 12 represents variations of the fully developed Nusselt number with the dimensionless round corners of the lumen for the various dimensionless center distances of the lumen of $e = 0.1$, 0.19, 0.4, and 0.9. It is apparent from this figure that the same $Nu_{z,T}$ is achieved at $\delta = 0.46$ for $e = 0.1$, 0.19, and 0.4.

Concluding Remarks

Fluid flow, frequency response, in the fully develop region and convective heat transfer in the entrance region of the crescent-shaped lumen catheter is numerically analyzed for various parameters of dimensionless center distances and round corners of the lumen. The boundary fitted coordinate system is used to solve the difficulty induced by the computational domain. To prove the accuracy of the proposed methodology, an independent grid size test has been performed and the values are tabulated in Table 1. Thermally developing heat transfer with a fully developed velocity field, frequency response, and damping coefficient is obtained and presented in this paper. The results indicate that an optimum value of $\delta \cong 0.9$ exists, which gives a maximum local Nusselt number for a given value of e. The isotherms, bulk temperature, and the local Nusselt number variations with the axial distance are graphically illustrated. As expected, a large Nusselt number in the entrance region of the catheter is obtained, approaching asymptotically the fully developed value at a greater axial distance.

Acknowledgment

The results presented in this paper were obtained in the course of research sponsored by the Florida High Technology and Industry Council.

References

Brathwaite, M. A., and Bradley, R. D., 1968, "Measurement of Cardiac Output by Thermal Dilution in Man," *Journal of Applied Physiology*, Vol. 24, pp. 434–438.

Doebelin, E. O., 1990, *Measurement Systems, Application and Design*, McGraw-Hill, New York.

Eckert, E. R. G., Goldstein, R. G., Pfender, E., Ibele, W. E., Patankar, S. W., Ramsey, S. W., Simon, T. W., Decker, N. A., Kuehn, T. H., Lee, H. O., and Girshick, S. L., 1989, "Heat Transfer—A Review of the 1988 Literature," *Int. J. Heat and Mass Transfer*, Vol. 32, pp. 2211–2280.

Eckert, E. R. G., Irvine, Jr., T. F., Goldstein, R. J., and Hartnett, J. P., 1990, *Heat Transfer—A Review of 1976–1986—A Wiley Interscience Publication*, John Wiley and Sons, Inc., New York.

Intaglietta, M., 1987, "Blood Pressure and Flow Measurements," *Handbook of Bioengineering*, Chapter 33, pp. 33.1–33.15.

Kakac, S., Shah, R. K., and Aung, W., 1987, *Handbook of Single-Phase Convection Heat Transfer*, John Wiley and Sons, New York.

Martynenko, O. G., 1988, "Heat Mass Transfer Bibliography—Soviet Literature," *Int. J. Heat and Mass Transfer*, Vol. 31, pp. 2489–2503.

Pepine, C. J., Hill, J. A., and Lambert, C. R., 1989, *Diagnostic and Therapeutic Cardiac Catheterization*, Williams and Wilkins, Baltimore.

Shah, R. K., and London, S. L., 1978, "Laminar Forced Convection in Ducts," Supplement I to *Advances in Heat Transfer*, Academic Press, New York.

Thomas, P., and Middlecoff, J., 1982, "Direct Control of Grid Point Distribution in Meshes Generated by Elliptic Equations," *AIAA J.*, Vol. 10, pp. 305–306.

Thompson, J. F., Thames, F. C., and Mastin, C. W., 1977, "TOMCAT—A Code to a Numerical Generation of Boundary-Fitted Curvilinear Coordinate System of Fields Containing any Number of Arbitrary Two-Dimensional Bodies," *J. Computational Physics*, Vol. 24, pp. 274–302.

Thompson, J. F., Thames, F. C., and Mastin, C. W., 1974, "Automatic Numerical Generation of Body-Fitted Curvilinear Coordinate System for Field Containing Any Number of Arbitrary Two-Dimensional Bodies," *Journal of Computational Physics*, Vol. 15, pp. 299–319.

Thompson, J. F., Warsi, U. A., and Mastin, C. W., 1982, "Boundary-Fitted Coordinate Systems for Numerical Solution of Partial Differential Equations—A Review," *Journal of Computational Physics*, Vol. 47, pp. 1–108.

Weisel, R. D., Berger, R. L., and Hechtman, H. B., 1975, "Measurement of Cardiac Output by Thermodilution," *New England Journal of Medicine*, Vol. 292, pp. 682–684.

S. H. Crandall
Department of Mechanical Engineering,
Massachusetts Institute of Technology,
Cambridge, MA 02139
Fellow ASME

A. El-Shafei
Assistant Professor,
Department of Mechanical Design and Production,
Cairo University, Giza, Egypt
Assoc. Mem. ASME

Momentum and Energy Approximations for Elementary Squeeze-Film Damper Flows

To provide understanding of the effects of inertia on squeeze-film damper performance, two elementary flow patterns are studied. These elementary flows each depend on a single generalized motion coordinate whereas general planar motions of a damper are described by two independent generalized coordinates. Momentum and energy approximations for the elementary flows are compared with exact solutions. It is shown that the energy approximation, not previously applied to squeeze films, is superior to the momentum approximation in that at low Reynolds number the energy approximations agree with the exact solutions to first order in the Reynolds number whereas there are 20 percent errors in the first-order terms of the momentum approximations.

Introduction

Exact solutions for the response of squeeze-film dampers including the effects of fluid inertia do not appear to be obtainable. A number of approximate solutions for the effects of fluid inertia in hydrodynamic bearings have been proposed. Smith (1964-1965) obtained approximate inertia force coefficients for journal bearings and concluded that the principal effect of fluid inertia was to introduce a virtual added mass to the rotor. Subsequent studies of inertia effects have generally employed methods which can be divided into three categories. The first category, in which a perturbation series in Reynolds number is used, is represented by the papers of Tichy and Winer (1970), Jones and Wilson (1975), and Reinhardt and Lund (1975). The second category, in which the inertia forces are averaged across the film, is represented by the papers of Constantinescu (1970), Szeri et al. (1983), and San Andrés and Vance (1986). A third category represented by Tichy and Modest (1978) is based on a stream function approach using a linearized momentum equation. Recently Ramli et al. (1987) compared the results of Smith (1964-1965), Reinhardt and Lund (1975) and Szeri et al. (1983) and concluded that they were in good agreement, especially for short bearings.

In an attempt to clarify the mechanics of squeeze-film dampers we identify two elementary flow patterns which are combined in a complete damper. We study these mechanisms separately and take advantage of exact solutions to compare energy and momentum approximations for the inertia forces developed. Both approximations rely on the fact, developed in the previous literature, that the introduction of fluid inertia in a thin film does not appreciably alter the velocity profile within the film in the low Reynolds number range of typical squeeze-film dampers. The fundamental approximation is that the velocity field with fluid inertia remains exactly the same as in the inertialess case. The pressure field and the force response do, however, change when fluid inertia is introduced. In the *momentum approximation*, the inertialess velocity profiles are introduced into the Navier-Stokes momentum equation and the equation integrated across the film to provide a differential equation for the pressure. Integration yields the pressure field and the force response. The *energy approximation* can generally be carried out by two procedures which lead to equivalent results. In the first procedure the Navier-Stokes momentum equation is premultiplied by the flow velocity (making each term represent power per unit volume). The inertialess profiles are then introduced and each term integrated across the film to provide a differential equation for the pressure. Integration yields the pressure field and the force response in a procedure similar to that followed in the momentum approximation. In the second procedure the inertialess velocity profile is used to construct the fluid kinetic energy and dissipation function and then Lagrange's equation is used to obtain the force response. In systems with a single generalized coordinate, simple energy balance may also be used to obtain the force response. Both the momentum and the energy approximations fall in the second category of methods mentioned above. Most workers have adopted procedures essentially equivalent to the momentum approximation. The energy approximation was introduced by El-Shafei (1988). For the elementary flow patterns studied here the energy approximation gives more accurate results.

Contributed by the Applied Mechanics Division of THE AMERICAN SOCIETY OF MECHANICAL ENGINEERS for publication in the ASME JOURNAL OF APPLIED MECHANICS.

Discussion on this paper should be addressed to the Technical Editor, Professor Lewis T. Wheeler, Department of Mechanical Engineering, University of Houston, Houston, TX 77204-4792, and will be accepted until four months after final publication of the paper itself in the ASME JOURNAL OF APPLIED MECHANICS.

Manuscript received by the ASME Applied Mechanics Division, Aug. 20, 1990; final revision, June 3, 1992. Associate Technical Editor: S. A. Berger.

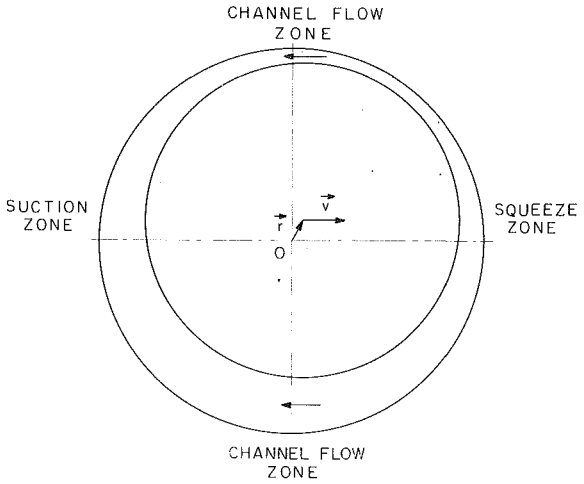

Fig. 1 Inner cylinder of squeeze-film damper has displacement r and velocity v with respect to outer cylinder

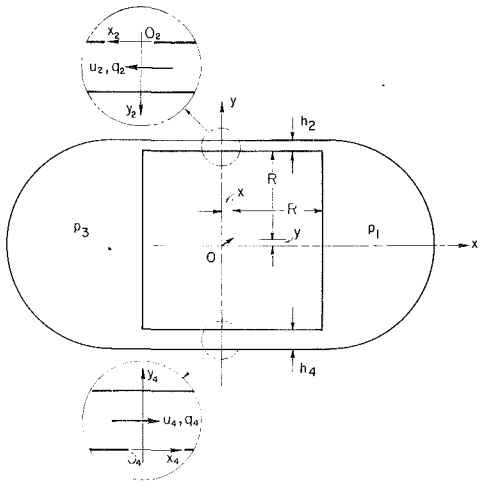

Fig. 2 Block has velocity $\dot{x}$ and acceleration $\ddot{x}$ with fixed y. Pressure difference $p_1 - p_3$ causes return flow through channels of width h_2 and h_4.

Two Elementary Flow Patterns

Consider the squeeze film damper sketched in Fig. 1. The outer cylinder is fixed. The inner cylinder, which contains a rolling element bearing and shaft, is free to move in the clearance space. The annular space between cylinders is filled with liquid. The fluid film is taken to have a depth b normal to the sketch and the fluid flow is assumed to remain parallel to the plane of the sketch in accord with the long-bearing approximation of lubrication theory. At the instant shown the inner cylinder has arbitrary displacement **r** and arbitrary velocity **v**. The region of the fluid film toward which the velocity is directed is identified as the squeeze zone. Directly opposite is the suction zone. Halfway between, where the film thickness is temporarily stationary, are the channel flow zones. At intermediate locations the film undergoes a combination of the squeeze-suction flow pattern and the channel flow pattern.

To see the channel flow pattern in its pure form consider the square block of side $2R$ moving with velocity $\dot{x}$ in the chamber of width $2(R+c)$ shown in Fig. 2. The clearance c is taken to be small compared to R ($c/R = O$ (0.001) is typical for a squeeze-film damper). The pressures in the enlarged squeeze and suction zones are taken to be constants with the only pressure gradients occurring in the thin films of thickness $h_2 = c - y$ and $h_4 = c + y$. We shall study the force response (i.e., the force required to move the block with specified velocity $\dot{x}$ and acceleration $\ddot{x}$) for the system of Fig. 2 and compare the results of momentum and energy approximations with the exact solution.

To see the squeeze-suction flow pattern in its pure form consider the square block of side $2R$ moving with velocity $\dot{x}$ in the chamber of length $2(R+c)$ shown in Fig. 3. Here the pressures in the enlarged flow zones are taken to be constants with the only pressure gradients occurring in the thin films of thickness $h_1 = c - x$ in the squeeze zone and $h_3 = c + x$ in the suction zone. Despite the simplicity of this flow pattern, an exact solution accounting for the inertia in the fluid film is apparently unknown if there is no limitation on the displacement beyond $|x| < c$. Here we obtain an exact solution for the linearized limit of small displacement $|x/c| \to 0$ and use it as a basis for comparing the results of momentum and energy approximations.

It should be emphasized that the models shown in Figs. 2 and 3 are introduced to clarify the mechanics of squeeze-film damper flows and not for any resemblance to practical devices. We believe that the energy approximation developed by El-Shafei (1988) and applied here has not been previously applied to squeeze-film flows. In particular, the extension of La-

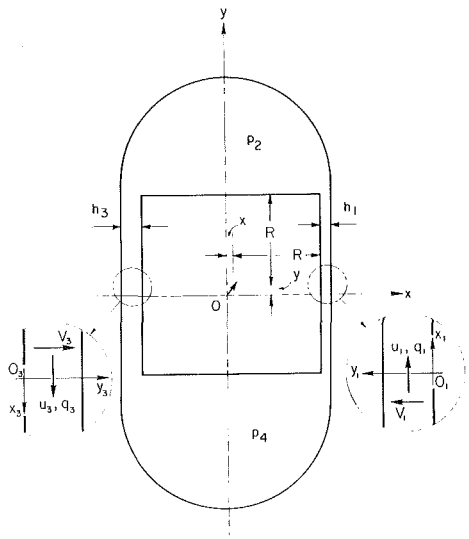

Fig. 3 Block has velocity $\dot{x}$ and acceleration $\ddot{x}$ with fixed y. Fluid expelled from squeeze zone enters enlarged channel flow zones while fluid from enlarged flow zones is drawn into suction zones.

grange's equation to control volumes by means of Reynolds's transport theorem, as indicated by Eqs. (42) and (43) and Appendix B, is believed to be new. This approach has been applied to realistic squeeze-film damper models by El-Shafei and Crandall (1991).

Elementary Channel Flow Pattern

We focus our attention first on Fig. 2. The classical inertialess flow is described and used as input to the momentum and energy approximations for the case where fluid inertia is included. The exact solution including inertia is then obtained and the approximations are compared against it. In classical lubrication theory a number of assumptions are made. The fluid film is taken to be incompressible with homogeneous viscosity μ. Because the film thickness is so small and the pressure gradient across the film is $O(c^2/R^2)$ (El-Schafei, 1991), the pressure is assumed not to vary across the thickness. As a consequence all velocity profiles in a uniform channel are linear combinations of a linear profile (Couette flow) and a parabolic profile (Poiseuille flow). In squeeze-film dampers the velocities in the Couette component are of order c/R smaller than the

velocities in the Poiseuille component and hence may be neglected. Another consequence of the thinness of the films is that the resultant of the wall shear stresses acting on the moving element are of order c/R smaller than the resultant of the wall pressures and hence can be neglected in calculating the force response. We assume that cavitation does not occur anywhere within the fluid.

In Fig. 2 when the square block moves to the right, continuity requires flow to the left through the channels of width h_2 and h_4. To describe the flows we use local x_i, y_i directed to the left (in the positive x_i-direction). The classical Poiseuille flow in the top channel has

$$u_2=\frac{h_2^2}{2\mu}\frac{p_2-p_3}{2R}\left(\frac{y_2}{h_2}-\frac{y_2^2}{h_2^2}\right) \tag{1}$$

with v_2 identically zero. The volume rate of flow through the channel of depth b is

$$q_2=\int_0^{h_2}u_2 b dy_2=\frac{bh_2^3}{24\mu R}(p_1-p_3). \tag{2}$$

A parallel calculation for the bottom channel gives a similar for q_4. Global continuity requires

$$2Rb\dot{x}=q_2-q_4 \tag{3}$$

which permits evaluation of the pressure difference p_1-p_3 and the force F required to move the block at velocity $\dot{x}$

$$F=(p_1-p_3)\ 2Rb=\frac{96\mu R^3 b}{h_2^3+h_4^3}\dot{x}. \tag{4}$$

In the case where the block is centered so that $y=0$ and $h_2=h_4=c$ the fluid velocity (1) reduces to

$$u_2=\frac{6q_2}{bc}\left(\frac{y_2}{c}-\frac{y_2^2}{c^2}\right)=6\frac{R}{c}\left(\frac{y_2}{c}-\frac{y_2^2}{c^2}\right)\dot{x} \tag{5}$$

and the force response (4) becomes

$$F=48\mu\frac{R^3}{c^3}b\dot{x}. \tag{6}$$

We next consider approximate solutions taking account of fluid inertia when the block has acceleration $\ddot{x}$ as well as velocity $\dot{x}$. For simplicity of exposition we consider only the centered case, $y=0$. The case $y\neq 0$ is treated in Appendix A.

Approximate Inertial Solutions for the Channel Flow Pattern

In the *momentum approximation* we begin with the assumption that the velocity profiles with inertia are the same as those for the inertialess case. Thus in the upper channel of Fig. 2 we insert the velocity (5) in the Navier-Stokes equation applicable when $v_2=0$.

$$-\frac{\partial p_2}{\partial x_2}=\rho\left(\frac{\partial u_2}{\partial t}+u_2\frac{\partial u_2}{\partial x_2}\right)-\mu\frac{\partial^2 u_2}{\partial y_2^2} \tag{7}$$

and integrate with respect y_2 across the channel of width c. Under the assumption that the pressure gradient is independent of y_2 we obtain, after division by c,

$$-\frac{dp_2}{dx_2}=12\mu\frac{R}{c^3}\dot{x}+\rho\frac{R}{c}\ddot{x}. \tag{8}$$

A similar result applies to the lower channel by symmetry. Integration of (8) along the channel of length $2R$ provides the pressure difference p_1-p_3 and the force F required to develop the velocity $\dot{x}$ and the acceleration $\ddot{x}$,

$$F=(p_1-p_3)2Rb=48\mu\frac{R^3}{c^3}b\left(\dot{x}+\frac{\rho c^2}{12\mu}\ddot{x}\right). \tag{9}$$

This is the force response according to the momentum approximation.

In this case there are three ways to obtain the *energy approximation*. The first procedure is parallel to the momentum approximation. We begin with the same velocity profile (5) but we first multiply each term of the Navier Stokes Eq. (7) by $u_2(y_2)$. Then after integration across the channel width and division by the common factor $R\dot{x}$ we obtain the pressure gradient

$$-\frac{dp_2}{dx_2}=12\mu\frac{R}{c^3}\dot{x}+\frac{12}{10}\rho\frac{R}{c}\ddot{x}. \tag{10}$$

Integration along the channel then leads to the force response

$$F=48\ \mu\frac{R^3}{c^3}b\left(\dot{x}+\frac{\rho c^2}{10\mu}\ddot{x}\right) \tag{11}$$

according to the energy approximation.

The second procedure makes use of Lagrange's equation. The kinetic energy in the two channels is

$$T=2b\int_0^{2R}dx\int_0^c\frac{1}{2}\rho u_2^2 dy_2$$
$$=\frac{1}{2}\frac{48}{10}\rho\frac{R^3 r}{c}\dot{x}^2 \tag{12}$$

if the inertialess velocity profile (5) is inserted for u_2. The Rayleigh dissipation function is one-half the rate of dissipation of energy due to viscosity. For the two channels it is

$$D=2b\int_0^{2R}dx\int_0^c\frac{1}{2}\mu\left(\frac{\partial u_2}{\partial y_2}\right)^2 dy_2$$
$$=\frac{1}{2}48\mu\frac{R^3 b}{c^3}\dot{x}^2 \tag{13}$$

if (5) is inserted for u_2. Since the fluid is incompressible there is no potential energy. We now apply Lagrange's equation for the complete system of Fig. 2, neglecting the mass of the block while assuming that an external force F in the positive x-direction acts on the block. Furthermore, since most of the fluid in the enlarged squeeze and suction zones is stagnant, we neglect the small contributions to the kinetic energy and dissipation function located in the vicinity of the entrances and exists of the narrow channels. With these assumptions Lagrange's equation reduces to

$$F=\frac{\partial D}{\partial\dot{x}}+\frac{d}{dt}\left(\frac{\partial T}{\partial\dot{x}}\right)-\frac{\partial T}{\partial x}. \tag{14}$$

When (12) and (13) are inserted in (14) the force response (11) is obtained directly.

The third energy method makes use of simple energy balance. During time interval dt the work done by the external force F is partly dissipated by viscosity and partly stored as an increase in kinetic energy; i.e., on dividing by dt we have

$$F\dot{x}=2D+\frac{dT}{dt}. \tag{15}$$

When (12) and (13) are inserted in (15) and the result divided through by $\dot{x}$, the force response (11) is once more obtained.

There is a subtle point concealed in the preceding two energy methods which make use of the kinetic energy (12) in the two channels. The fluid in the channels does not remain a mass system of fixed identity. The identity of mass in a channel is continually changing as new mass enters one end and old mass departs at the other end. In the configuration of Fig. 2, however, the velocity profile of the fluid entering a channel is identical with that of the departing fluid so that the derivatives of the energy for the mass in a channel are also the same as those for a slug of fluid of fixed identity which is just passing through. This situation does not occur in the configuration of Fig. 3 and special steps must be taken to redress the difference between the derivative of the energy for a system of fixed identity and that for the energy within a control volume.

For a steady-state oscillation of the block in Fig. 2 with $x = x_0 \sin \omega t$ the forces response (9) provided by the momentum approximation is

$$F = 48\mu b x_0 \omega \frac{R^3}{c^3}\left(\cos\omega t - \frac{\mathrm{Re}}{12}\sin\omega t\right) \tag{16}$$

where Re stands for the squeeze Reynolds number

$$\mathrm{Re} = \frac{\rho c^2 \omega}{\mu}. \tag{17}$$

The corresponding response (11) provided by the energy approximation is

$$F = 48\mu b x_0 \omega \frac{R^3}{c^3}\left(\cos\omega t - \frac{\mathrm{Re}}{10}\sin\omega t\right). \tag{18}$$

Both (16) and (18) approach the inertialess response provide by (6) as the Reynolds number approaches zero. The coefficients of the inertia terms in (16) and (18) differ by about 20 percent.

Exact Solution for the Channel Flow Pattern

We now obtain an exact solution to compare with the approximations (16) and (18). By "exact" we mean that it is the correct leading term in an expansion in powers of the clearance ratio c/R. It is, however, valid for arbitrary Reynolds number as long as the flow remains laminar, and valid for arbitrary amplitude of motion within the limits imposed by the geometric requirement of uniform channel thickness.

An exact solution for the pressure and velocities in the i-th film must satisfy the continuity equation

$$\frac{\partial u_i}{\partial x_i} + \frac{\partial v_i}{\partial y_i} = 0, \tag{19}$$

the thin film momentum equations

$$-\frac{\partial p_i}{\partial x_i} = \rho\left(\frac{\partial u_i}{\partial t} + u_i\frac{\partial u_i}{\partial x_i} + v_i\frac{\partial u_i}{\partial y_i}\right) - \mu\nabla^2 u_i \tag{20}$$

$$-\frac{\partial p_i}{\partial y_i} = 0, \tag{21}$$

and the appropriate boundary conditions. In the upper channel of Fig. 2 with $h_2 = c$, the assumption that v_2 vanishes identically requires that $\partial u_2/\partial x_2$ also vanishes if (19) is to be satisfied. This leaves only the following linear version of (20)

$$-\frac{\partial p_2}{\partial x_2} = \rho\frac{\partial u_2}{\partial t} - \mu\frac{\partial^2 u_2}{\partial y_2^2} \tag{22}$$

and the boundary conditions $u_2 = 0$ at $y_2 = 0$ and $y_2 = c$ to be satisfied. For steady-state oscillation at frequency ω, $x(t)$, $u_2(y_2, t)$, $p_2(x_2, t)$, and $F(t)$ are taken as the real part of $-ix_0e^{i\omega t}$, $U_2(y_2)e^{i\omega t}$, $P_2(x_2)e^{i\omega t}$ and $F_0e^{i\omega t}$, respectively. Straightforward solution leads to

$$U_2(y_2) = -\frac{1}{\mu s^2}\frac{dP_2}{dx_2}\left[1 - \phi(y_2, c)\right] \tag{23}$$

with

$$\phi(y_2, c) = \frac{\sinh sy_2 + \sinh s(c - y_2)}{\sinh sc} \tag{24}$$

where s is the complex root in the first quadrant given by

$$s^2c^2 = i\frac{\rho c^2\omega}{\mu} = i\mathrm{Re}. \tag{25}$$

The solution for $U_4(y_4)$ is of the same form as (23) when the block is centered so that application of the continuity requirement (3) yields the pressure gradient and the amplitude of the force response

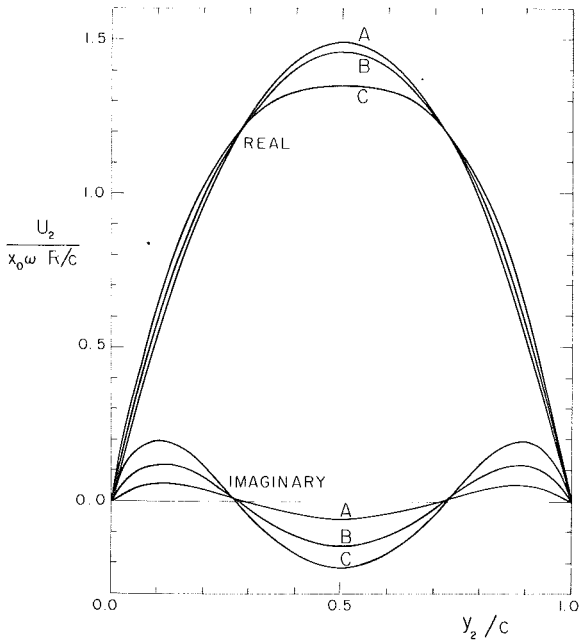

Fig. 4 Real and imaginary parts of complex amplitude $U_2(y_2)$ of velocity profile for Re = 10 (A), Re = 25 (B), and Re = 50 (C)

$$F_0 = -4R^2b\frac{dP_2}{dx_2} = 4\mu b x_0\omega\frac{R^3}{c^3}\frac{s^2c^2}{1 - \psi(c)} \tag{26}$$

with

$$\psi(c) = \frac{2(\cosh sc - 1)}{sc\sinh sc}. \tag{27}$$

Note that in the exact solution the pressure gradient is independent of x_2 which implies that the velocity profile (23) is uniform along the length of the film. The shape of the velocity profile does, however, vary with the Reynolds number Re. For small Re($0 < \mathrm{Re} < 10$), the velocity (23) does not deviate appreciably from the parabolic profile (5). In Fig. 4 the real and imaginary parts of the complex velocity amplitude (23) are displayed for Re = 10, Re = 25, and Re = 50. At Re = 10 the deviation of the real part from the parabola (5) is not visible with the line width employed in drawing Fig. 4. What is apparent is the emergence of a small imaginary part which has little effect on the velocity amplitude but does indicate a departure from uniform phase. At Re = 25 and Re = 50 the deviations from a parabolic uniform phase profile become increasingly evident.

The complex force response (26) also depends on the Reynolds number. The low Re approximation to (26) obtained by expanding numerator and denominator of (27) in powers of sc and retaining terms up to the sixth power is

$$F_0 = 48\mu b x_0\omega\frac{R^3}{c^3}\left(1 + \frac{i\mathrm{Re}}{10}\right). \tag{28}$$

Note that the real part of $F_0e^{i\omega t}$ using (28) is the same as the inertialess solution (6) and that the imaginary part is the same as the energy approximation (18). We call the real and imaginary parts of (26) the amplitudes of the viscous and inertial responses, respectively. The viscous force has the same phase as the velocity phasor $x_0\omega e^{i\omega t}$ while the inertial force has the same phase as the acceleration phasor $ix_0\omega^2e^{i\omega t}$. The exact amplitudes obtained from (26) are plotted as functions of the Reynolds number in Fig. 5 along with the corresponding amplitudes given by the momentum approximation (16) and the energy approximation (18). We note that for small Reynolds number, the response is primarily viscous, while for large Reyn-

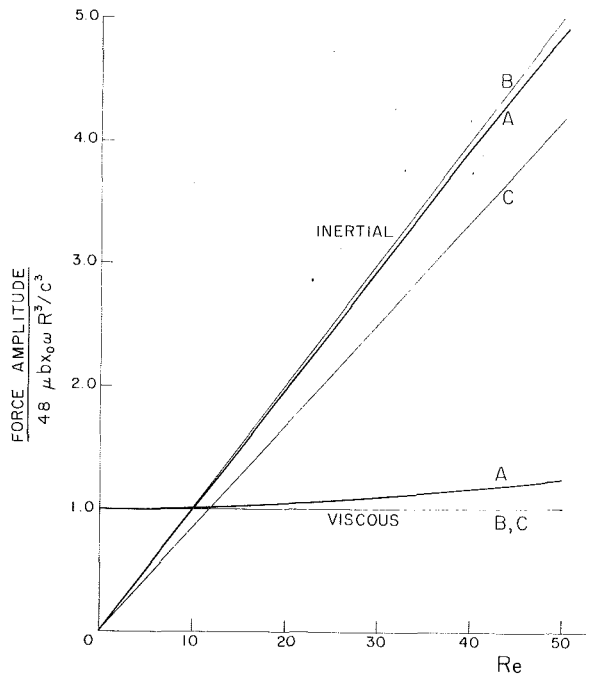

Fig. 5 Viscous and inertial force response to oscillation with displacement amplitude x_0 and frequency ω by exact solution (A), by energy approximation (B), and by momentum approximation (C)

olds number, the response is primarily inertial—the crossover occurring at Re ≈ 10. The energy approximation for the inertial response is quite accurate in the range < Re < 50. Both approximations underestimate the viscous response while the inertial response is overestimated by the energy approximation and underestimated by the momentum approximation.

The inertial response of the energy approximation (18), $F_{in} = -48\mu b x_0 \omega$ (Re/10) $\sin\omega t$, can be decomposed into the product

$$F_{in} = \frac{12}{10}\frac{R}{c} ma \tag{29}$$

where $m = 4R^2 b\rho$ is the mass of the fluid displaced by the block and $a = -x_0\omega^2 \sin\omega t$ is the acceleration of the block. The effective virtual mass of the fluid in the two narrow channels in Fig. 2 is thus $1.2mR/c$, which is about three orders of magnitude greater than the mass of the fluid displaced by the block or about two orders of magnitude greater than the mass of the block itself if the fluid is lube oil and the block is metal. Note that as the clearance c is diminished we have the paradoxical situation that the virtual mass increases as the actual mass of the fluid in the channels decreases.

Elementary Squeeze-Suction Pattern

We turn to the configuration of Fig. 3 where the film on the right is being squeezed while the film on the left undergoes suction. The inertialess flow is described and used as input to the momentum and energy approximations for the flow with inertia. The results here are nonlinear in the displacement x due to the varying film thickness ($h_1 = c - x$ and $h_3 = c + x$) and nonlinear in the velocity $\dot{x}$ due to the convective terms in the fluid acceleration. An exact solution for these nonlinear effects is unknown. We obtain an exact solution for a linearized small amplitude oscillation and find as in the channel flow case that the energy approximation is superior to the momentum approximation.

In the squeeze film at the right in Fig. 3 there is small transverse velocity $v_1(y_1, t)$ of order $\dot{x}$ and large longitudinal velocity $u_1(x_1, y_1, t)$ of order $\dot{x}R/c$. With large constant pressure reservoirs at top and bottom the film flows are independent of the fixed value of y. The longitudinal flow pattern is symmetric about the block center with the flow upward in the upper half and downward in the lower half. The symmetry of the squeeze and suction flows implies that $p_2 = p_4$. Global continuity applied to those films shows that the flow rates away from the block center in the squeeze film, and towards the block center in the suction film, must increase linearly with the distance x_i from the block center. The profile of the longitudinal velocity in the squeeze film of thickness h_1 in the inertialess case has the parabolic form (5) but must have linearly increasing flow rate $q_1(x_1)$ in order to satisfy the global continuity requirement

$$q_1(x_1) = x_1 b\dot{x}. \tag{30}$$

The resulting velocity field

$$u_1 = \frac{6q_1}{bh_1}\left(\frac{y_1}{h_1} - \frac{y_1^2}{h_1^2}\right) = 6\dot{x}\,\frac{x_1}{h_1}\left(\frac{y_1}{h_1} - \frac{y_1^2}{h_1^2}\right) \tag{31}$$

varies linearly with x_1 and parabolically with y_1 and also depends linearly on the block velocity $\dot{x}$ and nonlinearly on the block displacement $x = c - h_1$. The transverse velocity which satisfies the local continuity requirement (19) and the boundary conditions $v_1(0) = 0$ and $v_1(h_1) = -\dot{x}$ is

$$v_1(y_1) = -6\dot{x}\left(\frac{y_1^2}{2h_1^2} - \frac{y_1^3}{3h_1^3}\right). \tag{32}$$

The film pressure p_1 which satisfies the inertialess versions of the momentum Eqs. (20) and (21) along with (31) and (32) is

$$p_1(x_1) = 6\mu\,\frac{\dot{x}}{h_1}\left(\frac{R^2 - x_1^2}{h_1^2}\right) + p_2. \tag{33}$$

A parallel analysis applies to the suction film at the left of Fig. 3 so that the force F required to impart the velocity $\dot{x}$ to the block is

$$F = b\int_{-R}^{R} [p_1(x_1, h_1)dx_1 - p_3(x_3, h_3)dx_3]$$

$$= 8\mu b R^3\left(\frac{1}{h_1^3} + \frac{1}{h_3^3}\right)\dot{x}. \tag{34}$$

Note that when $h_1 = h_3 = c$ the force required in the inertialess squeeze-suction case here is one-third the corresponding channel flow force (6) for the same block velocity $\dot{x}$. The force here is linear in the block velocity $\dot{x}$ but nonlinear in the block displacement x.

Approximate Inertial Solutions for the Squeeze-Suction Pattern

In the *momentum approximation* for the squeeze film at the right of Fig. 3 we begin with the longitudinal momentum Eq. (20) and insert the inertialess velocity profiles (31) and (32). Assuming that the pressure gradient is independent of y_1 we integrate with respect to y_1 across the channel of width h_1 and divide through by h_1 to obtain

$$-\frac{\partial p_1}{\partial x_1} = x_1\left(12\,\frac{\mu}{h_1^3}\,\dot{x} + \frac{\rho}{h_1}\,\ddot{x} + \frac{12}{5}\,\frac{\dot{x}^2}{h_1^2}\right). \tag{35}$$

Taking $p_1(R, h_1) = p_2$ and $p_1(-R, h_1) = p_4 = p_2$ we integrate (35) to get

$$p_1 - p_2 = \frac{R^2 - x_1^2}{2}\left(12\,\frac{\mu}{h_1^3}\,\dot{x} + \frac{\rho}{h_1}\,\ddot{x} + \frac{12}{5}\,\frac{\dot{x}^2}{h_1^2}\right). \tag{36}$$

After a parallel analysis for $p_3 - p_2$, the force F required to move the block with velocity $\dot{x}$ and acceleration $\ddot{x}$ according to the momentum approximation is

$$F = b\int_{-R}^{R} (p_1 dx_1 - p_3 dx_3)$$

$$= 8bR^3\left[\mu\left(\frac{1}{h_1^3}+\frac{1}{h_3^3}\right)\dot{x}\right.$$

$$\left.+\frac{\rho}{12}\left(\frac{1}{h_1}+\frac{1}{h_3}\right)\ddot{x}+\frac{\rho}{5}\left(\frac{1}{h_1^2}-\frac{1}{h_3^2}\right)\dot{x}^2\right]. \quad (37)$$

The first two terms are linear in the block velocity and acceleration while the final term arising from the two convective terms in (20) is quadratic in the velocity. When $\rho = 0$, (37) reduces to the inertialess result (34).

There are again three ways to obtain the *energy approximation*. In the first procedure the longitudinal momentum Eq. (20) for the squeeze film at the right of Fig. 3 is premultiplied by u_1, the velocity profiles (31) and (32) are inserted, each term is integrated with respect to y_1 across the channel, and divided by $\dot{x}x_1$ to obtain

$$-\frac{\partial p_1}{\partial x} = x_1\left(12\frac{\mu}{h_1^3}\dot{x}+\frac{6}{5}\frac{\rho}{h_1}\ddot{x}+\frac{102}{35}\frac{\rho}{h_1^2}\dot{x}^2\right) \quad (38)$$

in place of the momentum approximation (35). The subsequent integrations for the pressure and the required force follow the same path as outlined above and lead to the energy approximation

$$F = 8bR^3\left[\mu\left(\frac{1}{h_1^3}+\frac{1}{h_3^3}\right)\dot{x}+\frac{\rho}{10}\left(\frac{1}{h_1}+\frac{1}{h_3}\right)\ddot{x}\right.$$

$$\left.+\frac{17\rho}{70}\left(\frac{1}{h_1^2}-\frac{1}{h_3^2}\right)\dot{x}^2\right] \quad (39)$$

in place of (37).

The second energy procedure uses Lagrange's Eq. (14). Since the transverse velocity is of order c/R smaller than the longitudinal velocity the kinetic energy in the squeeze and suction channels may be taken as

$$T = b\int_{-R}^{R} dx_1\int_0^{h_1}\frac{1}{2}\rho u_1^2 dy_1 + b\int_{-R}^{R} dx_3\int_0^{h_3}\frac{1}{2}\rho u_3^2 dy_3$$

$$= \frac{2}{5}\rho bR^3\left(\frac{1}{h_1}+\frac{1}{h_3}\right)\dot{x}^2 \quad (40)$$

and the Rayleigh dissipation function may be taken as

$$D = b\int_{-R}^{R} dx_1\int_0^{h_1}\frac{1}{2}\mu\left(\frac{\partial u_1}{\partial y_1}\right)^2 dy_1$$

$$+ b\int_{-R}^{R} dx_3\int_0^{h_3}\frac{1}{2}\mu\left(\frac{\partial u_3}{\partial y_3}\right)^2 dy_3$$

$$= 4\mu bR^3\left(\frac{1}{h_1^3}+\frac{1}{h_3^3}\right)\dot{x}^2. \quad (41)$$

The kinetic energy (40) is that of a fixed identity of fluid mass which occupies the two channels at a particular instant of time. It is convenient to set up a control volume congruent with the boundary of this fluid mass at a particular time t. As time evolves the control volume remains fixed in space while the fixed identity of fluid mass changes its shape: the squeeze film gets thinner and the suction film gets thicker. Some of the fluid of fixed identity near the ends of the squeeze film is expelled from the control volume and some new fluid, not part of the mass of fixed identity, is drawn into the control volume at the ends of the suction film. In order to evaluate the energy derivatives required in Lagrange's Eq. (14) it is convenient to use the relations (see Appendix B)

$$\frac{d}{dt}\left(\frac{\partial T_{fi}}{\partial \dot{x}}\right) = \frac{d}{dt}\left(\frac{\partial T_{cv}}{\partial \dot{x}}\right) + \oint_S \frac{\partial \tau}{\partial \dot{x}} v_n dS \quad (42)$$

$$\frac{\partial T_{fi}}{\partial x} = \frac{\partial T_{cv}}{\partial x} + \oint_S \tau\frac{\partial v_n}{\partial \dot{x}} dS \quad (43)$$

where T_{cv} is the total kinetic energy (40) in the control volume, and τ is the kinetic energy per unit volume at points on the surface S of the control volume where the normal component of fluid velocity, out of the control volume, is v_n. For the control volume enclosing the squeeze and suction films in Fig. 3, the two regions where fluid is being expelled extend from $y_1 = 0$ to $y_1 = h_1$ at $x_1 = -R$ and at $x_1 = R$ and the two regions where new fluid is drawn into the control surface extend from $y_3 = 0$ to $y_3 = h_3$ at $x_3 = -R$ and at $x_3 = R$. These four regions contribute to the second term on the right of (42). In each region the kinetic energy per unit volume is of the form $\tau = -1/2\ \rho u_i^2$ and $v_n = u_i \mathrm{sgn}\ x_i$ where u_1 is given by (31) evaluated at $x_1 = \pm R$ and u_3 is given by the corresponding inertialess suction profile

$$u_3(x_3, y_3, t) = -6\dot{x}\frac{x_3}{h_3}\left(\frac{y_3}{h_3}-\frac{y_3^2}{h_3^2}\right) \quad (44)$$

evaluated at $x_3 = \pm R$. The total contribution to the second term on the right of (42) is

$$2\rho b\dot{x}^2\left\{\int_0^{h_1}\left[6\frac{R}{h_1}\left(\frac{y_1}{h_1}-\frac{y_1^2}{h_1^2}\right)\right]^3 dy_1\right.$$

$$\left.-\int_0^{h_3}\left[6\frac{R}{h_3}\left(\frac{y_3}{h_3}-\frac{y_3^2}{h_3^2}\right)\right]^3 dy_3\right\} = \frac{108}{35}\rho bR^3\dot{x}^2\left(\frac{1}{h_1^2}-\frac{1}{h_3^2}\right). \quad (45)$$

The corresponding evaluation of the second term on the right of (43) leads to a result which is just one half of (45). With these results included, the use of (42) and (43) to evaluate the energy derivatives when Lagrange's Eq. (14) is applied to (40) and (41) leads directly to the required driving force (39).

The third energy method is based on the energy balance statement (15). Here again it is necessary to realize that the kinetic energy involved is that of a system of fixed identity. To compute its time derivative using a control volume, it is convenient to use the relation (see Appendix B)

$$\frac{dT_{fi}}{dt} = \frac{dT_{cv}}{dt} + \oint_S \tau v_n dS \quad (46)$$

for the control volume enclosing the squeeze and suction films in Fig. 3. The second term on the right of (46), evaluated like the corresponding terms in (42) and (43), has the value

$$\frac{54}{35}\rho bR^3\dot{x}^2\left(\frac{1}{h_1^2}-\frac{1}{h_3^2}\right). \quad (47)$$

When (15) is applied to (40) and (41), with the derivative evaluated by use of (47), the result, after division by $\dot{x}$, is precisely the same driving force (39) as obtained by the other two energy methods.

For steady-state oscillation of the block in Fig. 3 with $x = x_0 \sin\omega t$, the force response (37) provided by the momentum approximation becomes

$$F = 16\mu bx_0\omega\frac{R^3}{c^3}\left[\frac{1+3\epsilon^2\sin^2\omega t}{(1-\epsilon^2\sin^2\omega t)^3}\cos\omega t\right.$$

$$\left.-\frac{\mathrm{Re}}{12}\frac{\sin\omega t}{1-\epsilon^2\sin^2\omega t}\left(1-\frac{24}{5}\frac{\epsilon^2\cos^2\omega t}{1-\epsilon^2\sin^2\omega t}\right)\right] \quad (48)$$

where $\epsilon = x_0/c$. The energy approximation (39) becomes

$$F = 16\mu b x_0 \omega \frac{R^3}{c^3}\left[\frac{1+3\epsilon^2\sin^2\omega t}{(1-\epsilon^2\sin^2\omega t)^3}\cos\omega t - \frac{\mathrm{Re}}{10}\frac{\sin\omega t}{1-\epsilon^2\sin^2\omega t}\left(1-\frac{34}{7}\frac{\epsilon^2\cos^2\omega t}{1-\epsilon^2\sin\omega t}\right)\right] \quad (49)$$

under the same circumstances. Both these approximations reduce to the inertialess result obtained from (34) when $\mathrm{Re}=0$. The discrepancies in the coefficients in the inertia terms of the two approximations are of the order of 20 percent.

Linearized Solution for the Squeeze-Suction Pattern

An exact solution to the momentum Eqs. (20) and (21) and the continuity Eq. (19) for squeeze-film geometry must include the nonlinear contributions of the convective acceleration terms and satisfy boundary conditions on the moving channel walls. The low Re approximations furnished by (48) and (49) suggest that these two phenomena contribute $O(\epsilon^2)$ effects to the force response where $\epsilon = x_0/c$ is a measure of the smallness of the motion. Here we obtain a linearized solution correct to first order in ϵ, but not restricted to low Re, by neglecting the convective acceleration terms in (20) and by satisfying the boundary conditions at the average locations of the moving channel walls.

For steady-state oscillation at frequency ω, $x(t)$, $F(t)$, and the fluid film parameters in the squeeze film at the right of Fig. 3, $u_1(x_1, y_1, t)$, $v_1(y_1, t)$, and $p_1(x_1, t)$ are taken as the real parts of $-ix_0e^{i\omega t}$, $F_0e^{i\omega t}$, $U_1(x_1, y_1)e^{i\omega t}$, $V_1(y_1)e^{i\omega t}$, and $P_1(x_1)e^{i\omega t}$, respectively. The longitudinal velocity amplitude profile U_1 which satisfies the global continuity requirement (30) as well as the linearized version of the longitudinal momentum Eq. (20) is

$$U_1 = x_0\omega\frac{x_1}{c}\frac{1-\phi(y_1, c)}{1-\psi(c)} \quad (50)$$

where the functions ϕ and ψ are defined in (24) and (27). The transverse velocity amplitude $V_1(y_1)$ which satisfies the continuity Eq. (19) and the boundary conditions $V_1(0)=0$ and $V_1(c) = -x_0\omega$ is

$$V_1 = -\frac{x_0\omega}{1-\psi(c)}\left[\frac{y_1}{c}+\frac{\cosh s(c-y_1)-\cosh sy_1-\cosh sc+1}{sc\sinh sc}\right]. \quad (51)$$

The pressure amplitude $P_1(x_1)$ which satisfies both the longitudinal and transverse momentum equations, (20) and (21), is

$$P_1 = \frac{\mu x_0\omega}{2c}\frac{s^2c^2}{1-\psi(c)}\left[\frac{R^2-x_1^2}{c^2}\right]+P_2. \quad (52)$$

A parallel calculation provides the pressure amplitude P_3 in the suction film so that the force amplitude F_0 required to maintain the oscillation is

$$F_0 = \int_{-R}^{R} b(P_1dx_1 - P_3dx_3) = \frac{4}{3}\mu b x_0\omega\frac{R^3}{c^3}\frac{s^2c^2}{1-\psi(c)}. \quad (53)$$

This force applies to any Reynolds number so long as the flow is laminar, but is only valid to first order in $\epsilon = x_0/c$. The low Re approximation to (53), obtained by expanding $\psi(c)$ up to the sixth power in sc, is

$$F_0 = 16\mu b x_0\omega\frac{R^3}{c^2}\left(1+i\frac{\mathrm{Re}}{10}\right). \quad (54)$$

note that this is equivalent to the force provided by the energy approximation (49) when terms of order ϵ^2 are neglected. For small ϵ, the relative accuracy of the momentum and energy approximations as functions of Reynolds number for the squeeze-suction flow pattern is the same as that for the channel flow pattern displayed in Fig. 5.

Conclusion

Two elementary flow patterns, which are combined in practical squeeze-film dampers, were analyzed separately. Momentum and energy approximations for inertial flows, based on the assumption that the inertialess velocity profiles remained unaffected by the presence of inertia forces, were presented. These approximations were compared with an exact solution in the case of the channel flow pattern, and with an exact linearized solution, valid for small amplitude oscillation, in the case of the squeeze-suction flow pattern. It was verified that in these cases the velocity profile with inertia does not deviate much from the inertialess profile in the Reynolds number range $0 < \mathrm{Re} < 50$. The force responses are satisfactorily estimated by either momentum or energy approximations in this range. The energy approximations are, however, more accurate (see Fig. 5). They agree to first order in Re with expansions of the exact solutions in powers of Re whereas the momentum approximations have deviations in the inertial components of the order of 20 percent.

For films of comparable dimensions and with small displacements of the block from the central position, the viscous and inertial components of the force response for the elementary channel flow pattern are about three times greater than the corresponding components of the force response for the squeeze-suction flow pattern, and these components are nearly linearly proportional to the block velocity and acceleration, respectively. The magnitude of the inertial component increases nearly linearly with Re and crosses over the magnitude of the viscous component at about $\mathrm{Re}=10$. For larger displacements the force response becomes nonlinear as indicated by (A9) for the elementary channel flow pattern and by (49) for the squeeze-suction pattern.

The momentum approximation and the first method of applying the energy approximation involve substantially similar calculations. The second energy method using Lagrange's equation can be significantly simpler, although care must be exercised to distinguish between a system of fixed identity and the changing contents of a fixed control volume (see Appendix B). In systems with more than one generalized coordinate, energy balance does not provide a complete solution. However, for the elementary flow patterns considered here with the single generalized coordinate x, energy balance does provide a complete solution with slightly less calculation than Lagrange's equation.

References

Constantinescu, V. N., 1970, "On the Influence of Inertia Forces in Turbulent and Laminar Self-Acting Films," ASME *Journal of Lubrication Technology*, Vol. 92, pp. 473–479.

El-Shafei, A., 1988, "Dynamics of Rotors Incorporating Squeeze Film Dampers," Ph.D. Thesis, Department of Mechanical Engineering, M.I.T., Cambridge, MA.

El-Shafei, A., 1991, "A New Approach to the Derivation of Reynolds Equation," EGTRIB '91 preprints, Egyptian Soc. of Tribology, pp. II-52 to II-59.

El-Shafei, A., and Crandall, S. H., 1991, "Fluid Inertia Forces in Squeeze Film Dampers," *Rotating Machinery and Vehicle Dynamics*, T. C. Huang, J. Wolf, F. Ehrich, D. J., Segalman, D. K. Rao, and A. V. Srinivasan, eds., ASME Publication DE-Vol. 35, ASME, New York, pp. 219–228.

Goldstein, H., 1959, *Classical Mechanics*, Addison-Wesley, Reading, MA, p. 17.

Jones, A. F., and Wilson, S. D. R., 1975, "On the Failure of Lubrication Theory in Squeezing Flows," ASME *Journal of Lubrication Technology*, Vol. 97, pp. 101–104.

Modest, M. F., and Tichy, J. A., 1978b, "Squeeze Film Flow in Arbitrarily Shaped Journal Bearings Subject to Oscillations," ASME *Journal of Lubrication Technology*, Vol. 100, pp. 323–329.

Reinhardt, E., and Lund, J. W., 1975, "The Influence of Fluid Inertia on the Dynamic Properties of Journal Bearings, ASME *Journal of Lubrication Technology*, Vol. 97, pp. 159–167.

Ramli, M. D., Ellis, J., and Roberts, J. B., 1987, "On the Computation of Inertial Coefficients in Squeeze-Film Bearings," *Proc. I. Mech. E*, Vol. 201 C2, pp. 125–131.

San Andrés, L. A., and Vance, J. M., 1986, "Effects of Fluid Inertia and

Turbulence on the Force Coefficients for Squeeze Film Dampers," ASME *Journal of Engineering for Gas Turbine and Power*, Vol. 108, pp. 332–339.

Shames, I. H., 1982, *Mechanics of Fluids*, 2nd ed., McGraw-Hill, New York, p. 112.

Smith, D. M., 1964-5, "Journal Bearing Dynamic Characteristics—Effect of Inertia of Lubricant," *Proc. I Mech. E.*, Vol. 179, pp. 37–44.

Szeri, A. Z., Raimondi, A. A., and Giron-Durate, A., 1983, "Linear Force Coefficients of Squeeze Film Dampers," ASME *Journal of Lubrication Technology*, Vol. 105, pp. 326–334.

Tichy, J. A., and Modest, M. F., 1978, "Squeeze Film Flow Between Arbitrary Two-Dimensional Surfaces Subject to Normal Oscillation," ASME *Journal of Lubrication Technology*, Vol. 100, pp. 316–322.

Tichy, J. A., and Winer, W. O.,.1970, "Inertial Considerations in Parallel Circular Squeeze Film Bearings," ASME *Journal of Lubrication Technology*, Vol. 92, pp. 588–592.

APPENDIX A

Channel Flow Pattern When $h_2 \neq h_4$

For the momentum and energy approximations the velocity profiles of the inertialess case are taken as

$$u_2 = \frac{6q_2}{bh_2}\left(\frac{y_2}{h_2} - \frac{y_2^2}{h_2^2}\right) \quad u_4 = \frac{6q_4}{bh_4}\left(\frac{y_4}{h_4} - \frac{y_4^2}{h_4^2}\right). \tag{A1}$$

When these are inserted in (7) and in the corresponding equation for u_4, and the equations integrated across the films, and divided by the film thicknesses, the momentum approximation yields

$$\frac{p_1 - p_3}{2R} = 12\,\frac{\mu}{bh_2^3}\,q_2 + \frac{\rho}{bh_2}\,\dot{q}_2 = -12\,\frac{\mu}{bh_4^3}\,q_4 - \frac{\rho}{bh_4}\,\dot{q}_4. \tag{A2}$$

The flow rates q_2 and q_4 and their derivatives are eliminated between the two equations of (A2) and the continuity Eq. (3) to obtain a linear differential equation for the pressure difference $p_1 - p_3$ as a function of the block velocity $\dot{x}(t)$. The force $F(t) = 2Rb(p_1 - p_2)$ required to produce this motion satisfies the differential equation

$$\left[\left(\frac{\mu}{h_2^3} + \frac{\rho}{12h_2}\frac{d}{dt}\right) + \left(\frac{\mu}{h_4^3} + \frac{\rho}{12h_4}\frac{d}{dt}\right)\right]F = 96R^3 b\left(\frac{\mu}{h_2^3} + \frac{\rho}{12h_2}\frac{d}{dt}\right)\left(\frac{\mu}{h_4^3} + \frac{\rho}{12h_4}\frac{d}{dt}\right)\dot{x} \tag{A3}$$

according to the momentum approximation.

The energy approximation starting from (A1) proceeds in a parallel manner. All three energy techniques lead to a pair of equations similar in form to (A2) but with coefficients of 12/10 before the $\dot{q}_2$ and $\dot{q}_4$ terms (compare Eqs. (8) and (10) for the corresponding different when $h_2 = h_4$). The force required, according to the energy approximation, thus satisfies the differential equation

$$\left[\left(\frac{\mu}{h_2^3} + \frac{\rho}{10h_2}\frac{d}{dt}\right) + \left(\frac{\mu}{h_4^3} + \frac{\rho}{10h_4}\frac{d}{dt}\right)\right]F = 96R^3 b\left(\frac{\mu}{h_2^3} + \frac{\rho}{10h_2}\frac{d}{dt}\right)\left(\frac{\mu}{h_4^3} + \frac{\rho}{10h_4}\frac{d}{dt}\right)\dot{x}. \tag{A4}$$

Note that (A3) and (A4) reduce to the simpler relations (9) and (11) when $h_2 = h_4 = c$.

Within the channels 2 and 4 the *exact* solution (23) for the velocity amplitudes are

$$U_i(y_i) = -\frac{1}{\mu s^2}\frac{dP_i}{dx_i}\left[1 - \phi(y_i, h_i)\right] \tag{A5}$$

where the subscript i takes the value 2 or 4 corresponding to the channel. The corresponding flow rate amplitudes

$$Q_i = b\int_0^{h_i} U_i dy_i \tag{A6}$$

are

$$Q_i = -\frac{bh_i}{\mu s^2}\frac{dP_i}{dx_i}\left[1 - \psi(h_i)\right] \tag{A7}$$

where the ψ function is defined in (27). If these flow rates are inserted in the continuity Eq. (3) and the equality of the pressure gradients in the two channels is noted, the pressure drop amplitude $P_1 - P_3$ and the force amplitude F_0 are obtained as follows:

$$F = 2Rb(P_1 - P_3) = \frac{8\mu bR^3 x_0 \omega s^2}{2c - h_2\psi(h_2) - h_4\psi(h_4)}. \tag{A8}$$

This is the exact solution for the complex force amplitude required to oscillate the block in Fig. 2 at frequency ω and amplitude x_0, taking account of the inertia and viscosity in the channels of width h_2 and h_4. Note that it reduces to (26) when $h_2 = h_4 = c$. The small Reynolds number approximation, obtained by expanding the ψ functions up to the sixth power in sh_i, is

$$F_0 = 96\mu bR^3 x_0 \omega \frac{\left(1 + i\frac{\mathrm{Re}}{10}\frac{h_2^2}{c^2}\right)\left(1 + i\frac{\mathrm{Re}}{10}\frac{h_4^2}{c^2}\right)}{h_4^3\left(1 + i\frac{\mathrm{Re}}{10}\frac{h_2^2}{c^2}\right) + h_2^3\left(1 + \frac{\mathrm{Re}}{10}\frac{h_4^2}{c^2}\right)} \tag{A9}$$

which is equivalent to the energy approximation (A4) for the special case when $x(t)$ is the real part of $-ix_0 e^{i\omega t}$.

APPENDIX B

Control Volume Evaluation of Energy Derivatives for a System of Fixed Identity

Let $\phi(q_1, \ldots, q_n, \dot{q}_1, \ldots, \dot{q}_n)$ be the density of some extensive fluid property that depends on n generalized coordinates $q_i(t)$ and n generalized velocities $\dot{q}_i(t)$, $i = 1, \ldots, n$. Let the total mass of fluid within an enveloping surface S_{fi} constitute a system of fixed identity. As time evolves, the volume V_{fi} enclosed by S_{fi} will, in general, change its shape and move about. At a particular time t let V_{fi} coincide with a stationary control volume V with boundary surface S which coincides with the system envelope S_{fi}. At this instant the total system property corresponding to the density ϕ is

$$\Phi_{fi} = \int_{V_{fi}} \phi dV = \int_V \phi dV = \Phi_{cs}. \tag{B1}$$

The time rate of change of Φ_{fi} at this same instant can be evaluated by using Reynolds transport theorem (Shames, 1982) which accounts for the rate of change of ϕ within the control volume and for the transport of matter across the control volume surface S. If the vector particle velocity at an element dS of the surface S is $\dot{\mathbf{r}}$ and $\mathbf{n}$ is the unit outward normal vector, Reynolds theorem may be written in the form

$$\frac{d\Phi_{fi}}{dt} = \int_V \frac{d\phi}{dt}\,dV + \oint_S \phi\mathbf{n}\cdot\dot{\mathbf{r}}\,dS \tag{B2}$$

or as

$$\frac{d\Phi_{fi}}{dt} = \frac{d\Phi_{cv}}{dt} + \oint_S \phi v_n\,dS \tag{B3}$$

where v_n is the outward normal component of fluid velocity on S. The density function ϕ may stand for the kinetic energy per unit volume, τ, in which case (B3) reduces to (46), or ϕ may stand for the derivative of the kinetic energy density with respect to a generalized velocity, $\partial\tau/\partial\dot{q}_i$ in which case (B3) becomes the justification for (42).

The concept underlying the Reynolds theorem for the evaluation of time derivatives can be extended to derivatives with respect to generalized coordinates. When a generalized variable has a differential increment dq_i, the vector displacement $\mathbf{r}$ of a particle on the surface S has the differential increment

$$d\mathbf{r} = \frac{\partial \mathbf{r}}{\partial q_i}\, dq_i. \tag{B4}$$

The derivative of the system property Φ_{fi} with respect to q_i at time t is obtained by summing $\partial\phi/\partial q_i$ over the control volume and accounting for the transport of matter across its surface S as follows:

$$\frac{\partial \Phi_{fi}}{\partial q_i} = \int_V \frac{\partial \phi}{\partial q_i}\, dV + \oint_S \phi \mathbf{n} \cdot \frac{\partial \mathbf{r}}{\partial q_i}\, dS. \tag{B5}$$

By inserting the classical identity (Goldstein, 1959)

$$\frac{\partial \mathbf{r}}{\partial q_i} = \frac{\partial \dot{\mathbf{r}}}{\partial \dot{q}_i}, \tag{B6}$$

and introducing $v_n = \mathbf{n} \cdot \dot{\mathbf{r}}$ we write (B5) in the form

$$\frac{\partial \Phi_{fi}}{\partial q_i} = \frac{\partial \Phi_{cv}}{\partial q_i} + \oint \phi \frac{\partial v_n}{\partial \dot{q}_i}\, dS. \tag{B7}$$

With ϕ representing the kinetic energy density τ and q_i representing the block displacement x in Fig. 3, (B7) reduces to (43).

Contact With Friction Between Two Elastic Half-Planes

L. Johansson
Linköping Institute of Technology,
Department of Mechanical Engineering,
Division of Solid Mechanics and
Strength of Materials,
S-581 83, Linköping, Sweden

In the present paper the problem of contact with friction between two elastic bodies is formulated in the form of variational inequalities using half-plane assumptions for the elastic behavior. The formulation fits directly into a computational method developed in a previous paper and some numerical examples investigating the effects of using dissimilar elastic constants in the bodies and of using different load paths in the application of the external forces are given.

1 Introduction

The purpose of the present paper is to give a variational formulation of the contact with friction between two elastic half-planes with dissimilar elastic constants. The contacting half-planes are assumed to be linearly elastic and isotropic so that their elastic behavior is given by Flamant's solution for a point force on the edge of an elastic half-plane. For the contact interface we assume unilateral contact conditions in the normal direction and Coulomb's law of friction in the tangential direction. These assumptions can of course be questioned from both a physical-experimental and from a mathematical point of view. These issues are, however, not addressed in the present paper. The stated constitutive laws are assumed to be valid, and the analysis proceeds from that point.

An inherent difficulty when treating contact problems using half-plane assumptions is the arbitrary constants present in the force-displacement relations (see Eqs. (1) through (3) and comments in Johnson (1985) and in Gladwell (1980)). In three-dimensional problems using half-space assumptions this difficulty does not occur since it is possible to determine the rigid-body constants by assuming that displacements and rotations at points infinitely distant from the applied load are zero. But in the plane case this removes only the constants associated with rigid-body rotation and not the constants associated with rigid-body translation; and making an arbitrary choice of constants cannot be readily interpreted as fixing a particular reference point. In previous works where contact problems have been solved using the Flamant solution for a point force on an elastic half-plane, this difficulty has been circumvented by differentiating the relations to obtain a system of integral equations involving the surface gradients of the displacements.

In the present paper it is shown how the difficulty of the half-plane case can be avoided by calculating the displacements relative to a point on the contact surface itself and how the contact between two elastic half-planes can thus be given a reciprocal variational formulation. This formulation is formally identical to the formulation used by Johansson and Klarbring (1992) for a rigid punch problem and the numerical method developed in this paper can be used directly. Thus a method is obtained which solves half-plane contact problems very accurately yet is completely general in the choice of elastic constants, initial gap between the bodies, and load-path, and which also includes a rotational degree-of-freedom and a moment in the loading.

In Johnson (1985) solutions are given for some two-dimensional cases, without coupling between the normal and tangential directions, by using integral equations based on relations between the contact tractions and the derivatives of the displacements. Important progress with formulations of this type was made by Spence (1973) who solved the case of normal indentation with friction of a flat or power-law profiled punch into an elastic half-plane. This line is followed by Nowell et al. (1988), where the coupled case is solved for a case with second-order initial gap and normal and tangential loading using a method involving numerical solution of integral equations. A similar approach is also followed by Bjarnehed (1991) for the normal indentation of a rigid punch into a prestressed orthotropic half-plane.

2 Governing Equations

Consider two elastic bodies that are pressed together by some external forces, Fig. 1. The problem is considered as two-dimensional and the bodies are modeled as elastic half-planes. Quantities associated with the lower half-plane will be denoted by superscript 1 and quantities associated with the upper half-plane by superscript 2. The displacement fields of the bodies, in the coordinate directions, will be denoted by v_T^1 and v_T^2 in the x-direction and v_N^1 and v_N^2 in the y-direction.

The bodies are assumed to be in contact on some segment S_c of the plane $y=0$ and the traction on the bodies in this segment can be represented by the components p_T and p_N in the x and y-directions, respectively. These tractions are equal in magnitude but opposite in direction for the upper and lower body, respectively. Here the convention that p_N and p_T are positive when acting in positive coordinate directions on the lower body is chosen. The externally applied loads M, N, and T will be defined at the end of Section 2, and are positive when acting in positive coordinate directions on the upper body.

Contributed by the Applied Mechanics Division of THE AMERICAN SOCIETY OF MECHANICAL ENGINEERS for publication in the ASME JOURNAL OF APPLIED MECHANICS. Discussion on this paper should be addressed to the Technical Editor, Professor Lewis T. Wheeler, Department of Mechanical Engineering, University of Houston, Houston, TX 77204-4792, and will be accepted until four months after final publication of the paper itself in the ASME JOURNAL OF APPLIED MECHANICS.

Manuscript received by the ASME Applied Mechanics Division, Sept. 10, 1991; final revision, Jan. 21, 1992. Associate Technical Editor: R. Abeyaratne.

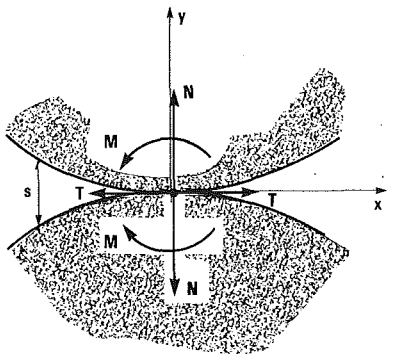

Fig. 1 Contact between two elastic half-planes

In the following discussion the origin of coordinates will be used as a reference point and referred to as x_0. This point is conveniently chosen to be the point where contact first occurs but can also be any other point of the x-axis.

For a homogeneous isotropic linearly elastic half-plane in plane stress, the relations between displacement and normal pressure and tangential traction on the boundary can be written as

$$v_N^l(x, y) = \int_{S_c} g_{NN}^l(x, \xi) p_N(\xi) d\xi + \int_{S_c} g_{NT}^l(x, \xi) p_T(\xi) d\xi \tag{1a}$$

$$v_T^l(x, y) = \int_{S_c} g_{TN}^l(x, \xi) p_N(\xi) d\xi + \int_{S_c} g_{TT}^l(x, \xi) p_T(\xi) d\xi \tag{1b}$$

$$v_N^2(x, y) = -\int_{S_c} g_{NN}^2(x, \xi) p_N(\xi) d\xi + \int_{S_c} g_{NT}^2(x, \xi) p_T(\xi) d\xi \tag{1c}$$

$$v_T^2(x, y) = \int_{S_c} g_{TN}^2(x, \xi) p_N(\xi) d\xi - \int_{S_c} g_{TT}^2(x, \xi) p_T(\xi) d\xi. \tag{1d}$$

Here

$$g_{NN}^l = \frac{1}{\pi E^l}\left[-2ln(r/d) - (1+\nu^l)\frac{(x-\xi)^2}{r^2}\right] + b_N^l + c_N^l(x-\xi), \quad l=1, 2 \tag{2a}$$

$$g_{TT}^l = \frac{1}{\pi E^l}\left[-2ln(r/d) - (1+\nu^l)\frac{y^2}{r^2}\right] + b_T^l + c_T^l y, \quad l=1, 2 \tag{2b}$$

$$g_{TN}^l = \frac{-(-1)^l}{\pi E^l}\left[(1+\nu^l)\frac{y(x-\xi)}{r^2} - (1-\nu^l)\arctan\left(\frac{x-\xi}{y}\right)\right] + a_N^l - c_N^l y, \quad l=1, 2 \tag{2c}$$

$$g_{NT}^l = \frac{-(-1)^l}{\pi E^l}\left[(1+\nu^l)\frac{y(x-\xi)}{r^2} + (1-\nu^l)\arctan\left(\frac{x-\xi}{y}\right)\right] + a_T^l - c_T^l(x-\xi), \quad l=1, 2 \tag{2d}$$

$$r = [(x-\xi)^2 + y^2]^{1/2} \tag{2e}$$

where E^l, $l=1, 2$ are the Young's moduli for the lower and upper body, respectively, and ν^l, $l=1, 2$ are the Poisson's ratios. In Eqs. (2), a_N^l, b_N^l, c_N^l, a_T^l, b_T^l, and c_T^l are undetermined constants, with $l=1$ for the lower half-plane and $l=2$ for the upper half-plane. In Eqs. (2a) and (2b), d is a constant inserted to give the logarithm a nondimensional argument. This constant will be assumed to have the value of one in the units the coordinate values are measured in, and will be dropped below without loss of generality.

Constants with subscript N will be multiplied by p_N in Eqs. (1) and constants with subscript T will be multiplied by p_T. Combining (2) and (1), a_N^l, b_N^l, and c_N^l will give rise to a rigid-body displacement and rotation of each half-plane depending on p_N, and a_T^l, b_T^l, and c_T^l will give rise to a rigid-body displacement and rotation depending on p_T. Similar constants occur in three-dimensional problems in which case it is customary to determine these constants by prescribing that the displacements and rotation should be zero at points infinitely distant from the applied surface load. In the two-dimensional case, if we prescribe that the rotation $\omega = 1/2[(\partial v_N/\partial x) - (\partial v_T/\partial y)]$ is zero as x, y tend towards infinity, we find that $c_N^l = c_T^l = 0$. The remaining constants, however, cannot be determined in this manner. Next we specialize Eqs. (2) to points on the surface $y=0$ and introduce $d_N^l = b_N^l - (1-\nu^l)/\pi E^l$ and $d_T^l = b_T^l$ and also put $c_N^l = c_T^l = 0$ to obtain

$$g_{NN}^l = -\frac{2}{\pi E^l} ln|x-\xi| + d_N^l, \quad l=1, 2 \tag{3a}$$

$$g_{TT}^l = -\frac{2}{\pi E^l} ln|x-\xi| + d_T^l, \quad l=1, 2 \tag{3b}$$

$$g_{TN}^l = \begin{cases} -\dfrac{1-\nu^l}{2E^l} + a_N^l, & x<\xi \\ \dfrac{1-\nu^l}{2E^l} + a_N^l, & x>\xi \end{cases} \quad l=1, 2 \tag{3c}$$

$$g_{NT}^l = \begin{cases} \dfrac{1-\nu^l}{2E^l} + a_T^l, & x<\xi \\ -\dfrac{1-\nu^l}{2E^l} + a_T^l, & x>\xi. \end{cases} \quad l=1, 2 \tag{3d}$$

The Green's functions g_{NN}^l and g_{TN}^l can be interpreted as the normal and tangential displacement at x due to a unit normal force at ξ. Thus, these Green's functions can be deduced from the Flamant Solution of a concentrated normal force at the edge of an elastic half-plane (see Gladwell (1980), Timoshenko and Goodier (1982), and Johansson (1990)). Similarly, g_{TT}^l and g_{NT}^l can be deduced from the solution for a concentrated tangential force. The same results can be obtained from equations derived in, for example, Muskhelishvili (1963), without the use of a point force.

The relations between deformation of the surfaces of the bodies and traction on the surfaces implied by Eqs. (1) and (3) can be written compactly using an operator notation as

$$v_N^1 = G_{NN}^1(x, p_N) + G_{NT}^1(x, p_T) + D_N^1(p_N) + A_T^1(p_T) \tag{4a}$$

$$v_T^1 = G_{TN}^1(x, p_N) + G_{TT}^1(x, p_T) + A_N^1(p_N) + D_T^1(p_T) \tag{4b}$$

$$v_N^2 = -G_{NN}^2(x, p_N) + G_{NT}^2(x, p_T) - D_N^2(p_N) + A_T^2(p_T) \tag{4c}$$

$$v_T^2 = G_{TN}^2(x, p_N) - G_{TT}^2(x, p_T) + A_N^2(p_N) - D_T^2(p_T). \tag{4d}$$

In this notation the operators $G_{NN}^l(\cdot,\cdot)$, $l=1, 2$ correspond to the integration of the first term to the right in (3a) multiplied by $p_N(\xi)$ and similarly for $G_{TT}^l(\cdot,\cdot)$, $G_{NT}^l(\cdot,\cdot)$ and $G_{TN}^l(\cdot,\cdot)$. The operators $D_N^l(\cdot)$, $l=1, 2$ correspond to the integration along S_c of the second term to the right in (3a) multiplied by $p_N(\xi)$, that is the integral of $p_N(\xi)$ multiplied by the constant d_N^l, and similarly for $D_T^l(\cdot)$, $A_N^l(\cdot)$, and $A_T^l(\cdot)$. Note that the operators $D_N^l(\cdot)$, $D_T^l(\cdot)$, $A_N^l(\cdot)$, and $A_T^l(\cdot)$, $l=1, 2$ do not depend on the coordinate x and thus give the same contributions at every point along S_c.

The displacements v_N^l and v_T^l, $l=1, 2$ can only be computed to within arbitrary constants due to $D_N^l(\cdot)$, $D_T^l(\cdot)$, $A_N^l(\cdot)$, and $A_T^l(\cdot)$, but if we compute the relative displacement between two points on one of the half-planes, the contributions from $D_N^l(\cdot)$, $D_T^l(\cdot)$, $A_N^l(\cdot)$, and $A_T^l(\cdot)$ will cancel. Thus, the displacement of an arbitrary surface point relative to x_0 can be written as

$$\bar{v}_N^1 = G_{NN}^1(x, p_N) + G_{NT}^1(x, p_T) - [G_{NN}^1(x, p_N) + G_{NT}^1(x, p_T)]|_{x_0} \tag{5a}$$

$$\bar{v}_T^1 = G_{TN}^1(x, p_N) + G_{TT}^1(x, p_T) - [G_{TN}^1(x, p_N) + G_{TT}^1(x, p_T)]|_{x_0} \quad (5b)$$

$$\bar{v}_N^2 = -G_{NN}^2(x, p_N) + G_{NT}^2(x, p_T) - [-G_{NN}^2(x, p_N) + G_{NT}^2(x, p_T)]|_{x_0} \quad (5c)$$

$$\bar{v}_T^2 = G_{TN}^2(x, p_N) - G_{TT}^2(x, p_T) - [G_{TN}^2(x, p_N) - G_{TT}^2(x, p_T)]|_{x_0} \quad (5d)$$

where the notation $|_{x_0}$ means that the preceding term is evaluated at x_0.

If the surface of the lower body modes in the positive y-direction and the surfaces of the upper body moves in the negative y-direction, the gap between the bodies will become smaller. This closure of corresponding surface points on the upper and lower half-planes is the displacement relative to x_0 in the positive y-direction of a point on the lower half-plane plus the displacement relative to x_0 in the negative y-direction of the corresponding point on the upper half-plane plus the closure at x_0. Thus

$$\begin{aligned}\hat{u}_N &= v_N^1 - v_N^1|_{x_0} - [v_N^2 - v_N^2|_{x_0}] + \hat{u}_{NO} = \bar{v}_N^1 - \bar{v}_N^2 + \hat{u}_{NO} \\ &= G_{NN}^1(x, p_N) + G_{NN}^2(x, p_N) + G_{NT}^1(x, p_T) - G_{NT}^2(x, p_T) \\ &\quad - [G_{NN}^1(x, p_N) + G_{NN}^2(x, p_N) + G_{NT}^1(x, p_T) - G_{NT}^2(x, p_T)]|_{x_0} + \hat{u}_{NO} \quad (6)\end{aligned}$$

where $\hat{u}_{NO}$ is the closure at x_0. When the bodies are in contact at x_0 we have $\hat{u}_{NO} = 0$.

Next we define

$$u_N \equiv G_{NN}^1(x, p_N) + G_{NN}^2(x, p_N) + G_{NT}^1(x, p_T) - G_{NT}^2(x, p_T) \quad (7a)$$

$$\beta \equiv [G_{NN}^1(x, p_N) + G_{NN}^2(x, p_N) + G_{NT}^1(x, p_T) - G_{NT}^2(x, p_T)]|_{x_0} - \hat{u}_{NO} \quad (7b)$$

so that $\hat{u}_N$ is expressed compactly as

$$\hat{u}_N = u_N - \beta. \quad (8)$$

We have now made definitions necessary to express the kinematical impenetrability condition between the bodies. The closure of corresponding surface points must be smaller than the initial gap $s(x)$ plus any increase in the gap due to relative rigid body rotation θ of the bodies. Thus,

$$u_N(x) - \beta \le s(x) + \theta x. \quad (9)$$

The assumptions of unilateral contact can now be expressed as

$$p_N \le 0 \quad (10a)$$

$$p_N(u_N - \beta - s - \theta x) = 0 \quad (10b)$$

i.e., the contact pressure is always compressive and (10b) holds since (9) is always fulfilled with equality if $p_N \neq 0$.

Next we will study the tangential direction. To this end we will compute the relative speed between the two surface points corresponding to the same x-coordinate—one at the surface of each body. If the bodies are in contact at this x-coordinate this will be the slip speed. The relative speed is the speed of a point on the lower plane relative to the speed of the lower plane at x_0 minus the speed of the corresponding point on the upper plane relative to the speed of the upper plane at x_0 plus the relative speed at x_0. Thus

$$\begin{aligned}\dot{\lambda}_T &= \dot{v}_T^1 - \dot{v}_T^1|_{x_0} - [\dot{v}_T^2 - \dot{v}_T^2|_{x_0}] + \dot{\lambda}_{TO} \\ &= G_{TN}^1(x, \dot{p}_N) - G_{TN}^2(x, \dot{p}_N) + G_{TT}^1(x, \dot{p}_T) + G_{TT}^2(x, \dot{p}_T) \\ &\quad - [G_{TN}^1(x, \dot{p}_N) - G_{TN}^2(x, \dot{p}_N) + G_{TT}^1(x, \dot{p}_T) + G_{TT}^2(x, \dot{p}_T)]|_{x_0} + \dot{\lambda}_{TO} \quad (11)\end{aligned}$$

where $\dot{\lambda}_{TO}$ is the relative speed at x_0. Here and elsewhere in this paper a superposed dot denotes the time derivative. We now define

$$\dot{u}_T \equiv G_{TN}^1(x, \dot{p}_N) - G_{TN}^2(x, \dot{p}_N) + G_{TT}^1(x, \dot{p}_T) + G_{TT}^2(x, \dot{p}_T) \quad (12a)$$

$$\dot{\alpha} \equiv G_{TN}^1(x, \dot{p}_N) - G_{TN}^2(x, \dot{p}_N) + G_{TT}^1(x, \dot{p}_T) + G_{TT}^2(x, \dot{p}_T)]|_{x_0} - \dot{\lambda}_{TO}. \quad (12b)$$

We can now write (11) as

$$\dot{\lambda}_T = \dot{u}_T - \dot{\alpha}. \quad (13)$$

For the frictional behavior we assume Coulomb's law, i.e.,

$$|p_T(x)| \le \mu |p_N(x)| \equiv \tau(x) \quad (14a)$$

$$|p_T(x)| < \tau(x) \Rightarrow \dot{u}_T(x) - \dot{\alpha} = 0 \quad (14b)$$

$$p_T(x) = \tau(x) \Rightarrow \dot{u}_T(x) - \dot{\alpha} \le 0 \quad (14c)$$

$$p_T(x) = -\tau(x) \Rightarrow \dot{u}_T(x) - \dot{\alpha} \ge 0. \quad (14d)$$

That is, there is a friction bound $\tau(x)$. If the absolute value of the tangential traction is below this bound, there is no slip, and if it is equal to this bound, the sign of the slip is opposite to the sign of the tangential traction.

Finally, the externally applied forces, which give rise to the contact traction, are characterized by their resultants at x_0. Thus

$$N = \int_{S_c} p_N dx \quad (15a)$$

$$T = \int_{S_c} p_T dx \quad (15b)$$

$$M = \int_{S_c} x p_N dx. \quad (15c)$$

3 A Variational Inequality Formulation

As a basis for time and space discretizations the problem will be formulated using variational inequalities. First, let Σ_N be a space of sufficiently smooth fields of contact pressures, and define a convex set of admissible such fields:

$$S_N^t = \left\{ q_N \in \Sigma_N;\ q_N(x) \le 0,\quad N(t) = \int_{S_c} q_N dx,\quad M(t) = \int_{S_c} x q_N dx \right\}.$$

Here, N and M are regarded as prescribed functions of time.

Then, letting u_N and p_N satisfy the relations of Section 2, we have for all $q_N \in S_N^t$

$$\int_{S_c} (u_N - s)(q_N - p_N) dx = \int_{S_c} (u_N - s - \beta - \theta x)(q_N - p_N) dx + \beta \int_{S_c} (q_N - p_N) dx + \theta \int_{S_c} x(q_N - p_N) dx \ge 0. \quad (16)$$

The inequality follows since the last two integrals vanish when both q_N and p_N satisfy (15a) and (15c) since they belong to S_N^t, and the first integral can not be negative because of (8) and (10). Note that β can be moved outside the integration since it is independent of x according to its definition (7b).

Similarly, let Σ_T be a space of fields of tangential tractions, and define a convex set of admissible fields

$$S_T^t(p_N) = \left\{ q_T \in \Sigma_T;\ |q_T(x)| \le \mu |p_N(x)|,\ T(t) = \int_{S_c} q_T dx \right\}.$$

Note that this set is dependent on the field $p_N \in S_N^t$. Letting $\dot{u}_T$ and p_T satisfy the relations of Section 2 we have, similarly to (16) for all $q_T \in S_T^t(p_N)$,

$$\int_{S_c} \dot{u}_T(q_T - p_T)dx = \int_{S_c} (\dot{u}_T - \dot{\alpha})(q_T - p_T)dx + \dot{\alpha}\int_{S_c} (q_T - p_T)dx \geq 0. \quad (17)$$

The inequality follows since the last term vanishes, since q_T and p_T belong to $S_T^t(p_N)$ and the first integral to the right is found to be non-negative by considering different slip situations according to (14). Note that $\dot{\alpha}$ can be moved outside the integration since it is independent of x according to (12b).

Finally, introducing (7a) and (12a) into (16) and (17) we obtain the following problem:

Problem V. Find p_N: $[0, T] \to S_N^t$ and p_T: $[0, T] \to S_T^t(p_N)$ such that for all $q_N \in S_N^t$, $q_T \in S_T^t(p_N)$ and $t \in [0, T]$

$$\int_{S_c} (\tilde{G}_{NN}(x, p_N) + \tilde{G}_{NT}(x, p_T) - s)(q_N - p_N)dx \geq 0 \quad (18a)$$

$$\int_{S_c} (\tilde{G}_{TN}(x, \dot{p}_N) + \tilde{G}_{TT}(x, \dot{p}_T))(q_T - p_T)dx \geq 0 \quad (18b)$$

where

$$\tilde{G}_{NN}(\cdot,\cdot) = G_{NN}^1(\cdot,\cdot) + G_{NN}^2(\cdot,\cdot) \quad (19a)$$

$$\tilde{G}_{NT}(\cdot,\cdot) = G_{NT}^1(\cdot,\cdot) + G_{NT}^2(\cdot,\cdot) \quad (19b)$$

$$\tilde{G}_{TN}(\cdot,\cdot) = G_{TN}^1(\cdot,\cdot) + G_{TN}^2(\cdot,\cdot) \quad (19c)$$

$$\tilde{G}_{TT}(\cdot,\cdot) = G_{TT}^1(\cdot,\cdot) + G_{TT}^2(\cdot,\cdot) \quad (19d)$$

with appropriate initial conditions prescribed. Here $[0, T]$ is some time interval during which we are investigating the problem.

4 The Computational Method

Equations (18) are identical to the equations obtained in Johansson and Klarbring (1992) except that the flexibility operator now contains contributions from both bodies according to Eqs. (19). The computational method deviced in Johansson and Klarbring (1989), which will be outlined as follows, can therefore be used directly, if the calculation of the discrete counterparts of these flexibility operators are modified.

The problem **V** is first discretized in time by introducing a backward finite difference for the time derivative

$$\dot{p}_N(t_l) \approx \frac{p_N(t_l) - p_N(t_{l-1})}{t_l - t_{l-1}}. \quad (20)$$

It is then assumed that the tractions are piecewise constant in space over intervals of length h^i. The integrals over ξ in Eqs. (1) can then be performed in closed form. Finally, the integrals over x explicit in Eqs. (18) are evaluated using a one point Gauss integration with the midpoints of the intervals h^i as integration points. We then have problem **V** discretized in time and space as follows:

Problem $\mathbf{V}_l^h$. Find $\mathbf{P}_N \in S_N^h$ and $\mathbf{P}_T \in S_T^h(\mathbf{P}_N)$ such that for all $\mathbf{Q}_N \in S_N^h$ and $\mathbf{Q}_T \in S_T^h$

$$(\tilde{\mathbf{G}}_{NN}\mathbf{P}_N + \tilde{\mathbf{G}}_{NT}\mathbf{P}_T - \mathbf{s})^t(\mathbf{Q}_N - \mathbf{P}_N) \geq 0 \quad (21a)$$

$$(\tilde{\mathbf{G}}_{TN}\mathbf{P}_N + \tilde{\mathbf{G}}_{TT}\mathbf{P}_T)^t(\mathbf{Q}_T - \mathbf{P}_T) \geq (\tilde{\mathbf{G}}_{TN}\mathbf{P}_N(t_{l-1}) + \tilde{\mathbf{G}}_{TT}\mathbf{P}_T(t_{l-1}))^t(\mathbf{Q}_T - \mathbf{P}_T) \quad (21b)$$

where

$$S_N^h = \{\mathbf{Q}_N \mid Q_N^j \leq 0,\ j = 1, \ldots, M,\ N(t) = \mathbf{l}^t\mathbf{Q}_N,\ M(t) = \mathbf{x}^t\mathbf{Q}_N\} \quad (22a)$$

$$S_T^h(\mathbf{P}_N) = \{\mathbf{Q}_T \mid |Q_T^j| \leq \mu |P_N^j|,\ j = 1, \ldots, M,\ T(t) = \mathbf{l}^t\mathbf{Q}_T\}. \quad (22b)$$

Here the product $\tilde{\mathbf{G}}_{NN}\mathbf{P}_N$ of a square matrix and a column matrix results in a column matrix of displacements and is the discretized counterpart of the notation $\tilde{G}_{NN}(x, p_N)$ used in the continuous case above. Column matrices $\mathbf{P}_N$, $\mathbf{P}_T$, $\mathbf{s}$, and $\mathbf{x}$ are the values of the functions p_N, p_T, s, and x at the Gauss integration points mentioned above and $\mathbf{l}$ is a column matrix of ones.

Finally it can be shown (Johansson and Klarbring, 1992) that the problem $\mathbf{V}_l^h$ is equivalent to the following problem:

Problem $\mathbf{V}_l^h$. Find $\mathbf{P}_T$, $\mathbf{P}_N$, λ_N, λ_{T1}, λ_{T2}, ϕ_1, ϕ_2, γ_1, γ_2, and γ_3 such that

$$\begin{bmatrix} \mathbf{0} \\ 0 \\ 0 \\ 0 \\ \lambda_N \\ -\phi_1 \\ -\phi_2 \end{bmatrix} = \begin{bmatrix} \mathbf{A} \\ T \\ M \\ N \\ \mathbf{s} \\ \mathbf{0} \\ \mathbf{0} \end{bmatrix} + \begin{bmatrix} \tilde{\mathbf{G}}_{TT} & -\mathbf{1} & \mathbf{0} & \mathbf{0} & \tilde{\mathbf{G}}_{TN} & -\mathbf{I} & \mathbf{I} \\ \mathbf{l}^t & 0 & 0 & 0 & \mathbf{0} & 0 & 0 \\ \mathbf{0} & 0 & 0 & 0 & \mathbf{x}^t & 0 & 0 \\ \mathbf{0} & 0 & 0 & 0 & \mathbf{l}^t & 0 & 0 \\ \tilde{\mathbf{G}}_{NT} & \mathbf{0} & -\mathbf{x} & -\mathbf{1} & \tilde{\mathbf{G}}_{NN} & \mathbf{0} & \mathbf{0} \\ \mathbf{I} & \mathbf{0} & \mathbf{0} & \mathbf{0} & \mu\mathbf{I} & \mathbf{0} & \mathbf{0} \\ -\mathbf{I} & \mathbf{0} & \mathbf{0} & \mathbf{0} & \mu\mathbf{I} & \mathbf{0} & \mathbf{0} \end{bmatrix} \begin{bmatrix} -\mathbf{P}_T \\ \gamma_3 \\ \gamma_2 \\ \gamma_1 \\ -\mathbf{P}_N \\ \lambda_{T1} \\ \lambda_{T2} \end{bmatrix} \quad (23a)$$

$$\left.\begin{array}{lll} \lambda_N \geq \mathbf{0} & -\mathbf{P}_N \geq \mathbf{0} & \lambda_N^t\mathbf{P}_N = 0 \\ \lambda_{T1} \geq \mathbf{0} & -\phi_1 \geq \mathbf{0} & \lambda_{T1}^t\phi_1 = 0 \\ \lambda_{T2} \geq \mathbf{0} & -\phi_2 \geq \mathbf{0} & \lambda_{T2}^t\phi_2 = 0 \end{array}\right\} \quad (23b)$$

$$\mathbf{A} = \tilde{\mathbf{G}}_{TT}\mathbf{P}_T(t_{l-1}) + \tilde{\mathbf{G}}_{TN}\mathbf{P}_N(t_{l-1}) \quad (23c)$$

where $\mathbf{I}$ is the identity matrix.

It is possible to make physical interpretations of the various multipliers in Eqs. (23). Thus λ_{T1} and λ_{T2} are related to the slip speed between points in contact and γ_2 can be identified as the rotation $-\theta$. γ_1 and γ_2 can be identified with the relative rigid-body motions of the bodies, but of course this interpretation is useless in the present case since there are no definite reference points for this motion. (See Johansson and Klarbring (1992) for more details on these interpretations.)

The solution of Eqs. (23) provides the contact forces at time t_l provided that they are known at time t_{l-1}. Thus, to proceed with the solution we assign loads N, T, and M to the times t_1, ..., t_{l-1}, t_l, ..., t_N, in agreement with the previous time discretization. The problem is then solved as follows:

(1) Find $\mathbf{P}_T$, $\mathbf{P}_N$, λ_N, λ_{T1}, λ_{T2}, ϕ_1, ϕ_2, γ_1, γ_2, and γ_3 such that (23a) and (23b) is satisfied for $\mathbf{A} = \mathbf{0}$, $N = N(t_1)$, $T = T(t_1)$, $M = M(t_1)$, $\mathbf{s}$.

(2) Compute $\mathbf{A}(t_1)$.

(3) Find $\mathbf{P}_T$, $\mathbf{P}_N$, λ_N, λ_{T1}, λ_{T2}, ϕ_1, ϕ_2, γ_1, γ_2, and γ_3 such that (23a) and (23b) are satisfied for $\mathbf{A} = \mathbf{A}(t_1)$, $N = N(t_2)$, $T = T(t_2)$, $M = M(t_2)$, $\mathbf{s}$.

(4) Repeat steps (2) and (3) for $t = t_l$ until $t = t_N$.

To obtain a solution to problem $\mathbf{V}_l^h$ we note that this is a linear complementary problem (in the second statement of the problem), save for the fact that the unknowns of the first four equations are not required to satisfy inequality constraints and complementary conditions. To obtain an LCP the first two equations are eliminated with a simple Gauss elimination. The following two equations cannot be eliminated in this manner since this would imply the inversion of a singular matrix, but a more involved rearrangement suggested by Canarozzi (1980) can be used. The remaining equations are then solved as an LCP. We then obtain $\mathbf{P}_N$ directly, and $\mathbf{P}_T$ is obtained by noting that the last two equations imply

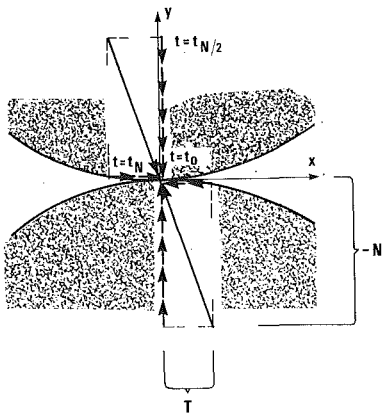

Fig. 2 Nonproportional loading

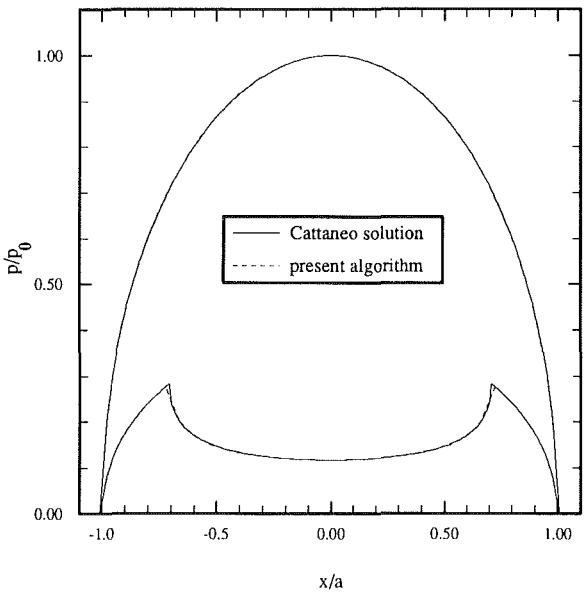

Fig. 3 Comparison between present algorithm and Cattaneo solution

$$\mathbf{P}_T = \frac{\phi_1 + \phi_2}{2}. \tag{24}$$

Finally it is noted that in the implementation of the foregoing method, numerical problems were encountered due to large differences in absolute value between elements of the Eqs. (23*a*). These problems were overcome by multiplying the first and fifth equations of Eqs. (23*a*) with a large but arbitrary factor. Thus $\mathbf{A}$, $\tilde{\mathbf{G}}_{TT}$, $\tilde{\mathbf{G}}_{TN}$, $\mathbf{s}$, $\tilde{\mathbf{G}}_{NT}$, and $\tilde{\mathbf{G}}_{NN}$ were multiplied by this factor when setting up the problem, and γ_1, γ_2, γ_3, λ_N, λ_{T1}, and λ_{T2} appeared in multiplied form in the solution.

5 Numerical Examples

The first example concerns the contact between two half-planes with the same elastic constants, so that no coupling between the normal and tangential directions occur. The initial gap was taken as $s(x) = x^2/R$, i.e., a Hertz-type problem. The half-planes were first pressed together by a normal force $-N$ per unit thickness and then subjected to a tangential load $T = 0.5 \cdot \mu \cdot |N|$ (see Fig. 2). The friction coefficient was taken to be $\mu = 0.4$. For this case a closed-form solution due to Cattaneo exists (see Johnson (1985)) and this solution is compared to the solution with the present algorithm in Fig. 3 where

$$p_0 = \frac{2|N|}{\pi a} \tag{25a}$$

$$a = \left(\frac{4|N|R}{\pi E}\right)^{1/2}. \tag{25b}$$

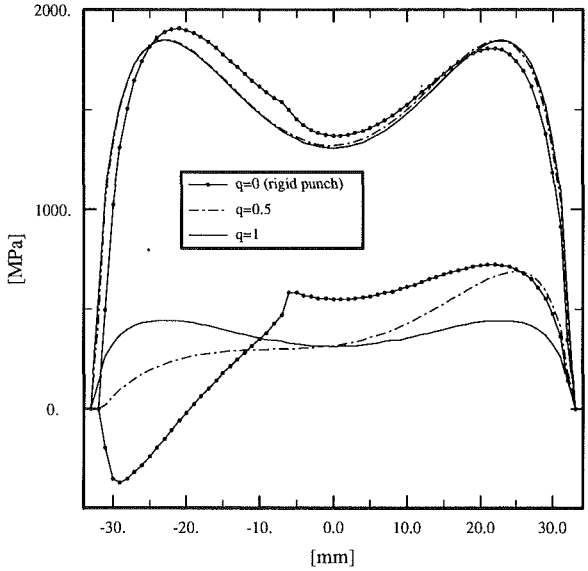

Fig. 4 Normal pressures and tangential tractions due to normal and tangential loads with proportional loading

Here, $E = E^1 = E^2$ is the common modulus of elasticity and R is defined above. In Fig. 3 and in the other examples in this section the normal pressures were multiplied by a factor -1 to obtain positive pressures.

It is noted in Fig. 3 that the two solutions are almost indistinguishable, except for a small discrepancy in tangential tractions at the point where the solution changes from stick to slip conditions. This discrepancy is in part due to the particular discretization chosen in the calculations for the example, since the approximate solution must necessarily break off at a discretization point, and it does so at the discretization point immediately outside the point where the Cattaneo solution changes from stick to slip conditions.

Next a few examples with no known closed-form solution will be studied. In particular, the dependence of contact tractions on the load path and on the difference in Young's moduli E^1 and E^2 between the bodies will be investigated. To this end we introduce S as a measure of combined flexibility and q as the quotient between the Young's moduli of the bodies

$$S = \frac{1}{E^1} + \frac{1}{E^2} \tag{26a}$$

$$q = E^1/E^2. \tag{26b}$$

It is seen from Eqs. (3) and (19) that $\tilde{G}_{NN}$ and $\tilde{G}_{TT}$ will not change if the Young's moduli are changed provided S is kept constant. The changes in contact tractions will then depend only on the coupling terms between the normal and tangential directions, i.e., on $\tilde{G}_{NT}$ and $\tilde{G}_{TN}$. In the following examples the value of S was kept constant at the value obtained with $E^1 = E^2 = 205000$ [MPa]. A value of q was then chosen and E^1 and E^2 were calculated from Eqs. (26). Poisson's constants were $\nu^1 = \nu^2 = 0.3$ in all cases. In the examples the initial gap was taken to be $s = cx^4$ with c such that s (34 mm) = 0.5 [mm]. The half-planes were discretized over a 69 [mm] wide segment into 69 elements of equal width, the circular markers on some of the curves indicating the midpoints of these intervals. The friction coefficient was taken to be $\mu = 0.4$. First, the tractions due to a normal force of $N = -100000$ [N] per unit thickness and a tangential force of $T = 0.6\mu|N|$ were investigated. In Fig. 4 the results are shown when the tangential load was applied proportionally to the normal load as indicated in Fig. 5. The normal pressures show the typical saddle form of a fourth-order problem. It can be noted that the tangential tractions are much more dependent on the value of q than the normal pressures.

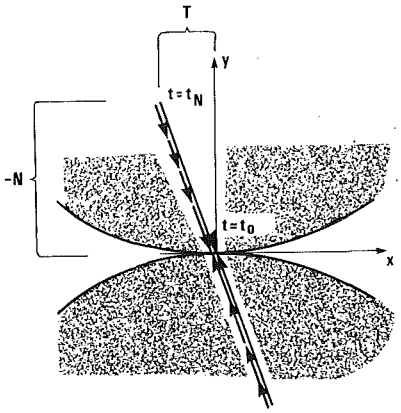

Fig. 5 Proportional loading

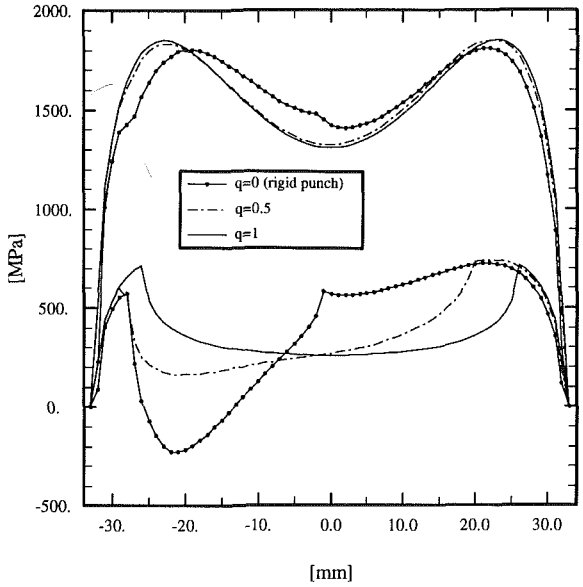

Fig. 6 Normal pressures and tangential tractions due to normal and tangential load with nonproportional loading

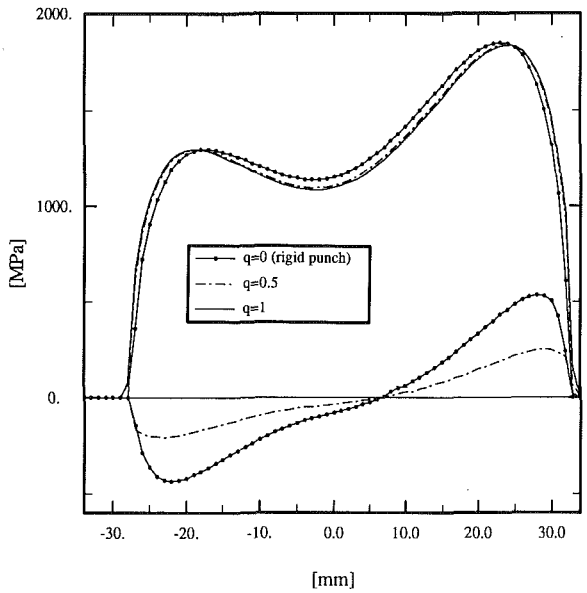

Fig. 7 Normal pressures and tangential tractions due to normal load and applied moment with proportional loading

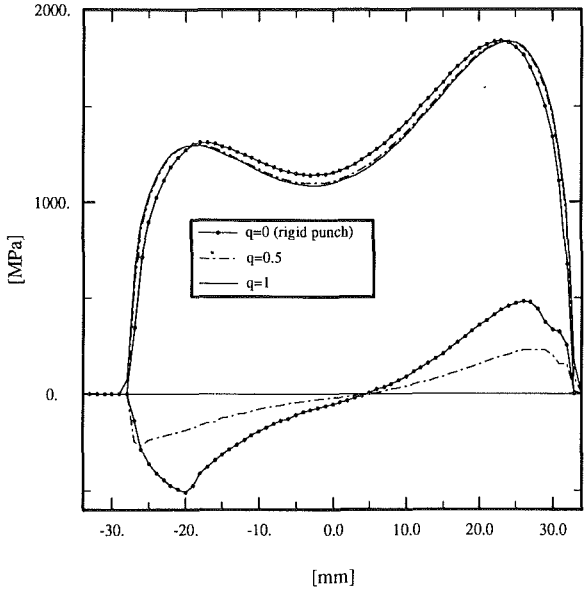

Fig. 8 Normal pressures and tangential tractions due to normal load and applied moment with nonproportional loading

Figure 6 shows the corresponding results when the normal load was first applied and the tangential load was applied after the normal load had been applied as indicated in Fig. 2. Comparing Figs. 4 and 6 it is seen that the tangential traction is heavily load-path dependent, and this is also the case with the same elastic constants in both half-planes.

In the final example a normal load of $N = -80000$ [n] and a moment of $M = -400000$ [Nmm] were applied. Figure 7 shows the result when the normal load and the moment were applied proportionally, analogously to Fig. 5, and Fig. 8 shows the result when the normal load had first been applied and the moment was applied after the normal load had been applied analogously to Fig. 2. Again the tangential tractions are much more dependent of the value of q than the normal pressures, but does not show the large degree of load-path dependence as when a tangential force is applied. Note that no tangential tractions at all occur when $q = 1$ with this loading.

References

Bjarnehed, H. L., 1991, "Rigid Punch on Stressed Orthotropic Half-plane with Partial Slip," ASME Journal of Applied Mechanics, Vol. 58, pp. 128–133.

Canarozzi, A. A., 1980, "On the Resolution of Some Unilaterally Constrained Problems in Engineering," *Computer Methods in Applied Mechanics and Engineering*, Vol. 24, pp. 339–357.

Gladwell, G. M. L., 1980, *Contact Problems of the Classical Theory of Elasticity*, Sijthoff and Nordhoff.

Johansson, L., and Klarbring, A., 1992, "The Rigid Punch Problem with Friction using Variational Inequalities and Linear Complementarity," *Mechanics of Structures and Machines*, Vol. 20, No. 3, pp. 293–319.

Johansson, L., 1990, "Rigid Punch Problems and Green's Functions," Thesis for the Degree of Licentiate of Engineering, University of Linköping, Linköping, Sweden.

Johnson, K. L., 1985, *Contact Mechanics*, Cambridge University Press, Cambridge, U.K.

Muskhelishvili, N. I., 1963, *Some Basic Problems of the Mathematical Theory of Elasticity*, P. Nordhoff.

Nowell, D., Hills, D. A., and Sackfield, A., 1988, "Contact of Dissimilar Elastic Cylinders Under Normal and Tangential Loading," *J. Mech. Phys. Solids*, Vol. 36, No. 1, pp. 59–75.

Spence, D. A., 1973, "An Eigenvalue Problem for Elastic Contact with Finite Friction," *Proc. Camb. Phil. Soc.*, Vol. 73, pp. 249–268.

Timoshenko, S. P., and Goodier, J. N., 1982, *Theory of Elasticity*, McGraw-Hill, New York.

P. Kelly

D. A. Hills

D. Nowell

Department of Engineering Science,
Oxford University,
Oxford OX1 3PJ, England

Stress Field due to a Dislocation on the Interface Between Two Quarter Planes

Solutions are found for the state of stress obtaining along the interface between two bonded quarter planes, induced by an edge dislocation located at an arbitrary point on the interface. Explicit asymptotic expressions are given for the stress at points close to the free surfaces.

1 Introduction

The characteristics of dislocations located at interfaces are of great interest in applied mechanics; first, they enable us to describe the motion, stability, and self-stress associated with "real" dislocations, in the sense of lattice flaws, and secondly, they provide a useful Green's function for the solution of cracks located at the interface. The now classical solution of Dundurs and Sendeckyj (1965) giving the solution for the behavior of an edge dislocation at or near an elastically dissimilar circular inclusion embedded in an infinite matrix has been used as the starting point for many crack solutions. For example, it is ideal for use as a Green's function for solving the problem of a crack between bonded semi-infinite planes (Gautesen and Dundurs, 1987), for cracks at or near circular inclusions (Erdogan et al. 1974) or for cracks in a half-plane near a free surface (Nowell and Hills, 1987). The state of stress for an edge dislocation at the junction of two half-planes has also been found by Hui and Lagoudas (1990). A further fundamental problem which is of great practical interest is that of an interface dislocation in the neighborhood of a free surface (Fig. 1). As well as adding to the repertoire of solutions describing the behavior of real dislocations, the solution provides the means of solving the surface breaking interface crack. This problem is of great fundamental interest, as failure of interfaces may often be initiated at the edge of the joint, where, for some material pairs, a singularity in the stress field occurs. This singularity may be relieved by localized plasticity or by immediate failure of the bond, both of which promote the development of an edge-initiated interface crack.

2 Formulation

Consider two quarter planes (Fig. 1(*a*)), region "1", $x \geq 0$, $y \leq 0$ and region "2", $x \geq 0$, $y \geq 0$ bonded along the interface $x \geq 0, y = 0$ with a dislocation having Burgers vectors b_x, b_y located at a position $(d, 0)$.

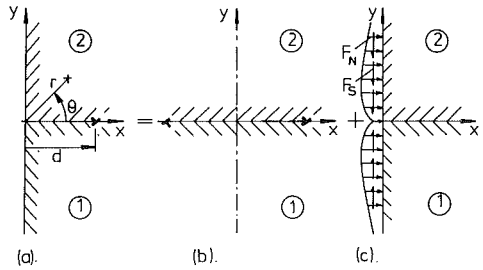

Fig. 1 Geometry of the problem

The primary purpose of this paper is to determine the stress field σ due to the dislocation and this may be found by the superposition of two solutions (as was done by Keer et al. (1983) for the case of a dislocation in a quarter plane). These are as follows:

(i) the stress field $\tilde{\sigma}$ which is itself a composite of two solutions, viz. the state of stress induced in two perfectly bonded half-planes by a dislocation having Burgers components b_x, b_y located at $(d, 0)$, and the state of stress induced by an image dislocation, having Burgers components $-b_x$, $-b_y$ located at $(-d, 0)$, Fig. 1(*b*).

(ii) a stress field $\bar{\sigma}$ intended to clear the boundary $x = 0$ of any remaining tractions, Fig. 1(*c*).

The net stress is then given by

$$\sigma(x, y) = \tilde{\sigma}(x, y) + \bar{\sigma}(x, y). \tag{1}$$

We shall be primarily interested in the stress arising on the interface $y = 0$, $x > 0$, where the stress $\tilde{\sigma}$ may be readily derived from the Airy stress function of a dislocation at the junction of two half-planes given by Dundurs and Mura (1964). Thus[1]

Contributed by the Applied Mechanics Division of THE AMERICAN SOCIETY OF MECHANICAL ENGINEERS for publication in the ASME JOURNAL OF APPLIED MECHANICS.

Discussion on this paper should be addressed to the Technical Editor, Professor Lewis T. Wheeler, Department of Mechanical Engineering, University of Houston, Houston, TX 77204-4792, and will be accepted until four months after final publication of the paper itself in the ASME JOURNAL OF APPLIED MECHANICS.

Manuscript received by the ASME Applied Mechanics Division, Nov. 11, 1991; final revision, May 14, 1992. Associate Technical Editor: R. Abeyaratne.

[1]The normal and shear stresses are continuous across the interface, but the $\tilde{\sigma}_{xx}$ stress component is discontinuous.

$$\frac{\pi}{C}\begin{Bmatrix}\tilde{\sigma}^{(2)}_{xx}(x,0)\\ \tilde{\sigma}^{(1)}_{xx}(x,0)\\ \tilde{\sigma}_{yy}(x,0)\\ \tilde{\sigma}_{xy}(x,0)\end{Bmatrix}=b_x\begin{Bmatrix}-(2+\beta)\pi\delta(x-d)\\ +(2-\beta)\pi\delta(x-d)\\ -\beta\pi\delta(x-d)\\ \dfrac{1}{x-d}-\dfrac{1}{x+d}\end{Bmatrix}$$

$$+b_y\begin{Bmatrix}(1+2\beta)\left[\dfrac{1}{x-d}-\dfrac{1}{x+d}\right]\\ (1-2\beta)\left[\dfrac{1}{x-d}-\dfrac{1}{x+d}\right]\\ \dfrac{1}{x-d}-\dfrac{1}{x+d}\\ \beta\pi\delta(x-d)\end{Bmatrix},\quad x>0 \tag{2}$$

where $\delta(\bullet)$ is the dirac delta function,

$$C=\frac{2\mu_1(1+\alpha)}{(\kappa_1+1)(1-\beta^2)}=\frac{2\mu_2(1-\alpha)}{(\kappa_2+1)(1-\beta^2)}, \tag{3}$$

and α, β are the Dundurs elastic composite parameters defined as (Dundurs, 1969)

$$\alpha=\frac{\Gamma(\kappa_1+1)-(\kappa_2+1)}{\Gamma(\kappa_1+1)+(\kappa_2+1)},\quad \beta=\frac{\Gamma(\kappa_1-1)-(\kappa_2-1)}{\Gamma(\kappa_1+1)+(\kappa_2+1)}, \tag{4}$$

and $\kappa_j = 3 - 4\nu_j$ ($j = 1, 2$) in plane strain, $\kappa_j = (3 - \nu_j)/(1 + \nu_j)$ in plane stress and $\Gamma = \mu_2/\mu_1$ where ν_j, μ_j are, respectively, the Poissons' ratio and shear modulus of material j. (The superscripts on the stress components in Eq. (2) and in what follows refer to regions "1", "2".)

Similarly, the stress arising along the intended free surface $x = 0$ due to the dislocation pair is

$$\frac{\pi}{C}\begin{Bmatrix}\tilde{\sigma}^{(2)}_{xx}(0,y)\\ \tilde{\sigma}^{(2)}_{yy}(0,y)\\ \tilde{\sigma}^{(2)}_{xy}(0,y)\end{Bmatrix}=b_x\begin{Bmatrix}0\\ 0\\ \dfrac{2d}{r_1^4}\,(y^2(1+2\beta)-d^2)\end{Bmatrix}$$

$$+b_y\begin{Bmatrix}\dfrac{2d}{r_1^4}\,(y^2-d^2(1+2\beta))\\ -\dfrac{2d}{r_1^4}\,(y^2(3+2\beta)+d^2)\\ 0\end{Bmatrix} \tag{5}$$

where $r_1^2 = y^2 + d^2$ and

$$\tilde{\sigma}^{(1)}_{ij}(0, y; \beta)=\tilde{\sigma}^{(2)}_{ij}(0, y; -\beta). \tag{6}$$

The choice of image dislocations has, of course, already rendered the $x = 0$ line free of direct tractions for the case of a dislocation b_x and free of shear tractions for a dislocation b_y. Thus, from Eqs. (5), we need now to apply direct tractions $F_N(y)$ and shear tractions $F_s(y)$ along the $x = 0$ line in order to satisfy the free boundary conditions, where these distributions are given by

$$F^{(2)}_N(r;\beta)=\bar{\sigma}^{(2)}_{\theta\theta}(r,\pi/2)=\frac{C}{\pi}\,b_y\left\{-\frac{2d}{r_1^4}\,[r^2-d^2(1+2\beta)]\right\}$$

$$F^{(2)}_S(r;\beta)=\bar{\sigma}^{(2)}_{r\theta}(r,\pi/2)=\frac{C}{\pi}\,b_x\left\{\frac{2d}{r_1^4}\,[r^2(1+2\beta)-d^2]\right\}$$

$$F^{(1)}_i(r;\beta)=\bar{\sigma}^{(1)}(r,-\pi/2)=F^{(2)}_i(r;-\beta),\quad i=N, S \tag{7}$$

where along $x = 0$, $y^2 = r^2$, $r_1^2 = r^2 + d^2$ and we have now employed a polar coordinate set (Fig. 1(*a*)).

The next step is to deduce the state of stress induced by the tractions F_N, F_S, and the most convenient way to do this is to transform the problem into the complex plane by employing Mellin transforms. The Mellin transforms of r^2F_N, r^2F_S are defined as

$$\hat{F}_i(s;\beta)=\int_0^\infty F_i(r;\beta)r^{s+1}dr,\quad i=N, S. \tag{8}$$

Substituting in from Eqs. (7) the transforms of the applied loads may be found explicitly (Erdélyi et al. 1954), and are

$$\hat{F}^{(2)}_N(s;\beta)=\frac{Cb_yd^{s+1}}{\sin(s\pi/2)}\,\{(s+1)+\beta s\},\ \hat{F}^{(1)}_N(s;\beta)=\hat{F}^{(2)}_N(s;-\beta)$$

$$\hat{F}^{(2)}_S(s;\beta)=-\frac{Cb_xd^{s+1}}{\sin(s\pi/2)}\,\{(s+1)+\beta(s+2)\},$$

$$\hat{F}^{(1)}_S(s;\beta)=\hat{F}^{(2)}_S(s;-\beta). \tag{9}$$

Once the transforms of the applied loads are known, the transforms of the stress field along the interface $y = 0$ due to these loads may be found from results given by Bogy (1970). Let the transforms of $r^2\bar{\sigma}_{\theta\theta}(r,\theta)$, $r^2\bar{\sigma}_{r\theta}(r,\theta)$, $r^2\sigma_{rr}(r,\theta)$ obtaining along the interface ($\theta = 0$) be

$$\begin{aligned}\hat{\sigma}_{\theta\theta}(s,0)&=b_x\hat{\sigma}_{x\theta\theta}(s,0)+b_y\hat{\sigma}_{y\theta\theta}(s,0)\\ \hat{\sigma}_{r\theta}(s,0)&=b_x\hat{\sigma}_{xr\theta}(s,0)+b_y\hat{\sigma}_{yr\theta}(s,0)\\ \hat{\sigma}^{(2)}_{rr}(s,0^+)&=b_x\hat{\sigma}^{(2)}_{xrr}(s,0^+)+b_y\hat{\sigma}^{(2)}_{yrr}(s,0^+)\\ \hat{\sigma}^{(1)}_{rr}(s,0^-)&=b_x\hat{\sigma}^{(1)}_{xrr}(s,0^-)+b_y\hat{\sigma}^{(1)}_{yrr}(s,0^-)\end{aligned} \tag{10}$$

so that each stress component is made up of two contributions, one for each component of the Burgers vector. Then, from Bogy (1970, Eqs. 3.14, 3.15):

$$\hat{\sigma}_{x\theta\theta}(s,0)=\frac{Cd^{s+1}}{\Delta(s)}\,\{-(1-\alpha\beta)(\alpha-\beta)(s+1)^4$$
$$+\alpha(1-\beta^2)(s+1)[(s+1)^2-\cos^2(s\pi/2)]+\beta\cos^2(s\pi/2)$$
$$-[\alpha^2\beta-(\alpha-2\beta+\alpha\beta^2)\cos^2(s\pi/2)](s+1)^2\}$$

$$\hat{\sigma}_{y\theta\theta}(s,0)=\frac{Cd^{s+1}\cos(s\pi/2)}{\Delta(s)\sin(s\pi/2)}\,\{(\alpha-\beta)^2(s+1)^4$$
$$+[1-\alpha^2-\beta^2-(1-2\alpha\beta+\beta^2)\cos^2(s\pi/2)](s+1)^2+\beta^2\cos^2(s\pi/2)$$

$$\hat{\sigma}_{xr\theta}(s,0)=\hat{\sigma}_{y\theta\theta}(s,0)$$

$$\hat{\sigma}_{yr\theta}(s,0)=\frac{Cd^{s+1}}{\Delta(s)}\,\{+(1-\alpha\beta)(\alpha-\beta)(s+1)^4$$
$$+\alpha(1-\beta^2)(s+1)[(s+1)^2-\cos^2(s\pi/2)]-\beta\cos^2(s\pi/2)$$
$$+[\alpha^2\beta-(\alpha-2\beta+\alpha\beta^2)\cos^2(s\pi/2)](s+1)^2\}$$

$$\hat{\sigma}^{(1)}_{xrr}(s,0^-)=\frac{Cd^{s+1}}{\Delta(s)}\,\{(\alpha-\beta)(s+1)^4[(1-\beta)(2\beta-\alpha)+(1-\alpha)]$$
$$+(1-\beta^2)(\alpha-2\beta)(s+1)[(s+1)^2-\cos^2(s\pi/2)]$$
$$+(s+1)^2[2\alpha(\alpha-1)-\alpha\beta(\alpha-2\beta)+(\alpha-4\beta(\alpha-\beta)$$
$$+\beta^2(\alpha-2\beta))\cos^2(s\pi/2)]+\beta(1-2\beta)\cos^2(s\pi/2)\}$$

$$\hat{\sigma}^{(1)}_{yrr}(s,0^-)=\frac{Cd^{s+1}\cos(s\pi/2)}{\Delta(s)\sin(s\pi/2)}\,\{(\alpha-\beta)^2(1-2\beta)(s+1)^4$$
$$+2(\alpha-1)(1-\beta^2)(s+1)[1-\cos^2(s\pi/2)]$$
$$+(s+1)^2[-(\alpha-1)^2+\beta(\beta-2)+2\beta(\alpha^2-\alpha\beta+\beta^2)$$
$$+(1-2\alpha+2\beta(1+\alpha)-\beta^2(3-2\beta+2\alpha))\cos^2(s\pi/2)]$$
$$+\beta^2(1-2\beta)\cos^2(s\pi/2)\}$$

$$\hat{\sigma}^{(2)}_{xrr}(s,0^+;\alpha,\beta)=\frac{1+\alpha}{1-\alpha}\,(-\hat{\sigma}^{(1)}_{xrr}(s,0^-;-\alpha,-\beta))$$

$$\hat{\sigma}^{(2)}_{yrr}(s,0^+,\alpha,\beta)=\frac{1+\alpha}{1-\alpha}\,(+\hat{\sigma}^{(1)}_{yrr}(s,0^-;-\alpha,-\beta)) \tag{11}$$

and

$$\Delta(s)=(\alpha-\beta)^2(s+1)^4+[2\beta(\alpha-\beta)\cos^2(s\pi/2)-\alpha^2](s+1)^2$$
$$+[(\beta^2-1)\cos^2(s\pi/2)+1]\cos^2(s\pi/2). \tag{12}$$

To obtain the stresses in the physical problem, we apply the inverse transform, namely

$$\bar{\sigma}_{ij}(r, \theta)=\frac{1}{2\pi i}\int_{c-i\infty}^{c+i\infty}\hat{\sigma}_{ij}(s, \theta)r^{-(s+2)}ds. \tag{13}$$

The transformed stresses $\hat{\sigma}_{\theta\theta}(s, 0)$, $\hat{\sigma}_{r\theta}(s, 0)$ and $\hat{\sigma}_{rr}(s, 0)$ are regular at $s = -1$ and so we may use the path of integration in (13) defined by $c = -1$. To convert Eq. (13) into a line integral[2] we make the substitution $-(s + 1) = \varphi + i\xi$ and integrate along the $\varphi = 0$ axis which yields, in terms of the $x - y$ cartesian coordinate set

$$\frac{\pi}{C}\bar{\sigma}_{xij}(x, 0)=\frac{1}{x}\int_0^\infty\left[A_{xij}(\xi;\alpha,\beta)\cos\left(\xi\log\frac{x}{d}\right)+B_{xij}(\xi,\alpha,\beta)\sin\left(\xi\log\frac{x}{d}\right)\right]d\xi \tag{14a}$$

$$\frac{\pi}{C}\bar{\sigma}_{yij}(x, 0)=\frac{1}{x}\int_0^\infty\left[A_{yij}(\xi;\alpha,\beta)\cos\left(\xi\log\frac{x}{d}\right)+B_{yij}(\xi;\alpha,\beta)\sin\left(\xi\log\frac{x}{d}\right)\right]d\xi \tag{14b}$$

where[3]

$$A_{xyy}=\{-(1-\alpha\beta)(\alpha-\beta)\xi^4+[\alpha^2\beta+(\alpha-2\beta+\alpha\beta^2)\sinh^2(\xi\pi/2)]\xi^2-\beta\sinh^2(\xi\pi/2)\}/\Delta(\xi)$$

$$B_{xyy}=\{-\alpha(1-\beta^2)\xi[\xi^2-\sinh^2(\xi\pi/2)]\}/\Delta(\xi)$$

$$A_{yyy}=0$$

$$B_{yyy}=\frac{\sinh(\xi\pi/2)}{\cosh(\xi\pi/2)}\{-(\alpha-\beta)^2\xi^4+[1-\alpha^2-\beta^2+(1-2\alpha\beta+\beta^2)\sinh^2(\xi\pi/2)]\xi^2+\beta^2\sinh^2(\xi\pi/2)\}/\Delta(\xi)$$

$$A_{xxy}=A_{yyy}=0,\quad B_{xxy}=B_{yyy},\quad A_{yxy}=-A_{xyy},\quad B_{yxy}=B_{xyy}$$

$$A^{(1)}_{xxx}=\{(\alpha-\beta)[(1-\beta)(2\beta-\alpha)+(1-\alpha)]\xi^4-\beta(1-2\beta)\sinh^2(\xi\pi/2)-\xi^2[2\alpha(\alpha-1)-\alpha\beta(\alpha-2\beta)-(\alpha-4\beta(\alpha-\beta)+\beta^2(\alpha-2\beta))\sinh^2(\xi\pi/2)]\}/\Delta(\xi)$$

$$B^{(1)}_{xxx}=\{-(\alpha-2\beta)(1-\beta^2)\xi[\xi^2-\sinh^2(\xi\pi/2)\}/\Delta(\xi)$$

$$A^{(1)}_{yxx}=\frac{\sinh(\xi\pi/2)}{\cosh(\xi\pi/2)}\{2(\alpha-1)(1-\beta^2)\xi[1+\sinh^2(\xi\pi/2)]\}/\Delta(\xi)$$

$$B^{(1)}_{yxx}=\frac{\sinh(\xi\pi/2)}{\cosh(\xi\pi/2)}\{-(\alpha-\beta)^2(1-2\beta)\xi^4+\beta^2(1-2\beta)\sinh^2(\xi\pi/2)+\xi^2[-(\alpha-1)^2+\beta(\beta-2)+2\beta(\alpha^2-\alpha\beta+\beta^2)-(1-2\alpha+2\beta(1+\alpha)-\beta^2(3-2\beta+2\alpha))\sinh^2(\xi\pi/2)]\}/\Delta(\xi)$$

$$A^{(2)}_{xxx}(\xi;\alpha,\beta)=-A^{(1)}_{xxx}(\xi;-\alpha,-\beta),$$

$$B^{(2)}_{xxx}(\xi;\alpha,\beta)=-B^{(1)}_{xxx}(\xi;-\alpha,-\beta)$$

$$A^{(2)}_{yxx}(\xi;\alpha,\beta)=A^{(1)}_{yxx}(\xi;-\alpha,-\beta),$$

$$B^{(2)}_{yxx}(\xi;\alpha,\beta)=B^{(1)}_{yxx}(\xi;-\alpha,-\beta) \tag{15}$$

and, in terms of the new variable ξ,

$$\Delta(\xi)=(\alpha-\beta)^2\xi^4+[2\beta(\alpha-\beta)\sinh^2(\xi\pi/2)+\alpha^2]\xi^2+[(\beta^2-1)\sinh^2(\xi\pi/2)-1]\sinh^2(\xi\pi/2). \tag{16}$$

The integrals contained in Eqs. (14) are, perhaps not surprisingly, intractable analytically. However, a useful check on the algebra to this point may be made by specializing the elastic constants to render $\alpha = \beta = 0$, i.e., make the quarter planes similar, whereupon the integrals do become feasible and we are able to recover the solution for a dislocation in a homogeneous half-plane. In this case, the only nonzero functions in Eqs. (15) which remain are

$$B_{yyy}(\xi)=B_{xxy}(\xi)=\frac{-2\xi^2}{\sinh(\pi\xi)}$$

$$B_{yxx}(\xi)=\frac{2\xi^2}{\sinh(\pi\xi)},\quad A_{yxx}(\xi)=\frac{4\xi}{\sinh(\pi\xi)}. \tag{17}$$

Using the integrals

$$\int_0^\infty\frac{\xi^2\sin[\xi\log(x/d)]}{\sinh(\pi\xi)}d\xi=-\frac{1}{2}\frac{\partial^2}{\partial^2 a}\tanh\left(\frac{a}{2}\right)$$

$$\int_0^\infty\frac{\xi\cos[\xi\log(x/d)]}{\sinh(\pi\xi)}d\xi=\frac{1}{2}\frac{\partial}{\partial a}\tanh\left(\frac{a}{2}\right) \tag{18}$$

where $a = \log(x/d)$ and from Eqs. (1), (2), (3), and (14), we find that the stress field due to a dislocation in a half-plane a distance d from the surface is given by

$$\frac{\pi(\kappa+1)}{2\mu}\sigma_{yyy}(x, 0)=\frac{\pi(\kappa+1)}{2\mu}\sigma_{xxy}(x, 0)=\frac{1}{x-d}-\frac{1}{x+d}-\frac{2d}{(x+d)^2}+\frac{4d^2}{(x+d)^3} \tag{19a}$$

$$\frac{\pi(\kappa+1)}{2\mu}\sigma_{yxx}(x, 0)=\frac{1}{x-d}-\frac{1}{x+d}+\frac{6d}{(x+d)^2}-\frac{4d^2}{(x+d)^3}, \tag{19b}$$

which agrees with the general stress field given by Nowell and Hills (1987).

3 Numerical Solution

For dissimilar pairs of materials the integrals in Eqs. (14) must be solved numerically. It will be noted that the integrals are all of the form

$$\int_0^\infty f(\xi)\begin{pmatrix}\cos\\ \sin\end{pmatrix}\left(\xi\log\frac{x}{d}\right)d\xi. \tag{20}$$

These integrals are difficult to evaluate efficiently since, as $x/d \to 0$, the argument of the trigonometric functions can be quite large resulting in rapidly oscillating integrands. Special care is needed with the numerical quadrature and a procedure due to Filon (see Tranter, 1956) is utilized. First, we write the integrals as

$$\int_0^\infty f(\xi)\begin{pmatrix}\cos\\ \sin\end{pmatrix}\left(\xi\log\frac{d}{x}\right)d\xi=\int_0^N f(\xi)\begin{pmatrix}\cos\\ \sin\end{pmatrix}\left(\xi\log\frac{d}{x}\right)d\xi+\int_N^\infty f(\xi)\begin{pmatrix}\cos\\ \sin\end{pmatrix}\left(\xi\log\frac{d}{x}\right)d\xi. \tag{21}$$

The second term on the right-hand side of (21) can be made arbitrarily small for sufficiently large N, since the functions A_{kij} and $B_{kij} \to$ order $0(\xi^2 e^{-\xi\pi})$ or less as $\xi \to \infty$. Considering the first term and dividing the interval $[0, N]$ into $2n$ equal parts of length h, we have (Tranter, 1956)

$$\frac{1}{x}\int_0^\infty f(\xi)\cos\left(\xi\log\frac{x}{d}\right)d\xi\approx\frac{h}{x}\left\{\bar{\alpha}f(N)\sin\left(N\log\frac{x}{d}\right)+\bar{\beta}\left[\frac{1}{2}f(0)+\sum_{i=1}^{n-1}f(\xi_{2i})\cos\left(\xi_{2i}\log\frac{x}{d}\right)+\frac{1}{2}f(N)\cos\left(N\log\frac{x}{d}\right)\right]+\bar{\gamma}\sum_{i=1}^{n}f(\xi_{2i-1})\cos\left(\xi_{2i-1}\log\frac{x}{d}\right)\right\}$$

[2]See Pipes and Harvill (1971), Chapter 1, for further information regarding integrals of the type given in Eq. (13).

[3]In the following expressions, (1), (2) have been added as in the earlier equations to denote the half-plane in which the result applies.

$$\frac{1}{x}\int_0^\infty f(\xi)\sin\left(\xi\log\frac{x}{d}\right)d\xi$$

$$\approx\frac{h}{x}\left\{\bar{\alpha}\left[f(0)-f(N)\cos\left(N\log\frac{x}{d}\right)\right]\right.$$

$$+\bar{\beta}\left[\sum_{i=1}^{n-1}f(\xi_{2i})\sin\left(\xi_{2i}\log\frac{x}{d}\right)+\frac{1}{2}f(N)\sin\left(N\log\frac{x}{d}\right)\right]$$

$$\left.+\bar{\gamma}\sum_{i=1}^{n}f(\xi_{2i-1})\sin\left(\xi_{2i-1}\log\frac{x}{d}\right)\right\} \quad (22a, b)$$

where $\xi_i = ih$,

$$\bar{\alpha}=[\Theta^2+\Theta\sin\Theta\cos\Theta-2\sin^2\Theta]/\Theta^3$$

$$\bar{\beta}=2[\Theta(1+\cos^2\Theta)-2\sin\Theta\cos\Theta]/\Theta^3$$

$$\bar{\gamma}=4[\sin\Theta-\Theta\cos\Theta]/\Theta^3 \quad (23)$$

and $\Theta = h \cdot \log(x/d)$. Also, by examining Eqs. (15) in the limit as $\xi \to 0$ we find that in Eqs. (22) we have

$$A_{xyy}(0;\alpha,\beta)=+\beta, \quad A_{yxy}(0;\alpha,\beta)=-\beta$$

$$A_{(1)xxx}(0;\alpha,\beta)=-\frac{2\alpha(\alpha-1)+\alpha\beta(2\beta-\alpha)+\beta\pi^2(1-2\beta)/4}{\alpha^2-\pi^2/4}$$

$$A^{(1)}_{yxx}(0;\alpha,\beta)=-\frac{\pi(1-\alpha)(1-\beta^2)}{\alpha^2-\pi^2/4}$$

$$A^{(2)}_{xxx}(0;\alpha,\beta)=-A^{(1)}_{xxx}(0;-\alpha,-\beta),$$

$$A^{(2)}_{yxx}(0;\alpha,\beta)=A^{(1)}_{yxx}(0;-\alpha,-\beta) \quad (24)$$

with the remaining functions A_{kij}, $B_{kij} \to 0$ as $\xi \to 0$. Convergence of Eq. (21) was obtained with $N = 12$, $n = 50$ for $x/d > 0.01$, but values of x/d down to 1.0×10^{-7} demanded n be set as high as 300.

4 Asymptotic Analysis

As $(x/d) \to 0$ the characteristics of the solution are dominated by the well-known asymptotic behavior at the apex of two bonded quarter planes (Bogy, 1970). (The most general problem, i.e., the asymptotic behavior at the apex of two bonded wedges of arbitrary angles has been investigated separately (Bogy, 1971; Kelly et al., 1992)).

The asymptotic behavior of the stress field along $y = 0$ due to the prescribed tractions F_N, F_S is obtained by evaluating the most dominant terms of $\bar{\sigma}_{ij}(r, \theta)$ in Eq. (13). This is achieved by carrying out residue computations at the poles of the integrand in Eq. (13). An elementary example of the procedure is outlined by Bogy and Sternberg (1968). Three kinds of behavior may be anticipated depending on the combination of elastic constants obtaining:

I $\alpha(\alpha - 2\beta) > 0$. The stress field is in this case singular with the asymptotic behavior of the stress field being given by the residue of the integrand in (13) at the simple pole $s = s_1$, where s_1 is the zero of $\Delta(s)$ in the range $-2 < s < -1$. Thus,

$$\frac{\pi d}{C}\bar{\sigma}_{kij}(x,0)=\left\{\frac{\hat{\sigma}_{kij}(s_1,0)\Delta(s_1)}{Cd^{s_1+1}}\right\}\frac{\pi}{\Delta'(s_1)}\left(\frac{x}{d}\right)^{-\lambda}$$

$$+O\left[\left(\frac{x}{d}\right)^{-\lambda}\right] \quad (25)$$

where $\lambda = s_1 + 2$. λ can take values in the range $0 < \lambda < 0.41$ depending on the values of α and β (Bogy, 1970). These material combinations also have a simple pole at $s = -2$, and the residue there gives a bounded second term to the above expansion. These terms are presented in Case III.

II $\alpha(\alpha - 2\beta) = 0$. These combinations of materials give rise to the possibility of a logarithmically varying stress field (Eqs. 4.6, 4.7 Bogy, 1970). However, it transpires for the present problem the stress field is bounded as $x/d \to 0$ with the asymptotic behavior given by

$$\bar{\sigma}_{xyy}(x,0)=\frac{16\pi\alpha(1-\beta^2)}{16\beta^2+\pi^2(1-\alpha^2)}\frac{C}{\pi d}+o(1)$$

$$\bar{\sigma}_{yyy}(x,0)=\frac{2C}{\pi d}+o(1)$$

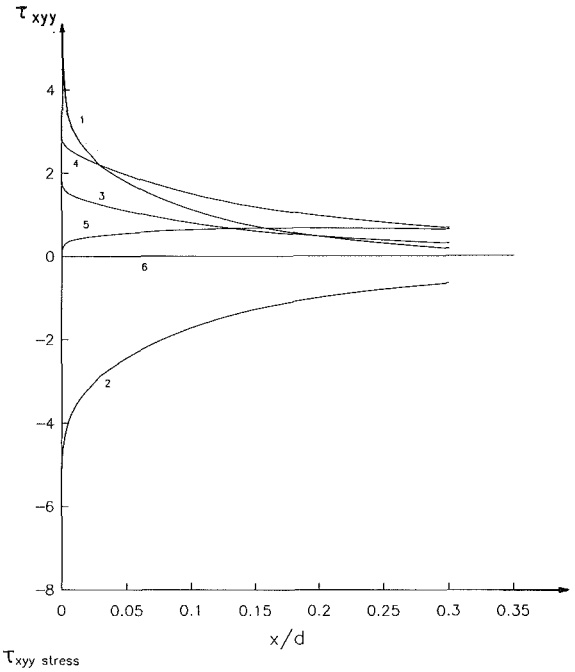

Fig. 2 Variation of the stress component τ_{yy} with position along the interface for a dislocation having a Burgers vector in the x-direction

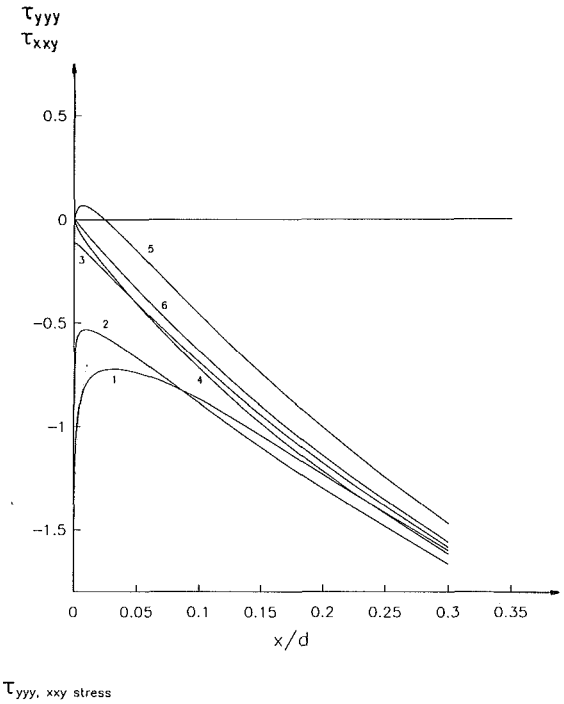

Fig. 3 Variation of the stress component τ_{yy} with position along the interface for a dislocation having a Burgers vector in the y-direction

$$\bar{\sigma}_{xxy}(x, 0) = \frac{2C}{d\pi} + o(1) = -F_s(0, \beta)/b_x$$

$$\frac{\pi d}{C}\,\bar{\sigma}_{yxy}(x, 0) = \frac{\pi d}{C}\,\bar{\sigma}^{(1)}_{xxx}(x, 0) = \frac{\pi d}{C}\,\bar{\sigma}^{(2)}_{xxx}(x, 0) = o(1)$$

$$\bar{\sigma}^{(1)}_{yxx}(x, 0^-) = \frac{2C}{d\pi}\,(1-2\beta) + o(1) = +F^{(1)}_N(0, \beta)/b_y$$

$$\bar{\sigma}^{(2)}_{yxx}(x, 0^+) = \frac{2C}{d\pi}\,(1+2\beta) + o(1) = +F^{(2)}_N(0, \beta)/b_y. \quad (26)$$

These expressions take on the values of the applied clearing tractions F_N, F_s at $x = 0$, $\theta = \mp\pi/2$. (see Eq. (7)). Note that the expressions in Eqs. (26) agree with those considered by Bogy but include one further term in the series expansion.

III $\alpha(\alpha - 2\beta) < 0$. Here, again, the stress field is not singular with the stress components having the same values as for Case II above except σ_{xyy}, which is of order $o(1)$ as $(x/d) \to 0$.

5 Results

Using normalized dimensionless stress components defined as

$$\tau_{kij}(x/d, 0) = \frac{d\pi}{Cb_k}\,\sigma_{kij}(x/d, 0), \quad i, j, k = x, y, \quad (27)$$

Figs. 2, 3, 4, 5, and 6 show, respectively, the stresses τ_{xyy}, $\tau_{yyy} = \tau_{xxy}$, τ_{yxy}, τ_{xxx} and τ_{yxx}[4] along the interface $y = 0$ as given by Eqs. (1), (2), (14), and (27) as a function of (x/d) for the material combinations, i.e., (α, β) values, listed in Table 1, column 2. The labels on the graphs refer to the numbers in column 1 of the table while column 3 refers to the asymptotic nature of the stress field as defined in Section 4.

The graphs display the nature of the stress field as $(x/d) \to 0$ as given by Eqs. (1), (2), (25)-(26). For example, with $(\alpha, \beta) = (.5, 0)$ (Case I) we find that, in Eq. (25), $\lambda = 0.147$ and the following asymptotic stress fields arise:

$$\tau_{xyy} \to 1.265\left(\frac{x}{d}\right)^{-0.147} + o(1)$$

$$\tau_{xxy} = \tau_{yyy} \to -0.356\left(\frac{x}{d}\right)^{-0.147} + o(1)$$

$$\tau_{yxy} \to 0.100\left(\frac{x}{d}\right)^{-0.147} + o(1)$$

$$\tau^{(1)}_{xxx} \to 0.544\left(\frac{x}{d}\right)^{-0.147} + o(1)$$

$$\tau^{(1)}_{yxx} \to -0.153\left(\frac{x}{d}\right)^{-0.147} + o(1)$$

$$\tau^{(2)}_{xxx} \to -0.898\left(\frac{x}{d}\right)^{-0.147} + o(1)$$

$$\tau^{(2)}_{yxx} \to 0.253\left(\frac{x}{d}\right)^{-0.147} + o(1). \quad (28)$$

These one-term expansions agree with the full numerical solution for material combination 1 (see Table 1) for values of $(x/d) < .001$. For some stress components, the asymptotes remain reasonably accurate up to much larger values of x/d. However, the range of validity of these asymptotes depends on the (α, β) values of the material pair under consideration and under the stress component under consideration. Similar expressions to those given by Eq. (28) can be obtained for material combinations 2, $(\alpha, \beta) = (-.6, -.2)$, and 3, $(\alpha, \beta) = (.3, .1)$, for which $\lambda = 0.0929$ and $\lambda = 0.0239$, respectively.

[4]Since the strain in the x direction, ϵ_{xx}, is continuous across the interface, $\tau^{(2)}_{kxx}$ may be derived from $\tau^{(1)}_{kxx}$ by use of Hookes law and is omited for brevity.

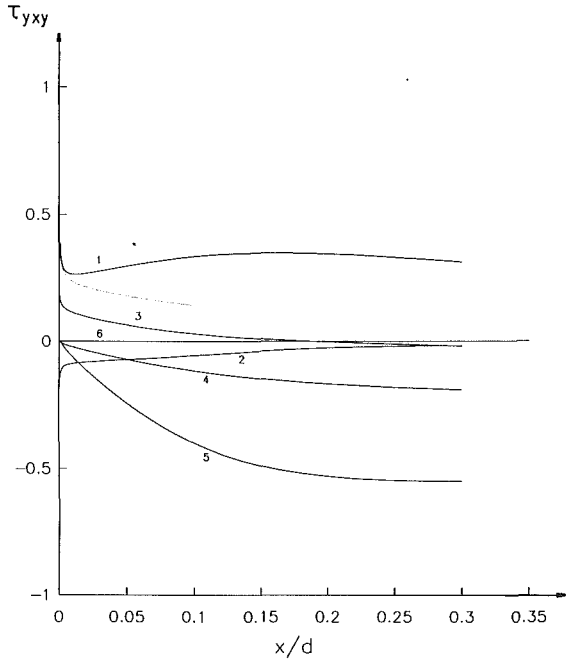

Fig. 4 Variation of the stress component τ_{xy} with position along the interface for a dislocation having a Burgers vector in the y-direction

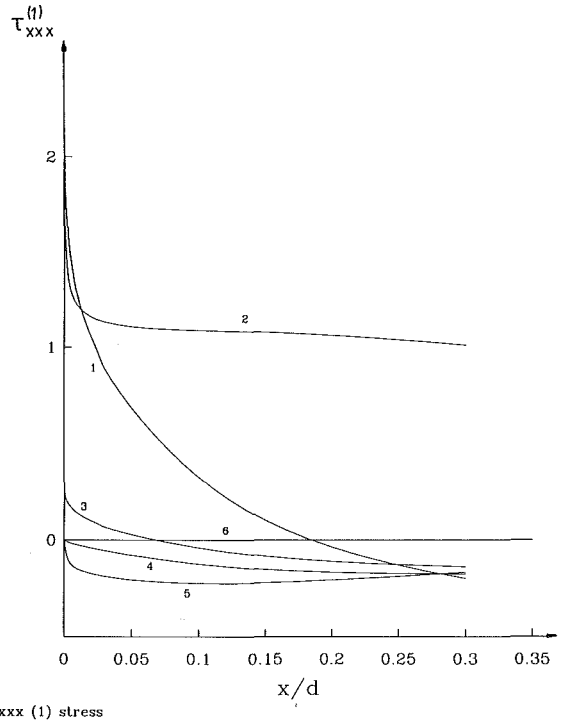

Fig. 5 Variation of the stress component τ_{xx} in body "1" with position along the interface for a dislocation having a Burgers vector in the x-direction

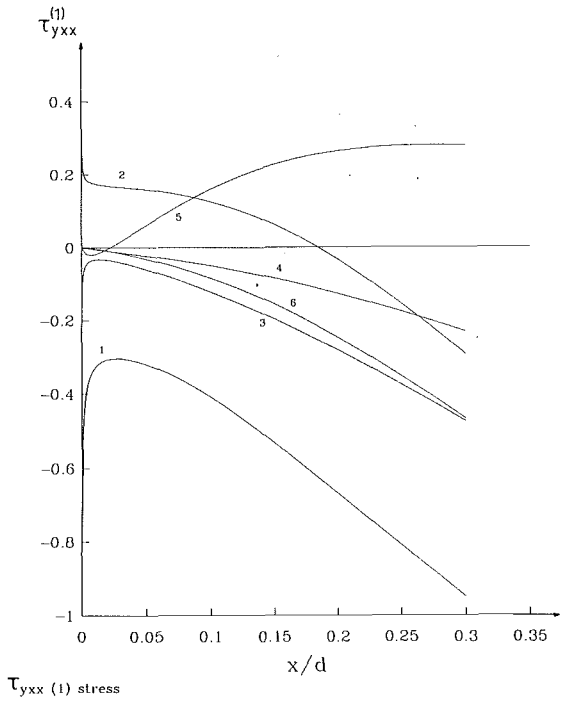

Fig. 6 Variation of the stress component τ_{xx} in body "1" with position along the interface for a dislocation having a Burgers vector in the *y*-direction

Table 1

	(α,β)	asymptotic case	
1	(.5,0)	I	Power singularity
2	(−.6,−.2)	I	Power singularity
3	(.3,.1)	I	Power singularity
4	(.5,.25)	II	Bounded stress
5	(.1,.3)	III	Bounded stress
6	(0,0)	Homogeneous	Bounded stress

For material combinations satisfying $\alpha(\alpha - 2\beta) \leq 0$, all stress components τ are of order $o(1)$ except τ_{xyy} which goes to either $16\pi\alpha(1 - \beta^2)/(16\beta^2 + \pi^2(1 - \alpha^2))$ (Case II) or $o(1)$ (Case III).

The values have been plotted for $x/d < 0.3$ as this is the region of greatest interest, where the influence of the free surface is strong. Remote from the free surface the bonded half-planes solution given by Eq. (2) is recovered.

For the material pairs chosen (Table 1) the influence of the free surface becomes very small by the time x/d reaches 0.5 for all the stress components except τ_{yxx}. In the case of this stress the influence of the surface persists up to $x/d \approx 1.0$.

6 Conclusions

The burden of this paper is to deduce the display the influence functions for an edge dislocation at the interface of two bonded quarter planes. This has been achieved through Eqs. (1), (2), (14), and (27), but inevitably closed-form expressions are not attainable although the case of similar quarter planes; i.e., a half-plane can be evaluated and is shown to agree with earlier results. Further, we have investigated carefully the behavior of the stress field very near to the surface of the solid and given explicit asymptotic expressions for this case. The intended principal use of the results is to provide a Green's function for the solution of an interface crack breaking a free surface.

References

Body, D. B., and Sternberg, E., 1968, "The Effect of Couple Stresses on the Corner Singularity due to an Asymmetric Shear Loading," *Int. J. Sol. Struct.*, Vol. 4, pp. 159–174.

Bogy, D. B., 1970, "On the Problem of Edge Bonded Elastic Quarter-Planes Loaded at the Boundary," *Int. J. Sol. Struct.*, Vol. 6, pp. 1287–1313.

Bogy, D. B., 1971, "Two Edge Bonded Elastic Wedges of Different Materials and Wedge Angles Under Surface Tractions," ASME JOURNAL OF APPLIED MECHANICS, Vol. 38, pp. 377–386.

Comninou, M., 1977, "A Property of Interface Dislocations," *Phil. Mag.*, Vol. 36, No. 5, pp. 1281–1283.

Comninou, M., 1977, "The Interface Crack," ASME JOURNAL OF APPLIED MECHANICS, Vol. 44, pp. 631–636.

Dundurs, J., and Mura, T., 1964, "Interaction Between an Edge Dislocation and a Circular Inclusion," *J. Mech. Phys. Solids*, Vol. 12, pp. 177–189.

Dundurs, J., and Sendeckyj, G. P., 1965, "An Edge Dislocation Inside a Circular Inclusion," *J. Mech. Phys. Sols.*, Vol. 13, pp. 141–147.

Dundurs, J., 1969, discussion, ASME JOURNAL OF APPLIED MECHANICS, Vol. 36, pp. 650–652.

Erdélyi, A., Magnus, W., Oberhettinger, F., and Tricomi, F. G., 1954, *Tables of Integral Transforms*, Vol. I, McGraw-Hill, New York, Chapter 6.

Erdogan, F., Gupta, G. D., and Ratwani, M., 1974, "Interaction Between a Circular Inclusion and an Arbitrarily Oriented Crack," ASME JOURNAL OF APPLIED MECHANICS, Vol. 41, pp. 1007–1013.

Gautesen, A. K., and Dundurs, J., 1987, "The Interface Crack in a Tension Field," ASME JOURNAL OF APPLIED MECHANICS, Vol. 54, pp. 93–98.

Hui, C.-Y., and Lagoudas, D. C., 1990, "Stress Fields of Interface Dislocations," ASME JOURNAL OF APPLIED MECHANICS, Vol. 57, pp. 247–248.

Keer, L. M., Lee, J. C., and Mura, T., 1983, "Stress Distributions for a Quarter Plane Containing an Arbitrarily Oriented Crack," ASME JOURNAL OF APPLIED MECHANICS, Vol. 50, pp. 43–49.

Kelly, P., Hills, D. A., and Nowell, D., 1992, "The Design of Joints Between Elastically Dissimilar Components," *J. Strain Analysis*, Vol. 27, pp. 15–20.

Nowell, D., and Hills, D. A., 1987, "Open Cracks at or Near a Free Edge," *J. Strain Analysis*, Vol. 22, No. 3, pp. 177–185.

Pipes, L., and Harvill, L., 1971, *Applied Mathematics for Engineers and Physicists*, 3rd ed., McGraw-Hill, New York.

Tranter, C. J., 1956, *Integral Transforms in Mathematical Physics*, 2nd ed., John Wiley and Sons, New York, Chapter 5.

A Computational Model for Fe Ductile Plastic Damage Analysis of Plate Bending

Guangyu Shi[1]
Research Associate.

G. Z. Voyiadjis
Professor,
Mem. ASME.

Department of Civil Engineering,
Louisiana State University,
Baton Rouge, LA 70893

This paper presents a computational model for the finite element plastic damage analysis of ductile flexural plates. The phenomenological damage model proposed by Lemaitre is adopted here. The damage effect parameters of a cross-section are defined and employed to account for the damage effect across the thickness of a bending plate. Similar to the effective stresses used in many damage models, the effective stress couples are introduced in this work and used in the yield function. The damage criterion is defined in terms of damage strain energy release rates. Based on the damage node model proposed here, the elastoplastic-damage stiffness matrix of element is derived. When the corresponding elastic stiffness matrix is given explicitly, the resulting elastoplastic-damage stiffness matrix can be evaluated without use of numerical integration. The feature of the expicit form of element stiffness matrix makes the computational model proposed here very efficient. Several numerical examples of ductile plastic damage analysis of plates are also given in this work to demonstrate the validity of the computational model.

1 Introduction

A ductile material is capable of undergoing large plastic deformations. The accumulated plastic deformation can induce the changes of microstructures of the material through, for example, the nucleation, growth, and coalescence of microvoids. These changes in material microstructures are the irreversible thermodynamic processes and result in a progressive degradation on the material properties. The process of the initiation and growth of microvoids and other microdefects induced by plastic deformations in ductile solids is called the ductile plastic damage. The primary interest of the ductile plastic damage is to study the influence of microvoids resulting from plastic deformations on the degradation of material properties. The changes on material properties can be studied by either a phenomenological damage model or a micromechanical damage model. A number of damage definitions and measures were proposed for both the models (vide the review papers of Krajcinovic, 1984, 1989; Chaboche, 1988; among others). Within the framework of phenomenological damage model, the damage of a material can be measured in macroscale by the deduction of mechanical properties, such as the elasticity constants (Lemaitre et al., 1979). Moreover, the changes of the macromechanical properties can be characterized by the damage effect parameters which are able to be determined from experiments (Lemaitre, 1985). These damage parameters are the internal state variables in thermodynamics. The phenomenological damage model in conjunction with thermodynamics is not only simple in material modeling, but also quite accurate for the representation of a damage process. Therefore, the phenomenological model is very attractive in the practical application of the damage mechanics for engineering structures. The present study is based on the phenomenological damage model.

Quite a large number of papers on continuum damage mechanics have been published (see the references given in reviews of Krajcinovic, 1984, 1989; Chaboche, 1988). However, the ductile plastic damage of plate bending has received little attention up to now even though some damage models for the bending analysis of brittle beams have been proposed, e.g., Krajcinovic (1979). The flexural plates made of ductile metals, a very important type of structure, may undergo large plastic deformations under certain boundary and loading conditions. The large plastic deformations in a metal plate can induce the initiation and growth of microvoids and consequently cause the deterioration of the mechanical properties of the plate, a damage process. The load-carrying capacity of the damaged plate is lower than the one predicted from the elastoplastic analysis. Therefore, the ductile plastic damage analysis can provide a useful tool for a safe design of metal plates.

The objective of this paper is to present a computational model for the ductile plastic analysis of plates. The application and numerical examples of the proposed model is also presented in this study.

[1]Presently at the Research Institute of Engineering Mechanics, Dalian University of Technology, Dalian, Liaoning, China.

Contributed by the Applied Mechanics Division of THE AMERICAN SOCIETY OF MECHANICAL ENGINEERS for publication in the ASME JOURNAL OF APPLIED MECHANICS.

Discussion on this paper should be addressed to the Technical Editor, Professor Lewis T. Wheeler, Department of Mechanical Engineering, University of Houston, Houston, TX 77204-4792, and will be accepted until four months after final publication of the paper itself in the ASME JOURNAL OF APPLIED MECHANICS.

Manuscript received by the ASME Applied Mechanics Division, Aug. 29, 1991; final revision, Jan. 21, 1992. Associate Technical Editor: A. K. Noor.

In the present computational model, the damage effect parameters of a cross-section are introduced from irreversible thermodynamics to take into account the damage effect across the plate thickness. Analogous to the concept of effective stresses, the effective stress couples are defined for plate bending problems. The yield function is then defined in the effective stress couple space. The evolution law of ductile plastic damage proposed by Lemaitre (1985), in which the damage evolution is a linear function of the equivalent plastic strain, is adopted. The concept of the plastic node model presented by Shi and Voyiadjis (1992a) is extended here to discretize the distribution of the damage matrix in an element. Finally, by using the principle of virtual work together with the damage node model proposed here, the elastoplastic-damage stiffness matrix of element is derived. The resulting element stiffness matrix can be obtained explicitly as long as the elastic part of the element stiffness matrix is given explicitly. Consequently, the computational model presented here is very simple and efficient for the damage analysis of elastoplastic bending plates.

The damage-related matrices in the elastoplastic-damage stiffness matrix are dependent on the damage effect matrix (or tensor). The damage model used for the application presented here is the scalar isotropic damage model which is the simplest and most widely used model for the one-dimensional and isotropic phenomenological damage (vide, e.g., the review papers of Chaboche, 1988; Krajcinovic, 1989). In this model, the change of macromechanical properties of a material caused by microdefects is described by a simple scalar variable: a damage parameter. A new damage strain release rate proposed by the authors (Shi and Voyiadjis, 1992b), in which the influence of damage on the plastic deformations is taken into account, is used in this work. This damage strain release rate can be defined in the effective stress couple space.

The four-noded quadrilateral (12 degree-of-freedom) C^0 strain element for plate bending developed by the authors (Shi and Voyiadjis, 1991) is employed here to evaluate the elastic stiffness matrix. This assumed strain plate element is based upon the shear deformable plate theory proposed by Voyiadjis and Shi (1991a) and the quasi-conforming element method presented by Tang et al. (1980). Unlike most C^0 plate elements where the element stiffness matrix is evaluated by numerical integration, the element stiffness matrix of the C^0 plate element used here is given explicitly. Consequently, the assumed strain C^0 plate element presented by the authors is very computationally efficient. Furthermore, this four-noded quadrilateral (12 degree-of-freedom) C^0 plate element possesses a linear bending strain field and is free of shearing locking and numerical ill-condition. Therefore, this finite element is capable of giving reliable and accurate results for both thick and thin plate analysis.

Several numerical examples of the ductile plastic damage analysis of plate bending are presented in this paper to demonstrate the validity of the proposed computational model. The damage analysis results are compared with the elastoplastic analysis results.

2 Ductile Plastic Damage in Plate Bending Problems

The damage analysis presented here is based on the phenomenological method. As mentioned earlier, so far there is not much information about the ductile plastic damage analysis of plate bending in the literature. As an earlier step towards the ductile damage analysis of plates, the following assumptions are adopted in the present study for simplicity:

(1) The damage process in ductile plastic damage is induced by plastic deformations.

(2) Tension and compression have the same influence on the damage development (Lemaitre, 1985).

The first assumption is reasonable for ductile materials since the degradation of elastic modulus in elastic range is really negligible. The second assumption is similar to the plastic behavior of ductile materials. It has some limitations in application. Nevertheless, when the degradation of mechanical properties of a ductile material is primarily induced by microvoids rather than by microcracks, this assumption will be quite feasible.

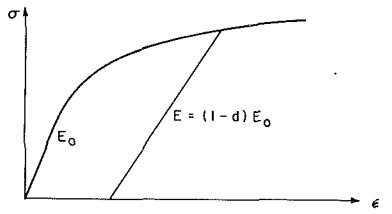

Fig. 1(a) The variation of elastic modulus

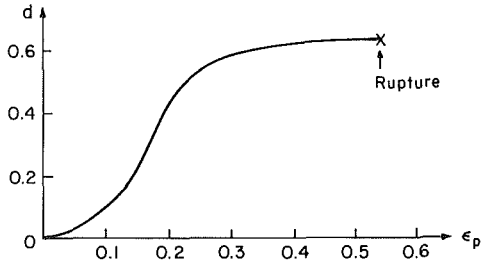

Fig. 1(b) The damage curve for annealed 30CrMnSi (Li et al., 1990)

Fig. 1 Ductile plastic damage in the extension of a bar

In order to demonstrate the ductile plastic damage of plate bending more easily, the corresponding one-dimensional case will be examined first.

2.1 Ductile Plastic Damage of Beams. Within the framework of the phenomenological damage, the measure of damage can be characterized by the degradation of the elastic modulus of the material (Lemaitre, 1985; Voyiadjis, 1988), as shown in Fig. 1 (Li et al., 1990). If one lets E_0 be the Young's modulus of the material in the undamaged state (virgin material), then the instantaneous Young's modulus E can be determined by the damage effect parameter d ($0 \le d \le 1$) as

$$E = (1-d)E_0. \tag{1}$$

Since the stress induced by bending is nonuniformly distributed along the thickness direction z, the damage parameter d, in general, varies through the thickness of a beam, i.e., $d = d(z)$.

Let $\epsilon_e(z)$ be the elastic axial strain of the cross-section of a beam, $\sigma(z)$ be the corresponding axial stress. According to the assumption of the plane cross-section, $\epsilon_e(z)$ can be expressed in terms of the elastic rotation of cross-section ϕ as

$$\epsilon_e(z) = \frac{\partial \phi}{\partial x} z. \tag{2}$$

The corresponding stress then is given by the Hooke's law as follows:

$$\sigma(z) = E\epsilon_e = (1-d)E_0\epsilon_e = (1-d)E_0 \frac{\partial \phi}{\partial x} z \tag{3}$$

where x is the coordinate in the axial direction of the beam. It should be noted that $\sigma(z)$ might be nonlinear across the thickness since $d(z)$ can also be a function of z.

The elastic bending strain energy density of the beam, W_e, is of the form

$$W_e = \frac{b}{2}\int_{-h/2}^{h/2} \epsilon_e \sigma dz = \frac{b}{2}\frac{\partial \phi}{\partial x}\int_{-h/2}^{h/2} \sigma z dz = \frac{1}{2}\frac{\partial \phi}{\partial x} M \tag{4}$$

with

$$M = b\int_{-h/2}^{h/2} \sigma z dz = b\frac{\partial \phi}{\partial x} E_0 \int_{-h/2}^{h/2} [1-d(z)]z^2 dz \qquad (5)$$

in which h and b are, respectively, the thickness and width of the beam. If one lets

$$\bar{\sigma} = E_0\epsilon_e = \frac{E}{1-d}\epsilon_e = \frac{\sigma}{1-d}, \qquad (6)$$

then the stress couple also takes the form

$$M = b\int_{-h/2}^{h/2} [1-d(z)]\bar{\sigma} z dz = \overline{M} - b\int_{-h/2}^{h/2} d(z)\bar{\sigma} z dz \qquad (7a)$$

with

$$\overline{M} = b\int_{-h/2}^{h/2} \bar{\sigma} z dz = bE_0\frac{\partial \phi}{\partial x}\int_{-h/2}^{h/2} z^2 dz = E_0\frac{\partial \phi}{\partial x}\frac{bh^3}{12}. \qquad (7b)$$

$\bar{\sigma}$ in Eq. (6) is the so-called effective stress. The quantity $\overline{M}$ defined in Eq. (7b) can be considered as the effective stress couple. In the beam bending problem considered here, the product of $\bar{\sigma}$ and z does not change its sign across the beam thickness $-h/2 \le z \le h/2$. Therefore, by using the weighted mean-value theorem for integrals, the last term in Eq. (7a) can be expressed as

$$b\int_{-h/2}^{h/2} d(z)\bar{\sigma} z dz = bd(\xi)\int_{-h/2}^{h/2} \bar{\sigma} z dz = d(\xi)\overline{M} = d^*\overline{M} \quad \text{for some } \xi \text{ in } [-h/2, h/2]. \qquad (8)$$

The parameter d^* in the above equation is the mean value of damage parameter $d(z)$ across the beam thickness. In the present study, d^* is taken as the damage effect parameter of a cross-section of the beam. The determination of d^* will be presented later. Substituting Eq. (8) into Eq. (7a) gives

$$M = (1-d^*)\overline{M}. \qquad (9)$$

The rate form of Eq. (9) can be written as

$$\dot{M} = (1-d^*)\dot{\overline{M}} - \dot{d}^*\overline{M} \qquad (10)$$

where the symbol " $\dot{}$ " signifies the material rate.

Similar to the strain energy release rate in fracture mechanics which is used for the fracture criterion, a damage strain energy release rate associated with a unit damage growth is defined in damage mechanics (Lemaitre, 1985). From thermodynamics, there is an internal variable, named D here for a one-dimensional problem, corresponding to the damage strain energy release rate $-Y$. By taking the free-energy Ψ as the thermodynamic potential, the damage strain energy release rate $-Y$ of a beam can be defined as

$$Y = \frac{\partial \Psi}{\partial D}. \qquad (11)$$

In general, the free energy Ψ is the function of elastic strains ϵ_e, equivalent plastic strain $\bar{\epsilon}_p$, internal variables $\mathbf{d}$, and absolute temperature T, i.e.,

$$\Psi = \Psi_1(\epsilon_e, \bar{\epsilon}_p, \mathbf{d}, T). \qquad (12)$$

Ψ can also be expressed in terms of effective stresses $\bar{\sigma}$ as

$$\Psi = \Psi_2(\bar{\sigma}, \bar{\epsilon}_p, \mathbf{d}, T). \qquad (13a)$$

For the one-dimensional problem considered here, the above equation takes the form

$$\Psi = \Psi(\overline{M}, \kappa_p, D, T) \qquad (13b)$$

where κ_p is the plastic curvature. In damage mechanics, the internal variables $\mathbf{d}$ are the damage effect parameters. It should be noted that both elastic and plastic strains in a damaged material are associated with the damage parameters $\mathbf{d}$, even in the case where the elastic and plastic free energies can be decoupled.

The damage evolution D can be determined by the normality property of the dissipation potential. By defining a suitable dissipation potential, Lemaitre (1985) proposed a damage evolution model for ductile plastic damage as follows:

$$\dot{D} = \left(\frac{-Y}{S_0}\right)^{s_0}\dot{\epsilon}_p \qquad (14)$$

with

$$-Y\dot{D} \ge 0 \qquad (15)$$

$$\dot{D} = 0 \quad \text{when } -Y \le Y_c \qquad (16)$$

$$D = D_c \quad \text{ruptured} \qquad (17)$$

in which S_0 and s_0 are the material constants; Y_c is the critical value of the damage strain energy release rate $-Y$; D_c is the critical value of the damage parameter D. Both Y_c and D_c are material constants and can be determined from experiments. The damage parameter D then can be evaluated from $\dot{D}$ by integration.

When the stresses rather than stress resultants are used, Eq. (11) takes the form

$$Y = \frac{\partial \Psi}{\partial \mathbf{d}}. \qquad (18)$$

Because of the analogy between Eqs. (6) and (9) as well as between Eqs. (18) and (11), it is feasible to assume $d^* = D$. From now on, d^* will be used to represent the damage parameter of a cross-section determined from the free energy in terms of stress couples.

2.2 Ductile Plastic Damage of Plate Bending. In the plane stress problem of plate bending, the in-plane strains ϵ and stresses σ can be written in the matrix forms, respectively, as

$$\epsilon = \begin{Bmatrix} \epsilon_x \\ \epsilon_y \\ 2\epsilon_{xy} \end{Bmatrix}, \quad \sigma = \begin{Bmatrix} \sigma_x \\ \sigma_y \\ \sigma_{xy} \end{Bmatrix}. \qquad (19)$$

For a linear elastic, isotropic material, the stresses σ and elastic strains ϵ_e in the undamaged state have the following relation:

$$\sigma = \mathbf{S}_0\epsilon_e$$

with

$$\mathbf{S}_0 = \frac{E_0}{1-\nu_0^2}\begin{bmatrix} 1 & \nu_0 & 0 \\ \nu_0 & 1 & 0 \\ 0 & 0 & \dfrac{1-\nu_0}{2} \end{bmatrix} \qquad (20)$$

in which ν_0 is the Poisson's ratio of the undamaged material. After the material is subjected to damage, the corresponding damaged elasticity matrix $S(d)$ can be written as (Krajcinovic, 1989)

$$\mathbf{S(d)} = [\mathbf{I} - \mathbf{D(d)}]\mathbf{S}_0 \qquad (21)$$

where $\mathbf{I}$ is the identity matrix and $\mathbf{D(d)}$ signifies the damage effect matrix (or tensor) which is symmetric and composed of damage parameters $\mathbf{d}$. The expression of $\mathbf{D(d)}$ can be determined from suitable micromechanical models (Krajcinovic, 1989). The evolution of the damage parameters $\mathbf{d}$ can be evaluated from the free energy as described earlier.

The stress-strain relation in a damaged state takes the form

$$\sigma = \mathbf{S(d)}\epsilon_e = [\mathbf{I} - \mathbf{D(d)}]\mathbf{S}_0\epsilon_e = [\mathbf{I} - \mathbf{D(d)}]\bar{\sigma} \qquad (22)$$

with the introduction of the effective stresses $\bar{\sigma}$ defined as

$$\bar{\sigma} = \mathbf{S}_0\epsilon_e. \qquad (23)$$

The increment of σ can be expressed as

$$\Delta\sigma = [\mathbf{I} - \mathbf{D(d)}]\Delta\bar{\sigma} - \Delta\mathbf{D}(\mathbf{d}, \Delta\mathbf{d})\bar{\sigma} \qquad (24)$$

in which $\Delta\mathbf{D}$ is the increment of $\mathbf{D}$ and is composed of $\mathbf{d}$ and $\Delta\mathbf{d}$.

Under the assumption of the plane cross-section, the elastic strains ϵ_e across a cross-section can be expressed as

$$\epsilon_e = \begin{Bmatrix} \dfrac{\partial \phi_{xe}}{\partial x} \\ \dfrac{\partial \phi_{ye}}{\partial y} \\ \dfrac{\partial \phi_{xe}}{\partial y} + \dfrac{\partial \phi_{ye}}{\partial x} \end{Bmatrix} z = \kappa_e z \tag{25}$$

where ϕ_{xe} and ϕ_{ye} are the generalized elastic rotations of the cross-section at x = constant and y = constant, respectively, and κ_e signifies the elastic curvatures of the plate. The incremental form of Eq. (25) is as follows:

$$\Delta\epsilon_e = \begin{Bmatrix} \dfrac{\partial \Delta\phi_{xe}}{\partial x} \\ \dfrac{\partial \Delta\phi_{ye}}{\partial y} \\ \dfrac{\partial \Delta\phi_{xe}}{\partial y} + \dfrac{\partial \Delta\phi_{ye}}{\partial x} \end{Bmatrix} z = \Delta\kappa_e z. \tag{26}$$

Consequently, the increment of the elastic bending strain energy density of a plate, ΔW_e, can be expressed as

$$\Delta W_e = \frac{1}{2}\int_{-h/2}^{h/2} \Delta\epsilon_e^T \Delta\sigma dz = \frac{1}{2}\Delta\kappa_e^T \int_{-h/2}^{h/2} \times [(\mathbf{I}-\mathbf{D})\Delta\bar{\sigma} - \Delta\mathbf{D}\bar{\sigma}]z dz = \frac{1}{2}\Delta\kappa_e^T \times [(\mathbf{I}-\mathbf{D}^*)\Delta\bar{\mathbf{M}} - \Delta\mathbf{D}^*\bar{\mathbf{M}}] = \frac{1}{2}\Delta\kappa_e^T \Delta\mathbf{M} \tag{27}$$

in which the right superscript T signifies the matrix transpose and

$$\Delta\bar{\mathbf{M}} = \int_{-h/2}^{h/2} \Delta\bar{\sigma} z dz = \frac{h^3}{12}\mathbf{S}_0\Delta\kappa_e = \mathbf{S}_{b0}\Delta\kappa_e \tag{28}$$

$$\mathbf{D}^*\Delta\bar{\mathbf{M}} = \mathbf{D}(\mathbf{d}(\xi))\Delta\bar{\mathbf{M}} = \int_{-h/2}^{h/2} \mathbf{D}(\mathbf{d}(z))\Delta\bar{\sigma} z dz, \tag{29}$$

some ξ in $[-h/2, h/2]$

$$\Delta\mathbf{D}^*\bar{\mathbf{M}} = \Delta\mathbf{D}^*(\Delta\mathbf{d}(\xi), \mathbf{d}(\xi))\bar{\mathbf{M}} = \int_{-h/2}^{h/2} \Delta\mathbf{D}(\mathbf{d}(z), \Delta\mathbf{d}(z))\bar{\sigma} z dz. \tag{30}$$

In Eqs. (29) and (30), the weighted mean-value theorem for integrals is utilized. The parameters $\mathbf{d}(\xi)$ and $\Delta\mathbf{d}(\xi)$ are the mean values of damage parameter $\mathbf{d}(z)$ and its increment $\Delta\mathbf{d}(z)$ along the plate thickness, respectively. $\mathbf{d}(\xi)$ and $\Delta\mathbf{d}(\xi)$ are defined as, respectively, the damage effect parameter and its increment of a plate at the point of the plate under consideration. Similar to the one-dimensional problem, $\Delta\mathbf{d}(\xi)$ and $\mathbf{d}(\xi)$ can also be evaluated by the internal variables $\mathbf{D}_I$ corresponding to the damage strain energy release rates $-\mathbf{Y}$. For plate bending problem, $-\mathbf{Y}$ takes the form $-\mathbf{Y} = \{Y_1, Y_2\}$, and is given by the free energy of the plate $\Psi(\bar{\mathbf{M}}, \bar{\kappa}_p, \mathbf{D}_I, T)$ as

$$\mathbf{Y} = \frac{\partial\Psi}{\partial\mathbf{D}_I}. \tag{31}$$

The increments of the damage effect parameters of a cross-section, $\Delta\mathbf{d}(\xi)$, are given by

$$\Delta\mathbf{d}^* = \Delta\mathbf{d}(\xi) = \Delta\mathbf{D}_I = \left(\frac{1}{S_0}\right)^{s_0} \begin{Bmatrix} -Y_1^{s_0} \\ -Y_2^{s_0} \end{Bmatrix} \Delta\bar{\kappa}_p \tag{32}$$

where $\Delta\bar{\kappa}_p$ is the increment of the equivalent plastic curvature. Let $\Delta\kappa_{xp}$, $\Delta\kappa_{yp}$, and $\Delta\kappa_{xyp}$ be the increments of plastic curvatures, then $\Delta\bar{\kappa}_p$ can be expressed as

$$\Delta\bar{\kappa}_p = \frac{2}{3^{1/2}}(\Delta\kappa_{xp}^2 + \Delta\kappa_{yp}^2 + \Delta\kappa_{xp}\Delta\kappa_{yp} + \Delta\kappa_{xyp}^2/4)^{1/2}. \tag{33}$$

Following the concept used in the three-dimensional problem presented by Lee et al. (1985), the damage criterion of a plate can be written as

$$F_d(\mathbf{Y}, \beta) = \frac{1}{2}(\mathbf{Y}^T\mathbf{J}\mathbf{Y})^{1/2} - [B_0 + B(\beta)] = 0 \tag{34}$$

in which $\mathbf{J}$ is a symmetric matrix; B_0 is the initial damage threshold; $B(\beta)$ is the damage threshold strengthening; and β is a overall damage parameter. The determination of $\mathbf{J}$ can be found in Lee et al. (1985) and Chaw and Lu (1989). B_0 and $B(\beta)$ can be obtained from experiments (Chaw and Wang, 1988). The increment of β can be expressed as (Lee et al., 1985)

$$\Delta\beta = 2\left(\frac{1}{2}\Delta\mathbf{D}_I^T\mathbf{J}\Delta\mathbf{D}_I\right)^{1/2}. \tag{35}$$

The following expression can be used as a rupture criterion (Lee et al., 1985)

$$\beta = \Sigma\Delta\beta = \beta_c \tag{36}$$

where β_c is the critical value of overall damage which is a material constant and can be obtained from experiments (Chaw and Wang, 1988).

3 A Damage Node Model for Ductile Plastic Damage of Plate Bending

A new plastic node model for the finite element plastic analysis of plates and shells was presented in the authors' previous paper (Shi and Voyiadjis, 1992a). In this plastic node model, the yield function, in terms of stress couples and stress resultants, is checked only at the element nodes. When the stress couples and stress resultants at a node satisfy the yield function, the node of the element is considered to become a plastic node. The plastic deformations are developed only at these plastic nodes, and the interior of the element is always elastic. The concept of plastic nodes is extended to damage analysis in the present work. That is, the damage criterion is only checked at the element nodes and it is assumed that the damage only undergoes at the damaged nodes.

Because of the nonlinear nature of the plastic analysis, the incremental scheme is used in the evaluation of the elastoplastic stiffness matrix. It is assumed in this work that the incremental bending strains of a plate, i.e., incremental curvature $\Delta\kappa$, can be decomposed into two parts: elastic parts $\Delta\kappa_e$ and plastic parts $\Delta\kappa_p$, i.e.,

$$\Delta\kappa = \Delta\kappa_e + \Delta\kappa_p. \tag{37}$$

Similarly, the incremental nodal displacement vector of an element $\Delta\mathbf{q}$ takes the form

$$\Delta\mathbf{q} = \Delta\mathbf{q}_e + \Delta\mathbf{q}_p. \tag{38}$$

In the finite element modeling of plate bending using the generalized displacement method, $\Delta\kappa_e$ in an element can be expressed in terms of the strain-displacement matrix $\mathbf{B}$ and the nodal elastic displacement vector of the element $\Delta\mathbf{q}_e$ as

$$\Delta\kappa_e(x,y) = \mathbf{B}(x,y)\Delta\mathbf{q}_e = \mathbf{B}\Delta\mathbf{q}_e. \tag{39}$$

If one lets $\mathbf{S}_b$ be the flexural rigidity matrix, the element stress couples $\Delta\mathbf{M}$ are then given by

$$\Delta\mathbf{M}(x,y)=\begin{Bmatrix}\Delta M_x\\ \Delta M_y\\ \Delta M_{xy}\end{Bmatrix}=\mathbf{S}_b\Delta\boldsymbol{\kappa}_e(x,y)=\mathbf{S}_b\mathbf{B}\Delta\mathbf{q}_e. \tag{40}$$

Consequently, the elastic stiffness matrix of an element, $\mathbf{K}_e$, can be written as

$$\mathbf{K}_e=\int_\Omega \mathbf{B}^T\mathbf{S}_b\mathbf{B}\,dxdy \tag{41}$$

where Ω denotes the element domain.

The plastic curvatures can be obtained from the yield function and the associated flow rule. If one lets $F_i(\mathbf{M}_i)$ be the yield function, and $d\lambda_i$ be the plastic proportionality parameter at node i, then by recalling that the plastic deformations are only developed at the plastic nodes, the increment of the plastic curvature κ_{xp} in an element is given by

$$\Delta\kappa_{xp}(x,y)=\sum_{i=1}^{NPN}\delta(x-x_i,y-y_i)\,d\lambda_i\frac{\partial F_i}{\partial M_{xi}} \tag{42}$$

in which NPN denotes the number of plastic nodes in the element under consideration.

By using the variational principle to determine $d\lambda_i$ in terms of elastic nodal displacement vector $\Delta\mathbf{q}$ (Shi and Voyiadjis, 1992a), then the elastoplastic stiffness matrix of a finite element, $\mathbf{K}_{ep}$, takes the form

$$\mathbf{K}_{ep}=\mathbf{K}_e[\mathbf{I}-\mathbf{a}(\mathbf{a}^T\mathbf{K}_e\mathbf{a}+\mathbf{H})^{-1}\mathbf{a}^T\mathbf{K}_e] \tag{43}$$

where $\mathbf{a}$ is the plastic nodal displacement matrix which is associated with the yield function in terms of the stress couples, and $\mathbf{H}$ is a matrix related to the plastic stiffness of the given material (Shi and Voyiadjis, 1992a).

It is worthwhile to mention that $\mathbf{K}_{ep}$ presented here can be evaluated explicitly, i.e., without numerical integration, when the elastic stiffness matrix $\mathbf{K}_e$ can be given explicitly. This feature makes the present plastic node model very computationally efficient and attractive.

When a material is subjected to a damage process, the mechanical properties of the material are degraded. Consequently, the yield stress of the damaged material decreases as the damage increases. However, when the stresses σ are replaced by the effective stresses $\bar{\sigma}$ which are associated with the virgin material, the yield function of the virgin material can be used for the damaged material. For example, in the plastic damage analysis of plates, the yield function takes the form

$$F(\mathbf{M},\sigma_{yd}(\mathbf{D}),k)=\bar{F}(\bar{\mathbf{M}},\sigma_{yo},k_o)=0 \tag{44}$$

where $\mathbf{M}$ is the stress couple vector of the plate; $\sigma_{yd}(\mathbf{D})$ is the yield stress of the damaged material which is the function of the damage tensor $\mathbf{D}$; $\bar{\mathbf{M}}$ is the effective stress couple; σ_{yo} is the yield stress of the virgin material; and k and k_o are the strain hardening parameters of the damaged and virgin materials, respectively.

From the associated flow rule, the incremental plastic curvatures at node i are given by

$$\Delta\kappa_{p_i}=\frac{\partial\bar{F}_i}{\partial\mathbf{M}_i}d\lambda_i=\frac{\partial\bar{\mathbf{M}}_i}{\partial\mathbf{M}_i}\frac{\partial\bar{F}_i}{\partial\bar{\mathbf{M}}_i}d\lambda_i=(\mathbf{I}-\mathbf{D}_i^*)^{-1}\frac{\partial\bar{F}_i}{\partial\bar{\mathbf{M}}_i}d\lambda_i \tag{45}$$

(no summation on i)

in which Eqs. (22) and (27) are used. It should be noted that there is no summation on the repeated indices in this work.

For an element in the damaged state, corresponding to a virtual nodal displacement vector $\delta\Delta\mathbf{q}=\delta\Delta\mathbf{q}_e+\delta\Delta\mathbf{q}_p$ and a virtual bending strain field $\delta\Delta\boldsymbol{\kappa}=\delta\Delta\boldsymbol{\kappa}_e+\delta\Delta\boldsymbol{\kappa}_p$, the principle of virtual work for the element gives

$$\begin{aligned}\delta\Delta\mathbf{q}^T\Delta\mathbf{f}&=\int_\Omega\delta\Delta\boldsymbol{\kappa}^T\Delta\mathbf{M}\,dxdy\\&=\int_\Omega(\delta\Delta\boldsymbol{\kappa}_e^T+\delta\Delta\boldsymbol{\kappa}_p^T)[(\mathbf{I}-\mathbf{D}^*)\Delta\bar{\mathbf{M}}-\Delta\mathbf{D}^*\bar{\mathbf{M}}]\,dxdy\\&=\int_\Omega[\delta\Delta\boldsymbol{\kappa}_e^T\Delta\bar{\mathbf{M}}+\delta\Delta\boldsymbol{\kappa}_p^T(\mathbf{I}-\mathbf{D}^*)\Delta\bar{\mathbf{M}}-\delta\Delta\boldsymbol{\kappa}_e^T\mathbf{D}^*\Delta\bar{\mathbf{M}}\\&\quad-\delta\Delta\boldsymbol{\kappa}_e^T\Delta\mathbf{D}^*\bar{\mathbf{M}}-\delta\Delta\boldsymbol{\kappa}_p^T\Delta\mathbf{D}^*\bar{\mathbf{M}}]\,dxdy\end{aligned} \tag{46}$$

where $\Delta\mathbf{f}$ represents the increment of the internal nodal force vector of the element. In Eq. (46), $\mathbf{D}^*(x,y)$ and $\Delta\mathbf{D}^*(x,y)$ are yet undefined fields.

Similar to the concept of the plastic nodes, a damage node model is proposed here to construct $\mathbf{D}^*(x,y)$ and $\Delta\mathbf{D}^*(x,y)$. In this damage node model, the damage is assumed to be developed at the element nodes only, and the interior of the element is always in the undamaged state. Consequently, the damage matrix or tensor in an element $\mathbf{D}^*$ and $\Delta\mathbf{D}^*$ can be expressed as

$$\mathbf{D}^*(x,y)=\sum_{j=1}^{NDN}\delta(x-x_j,y-y_j)\mathbf{D}_j^* \tag{47}$$

$$\Delta\mathbf{D}^*(x,y)=\sum_{j=1}^{NDN}\delta(x-x_j,y-y_j)\Delta\mathbf{D}_j^* \tag{48}$$

where $\mathbf{D}_j^*$ and $\Delta\mathbf{D}_j^*$ are the damage matrix and its increment at node j of the element under consideration; and NDN represents the number of damage nodes of the element. Substituting Eqs. (41), (45), (47) and (48) into Eq. (46) leads to

$$\begin{aligned}\delta\Delta\mathbf{q}^T\Delta\mathbf{f}&=\delta\Delta\mathbf{q}_e^T\mathbf{K}_e\Delta\mathbf{q}_e+\delta d\lambda^T\mathbf{H}d\lambda\\&\quad-\sum_{j=1}^{NDN}\left[\delta\Delta\boldsymbol{\kappa}_{ej}^T\mathbf{D}^*\Delta\bar{\mathbf{M}}_j+\delta\Delta\boldsymbol{\kappa}_{ej}^T\Delta\mathbf{D}_j^*\bar{\mathbf{M}}_j\right.\\&\quad\left.+\delta d\lambda_j\frac{\partial\bar{F}_j^T}{\partial\bar{\mathbf{M}}_j}(\mathbf{I}-\mathbf{D}_j^*)^{-T}\Delta\mathbf{D}_j^*\bar{\mathbf{M}}_j\right].\end{aligned} \tag{49}$$

In the above derivation, the consistency condition of yield function

$$\frac{\partial\bar{F}_i^T}{\partial\bar{\mathbf{M}}_i}d\bar{\mathbf{M}}_i=-\frac{\partial\bar{F}_i}{\partial k_{0i}}dk_{0i}=H_i d\lambda_i$$

is also utilized. It follows from Eqs. (39) and (40) that the elastic bending strains and stress couples at node j of the element can be written as

$$\Delta\boldsymbol{\kappa}_{ej}=\Delta\boldsymbol{\kappa}_e(x_j,y_j)=\mathbf{B}(x_j,y_j)\Delta\mathbf{q}_e=\mathbf{B}_{nj}\Delta\mathbf{q}_e \tag{50}$$

$$\Delta\bar{\mathbf{M}}_j=\mathbf{S}_{b0}\Delta\boldsymbol{\kappa}_e(x_j,y_j)=\mathbf{S}_{b0}\mathbf{B}_{nj}\Delta\mathbf{q}_e. \tag{51}$$

After some mathematical manipulations, one can obtain

$$\sum_{j=1}^{NDN}\delta\Delta\boldsymbol{\kappa}_{ej}^T\mathbf{D}^*\Delta\bar{\mathbf{M}}_j=\delta\Delta\mathbf{q}_e^T\mathbf{B}_n^T\mathbf{D}_e^*\mathbf{S}_{be}\mathbf{B}_n\Delta\mathbf{q}_e \tag{52}$$

in which $\mathbf{B}_n$ is the matrix consisting of $\mathbf{B}_{nj}$ ($j=1, 2, NDN$), $\mathbf{D}_e^*$ is the damage matrix of the element, and $\mathbf{S}_{be}$ is the enlarged diagonal matrix of $\mathbf{S}_{b0}$. $\mathbf{D}_e^*$ takes the form

$$\mathbf{D}_e^*=\begin{bmatrix}\mathbf{D}_1^* & \mathbf{0} & \mathbf{0}\\ \mathbf{0} & \mathbf{D}_j^* & \mathbf{0}\\ \mathbf{0} & \mathbf{0} & \mathbf{D}_{NDN}^*\end{bmatrix}. \tag{53}$$

In the ductile plastic damage, the increment of the damage tensor $\Delta\mathbf{D}_j^*$ at node j is the function of the damage parameters $\Delta\mathbf{d}_j^*$ at the node, and $\Delta\mathbf{d}_j^*$ depends on the increment of the equivalent plastic curvature $\Delta\kappa_{pj}$ shown in Eq. (32). By using Eqs. (33) and (45), $\Delta\mathbf{D}_j^*(\Delta\mathbf{d}_j^*)$ can be transformed into

$$\Delta \mathbf{D}_j^*(\Delta \mathbf{d}_j^*) = \mathbf{D}_1(\Delta \kappa_{pj}) = \mathbf{D}_2(d\lambda_j). \tag{54}$$

Therefore, in the case when $\Delta \mathbf{D}_j^*$ is a linear function of $\Delta \mathbf{d}_j^*$, after a simple rearrangement the last two terms in Eq. (49) can be written as

$$\sum_{j=1}^{NDN} \delta \Delta \kappa_{ej}^T \Delta \mathbf{D}_j^* \overline{\mathbf{M}}_j = \sum_{j=1}^{NDN} \delta \Delta \kappa_{ej}^T \mathbf{D}_2(d\lambda_j) \overline{\mathbf{M}}_j = \delta \Delta \mathbf{q}_e^T \mathbf{B}_n^T (\mathbf{DM}) d\lambda \tag{55}$$

$$\sum_{j=1}^{NDN} \delta d\lambda_j \frac{\partial \overline{F}_j^T}{\partial \overline{\mathbf{M}}_j} (\mathbf{I} - \mathbf{D}_j^*)^{-T} \Delta \mathbf{D}_j^* \overline{\mathbf{M}}_j = \delta d\lambda^T (\mathbf{DF})^T (\mathbf{ID}) (\mathbf{DM}) d\lambda \tag{56}$$

with

$$d\lambda^T = \{d\lambda_1, d\lambda_j, d\lambda_{NDN}\}. \tag{57}$$

By substituting Eqs. (52), (55), and (56), Eq. (49) becomes

$$\begin{aligned} \delta \Delta \mathbf{q}^T \Delta \mathbf{f} &= \delta \Delta \mathbf{q}_e^T \mathbf{K}_e \Delta \mathbf{q}_e + \delta d\lambda^T \mathbf{H} d\lambda - \delta \Delta \mathbf{q}_e^T \mathbf{B}_n^T \mathbf{D}_e^* \mathbf{S}_{be} \mathbf{B}_n \Delta \mathbf{q}_e \\ &\quad - \delta \Delta \mathbf{q}_e^T \mathbf{B}_n^T (\mathbf{DM}) d\lambda - \delta d\lambda^T (\mathbf{DF})^T (\mathbf{ID}) (\mathbf{DM}) d\lambda \\ &= \delta \Delta \mathbf{q}_e^T [(\mathbf{K}_e - \mathbf{B}_n^T \mathbf{D}_e^* \mathbf{S}_{be} \mathbf{B}_n) \Delta \mathbf{q}_e - \mathbf{B}_n^T (\mathbf{DM}) d\lambda] \\ &\quad + \delta d\lambda^T [\mathbf{H} d\lambda - (\mathbf{DF})^T (\mathbf{ID}) (\mathbf{DM}) d\lambda]. \end{aligned} \tag{58}$$

By recalling Eqs. (38), Eq. (58) can be rewritten as

$$\begin{aligned} &\delta \Delta \mathbf{q}^T [\mathbf{K}_e^* (\Delta \mathbf{q} - \bar{\mathbf{a}} d\lambda) - \mathbf{B}_n^T (\mathbf{DM}) d\lambda - \Delta \mathbf{f}] \\ &\quad + \delta d\lambda^T [\mathbf{H} d\lambda - (\mathbf{DF})^T (\mathbf{ID}) (\mathbf{DM}) d\lambda - \bar{\mathbf{a}}^T \mathbf{K}_e^* (\Delta \mathbf{q} - \bar{\mathbf{a}} d\lambda) \\ &\quad + \bar{\mathbf{a}}^T \mathbf{B}_n^T (\mathbf{DM}) d\lambda] = 0 \end{aligned} \tag{59}$$

where $\bar{\mathbf{a}}$ is the modified plastic nodal displacement matrix because of the damage and $\mathbf{K}_e^*$ is the modified elastic stiffness matrix. Matrix $\bar{\mathbf{a}}$ gives the plastic nodal displacement vector as (Shi and Voyiadjis, 1992a)

$$\Delta \mathbf{q}_p = \bar{\mathbf{a}} d\lambda \tag{60}$$

$\mathbf{K}_e^*$ is of the form

$$\mathbf{K}_e^* = \mathbf{K}_e - \mathbf{B}_n^T \mathbf{D}_e^* \mathbf{S}_{be} \mathbf{B}_n. \tag{61}$$

Since $\delta \Delta \mathbf{q}$ and $\delta d\lambda$ are independent of each other and arbitrary, Eq. (59) then gives the following two equations:

$$\mathbf{K}_e^* (\Delta \mathbf{q} - \bar{\mathbf{a}} d\lambda) - \mathbf{B}_n^T (\mathbf{DM}) d\lambda = \Delta \mathbf{f} \tag{62}$$

$$\mathbf{A} d\lambda - \bar{\mathbf{a}}^T \mathbf{K}_e^* \Delta \mathbf{q} = \mathbf{0} \tag{63}$$

where $\mathbf{A}$ is the nonsingular square matrix and of the form

$$\mathbf{A} = \mathbf{H} + \bar{\mathbf{a}}^T \mathbf{K}_e^* \bar{\mathbf{a}} + \bar{\mathbf{a}}^T \mathbf{B}_n^T (\mathbf{DM}) - (\mathbf{DF})^T (\mathbf{ID}) (\mathbf{DM}). \tag{64}$$

Equation (63) gives

$$d\lambda = \mathbf{A}^{-1} \bar{\mathbf{a}}^T \mathbf{K}_e^* \Delta \mathbf{q}. \tag{65}$$

Substituting Eq. (65) into Eq. (62), one finally obtains

$$\mathbf{K}_{epd} \Delta \mathbf{q} = \Delta \mathbf{f} \tag{66}$$

in which $\mathbf{K}_{epd}$ is the elastoplastic-damage stiffness matrix of an element and takes the form

$$\mathbf{K}_{epd} = \mathbf{K}_e^* (\mathbf{I} - \bar{\mathbf{a}}^T \mathbf{A}^{-1} \bar{\mathbf{a}}^T \mathbf{K}_e^*) - \mathbf{B}_n^T (\mathbf{DM}) \mathbf{A}^{-1} \bar{\mathbf{a}}^T \mathbf{K}_e^*. \tag{67}$$

It should be noted that $\mathbf{K}_{epd}$ is, in general, unsymmetric in the presence of damage. It can be seen that $\mathbf{K}_{epd}$ reduces to $\mathbf{K}_{ep}$ when the damage tensor is null which results in $\mathbf{D}_e^* = \mathbf{0}$, $(\mathbf{DM}) = \mathbf{0}$ and $(\mathbf{ID}) = \mathbf{I}$. Similar to $\mathbf{K}_{ep}$, $\mathbf{K}_{epd}$ can also be evaluated explicitly as long as the elastic stiffness matrix $\mathbf{K}_e$ is given explicitly. A four-noded strain element with the explicit stiffness matrix for the elastic plate bending analysis can be found in the paper of Shi and Voyiadjis (1991).

4 Application

4.1 Scalar Isotropic Damage Model for Bending Plates. Based on Kachanov's pioneering work (1958), the scalar isotropic damage model has been widely used by many researchers (e.g., Chaboche, 1988; Krajcinovic, 1989; Lemaitre, 1985). In the scalar isotropic damage model, it is assumed that the degradation of macromechanical properties induced by microstructural changes of a material can be represented by a scalar parameter. For the plate bending problem considered here, the damage will be quite isotropic if the principal stress couples at any point of the plate are quite close in magnitude. Under such a model, if one lets $\mathbf{S}_{bo}$ be the elastic flexural rigidity matrix in the undamaged state, then the flexural rigidity matrix $\mathbf{S}_b$ in a damage state can be expressed as

$$\mathbf{S}_b = (1 - d^*) \mathbf{S}_{bo} \tag{68a}$$

or

$$\mathbf{S}_b = (\mathbf{I} - d^* \mathbf{I}) \mathbf{S}_{bo} \tag{68b}$$

where d^* is the scalar damage parameter of the plate. This scalar isotropic damage model is very attractive because of its simplicity. However, this damage model implies that the damage process has no influence on the Poisson's ratio. It was shown that even for an isotropic material, the Poisson's ratio changes as the microstructures of the material change (Sumarac and Krajcinovic, 1989; among others). Consequently, the scalar isotropic damage model is too restrictive. Nevertheless, it is feasible to employ this simple damage model here to demonstrate the validity of the computational model presented in this work.

Within the framework of scalar isotropic damage model, the effective stress couple vector $\overline{\mathbf{M}}$ takes the form

$$\overline{\mathbf{M}} = \mathbf{M}/(1 - d^*). \tag{69}$$

By recalling Eq. (68), the damage effect matrix at node j of an element $\mathbf{D}_j^*$ defined in Eq. (29) can be expressed as

$$\mathbf{D}_j^*(d_j^*) = d_j^* \mathbf{I} \tag{70}$$

where d_j^* is the damage parameter across the plate thickness at node j.

The damage strain energy release rate of a system is derived from the free energy of the system. The assumption that the elastic and plastic parts in the free energy are uncoupled is widely used (Lemaitre, 1985; Lehmann, 1991). This assumption is also adopted here even though it is not necessary. However, it should be noted that in a damage state, both elastic and plastic parts in the free energy are associated with the damage parameter. Consequently, Eq. (12) can be rewritten as

$$\Psi = \Psi_e(\epsilon_e, d, T) + \Psi_p(\bar{\epsilon}_p(d), T) \tag{71}$$

where $\bar{\epsilon}_p(d)$ represents that the equivalent plastic strain $\bar{\epsilon}_p$ also depends on the damage parameter d. Under isothermal conditions, the scalar isotropic damage gives the free energy in tensor form as (Lemaitre, 1985)

$$\Psi_e = \frac{1}{2} (1 - d) \boldsymbol{\epsilon}_e : \mathbf{S}_o : \boldsymbol{\epsilon}_e \tag{72}$$

in which $\boldsymbol{\epsilon}_e$ is the elastic strain tensor; $\mathbf{S}_o$ is the elasticity tensor in the undamaged state; and symbol ":" signifies the tensor contraction.

Substituting ψ_e from Eq. (72) into Eq. (71) leads to

$$\Psi = \frac{1}{2} (1 - d) \boldsymbol{\epsilon}_e : \mathbf{S}_o : \boldsymbol{\epsilon}_e + \Psi_p(\bar{\epsilon}_p(d), T). \tag{73}$$

The free energy defined here is different from the one presented by Lemaitre (1985) in which $\partial \Psi_p / \partial d = 0$, although the elastic part is identical. By accounting for the influence of damage on the plastic deformations, a new damage strain energy release rate proposed by Shi and Voyiadjis (1992b) is as follows:

$$-Y = -\frac{\partial \Psi}{\partial d} = -\left(\frac{\partial \Psi_e}{\partial d} + \frac{\partial \Psi_p}{\partial d} \right) = (1 - d) \boldsymbol{\epsilon}_e : \mathbf{S}_o : \boldsymbol{\epsilon}_e. \tag{74}$$

For the plate bending problem considered here, the elastic bending strains $\boldsymbol{\kappa}_e$ can be expressed in a matrix form as

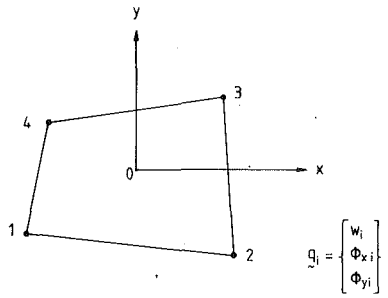

Fig. 2 A typical four-noded quadrilateral plate element

$$\kappa_e = \mathbf{S}_b^{-1}\mathbf{M} = \mathbf{S}_{bo}^{-1}\mathbf{M}/(1-d^*) = \mathbf{S}_{bo}^{-1}\overline{\mathbf{M}} \tag{75}$$

where Eqs. (68) and (69) are utilized. Therefore, the damage strain energy release rate $-Y$ of a bending plate can be expressed in terms of the effective stress couple vector $\overline{\mathbf{M}}$ as

$$-Y = (1-d^*)\overline{\mathbf{M}}^T\mathbf{S}_{bo}^{-T}\mathbf{S}_{bo}\mathbf{S}_{bo}^{-1}\overline{\mathbf{M}} = (1-d^*)\overline{\mathbf{M}}^T\mathbf{S}_{bo}^{-1}\overline{\mathbf{M}}. \tag{76}$$

By substituting Eq. (76) into the damage evolution law given in Eq. (32), one obtains

$$\Delta d^* = \Delta D_I = [(1-d^*)\overline{\mathbf{M}}^T\mathbf{S}_{bo}^{-1}\overline{\mathbf{M}}/S_o]^{s_o}\Delta\bar{\kappa}_p. \tag{77}$$

If one lets ${}^k d_j^*$ be the damage parameter of node j at configuration k, then the damage parameter at configuration $k+1$ can be written as

$${}^{k+1}d_j^* = {}^k d_j^* + \Delta d_j^*. \tag{78}$$

Making use of Eqs. (33) and (45) and recalling Eq. (70), the increment of equivalent plastic curvature at node j from configurations k to $k+1$, $\Delta\bar{\kappa}_{pj}$, takes the form

$$\Delta\bar{\kappa}_{pj} = \frac{1}{1-{}^k d_j^*}\, dF_{mj}\, d\lambda_j \quad \text{(no summation on } j\text{)} \tag{79}$$

with

$$dF_{mj} = \frac{2}{3^{1/2}}\left[\left(\frac{\partial\bar{F}_j}{\partial\overline{M}_{xj}}\right)^2 + \left(\frac{\partial\bar{F}_j}{\partial\overline{M}_{yj}}\right)^2 + \frac{\partial\bar{F}_j}{\partial\overline{M}_{xj}}\frac{\partial\bar{F}_j}{\partial\overline{M}_{yj}} + \left(\frac{\partial\bar{F}_j}{\partial\overline{M}_{xyj}}\right)^2\Big/4\right]^{1/2}. \tag{80}$$

Therefore, the increment of damage parameter at node j of a plate from configurations k to $k+1$ can be written as

$$\Delta d_j^* = \Lambda_j d\lambda_j \tag{81}$$

with

$$\Lambda_j = [(1-{}^k d_j^*)\,{}^k\overline{\mathbf{M}}_j^T\mathbf{S}_{bo}^{-1}{}^k\overline{\mathbf{M}}_j/S_o]^{s_o}\frac{1}{1-{}^k d_j^*}\, dF_{mj}. \tag{82}$$

Equation (81) indicates that the increment of damage parameter at a nodal point is a function of the plastic proportionality parameter of the same node.

4.2 Elastoplastic-damage Stiffness Matrix of Element Based on the Scalar Isotropic Damage Model. The incremental form of Eq. (67) at configuration k, which gives the elastoplastic-damage tangent stiffness matrix at configuration k, can be expressed as follows:

$${}^k\mathbf{K}_{epd} = \mathbf{K}_e^*(\mathbf{I} - \bar{\mathbf{a}}^T({}^k\mathbf{A}^{-1})\bar{\mathbf{a}}\mathbf{K}_e^*) - \mathbf{B}_n^T({}^k\mathbf{DM}^k)(\mathbf{A}^{-1})\bar{\mathbf{a}}^T\mathbf{K}_e^* \tag{83}$$

where the left superscript k denotes configuration k, and $\mathbf{K}_e^*$ and ${}^k\mathbf{A}$ are of the form

$$\mathbf{K}_e^* = \mathbf{K}_e - \mathbf{B}_n^{Tk}(\mathbf{D}_e^*)\mathbf{S}_{be}\mathbf{B}_n \tag{84}$$

$${}^k\mathbf{A} = \mathbf{H} + \bar{\mathbf{a}}^T\mathbf{K}_e^*\bar{\mathbf{a}} + \bar{\mathbf{a}}^T\mathbf{B}_n^{Tk}(\mathbf{DM}) - (\mathbf{DF})^{Tk}(\mathbf{ID})({}^k\mathbf{DM}). \tag{85}$$

In Eqs. (83) to (84), $\mathbf{K}_e$ is the elastic part of the element stiffness matrix; $\mathbf{B}_n$ can be constructed by $\mathbf{B}_b$ (see Eqs. (87) and (94)); matrices $\mathbf{H}$, $\bar{\mathbf{a}}$, and $\mathbf{DF}$, associated with plastic deformations, were presented in Section 3.

The finite element considered here is the four-noded quadrilateral plate element shown in Fig. 2. The assumed strain C^0 element for the thick/thin plate analysis developed by the authors (Shi and Voyiadjis, 1991) is employed in this work for the elastic stiffness matrix. The element stiffness matrix of this element is of the form

$$\mathbf{K}_e = \int_\Omega \mathbf{B}_b^T(x,y)\mathbf{S}_b\mathbf{B}_b(x,y)\,dxdy + \int_\Omega \mathbf{B}_s^T\mathbf{T}_s\mathbf{B}_s dxdy \tag{86}$$

in which Ω signifies the element domain; $\mathbf{S}_b$ and $\mathbf{T}_s$ are the customary flexural and transverse shear rigidity matrices, respectively; $\mathbf{B}_b$ and $\mathbf{B}_s$ are the bending and transverse shearing strain-displacement matrices, respectively. The quasi-conforming element method gives $\mathbf{B}_b$ and $\mathbf{B}_s$ as

$$\mathbf{B}_b(x,y) = \mathbf{P}_b(x,y)\mathbf{A}_b^{-1}\mathbf{C}_b \tag{87}$$

$$\mathbf{B}_s = \mathbf{C}_s/\Delta \tag{88}$$

where $\mathbf{P}_b(x,y)$ is the interpolation function matrix for element bending strains; $\mathbf{A}_b$, $\mathbf{C}_b$, and $\mathbf{C}_s$ are matrices independent of x and y; and Δ represents the area of the element. $\mathbf{P}_b$, $\mathbf{A}_b$, $\mathbf{C}_b$, and $\mathbf{C}_s$ for the element shown in Fig. 2 can be found in the authors' previous paper (Shi and Voyiadjis, 1991). Substituting Eqs. (87) and (88) into Eq. (86) gives

$$\mathbf{K}_e = \mathbf{C}_b^T\mathbf{A}_b^{-1}\int_\Omega \mathbf{P}_b^T(x,y)\mathbf{S}_b\mathbf{P}_b(x,y)\,dxdy\mathbf{A}_b^{-1}\mathbf{C}_b + \mathbf{C}_s^T\mathbf{T}_s\mathbf{C}_s/\Delta. \tag{89}$$

It is worthwhile to mention that the element stiffness matrix presented here can be evaluated explicitly since the integrands appearing in Eq. (89) are only simple polynomials.

In order to illustrate the validity of the proposed computational model by solving some numerical examples, the derivation of $\mathbf{D}_e^*$, **DM** and **ID** will be presented for the scalar isotropic damage model in this section.

By substituting Eq. (70) into Eq. (53), the damage effect matrix of an element at configuration k can be expressed as

$${}^k\mathbf{D}_e^* = \begin{bmatrix} ({}^k d_1^*)\mathbf{I} & \mathbf{0} & \mathbf{0} \\ \mathbf{0} & ({}^k d_j^*)\mathbf{I} & \mathbf{0} \\ \mathbf{0} & \mathbf{0} & ({}^k d_{NDN}^*)\mathbf{I} \end{bmatrix} \tag{90}$$

in which NDN represents the number of damaged nodes in the element under consideration.

The incremental form of Eq. (70) takes the form

$$\Delta\mathbf{D}_j^*(d_j^*) = \Delta d_j^*\mathbf{I} = \Lambda_j d\lambda_j\mathbf{I} \tag{91}$$

By comparing the above equation with Eq. (54), one can obtain

$$\mathbf{D}_2(d\lambda_j) = \Lambda_j\mathbf{I}d\lambda_j. \tag{92}$$

According to the definition given in Eq. (55)

$$\delta\Delta\mathbf{q}_e^T\mathbf{B}_n^T(\mathbf{DM})d\lambda = \sum_{j=1}^{NDN}\delta\Delta\kappa_{ej}^T\mathbf{D}_2(d\lambda_j)\overline{\mathbf{M}}_j \tag{93}$$

together with

$$\mathbf{B}_n = \begin{bmatrix} \mathbf{B}_{n1}(x_1,y_1) \\ \mathbf{B}_{nj}(x_j,y_j) \\ \mathbf{B}_{nNDN}(x_{NDN},y_{NDN}) \end{bmatrix}, \quad d\lambda = \begin{Bmatrix} d\lambda_1 \\ d\lambda_j \\ d\lambda_{NDN} \end{Bmatrix}, \tag{94}$$

matrix **DM** at configuration k can be written as

$$
{}^{k}\mathbf{DM}=\begin{bmatrix} {}^{k}\overline{M}_{x1} & {}^{k}\overline{M}_{y1} & {}^{k}\overline{M}_{xy1} & 0 & 0 & 0 & 0 & 0 & 0 \\ 0 & 0 & 0 & {}^{k}\overline{M}_{xj} & {}^{k}\overline{M}_{yj} & {}^{k}\overline{M}_{xyj} & 0 & 0 & 0 \\ 0 & 0 & 0 & 0 & 0 & 0 & {}^{k}\overline{M}_{xNDN} & {}^{k}\overline{M}_{yNDN} & {}^{k}\overline{M}_{xyNDN} \end{bmatrix}^{T}
$$

$$
\cdot\begin{bmatrix} \Lambda_1 & 0 & 0 \\ 0 & \Lambda_j & 0 \\ 0 & 0 & \Lambda_{NDN} \end{bmatrix}. \quad (95)
$$

By recalling Eq. (56)

$$
\delta d\lambda^{T}(\mathbf{DF})^{T}(\mathbf{ID})(\mathbf{DM})d\lambda=\sum_{j=1}^{NDN}\delta d\lambda_j\frac{\partial\overline{\mathbf{F}}_j^{T}}{\partial\overline{\mathbf{M}}_j}(\mathbf{I}-\mathbf{D}_j^{*})^{-T}\Delta\mathbf{D}_j^{*}\overline{\mathbf{M}}_j, \quad (96)
$$

matrix **ID** at configuration k takes the form

$$
{}^{k}\mathbf{ID}=\begin{bmatrix} \mathbf{I}/(1-{}^{k}d_1^{*}) & \mathbf{0} & \mathbf{0} \\ \mathbf{0} & \mathbf{I}/(1-{}^{k}d_j^{*}) & \mathbf{0} \\ \mathbf{0} & \mathbf{0} & \mathbf{I}/(1-{}^{k}d_{NDN}^{*}) \end{bmatrix}. \quad (97)
$$

$\mathbf{D}_e^{*}$, **DM**, and **ID** are the only matrices associated with damage. Having obtained these matrices related to damage, the elastoplastic-damage stiffness matrix of an element given by Eq. (83) can be evaluated easily. It is worthwhile to emphasize it again that the elastoplastic-damage stiffness matrix presented here is given explicitly.

4.3 Numerical Examples. Three numerical examples of the damage analysis of elastoplastic plates are presented in this section. The computer program NAPSASE (Nonlinear Analysis of Plates and Shells by Assumed Strain Elements) developed by the authors (Voyiadjis and Shi, 1991b) is used here. The updated Lagrangian formulation is adopted in NAPSASE. The yield function in terms of the stress couples is employed here. The notations of the yield function used in this section are of the form

$$
F(\overline{\mathbf{M}})=\frac{|\overline{M}|}{M_0}-1=0 \quad (98)
$$

$$
F(\overline{\mathbf{M}},k)=\frac{|\overline{M}|}{M_0}-\frac{Y_p(k)}{\sigma_0^2}=0 \quad (99)
$$

$$
F(\overline{\mathbf{M}},\alpha)=\frac{|\overline{M}|}{\alpha M_0}-1=0 \quad (100)
$$

$$
F(\overline{\mathbf{M}},\alpha,k)=\frac{|\overline{M}|}{\alpha M_0}-\frac{Y_p(k)}{\sigma_0^2}=0 \quad (101)
$$

with

$$
|\overline{M}|=(\overline{M}_{xi}^2+\overline{M}_{yi}^2-\overline{M}_{xi}\overline{M}_{yi}+3\overline{M}_{xyi}^2)^{1/2} \quad (102)
$$

$$
M_0=\sigma_0 h^2/4 \quad (103)
$$

where σ_0 is the uniaxial yield stress of the virgin material; h is the thickness of the plate; α ($2/3 \le \alpha \le 1$) is the plastic curvature parameter used to take into account the progressive development of plastic deformations across the plate thickness in plate bending problems (Crisfield, 1981); and k represents the strain hardening of a material. A linear hardening with plastic stiffness $H' = E/9$ is used in all the examples presented here. The material constants appearing in the damage evaluation of Eq. (80) and the rupture criterion of Eq. (17) are taken as

$$
s_o=1.0, \quad S_o=Y_c, \quad D_c=0.2 \quad (104)
$$

in which Y_c is the critical value of the strain energy release rate. Different values of Y_c are used in each example.

Since not much information about the ductile plastic damage analysis of bending plates is available for comparison, the numerical study of the damage analysis presented here is less ambitious.

Example 1. Clamped Circular Plate Under a Uniform Load. A clamped circular plate subjected to a uniformly distributed load is considered in this example. Because of the symmetry, only one-quarter of the plate is analyzed here and the finite element layout is depicted in Fig. 3. The critical value of strain energy release rate used in this example is $Y_c = 3\sigma_0^2 h/4E$. The curves of central deflections versus the load for both elastoplastic and elastoplastic-damage analysis are illustrated in Fig. 4. In this example, the edge of the plate becomes a plastic hinge line first. The collapse load given by the plastic analysis with $F = F(\mathbf{M})$ is very close to the lower bound obtained by Hopkins and Wang (1954). When the yield function $F = F(\overline{\mathbf{M}})$ is used, the result of the elastoplastic-damage analysis is almost identical to that of the elastoplastic analysis. Corresponding to yield function $F = F(\mathbf{M}, k)$, the difference between the load-deflection curves with and without damage is not considerable either. Nevertheless, when the damage effect is taken into account, the load-carrying capacity of the plate is lower than that of the plate without damage, since the damage parameter can cause the plate to become unstable even though the damage parameter is much lower than the critical value. In the present example, the plate becomes unstable when the damage parameter at the central point of the plate is of the value $d^* = 0.0315$.

Example 2. Circular Plate Subjected to a Central Load. The clamped circular plate considered in the previous example is studied here again, but in this case, the plate is subjected to a central load. The elastoplastic analysis of this

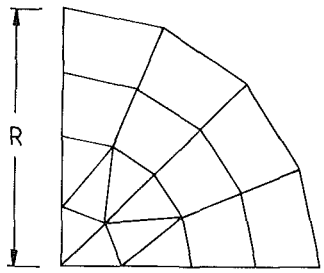

Fig. 3 Element mesh of a quarter of circular plate

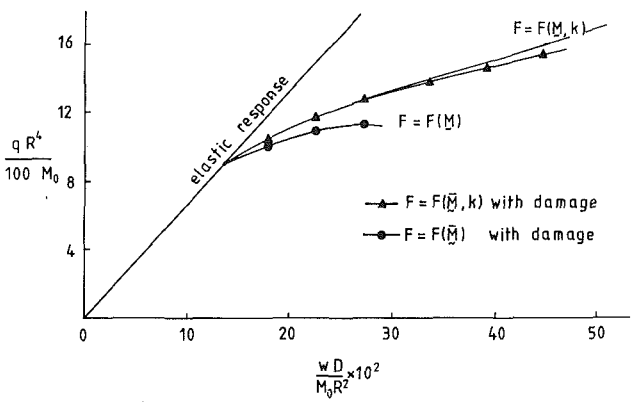

Fig. 4 Central deflections of clamped circular plate under a uniform load

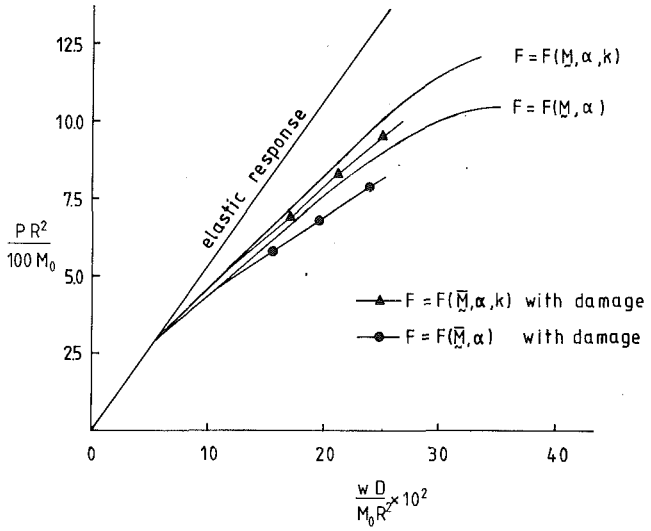

Fig. 5 Central deflections of clamped circular plate subjected to a central load

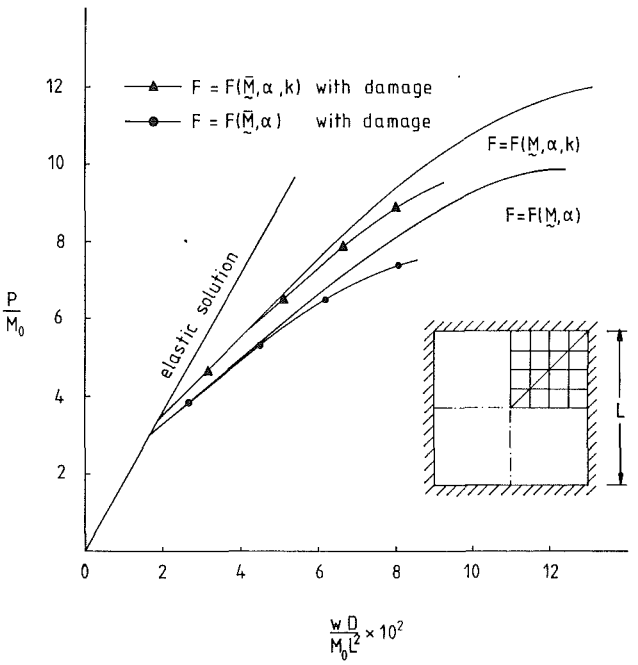

Fig. 6 Central deflections of clamped square plate subjected to a central load

structure was solved in the authors previous paper (Shi and Voyiadjis, 1992a) for various yield conditions. The progressive development of the plastic curvatures across the plate thickness is taken into account here. The critical strain energy release rate in this example is taken as $Y_c = 3\sigma_0^2 h(1-\nu)/4E$ where ν is the Poisson ratio. The element mesh shown in Fig. 3 is employed here again. The load-deflection curves at the plate center are depicted in Fig. 5. The plastic deformation pattern in this example is that the center of the plate becomes a plastic node first. As shown in Fig. 5, the damage process causes the plate to become softer. Furthermore, if no strain hardening is considered, the damaged plate becomes unstable when the damage parameter at the plate center is of the value $d^* = 0.057$. If the strain hardening is considered, the plate is ruptured when the damage parameter at the central point reaches the given critical value $D_c = 0.2$.

Example 3. Clamped Square Plate Subjected to a Central Load. This example concerns a clamped square plate with an aspect ratio of $L/h = 20$ where L is the length and h is the thickness. In order to have considerable damage effect, the centrally concentrated load is considered here. Making use of the symmetry, only a quarter of the plate is studied, and a 4×4 mesh is used for the finite element descritization. As illustrated in Fig. 6, eight triangular elements are used along the diagonal connecting the center and the corner, and twelve rectangular elements are employed elsewhere. There is no analytical solution for the critical load of the clamped square plate considered here. For such a plate made of elastic perfectly plastic material, one of the upper bounds of the critical load obtained from the limit analysis is $P_c = 4\pi M_0$ (Johnson and Mellor, 1973). The present critical load given by yield function $F = F(\mathbf{M}, \alpha)$ is about $P_c = 10\,M_0$. Two yield functions are used for the damage analysis, i.e., $F = F(\overline{\mathbf{M}}, \alpha)$ and $F = F(\overline{\mathbf{M}}, \alpha, k)$. The damage load-deflection curves depicted in Fig. 6 indicate that in both cases, the damage processes reduce the plate stiffness considerably, which is similar to the results presented in the previous example. Corresponding to $F = F(\overline{\mathbf{M}}, \alpha)$, the solution becomes divergent when the damage parameter of the plate at the center is of the value $d^* = 0.0482$. For $F = F(\overline{\mathbf{M}}, \alpha, k)$, the solution becomes unstable when $d^* = 0.0861$. In both cases, the solutions fluctuate somewhat when the damage parameters are close to the values corresponding to the points where divergence occurs.

5 Summary and Conclusions

A computational model for the finite element damage analysis of elastoplastic bending plates is presented in this paper. This computational model can account for the degradation of the mechanical properties resulting from microvoids induced by plastic deformations in ductile plates. When the elastic part of the element stiffness matrix is given explicitly, the elastoplastic-damage stiffness matrix resulting from the proposed computational model can also be evaluated explicitly. The explicit form of the tangent stiffness matrix presented here makes the resulting element very attractive in computation.

The proposed model is based on:

(1) the ductile plastic damage model presented by Lemaitre (1985);
(2) effective stress couples introduced in this work;
(3) damage effect parameters of a cross-section of bending plates defined here which can also be extended to account for partial damage of the cross-section; and
(4) the damage node model proposed here.

The introduction of effective stress couples for bending analysis is the natural extension of the effective stresses. The purpose of the use of the effective stress couples is to construct the yield function in the effective stress space which is associated with the virgin materials. The mean values of the damage parameters across the plate thickness are taken as the damage effect parameters of a cross-section, and these parameters are the conjugate variables of the damage bending strain energy release rates in the irreversible thermodynamics. The damage node model is employed to discretize the damage effect matrices in the element domain. The use of the damage node model makes it possible that the elastoplastic-damage stiffness matrix can be evaluated easily.

The assumption that compression and extension have the same influence on the initiation and growth of microvoids in a ductile material is used in the present computational model. Even though this assumption has certain limitations, it is quite feasible in ductile plates when the macrodefects induced by plastic deformations are dominated by microvoids rather than by microcracks.

The application of the proposed computational model is also given in this work. Because the purpose of this paper is merely to demonstrate the validity of the proposed model by solving some numerical examples, the widely used scalar isotropic damage model is adopted here. The four-noded quadrilateral C^0 strain element for plate bending presented by the authors is employed to evaluate the element stiffness matrix. Since the element stiffness matrix is given explicitly in this four-node C^0 strain plate element, the elastoplastic-damage stiffness matrix presented here can also be evaluated explicitly. Compared with the elastoplastic analysis, only a little additional computational effort is needed in the corresponding damage analysis.

Three examples are solved here to demonstrate the proposed computational model. The numerical results show that the influence of damage on the deformation and load-carrying capacity of flexural plates depends on the boundary condition, loading condition, and material properties. Generally speaking, the damage induced by the plastic deformations has considerable influence on the plates subjected to concentrated load and those made of hardening materials.

It should be pointed out that the ductile plastic damage affects the dynamic response of bending plates more significantly than it does on the static response. This is because the damage process considerably influences the energy dissipation induced by the plastic hysteresis loop and the energy dissipation is a very important source of damping in the plastic dynamic analysis. The present computational model can be extended to the dynamic damage analysis of ductile plates undergoing plastic deformations.

Acknowledgment

The authors would like to express appreciation for the support provided by the Air Force Office of Scientific Research under the grant AFOSR-90-0227DEF. The authors thank Ms. Susan Sartwell for her expert help in preparing this typescript.

References

Chaboche, J. L., 1988, "Continuum Damage Mechanics," ASME JOURNAL OF APPLIED MECHANICS, Vol. 55, pp. 55–72.

Chaw, C. L., and Wang, J., 1988, "A Finite Element Analysis of Continuum Damage Mechanics for Ductile Fracture," *Int. J. Fracture*, Vol. 38, pp. 83–102.

Chaw, C. L., and Lu, T. J., 1989, "On Evolution Laws of Anisotropic Damage," *Eng. Fracture Mech.*, Vol. 34, pp. 679–701.

Crisfield, M. A., 1981, "Finite Element Analysis of Combined Material and Geometric Nonlinearities," *Nonlinear Finite Element Analysis in Structural Mechanics*, W. Wunderlin, et al., eds., Springer-Verlag, New York, pp. 325–338.

Hopkins, H. G., and Wang, A. J., 1954, "Load-Carrying Capacities for Circular Plates of Perfectly-Plastic Material with Arbitrary Yield Conditions," *J. Mech. Phys. Solids*, Vol. 3, pp. 117–129.

Johnson, W., and Mellor, P. B., 1973, *Engineering Plasticity*, Von Nostrand Reinhold, London.

Kachanov, L. M., 1958, "Time of Rupture Process Under Creep Conditions," *IVZ Akad Nauk USSR*, Otd Tech. Nauk., No. 8, pp. 26–31 (in Russian).

Krajcinovic, D., 1979, "Distributed Damage Theory of Beams in Pure Bending," ASME JOURNAL OF APPLIED MECHANICS, Vol. 46, pp. 592–596.

Krajcinovic, D., 1984, "Continuum Damage Mechanics," ASME *Applied Mechanics Reviews*, Vol. 37, pp. 1–6.

Krajcinovic, D., 1989, "Damage Mechanics," *Mech. Mater.*, Vol. 8, pp. 117–197.

Lee, H., Peng, K., and Wang, J., 1985, "An Anisotropic Damage Criterion for Deformation Instability and Its Application to Forming Limit Analysis of Metal Plates," *Eng. Fracture Mech.*, Vol. 21, pp. 1031–1054.

Lehmann, Th., 1991, "Thermodynamical Foundation of Large Inelastic Deformations of Solid Bodies Including Damage," *Int. J. Plasticity*, Vol. 7, pp. 79–98.

Lemaitre, J., Cordebois, J. P., and Dufailly, J., 1979, "Sur le Couplage Endommagement—elasticite," *Compte-rendu a l'Academie des Sciences*, Paris, Vol. 391.

Lemaitre, J., 1985, "A Continuous Damage Mechanics Model for Ductile Fracture," *J. Eng. Mater. Technol.*, Vol. 107, pp. 83–89.

Li, M., Wu, S., and Dang, Z., 1990, "Determination of the Ductile Plastic Damage Variable for the Annealed 30CrMnSi," *Int. J. Fracture*, Vol. 46, pp. R51–R54.

Shi, G., and Voyiadjis, G. Z., 1991, "Efficient and Accurate Four-node Quadrilateral C^0 Plate Bending Element Based on Assumed Strain Fields," *Int. J. Num. Meth. Eng.*, Vol. 32, pp. 1041–1055.

Shi, G., and Voyiadjis, G. Z., 1992a, "A Simple Nonlayered Finite Element for the Elasto-plastic Analysis of Shear Flexible Plates," *Int. J. Num. Meth. Eng.*, Vol. 33, pp. 85–99.

Shi, G., and Voyiadjis, G. Z., 1992b, "A New Damage Strain Energy Release Rate for Plastic Damage Analysis," submitted for publication.

Sumarac, D., and Krajcinovic, D., 1989, "A Mesomechanical Model for Brittle Deformation Processes: Part II," ASME JOURNAL OF APPLIED MECHANICS, Vol. 56, pp. 57–62.

Tang, L., Chen, W., and Liu, Y., 1980, "Quasi-Conforming Elements for Finite Element Analysis," *J. Dalian Inst. Tech.*, Vol. 19, No. 2, pp. 19–36 (in Chinese).

Voyiadjis, G. Z., 1988, "Degradation of Elastic Modulus in Elastoplastic Coupling with Finite Strains," *Int. J. Plasticity*, Vol. 4, pp. 335–353.

Voyiadjis, G. Z., and Shi, G., 1991a, "A Refined Two-Dimensional Theory for Thick Cylindrical Shells," *Int. J. Solids Struct.*, Vol. 27, pp. 261–282.

Voyiadjis, G. Z. and Shi, G., 1991b, "Buckling and Damage Analysis of Plates and Shells," Report to Martin Marietta Manned Space Systems at New Orleans.

A Doubly Periodic Rectangular Array of Fiber-Matrix Interfacial Cracks Under Longitudinal Shearing

Hong Teng

A. Agah-Tehrani
Assoc. Mem. ASME.

Department of Theoretical and Applied Mechanics,
University of Illinois at Urbana-Champaign,
Urbana, IL 61801

The antiplane strain problem of a unidirectional fiber composite consisting of a doubly periodic rectangular array of fibers containing interfacial cracks in an infinite matrix is considered. The interfacial cracks are assumed to exhibit the same periodicity as the fibers. The periodicity of the geometry allows the use of a unit cell in the formulation of the problem. The governing weakly singular integral equation of the mixed boundary value problem permits an explicit solution which contains a set of unknown constants. The unknown constants are then determined by satisfying the boundary conditions on the external surfaces of the unit cell through the method of least squares. The stress intensity factor is calculated for various crack lengths, fiber volume fractions, and fiber spacings. Unlike the plane strain or plane stress deformation, the oscillations in stress and displacement around the interface crack tip are absent in the current antiplane strain problem.

Introduction

In this paper we consider longitudinal shearing of a unidirectional fiber composite consisting of a doubly periodic rectangular array of fibers with interfacial cracks in an infinite matrix. The interfacial cracks are assumed to exhibit the same periodicity as the fibers. A unit cell consisting of a circular fiber and a surrounding rectangular region of matrix material is employed in the formulation of the problem. The resulting mixed boundary value problem leads to a Fredholm integral equation of the first kind with a logarithmically singular kernel, which can be reduced to the airfoil integral equation that permits an explicit solution. The solution contains a set of unknown constants which are determined by satisfying the boundary conditions on the external surfaces of the unit cell through the method of least squares.

Although studies of periodic arrays of cracks in homogeneous materials have been carried out by many authors, for example, Delameter, Herrmann, and Barnett (1975), and Nied (1975), few solutions exist for periodic arrays of interface cracks. Comninou (1979) has given a solution for a periodic array of cracks at the interface between two half-planes.

The problem of a rectangular array fiber composite with perfect interface subjected to longitudinal shear has been solved by Adams and Doner (1967) and Chen (1970). The analysis of interface crack problems related to fiber composite materials based on the treatment of a single fiber in an infinite matrix has been given by a number of authors (Erdogan and Ozbek, 1969; Smith, 1969; Toya, 1974).

Formulation of the Problem

Consider a doubly periodic rectangular array of fiber-matrix interfacial cracks subjected to a remote longitudinal shear stress τ_0 as illustrated in Fig. 1. The fibers are of radius a, and the fiber spacings in the x and y-directions are $2b_1$ and $2b_2$ respectively. Both the fibers and the matrix are taken to be homogeneous, isotropic, and linearly elastic, with shear moduli of G_f and G_m, respectively. It is assumed that the cracks are located symmetrically at the top and the bottom of the fibers as shown in Fig. 1. The assumption is made on the physical grounds that for a rectangular array of fibers with perfect interface under longitudinal shear, the magnitude of the interfacial shear traction attains its maximum at both the top and the bottom of each fiber (Adams and Doner, 1967), suggesting that cracks, if they do develop, are more likely to occur at these locations.

The periodicity of the problem allows us to confine the analysis to a unit cell as shown in Fig. 1. The problem is that of the antiplane strain deformation. The extent of the cracked interface is defined by $\alpha < \theta < \pi - \alpha$ and $\alpha + \pi < \theta < 2\pi - \alpha$, with the half crack length given by $c = \alpha_c a$, where $\alpha_c = \pi/2 - \alpha$.

The symmetries of the problem imply that the analysis can

Contributed by the Applied Mechanics Division of THE AMERICAN SOCIETY OF MECHANICAL ENGINEERS for publication in the ASME JOURNAL OF APPLIED MECHANICS.

Discussion on this paper should be addressed to the Technical Editor, Professor Lewis T. Wheeler, Department of Mechanical Engineering, University of Houston, Houston, TX 77204-4792, and will be accepted until four months after final publication of the paper itself in the ASME JOURNAL OF APPLIED MECHANICS.

Manuscript received by the ASME Applied Mechanics Division, July 12, 1991; final revision, June 4, 1992. Associate Technical Editor: C. F. Shih.

be limited to the first quadrant defined by $0 \le x \le b_1$, $0 \le y \le b_2$. Due to the symmetry and periodicity, the boundary conditions on the sides of the first quadrant of the unit cell are

$$\tau_{xz} = 0,\ x = 0,\ 0 \le y \le b_2 \tag{1}$$

$$\tau_{xz} = 0,\ x = b_1,\ 0 \le y \le b_2 \tag{2}$$

$$w = 0,\ y = 0,\ 0 \le x \le b_1 \tag{3}$$

$$w = w_0,\ y = b_2,\ 0 \le x \le b_1. \tag{4}$$

In (4), w_0 is an unknown constant. In addition, we have the following equilibrium condition:

$$\int_0^{b1} \tau_{\theta z}(r, 0)dr = b_1\tau_0. \tag{5}$$

The stress component τ_{xz} can be expressed in terms of τ_{rz} and $\tau_{\theta z}$ as

$$\tau_{xz} = \tau_{rz}\cos\theta - \tau_{\theta z}\sin\theta. \tag{6}$$

For the boundary conditions at the interface, we have

$$\tau^f_{rz} = \tau^m_{rz},\ r = a,\ 0 \le \theta \le \alpha \tag{7}$$

$$\tau^f_{rz} = \tau^m_{rz} = 0,\ r = a,\ \alpha \le \theta \le \pi/2 \tag{8}$$

$$w^f = w^m,\ r = a,\ 0 \le \theta \le \alpha \tag{9}$$

where the superscripts f and m refer to the fiber and the matrix, respectively.

The longitudinal displacement $w(r, \theta)$ can be represented by the following series:

$$w^f = a\sum_{n=1,3,\ldots}^{\infty} \overline{A}_n\left(\frac{r}{a}\right)^n \sin n\theta,\ 0 < r < a,\ 0 \le \theta \le \pi/2 \tag{10}$$

$$w^m = \frac{a}{G_m}\sum_{n=1,3,\ldots}^{\infty}\left[A_n\left(\frac{r}{a}\right)^n + B_n\left(\frac{a}{r}\right)^n\right]\sin n\theta,$$

$$r > a,\ 0 < x < b_1,\ 0 < y < b_2. \tag{11}$$

And the stress components can be expressed as

$$\tau^f_{rz} = G_f\sum_{n=1,3,\ldots}^{\infty} n\overline{A}_n\left(\frac{r}{a}\right)^{n-1}\sin n\theta,$$

$$0 < r < a,\ 0 \le \theta \le \pi/2 \tag{12}$$

$$\tau^f_{\theta z} = G_f\sum_{n=1,3,\ldots}^{\infty} n\overline{A}_n\left(\frac{r}{a}\right)^{n-1}\cos n\theta,\ 0 < r < a,\ 0 \le \theta \le \pi/2 \tag{13}$$

$$\tau^m_{rz} = \sum_{n=1,3,\ldots}^{\infty} n\left[A_n\left(\frac{r}{a}\right)^{n-1} - B_n\left(\frac{a}{r}\right)^{n+1}\right]\sin n\theta,$$

$$r > a,\ 0 < x < b_1,\ 0 < y < b_2 \tag{14}$$

$$\tau^m_{\theta z} = \sum_{n=1,3,\ldots}^{\infty} n\left[A_n\left(\frac{r}{a}\right)^{n-1} + B_n\left(\frac{a}{r}\right)^{n+1}\right]\cos n\theta,$$

$$r > a,\ 0 < x < b_1,\ 0 < y < b_2. \tag{15}$$

Notice that the Cartesian coordinates (x, y) are related to the polar coordinates (r, θ) by $x = r\cos\theta$, $y = r\sin\theta$.

For the shear traction to be continuous across the interface one has

$$B_n = A_n - G_f\overline{A}_n,\ n = 1, 3, \ldots \tag{16}$$

The boundary conditions (1) and (3) are identically satisfied. The remaining boundary conditions (9), (8), (2), and (4) lead to the following series equations (17), (18), (19), and (20), respectively.

$$G_m\sum_{n=1,3,\ldots}^{\infty}\overline{A}_n\sin n\theta - \frac{2}{\lambda+1}\sum_{n=1,3,\ldots}^{\infty} A_n\sin n\theta = 0,\ 0 \le \theta \le \alpha \tag{17}$$

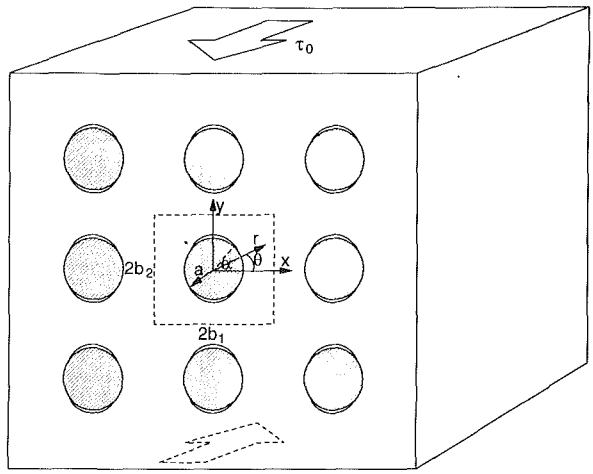

Fig. 1 A doubly periodic rectangular array of fiber-matrix interfacial cracks under longitudinal shearing

$$\sum_{n=1,3,\ldots}^{\infty} n\overline{A}_n\sin n\theta = 0,\ \alpha \le \theta \le \pi/2 \tag{18}$$

$$G_f\sum_{n=1,3,\ldots}^{\infty} n\left(\frac{a}{b_1}\right)^{n+1}\overline{A}_n\cos^{n+1}\theta\sin(n+1)\theta + \sum_{n=1,3,\ldots}^{\infty} nA_n \times\left[\left(\frac{b_1}{a}\right)^{n-1}\frac{\sin(n-1)\theta}{\cos^{n-1}\theta} - \left(\frac{a}{b_1}\right)^{n+1}\cos^{n+1}\theta\sin(n+1)\theta\right] = 0,$$

$$0 \le \theta \le \theta_0 \tag{19}$$

$$-G_f\sum_{n=1,3,\ldots}^{\infty}\left(\frac{a}{b_2}\right)^{n+1}\overline{A}_n\sin^n\theta\sin n\theta + \sum_{n=1,3,\ldots}^{\infty} A_n \times\left[\left(\frac{b_2}{a}\right)^{n-1}\frac{\sin n\theta}{\sin^n\theta} + \left(\frac{a}{b_2}\right)^{n+1}\sin^n\theta\sin n\theta\right] = G_m\gamma_0,$$

$$\theta_0 \le \theta \le \pi/2 \tag{20}$$

where $\lambda = G_f/G_m$, $\theta_0 = \tan^{-1}(b_2/b_1)$, and $\gamma_0 = w_0/b_2$, the average shear strain. The equilibrium condition (5) can be written as

$$G_f\sum_{n=1,3,\ldots}^{\infty}\left(\frac{a}{b_1}\right)^n\overline{A}_n + \sum_{n=1,3,\ldots}^{\infty}\left[\left(\frac{b_1}{a}\right)^{n-1} - \left(\frac{a}{b_1}\right)^{n+1}\right]A_n = \tau_0. \tag{21}$$

Solution of the Series Equations

Let $H(\theta)$ denote the shear traction along the uncracked portion of the interface. From (8) and (12) we have

$$G_f\sum_{n=1,3,\ldots}^{\infty} n\overline{A}_n\sin n\theta = \begin{cases} H(\theta), & 0 \le \theta \le \alpha \\ 0, & \alpha \le \theta \le \pi/2. \end{cases} \tag{22}$$

The Fourier coefficients $\overline{A}_n$ are then given by

$$\overline{A}_n = \frac{4}{\pi G_f n}\int_0^{\alpha} H(\phi)\sin n\phi d\phi$$

$$n = 1, 3, \ldots \tag{23}$$

Substituting (23) into (17), (18), (19), (20), and (21), and changing the order of integration and summation, we arrive at the following coupled integral-series equations:

$$\int_0^\alpha H(\phi)K_1(\theta,\phi)d\phi=\frac{\pi\lambda}{2(\lambda+1)}\sum_{n=1,3,\ldots}^{\infty}A_n\sin n\theta,\ 0\le\theta\le\alpha \tag{24}$$

$$\int_0^\alpha H(\phi)K_2(\theta,\phi)d\phi+\frac{\pi}{4}\sum_{n=1,3,\ldots}^{\infty}nA_n \times\left[\left(\frac{b_1}{a}\right)^{n-1}\frac{\sin(n-1)\theta}{\cos^{n-1}\theta}-\left(\frac{a}{b_1}\right)^{n+1}\cos^{n+1}\theta\sin(n+1)\theta\right]=0,\quad 0\le\theta\le\theta_0 \tag{25}$$

$$\int_0^\alpha H(\phi)K_3(\theta,\phi)d\phi-\frac{\pi}{4}\sum_{n=1,3,\ldots}^{\infty}A_n \times\left[\left(\frac{b_2}{a}\right)^{n-1}\frac{\sin n\theta}{\sin^n\theta}+\left(\frac{a}{b_2}\right)^{n+1}\sin^n\theta\sin n\theta\right]+\frac{\pi}{4}G_m\gamma_0=0,\quad \theta_0\le\theta\le\frac{\pi}{2} \tag{26}$$

$$\int_0^\alpha H(\phi)K_4(\phi)d\phi+\frac{\pi}{4}\sum_{n=1,3,\ldots}^{\infty}\left[\left(\frac{b_1}{a}\right)^{n-1}-\left(\frac{a}{b_1}\right)^{n+1}\right]A_n=\frac{\pi}{4}\tau_0 \tag{27}$$

where

$$K_1(\theta,\phi)=\frac{1}{4}\log\left|\tan\frac{\theta+\phi}{2}\right|-\frac{1}{4}\log\left|\tan\frac{\theta-\phi}{2}\right| \tag{28}$$

$$K_2(\theta,\phi)=\frac{1}{2}\rho_1^2(\theta)[1-\rho_1^2(\theta)]\cos\theta\left[\frac{\cos(\theta-\phi)}{1-2\rho_1^2(\theta)\cos2(\theta-\phi)+\rho_1^4(\theta)}-\frac{\cos(\theta+\phi)}{1-2\rho_1^2(\theta)\cos2(\theta+\phi)+\rho_1^4(\theta)}\right]+\frac{1}{2}\rho_1^2(\theta)[1+\rho_1^2(\theta)]\sin\theta \times\left[\frac{\sin(\theta+\phi)}{1-2\rho_1^2(\theta)\cos2(\theta+\phi)+\rho_1^4(\theta)}-\frac{\sin(\theta-\phi)}{1-2\rho_1^2(\theta)\cos(\theta-\phi)+\rho_1^4(\theta)}\right] \tag{29}$$

$$K_3(\theta,\phi)=\frac{1}{8}\frac{a}{b_2}\log\frac{1+2\rho_2(\theta)\cos(\theta-\phi)+\rho_2^2(\theta)}{1-2\rho_2(\theta)\cos(\theta-\phi)+\rho_2^2(\theta)}-\frac{1}{8}\frac{a}{b_2}\log\frac{1+2\rho_2(\theta)\cos(\theta+\phi)+\rho_2^2(\theta)}{1-2\rho_2(\theta)\cos(\theta+\phi)+\rho_2^2(\theta)} \tag{30}$$

$$K_4(\phi)=\frac{1}{2}\tan^{-1}\frac{2(a/b_1)\sin\phi}{1-(a/b_1)^2} \tag{31}$$

with

$$\rho_1(\theta)\equiv\frac{a}{b_1}\cos\theta,\ \rho_2(\theta)\equiv\frac{a}{b_2}\sin\theta. \tag{32}$$

Equation (24) is a Fredholm integral equation of the first kind with a logarithmic singularity. We can write its solution as

$$H(\theta)=\frac{2\lambda}{\pi(\lambda+1)}\sum_{n=1,3,\ldots}^{\infty}A_nH_n(\theta) \tag{33}$$

where $H_n(\theta)$ are the solutions to the following integral equations:

$$\frac{4}{\pi^2}\int_0^\alpha H_n(\theta)K_1(\theta,\phi)d\phi=\sin n\theta,\ 0\le\theta\le\alpha \quad n=1,3,\ldots \tag{34}$$

It can be shown that by differentiating both sides of (34) with respect to θ, the integral equations (34) can be reduced to the integral equations of the airfoil type and permit the following explicit solutions:

$$H_n(\theta)=\frac{\sin2\theta}{(\sin^2\alpha-\sin^2\theta)^{1/2}}n\int_0^\alpha\frac{(\sin^2\alpha-\sin^2\phi)^{1/2}}{\sin^2\theta-\sin^2\phi}\cos n\phi d\phi \quad n=1,3,\ldots \tag{35}$$

The integrals in (35) are to be interpreted as Cauchy principal value integrals. Since $H_n(0)=0$, it follows from (33) that $H(\theta)$ satisfies the end condition $H(0)=0$ as demanded by the symmetry of the problem.

Substituting (33) into (25) and (26) leads to a system of equations

$$\sum_{n=1,3,\ldots}^{\infty}A_n\psi_n(\theta)=f(\theta),\ 0\le\theta\le\pi/2 \tag{36}$$

for A_n, where

$$\psi_n(\theta)=\begin{cases}\psi_n^{(1)}(\theta), & 0\le\theta\le\theta_0\\ \psi_n^{(2)}(\theta), & \theta_0\le\theta\le\pi/2\end{cases} \tag{37}$$

$$f(\theta)=\begin{cases}0, & 0\le\theta\le\theta_0\\ -\frac{\pi}{4}G_m\gamma_0, & \theta_0\le\theta\le\pi/2\end{cases} \tag{38}$$

$$\psi_n^{(1)}(\theta)=\frac{\pi}{4}n\times\left[\left(\frac{b_1}{a}\right)^{n-1}\frac{\sin(n-1)\theta}{\cos^{n-1}\theta}-\left(\frac{a}{b_1}\right)^{n+1}\cos^{n+1}\theta\sin(n+1)\theta\right]+\frac{2\lambda}{\pi(\lambda+1)}\int_0^\alpha H_n(\phi)K_2(\theta,\phi)d\phi \tag{39}$$

$$\psi_n^{(2)}(\theta)=-\frac{\pi}{4}\left[\left(\frac{b_2}{a}\right)^{n-1}\frac{\sin n\theta}{\sin^n\theta}+\left(\frac{a}{b_2}\right)^{n+1}\sin^n\theta\sin n\theta\right]+\frac{2\lambda}{\pi(\lambda+1)}\int_0^\alpha H_n(\phi)K_3(\theta,\phi)d\phi. \tag{40}$$

Substituting (33) into (27), we obtain

$$\sum_{n=1,3,\ldots}^{\infty}\alpha_nA_n=\frac{\pi}{4}\tau_0 \tag{41}$$

where

$$\alpha_n=\frac{\pi}{4}\left[\left(\frac{b_1}{a}\right)^{n-1}-\left(\frac{a}{b_1}\right)^{n+1}\right]+\frac{2\lambda}{\pi(\lambda+1)}\int_0^\alpha H_n(\phi)K_4(\phi)d\phi. \tag{42}$$

Following Smith (1969), the stress intensity factor is defined by

$$K=\lim_{\theta\to\alpha}\sqrt{2\pi a(\alpha-\theta)}\,\tau_{rz}(a,\theta). \tag{43}$$

Notice that $\tau_{rz}(a,\theta)$ in (43) is the shear traction $H(\theta)$ on the uncracked portion of the interface as given by (33). It can be shown that the stress intensity factor can be expressed as

$$\frac{K}{\sqrt{\pi a}}=\frac{\lambda}{\lambda+1}\sqrt{2\sin2\alpha}\left(A_1+\sum_{n=3,5,\ldots}^{\infty}A_nK_n\right) \tag{44}$$

with K_n given by

$$K_n=\frac{2}{\pi}n\int_0^\alpha\frac{\cos n\phi}{(\sin^2\alpha-\sin^2\phi)^{1/2}}d\phi. \tag{45}$$

Unlike the plane strain or plane stress deformation, the oscillatory behavior of stresses and displacements around the interface crack tip does not appear in the antiplane strain deformation (also see Smith, 1969).

For a single fiber in an infinite matrix, we have $a/b_1=0$, $a/b_2=0$, and it can be easily shown that $A_1=\tau_0$, $A_n=0$ for $n\neq1$ so that Smith's close-form solution (1969) is recovered.

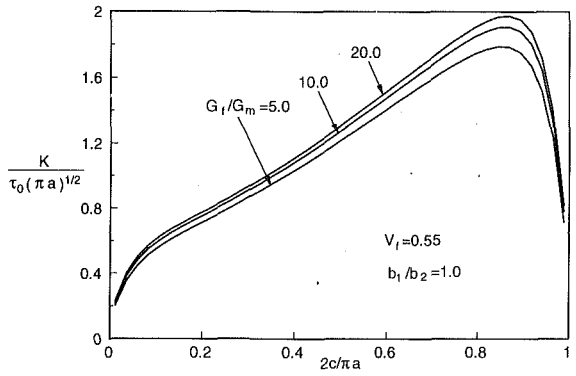

Fig. 2 Stress intensity factor versus crack length, $V_f = 0.55$, for various values of G_f / G_m

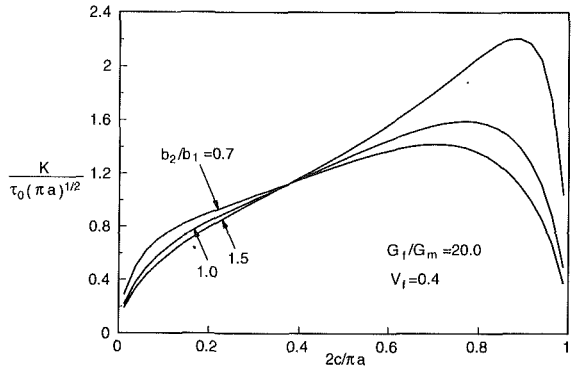

Fig. 4 Stress intensity factor versus crack length, $G_f / G_m = 20.0$, $V_f = 0.4$, for various values of b_1/b_2

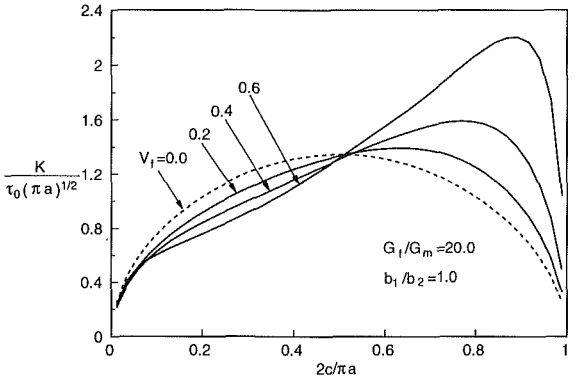

Fig. 3 Stress intensity factor versus crack length, $G_f / G_m = 20.0$, for various values of V_f

Numerical Solution and Results

The method of least squares is used to solve for the coefficients A_n. The method, in the present context, consists of truncating the series equation (36) to N terms and minimizing the mean square error E_N defined by

$$E_N = \int_0^{\pi/2} \left[\sum_{n=1,3,\ldots}^{2N-1} A_n \psi_n(\theta) - f(\theta) \right]^2 d\theta \qquad (46)$$

Accordingly, Eq. (41) is also truncated to N terms so that we have

$$\sum_{n=1,3,\ldots}^{2N-1} \alpha_n A_n = \frac{\pi}{4} \tau_0. \qquad (47)$$

Some of the results for the stress intensity factor are presented in Figs. 2–4. The values of number N used in the computations range from 6 to 40. In general larger values of N are needed when fibers are more closely packed.

Figures 2–4 show that the value of K first increases, then decreases with crack length. Figure 2 shows that the stress intensity factor increases as fibers become stiffer. It is of interest to note that with perfect interface, the local stress concentration factor also becomes higher when the fiber stiffness increases (Adams and Doner, 1967). Thus, high composite stiffness may well result in low strength. As observed from Fig. 3, for small to medium crack lengths, increase in fiber volume content will decrease the stress intensity factor whereas for large crack lengths, higher fiber volume content tends to magnify the stress intensity factor. This suggests that the fiber-reinforcing effect on the resistence to interfacial cracking is apparent only at small to medium crack lengths.

References

Adams, D. F., and Doner, D. R., 1967, "Longitudinal Shear Loading of a Unidirectional Composite," *J. Composite Materials*, Vol. 1, pp. 4–17.

Chen, C. H., 1970, "Fiber-Reinforced Composites Under Longitudinal Shearing," ASME JOURNAL OF APPLIED MECHANICS, Vol. 37, pp. 198–201.

Comninou, M., 1979, "The Periodic Array of Interface Cracks and Their Interaction," *Int. J. Solids Structures*, Vol. 15, pp. 927–934.

Delameter, W. R., Herrmann, G., and Barnett, D. M., 1975, "Weakening of an Elastic Solid by a Rectangular Array of Cracks," ASME JOURNAL OF APPLIED MECHANICS Vol. 42, pp. 74–80.

Erdogan, F., and Ozbek, T., 1969, "Stresses in Fiber-Reinforced Composite with Imperfect Bonding," ASME JOURNAL OF APPLIED MECHANICS, Vol. 36, pp. 865–869.

Nied, H. F., 1987, "Periodic Array of Cracks in Half-plane Subjected to Arbitrary Loading," ASME JOURNAL OF APPLIED MECHANICS, Vol. 54, pp. 642–648.

Smith, E., 1969, "The Extension of Circular-arc Cracks in Antiplane Strain Deformation," *Int. J. Engng. Sci.*, Vol. 7, pp. 973–991.

Toya, M., 1974, "A Crack Along the Interface of a Circular Inclusion Embedded in an Infinite Solid," *J. Mech. Phys. Solids*, Vol. 22, pp. 325–348.

Transient Wave Propagation Methods for Determining the Viscoelastic Properties of Solids

R. H. Blanc
Centre National de la Recherche Scientifique,
Laboratoire de Mécanique et d'Acoustique,
F-13402 Marseille, France

The following two solutions are proposed for deducing the viscoelastic properties of a solid from the change in the shape of a one-dimensional transient mechanical wave as it propagates through the medium: (i) The general solution:—the phase velocity and the attenuation coefficient are expressed in terms of the Fourier transforms of the pulse after two distances of travel, and (ii) A filter method. An experimental set-up is described. The results, which are obtained with no heating of the material, come within the audiofrequency range. This method fills a gap between the existing vibratory and ultrasonic methods.

1 Introduction

The aim of the present study is to deduce the mechanical characteristics of a linear viscoelastic medium from the change in the shape of a transient mechanical wave propagating through a sample of the medium.

In the mathematical study of a one-dimensional viscoelastic wave propagating along a semi-infinite rod, the medium can be represented by means of viscoelastic functions of either the time (Brun, 1974) or the frequency (Hunter, 1960). Sackman and Kaya (1968) have established the analytical bases for determining short time portions of creep or relaxation functions; the four theories proposed so far involve, however, either various operations on observables or related quantities, partial sum expansions, or the resolution of Volterra integral equations. For determining viscoelastic characteristics in terms of the frequency, there exist two modes of excitation: fixed frequency wave trains and transients. The former procedure, which extends to viscoelasticity acoustical methods previously used in elasticity, was applied in particular by A. W. Nolle (1947) and by Hillier and Kolsky (1949) to stretched filaments. Here it is proposed to use the second mode of excitation, that involving brief transient pulses.

Any homogeneous viscoelastic medium subjected to one-dimensional tension or compression can be characterized in terms of the phase velocity $c(\omega)$ and the attenuation coefficient $\alpha(\omega)$ of the longitudinal wave, from which it is possible to deduce the complex modulus and the other equivalent viscoelastic functions (Pierrard, 1969; Ferry, 1980). To determine these functions, a slender bar of the medium under investigation is subjected to a single mechanical transient and the resulting wave is observed. This wave can be represented by a Fourier integral involving the functions $c(\omega)$ and $\alpha(\omega)$ as well as the pulse at the origin. There exist several possible ways of deriving $c(\omega)$ and $\alpha(\omega)$ from this integral. First, one can attempt to integrate it exactly by forming hypotheses as to the form of the functions $c(\omega)$ and $\alpha(\omega)$ and that of the initial pulse. This approach was first used by Bodner and Kolsky (1958) and then developed by Champomier and the present author for use in cases where only the wave front can be observed (Blanc and Champomier, 1976). Another possibility consists of looking for a numerical solution. Kolsky and Lee (1962) have investigated this problem without solving it completely: these authors used a partial Fourier series development to represent the wave, but the expression they obtained for $c(\omega)$ was multivalued, and they did not completely overcome this difficulty. Satô (1955) previously encountered a similar indetermination in formulating the celerity of an elastic surface wave. Theocaris and Papadopoulou (1978) and Christensen (1982) have developed theories on the same lines as Kolsky and Lee. We shall not review here other previous studies, the general validity of which is restricted because they involve the use of mechanical models with only a few elements to represent the medium investigated: Kolsky and Lee (1962) have mentioned that these models are generally inadequate, "except in problems where only narrow frequency ranges are involved". We have established (Blanc, 1971) expressions for the phase velocity and the attenuation coefficient in terms of the argument and the modulus, respectively, of the Fourier transforms of the pulse. Sogabe, Kishida, and Nakagawa (1982) have proposed a similar method. We now propose to completely re-examine this problem and to fully solve it.

The plan of the present paper is as follows. After describing the principle of the method we propose two theoretical solutions. Expressions are first established for $c(\omega)$ and $\alpha(\omega)$ in terms of the Fourier transforms of the wave shapes after two distances of travel. This is the general solution of the problem. It is expressed quite simply in terms of the transfer function of these two wave shapes. On the other hand, the behavior of the medium is completely determined by measuring the real

Contributed by the Applied Mechanics Division of The American Society of Mechanical Engineers for publication in the ASME Journal of Applied Mechanics.

Discussion on this paper should be addressed to the Technical Editor, Professor Lewis T. Wheeler, Department of Mechanical Engineering, University of Houston, Houston, TX 77204-4792, and will be accepted until four months after final publication of the paper itself in the ASME Journal of Applied Mechanics.

Manuscript received by the ASME Applied Mechanics Division, Feb. 5, 1991; final revision, Dec. 9, 1991. Associate Technical Editor: R. M. Bowen.

or complex Poisson's ratio. Secondly, the same pulses are applied to selective frequency filters, and again the required results are obtained from their responses. An appropriate experimental set-up is described. As an illustration, the method is applied to the study of a bitumen.

2 Principle

The principle of the method is as follows. Let us consider a slender bar of the medium, with a constant cross-section area. A short axial disturbance is produced at one end of the bar, resulting in the propagation of a wave. In viscoelastic media, the high frequency waves propagate and are damped more quickly than the low frequency ones, so that the shape of the wave will change continuously as it propagates. Let us assume that we know the successive shapes of the pulse as a function of time after it has travelled two distances x_1 and x_2 along the bar. It is proposed to deduce the corresponding functions $c(\omega)$ and $\alpha(\omega)$.

The bar is assumed to be thin, which means that the largest dimension of its cross-section is small in comparison with the wavelengths involved in the disturbance. The one-dimensional theory will then be valid (Kolsky, 1963).

It is worth mentioning that the results established below in the framework of the present theory in the case of a thin bar will in fact be more general, since they can be extended to other types of waves defined in terms of a single parameter in both rods and extended media (Sackman and Kaya, 1968).

3 General Theory

At distance x and time t, let us consider the stress σ, the displacement u, or any of its successive derivatives with respect to time, particularly the particle velocity $v = \partial u/\partial t$ or the strain ϵ. Let us write $f(x, t)$ for functions of the kind

$$f(x, t) \in \left\{\sigma, u, \ldots, \frac{\partial^i u}{\partial t^i}, \ldots, \epsilon\right\}. \tag{1}$$

$f(x, t)$ can be represented by the Fourier integral (Hunter, 1960)

$$f(x, t) = \frac{1}{2\pi}\int_{-\infty}^{+\infty} \bar{f}(0, \omega) e^{-\alpha(\omega)x + i\omega\left[t - \frac{x}{c(\omega)}\right]} d(\omega) \tag{2}$$

where $\bar{f}(x, \omega)$ stands for the Fourier transform of $f(x, t)$.

Taking the inverse transform of (2),

$$\bar{f}(x, \omega) = \bar{f}(0, \omega) e^{-\alpha(\omega)x - i\omega\frac{x}{c(\omega)}} \tag{3}$$

and writing this transform in polar form

$$\bar{f}(x, \omega) = \rho(x, \omega) e^{i\theta(x, \omega)} \tag{4}$$

yields

$$\rho(x, \omega) e^{i\theta(x, \omega)} = \rho(0, \omega) e^{-\alpha(\omega)x + i\left[\theta(0,\omega) - \frac{\omega x}{c(\omega)}\right]}.$$

This relation can be decomposed into two parts by taking the arguments and the moduli:

$$\theta(x, \omega) = \theta(0, \omega) - \frac{\omega x}{c(\omega)} \tag{5}$$

$$\rho(x, \omega) = \rho(0, \omega) e^{-\alpha(\omega)x}. \tag{6}$$

Let us write these relations for the two distances of travel x_1 and x_2; the following two relations can then be derived:

$$c(\omega) = -\omega \frac{x_2 - x_1}{\theta(x_2, \omega) - \theta(x_1, \omega)} \tag{7}$$

$$\alpha(\omega) = -\frac{1}{x_2 - x_1} \ln \frac{\rho(x_2, \omega)}{\rho(x_1, \omega)}. \tag{8}$$

These general relations completely solve the problem. It can be noted that $c(\omega)$ and $\alpha(\omega)$ are remarkably simple functions of the phase $\theta(x_2, \omega) - \theta(x_1, \omega)$ and the gain $\rho(x_2, \omega)/\rho(x_1, \omega)$ of the transfer function of the two waves (which can be directly obtained experimentally by means of a spectrum analyzer).

3.1 Wave Area Conservation. Let us note that $\alpha(0) = 0$ (Hunter, 1960). Substituting into Eq. (8), this results in

$$\rho(x_2, 0) = \rho(x_1, 0), \tag{9}$$

which is usually not null.

On the other hand, since the transform of a real function is real with $\omega = 0$, it follows that $\theta(x_1, 0) = k_1\pi$ and $\theta(x_2, 0) = k_2\pi$, where k_1 and k_2 are both integers. If one takes $x_2 = x_1$, one obtains $k_2 = k_1$. This gives

$$\theta(x_2, 0) = \theta(x_1, 0). \tag{10}$$

Note that this result can be obtained using a different approach, taking as a starting point the behavior of $c(\omega)$ when $\omega \to 0$ (see Hunter, 1960).

From the definition of the Fourier transform,

$$\bar{v}(x, 0) = \int_{-\infty}^{+\infty} v(x, t) dt = |u(x, t)|_{-\infty}^{+\infty} = \Delta_x u.$$

Substituting from (9) and (10) gives

$$\Delta_{x_2} u = \Delta_{x_1} u. \tag{11}$$

The total displacement of any particle of the material due to the passing of the wave is therefore invariant with respect to the distance covered by the wave, which generalizes the validity of a result established for the elastic case (Kolsky, 1963). According to (1), the area of any wave, whatever its mechanical nature, remains the same as it propagates through the medium.

3.2 Linear Distortion Invariance. Let us examine the effects of a possible linear phase and amplitude distortion which is liable to affect the measurement of the mechanical quantity $f(x, t)$ given by (2). Let us assume that at each angular frequency ω, the transducer (for example) multiplies the amplitude by $\mu(\omega)$ and causes a change of $\psi(\omega)$ in the phase. In this case, the signal obtained will be as follows (Rocard, 1960):

$$f^*(x, t) = \frac{1}{2\pi}\int_{-\infty}^{+\infty} \mu(\omega)\bar{f}(0, \omega) e^{-\alpha(\omega)x + i\left\{\omega\left[t - \frac{x}{c(\omega)}\right] + \psi(\omega)\right\}} d\omega.$$

Inverting this transform yields

$$f^*(x, \omega) = \mu(\omega)\bar{f}(0, \omega) e^{-\alpha(\omega)x + i\left[\frac{-\omega x}{c(\omega)} + \psi(\omega)\right]}$$

and hence

$$\rho^*(x, \omega) e^{i\theta^*(x,\omega)} = \mu(\omega)\rho(0,\omega) e^{-\alpha(\omega)x + i\left[\theta(0,\omega) - \frac{\omega x}{c(\omega)} + \psi(\omega)\right]},$$

which can be decomposed into

$$\theta^*(x, \omega) = \theta(0, \omega) - \frac{\omega x}{c(\omega)} + \psi(\omega)$$

$$\rho^*(x, \omega) = \mu(\omega)\rho(0, \omega) e^{-\alpha(\omega)x}.$$

We obtain

$$\theta^*(x_2, \omega) - \theta^*(x_1, \omega) = \theta(x_2, \omega) - \theta(x_1, \omega)$$

$$\frac{\rho^*(x_2, \omega)}{\rho^*(x_1, \omega)} = \frac{\rho(x_2, \omega)}{\rho(x_1, \omega)}.$$

Applying relations (7) and (8) to the distorted wave shapes therefore does not change the results. Here it should be mentioned that the useful frequency range of the transducers is thus extended to the whole interval within which their sensitivity is appreciable. This increases the variety and number of the gauges which are suitable for use with this method.

Note that this invariance can be said to be a generalization of relation (1), where each element of the set was taken to be the distorted image of any other one. The invariance does not, however, include the case of nonlinear distortions (such as chopping or pulse clipping).

3.3 Complete Determination of the Behavior. In order to completely determine the mechanical behavior, it is necessary to know a second viscoelastic function: we propose the complex Poisson's ratio (Tschoegl, 1989). The longitudinal and radial pulses can be measured at a single point using appropriate strain gauges. The reverse-sign ratio between the Fourier transforms of these pulses yields $\nu(\omega)$. Experience has shown that in fact, $\nu(\omega)$ usually reduces to a real constant which can then be obtained without performing any transforms.

4 The Filter Method

It is now proposed to determine functions $c(\omega)$ and $\alpha(\omega)$ without having to calculate the Fourier transforms which occur in (7) and (8). For this purpose, transients are applied to a frequency filter. The signal delivered each time in response to these transients will depend not only on the input signal but also on the filter characteristics. In order to eliminate the latter, we apply to one same filter a single transient which has been picked up after two distances, x_1 and x_2, along the bar, and compare the results obtained. In a previous study (Blanc, 1974), we solved this problem in the case of an oscillating circuit. It is now proposed to generalize the method by extending it to the case of a narrow band filter system. Let us consider a bandpass filter having ω_0 as the center frequency. Let $h_1(t)$ be the envelope of the impulse response of the equivalent low-pass filter. Let us assume the bandpass of the filter to be sufficiently narrow for the Fourier transform of the input signal to be approximately constant. Papoulis (1962) has established that the filter response to the signal $f(x, t)$ can be expressed as follows:

$$y(x, t) = 2\rho(x, \omega_0)h_1(t)\cos[\omega_0 t + \theta(x, \omega_0) - \chi(\omega_0)]. \quad (12)$$

4.1 Damping Measurement. Let us consider the envelope of the response:

$$y_1(x, t) = 2\rho(x, \omega_0)h_1(t)$$

after two distances of travel, x_1 and x_2, along the bar. Let us take each of these two responses after the same time t' has elapsed from the onset of each response, i.e., making the two auxiliary time origins coincide. Let us write the latter relation with x_1 and x_2 and divide the two equations thus obtained part by part. It emerges that the ratio between the two response envelopes

$$\frac{y_1(x_2, t')}{y_1(x_1, t')} = \frac{\rho(x_2, \omega_0)}{\rho(x_1, \omega_0)}$$

is independent of t'. Substituting this ratio into expression (8) yields the damping coefficient $\alpha(\omega)$ with the angular frequency value $\omega = \omega_0$.

This result is immediately verified in the elastic case where the wave propagates without changing shape. We therefore obtain $y_1(x_2, t') \equiv y_1(x_1, t')$, and hence $\alpha(\omega_0) \equiv 0$.

4.2 Phase Velocity Measurement. The filter response phase is given by the sum between square brackets in expression (12). Let us write t_1 for the time in the filter response at point $x = x_1$ and t_2 at $x = x_2$. As previously, let us then take each of the two responses after the same time t' has elapsed since their time origins, t_{0_1} and t_{0_2}, i.e., at instants

$$t_1 = t_{0_1} + t'$$

and

$$t_2 = t_{0_2} + t'.$$

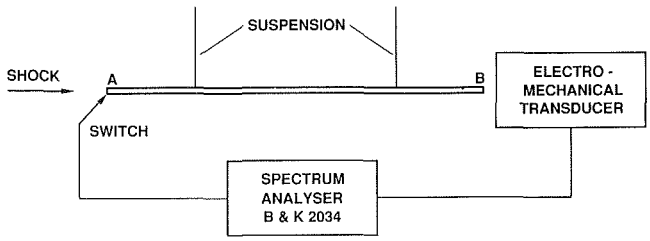

Fig. 1 Experimental set-up

Substituting these values into the corresponding expressions for the phases and subtracting them, the difference is independent of t'. Let us write $\xi(x_1, x_2, \omega_0)$ for this observable difference. This gives

$$\omega_0(t_{0_2} - t_{0_1}) + \theta(x_2, \omega_0) - \theta(x_1, \omega_0) = \xi(x_1, x_2, \omega_0) + 2k\pi$$

which yields modulo $2k\pi$, the denominator of expression (7) for $c(\omega)$ which we were looking for.

The present relation is immediately satisfied in the elastic case, where $\xi + 2k\pi = 0$, so that one again obtains

$$c(\omega_0) = (x_2 - x_1)/(t_{0_2} - t_{0_1}) = \text{const.}$$

In the viscoelastic case, it is necessary to determine k in order to remove the indetermination as to $c(\omega_0)$. Let us consider relation (7). Let us now refer each pulse to an auxiliary time origin, the abscissa t_G of the center of gravity of its area. The argument θ of the Fourier transform of each pulse therefore becomes stationary around the value $n\pi$, and the difference between the arguments becomes stationary around the value 0. In order to relate all the functions to the same time origin, one needs then only to subtract the quantity $\omega(t_{G_2} - t_{G_1})$ from the difference between arguments thus obtained. Since $c(\omega)$ is an increasing function, it is worth noting that the bottom limit of $c(\omega)$

$$c_{\min} = \frac{x_2 - x_1}{t_{G_2} - t_{G_1}}$$

is obtained on the left of the pulse spectrum curve.

5 Experimental Set-Up

5.1 Principle. Let us consider a slender bar of the medium under investigation, ending in two plane cross-sections A and B which are distance 1 apart (cf. Fig. 1). An axial shock is produced against A, which results in the propagation of a compression pulse. On being reflected at free end B, this pulse becomes a tension pulse. It returns to the original end A, which has meanwhile become free, and is again reflected as a compression pulse, and so on. The experimental set-up described below gives the wave shape as a function of time as it reaches B (Hunter, 1960) on two occasions, corresponding to distances of travel chosen from the sequence 1, 31, 51, etc. This set-up is basically similar to that described by Kolsky (1956). On the other hand, it would have been possible to measure the wave shape at any two points x_1 and x_2 along the bar. By comparing functions $f(x_1, t)$ and $f(x_2, t)$, the phase velocity $c(\omega)$ and the attenuation coefficient $\alpha(\omega)$ can be determined using the solutions we established above, and hence the complex modulus $E(\omega)$ can also be obtained, for example. On the other hand, it is furthermore possible to measure Poisson's ratio, as mentioned in Section 3.3. Once these two functions are known, it is then possible to calculate any other complex modulus which may be required to completely characterize a medium (Staverman and Schwarzl, 1956; Waterman, 1977).

The principle of the present method requires that pulses $f(x_1, t)$ and $f(x_2, t)$ be observed separately. B. Lundberg and the

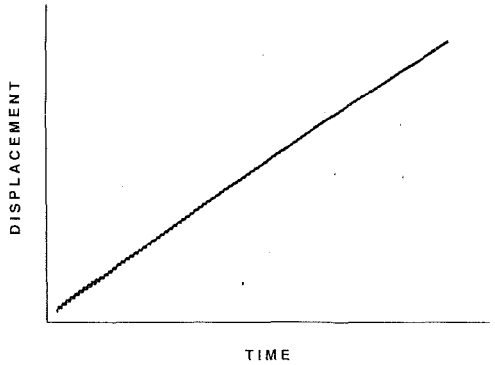

Fig. 2 Longitudinal displacement versus time of one end of a suspended duralumin bar after receiving an axial shock

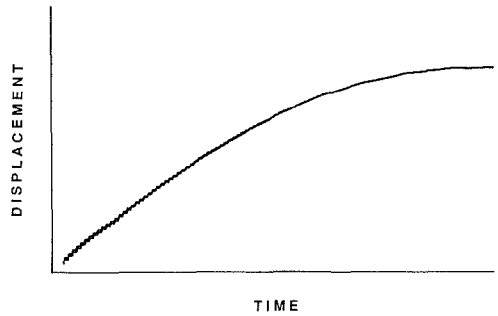

Fig. 3 Bar supported by roller bearings, under identical shock conditions to those pertaining in Fig. 2

author (1988) have solved elsewhere the problem where, on the contrary, one waits until observing the superimposition of the successive reflections of the pulse produced by the two ends of the bar.

5.2 General Description. Figure 1 shows the experimental set-up, which can be seen to be very simple. The suspended bar is free to undergo any small horizontal movement. The axial shock is produced at one of its ends by means of a hammer or an air gun. This shock also activates an electrical switch causing a single sweep to be made on either a spectrum analyzer, a transient recorder or a digital oscilloscope. An electromechanical transducer placed at the opposite end of the bar gives the pulse with respect to time at two passages, successive or otherwise.

5.3 Bar Suspension Mode. We have previously studied the limitations associated with two means of supporting the bar (Blanc, 1971). For this purpose, we recorded the displacement u of the end of a bar while the pulse was travelling back and forth several tens of times along the bar. It was observed that the movement of the end of the suspended bar (cf. Fig. 2) consisted of a series of equal, regularly spaced displacements u, in agreement with relation (11). When the bar was placed on a support (cf. Fig. 3), the kinetic energy began to dissipate as soon as the pulse had travelled only a few tens of times along the bar. It is therefore preferable to suspend the bar using flexible threads with no appreciable mass.

5.4 The Electromechanical Transducer. It is first worth mentioning that in the case of the two theories proposed above, the pulses $f(x_1, t)$ and $f(x_2, t)$ can be determined with an arbitrary unit; only the time axis requires calibration.

From (1), it follows that the quantity to be measured can be either σ, u, v, or ϵ. Now it is not possible to measure the stress σ directly, and in the case of a shock the displacement u is not susceptible to Fourier transform (cf. Figs. 2 and 4). We are left with a choice between measuring v or ϵ.

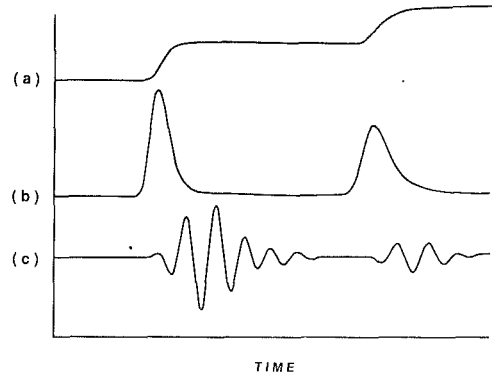

Fig. 4 Upper trace (a): displacement versus time of one end of a bar of polyvinyl chloride 0.80 m in length after receiving a shock at the opposite end. Middle trace (b): direct recording of the corresponding particle velocity. Lower trace (c): response to the above transients (b) of an Alison narrow band-pass filter, type 2D, centered on a frequency of 8.5 kHz.

Both the general method and the filter method are insensitive to distortion, so that one does not have to worry about the severe limitations which often have to be taken into consideration when choosing gauges (Kolsky, 1962). With these two methods, it is thus possible to use either electromagnetic transducers, which are sensitive to the particle velocity v but are otherwise not suitable for measuring mechanical waves because their pass-band is too narrow, or metallic resistance strain gauges, which are sometimes unsuitable because they have an indesirable stiffening effect on soft materials (Swan, 1973).

In the present study we used a velocity-sensitive pick-up, the Brüel and Kjaer Magnetic Transducer MM 0002, a variable reluctance device. It is also possible to use a capacitance gauge which is directly sensitive to v (Blanc, 1971; Graham and Asay, 1978). In fact, gauges of this kind and electromagnetic gauges, both of which are contact-free, are the most convenient types of transducers to use when working at the end of a bar.

5.5 Signal Analysis. The electrical signal delivered by the transducer can be processed in either of two possible ways. First it can be fed into a spectrum analyzer such as the Brüel and Kjaer model 2034 equipped with input time windows in order to separate the pulses. In this case, the transfer function of the two pulse shapes, which occurs in relations (7) and (8), is obtained directly; this yields $c(\omega)$ and $\alpha(\omega)$ without requiring the use of a computer. The second possibility consists of feeding the signal to a transient recorder; we used the Datalab model DL 905. After being thus stored on memory, the signal can again be used in 2 possible ways as follows: (i) it can be displayed on an oscilloscope screen; (ii) since it is digitized, it can be transferred to a computer to have the Fourier transforms and transfer functions of the two pulses calculated. Furthermore, when applying the filter method, the selective frequency filter is placed between the transducer and the transient recorder.

It is also possible, however, to bond two sets of gauges onto the bar. The pulses $f(x_1, t)$ and $f(x_2, t)$ are then obtained on two separate channels. This procedure is used when the pulses overlap in B.

Lastly, in order to measure Poisson's ratio, appropriate two-element strain gauges are used.

6 Results

As an illustration, Fig. 4 gives three typical examples of recordings obtained with a viscoelastic material.

In addition to numerous polymers and elastomers, the above set-up has been used to study a wide range of other materials with internal damping, such as composites, aggregates, and even foams.

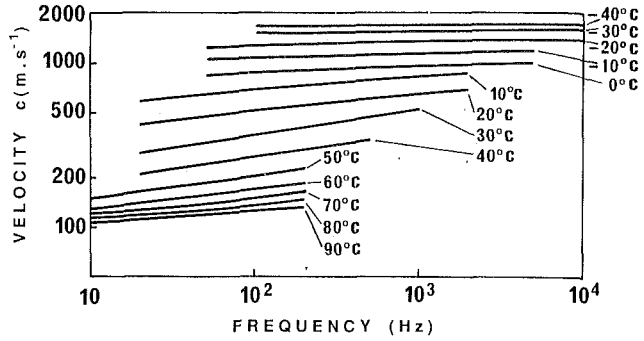

Fig. 5 Phase velocity versus frequency in a bitumen between −40 and +90°C

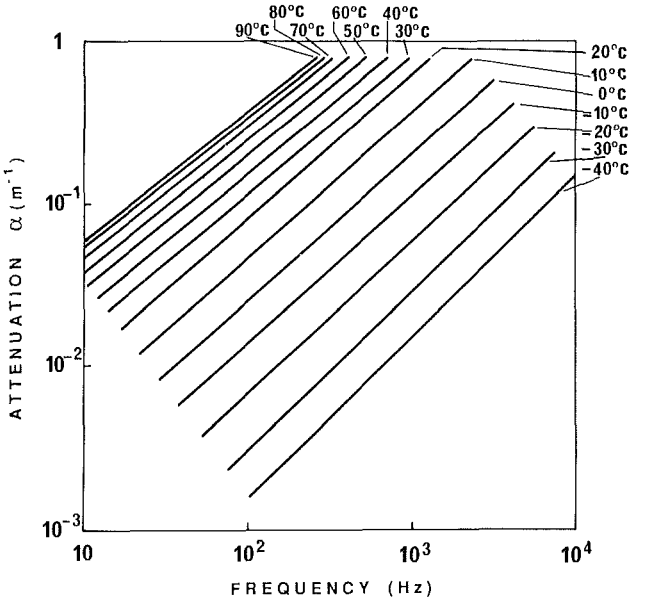

Fig. 6 Attenuation versus frequency in a bitumen between −40 and +90°C

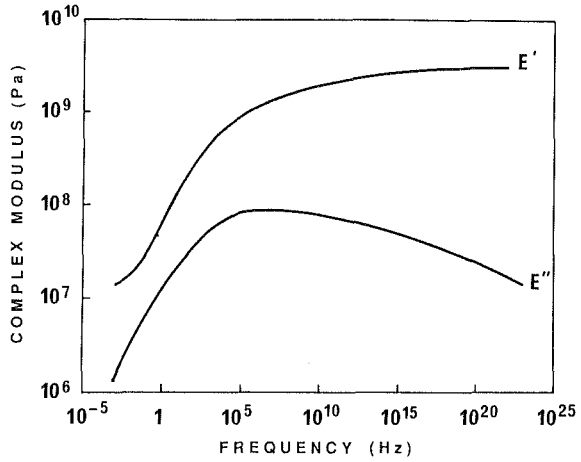

Fig. 7 Complex modulus of a bitumen at 20°C

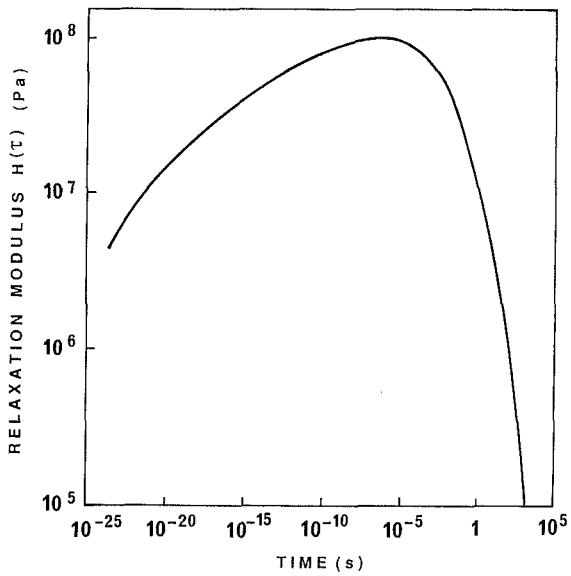

Fig. 8 Relaxation spectrum of a bitumen at 20°C

6.1 Example of a Bitumen. The general theory established in Section 3 was applied to the mechanical characterization of an industrial bitumen, Mexphalte R type 135/10 manufactured by Shell company, which is a highly oxydated gel. The method was applied at 14 temperatures ranging in ten-degree steps between −40 and +90°C. From relations (7) and (8), the families of curves shown in Figs. 5 and 6 were obtained.

The real and imaginary parts of the complex modulus $E = E' + iE''$ can then be built up using the following classical relations:

$$\tan\frac{\varphi(\omega)}{2}=\frac{\alpha(\omega)c(\omega)}{\omega}$$

$$|E(\omega)|=\rho c^2(\omega)\cos^2\frac{\varphi(\omega)}{2}$$

$$E'(\omega)=|E(\omega)|\cos\varphi(\omega)$$

$$E''(\omega)=|E(\omega)|\sin\varphi(\omega),$$

ρ being the specific mass.

These families of curves show that we are dealing with a thermorheologically simple medium (Ferry, 1980). Taking $T_0 = 293$ K as the reference temperature, the shift factor a_T obtained obeys the following W.L.F. equation:

$$lga_T=\frac{-10(T-293)}{92+T-293}.$$

One thus obtains the master curves given in Fig. 7. Knowing $E(\omega)$ makes it possible to calculate the relaxation spectrum, for example, using the method described by Williams and Ferry (Pierrard, 1976; Ferry, 1980), cf. Fig. 8.

7 Discussion and Conclusion

Transient wave propagation methods are proposed for determining the viscoelastic properties of solids. Two solutions are provided for deducing these properties from the change in the shape of a transient mechanical wave as it propagates along a slender bar of the medium under investigation:

(1) the general solution, i.e., one which is valid with any transient excitation. Very simple expressions are established for the phase velocity and the attenuation coefficient in terms of the Fourier transforms of the wave shapes after two distances of travel. These results are shown to be linear distortion invariant.

(2) a physical filter method, which is applicable in the case of brief pulses and does not require calculation of the Fourier transforms. It is again insensitive to distortion.

An appropriate experimental set-up is described for use with these theoretical solutions. With this method, it suffices to

determine the wave shapes with an arbitrary unit, and only the time axis requires to be calibrated. In addition, the distortion invariance implies that a larger number of gauges can be used, and that their useful range is extended to the whole frequency band within which the gauge sensitivity continues to be appreciable. These two characteristics, along with the simplicity of the set-up as a whole, make the present method particularly easy to use. The results occupy a frequency band of one and a half to two decades within the audiofrequency range (20–20,000 Hz). The slight shock required entails practically no heating of the medium. As an illustration, the method was applied to studying a bitumen between -40 and $+90°C$.

The present impulse method fills a gap (see for example Perepechko (1975), Read and Dean (1978), Whorlow (1992), and Masson and Thurston (1990)) between the available vibratory and ultrasonic methods.

Acknowledgments

The author is grateful to Dr. Jessica Blanc for her help with the English translation.

References

Blanc, R. H., 1971, "Détermination de l'équation de Comportement des Corps Viscoélastiques Linéaires par une Méthode d'impulsion," Doctoral Thesis, Université d'Aix-Marseille, Faculté des Sciences, Marseille, France.

Blanc, R. H., 1974, "Spectre Instantané d'une Impulsion dans un Barreau Viscoélastique," *Rheologica Acta*, Vol. 13, No. 2, pp. 228–232.

Blanc, R. H., and Champomier, F. P., 1976, "A Wave-Front Method for Determining the Dynamic Properties of High Damping Materials," *Journal of Sound and Vibration*, Vol. 49, No. 1, pp. 37–44.

Bodner, S. R., and Kolsky, H., 1958, "Stress Wave Propagation in Lead," *Proceedings of the third U.S. National Congress of Applied Mechanics*, R. M. Haythornthwaite, ed., ASME, New York, pp. 495–501.

Brun, L., 1974, "L'onde Simple Viscoélastique Linéaire," *Journal de Mécanique*, Vol. 13, No. 3, pp. 449–498.

Christensen, R. M., 1982, *Theory of Viscoelasticity: An Introduction*, Academic Press, New York.

Ferry, J. D., 1980, *Viscoelastic Properties of Polymers*, John Wiley and Sons, New York.

Graham, R. A., Asay, J. R., 1978, "Measurement of Wave Profiles in Shock-Loaded Solids," *High Temperatures—High Pressures*, Vol. 10, No. 4, pp. 355–390.

Hillier, W., and Kolsky, H., 1949, "An Investigation of the Dynamic Elastic Properties of Some High Polymers," *Proceedings of the Physical Society, London*, Vol. 62, Part 2, No. 350, pp. 111–121.

Hunter, S. C., 1960, "Viscoelastic Waves," *Progress in Solid Mechanics*, Vol. 1, I. N. Sneddon, and R. Hill, eds., North-Holland, Amsterdam, pp. 1–57.

Kolsky, H., 1956, "The Propagation of Stress Pulses in Viscoelastic Solids," *The Philosophical Magazine*, Vol. 1, No. 8, pp. 693–710, pl. 35–36.

Kolsky, H., 1962, "The Detection and Measurement of Stress Waves," *Experimental Techniques in Shock and Vibration*, W. J. Worley, ed., ASME, New York, pp. 11–24.

Kolsky, H., 1963, *Stress Waves in Solids*, Dover, New York.

Kolsky, H., and Lee, S. S., 1962, "The Propagation and Reflection of Stress Pulses in Linear Viscoelastic Media," Contract Nonr 562(30), Office of Naval Research, Washington, D.C., Technical Report No. 5, Brown University, Providence, RI.

Lundberg, B., and Blanc, R. H., 1988, "Determination of Mechanical Material Properties from the Two-Point Response of an Impacted Linearly Viscoelastic Rod Specimen," *Journal of Sound and Vibration*, Vol. 126, No. 1, pp. 97–108.

Mason, W. P., and Thurston, R. N., 1990, *Physical Acoustics* (19 volumes), Academic Press, New York.

Nolle, A. W., 1947, "Acoustic Determination of the Physical Constants of Rubber-Like Materials," *Journal of the Acoustical Society of America*, Vol. 19, No. 1, pp. 194–201.

Papoulis, A., 1962, *The Fourier Integral and its Applications*, McGraw-Hill, New York.

Perepechko, I., 1975, *Acoustic Methods of Investigating Polymers*, Mir, Moscow.

Pierrard, J. M., 1969, "Modèles et Fonctions Visco-élastiques Linéaires," *La Rhéologie*, Persoz, B., coord., Masson, Paris.

Read, B. E., and Dean, G. D., 1978, *The Determination of Dynamic Properties of Polymers and Composites*, Adam Hilger, Bristol, U.K.

Rocard, Y., 1960, *Dynamique Générale des Vibrations*, Masson, Paris.

Sackman, J. L., and Kaya, I., 1968, "On the Determination of Very Early-Time Viscoelastic Properties," *Journal of the Mechanics and Physics of Solids*, Vol. 16, pp. 121–132.

Satô, Y., 1955, "Analysis of Dispersed Surface Waves by Means of Fourier Transform I," *Bull. Earthquake Research Inst.*, (Tokyo), Vol. 33, Part 1, pp. 33–48.

Sogabe, Y., Kishida, K., and Nakagawa, K., 1982, "Wave Propagation Analysis for Determining the Dynamic Properties of High Damping Alloys," *Bull. J.S.M.E.*, Vol. 25, No. 201, pp. 321–327.

Staverman, A. J., and Schwarzl, F., 1956, "Linear Deformation Behaviour of High Polymers," *Die Physik der Hochpolymeren*, Vol. 4, H. A. Stuart, ed., Springer-Verlag, Berlin, Ch. 1.

Swan, J. W., 1973, "Resistance Strain Gauges on Thermoplastics," *Strain*, Apr., pp. 56–59.

Theocaris, P. S., and Papadopoulou, N., 1978, "Propagation of Stress Waves in Viscoelastic Media," *Polymer*, Vol. 19, No. 2, pp. 215–219.

Tschoegl, N. W., 1989, *The Phenomenological Theory of Linear Viscoelastic Behavior*, Springer-Verlag, Berlin.

Waterman, H. A., 1977, "Relations between Loss Angles in Isotropic Linear Viscoelastic Materials," *Rheologica Acta*, Vol. 16, No. 1, pp. 31–42.

Whorlow, R. W., 1992, *Rheological Techniques*, Ellis Horwood, Chichester, U.K.

Journal of Applied Mechanics

Brief Notes

A Brief Note is a short paper that presents a specific solution of technical interest in mechanics but which does not necessarily contain new general methods or results. A Brief Note should not exceed 1500 words *or equivalent* (a typical one-column figure or table is equivalent to 250 words; a one line equation to 30 words). Brief Notes will be subject to the usual review procedures prior to publication. After approval such Notes will be published as soon as possible. The Notes should be submitted to the Technical Editor of the JOURNAL OF APPLIED MECHANICS. Discussions on the Brief Notes should be addressed to the Editorial Department, ASME, United Engineering Center, 345 East 47th Street, New York, N. Y. 10017, or to the Technical Editor of the JOURNAL OF APPLIED MECHANICS. Discussions on Brief Notes appearing in this issue will be accepted until two months after publication. Readers who need more time to prepare a Discussion should request an extension of the deadline from the Editorial Department.

The Scattering of Plane SH-Waves by Noncircular Cavity in Anisotropic Media[1]

Liu Diankui[2] and Han Feng[2]

1 Introduction

The scattering of elastic waves has been the subject of study for over a hundred years, but only in the last 20 years has the subject received a good deal of attention from seismology and applied mechanics. A comprehensive review of them was given by Pao and Mow (1973) and Pao (1983). The problems of scattering by inclusions of arbitrary shape are not amenable to an exact solution, and only in recent years has it been possible to obtain numerical and approximate asymptotic solutions for that. Datta (1978, 1982, 1988) and others have made a greater contribution to these problems. The method of complex function presented by Liu (1982) offers a new approach to two-dimensional scattering problems. Despite the fact that the wave equation is not conserved by a conformal mapping, the scattering of cavities of arbitrary shape can still be treated numerically.

In general, wave in homogeneous anisotropic media cannot be represented by the compressional (P—) wave and shear (S—) wave parts as in an isotropic case, so there are some inherent mathematical difficulties in solving scattering problems in anisotropic media. Until now, references of scattering and dynamic stress concentration in anisotropic media are extremely few. Liu (1988, 1990) tried to meet this challenge by choosing antiplane shear motion as a simple mathematical model to approach anisotropic media character. By means of complex function and mapping techniques, the authors have successfully evaluated the dynamic stress concentration around a circular hole and the displacements along the surface of the cylindrical canyon of arbitrary shape.

[1]This work is supported by the National Natural Science Foundation of the Peoples Republic of China.

[2]Department of Aerospace Engineering, Harbin Shipbuilding Engineering Institute, Harbin 150001, P.R. China.

Contributed by the Applied Mechanics Division of THE AMERICAN SOCIETY OF MECHANICAL ENGINEERS for publication in the ASME JOURNAL OF APPLIED MECHANICS. Manuscript received by the ASME Mechanics Division, June 25, 1991; final revision, Nov. 24, 1992. Associate Technical Editor: S. K. Datta.

In this paper the authors will extend this method in the case of scattering of a plane SH-wave due to cavities with arbitrary shape in anisotropic media by adding the technique of conformal mapping.

2 Statement of Problem

Under an antiplane shear model for the problem of scattering of elastic waves and dynamic stress concentration around a cavity in anisotropic media, the equation of motion can be written as (Liu, 1988)

$$C_{55}\frac{\partial^2 W}{\partial x^2}+2C_{45}\frac{\partial^2 W}{\partial x\partial y}+C_{44}\frac{\partial^2 W}{\partial y^2}=\rho\frac{\partial^2 W}{\partial t^2}. \tag{2.1}$$

The relationships between stresses and displacements in anisotropic media are

$$\tau_{xz}=C_{55}\frac{\partial W}{\partial x}+C_{45}\frac{\partial W}{\partial y},\quad \tau_{yz}=C_{45}\frac{\partial W}{\partial x}+C_{44}\frac{\partial W}{\partial y} \tag{2.2}$$

where (x, y, t) is the displacement of an anti plane shear motion normal to the (x, y) plane and independent of the z-axis; ρ is the density of the media; and C_{55}, C_{45}, C_{44} are elastic constants.

Introduce complex variables $Z = x + iy$, $\bar{Z} = x - iy$. Then, on our study of steady-state waves, w can be expressed as

$$W(Z, \bar{Z}, t)=\mathrm{Re}[W(Z, \bar{Z})e^{-i\omega t}] \tag{2.3}$$

where $w(z, \bar{z})$ is a function of z and $\bar{z}$, ω is the circular frequency of wave.

Here, with the aids of complex variables and the technique of conformal mapping, it is possible to transform the external domain bounded by noncircular curve in the z-plane into the external domain of a unit circle bounded by S in the λ-plane. If both L and S are unlimited and mapped in finite points, the mapping function $\omega(\lambda)$ will be of the following form:

$$Z=\omega(\lambda)=C\lambda+\text{ a holomorphic function.} \tag{2.4}$$

Using the mapping function (2.4), the equation of motion in the λ-plane can be written as (Liu et al., 1990)

$$\begin{aligned}&(C_{55}-C_{44}+2iC_{45})\frac{1}{\omega'(\lambda)}\frac{\partial}{\partial\lambda}\left(\frac{1}{\omega'(\lambda)}\frac{\partial W}{\partial\lambda}\right)\\&\quad+2(C_{55}+C_{44})\frac{1}{\omega'(\lambda)}\frac{\partial}{\partial\lambda}\left(\frac{1}{\overline{\omega'(\lambda)}}\frac{\partial W}{\partial\bar{\lambda}}\right)\\&\quad+(C_{55}-C_{44}-2iC_{45})\frac{1}{\overline{\omega'(\lambda)}}\frac{\partial}{\partial\bar{\lambda}}\left(\frac{1}{\overline{\omega'(\lambda)}}\frac{\partial W}{\partial\bar{\lambda}}\right)+\rho\omega^2 W=0.\end{aligned} \tag{2.5}$$

3 Analytical Method

In order to solve Eq. (2.5), we introduce a new transformation for mapping function $\omega(\lambda)$ as follows:

$$\zeta=\frac{1}{2}\left[(1-i\gamma)\omega(\lambda)+(1+i\gamma)\overline{\omega(\lambda)}\right]$$

$$\bar{\zeta}=\frac{1}{2}\left[(1-i\bar{\gamma})\omega(\lambda)+(1+i\bar{\gamma})\overline{\omega(\lambda)}\right] \tag{3.1}$$

where γ is a complex constant, $\gamma = -C_{45}/C_{44} + i(C_{55}C_{44} - C_{45}^2)^{1/2}/C_{44}$.

Using the transformation (3.1), Eq. (2.5) can be written as

$$\frac{\partial^2 W}{\partial\zeta\partial\bar{\zeta}}=\left(\frac{iK_T}{2}\right)^2 W \tag{3.2}$$

where $K_T = \omega/C_T$, $C_T^2 = \mu/\rho$ and $\mu = (C_{55}C_{44} - C_{45}^2)/C_{44}$.

Following our previous works (Liu et al., 1982), the scattering wave governed by Eq. (3.2) can be written as

$$W^{(s)}(\zeta,\bar{\zeta})=\sum_{-\infty}^{\infty} A_n H_n^{(1)}(K_T|\zeta|)\left[\frac{\zeta}{|\zeta|}\right]^n \tag{3.3}$$

where A_n are undetermined coefficients, and $H_n^{(1)}(.)$ is the first kind Hankel function of the nth order with argument $K_T|\zeta|$.

The incident plane SH-wave in the **n**-direction in anisotropic media can be written as

$$W^{(i)}=W\left(t-\frac{x\cos\alpha+y\sin\alpha}{c_\alpha}\right) \tag{3.4}$$

where $\cos\alpha = n_x$, $\sin\alpha = n_y$; C_α is the wave velocity in the **n**-direction. Then we shall get the expression of velocity C_α as follows:

$$c_\alpha=\left[\frac{1}{\rho}\left(C_{55}\cos^2\alpha+2C_{45}\sin\alpha\cos\alpha+C_{44}\sin^2\alpha\right)\right]^{1/2} \tag{3.5}$$

In the steady-state case, the incident plane SH-wave propagating in the **n**-direction can be written as

$$W^{(i)}=W_0 e^{i[K_\alpha(x\cos\alpha+y\sin\alpha)-\omega t]} \tag{3.6}$$

where W_0 is an amplitude of the incident wave and $\omega = K_\alpha C_\alpha$.

In a polar coordinate system, $x = r\cos\theta$, $y = r\sin\theta$. So the incident wave can be written as

$$W^{(i)}=W_0 e^{i[K_\alpha r\cos(\theta-\alpha)]}e^{-i\omega t}. \tag{3.7}$$

In the λ-plane, the expression (3.6) can be written as

$$W^{(i)}=W_0 e^{\frac{iK_\alpha}{2}[\omega(\lambda)e^{-i\alpha}+\overline{\omega(\lambda)}e^{i\alpha}]}. \tag{3.8}$$

The expression (3.8) can be expanded into the Fourier series in complex form

$$W^{(i)}=W_0\sum_{-\infty}^{\infty}(i)^n J_n(K_\alpha|\omega(\lambda)|)\left[\frac{\omega(\lambda)}{|\omega(\lambda)|}\right]^n e^{-in\alpha}e^{-i\omega t} \tag{3.9}$$

where $J_n(.)$ is the nth order of the Bessel function with the argument $K_\alpha|\omega(\lambda)|$.

In the complex plane Z, stresses can be written as

$$\tau_{xz}-i\tau_{yz}=(C_{55}+C_{44})\frac{\partial W}{\partial Z}+(C_{55}-C_{44}-2iC_{45})\frac{\partial W}{\partial\bar{Z}} \tag{3.10}$$

$$\tau_{rz}-i\tau_{\theta z}=\left[(C_{55}+C_{44})\frac{\partial W}{\partial Z}+(C_{55}-C_{44}-2iC_{45})\frac{\partial W}{\partial\bar{Z}}\right]e^{i\theta}. \tag{3.11}$$

Similarly, in the complex plane λ, (3.11) can be written as

$$\tau_{rz}-i\tau_{\theta z}=\frac{1}{2}\left\{\left[(C_{55}+C_{44})(1-i\gamma)+(C_{55}-C_{44}-2iC_{45})(1+i\gamma)\right]\frac{\partial W}{\partial\zeta}+\left[(C_{55}+C_{44})(1-i\bar{\gamma})+(C_{55}-C_{44}-2iC_{45})(1+i\bar{\gamma})\right]\frac{\partial W}{\partial\bar{\zeta}}\right\}\frac{\lambda}{\rho}\frac{\omega'(\lambda)}{|\omega'(\lambda)|}. \tag{3.12}$$

When the incident steady-state plane SH-wave is from an infinite distance, the controlling condition for stress along the circumference of a scatter should be given, i.e., along $\lambda = e^{i\theta}$, we have

$$\tau_{rz}^{(i)}+\tau_{rz}^{(s)}=F \tag{3.13}$$

where $\tau_{rz}^{(i)}$, $\tau_{rz}^{(s)}$ and F are incident stress, scattering stress, and applied stress along the circumference of the scatterer. Again, assuming that the time dependence of F can be the same as that of the incident wave, we have

$$F=\mathrm{Re}[f\cdot e^{-i\omega t}]. \tag{3.14}$$

Substituting (3.9) and (3.3) into (3.12) and (3.13), respectively, we have

$$\sum_{-\infty}^{\infty}\epsilon_n A_n=\epsilon \tag{3.15}$$

where

$$\epsilon_n=\frac{K_T}{K_\alpha}\left\{\left[(a+ic)H_{n-1}^{(1)}(K_T|\zeta|)\left[\frac{\zeta}{|\zeta|}\right]^{n-1}-(b-ic)H_{n+1}^{(1)}(K_T|\zeta|)\left[\frac{\zeta}{|\zeta|}\right]^{n+1}\right]\frac{\lambda\omega'(\lambda)}{|\omega'(\lambda)|}+\left[(b+ic)\times H_{n-1}^{(1)}(K_T|\zeta|)\left[\frac{\zeta}{|\zeta|}\right]^{n-1}-(a-ic)H_{n+1}^{(1)}(K_T|\zeta|)\left[\frac{\zeta}{|\zeta|}\right]^{n+1}\right]\frac{\bar{\lambda}\,\overline{\omega'(\lambda)}}{|\omega'(\lambda)|}\right\}$$

$$\epsilon=F'-W_0\left\{\left[(1-\eta)\sum_{-\infty}^{\infty}(i)^n\times J_{n-1}(K_\alpha|\omega(\lambda)|)e^{-in\alpha}\left[\frac{\omega(\lambda)}{|\omega(\lambda)|}\right]^{n-1}-(1-\eta-2i\xi)\sum_{-\infty}^{\infty}(i)^n\times J_{n+1}(K_\alpha|\omega(\lambda)|)e^{-in\alpha}\left[\frac{\omega(\lambda)}{|\omega(\lambda)|}\right]^{n+1}\right]\frac{\lambda\omega'(\lambda)}{|\omega'(\lambda)|}+\left[(1-\eta+2i\xi)\sum_{-\infty}^{\infty}(i)^n J_{n-1}(K_\alpha|\omega(\lambda)|)e^{-in\alpha}\left[\frac{\omega(\lambda)}{|\omega(\lambda)|}\right]^{n-1}-(1+\eta)\sum_{-\infty}^{\infty}(i)^n J_{n+1}(K_\alpha|\omega(\lambda)|)e^{-in\alpha}\left[\frac{\omega(\lambda)}{|\omega(\lambda)|}\right]^{n+1}\right]\frac{\bar{\lambda}\,\overline{\omega'(\lambda)}}{|\omega'(\lambda)|}\right\}$$

and

$$F'=F/C_{55}K_\alpha,\quad a=(\eta-\xi^2)^{1/2}\left\{1+\left(\frac{1}{\eta}-\frac{\xi^2}{\eta^2}\right)^{1/2}\right\},$$

$$b=-(\eta-\xi^2)^{1/2}\left\{1-\left(\frac{1}{\eta}-\frac{\xi^2}{\eta^2}\right)^{1/2}\right\},\quad c=\frac{\xi(\eta-\xi^2)^{1/2}}{\eta}$$

and $\xi = C_{45}/C_{55}$, $\eta = C_{45}/C_{55}$.

Multiplying both sides of Eq. (3.15) with $e^{-is\theta}$ and integrating on the interval $[-\pi, \pi]$, we find

$$\sum_{-\infty}^{\infty}\epsilon_{ns}A_n=\epsilon_s \qquad s=0,\ \pm1,\ \pm2\ldots \tag{3.16}$$

where

$$\epsilon_{ns}=\frac{1}{2\pi}\int_{-\pi}^{\pi}\epsilon_n e^{-is\theta}d\theta,\quad \epsilon_s=\frac{1}{2\pi}\int_{-\pi}^{\pi}\epsilon_n e^{-is\theta}d\theta.$$

Dynamic stress concentration factor $\tau^*_{\theta z}$ along the circumference of a scatterer is defined as the ratio of the stress along the circumference to the maximum amplitude of the stress at the same point, i.e. (Pao, 1973; Liu, 1988),

$$\tau^*_{\theta z}=\tau_{\theta z}/\tau_0 \tag{3.17}$$

where $\tau_{\theta z}=\tau^{(i)}_{\theta z}+\tau^{(s)}_{\theta z}$ and $\tau_0=C_{55}K_\alpha W_0$.

Using (3.9), (3.3), (3.12), and (3.17), we have

$$\begin{aligned}\tau^*_{\theta z}=\frac{1}{4}\Bigg\{&i(1+\eta)\sum_{-\infty}^{\infty}(i)^n J_{n-1}(K_\alpha|\omega(\lambda)|)\left[\frac{\omega(\lambda)}{|\omega(\lambda)|}\right]^{n-1}e^{-in\alpha}\\&-[2\xi+i(1-\eta)]\sum_{-\infty}^{\infty}(i)^n\\&\times J_{n+1}(K_\alpha|\omega(\lambda)|)\left[\frac{\omega(\lambda)}{|\omega(\lambda)|}\right]^{n+1}e^{-in\alpha}\Bigg\}\frac{\lambda\omega'(\lambda)}{|\omega(\lambda)|}\\&+\frac{1}{4}\Bigg\{(2\xi+i(\eta-1))\sum_{-\infty}^{\infty}(i)^n\\&\times J_{n-1}(K_\alpha|\omega(\lambda)|)\left[\frac{\omega(\lambda)}{|\omega(\lambda)|}\right]^{n-1}e^{-in\alpha}\\&+i(1+\eta)\sum_{-\infty}^{\infty}(i)^n\\&\times J_{n+1}(K_\alpha|\omega(\lambda)|)\left[\frac{\omega(\lambda)}{|\omega(\lambda)|}\right]^{n+1}e^{-in\alpha}\Bigg\}\frac{\bar\lambda\,\overline{\omega'(\lambda)}}{|\omega'(\lambda)|}\\&+\frac{\eta^{1/2}(\cos^2\alpha+2\xi\sin\alpha\cos\alpha+\eta^2\sin^2\alpha)^{1/2}}{4(\eta-\xi^2)^{1/2}}\Bigg\{(-c+ia)\sum_{-\infty}^{\infty}A_n\\&\times H^{(1)}_{n-1}\left(\frac{c_\alpha}{c_T}K_\alpha|\zeta|\right)\left[\frac{\zeta}{|\zeta|}\right]^{n-1}\\&-(c+ib)\sum_{-\infty}^{\infty}A_nH^{(1)}_{n+1}\left(\frac{c_\alpha}{c_T}K_\alpha|\xi|\right)\left[\frac{\zeta}{|\zeta|}\right]^{n+1}\Bigg]\\&\times\frac{\lambda\omega'(\lambda)}{|\omega'(\lambda)|}+\Bigg[(c+ib)\sum_{-\infty}^{\infty}A_nH^{(1)}_{n-1}\left(\frac{c_\alpha}{c_T}K_\alpha|\zeta|\right)\left[\frac{\zeta}{|\zeta|}\right]^{n-1}\\&\times(c+ia)\sum_{-\infty}^{\infty}A_nH^{(1)}_{n+1}\left(\frac{c_\alpha}{c_T}K_\alpha|\zeta|\right)\left[\frac{\zeta}{|\zeta|}\right]^{n+1}\Bigg]\frac{\bar\lambda\,\overline{\omega'(\lambda)}}{\omega'(\lambda)|}\Bigg\}.\end{aligned} \tag{3.18}$$

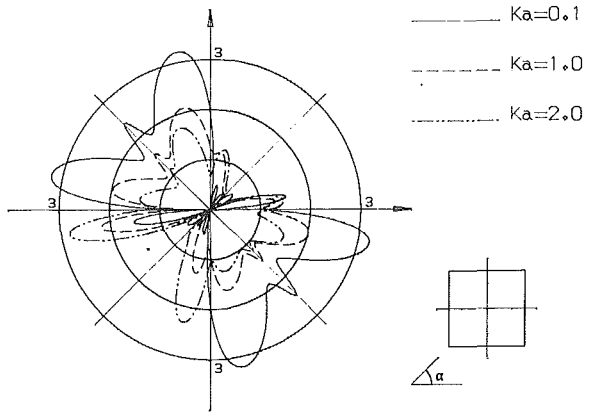

Fig. 1 Distribution of dynamic stress concentration factor: b/a = 0.75, α = 45, ζ = 0.0, η = 0.8

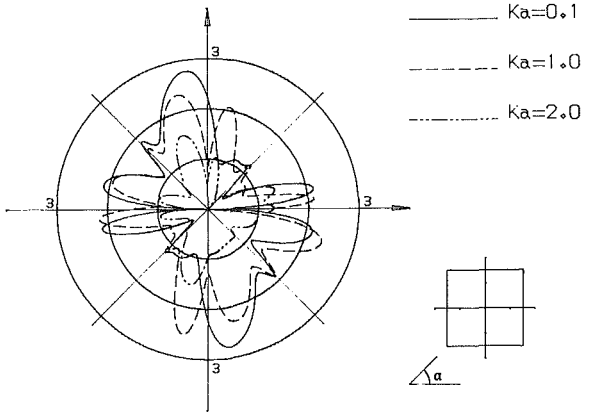

Fig. 2 Distribution of dynamic stress concentration factor: side length of the square cavity is 2a, α = 0, ζ = 0.2, η = 0.8

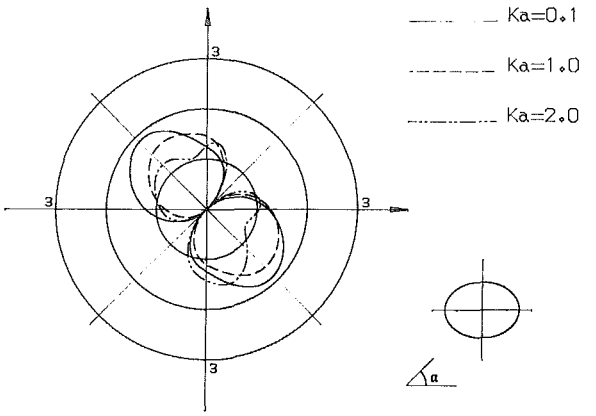

Fig. 3 Distribution of dynamic stress concentration factor: side length of the square cavity is 2a, α = 45, ζ = 0.2, η = 0.8

4 Numerical Results and Conclusions

(1) Case I, for Elliptic Cavity: The distribution of dynamic stress concentration factor in the neighborhood of an elliptic cavity with a and b as its semi-major and semi-minor axis, respectively, can be expressed by choosing mapping function as

$$Z=\omega(\lambda)=R(\lambda+m/\lambda) \tag{4.1}$$

where $R=(a+b)/2$, $m=(a-b)/(a+b)$.

We assume that $b/a=0.75$, the boundary of ellipse is free, and the parameters of media are $\xi=0.0$, $\eta=0.8$. Substituting (4.1) into (3.16) and choosing $n=s=3$ for $K_\alpha a=0.1$, 1.0, and 2.0, the coefficients A_n can be calculated. Figure 1 shows the distribution of dynamic stress concentration factors along the circumference of the cavity.

(2) Case II, for Square Cavity: The function to map the external region of the square cavity with $2a$ as its side length into the unit circle in the λ-plane can be written as

$$Z=\omega(\lambda)=R\left(\lambda-\frac{1}{6\lambda^2}+\frac{1}{56\lambda^7}-\frac{1}{176\lambda^{11}}\right) \tag{4.2}$$

where $R=1.2a$.

Similarly, the boundary condition is free from applied stress and the media are $\xi = 0.2$, $\eta = 0.8$.

By truncating the infinite algebraic Eq. (3.16) to $n = s = 3$ for $K_\alpha a = 0.1$ and $n = s = 4$ for $K_\alpha a = 1.0, 2.0$, we find the coefficients A_n. Figures 2 and 3 show the results of stress concentration factors of calculation.

Now, we conclude this paper with the following discussions:

(a) From the numerical results indicated above, we can see that the effect of anisotropy on dynamic stress concentration is quite significant in engineering sense.

(b) The convergence of Eq. (3.16) depends on wave number $K_\alpha a$ and on cavity shapes. For low $K_\alpha a$, a few terms of the series are sufficient; while for high $K_\alpha a$, the convergence is rather slow. So, in this case, the number of terms needed becomes large in order to get reasonably good results.

(c) For the square cavity case, the mapping function (4.2) maps the unit circle only to "nearly square cavity" with corners as shown in the figure attached. Such shape of course misses the character of sharp corners. This is the weak point of the method of mapping as noted universally in static case. Increasing the number of terms of the mapping functions is a way to make the corners of the figure rather sharp.

References

Datta, S. K., 1978, "Scattering of Elastic Wave," Vol. 4, *Mechanics Today*, pp. 149–208.

Datta, S. K., and Shah, A. H., 1982, "Scattering of SH-waves by Embedded Cavities," *Wave Motion*, Vol. 4, No. 3, pp. 265–283.

Datta, S. K., Ledbetter, H. M., Shindo, Y., and Shah, A. H., 1988, "Phase Velocity and Attenuation of Plane Elastic Waves in Particle-Reinforced Composite Medium," *Wave Motion*, Vol. 10, pp. 171–182.

Liu, Diankui, Gai, Bingzheng, and Tao, Guiyuan, 1982, "Application of the Complex Functions to Dynamic Stress Concentration," *Wave Motion*, Vol. 4, No. 3, pp. 293–304.

Liu, Diankui, 1988, "Dynamic Stress Concentration Around a Circular Hole Due to SH-wave in Anisotropic Media," *Acta Mechanica Sinica*, Vol. 4, No. 2, pp. 146–154.

Liu, Diankui, and Han, Feng, 1990, "Scattering of Plane SH-wave on Cylindrical Canyon of Arbitrary Shape in Anisotropic Media," *Acta Mechanica Sinica*, Vol. 6, No. 3, pp. 256–266.

Pao, Y. H., and Mow, C. C., 1973, *Diffraction of Elastic Waves and Dynamic Stress Concentration*, Crane and Russak, New York.

Pao, Y. H., 1983, "Elastic Wave in Solids," ASME JOURNAL OF APPLIED MECHANICS, Vol. 50, No. 4, pp. 1152–1164.

Steady-State Transonic Motion of a Line Load Over an Elastic Half-Space: The Corrected Cole/Huth Solution

H. G. Georgiadis[3] and J. R. Barber[4]

Introduction

Recently, the authors have investigated various *transient* and *steady-state* elastodynamic indentation problems, with a view to elucidating the paradoxes associated with such problems when the edge of the contact area has a speed in the super-Rayleigh/subseismic range (Georgiadis and Barber, 1993). In the course of this investigation, an *integral equation* formulation was developed for the steady-state problem of an indenter moving over a half-plane at constant speed, using the classical solution of Cole and Huth (1958) as a Green's function. However, the resulting equation exhibited different asymptotic behavior at the ends of the contact zone from other published solutions to elastodynamic *crack* and *contact* problems (see, e.g., Brock, 1977; Freund, 1979; Burridge et al., 1979; Georgiadis, 1986; Robinson and Thompson, 1974). Further investigation showed that this inconsistency was attributable to an error in the Cole/Huth solution in the transonic range. The purpose of the present Note is to rederive the solution for this speed range.

The Cole/Huth problem involves a concentrated load moving with a constant speed, V, over the surface of an elastic half-space under plane-stress or plane-strain conditions. This classical problem was formulated within steady-state elastodynamics and solved by a complex-variable method. A generalization involving an *inclined* load, i.e., a formulation including both normal and tangential tractions, was considered by Eringen and Suhubi (1975), but their final results exhibit the same error.

Obviously, the Cole/Huth problem possesses considerable engineering importance. For instance, it is of great interest in soil dynamics, where ground motions and stresses can be produced by blast waves (surface pressure waves due to explosions), or by supersonic aircraft. Other applications are encountered within the context of contact mechanics (see, e.g., Johnson, 1985); for instance, the problem of high-velocity rocket sleds sliding over steel guide rails (Gerstle and Pearsall, 1974). Consequently, this problem has attracted much interest being cited and fully presented in such classical texts as Sneddon (1951), Fung (1965), and Eringen/Suhubi (1975).

This Brief Note sets out to present the correct solution to the steady-state moving load problem for the *transonic* range, i.e., when the velocity of the load is between the shear and the longitudinal-wave velocities. It is this particular velocity range, where the results for displacements and stresses by Cole/Huth (1958) and Eringen/Suhubi (1975) are in error.

Analysis

We shall present very briefly the solution to the Cole/Huth problem for an inclined load. Our approach leads directly to the expressions for the real and imaginary parts of the complex potential function.

Assume that an elastic body in the form of a half-plane is set into motion by an inclined concentrated load moving over the surface with a constant velocity V (see Fig. 1). The longitudinal and shear-wave velocities are defined as $c_1 = [(\lambda + 2\mu)/\rho]^{1/2}$ and $c_2 = (\mu/\rho)^{1/2}$, in terms of the Lamé constants λ, μ and the mass density ρ. The quantities $M_j \equiv V/c_j$ ($j = 1, 2$) are the Mach numbers which define the speed range (subsonic, transonic, supersonic) of the motion.

The steady-state elastodynamic field can be described by introducing a moving coordinate system (x, y) as $x = x' -$

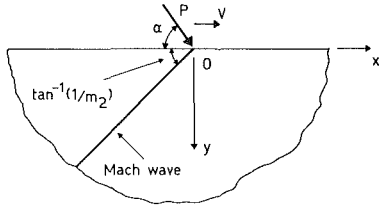

Fig. 1 Steadily moving load over the surface of an elastic half-plane. The Mach wave (shock wave in shear stress) is also shown for the transonic range.

[3]Mechanics Division, School of Technology, The Aristotle University of Thessaloniki, Thessaloniki 540 06, Greece. Mem. ASME.

[4]Department of Mechanical Engineering and Applied Mechanics, The University of Michigan, Ann Arbor, MI 48109-2125.

Contributed by the Applied Mechanics Division of THE AMERICAN SOCIETY OF MECHANICAL ENGINEERS for publication in the ASME JOURNAL OF APPLIED MECHANICS. Manuscript received by the ASME Applied Mechanics Division, Oct. 7, 1991; final revision, Apr. 23, 1992. Associate Technical Editor: S. K. Datta.

Similarly, the boundary condition is free from applied stress and the media are $\xi = 0.2$, $\eta = 0.8$.

By truncating the infinite algebraic Eq. (3.16) to $n = s = 3$ for $K_\alpha a = 0.1$ and $n = s = 4$ for $K_\alpha a = 1.0, 2.0$, we find the coefficients A_n. Figures 2 and 3 show the results of stress concentration factors of calculation.

Now, we conclude this paper with the following discussions:

(a) From the numerical results indicated above, we can see that the effect of anisotropy on dynamic stress concentration is quite significant in engineering sense.

(b) The convergence of Eq. (3.16) depends on wave number $K_\alpha a$ and on cavity shapes. For low $K_\alpha a$, a few terms of the series are sufficient; while for high $K_\alpha a$, the convergence is rather slow. So, in this case, the number of terms needed becomes large in order to get reasonably good results.

(c) For the square cavity case, the mapping function (4.2) maps the unit circle only to "nearly square cavity" with corners as shown in the figure attached. Such shape of course misses the character of sharp corners. This is the weak point of the method of mapping as noted universally in static case. Increasing the number of terms of the mapping functions is a way to make the corners of the figure rather sharp.

References

Datta, S. K., 1978, "Scattering of Elastic Wave," Vol. 4, *Mechanics Today*, pp. 149–208.

Datta, S. K., and Shah, A. H., 1982, "Scattering of SH-waves by Embedded Cavities," *Wave Motion*, Vol. 4, No. 3, pp. 265–283.

Datta, S. K., Ledbetter, H. M., Shindo, Y., and Shah, A. H., 1988, "Phase Velocity and Attenuation of Plane Elastic Waves in Particle-Reinforced Composite Medium," *Wave Motion*, Vol. 10, pp. 171–182.

Liu, Diankui, Gai, Bingzheng, and Tao, Guiyuan, 1982, "Application of the Complex Functions to Dynamic Stress Concentration," *Wave Motion*, Vol. 4, No. 3, pp. 293–304.

Liu, Diankui, 1988, "Dynamic Stress Concentration Around a Circular Hole Due to SH-wave in Anisotropic Media," *Acta Mechanica Sinica*, Vol. 4, No. 2, pp. 146–154.

Liu, Diankui, and Han, Feng, 1990, "Scattering of Plane SH-wave on Cylindrical Canyon of Arbitrary Shape in Anisotropic Media," *Acta Mechanica Sinica*, Vol. 6, No. 3, pp. 256–266.

Pao, Y. H., and Mow, C. C., 1973, *Diffraction of Elastic Waves and Dynamic Stress Concentration*, Crane and Russak, New York.

Pao, Y. H., 1983, "Elastic Wave in Solids," ASME JOURNAL OF APPLIED MECHANICS, Vol. 50, No. 4, pp. 1152–1164.

Steady-State Transonic Motion of a Line Load Over an Elastic Half-Space: The Corrected Cole/Huth Solution

H. G. Georgiadis[3] and J. R. Barber[4]

Introduction

Recently, the authors have investigated various *transient* and *steady-state* elastodynamic indentation problems, with a view to elucidating the paradoxes associated with such problems when the edge of the contact area has a speed in the super-Rayleigh/subseismic range (Georgiadis and Barber, 1993). In the course of this investigation, an *integral equation* formulation was developed for the steady-state problem of an indenter moving over a half-plane at constant speed, using the classical solution of Cole and Huth (1958) as a Green's function. However, the resulting equation exhibited different asymptotic behavior at the ends of the contact zone from other published solutions to elastodynamic *crack* and *contact* problems (see, e.g., Brock, 1977; Freund, 1979; Burridge et al., 1979; Georgiadis, 1986; Robinson and Thompson, 1974). Further investigation showed that this inconsistency was attributable to an error in the Cole/Huth solution in the transonic range. The purpose of the present Note is to rederive the solution for this speed range.

The Cole/Huth problem involves a concentrated load moving with a constant speed, V, over the surface of an elastic half-space under plane-stress or plane-strain conditions. This classical problem was formulated within steady-state elastodynamics and solved by a complex-variable method. A generalization involving an *inclined* load, i.e., a formulation including both normal and tangential tractions, was considered by Eringen and Suhubi (1975), but their final results exhibit the same error.

Obviously, the Cole/Huth problem possesses considerable engineering importance. For instance, it is of great interest in soil dynamics, where ground motions and stresses can be produced by blast waves (surface pressure waves due to explosions), or by supersonic aircraft. Other applications are encountered within the context of contact mechanics (see, e.g., Johnson, 1985); for instance, the problem of high-velocity rocket sleds sliding over steel guide rails (Gerstle and Pearsall, 1974). Consequently, this problem has attracted much interest being cited and fully presented in such classical texts as Sneddon (1951), Fung (1965), and Eringen/Suhubi (1975).

This Brief Note sets out to present the correct solution to the steady-state moving load problem for the *transonic* range, i.e., when the velocity of the load is between the shear and the longitudinal-wave velocities. It is this particular velocity range, where the results for displacements and stresses by Cole/Huth (1958) and Eringen/Suhubi (1975) are in error.

Analysis

We shall present very briefly the solution to the Cole/Huth problem for an inclined load. Our approach leads directly to the expressions for the real and imaginary parts of the complex potential function.

Assume that an elastic body in the form of a half-plane is set into motion by an inclined concentrated load moving over the surface with a constant velocity V (see Fig. 1). The longitudinal and shear-wave velocities are defined as $c_1 = [(\lambda + 2\mu)/\rho]^{1/2}$ and $c_2 = (\mu/\rho)^{1/2}$, in terms of the Lamé constants λ, μ and the mass density ρ. The quantities $M_j \equiv V/c_j$ ($j = 1, 2$) are the Mach numbers which define the speed range (subsonic, transonic, supersonic) of the motion.

The steady-state elastodynamic field can be described by introducing a moving coordinate system (x, y) as $x = x' -$

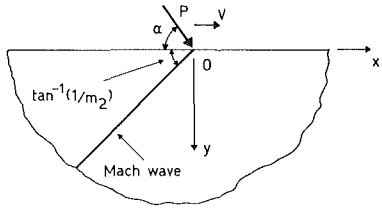

Fig. 1 Steadily moving load over the surface of an elastic half-plane. The Mach wave (shock wave in shear stress) is also shown for the transonic range.

[3]Mechanics Division, School of Technology, The Aristotle University of Thessaloniki, Thessaloniki 540 06, Greece. Mem. ASME.

[4]Department of Mechanical Engineering and Applied Mechanics, The University of Michigan, Ann Arbor, MI 48109-2125.

Contributed by the Applied Mechanics Division of THE AMERICAN SOCIETY OF MECHANICAL ENGINEERS for publication in the ASME JOURNAL OF APPLIED MECHANICS. Manuscript received by the ASME Applied Mechanics Division, Oct. 7, 1991; final revision, Apr. 23, 1992. Associate Technical Editor: S. K. Datta.

Vt, $y = y'$, where (x', y') is a fixed system. Then, for the *transonic* case ($c_2 < V < c_1$), the displacement and stress fields are given in terms of the so-called *potential functions* $W_1(z_1 = x + i\beta_1 y)$ and $W_2(x + m_2 y)$ (Eringen and Suhubi, 1975; Georgiadis, 1986)

$$u_x = 2\mathrm{Re}W_1 + 2m_2 W_2, \tag{1a}$$

$$u_y = -2\beta_1 \mathrm{Im}W_1 - 2W_2, \tag{1b}$$

$$\sigma_x = 2\mu[(2\beta_1^2 + m_2^2 + 1)\mathrm{Re}W_1' + 2m_2 W_2'], \tag{1c}$$

$$\sigma_y = 2\mu[-(1 - m_2^2)\mathrm{Re}W_1' - 2m_2 W_2'], \tag{1d}$$

$$\tau_{xy} = 2\mu[-2\beta_1 \mathrm{Im}W_1' - (1 - m_2^2) W_2'], \tag{1e}$$

where $\beta_1 = (1 - M_1^2)^{1/2}$ and $m_2 = (M_2^2 - 1)^{1/2}$ are real numbers.

The boundary conditions of the problem can be written as

$$\sigma_y(x,0) = -P \sin\alpha\, \delta(x), \tag{2a}$$

$$\tau_{xy}(x,0) = -P \cos\alpha\, \delta(x), \tag{2b}$$

where $\delta(\bullet)$ is the Dirac delta function, and the angle α defines the inclination of the load, as shown in Fig. 1. Introducing Eqs. (2) into (1) and then eliminating the function $W_2'(x)$ from the resulting system yields a relation between the real and imaginary parts of the function W_1'

$$\mathrm{Re}W_1'(x) = \frac{P \bullet f(\alpha, m_2)}{2\mu(1 - m_2^2)^2}\,\delta(x) + \frac{4\beta_1 m_2}{(1 - m_2^2)^2}\,\mathrm{Im}W_1'(x), \tag{3}$$

where $f(\alpha, m_2) \equiv \sin\alpha \bullet (1 - m_2^2) - 2\cos\alpha \bullet m_2$.

The boundary value problem in (3) is a *Riemann-Hilbert problem* (Gakhov, 1966) and can be solved by utilizing the *Hilbert transform* and elements from the theory of singular integral equations (Tricomi, 1985). By applying the operation $\mathrm{Im}W_1'(x) = \int_{-\infty}^{\infty} [\mathrm{Re}W_1'(\tau)/\pi(x - \tau)]d\tau$ to (3), we get a singular IE which has the solution

$$\mathrm{Re}W_1'(x) = \frac{P \bullet f(\alpha, m_2)}{2\mu R^*}\left[(1 - m_2^2)^2 \delta(x) + \frac{4\beta_1 m_2}{\pi}\frac{1}{x}\right], \tag{4}$$

where $R^* \equiv (1 - m_2^2)^4 + 16\beta_1^2 m_2^2$. Then, $\mathrm{Im}W_1'(x)$ follows from (3), whereas $W_2'(x)$ may be obtained from Eqs. (1) and (2). Finally, the functions $\mathrm{Re}W_1(x)$, $\mathrm{Im}W_1(x)$, and $W_2(x)$ are found by integrating the previous functions and omitting constants of integration, i.e., rigid-body displacements.

The next step involves evaluation of the functions $\mathrm{Re}W_1'(z_1)$, $\mathrm{Im}W_1'(z_1)$ and $W_2'(x + m_2 y)$ which enter (1) and give the stresses. The first two functions result from $\mathrm{Re}W_1'(x)$ through the *Schwarz integral formula* (Churchill et al., 1974)

$$W_1'(z_1) \equiv \mathrm{Re}W_1'(z_1) + i\mathrm{Im}W_1'(z_1) = \frac{1}{\pi}\int_{-\infty}^{\infty} \frac{\beta_1 y \bullet \mathrm{Re}W_1'(\tau) + i(x - \tau) \bullet \mathrm{Re}W_1'(\tau)}{(\tau - x)^2 + \beta_1^2 y^2}\, d\tau. \tag{5}$$

In combining (4) and (5) integrals which need to be evaluated are found in Tables (e.g., Petit Bois, 1961), and finally we obtain

$$\mathrm{Re}W_1'(z_1) = \frac{Bx + \pi^{-1}\beta_1 A y}{x^2 + \beta_1^2 y^2}, \tag{6a}$$

$$\mathrm{Im}W_1'(z_1) = \left(\pi^{-1}Ax + \frac{Bx^2}{\beta_1 y}\right)\frac{1}{x^2 + \beta_1^2 y^2} - \frac{B}{\beta_1 y}, \tag{6b}$$

where the constants A and B are given as

$$A = P(2\mu R^*)^{-1} \bullet f(\alpha, m_2) \bullet (1 - m_2^2)^2, \tag{7a}$$

$$B = P(2\pi\mu R^*)^{-1} \bullet f(\alpha, m_2) \bullet 4\beta_1 m_2. \tag{7b}$$

We also find

$$W_2'(x + m_2 y) = \frac{P}{\mu(1 - m_2^2)}[(1/2)\cos\alpha + 4\beta_1^2 m_2 (R^*)^{-1} \bullet f(\alpha, m_2)] \bullet \delta(x + m_2 y) - \frac{P\beta_1(1 - m_2^2) \bullet f(\alpha, m_2)}{\pi\mu R^*}\frac{1}{x + m_2 y}. \tag{8}$$

In a similar way, we can find the functions $\mathrm{Re}W_1(z_1)$, $\mathrm{Im}W_1(z_1)$, and $W_2(x + m_2 y)$, which are required for the determination of subsurface displacements,

$$\mathrm{Re}W_1(z_1) = \frac{P \bullet f(\alpha, m_2)}{2\pi\mu R^*}[4\beta_1 m_2 \bullet \log(r_1) - (1 - m_2^2)^2 \bullet \theta_1], \tag{9a}$$

$$\mathrm{Im}W_1(z_1) = \frac{P \bullet f(\alpha, m_2)}{2\pi\mu R^*}[4\beta_1 m_2 \bullet \theta_1 + (1 - m_2^2)^2 \bullet \log(r_1)], \tag{9b}$$

$$W_2(x + m_2 y) = \frac{P}{\mu(1 - m_2^2)}[(1/2)\cos\alpha + 4\beta_1^2 m_2 (R^*)^{-1} \bullet f(\alpha, m_2)] \bullet H(x + m_2 y) - 2\beta_1(1 - m_2^2)^{-1} \bullet A \bullet \log(|x + m_2 y|), \tag{10}$$

where $r_1 = (x^2 + \beta_1^2 y^2)^{1/2}$, $\theta_1 = \tan^{-1}(\beta_1 y/x)$, $0 < \theta_1 < \pi$, and $H(\bullet)$ is the Heaviside step function.

Neither Cole and Huth (1958) nor Eringen and Suhubi (1975) give expressions for $\mathrm{Re}W_1'$, $\mathrm{Im}W_1'$, $\mathrm{Re}W_1$, $\mathrm{Im}W_1$ (our Eqs. (6), (9)), but their expressions for W_2', W_2 are identical with our Eqs. (8), (10). However, as will be shown in the next section, the final expressions for the stress and displacement fields given by these authors are incorrect.

Results and Conclusions

Having available the functions given by Eqs. (6)–(10), one can readily obtain the stress and displacement field by substituting in Eq. (1). In particular, the expressions for the surface displacements $u_y(x, 0)$, $u_x(x, 0)$ and the normal stress immediately beneath the load $\sigma_y(0, y)$ are found to be

$$u_y(x,0) = \frac{P}{\mu}\left[\frac{\beta_1(1 - m_2^2)^4 \bullet f(\alpha, m_2)}{\pi R^*} \bullet \log(|x|) + \frac{1}{(1 - m_2^2)}\left[\frac{4\beta_1^2 m_2(1 + m_2^2) \bullet f(\alpha, m_2)}{R^*} - \cos\alpha\right] \bullet H(-x)\right], \tag{11}$$

$$u_x(x,0) = \frac{2P\beta_1 m_2(1 + m_2^2) \bullet f(\alpha, m_2)}{\pi\mu R^*} \bullet \log(|x|) + \frac{P}{\mu(1 - m_2^2)}\left[\frac{f(\alpha, m_2)}{R^*}[(1 - m_2^2)^3 + 8\beta_1^2 m_2^2] + \cos\alpha \bullet m_2\right] \bullet [1 - H(-x)], \tag{12}$$

$$\sigma_y(0,y) = \frac{P(1 - m_2^2) \bullet f(\alpha, m_2)}{\pi\beta_1 R^*}[4\beta_1^2 - (1 - m_2^2)^2]\frac{1}{y} - \frac{4Pm_2}{(1 - m_2^2)}[(1/2)\cos\alpha + 4\beta_1^2 m_2 (R^*)^{-1} \bullet f(\alpha, m_2)] \bullet \delta(m_2 y). \tag{13}$$

Equations (11)–(13) differ significantly from the corresponding expressions given by Cole and Huth (1958) and Eringen

and Suhubi (1975). These researchers do not give enough detail in their analyses for the cause of the difference to be identified with certainty, but a possible source of error could be an incorrect separation of their complex potentials into real and imaginary parts.

A check on the correctness of the present analysis and results are provided by our previous findings on the asymptotics of moving *contact* zones (Georgiadis and Barber, 1993). For the case of *normal* load, i.e., when $\alpha = \pi/2$, and for the $u_y(x, 0)$ displacement (which was utilized as a Green's function in Georgiadis and Barber, 1991), the Cole/Huth expression is in error by a factor $(2/M_2^2)$ multiplying the $H(-x)$ term.

With this correction, the asymptotic behavior of the stress and displacement field at the edges of the moving contact zone becomes consistent with that obtained in all other published solutions of elastodynamic crack and contact problems (Brock, 1977; Freund, 1979; Burridge et al., 1979; Georgiadis, 1986; Robinson and Thompson, 1974) involving the edge of a crack or contact zone moving at a speed in the transonic range.

In closing, we mention that the respective *transient* problem was considered by Payton (1967). In principle, one could get the present *steady-state* results by Payton's analysis, as time tends to infinity in the transient problem. However, the latter work does not provide pertinent results for field quantities in the interior of the half-space and, moreover, only the *horizontal* surface displacement caused by a *normal* load was worked out. Notice that we provide results for the more general case of an *inclined* load and stresses and displacements at all field points. It is felt thus, by also taking into account the very complicated expressions in Payton's analysis, that a *direct* steady-state analysis (as the present one) is preferable in some instances over a limiting procedure of exploiting already obtained transient results. This is especially true when one tries to correct some established and well-known analyses, as we did in the present case.

References

Brock, L. M., 1977, "Two Basic Problems of Plane Crack Extension—A Unified Treatment," *International Journal of Engineering Science*, Vol. 15, pp. 527–536.

Burridge, R., Conn, G., and Freund, L. B., 1979, "The Stability of a Rapid Mode II Shear Crack with Finite Cohesive Traction," *Journal of Geophysical Research*, Vol. 84, pp. 2210–2222.

Churchill, R. V., Brown, J. W., and Verhey, R. F., 1974, *Complex Variables and Applications*, McGraw-Hill, Tokyo.

Cole, J., and Huth, J., 1958, "Stresses Produced in a Half Plane by Moving Loads," ASME JOURNAL OF APPLIED MECHANICS, Vol. 25, pp. 433–436.

Eringen, A. C., and Suhubi, E. S., 1975, *Elastodynamics*, Vol. 2, Academic Press, New York.

Freund, L. B., 1979, "The Mechanics of Dynamic Shear Crack Propagation," *Journal of Geophysical Research*, Vol. 84, pp. 2199–2209.

Fung, Y. C., 1965, *Foundations of Solid Mechanics*, Prentice-Hall, Englewood Cliffs, NJ.

Gakhov, F. D., 1966, *Boundary Value Problems*, Pergamon Press, New York.

Georgiadis, H. G., 1986, "On the Stress Singularity in Steady-State Transonic Shear Crack Propagation," *International Journal of Fracture*, Vol. 30, pp. 175–180.

Georgiadis, H. G., and Barber, J. R., 1993, "On the Super-Rayleigh/Subseismic Elastodynamic Indentation Problem," *Journal of Elasticity*, to appear.

Gerstle, F. P., and Pearsall, G. W., 1974, "The Stress Response of an Elastic Surface to a High-Velocity, Unlubricated Punch," ASME JOURNAL OF APPLIED MECHANICS, Vol. 41, pp. 1036–1040.

Johnson, K. L., 1985, *Contact Mechanics*, Cambridge University Press, Cambridge, U.K.

Payton, R. G., 1967, "Transient Motion of an Elastic Half-Space due to a Moving Surface Line Load," *International Journal of Engineering Science*, Vol. 5, pp. 49–79.

Petit Bois, G., 1961, *Tables of Indefinite Integrals*, Dover, New York.

Robinson, A. R., and Thompson, J. C., 1974, "Transient Stresses in an Elastic Half-Space Resulting from the Frictionless Indentation of a Rigid Wedge-Shaped Die," *ZAMM*, Vol. 54, pp. 139–144.

Sneddon, I. N., 1951, *Fourier Transforms*, McGraw-Hill, New York.

Tricomi, F. G., 1985, *Integral Equations*, Dover, New York.

Capillary-Gravity Waves Generated Against a Vertical Cliff in a Fluid of Finite Depth

A. K. Pramanik[5] and D. Banik[5]

1 Introduction

This is the problem of two-dimensional capillary-gravity waves generated by some free surface oscillatory pressure distribution which moves with a uniform velocity. The fluid is incompressible, inviscid and is of uniform finite depth h and is bounded on one side by a vertical cliff.

This problem without the cliff has been studied by Pramanik and Majumdar (1984). The present problem with infinitely large depth has been discussed by Pramanik and Majumdar (1988). To understand the motivation of our paper we state the main results of the paper of Pramanik and Majumdar (1984). The ultimate steady state consists of six progressive waves, four gravity waves, and two capillary waves. There exists in the (a, b, c) space, where a, b, c are the nondimensional forms of the parameters of the problem, a surface called the critical surface, which divides the space into several regions in each of which the propagation is different.

The aim of the present paper is (i) to fully characterize the critical surfaces for all possible values of the parameters, (ii) to determine the waves for all possible values of the parameters, and (iii) to find the effect of the cliff on the reflection of waves.

As is already stated in Pramanik and Majumdar (1984), the waves were determined on the basis of two sections of the critical surface by the plane c = constant. However, the complete characterization of critical surface is possible. In this paper the critical surfaces are determined for all possible values of a, b, c. It is found that these surfaces divide the whole positive quadrant of the (a, b, c) space into five distinct regions for (a, b, c) in each of which the propagation of waves is different and the waves for all cases are determined. It is known that for (a, b, c) outside these surfaces, the waves are with constant amplitude while the amplitude is unbounded for (a, b, c) on the critical surfaces.

Previously, in linear theory, these waves for (a, b, c) on critical surfaces were not of interest where essentially nonlinear theory is to be developed for the complete understanding of the waves. However, to develop the nonlinear theory (Akylas, 1984) one has to take into account the order of the unboundedness on the critical surfaces. Motivated by this idea, waves are also determined for (a, b, c) on the critical surfaces.

Regarding the effect of the cliff it is found that one gravity wave is reflected for certain values of (a, b, c). In (a, b, c) space there is a surface called the surface of reflection, such that for (a, b, c) on one side of this surface, including those on the surface, reflection occurs. And the amplitude of the reflected wave remains the same as the original waves for all (a, b, c), excepting for those forming a curve on the surface of reflections. For (a, b, c) of this curve, the amplitude is found to be reduced.

2 Formulation and Formal Solution

We take the x-axis along the undisturbed free surface and

[5]Department of Applied Mathematics, Calcutta University, Calcutta, India.

Contributed by the Applied Mechanics Division of THE AMERICAN SOCIETY OF MECHANICAL ENGINEERS for publication in the ASME JOURNAL OF APPLIED MECHANICS.

Manuscript received by the ASME Applied Mechanics Division, Oct. 3, 1990; final revision, Feb. 20, 1992. Associate Technical Editor: K. R. Sreenivasan.

and Suhubi (1975). These researchers do not give enough detail in their analyses for the cause of the difference to be identified with certainty, but a possible source of error could be an incorrect separation of their complex potentials into real and imaginary parts.

A check on the correctness of the present analysis and results are provided by our previous findings on the asymptotics of moving *contact* zones (Georgiadis and Barber, 1993). For the case of *normal* load, i.e., when $\alpha = \pi/2$, and for the $u_y(x, 0)$ displacement (which was utilized as a Green's function in Georgiadis and Barber, 1991), the Cole/Huth expression is in error by a factor $(2/M_2^2)$ multiplying the $H(-x)$ term.

With this correction, the asymptotic behavior of the stress and displacement field at the edges of the moving contact zone becomes consistent with that obtained in all other published solutions of elastodynamic crack and contact problems (Brock, 1977; Freund, 1979; Burridge et al., 1979; Georgiadis, 1986; Robinson and Thompson, 1974) involving the edge of a crack or contact zone moving at a speed in the transonic range.

In closing, we mention that the respective *transient* problem was considered by Payton (1967). In principle, one could get the present *steady-state* results by Payton's analysis, as time tends to infinity in the transient problem. However, the latter work does not provide pertinent results for field quantities in the interior of the half-space and, moreover, only the *horizontal* surface displacement caused by a *normal* load was worked out. Notice that we provide results for the more general case of an *inclined* load and stresses and displacements at all field points. It is felt thus, by also taking into account the very complicated expressions in Payton's analysis, that a *direct* steady-state analysis (as the present one) is preferable in some instances over a limiting procedure of exploiting already obtained transient results. This is especially true when one tries to correct some established and well-known analyses, as we did in the present case.

References

Brock, L. M., 1977, "Two Basic Problems of Plane Crack Extension—A Unified Treatment," *International Journal of Engineering Science*, Vol. 15, pp. 527–536.

Burridge, R., Conn, G., and Freund, L. B., 1979, "The Stability of a Rapid Mode II Shear Crack with Finite Cohesive Traction," *Journal of Geophysical Research*, Vol. 84, pp. 2210–2222.

Churchill, R. V., Brown, J. W., and Verhey, R. F., 1974, *Complex Variables and Applications*, McGraw-Hill, Tokyo.

Cole, J., and Huth, J., 1958, "Stresses Produced in a Half Plane by Moving Loads," ASME JOURNAL OF APPLIED MECHANICS, Vol. 25, pp. 433–436.

Eringen, A. C., and Suhubi, E. S., 1975, *Elastodynamics*, Vol. 2, Academic Press, New York.

Freund, L. B., 1979, "The Mechanics of Dynamic Shear Crack Propagation," *Journal of Geophysical Research*, Vol. 84, pp. 2199–2209.

Fung, Y. C., 1965, *Foundations of Solid Mechanics*, Prentice-Hall, Englewood Cliffs, NJ.

Gakhov, F. D., 1966, *Boundary Value Problems*, Pergamon Press, New York.

Georgiadis, H. G., 1986, "On the Stress Singularity in Steady-State Transonic Shear Crack Propagation," *International Journal of Fracture*, Vol. 30, pp. 175–180.

Georgiadis, H. G., and Barber, J. R., 1993, "On the Super-Rayleigh/Subseismic Elastodynamic Indentation Problem," *Journal of Elasticity*, to appear.

Gerstle, F. P., and Pearsall, G. W., 1974, "The Stress Response of an Elastic Surface to a High-Velocity, Unlubricated Punch," ASME JOURNAL OF APPLIED MECHANICS, Vol. 41, pp. 1036–1040.

Johnson, K. L., 1985, *Contact Mechanics*, Cambridge University Press, Cambridge, U.K.

Payton, R. G., 1967, "Transient Motion of an Elastic Half-Space due to a Moving Surface Line Load," *International Journal of Engineering Science*, Vol. 5, pp. 49–79.

Petit Bois, G., 1961, *Tables of Indefinite Integrals*, Dover, New York.

Robinson, A. R., and Thompson, J. C., 1974, "Transient Stresses in an Elastic Half-Space Resulting from the Frictionless Indentation of a Rigid Wedge-Shaped Die," *ZAMM*, Vol. 54, pp. 139–144.

Sneddon, I. N., 1951, *Fourier Transforms*, McGraw-Hill, New York.

Tricomi, F. G., 1985, *Integral Equations*, Dover, New York.

Capillary-Gravity Waves Generated Against a Vertical Cliff in a Fluid of Finite Depth

A. K. Pramanik[5] and D. Banik[5]

1 Introduction

This is the problem of two-dimensional capillary-gravity waves generated by some free surface oscillatory pressure distribution which moves with a uniform velocity. The fluid is incompressible, inviscid and is of uniform finite depth h and is bounded on one side by a vertical cliff.

This problem without the cliff has been studied by Pramanik and Majumdar (1984). The present problem with infinitely large depth has been discussed by Pramanik and Majumdar (1988). To understand the motivation of our paper we state the main results of the paper of Pramanik and Majumdar (1984). The ultimate steady state consists of six progressive waves, four gravity waves, and two capillary waves. There exists in the (a, b, c) space, where a, b, c are the nondimensional forms of the parameters of the problem, a surface called the critical surface, which divides the space into several regions in each of which the propagation is different.

The aim of the present paper is (i) to fully characterize the critical surfaces for all possible values of the parameters, (ii) to determine the waves for all possible values of the parameters, and (iii) to find the effect of the cliff on the reflection of waves.

As is already stated in Pramanik and Majumdar (1984), the waves were determined on the basis of two sections of the critical surface by the plane c = constant. However, the complete characterization of critical surface is possible. In this paper the critical surfaces are determined for all possible values of a, b, c. It is found that these surfaces divide the whole positive quadrant of the (a, b, c) space into five distinct regions for (a, b, c) in each of which the propagation of waves is different and the waves for all cases are determined. It is known that for (a, b, c) outside these surfaces, the waves are with constant amplitude while the amplitude is unbounded for (a, b, c) on the critical surfaces.

Previously, in linear theory, these waves for (a, b, c) on critical surfaces were not of interest where essentially nonlinear theory is to be developed for the complete understanding of the waves. However, to develop the nonlinear theory (Akylas, 1984) one has to take into account the order of the unboundedness on the critical surfaces. Motivated by this idea, waves are also determined for (a, b, c) on the critical surfaces.

Regarding the effect of the cliff it is found that one gravity wave is reflected for certain values of (a, b, c). In (a, b, c) space there is a surface called the surface of reflection, such that for (a, b, c) on one side of this surface, including those on the surface, reflection occurs. And the amplitude of the reflected wave remains the same as the original waves for all (a, b, c), excepting for those forming a curve on the surface of reflections. For (a, b, c) of this curve, the amplitude is found to be reduced.

2 Formulation and Formal Solution

We take the x-axis along the undisturbed free surface and

[5]Department of Applied Mathematics, Calcutta University, Calcutta, India.

Contributed by the Applied Mechanics Division of THE AMERICAN SOCIETY OF MECHANICAL ENGINEERS for publication in the ASME JOURNAL OF APPLIED MECHANICS.

Manuscript received by the ASME Applied Mechanics Division, Oct. 3, 1990; final revision, Feb. 20, 1992. Associate Technical Editor: K. R. Sreenivasan.

the y-axis vertically upwards. The system being initially at rest, waves are produced by the continued application of the free surface pressure distribution $p(x, t) = f(x)\, e^{i\omega t}$ which at the same time moves along the positive x-axis with a uniform velocity V. Let $\varphi(x, y, t)$ be the velocity potential, $\eta(x, t)$ the surface elevation, ρ the density, and T_1 the surface tension of the fluid. Then in a moving coordinate system in which the origin initially coincides with the cliff and then moves with the velocity V, we have the following linearized initial value problem:

$$\varphi_{xx} + \varphi_{yy} = 0 \text{ in } 0 \le x < \infty,\ -h \le y \le 0,\ t \ge 0$$

$$\frac{p}{\rho} + D\varphi + g\eta = \frac{T_1}{\rho}\eta_{xx} \text{ and } D\eta = \varphi_y \text{ where } D \equiv \left(\frac{\partial}{\partial t} - V\frac{\partial}{\partial x}\right), \quad \text{at } y = 0$$

$$\varphi_x(-Vt, y, t) = 0,\ \varphi_y(x, -h, t) = 0,$$

$$\varphi(x, y, 0) = 0,\ \eta(x, 0) = 0.$$

Following the usual procedure as in Pramanik and Majumdar (1988), the integral representation for η with dimensionless variables can be obtained. For convenience we introduce the notation $g_m[A, x] = \int_0^\infty F_m e^{i(At + \lambda x)} d\lambda$, $m = 1$ to 4 and then we get

$$\eta = \frac{1}{4\pi\rho g h} \sum_{m=1}^{16} I_m \tag{1}$$

where

$$I_1 = g_1[a + 2b\lambda, x],\ I_2 = g_2[a + 2b\lambda, x],\ I_3 = g_1[\sigma + b\lambda, x],$$
$$I_4 = g_2[-\sigma + b\lambda, x],\ I_5 = g_3[a, x],\ I_6 = g_4[a, x],$$
$$I_7 = g_3[\sigma + b\lambda, x],$$
$$I_8 = g_4[-\sigma + b\lambda, x],\ I_9 = g_1[a, -x],$$
$$I_{10} = g_2[a, -x],$$
$$I_{11} = g_1[\sigma - b\lambda, -x],\ I_{12} = g_2[-\sigma - b\lambda, -x],$$
$$I_{13} = g_3[a - 2b\lambda, -x],$$
$$I_{14} = g_4[a - 2b\lambda, -x],\ I_{15} = g_3[\sigma - b\lambda, -x],$$
$$I_{16} = g_4[-\sigma - b\lambda, -x]$$

and

$$F_{1,2} = \frac{f_+(\lambda)}{a + b\lambda \mp \sigma},\ F_{3,4} = \frac{f_-(\lambda)}{a - b\lambda \mp \sigma},$$

$$f_\pm(\lambda) = \frac{\lambda h \tanh \lambda}{\sigma} \int_0^\infty f(hx) e^{\pm i\lambda x h} dx$$

$$a = \omega\left(\frac{h}{g}\right)^{1/2},\ b = \frac{V}{(gh)^{1/2}},\ c = \frac{T_1}{\rho g h^2},\ \sigma = [(\lambda + c\lambda^3)\tanh \lambda]^{1/2}.$$

3 Steady-State Waves

The steady-state waves at far field from the pressure segment will be determined by evaluating the integrals in (1) for large values of t and $|x|$. The ultimate steady state comes from the integrals as contributions from the residues at the real positive poles of the integrands. These poles are the solutions of the following equations:

$$a + b\lambda - \sigma = 0,\ a - b\lambda + \sigma = 0 \text{ and } a - b\lambda - \sigma = 0. \quad (2)\text{–}(4)$$

Pramanik and Majumdar (1984) have studied in detail the distribution of the roots of Eqs. (2), (3), and (4). However, for our purpose we state the results in short. Equation (2) has in general three real positive roots $\lambda_1, \lambda_2, \lambda_3$, say ($\lambda_1 < \lambda_2 < \lambda_3$); Eq. (3) has two such roots λ_4, λ_5, say ($\lambda_4 < \lambda_5$); and Eq. (4) has always one such root λ_6. The existence of the roots depends upon the values of the parameters a, b, c. This distribution can be known by a study of the cases where some roots coalesce. Following Pramanik and Majumdar (1984), the critical cases have the following representation:

$a = \Psi_1(\lambda)$ for $0 \le \lambda < \lambda'$, $a = -\Psi_1(\lambda)$ for $\lambda' \le \lambda < \infty$ and $b = \Psi_2(\lambda)$ for $0 \le \lambda < \infty$

where

$$\Psi_1(\lambda) = \frac{(\lambda - c\lambda^3)\tanh \lambda - \lambda(\lambda + c\lambda^3)\ \mathrm{sech}^2\lambda}{2[(\lambda + c\lambda^3)\tanh \lambda]^{1/2}}$$

$$\Psi_2(\lambda) = \frac{(1 + 3c\lambda^2)\tanh \lambda + (\lambda + c\lambda^3)\mathrm{sech}^2 \lambda}{2[(\lambda + c\lambda^3)\tanh \lambda]^{1/2}}$$

where λ_0 is the point of inflexion of the curve σ and λ', the value of λ for which the straight line $m = b\lambda$ is a tangent to the curve $m = \sigma$. These equations represent some surfaces, called the critical surfaces $f(a, b, c) = 0$ in (a, b, c) space. In general such a surface is divided in three portions, say S_1, S_2, and S_3, which represent the cases $\lambda_1 = \lambda_2$, $\lambda_2 = \lambda_3$, and $\lambda_4 = \lambda_5$, respectively.

To determine the nature of the critical surfaces, we take two sections of these surfaces as in Pramanik and Majumdar (1984) by the planes $c = .01$ and $c = 1$ which are respectively shown in Figs. 1 and 2 where C_1, C_2, and C_3 are the sections of S_1, S_2, and S_3, respectively, in Fig. 1 and C_3' is the section of S_3 in Fig. 2. These two sections as also the nature of the frequency curve for different values of c give some indications about the variation of the surface for different values of c. It is apparent that for $c \ge 1/3$, S_1 and S_2 are not present. For $c < 1/3$ all the portions S_1, S_2, and S_3 are present such that in every section a loop is present. As c increases from zero to 1/3, while the point A moves along a line L parallel to the c-axis starting from the point $a = 0$, $b = 1$, $c = 0$, the positions of the points A_0 and A_1 change such that both the points A_0 and A_1 approach to the line L along the space curves Γ_0, Γ_1, respectively. Consequently, the area of the loop approaches to zero. To verify this statement we consider the locii of the points A_0, A_1 which are, respectively, given by

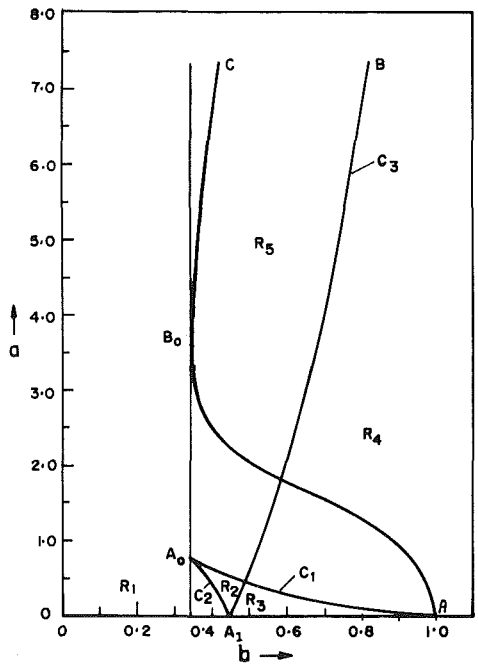

Fig. 1 Sections of the critical surface and surface of reflection in the (a, b) plane for $c = .01$

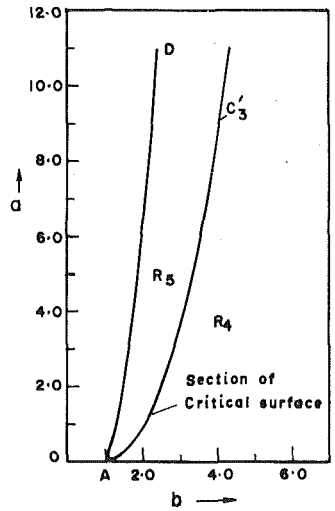

Fig. 2 Sections of the critical surface and surface of reflection in the (*a*, *b*) plane for *c* = 1

$$\sigma'' = 0,\ a = \Psi_1(\lambda),\ b = \Psi_2(\lambda) \tag{5}$$

$$\Psi_1(\lambda) = 0,\ b = \Psi_2(\lambda). \tag{6}$$

From each set of Eqs. (5), (6) it is clear that c can be expressed as a function of λ and then a, b will be so. Thus, Eqs. (5) and (6) respectively represent, in the parametric form, the two previous space curves Γ_0, Γ_1 in the (a, b, c) space. Now it is easy to verify by numerical calculation that the points A_0 and A_1 approach to the line L as c increases from 0 to 1/3.

The above descriptions give the clear idea about the shape of the critical surfaces. Thus, the whole positive quadrant of the (a, b, c) space is divided into five three-dimensional distinct regions R_n(n = 1 to 5) among which the regions R_1, R_2, and R_3 exist only below the plane c = 1/3. Now it is easy to say that only the surface S_3 is intersected by the plane c = 1/3 into the surfaces S_{31} and S_{32} which are, respectively, below and above the plane c = 1/3. Below this plane the surfaces S_1 and S_{31} are intersected each other by a space curve, say Γ_2. By this curve Γ_2, S_1 is divided into two parts, say S_1', S_1'', of which only S_1' contains the space curve Γ_0. Similarly, S_{31} is divided into two parts S_{31}' and S_{31}'' of which only S_{31}' contains the space curve Γ_1.

The distributions of the roots in the regions, on the surfaces and on the space curves are respectively shown in the following schemes:

Regions:	R_1	R_2	R_3	R_4	R_5
Roots:	λ_1	λ_1,λ_2	$\lambda_1,\lambda_2,\lambda_3$	λ_3,λ_4	λ_3
	λ_6	λ_3,λ_6	$\lambda_4,\lambda_5,\lambda_6$	λ_5,λ_6	λ_6

Surfaces:	S_1'	S_1''	S_2	S_{31}'	S_{31}''	S_{32}
Roots:	$\lambda_1=\lambda_2$	$\lambda_1=\lambda_2$	$\lambda_2=\lambda_3$	$\lambda_4=\lambda_5$	$\lambda_4=\lambda_5$	$\lambda_4=\lambda_5$
	λ_3,λ_6	$\lambda_3,\lambda_4,\lambda_5,\lambda_6$	λ_1,λ_6	$\lambda_1,\lambda_2,\lambda_3,\lambda_6$	λ_3,λ_6	λ_3,λ_6

Space curves:	Γ_0	Γ_1	Γ_2
Roots:	$\lambda_1=\lambda_2=\lambda_3,\lambda_6$	$\lambda_1,\lambda_2=\lambda_3,\lambda_4=\lambda_5,\lambda_6$	$\lambda_1=\lambda_2,\lambda_4=\lambda_5,\lambda_3,\lambda_6$.

We are now in a position to calculate the asymptotic values of the integrals in (1) for large time and distance from the origin in terms of the residue contributions at the poles. Now in a particular integral the poles occur in various ways for various values of the parameters a, b, c. Accordingly, the same integral has different values for a, b, c in various regions, on various surfaces, and on the space curves mentioned above. It is known Pramanik and Majumdar (1984) that an integral gives a steady-state wave with constant amplitude when the poles are distinct i.e., for (a, b, c) in the regions. For (a, b, c) on the surfaces where some of the poles are coincident, the corresponding integral gives a wave with an unbounded amplitude. However, the order of this unboundedness is different for different surfaces. To determine this order we consider the integral I_{11}. Following Pramanik and Majumdar (1984) it can be shown that for each double pole on the surfaces, the asymptotic value of I_{11} is of the order $t^{1/2}$ when $t \to \infty$. For (a, b, c) on Γ_0, three poles are coincident. To calculate I_{11} we use the transformation $m = a + b\lambda - \sigma$. Since the main contribution comes from the neighborhood of $\lambda = \lambda_0$, we can write

$$I_{11} \simeq \int_{\lambda_0-\epsilon}^{\lambda_0+\epsilon} \frac{f_+(\lambda)}{(a+b\lambda-\sigma)}\, e^{i[(\sigma-b\lambda)t-\lambda x]} d\lambda, \text{ where } 0<\epsilon\ll 1.$$

Now using the fact $\sigma'(\lambda_0) = b$, $\sigma''(\lambda_0) = 0$, $\sigma'''(\lambda_0) > 0$, we get

$$m \simeq -\frac{1}{3!}(\lambda-\lambda_0)^3\sigma'''(\lambda_0).$$

So

$$I_{11} \simeq \left(\frac{2}{9}\right)^{1/3} \frac{e^{iat}}{[\sigma'''(\lambda_0)]^{1/3}} \int_{-\infty}^{\infty} [f_+(\lambda)e^{-i\lambda x}] \frac{e^{-imt}}{|m|^{5/3}\mathrm{Sgn}m}\, dm$$

$$= \frac{i(-5/3)!}{\left[\frac{3^{1/2}}{2}\sigma'''(\lambda_0)\right]^{1/3}} f_+(\lambda_0)e^{i(at-\lambda_0 x)}t^{2/3} \text{ as } t\to\infty.$$

We now like to say something about the calculation of the integral I_{15}, since in the process of this calculation some typical feature of the problem comes out. For this purpose we use the transformation

$$m = \sigma - b\lambda. \tag{7}$$

There arise several cases in each of which the curve of transformation (7) has different shape and thus the asymptotic values are different. These cases are as follows: (i) $0 < b < b_0$, $c < 1/3$; (ii) $b_0 < b < 1$, $c < 1/3$; (iii) $b > 1$ for any value of c; (iv) $b < 1$, $c > 1/3$ where b_0 is the value of b corresponding to $\lambda = \lambda_0$. Since for the cases (i), (iv) the curve of transformation (7) has no extreme, by the usual method we get the asymptotic value of I_{15} as follows:

$$I_{15} \simeq -\frac{\pi i f_-(\lambda_6)}{[\sigma'(\lambda_6)+b]}\, e^{i[\{\sigma(\lambda_6)-b\lambda_6\}t-\lambda_6 x]} \text{ as } t\to\infty.$$

But since for the case (ii) the curve of transformation (7) has two extreme points, one maximum, say α_1 and other minimum, say α_2, the asymptotic value of I_{15} depends upon the position of the pole of the integrand λ_6 relative to α_1 or α_2. To find the position of λ_6 with respect to α_1 or α_2 we consider the case $\lambda_6 = \alpha_1$ or $\lambda_6 = \alpha_2$ which is represented by $\sigma' = b$ and $a = \sigma + b\lambda$.

This can be regarded as a surface, called the surface of reflection (the meaning of this term will be clarified later) in the parametric form in (a, b, c) space in the present case. The section AB_0C of this surface by the plane c = .01 is shown in Fig. 1, where the point B_0 corresponds the point of inflection $\lambda = \lambda_0$ and the equation to its locus for $c < 1/3$ is given by $\sigma'' = 0$, $\sigma' = b$ and $a = \sigma + b\lambda$.

This represents, in the parametric form, a space curve Γ_3 in

(a, b, c) space which divides the surface of reflection into two parts, say T and T' of which T is confined between L and Γ_3.

For other values of c, i.e., $c \geq 1/3$, we get a similar surface of reflection whose section AD by the plane $c = 1$ is shown in Fig. 2. Actually this is the continuation of the previous surface of reflection. But in this case, T is absent because the point B_0 approaches to the line L as c increases from 0 to 1/3. It is numerically verified from the equations representing the locus of B_0.

The above descriptions give the clear idea of the surface of reflection for all values of c.

So for the points (a, b, c), where $c < 1/3$, between the axis of b and T the asymptotic value of I_{15} is given by

$$I_{15} \simeq I \text{ as } t \to \infty \text{ where } I = -\frac{\pi i f_-(\lambda_6)}{[\sigma'(\lambda_6) + b]} e^{i[\{\sigma(\lambda_6) - b\lambda_6\}t - \lambda_6 x]}.$$

Also, for the points (a, b, c), where $c < 1/3$, between T and T', $I_{15} \simeq -I$ as $t \to \infty$. For the points (a, b, c) where $c < 1/3$ in the three-dimensional region bounded by the plane passing through B_0 and parallel to the $(b - c)$ plane, the $(a - c)$ plane and the surface T', $I_{15} \simeq I$ as $t \to \infty$.

Above the plane $c = 1/3$, $I_{15} \simeq \pm I$ as $t \to \infty$ according as the points (a, b, c) lie on the left or right to the surface of reflection. For the points (a, b, c) on the surface T excepting the space curve Γ_3 and on T'

$$I_{15} \simeq \frac{\pi i f_-(\lambda_6)}{2b} e^{i[\{\sigma(\lambda_6) - b\lambda_6\}t - \lambda_6 x]} \text{ as } t \to \infty.$$

Also for the points (a, b, c) on the space curve Γ_3, the asymptotic value of I_{15} is given by

$$I_{15} \simeq \frac{\pi i f_-(\lambda_6)}{6b} e^{i[\{\sigma(\lambda_6) - b\lambda_6\}t - \lambda_6 x]} \text{ as } t \to \infty.$$

From the above calculations it follows that for (a, b, c), on the critical surfaces, the asymptotic values of the integrals become unbounded and the order of the unboundedness is like $t^{1/2}$ where two roots coincide and like $t^{2/3}$ where three roots coincide. Now for (a, b, c) in a region R_n, the asymptotic values of the integrals are bounded leading to waves of constant amplitude. In the following we write down the waves. At first we write down the waves for (a, b, c) in the region R_3:

$$\left.\begin{aligned} \eta &= \eta_1 + \eta_3 + \eta_5 + \eta_r \text{ as } x \to \infty \text{ and } t \to \infty \\ &= \eta_2 + \eta_4 + \eta_6 + \eta_r \text{ as } x \to -\infty \text{ and } t \to \infty \end{aligned}\right\} \quad (8)$$

where

$$\eta_1 = H_+(\lambda_1) e^{i(at - \lambda_1 x)}, \quad \eta_3 = H_+(\lambda_3) e^{i(at - \lambda_3 x)},$$

$$\eta_5 = -H_-(\lambda_5) e^{i(at + \lambda_5 x)}$$

$$\eta_2 = -H_+(\lambda_2) e^{i(at - \lambda_2 x)}, \quad \eta_4 = H_-(\lambda_4) e^{i(at + \lambda_4 x)},$$

$$\eta_6 = G(\lambda_6) e^{i(at + \lambda_6 x)}$$

$$\eta_r = G(\lambda_6) e^{i[(a - 2b\lambda_6)t - \lambda_6 x]} \text{ and } H_\pm = \frac{\text{if}_\pm(\lambda)}{2\rho g h[\sigma'(\lambda) - b]},$$

$$G(\lambda) = \frac{\text{if}_-(\lambda)}{2\rho g h[\sigma'(\lambda) + b]}.$$

The wave system for the case when the values of the parameters a, b, c of the problem are such that the point (a, b, c) lies in the other regions is easy to determine. This is the same wave system as expressed in (8), only the wave corresponding to a pole not occurring in a region being deleted for that region.

The waves $\eta_n (n = 1 \text{ to } 6)$ are the original waves created by the source as found in the unbounded fluid Pramanik and Majumdar (1984). The wave η_r is an addition to this system due to the existence of the cliff. It is obviously seen that η_r is the reflection of the wave η_6 on the cliff. Among the six waves generated by the source, only the wave η_6 moves towards the cliff. So it must be reflected on reaching the cliff. Now the condition by which it reaches the cliff is obvious and its group velocity is greater than the velocity of source. One can verify that this is the same condition that the points (a, b, c) to the left of the surface of reflection. Thus, occurrence of reflection is physically reasonable. However, it is seen that the amplitude of the reflected wave is the same as the original wave excepting (a, b, c) on the curve Γ_3 where the amplitude of the wave η_r is reduced than the original wave. This seems to be a striking result. It is to be noted that we have dealt with the linear theory in an inviscid fluid. There is no obvious reason for the reduction of the amplitude in the reflected wave η_r.

References

Akylas, T. R., 1984, "On the Excitation of Nonlinear Water Waves by a Moving Pressure Distribution Oscillating at Resonant Frequency," *Phys. Fluids*, Vol. 27, pp. 2803–2807.

Pramanik, A. K., and Majumdar, S. R., 1984, "Small-amplitude Free-Surface Waves Generated by Moving Oscillatory Disturbances," *J. Fluid Mech.*, Vol. 145, pp. 405–415.

Pramanik, A. K., and Majumdar, S. R., 1988, "The Effect of Surface Tension on the Reflection of Gravity Waves from a Vertical Cliff," *Int. J. Engineering Science*, Vol. 26, pp. 549–558.

Analysis of the Interfacial Crack for Anisotropic Materials Under Displacement-Displacement or Traction-Displacement Boundary Conditions

Chien-Ching Ma[6,8] and Jyi-Jiin Luo[7,8]

Introduction

Many engineering structures are comprised of more than one material. The strength of composite materials is influenced by the orientation of existing cracks with respect to the bimaterial interface. A number of solutions for the stress and displacement fields for a crack lying along bimaterial interfaces have been obtained for isotropic materials by Williams (1959) and Rice and Sih (1965). Extensions to anisotropic elasticity have been made by Bogy (1972) and recently by Ting (1986, 1990). All these studies of in-plane problems have shown that the stresses share the inverse square root singularity of the crack and, in addition, exhibit an oscillatory behavior as the crack tip is approached. Recently, Ma and Hour (1989, 1990) investigated the antiplane problems of two dissimilar anisotropic wedges and an inclined crack terminating at a bimaterial interface. They found that the order of the stress singularity is always real for the antiplane anisotropic problems.

[6]Professor.

[7]Graduate Student.

[8]Department of Mechanical Engineering, National Taiwan University, Taipei, Taiwan 10763, Republic of China.

Contributed by the Applied Mechanics Division of THE AMERICAN SOCIETY OF MECHANICAL ENGINEERS for publication in the ASME JOURNAL OF APPLIED MECHANICS. Manuscript received by the ASME Applied Mechanics Division, Oct. 28, 1991; final revision, June 3, 1992. Associate Technical Editor: C. F. Shih.

(a, b, c) space which divides the surface of reflection into two parts, say T and T' of which T is confined between L and Γ_3.

For other values of c, i.e., $c \geq 1/3$, we get a similar surface of reflection whose section AD by the plane $c = 1$ is shown in Fig. 2. Actually this is the continuation of the previous surface of reflection. But in this case, T is absent because the point B_0 approaches to the line L as c increases from 0 to 1/3. It is numerically verified from the equations representing the locus of B_0.

The above descriptions give the clear idea of the surface of reflection for all values of c.

So for the points (a, b, c), where $c < 1/3$, between the axis of b and T the asymptotic value of I_{15} is given by

$$I_{15} \simeq I \text{ as } t \to \infty \text{ where } I = -\frac{\pi i f_-(\lambda_6)}{[\sigma'(\lambda_6) + b]} e^{i[\{\sigma(\lambda_6) - b\lambda_6\}t - \lambda_6 x]}.$$

Also, for the points (a, b, c), where $c < 1/3$, between T and T', $I_{15} \simeq -I$ as $t \to \infty$. For the points (a, b, c) where $c < 1/3$ in the three-dimensional region bounded by the plane passing through B_0 and parallel to the $(b - c)$ plane, the $(a - c)$ plane and the surface T', $I_{15} \simeq I$ as $t \to \infty$.

Above the plane $c = 1/3$, $I_{15} \simeq \pm I$ as $t \to \infty$ according as the points (a, b, c) lie on the left or right to the surface of reflection. For the points (a, b, c) on the surface T excepting the space curve Γ_3 and on T'

$$I_{15} \simeq \frac{\pi i f_-(\lambda_6)}{2b} e^{i[\{\sigma(\lambda_6) - b\lambda_6\}t - \lambda_6 x]} \text{ as } t \to \infty.$$

Also for the points (a, b, c) on the space curve Γ_3, the asymptotic value of I_{15} is given by

$$I_{15} \simeq \frac{\pi i f_-(\lambda_6)}{6b} e^{i[\{\sigma(\lambda_6) - b\lambda_6\}t - \lambda_6 x]} \text{ as } t \to \infty.$$

From the above calculations it follows that for (a, b, c), on the critical surfaces, the asymptotic values of the integrals become unbounded and the order of the unboundedness is like $t^{1/2}$ where two roots coincide and like $t^{2/3}$ where three roots coincide. Now for (a, b, c) in a region R_n, the asymptotic values of the integrals are bounded leading to waves of constant amplitude. In the following we write down the waves. At first we write down the waves for (a, b, c) in the region R_3:

$$\left.\begin{aligned} \eta &= \eta_1 + \eta_3 + \eta_5 + \eta_r \text{ as } x \to \infty \text{ and } t \to \infty \\ &= \eta_2 + \eta_4 + \eta_6 + \eta_r \text{ as } x \to -\infty \text{ and } t \to \infty \end{aligned}\right\} \quad (8)$$

where

$$\eta_1 = H_+(\lambda_1) e^{i(at - \lambda_1 x)}, \quad \eta_3 = H_+(\lambda_3) e^{i(at - \lambda_3 x)},$$

$$\eta_5 = -H_-(\lambda_5) e^{i(at + \lambda_5 x)}$$

$$\eta_2 = -H_+(\lambda_2) e^{i(at - \lambda_2 x)}, \quad \eta_4 = H_-(\lambda_4) e^{i(at + \lambda_4 x)},$$

$$\eta_6 = G(\lambda_6) e^{i(at + \lambda_6 x)}$$

$$\eta_r = G(\lambda_6) e^{i[(a - 2b\lambda_6)t - \lambda_6 x]} \text{ and } H_\pm = \frac{\text{if}_\pm(\lambda)}{2\rho g h[\sigma'(\lambda) - b]},$$

$$G(\lambda) = \frac{\text{if}_-(\lambda)}{2\rho g h[\sigma'(\lambda) + b]}.$$

The wave system for the case when the values of the parameters a, b, c of the problem are such that the point (a, b, c) lies in the other regions is easy to determine. This is the same wave system as expressed in (8), only the wave corresponding to a pole not occurring in a region being deleted for that region.

The waves $\eta_n (n = 1 \text{ to } 6)$ are the original waves created by the source as found in the unbounded fluid Pramanik and Majumdar (1984). The wave η_r is an addition to this system due to the existence of the cliff. It is obviously seen that η_r is the reflection of the wave η_6 on the cliff. Among the six waves generated by the source, only the wave η_6 moves towards the cliff. So it must be reflected on reaching the cliff. Now the condition by which it reaches the cliff is obvious and its group velocity is greater than the velocity of source. One can verify that this is the same condition that the points (a, b, c) to the left of the surface of reflection. Thus, occurrence of reflection is physically reasonable. However, it is seen that the amplitude of the reflected wave is the same as the original wave excepting (a, b, c) on the curve Γ_3 where the amplitude of the wave η_r is reduced than the original wave. This seems to be a striking result. It is to be noted that we have dealt with the linear theory in an inviscid fluid. There is no obvious reason for the reduction of the amplitude in the reflected wave η_r.

References

Akylas, T. R., 1984, "On the Excitation of Nonlinear Water Waves by a Moving Pressure Distribution Oscillating at Resonant Frequency," *Phys. Fluids*, Vol. 27, pp. 2803–2807.

Pramanik, A. K., and Majumdar, S. R., 1984, "Small-amplitude Free-Surface Waves Generated by Moving Oscillatory Disturbances," *J. Fluid Mech.*, Vol. 145, pp. 405–415.

Pramanik, A. K., and Majumdar, S. R., 1988, "The Effect of Surface Tension on the Reflection of Gravity Waves from a Vertical Cliff," *Int. J. Engineering Science*, Vol. 26, pp. 549–558.

Analysis of the Interfacial Crack for Anisotropic Materials Under Displacement-Displacement or Traction-Displacement Boundary Conditions

Chien-Ching Ma[6,8] and Jyi-Jiin Luo[7,8]

Introduction

Many engineering structures are comprised of more than one material. The strength of composite materials is influenced by the orientation of existing cracks with respect to the bimaterial interface. A number of solutions for the stress and displacement fields for a crack lying along bimaterial interfaces have been obtained for isotropic materials by Williams (1959) and Rice and Sih (1965). Extensions to anisotropic elasticity have been made by Bogy (1972) and recently by Ting (1986, 1990). All these studies of in-plane problems have shown that the stresses share the inverse square root singularity of the crack and, in addition, exhibit an oscillatory behavior as the crack tip is approached. Recently, Ma and Hour (1989, 1990) investigated the antiplane problems of two dissimilar anisotropic wedges and an inclined crack terminating at a bimaterial interface. They found that the order of the stress singularity is always real for the antiplane anisotropic problems.

[6]Professor.

[7]Graduate Student.

[8]Department of Mechanical Engineering, National Taiwan University, Taipei, Taiwan 10763, Republic of China.

Contributed by the Applied Mechanics Division of THE AMERICAN SOCIETY OF MECHANICAL ENGINEERS for publication in the ASME JOURNAL OF APPLIED MECHANICS. Manuscript received by the ASME Applied Mechanics Division, Oct. 28, 1991; final revision, June 3, 1992. Associate Technical Editor: C. F. Shih.

In this study, plane problems for bonded dissimilar half-planes of anisotropic material containing an interfacial crack are considered. The solutions obtained in this paper is valid only for anisotropic bimaterial having monoclinic symmetry with the axis of symmetry being the x_3-axis. Here the problem of displacement prescribed on both crack faces, and the problem of traction prescribed on one face with displacement prescribed on the other, is solved. The problem is solved by application of a generalized Mellin transform in conjunction with the complex stress function. The dependence of the order of the stress singularity on the material constants and boundary conditions is studied in detail. The result shows that the order of stress singularity has reduced dependence on material constants. The full-field solutions in the Mellin transform domain are obtained explicitly. It is very interesting to find that the solutions of the displacement prescribed problems can be obtained from the traction prescribed problems by a simple substitution.

Explicit Solutions in Mellin Transform Domain

The two-dimensional stress-strain relations for a homogeneous anisotropic body are

$$e_{\alpha\beta} = s_{\alpha\beta}^{\gamma\delta}\sigma_{\gamma\delta}. \tag{1}$$

Because of assumed elastic symmetry about $x_3 = 0$ for the plane problem, the six independent material constants are s_{11}^{11}, s_{22}^{11}, s_{12}^{11}, s_{12}^{12}, s_{22}^{12}, s_{22}^{22}. The solution of displacement for the two-dimensional problem has the following form in terms of complex potentials

$$u_r + iu_\theta = e^{-i\theta}\sum_{\alpha=1,2}\{\delta_\alpha\Omega_\alpha'(z_\alpha) + \rho_\alpha\overline{\Omega}_\alpha'(\overline{z}_\alpha)\}, \tag{2}$$

where Ω_α ($\alpha = 1, 2$) are arbitrary analytic functions of the complex variable z_α, $\overline{\Omega}_\alpha$ is complex conjugate and primes denote derivatives with respect to the indicated arguments. The relation between z and z_α is $z = re^{i\theta}$, $z_\alpha = z + \gamma_\alpha\bar{z}$. The complex constants δ_α, ρ_α, and γ_α are defined in terms of the components of the elasticity tensor $s_{\alpha\beta}^{\gamma\delta}$; see Bogy (1972) or Ma and Luo (1992). We now take Mellin transform of r^2 and r times the stress and displacement, respectively.

$$\hat{\sigma}_{\alpha\beta}(s,\theta) = \int_0^\infty \sigma_{\alpha\beta}(r,\theta)r^{s+1}dr, \tag{3}$$

$$\hat{u}_\alpha(s,\theta) = \int_0^\infty u_\alpha(r,\theta)r^s dr, \tag{4}$$

where s is the complex transform parameter. The physical stress and displacement fields are recovered as follows:

$$\sigma_{\alpha\beta}(r,\theta) = \frac{1}{2\pi i}\int_{c-i\infty}^{c+i\infty}\hat{\sigma}_{\alpha\beta}(s,\theta)r^{-s-2}ds, \tag{5}$$

$$u_\alpha(r,\theta) = \frac{1}{2\pi i}\int_{c-i\infty}^{c+i\infty}\hat{u}_\alpha(s,\theta)r^{-s-1}ds, \tag{6}$$

where $\mathrm{Re}(s) = c$ defines the path of integration. The choice of c has to be determined by the regularity of their integrands. Direct use of the transforms with the complex representation of the solution leads to (Bogy, 1972)

$$\hat{u}_r(s,\theta) + i\hat{u}_\theta(s,\theta) = e^{-i\theta}\sum_{\alpha=1,2}\times\left\{\frac{\delta_\alpha\phi_\alpha(s)}{(e^{i\theta}+\gamma_\alpha e^{-i\theta})^{s+1}} + \frac{\rho_\alpha\overline{\phi}_\alpha(s)}{(e^{-i\theta}+\overline{\gamma}_\alpha e^{i\theta})^{s+1}}\right\}, \tag{7}$$

$$\hat{\sigma}_{\theta\theta}(s,\theta) - i\hat{\sigma}_{r\theta}(s,\theta) = -2(s+1)e^{-i\theta}\sum_{\alpha=1,2}\times\left\{\frac{\gamma_\alpha\phi_\alpha(s)}{(e^{i\theta}+\gamma_\alpha e^{-i\theta})^{s+1}} + \frac{\overline{\phi}_\alpha(s)}{(e^{-i\theta}+\overline{\gamma}_\alpha e^{i\theta})^{s+1}}\right\}, \tag{8}$$

where $\phi_\alpha(s)$ is defined as

$$\phi_\alpha(s) = \int_{0(\theta)}^\infty \Omega_\alpha'(z_\alpha)z_\alpha^s dz_\alpha. \tag{9}$$

For convenience, define

$$H_\alpha(s,\theta) = (e^{i\theta}+\gamma_\alpha e^{-i\theta})^{-s-1}, \tag{10}$$

$$T(s,\theta) = [\hat{\sigma}_{\theta\theta}(s,\theta) - i\hat{\sigma}_{r\theta}(s,\theta)]/2(s+1), \tag{11}$$

$$D(s,\theta) = \hat{u}_r(s,\theta) + i\hat{u}_\theta(s,\theta). \tag{12}$$

Then (7) and (8) can be rewritten as

$$D(s,\theta) = e^{i\theta}\sum_{\alpha=1,2}\{\delta_\alpha H_\alpha(s,\theta)\phi_\alpha(s) + \rho_\alpha\overline{H}_\alpha(s,\theta)\overline{\phi}_\alpha(s)\}, \tag{13}$$

$$T(s,\theta) = -e^{-i\theta}\sum_{\alpha=1,2}\{\gamma_\alpha H_\alpha(s,\theta)\phi_\alpha(s) + \overline{H}_\alpha(s,\theta)\overline{\phi}_\alpha(s)\}. \tag{14}$$

We consider an anisotropic bimaterial interface crack, subjected to prescribed displacements at the crack faces $\theta = \pm\pi$ as shown in Fig. 1. Perfect bonding conditions along the interface $\theta = 0$ are ensured by the stress and displacement continuity conditions. It is very interesting to find that the form of solutions for the displacement prescribed problems are very similar to that of the traction prescribed problems solved by Ma and Luo (1992). For convenience, we define the following material constants:

$$\gamma_{d\alpha} = \delta_\alpha/\overline{\rho}_\alpha, \quad \delta_{d\alpha} = \gamma_\alpha/\overline{\rho}_\alpha, \quad \rho_{d\alpha} = 1/\rho_\alpha, \tag{15}$$

and

$$\lambda_d = \frac{\gamma_{d2}\delta_{d1} - \gamma_{d1}\delta_{d2}}{\gamma_{d1} - \gamma_{d2}} = \frac{\rho_{d1} - \rho_{d2}}{\overline{\gamma}_{d1} - \overline{\gamma}_{d2}}, \tag{16}$$

$$\eta_d = \overline{\eta}_d = \frac{\delta_{d1} - \delta_{d2}}{\gamma_{d1} - \gamma_{d2}}, \tag{17}$$

$$\xi_d = \overline{\xi}_d = \frac{\gamma_{d2}\overline{\rho}_{d1} - \gamma_{d1}\overline{\rho}_{d2}}{\gamma_{d1} - \gamma_{d2}}. \tag{18}$$

The subscript d indicates the displacement prescribed problems. It can be proved that η_d and ξ_d are all real values and we also find the following relations:

$$\lambda_d = \lambda\epsilon, \quad \xi_d = \eta\epsilon, \quad \eta_d = \xi\epsilon, \tag{19}$$

where

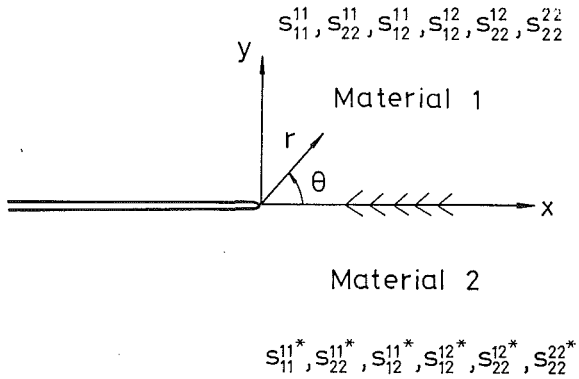

Fig. 1 Configuration of bonded anisotropic dissimilar interface crack

$$\epsilon=\bar{\epsilon}=\frac{1}{\eta\xi-|\lambda|^2}, \tag{20}$$

$$\lambda=\frac{\gamma_2\delta_1-\gamma_1\delta_2}{\gamma_1-\gamma_2}=\frac{\rho_1-\rho_2}{\bar{\gamma}_1-\bar{\gamma}_2}=\frac{S_{22}^{11}}{\gamma_1\gamma_2}[\gamma_1+\gamma_2-\gamma_1\gamma_2(\bar{\gamma}_1+\bar{\gamma}_2)], \tag{21}$$

$$\eta=\bar{\eta}=\frac{\delta_1-\delta_2}{\gamma_1-\gamma_2}=-2\left(S_{11}^{11}-\frac{S_{22}^{11}}{\gamma_1\gamma_2}\right), \tag{22}$$

$$\xi=\bar{\xi}=\frac{\gamma_2\bar{\rho}_1-\gamma_1\bar{\rho}_2}{\gamma_1-\gamma_2}=2(S_{11}^{11}-S_{22}^{11}\bar{\gamma}_1\bar{\gamma}_2). \tag{23}$$

The material constants λ, η, ξ are obtained for the traction prescribed problems analyzed by Ma and Luo (1992). It is very interesting to find that the solutions of the displacement prescribed problems can be obtained from the traction prescribed problems if we perform the following substitution:

Traction	ϕ_α	$T(s)$	G	H	U_α	V_α	γ_α	l	m	η	ξ	λ
Displacement	$\rho_\alpha\phi_\alpha$	$-D(s)$	G_d	H_d	$U_{d\alpha}$	$V_{d\alpha}$	$\gamma_{d\alpha}$	l_d	m_d	η_d	ξ_d	λ_d.

The solutions of the displacement prescribed problem in the Mellin transform domain can be expressed as follows:

$$\bar{\rho}_\alpha\phi_\alpha(s)H_\alpha(s,0)=\frac{p(G_dV_{d\alpha}-H_dU_{d\alpha})}{(-1)^\alpha(\gamma_{d2}-\gamma_{d1})(1-p^2)(l_dp^4+m_dp^2+l_d)}, \tag{24}$$

where

$$p=e^{-i(s+1)\pi}, \tag{25}$$

$$l_d=|\lambda_d+\lambda_d^*|^2-(\eta_d+\xi_d^*)(\xi_d+\eta_d^*), \tag{26}$$

$$m_d=2|\lambda_d+\lambda_d^*|^2-(\eta_d+\xi_d^*)^2-(\xi_d+\eta_d^*)^2, \tag{27}$$

$$\begin{aligned}G_d=&-D(s)[\xi_d-\xi_d^*-(\xi_d+\eta_d^*)p^2]\\&-\bar{D}(s)[-\lambda_d+\lambda_d^*+(\lambda_d+\lambda_d^*)p^2]\\&-D^*(s)(\eta_d^*+\xi_d^*)-\bar{D}^*(s)(-2\lambda_d^*),\end{aligned} \tag{28}$$

$$\begin{aligned}H_d=&-D(s)[\bar{\lambda}_d-\bar{\lambda}_d^*-(\bar{\lambda}_d+\bar{\lambda}_d^*)p^2]\\&-\bar{D}(s)[-\eta_d+\eta_d^*+(\eta_d+\xi_d^*)p^2]\\&-D^*(s)(2\bar{\lambda}_d^*)-\bar{D}^*(s)(-\eta_d^*-\xi_d^*),\end{aligned} \tag{29}$$

$$\begin{aligned}U_{d\alpha}=&\sum_{\beta=1,2}(1-\delta_{\alpha\beta})\gamma_{d\beta}[\eta_d+\xi_d^*+(\xi_d+\eta_d^*)p^2]\\&-(\lambda_d+\lambda_d^*)(1+p^2),\end{aligned} \tag{30}$$

$$\begin{aligned}V_{d\alpha}=&\sum_{\beta=1,2}(1-\delta_{\alpha\beta})\gamma_{d\beta}(\bar{\lambda}_d+\bar{\lambda}_d^*)(1+p^2)\\&-[\xi_d+\eta_d^*+(\eta_d+\xi_d^*)p^2],\end{aligned} \tag{31}$$

and $\delta_{\alpha\beta}$ is the Kronecker delta. The expressions for $\hat{u}_\alpha$ and $\hat{\sigma}_{\alpha\beta}$ now follow directly from the substitution of (24) into (7)–(8). This completes the formal solution for the transforms of the stress and displacement components. The location of the zeros of the characteristic function $(1-p^2)(l_dp^4+m_dp^2+l_d)=0$ is found to be

$$s=n, \tag{32}$$

or

$$s=n-\frac{1}{2}\pm i\beta_d \quad \text{if} \quad m_d/2l_d\geq 1; \tag{33}$$

$$s=n\pm i\beta_d \quad \text{if} \quad m_d/2l_d\leq -1; \tag{34}$$

$$s=n\pm\sigma \quad \text{if} \quad |m_d/2l_d|<1, \tag{35}$$

where

$$\beta_d=\frac{1}{2\pi}\cosh^{-1}\left|\frac{m_d}{2l_d}\right|=\frac{1}{2\pi}\ln\left|\frac{1+\kappa_d}{1-\kappa_d}\right|, \tag{36}$$

$$\sigma=\frac{1}{2\pi}\cos^{-1}\left(\frac{-m_d}{2l_d}\right), \tag{37}$$

$$\kappa_d=\sqrt{\frac{m_d-2l_d}{m_d+2l_d}}, \tag{38}$$

and n is an integer number. From the condition of the positive definite for the material constant it can be shown numerically that $m_d/2l_d\geq 1$. The similar results as shown in (32) and (33) are also obtained by Ting (1986). It is shown that β_d can be expressed in another form,

$$\beta_d=\frac{1}{\pi}\tanh^{-1}\frac{\eta_d-\xi_d-\eta_d^*+\xi_d^*}{\sqrt{(\eta_d+\xi_d+\eta_d^*+\xi_d^*)^2-4|\lambda_d+\lambda_d^*|^2}}. \tag{39}$$

The order of the power-type stress singularity is $\lambda=s_1+1$, where s_1 denotes the zero of the characteristic function with the largest value in the open strip $-2<\mathrm{Re}(s)<-1$. The order of the stress singularity λ is a complex number and the stress fields are oscillatory in the limit $r\to 0$. The magnitude of the oscillation is depend on the value β_d which is expressed in (36) and depends only on one material parameter κ_d. There are combinations of the material constants that will have the square root singularity, i.e., $\beta_d=0$, should satisfy the following equation:

$$\eta_d-\xi_d=\eta_d^*-\xi_d^*. \tag{40}$$

Homogeneous materials obviously satisfy Eq. (40). For the isotropic case, we have $\eta_d=\mu/(m-1)$, $\xi_d=\mu$ and $\lambda_d=0$. Equation (39) is reduced to

$$\beta_d=\frac{1}{\pi}\tanh^{-1}\frac{\mu(m-2)(m^*-1)-\mu^*(m^*-2)(m-1)}{\mu m(m^*-1)+\mu^*m^*(m-1)}, \tag{41}$$

which is in agreement with the result obtained by Ma and Wu (1990). The largest value of β_d in (41) is $(\ln\sqrt{3})/\pi(\approx 0.175)$, the same as the traction-prescribed boundary conditions.

Next, we consider the interfacial crack problem with the boundary conditions of traction prescribed along one crack face while displacement prescribed on the other crack face. Thus we consider the following boundary conditions:

$$\sum_{\alpha=1,2}\{\gamma_\alpha H_\alpha(s,\pi)\phi_\alpha(s)+\bar{H}_\alpha(s,\pi)\bar{\phi}_\alpha(s)\}=T(s), \tag{42}$$

$$\sum_{\alpha=1,2}\{\delta_\alpha^*H_\alpha^*(s,-\pi)\phi_\alpha^*(s)+\rho_\alpha^*\bar{H}_\alpha^*(s,-\pi)\bar{\phi}_\alpha^*(s)\}=-D^*(s). \tag{43}$$

By using the Cramer's rule and after some algebraic simplifications, we get

$$\phi_\alpha(s)H_\alpha(s,0)=\frac{pQ_\alpha}{(-1)^\alpha(\gamma_2-\gamma_1)Q}, \tag{44}$$

in which Q and Q_α are obtained from the determinant of eight-by-eight matrix. The characteristic equation Q, which presents the dependence of the stress singularity on material constants, is reduced to an explicit simple form as

$$Q=\begin{vmatrix}\eta+\xi p^2 & -\lambda(1+p^2) & 0 & 1-p^2\\ \bar{\lambda}(1+p^2) & -\xi-\eta p^2 & 1-p^2 & 0\\ 1-p^2 & 0 & \lambda_d^*(1+p^2) & -\xi_d^*-\eta_d^*p^2\\ 0 & 1-p^2 & \eta_d^*+\xi_d^*p^2 & -\lambda_d^*(1+p^2)\end{vmatrix}$$

$$= (1+p^2)^2\{[\lambda(\eta_d^* + \xi_d^* p^2) - \lambda_d^*(\eta + \xi p^2)\}$$
$$\times [\bar{\lambda}(\xi_d^* + \eta_d^* p^2) - \bar{\lambda}_d^*(\xi + \eta p^2)]\}$$
$$- \{(1-p^2)^2 + (\xi + \eta p^2)(\eta_d^* + \xi_d^* p^2) - \bar{\lambda}\lambda_d^*(1+p^2)^2\}$$
$$\cdot\{(1-p^2)^2 + (\eta + \xi p^2)(\xi_d^* + \eta_d^* p^2) - \lambda\bar{\lambda}_d^*(1+p^2)^2\}. \quad (45)$$

But Q_α can only be reduced to the determinant of a four-by-four matrix. The results are:

$$Q_\alpha = \begin{vmatrix} \xi T(s) - \lambda\bar{T}(s) - D^*(s) & -\lambda(1+p^2) + \Sigma_\beta(1-\delta_{\alpha\beta})\gamma_\beta(\eta + \xi p^2) & 0 & 1-p^2 \\ \bar{\lambda}T(s) - \eta\bar{T}(s) - \bar{D}^*(s) & -\xi - \eta p^2 + \Sigma_\beta(1-\delta_{\alpha\beta})\gamma_\beta\bar{\lambda}(1+p^2) & 1-p^2 & 0 \\ -T(s) - \eta_d^* D^*(s) + \lambda_d^*\bar{D}^*(s) & \Sigma_\beta(1-\delta_{\alpha\beta})\gamma_\beta(1-p^2) & \lambda_d^*(1+p^2) & -\xi_d^* - \eta_d^* p^2 \\ -\bar{T}(s) - \bar{\lambda}_d^* D^*(s) + \xi_d^*\bar{D}^*(s) & 1-p^2 & \eta_d^* + \xi_d^* p^2 & -\bar{\lambda}_d^*(1+p^2) \end{vmatrix}. \quad (46)$$

All the zeros of (45) can be obtained explicitly as shown in the following form:

$$s = n - \frac{1}{2} + \alpha \pm i\beta, \quad n - \frac{1}{2} - \alpha \pm i\beta,$$

$$\text{if } |q^+ - q^- + 16q_o| \le 2\sqrt{q^+ q^-}; \quad (47)$$

$$s = n - \frac{1}{2} + \alpha \pm \sigma, \quad n - \frac{1}{2} - \alpha \pm \sigma,$$

$$\text{if } \sqrt{q^+} + \sqrt{q^-} < \sqrt{16q_o}; \quad (48)$$

$$s = n - \frac{1}{2} + i(\beta \pm \tau), \quad n - \frac{1}{2} - i(\beta \pm \tau),$$

$$\text{if } \sqrt{q^+} - \sqrt{q^-} > \sqrt{16q_o}; \quad (49)$$

$$s = n + i(\beta \pm \tau), \quad n - i(\beta \pm \tau),$$

$$\text{if } \sqrt{q^+} - \sqrt{q^-} < -\sqrt{16q_o}; \quad (50)$$

$$s = n - \frac{1}{2} \pm i(\vartheta - \varsigma), \quad n \pm i(\vartheta + \varsigma), \quad \text{if } q_o < 0, \quad (51)$$

where

$$\alpha = \frac{1}{2\pi}\cos^{-1}(\sqrt{q^+/16q_o} - \sqrt{q^-/16q_o}),$$

$$\beta = \frac{1}{2\pi}\cosh^{-1}(\sqrt{q^+/16q_o} + \sqrt{q^-/16q_o}),$$

$$\sigma = \frac{1}{2\pi}\cos^{-1}(\sqrt{q^+/16q_o} + \sqrt{q^-/16q_o}),$$

$$\tau = \frac{1}{2\pi}\cosh^{-1}|\sqrt{q^+/16q_o} - \sqrt{q^-/16q_o}|,$$

$$\vartheta = \frac{1}{2\pi}\sinh^{-1}(\sqrt{-q^+/16q_o} + \sqrt{-q^-/16q_o}),$$

$$\varsigma = \frac{1}{2\pi}\sinh^{-1}(\sqrt{-q^+/16q_o} - \sqrt{-q^-/16q_o}),$$

$$q_o = -Q|_{p^2=0} = (\eta\xi - |\lambda|^2)(\eta_d^*\xi_d^* - |\lambda_d^*|^2) + \eta\xi_d^* + \xi\eta_d^* - \bar{\lambda}\lambda_d^* - \lambda\bar{\lambda}_d^* + 1, \quad (52)$$

$$q^+ = -Q|_{p^2=1} = [(\eta+\xi)^2 - 4|\lambda|^2][(\eta_d^* + \xi_d^*)^2 - 4|\lambda_d^*|^2], \quad (53)$$

$$q^- = -Q|_{p^2=-1} = [(\eta-\xi)(\eta_d^* - \xi_d^*) - 4]^2. \quad (54)$$

Equations (47)–(51) list all the mathematical possibility of the zeros of Eq. (45), but not all zeros are admissible. From the positive definite character of the material constant, it can be shown numerically that the admissible zeros are those expressed in (47), (48), and (49). The order of stress singularity for the mixed boundary condition can then be obtained explicitly. This is the first explicit results for the order of stress singularity of mixed boundary condition for anisotropic interfacial crack. While for the pure traction or displacement prescribed problems Ting (1986) also obtained the explicit results by using Stroh's formulations. For the isotropic interfacial crack subjected to mixed boundary condition, the solutions can be obtained from general results shown in (47)–(51) by setting

$$q_o = \left[1 + \frac{\mu^*(m-1)}{\mu}\right]\left[1 + \frac{\mu^*}{\mu(m^*-1)}\right], \quad (55)$$

$$q^+ = \left[\frac{\mu^* m m^*}{\mu(m^*-1)}\right]^2, \quad (56)$$

$$q^- = \left[4 + \frac{\mu^*(m-2)(m^*-2)}{\mu(m^*-1)}\right]^2. \quad (57)$$

This result of the order of stress singularity for an isotropic case is in agreement with the results obtained by Ting (1986) and Ma and Wu (1990).

Conclusions

The problem of plane deformation for a dissimilar anisotropic interface crack was solved by application of the Mellin transform. The explicit solutions of stresses and displacements are obtained for traction-displacement and displacement-displacement boundary conditions applied on the crack faces. It is very interesting to find that the solutions of the displacement prescribed problems can be obtained from the traction prescribed problems by a simple substitution. The dependence of the order of stress singularity on the material constants and boundary conditions is expressed in explicit closed form. It is shown that the order of stress singularity has reduced dependence on the elastic constants. It needs only one material parameter instead of 12 material constants for displacement-displacement boundary conditions. The reduction in the number of elastic constants may simplify the analysis and investigation of the interface crack problem.

Acknowledgments

The financial support by the National Science Council (Republic of China) through grant NSC 79-0401-E002-37 to National Taiwan University and helpful discussions with professor K. C. Wu are gratefully acknowledged.

References

Bogy, D. B., 1972, "The Plane Solution for Anisotropic Elastic Wedges Under Normal and Shear Loading," ASME JOURNAL OF APPLIED MECHANICS, Vol. 39, pp. 1103–1109.

Ma, C. C., and Hour, B. L., 1989, "Analysis of Dissimilar Anisotropic Wedges Subjected to Antiplane Shear Deformation," *Int. J. Solids Structures*, Vol. 25, pp. 1295–1309.

Ma, C. C., and Hour, B. L., 1990, "Antiplane Problems in Composite Anisotropic Materials with an Inclined Crack Terminating at a Bimaterial Interface," *Int. J. Solids Structures*, Vol. 26, pp. 1387–1400.

Ma, C. C., and Luo, J. J., 1992, "Plane Solutions of Interface Cracks in Anisotropic Dissimilar Media," submitted for publication.
Ma, C. C., and Wu, H. W., 1990, "Analysis of Inplane Composite Wedges under Traction-Displacement or Displacement-Displacement Boundary Conditions," *Acta Mechanica*, Vol. 85, pp. 149-167.
Rice, J. R., and Sih, G. C., 1965, "Plane Problems of Cracks in Dissimilar Media," ASME JOURNAL OF APPLIED MECHANICS, Vol. 32, pp. 418-422.
Ting, T. C. T., 1986, "Explicit Solution and Invariance of the Singularities at an Interface Crack in Anisotropic Composites," *Int. J. Solids Structures*, Vol. 22, pp. 965-983.
Ting, T. C. T., 1990, "Interface Cracks in Anisotropic Bimaterials," *J. Mech. Phys. Solids*, Vol. 38, pp. 505-513.
Williams, M. L., 1959, "The Stresses Around a Fault or Crack in Dissimilar Media," *Bulletin of the Seismological Society of America*, Vol. 49, pp.199-204.

Singularity Eigenvalue Analysis of a Crack Along a Wedge-Shaped Interface

Y. Z. Chen[9] and Norio Hasebe[10]

1 Introduction

Recently, there has been a resurgence of interest in the elastic interface crack problem. Works by Huchinson, Mear, and Rice (1987), Rice (1988), Mukai, Ballarini, and Miller (1990), Hasebe, Okumura, and Nakamura (1990), Toya (1990), and Wu (1990) provide examples of the recent contributions. The interface crack problem between dissimilar materials was first studied by Williams (1959). Williams showed that the stresses at the vicinity of a crack tip possess singularities of type $r^{a-i\epsilon}$, where r is the radial distance from the crack tip and ϵ is a bimaterial constant. The problem of two edge-bonded wedges of dissimilar materials was investigated by Bogy (1971). Bogy used the Mellin transform to investigate the nontrivial solution for the two edge-bonded wedges. He studied the order of the singularity in the case of some particular wedge angle and the material constants changing continuously.

In this paper, singularity eigenvalue analysis of a crack along a wedge-shaped interface is examined. The considered wedges are bonded along one edge and are debonding, or cracking, along another edge (Fig. 1). One wedge has an angle α and the elastic constants μ_1, κ_1 and another wedge has β, μ_2, and κ_2. Two angles are assumed to satisfy $\alpha + \beta = 2\pi$, and α changes from 0 to 2π. The eigenvalue is denoted by $E = a - ib$ in the following analysis. The complex variable function method proposed by Muskhelishvili (1953) is used for the eigenvalue analysis. Comparing with the Mellin transform method, the proposed method is straightforward, and the obtained results and eigenvalues can be directly related to the stress and displacement fields. It is obviously that $\alpha = 0$ or $\alpha = 2\pi$ corresponds to the isotropic case, and the eigenvalue for leading term (abbreviated as ELT) is a real one. Also, it is easily seen that $\alpha = \pi$ corresponds to the conventional interface crack problem, and the ELT is a complex value. Contrary to a previous study, in this paper the angle α is changing continuously and the material constants involved are assigned to be some particular value. Therefore, the change of ELT from a real value ($0 \le \alpha \le \alpha_c$), to a complex value ($\alpha_c \le \alpha \le \alpha_u$), and then to a real value ($\alpha_u \le \alpha \le 2\pi$) can clearly be seen from the obtained numerical results.

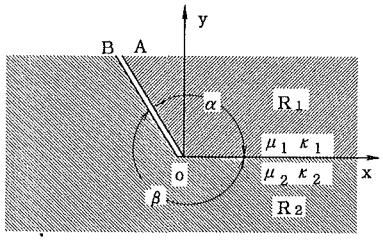

Fig. 1 A crack along a wedge-shaped interface

2 Analysis

It is well known that the complex variable function method proposed by Muskhelishvili (1953) provides a most effective approach to analyze the plane elastic problem. According to this method, the stresses (σ_{xx}, σ_{yy}, σ_{xy}), the resultant force functions (X, Y), and the displacements (u, v) can be described by two complex potentials $\phi(z)$ and $\omega(z)$

$$\sigma_{xx}+\sigma_{yy}=4\mathrm{Re}[\Phi(z)]$$

$$\sigma_{yy}-i\sigma_{xy}=\Phi(z)+(z-\bar{z})\overline{\Phi'(z)}+\overline{\Omega(z)} \tag{1}$$

$$P=-Y+iX=\phi(z)+(z-\bar{z})\overline{\phi'(z)}+\overline{\omega(z)} \tag{2}$$

$$2\mu(u+iv)=\kappa\phi(z)-(z-\bar{z})\overline{\phi'(z)}-\overline{\omega(z)} \tag{3}$$

where $\Phi(z) = \phi'(z)$ and $\Omega(z) = \omega'(z)$, μ is the shear modulus of elasticity, $\kappa = 3 - 4\nu$ for the plane strain problem, $\kappa = (3 - \nu)/(1 + \nu)$ for the plane stress problem, and ν is the Poisson's ratio.

We seek the solution of the problem in some region R ($R = R_1 + R_2$, Fig. 1) surrounding by a traction-free interface crack. The elastic constants and the complex potentials are denoted by μ_1, κ_1, $\phi_1(z)$, $\omega_1(z)$ and μ_2, κ_2, $\phi_2(z)$, $\omega_2(z)$ for the regions R_1 and R_2, respectively. From Eqs. (2) and (3) the continuation condition of the resultant force and the displacement along the positive part of real axis gives rise to the following relations:

$$\phi_1^+(x)+\overline{\omega_1^+(x)}=\phi_2^-(x)+\overline{\omega_2^-(x)} \quad (x>0) \tag{4}$$

$$\mu_2(\kappa_1\phi_1^+(x)-\overline{\omega_1^+(x)})=\mu_1(\kappa_2\phi_2^-(x)-\overline{\omega_2^-(x)}) \quad (x>0), \tag{5}$$

since along the crack faces OA and OB we have

$$z=\bar{z}\exp(2i\alpha) \quad (z\in\mathrm{OA} \text{ or } z\in\mathrm{OB}). \tag{6}$$

Therefore, the traction-free condition along the upper and lower crack faces can be expressed by

$$\phi_1(z)+(\exp(2i\alpha)-1)\bar{z}\,\overline{\phi_1'(z)}+\overline{\omega_1(z)}=0 \quad (z\in\mathrm{OA}) \tag{7}$$

$$\phi_2(z)+(\exp(2i\alpha)-1)\bar{z}\,\overline{\phi_2'(z)}+\overline{\omega_2(z)}=0 \quad (z\in\mathrm{OB}). \tag{8}$$

In the following analysis we let the complex potentials take the following expression:

$$\phi_1(z)=p_1z^{a-ib}+\bar{q}_1z^{a+ib}$$

$$\omega_1(z)=\bar{s}_1z^{a+ib}+t_1z^{a-ib} \tag{9}$$

$$\phi_2(z)=p_2z^{a-ib}+\bar{q}_2z^{a+ib}$$

$$\omega_2(z)=\bar{s}_2z^{a+ib}+t_2z^{a-ib} \tag{10}$$

where p_1, q_1, s_1, t_1, p_2, q_2, s_2, and t_2 are complex values. In addition, the value $E = a - ib$ (or $a + ib$) will be determined by the condition of a nontrivial solution of the problem and is called the eigenvalue for a crack problem in the bonded wedges.

Substituting Eqs. (9) and (10) in (4), (5), (7), and (8) yields eight equations. Furthermore, after eliminating s_1, t_1, s_2, and t_2 in these equations we get the following equations:

$$(1-e_1)p_1-e_3q_1-(1-e_1e_2)p_2+e_3q_2=0 \tag{11}$$

[9]Division of Engineering Mechanics, Jiangsu Institute of Technology, Zhenjiang, Jiangsu, 212013, P. R. China.
[10]Department of Civil Engineering, Nagoya Institute of Technology, Gokiso-cho, Showa-ku, Nagoya 466, Japan.

Contributed by the Applied Mechanics Division of THE AMERICAN SOCIETY OF MECHANICAL ENGINEERS for publication in the ASME JOURNAL OF APPLIED MECHANICS. Manuscript received by the ASME Applied Mechanics Division, Sept. 10, 1991; final revision, Apr. 10, 1992. Associate Technical Editor: C. F. Shih.

Ma, C. C., and Luo, J. J., 1992, "Plane Solutions of Interface Cracks in Anisotropic Dissimilar Media," submitted for publication.
Ma, C. C., and Wu, H. W., 1990, "Analysis of Inplane Composite Wedges under Traction-Displacement or Displacement-Displacement Boundary Conditions," *Acta Mechanica*, Vol. 85, pp. 149-167.
Rice, J. R., and Sih, G. C., 1965, "Plane Problems of Cracks in Dissimilar Media," ASME JOURNAL OF APPLIED MECHANICS, Vol. 32, pp. 418-422.
Ting, T. C. T., 1986, "Explicit Solution and Invariance of the Singularities at an Interface Crack in Anisotropic Composites," *Int. J. Solids Structures*, Vol. 22, pp. 965-983.
Ting, T. C. T., 1990, "Interface Cracks in Anisotropic Bimaterials," *J. Mech. Phys. Solids*, Vol. 38, pp. 505-513.
Williams, M. L., 1959, "The Stresses Around a Fault or Crack in Dissimilar Media," *Bulletin of the Seismological Society of America*, Vol. 49, pp.199-204.

Singularity Eigenvalue Analysis of a Crack Along a Wedge-Shaped Interface

Y. Z. Chen[9] and Norio Hasebe[10]

1 Introduction

Recently, there has been a resurgence of interest in the elastic interface crack problem. Works by Huchinson, Mear, and Rice (1987), Rice (1988), Mukai, Ballarini, and Miller (1990), Hasebe, Okumura, and Nakamura (1990), Toya (1990), and Wu (1990) provide examples of the recent contributions. The interface crack problem between dissimilar materials was first studied by Williams (1959). Williams showed that the stresses at the vicinity of a crack tip possess singularities of type $r^{a-i\epsilon}$, where r is the radial distance from the crack tip and ϵ is a bimaterial constant. The problem of two edge-bonded wedges of dissimilar materials was investigated by Bogy (1971). Bogy used the Mellin transform to investigate the nontrivial solution for the two edge-bonded wedges. He studied the order of the singularity in the case of some particular wedge angle and the material constants changing continuously.

In this paper, singularity eigenvalue analysis of a crack along a wedge-shaped interface is examined. The considered wedges are bonded along one edge and are debonding, or cracking, along another edge (Fig. 1). One wedge has an angle α and the elastic constants μ_1, κ_1 and another wedge has β, μ_2, and κ_2. Two angles are assumed to satisfy $\alpha + \beta = 2\pi$, and α changes from 0 to 2π. The eigenvalue is denoted by $E = a - ib$ in the following analysis. The complex variable function method proposed by Muskhelishvili (1953) is used for the eigenvalue analysis. Comparing with the Mellin transform method, the proposed method is straightforward, and the obtained results and eigenvalues can be directly related to the stress and displacement fields. It is obviously that $\alpha = 0$ or $\alpha = 2\pi$ corresponds to the isotropic case, and the eigenvalue for leading term (abbreviated as ELT) is a real one. Also, it is easily seen that $\alpha = \pi$ corresponds to the conventional interface crack problem, and the ELT is a complex value. Contrary to a previous study, in this paper the angle α is changing continuously and the material constants involved are assigned to be some particular value. Therefore, the change of ELT from a real value ($0 \le \alpha \le \alpha_c$), to a complex value ($\alpha_c \le \alpha \le \alpha_u$), and then to a real value ($\alpha_u \le \alpha \le 2\pi$) can clearly be seen from the obtained numerical results.

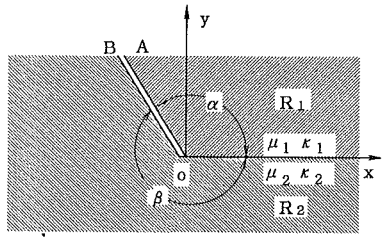

Fig. 1 A crack along a wedge-shaped interface

2 Analysis

It is well known that the complex variable function method proposed by Muskhelishvili (1953) provides a most effective approach to analyze the plane elastic problem. According to this method, the stresses (σ_{xx}, σ_{yy}, σ_{xy}), the resultant force functions (X, Y), and the displacements (u, v) can be described by two complex potentials $\phi(z)$ and $\omega(z)$

$$\sigma_{xx}+\sigma_{yy}=4\mathrm{Re}[\Phi(z)]$$

$$\sigma_{yy}-i\sigma_{xy}=\Phi(z)+(z-\bar{z})\overline{\Phi'(z)}+\overline{\Omega(z)} \quad (1)$$

$$P=-Y+iX=\phi(z)+(z-\bar{z})\overline{\phi'(z)}+\overline{\omega(z)} \quad (2)$$

$$2\mu(u+iv)=\kappa\phi(z)-(z-\bar{z})\overline{\phi'(z)}-\overline{\omega(z)} \quad (3)$$

where $\Phi(z) = \phi'(z)$ and $\Omega(z) = \omega'(z)$, μ is the shear modulus of elasticity, $\kappa = 3 - 4\nu$ for the plane strain problem, $\kappa = (3 - \nu)/(1 + \nu)$ for the plane stress problem, and ν is the Poisson's ratio.

We seek the solution of the problem in some region R ($R = R_1 + R_2$, Fig. 1) surrounding by a traction-free interface crack. The elastic constants and the complex potentials are denoted by μ_1, κ_1, $\phi_1(z)$, $\omega_1(z)$ and μ_2, κ_2, $\phi_2(z)$, $\omega_2(z)$ for the regions R_1 and R_2, respectively. From Eqs. (2) and (3) the continuation condition of the resultant force and the displacement along the positive part of real axis gives rise to the following relations:

$$\phi_1^+(x)+\overline{\omega_1^+(x)}=\phi_2^-(x)+\overline{\omega_2^-(x)} \quad (x>0) \quad (4)$$

$$\mu_2(\kappa_1\phi_1^+(x)-\overline{\omega_1^+(x)})=\mu_1(\kappa_2\phi_2^-(x)-\overline{\omega_2^-(x)}) \quad (x>0), \quad (5)$$

since along the crack faces OA and OB we have

$$z=\bar{z}\exp(2i\alpha) \quad (z\in\mathrm{OA} \text{ or } z\in\mathrm{OB}). \quad (6)$$

Therefore, the traction-free condition along the upper and lower crack faces can be expressed by

$$\phi_1(z)+(\exp(2i\alpha)-1)\bar{z}\,\overline{\phi_1'(z)}+\overline{\omega_1(z)}=0 \quad (z\in\mathrm{OA}) \quad (7)$$

$$\phi_2(z)+(\exp(2i\alpha)-1)\bar{z}\,\overline{\phi_2'(z)}+\overline{\omega_2(z)}=0 \quad (z\in\mathrm{OB}). \quad (8)$$

In the following analysis we let the complex potentials take the following expression:

$$\phi_1(z)=p_1z^{a-ib}+\bar{q}_1z^{a+ib}$$

$$\omega_1(z)=\bar{s}_1z^{a+ib}+t_1z^{a-ib} \quad (9)$$

$$\phi_2(z)=p_2z^{a-ib}+\bar{q}_2z^{a+ib}$$

$$\omega_2(z)=\bar{s}_2z^{a+ib}+t_2z^{a-ib} \quad (10)$$

where p_1, q_1, s_1, t_1, p_2, q_2, s_2, and t_2 are complex values. In addition, the value $E = a - ib$ (or $a + ib$) will be determined by the condition of a nontrivial solution of the problem and is called the eigenvalue for a crack problem in the bonded wedges.

Substituting Eqs. (9) and (10) in (4), (5), (7), and (8) yields eight equations. Furthermore, after eliminating s_1, t_1, s_2, and t_2 in these equations we get the following equations:

$$(1-e_1)p_1-e_3q_1-(1-e_1e_2)p_2+e_3q_2=0 \quad (11)$$

[9]Division of Engineering Mechanics, Jiangsu Institute of Technology, Zhenjiang, Jiangsu, 212013, P. R. China.
[10]Department of Civil Engineering, Nagoya Institute of Technology, Gokisocho, Showa-ku, Nagoya 466, Japan.

Contributed by the Applied Mechanics Division of THE AMERICAN SOCIETY OF MECHANICAL ENGINEERS for publication in the ASME JOURNAL OF APPLIED MECHANICS. Manuscript received by the ASME Applied Mechanics Division, Sept. 10, 1991; final revision, Apr. 10, 1992. Associate Technical Editor: C. F. Shih.

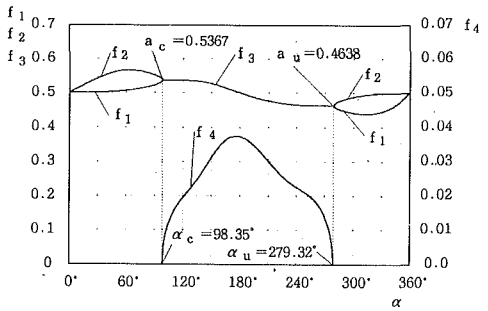

Fig. 2 Eigenvalue ($E = a - ib$) distribution for the leading term under the conditions of $\mu_1 = \mu_2 = 2.7/1.3$, $\mu_1 = 1.0$ and $\mu_2 = 2.0$ (see Eqs. (22) and (23))

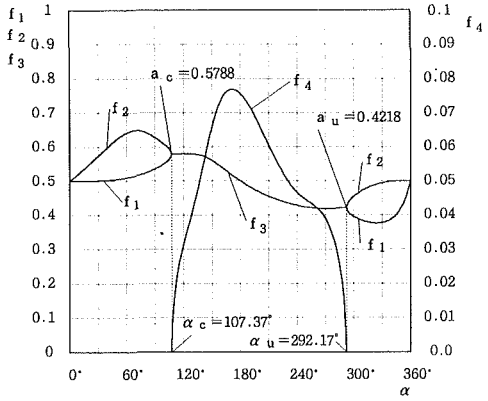

Fig. 3 Eigenvalue ($E = a - ib$) distribution for the leading term under the conditions of $\mu_1 = \mu_2 = 2.7/1.3$, $\mu_1 = 1.0$ and $\mu_2 = 5.0$ (see Eqs. (22) and (23))

$$\mu_2(\kappa_1+e_1)p_1+\mu_2e_3q_1-\mu_1(\kappa_2+e_1e_2)p_2-\mu_1e_3q_2=0 \quad (12)$$

$$-e_4p_1+(1-1/e_1)q_1+e_4p_2-(1-1/(e_1e_2))q_2=0 \quad (13)$$

$$\mu_2e_4p_1+\mu_2(\kappa_1+1/e_1)q_1-\mu_1e_4p_2-\mu_1(\kappa_2+1/(e_1e_2))q_2=0 \quad (14)$$

where

$$e_1=\exp(2(b+ia)\alpha) \qquad e_2=\exp(-4\pi(b+ia))$$

$$e_3=(a-ib)(\exp(2i\alpha)-1), \quad e_4=(a-ib)(\exp(-2i\alpha)-1). \quad (15)$$

After some manipulation, the condition of the nontrivial solution for p_1, q_1, p_2, and q_2 gives

$$\Delta=D_1+iD_2=0 \quad (16)$$

where

$$\Delta=(f_1f_2/e_2)e_1^{-2}+(g_2+g_1/e_2)/e_1+[-(f_1^2+f_2^2+f_3^2+f_4^2)+(3f_1^2+f_2^2)e_3e_4-f_1^2(e_3e_4)^2+f_3f_4(e_2+1/e_2)]+(g_2+g_1e_2)e_1+(f_1f_2e_2)e_1^2 \quad (17)$$

$$f_1=\mu_1-\mu_2, \quad f_2=\mu_1\kappa_2-\kappa_2\mu_1, \quad f_3=\mu_1+\mu_2\kappa_1, \quad f_4=\mu_2+\mu_1\kappa_2$$

$$g_1=-f_1f_4(1-e_3e_4)-f_2f_3, \quad g_2=f_1f_3(1-e_3e_4)+f_2f_4. \quad (18)$$

After using two parameters defined by Dundurs (1969)

$$\delta=\frac{\mu_2(\kappa_1+1)-\mu_1(\kappa_2+1)}{\mu_2(\kappa_1+1)+\mu_1(\kappa_2+1)}, \quad \gamma=\frac{\mu_2(\kappa_1-1)-\mu_1(\kappa_2-1)}{\mu_2(\kappa_1+1)+\mu_1(\kappa_2+1)}, \quad (19)$$

we get

$$f_1=\frac{\gamma-\delta}{1-\gamma}f_4, \quad f_2=-\frac{\gamma+\delta}{1-\gamma}f_4, \quad f_3=\frac{1+\gamma}{1-\gamma}f_4. \quad (20)$$

Therefore, Eq. (16) can be rewritten as

$$\Delta=f_4^2\Delta_1(a-ib,\delta,\gamma,\alpha)=0. \quad (21)$$

The above equation shows that the eigenvalue $E = a - ib$ depends on the material constants (δ and γ) and the wedge angle (α) only.

3 Results

The eigenvalue $E = a - ib$ was evaluated by some numerical technique. To shorten the length of the present Note the detail of computation is omitted here. It is well known that the most important eigenvalue in fracture analysis is the one relating to the leading term in the expansion form, which makes the stress infinite and the displacement finite. Clearly, the mentioned eigenvalue in the isotropic case is $E = a = 0.5$.

Thus, we first find the eigenvalue in the vicinity of $\mathrm{Re}(E) = 0.5$. The numerical computation shows the following results:

(a) If α is rather small ($\alpha \geq 0$) or rather large ($\alpha \leq 2\pi$), we always find two real eigenvalues a_1 and a_2 ($b = 0$) within the intervals $0 \leq \alpha \leq \alpha_c$ and $\alpha_u \leq \alpha \leq 2\pi$. The calculated eigenvalues can be expressed as

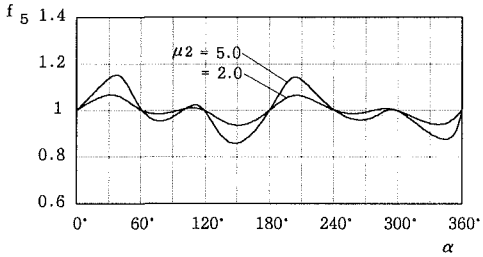

Fig. 4 Eigenvalue ($E = a - ib$) distribution at the vicinity of Re(E) = 1.0 under the conditions of $\mu_1 = \mu_2 = 2.7/1.3$, $\mu_1 = 1.0$ and $\mu_2 = 2.0$, 5.0 (see Eq. (24))

$$a_1=f_1(\alpha), \quad b_1=0, \quad (0\leq\alpha\leq\alpha_c \text{ and } \alpha_u\leq\alpha\leq2\pi)$$

$$a_2=f_2(\alpha), \quad b_2=0 \quad (0\leq\alpha\leq\alpha_c \text{ and } \alpha_u\leq\alpha\leq2\pi). \quad (22)$$

(b) If α is in the same vicinity of $\alpha = \pi$, we can find a complex eigenvalues $E = a - ib$ with the interval $\alpha_c \leq \alpha \leq \alpha_u$. In this case, the calculated eigenvalues can be expressed as

$$a=f_3(\alpha), \quad b=f_4(\alpha) \quad (\alpha_c\leq\alpha\leq\alpha_u). \quad (23)$$

The calculated results for two cases $\mu_2 = 2.0$, 5.0 ($\kappa_1 = \kappa_2 = 2.7/1.3$, $\mu_1 = 1.0$) are plotted in Figs. 2–3, respectively.

In addition, we also seek the eigenvalues in the vicinity of $\mathrm{Re}(E) = 1.0$. The calculated two eigenvalues can be expressed by

$$a_1=f_5(\alpha), \qquad b_1=0 \quad (0\leq\alpha\leq2\pi)$$

$$a_2=f_6(\alpha)=1, \quad b_2=0 \quad (0\leq\alpha\leq2\pi) \quad (24)$$

It is seen that the one eigenvalue is always equal to unity and another is variable depending on the angle α. The calculated results are plotted in Fig. 4.

References

Bogy, D. B., 1971, "Two Edge-Bonded Elastic Wedges of Different Materials and Wedge Angles under Surface Tractions," ASME JOURNAL OF APPLIED MECHANICS, Vol. 38, pp. 377–386.

Dundurs, J., discussion of "Edge-Bonded Dissimilar Orthogonal Elastic Wedges under Normal and Shear Loading," ASME JOURNAL OF APPLIED MECHANICS, Vol. 36, pp. 650–652.

Hasebe, N., Okumura, M., and Nakamura, T., 1990, "Partly Bonded Bimaterial Plane under Tension," *ASCE Journal of Engineering Mechanics*, Vol. 116, pp. 2017–2033.

Hutchinson, J. W., Mear, M. E., and Rice, J. R., "Crack Paralleling an Interface Between Dissimilar Materials," ASME JOURNAL OF APPLIED MECHANICS, Vol. 54, pp. 828–832.

Mukai, D. J., Ballarini, R., and Miller, G. R., 1990, "Analysis of Branched Interface Cracks," ASME JOURNAL OF APPLIED MECHANICS, Vol. 57, pp. 887–893.

Muskhelishvili, N. I., 1953, *Some Basic Problems of Mathematical Theory of Elasticity*, Noordhoff, Groningen.
Rice, J. R., 1988, "Elastic Fracture Mechanics Concept for Interfacial Cracks," ASME JOURNAL OF APPLIED MECHANICS, Vol. 55, pp. 98–103.
Toya, M., 1990, "Fracture Mechanics of Interfaces," *JSME International Journal Series I*, Vol. 33, pp. 413–424.
Williams, M. L., 1959, "The Stresses Around a Fault or Crack in Dissimilar Media," *Bull. Seismol. Soc. America*, Vol. 49, pp. 199–204.
Wu, K. C., 1990, "Stress Intensity Factor and Energy Release Rate for Interfacial Cracks between Dissimilar Anisotropic Materials," ASME JOURNAL OF APPLIED MECHANICS, Vol. 57, pp. 882–886.

On the Convergence of Karhunen-Loeve Series Expansion for a Brownian Particle

W. G. Paff[11] and G. Ahmadi[11,12]

A linear Langevin equation for the velocity of a Brownian particle is considered. The equation of motion is solved and the Karhunen-Loeve expansion for the particle velocity is derived. The mean-square velocity as obtained by the truncated Karhunen-Loeve expansion is compared with the exact solution. It is shown, as the number of terms in the series increases, the result approaches that of the exact solution asymptotically.

Introduction

Brownian motion was first observed by Robert Brown in 1827 while studying pollen particles suspended in liquid, and Brownian diffusivity was first estimated by Einstein (1903). An extensive exposition of the theory of Brownian motion was provided by Chandrasekhar (1943).

Use of the Karhunen-Loeve (KL) expansion (Loeve, 1955) for representing random data has attracted considerable attention in the field of turbulence (Lumley, 1967) and other areas (Lin and Yong, 1986). Here, the Karhunen-Loeve expansion for a Brownian particle is considered and analytical expressions for orthogonal basis are derived. The particle velocity response statistics as evaluated from the truncated series are compared with the exact values and the convergence of the KL series is discussed.

Analysis

Equation of Motion. The linear Langevin equation for the velocity of a Brownian particle is given as

$$\frac{du}{dt}+\beta u=n(t) \tag{1}$$

where

$$\beta=\frac{3\pi\mu d}{C_c m} \tag{2}$$

and $n(t)$ is a zero-mean Gaussian white noise process with a constant spectral intensity, S_o, given by

$$S_o=\frac{216\nu kT\rho}{\pi^2 d^5 \rho_p^2 C_c}. \tag{3}$$

Here, μ is the kinematic viscosity, d is the particle diameter, C_c is the Cunningham correction factor, m is the mass of the particle, ν is the kinematic viscosity, k is the Boltzmann constant, T is the temperature, ρ is the fluid density, and ρ_p is the particle density. A white noise process may be formally defined as the derivative of a Wiener process (Papoulis, 1984). A digital simulation procedure for generating white noise process corresponding to molecular agitation was described by Ounis et al. (1991).

Assuming that the motion starts from rest,

$$u(0)=0. \tag{4}$$

Equation (4) is the initial condition for particle velocity.

Karhunen-Loeve Expansion. According to the Karhunen-Loeve Theorem (Loeve, 1955), the random velocity has a series expansion of the form

$$u(t)=\sum_{n=1}^{\infty} C_n\Phi_n(t) \tag{5}$$

where $\Phi_n(t)$ are the KL orthonormal basis and C_n are independent random coefficients. The KL basis are the eigenfunctions of the Fredholm equation given by

$$\int_0^T R_{uu}(t_1,t_2)\Phi_n(t_2)dt_2=\lambda_n\Phi_n(t_1). \tag{6}$$

Here the kernel $R_{uu}(t_1, t_2)$ is the particle velocity autocorrelation function, and eigenvalues $\lambda_n = \langle |C_n|^2 \rangle$, with "$\langle\ \rangle$" denoting the expected value (ensemble average) and T, is a specified time duration.

Following the procedure outlined by Lin and Yong (1986), Eq. (6) may be restated as

$$L_{-t}L_t\Phi_n(t)=\frac{2\pi S_o}{\lambda_n}\Phi_n(t) \tag{7}$$

where

$$L_t=\frac{d}{dt}+\beta, \quad L_{-t}=-\frac{d}{dt}+\beta. \tag{8}$$

The required boundary conditions are

$$\Phi_n(0)=0, \quad L_t\Phi_n(T)=0. \tag{9}$$

The eigenfunctions for the boundary value problem, (7)–(9), are given by

$$\Phi_n(t)=A_n\sin(\xi_n t) \tag{10}$$

where

$$\xi_n=\sqrt{\frac{2\pi S_o}{\lambda_n}-\beta^2} \tag{11}$$

are solutions to the transcendental equation

$$\tan(\xi_n T)=\frac{-\xi_n}{\beta}. \tag{12}$$

The corresponding eigenvalues are

$$\lambda_n=\frac{2\pi S_o}{\beta^2+\xi_n^2}. \tag{13}$$

Using the normality condition,

[11]Department of Mechanical and Aeronautical Engineering, Clarkson University, Potsdam, NY 13699.
[12]Mem. ASME.

Contributed by the Applied Mechanics Division of THE AMERICAN SOCIETY OF MECHANICAL ENGINEERS for publication in the ASME JOURNAL OF APPLIED MECHANICS. Manuscript received by the ASME Applied Mechanics Division, Dec. 10, 1990; final revision, Aug. 17, 1992. Associate Technical Editor: J. T. C. Liu.

Muskhelishvili, N. I., 1953, *Some Basic Problems of Mathematical Theory of Elasticity*, Noordhoff, Groningen.
Rice, J. R., 1988, "Elastic Fracture Mechanics Concept for Interfacial Cracks," ASME JOURNAL OF APPLIED MECHANICS, Vol. 55, pp. 98–103.
Toya, M., 1990, "Fracture Mechanics of Interfaces," *JSME International Journal Series I*, Vol. 33, pp. 413–424.
Williams, M. L., 1959, "The Stresses Around a Fault or Crack in Dissimilar Media," *Bull. Seismol. Soc. America*, Vol. 49, pp. 199–204.
Wu, K. C., 1990, "Stress Intensity Factor and Energy Release Rate for Interfacial Cracks between Dissimilar Anisotropic Materials," ASME JOURNAL OF APPLIED MECHANICS, Vol. 57, pp. 882–886.

On the Convergence of Karhunen-Loeve Series Expansion for a Brownian Particle

W. G. Paff[11] and G. Ahmadi[11,12]

A linear Langevin equation for the velocity of a Brownian particle is considered. The equation of motion is solved and the Karhunen-Loeve expansion for the particle velocity is derived. The mean-square velocity as obtained by the truncated Karhunen-Loeve expansion is compared with the exact solution. It is shown, as the number of terms in the series increases, the result approaches that of the exact solution asymptotically.

Introduction

Brownian motion was first observed by Robert Brown in 1827 while studying pollen particles suspended in liquid, and Brownian diffusivity was first estimated by Einstein (1903). An extensive exposition of the theory of Brownian motion was provided by Chandrasekhar (1943).

Use of the Karhunen-Loeve (KL) expansion (Loeve, 1955) for representing random data has attracted considerable attention in the field of turbulence (Lumley, 1967) and other areas (Lin and Yong, 1986). Here, the Karhunen-Loeve expansion for a Brownian particle is considered and analytical expressions for orthogonal basis are derived. The particle velocity response statistics as evaluated from the truncated series are compared with the exact values and the convergence of the KL series is discussed.

Analysis

Equation of Motion. The linear Langevin equation for the velocity of a Brownian particle is given as

$$\frac{du}{dt}+\beta u=n(t) \tag{1}$$

where

$$\beta=\frac{3\pi\mu d}{C_c m} \tag{2}$$

and $n(t)$ is a zero-mean Gaussian white noise process with a constant spectral intensity, S_o, given by

$$S_o=\frac{216\nu kT\rho}{\pi^2 d^5 \rho_p^2 C_c}. \tag{3}$$

Here, μ is the kinematic viscosity, d is the particle diameter, C_c is the Cunningham correction factor, m is the mass of the particle, ν is the kinematic viscosity, k is the Boltzmann constant, T is the temperature, ρ is the fluid density, and ρ_p is the particle density. A white noise process may be formally defined as the derivative of a Wiener process (Papoulis, 1984). A digital simulation procedure for generating white noise process corresponding to molecular agitation was described by Ounis et al. (1991).

Assuming that the motion starts from rest,

$$u(0)=0. \tag{4}$$

Equation (4) is the initial condition for particle velocity.

Karhunen-Loeve Expansion. According to the Karhunen-Loeve Theorem (Loeve, 1955), the random velocity has a series expansion of the form

$$u(t)=\sum_{n=1}^{\infty} C_n\Phi_n(t) \tag{5}$$

where $\Phi_n(t)$ are the KL orthonormal basis and C_n are independent random coefficients. The KL basis are the eigenfunctions of the Fredholm equation given by

$$\int_0^T R_{uu}(t_1,t_2)\Phi_n(t_2)dt_2=\lambda_n\Phi_n(t_1). \tag{6}$$

Here the kernel $R_{uu}(t_1, t_2)$ is the particle velocity autocorrelation function, and eigenvalues $\lambda_n = \langle |C_n|^2 \rangle$, with "$\langle\ \rangle$" denoting the expected value (ensemble average) and T, is a specified time duration.

Following the procedure outlined by Lin and Yong (1986), Eq. (6) may be restated as

$$L_{-t}L_t\Phi_n(t)=\frac{2\pi S_o}{\lambda_n}\Phi_n(t) \tag{7}$$

where

$$L_t=\frac{d}{dt}+\beta, \quad L_{-t}=-\frac{d}{dt}+\beta. \tag{8}$$

The required boundary conditions are

$$\Phi_n(0)=0, \quad L_t\Phi_n(T)=0. \tag{9}$$

The eigenfunctions for the boundary value problem, (7)–(9), are given by

$$\Phi_n(t)=A_n\sin(\xi_n t) \tag{10}$$

where

$$\xi_n=\sqrt{\frac{2\pi S_o}{\lambda_n}-\beta^2} \tag{11}$$

are solutions to the transcendental equation

$$\tan(\xi_n T)=\frac{-\xi_n}{\beta}. \tag{12}$$

The corresponding eigenvalues are

$$\lambda_n=\frac{2\pi S_o}{\beta^2+\xi_n^2}. \tag{13}$$

Using the normality condition,

[11]Department of Mechanical and Aeronautical Engineering, Clarkson University, Potsdam, NY 13699.
[12]Mem. ASME.

Contributed by the Applied Mechanics Division of THE AMERICAN SOCIETY OF MECHANICAL ENGINEERS for publication in the ASME JOURNAL OF APPLIED MECHANICS. Manuscript received by the ASME Applied Mechanics Division, Dec. 10, 1990; final revision, Aug. 17, 1992. Associate Technical Editor: J. T. C. Liu.

Table 1 Listing of first nine eigenvalues for $\beta T = 5$

n	1	2	3	4	5	6	7	8	9
$\xi_n T$	2.654	5.454	8.391	11.409	14.47	17.556	20.657	23.769	26.887
$\frac{100\lambda_n}{2\pi S_o T^2}$	3.12	1.83	1.05	0.644	0.427	0.3	0.221	0.17	0.134

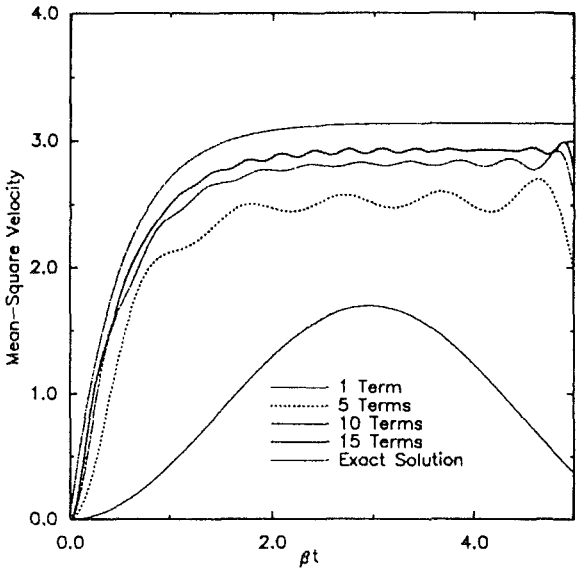

Fig. 1 Comparison of the mean-square velocities for the truncated Karhunen-Loeve series

$$\int_0^T \Phi_n(t)^2 dt = 1, \tag{14}$$

the coefficients A_n in Eq. (10) are given as

$$A_n = \sqrt{\frac{2\xi_n}{\xi_n T - \sin(\xi_n T)}}. \tag{15}$$

The mean-square velocity associated with the KL series is given by

$$\langle u^2(t)\rangle = \sum_n \lambda_n |\Phi_n(t)|^2 \tag{16}$$

and the exact transient mean-square velocity response as obtained by use of the impulse response method is

$$\langle u^2(t)\rangle = \frac{\pi S_o}{\beta}(1 - e^{-2\beta t}). \tag{17}$$

Results

For a nondimensional time duration of $\beta T = 5$, Table 1 provides a listing of the first nine values of $\xi_n T$ and λ_n. The weightings of different modes in Eq. (15) which correspond to eigenvalues λ_n can be clearly seen from this table. It is observed that λ_{n+1} is roughly about 80 percent of λ_n for higher modes. Figure 1 compares the dimensionless mean-square velocity responses, $\beta\langle u^2\rangle/S_o$, as obtained by the truncated KL expansion with the exact solution given by (17). The gradual convergence of the series solution to the exact mean-square response is clearly observed from this figure. Figure 2 shows

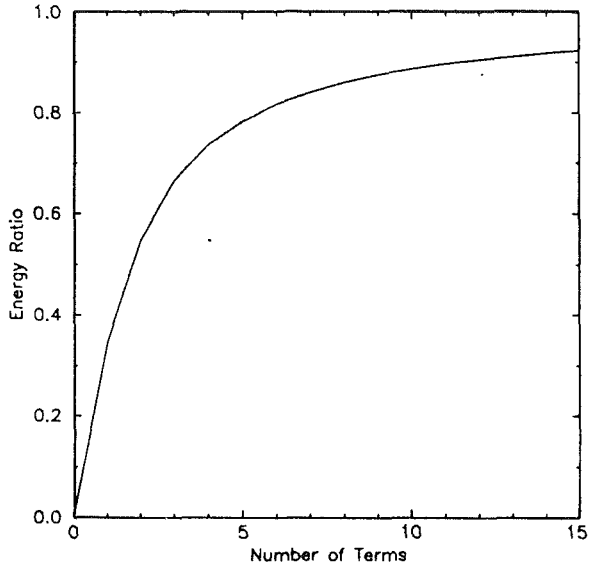

Fig. 2 Variation of energy ratio with order of truncation

the energy ratio for various orders of truncation of the KL series. Here the energy ratio is defined as the ratio of area under the mean-squared response curve as obtained by the truncated KL series to that of the exact one. From Fig. 2 it is observed that the first few terms of the KL series capture most of the energy. However, the convergence is asymptotic and a large number of terms are needed to recover the exact result.

Conclusion

For a finite time duration, the exact Karhunen-Loeve orthogonal basis for Brownian particles are derived. The mean-square velocities as evaluated from the truncated KL series expansion are compared with the exact one. It is shown that the first few terms of the series contains a substantial fraction of the energy of the response. However, for a high resolution description, consideration of a large number of terms are required.

Acknowledgments

The work of GA was supported by the US Department of Energy (University Coal Research Program, PETC) DE-GF22-91PC91297, and the New York State Science and Technology Foundation through the Center for Advanced Material Processing (CAMP) of Clarkson University.

References

Chandrasekhar, S., 1943, "Stochastic Problems in Physics and Astronomy," *Review of Modern Physics*, Vol. 15, pp. 1-89.

Einstein, A., 1903, "Investigation on the Theory of Brownian Movement," *Ann. D.,Physik*, Vol. 17, p. 549.

Lin, Y. K., and Yong, Y., 1986, "Some Observations on Spectral Analysis," *Random Vibration-Status and Recent Developments*, I. Elishckoff and R. H. Lyon, eds., Elsevier, New York, pp. 193-200.

Loeve, M., 1955, *Probability Theory*, Van Nostrand, New York.

Lumley, J. L., 1967, "The Structures of Inhomogeneous Turbulent Flow," *Atmospheric Turbulence and Radio Wave Propagation*, A. M. Yaglom and V. I. Tatarski, eds., Nauka, Moscow, pp. 166-178.

Papoulis, A., 1984, *Probability Random Variables, and/Stochastic Processes*, McGraw-Hill, New York.

Ounis, H., Ahmadi, G., and McLaughlin, J. B., 1991, "Brownian Diffusion of Submicrometer Particles in the Viscous Sublayer," *J. Colloid Interface Sci.*, Vol. 143, pp. 266-277.

Work-Conjugate Boundary Conditions Associated With the Total Rotation Angle of the Shell Boundary

W. Pietraszkiewicz[13]

Introduction

The general structure of four work-conjugate static and geometric boundary conditions for the nonlinear theory of thin shells expressed in terms of displacements of the reference surface as basic independent field variables was discussed by Makowski and Pietraszkiewicz (1989). It was proved, in particular, that the angle ω_t of total rotation of the shell boundary can be chosen as the fourth parameter which, together with three displacement components, describes an arbitrary deformation of the shell lateral boundary surface. In this report we present explicit derivation of the set of work-conjugate boundary conditions associated with the angle ω_t.

Notation and Basic Relations

Let the reference surface M of undeformed shell be defined by the position vector $\mathbf{r}(\Theta^\alpha)$, where Θ^α, $\alpha = 1, 2$, are surface curvilinear coordinates. On M we have the natural base vectors $\mathbf{a}_\alpha = \partial\mathbf{r}/\partial\Theta^\alpha$, the covariant (components of the surface) metric tensor $a_{\alpha\beta} = \mathbf{a}_\alpha \cdot \mathbf{a}_\beta$ with determinant $a = |a_{\alpha\beta}|$, and the unit normal vector $\mathbf{n} = a^{-1/2}\mathbf{a}_1 \times \mathbf{a}_2$. The boundary contour C of M consists of the finite set of piecewise smooth curves $\mathbf{r}(s) = \mathbf{r}[\Theta^\alpha(s)]$, where s is the arc length along C. With each regular point $M \in C$ we associate the unit tangent vector $\mathbf{t} = d\mathbf{r}/ds \equiv \mathbf{r}' = t^\alpha \mathbf{a}_\alpha$ and the outward unit normal vector $\boldsymbol{\nu} = \mathbf{r}_{,\nu} = \mathbf{t} \times \mathbf{n} = \nu^\alpha \mathbf{a}_\alpha$, where $(\ )_{,\nu}$ denotes the outward normal derivative at C.

Let $\overline{M}$ and $\overline{C}$ be deformed configurations of M and C defined by the position vectors $\bar{\mathbf{r}}(\Theta^\alpha) = \mathbf{r}(\Theta^\alpha) + \mathbf{u}(\Theta^\alpha)$ and $\bar{\mathbf{r}}[\Theta^\alpha(s)] = \mathbf{r}(s) + \mathbf{u}(s)$, respectively, where $\mathbf{u}$ is the displacement vector while Θ^α and s are convected coordinates. With $\overline{M}$ and $\overline{C}$ we can associate analogously defined geometric quantities, only now marked by an overbar: $\bar{\mathbf{a}}_\alpha$, $\bar{a}_{\alpha\beta}$, $\bar{a}$, $\bar{\mathbf{n}}$, $\bar{\mathbf{t}}$, $\bar{\boldsymbol{\nu}}$ etc. All the quantities can be expressed through the geometry of M and C and the displacement field $\mathbf{u}$ by the relations presented in more detail in Pietraszkiewicz (1989). In particular, on $\overline{C}$ we have

$$\bar{\mathbf{r}}' = \mathbf{t} + \mathbf{u}' = \bar{a}_t \bar{\mathbf{t}}, \quad \bar{\mathbf{n}} = j^{-1}\bar{\mathbf{r}}_{,\nu} \times \bar{\mathbf{r}}', \tag{1a}$$

$$\bar{\mathbf{r}}_{,\nu} = \boldsymbol{\nu} + \mathbf{u}_{,\nu} = \bar{a}_t^{-1}(j\bar{\boldsymbol{\nu}} + 2\gamma_{\nu t}\bar{\mathbf{t}}), \tag{1b}$$

$$\bar{a}_t = |\bar{\mathbf{r}}'|, \quad 2\gamma_{\nu t} = \bar{\mathbf{r}}_{,\nu} \cdot \bar{\mathbf{r}}', \tag{1c}$$

$$j^2 = \bar{a}/a = |\bar{\mathbf{r}}_{,\nu}|^2 |\bar{\mathbf{r}}'|^2 - (\bar{\mathbf{r}}_{,\nu} \cdot \bar{\mathbf{r}}')^2, \tag{1d}$$

$$\bar{\mathbf{a}}^\beta = j^{-1}(\bar{a}_t \nu^\beta - 2\gamma_{\nu t}\bar{a}_t^{-1} t^\beta)\bar{\boldsymbol{\nu}} + \bar{a}_t^{-1} t^\beta \bar{\mathbf{t}}. \tag{1e}$$

It follows from (5) of Makowski and Pietraszkiewicz (1989) that within the nonlinear theory of thin shells the work-conjugate boundary and corner conditions should follow from the line integral

$$\int_{C_f} [(\mathbf{T}^\beta \nu_\beta - \mathbf{T}) \cdot \delta\mathbf{u} + (M^{\alpha\beta}\bar{\mathbf{a}}_\alpha \nu_\beta - \mathbf{H}) \cdot \delta\bar{\mathbf{n}}]\, ds, \tag{2}$$

which should vanish identically for any kinematically admissible virtual displacement field $\delta\bar{\mathbf{r}} \equiv \delta\mathbf{u}$. Here $N^{\alpha\beta}$ and $M^{\alpha\beta}$ are symmetric Piola-Kirchhoff type stress resultant and stress couple tensors, C_f is the part of C where the external boundary force and moment resultant vectors $\mathbf{T}$ and $\mathbf{H}$ are prescribed, while $\mathbf{T}^\beta$ and $\delta\bar{\mathbf{n}}$ are given by

$$\mathbf{T}^\beta = N^{\alpha\beta}\bar{\mathbf{a}}_\alpha + M^{\alpha\beta}\bar{\mathbf{n}}_{,\alpha} + \{[(M^{\lambda\alpha}\bar{\mathbf{a}}_\lambda)_{|\alpha} + \mathbf{h}] \cdot \bar{\mathbf{a}}^\beta\}\bar{\mathbf{n}}, \tag{3}$$

$$\delta\bar{\mathbf{n}} = -\nu_\beta \bar{\mathbf{a}}^\beta (\bar{\mathbf{n}} \cdot \delta\mathbf{u}_{,\nu}) - t_\beta \bar{\mathbf{a}}^\beta (\bar{\mathbf{n}} \cdot \delta\mathbf{u}'), \tag{4}$$

where $\mathbf{h}$ in (3) is the external surface moment vector, $(\ )_{|\alpha}$ denotes the covariant derivative in the undeformed surface metric $a_{\alpha\beta}$ and the moment $\mathbf{H}$ used in (2) is related to the external boundary couple resultant vector $\mathbf{M}$ by $\mathbf{M} = \bar{\mathbf{n}} \times \mathbf{H}$.

All the vectors appearing in (1), (2), (3), and (4) are understood to be expressed in components with respect to the known triad $\boldsymbol{\nu}$, $\mathbf{t}$, $\mathbf{n}$ of C.

If (4) is introduced into (2) and integration by parts of terms containing $\delta\mathbf{u}'$ is performed, the vanishing of (2) allows us to derive natural static boundary and corner conditions to be satisfied on C_f. However, the effective force and couple resultants appearing in such natural boundary conditions do not possess corresponding work-conjugate geometric counterparts, because the differential 1-form $\bar{\mathbf{n}} \cdot \delta\mathbf{u}_{,\nu}$ is not integrable (see the Appendix of Makowski and Pietraszkiewicz, 1989). In what follows we derive an alternative formula for $\delta\bar{\mathbf{n}}$ expressed entirely in terms of $\delta\omega_t$ and $\delta\mathbf{u}'$.

Total Rotation of the Shell Boundary

The total rotation of the shell lateral boundary surface can be described either by the total rotation tensor $\mathbf{R}_t$ (proper orthogonal) or by an equivalent total finite rotation vector $\boldsymbol{\Omega}_t$, which according to Pietraszkiewicz (1979, 1980) are expressed in terms of displacement vector $\mathbf{u}$ by

$$\mathbf{R}_t = \bar{\boldsymbol{\nu}} \otimes \boldsymbol{\nu} + \bar{\mathbf{t}} \otimes \mathbf{t} + \bar{\mathbf{n}} \otimes \mathbf{n}, \quad \boldsymbol{\Omega}_t = \frac{1}{2}(\boldsymbol{\nu} \times \bar{\boldsymbol{\nu}} + \mathbf{t} \times \bar{\mathbf{t}} + \mathbf{n} \times \bar{\mathbf{n}}), \tag{5}$$

where $\bar{\boldsymbol{\nu}}$, $\bar{\mathbf{t}}$, $\bar{\mathbf{n}}$ are known functions of $\mathbf{u}_{,\nu}$ and $\mathbf{u}'$ following from (1).

On the other hand, $\mathbf{R}_t$ and $\boldsymbol{\Omega}_t$ can be represented through the unit vector $\mathbf{e}$ describing the rotation axis and the angle ω_t of rotation about $\mathbf{e}$ according to

$$\mathbf{R}_t = \cos\omega_t \mathbf{1} + \sin\omega_t \mathbf{e} \times \mathbf{1} + (1 - \cos\omega_t)\mathbf{e} \otimes \mathbf{e}, \ \boldsymbol{\Omega}_t = \sin\omega_t \mathbf{e}, \tag{6}$$

where $\mathbf{1}$ is the metric tensor of three-dimensional Euclidean space and $\otimes$ denotes the tensor product.

From (5) and (6) it follows that

$$\mathrm{tr}\mathbf{R}_t = 2\cos\omega_t + 1 = \bar{\boldsymbol{\nu}} \cdot \boldsymbol{\nu} + \bar{\mathbf{t}} \cdot \mathbf{t} + \bar{\mathbf{n}} \cdot \mathbf{n}, \tag{7}$$

$$\mathbf{e} = e_\nu \boldsymbol{\nu} + e_t \mathbf{t} + e_n \mathbf{n}, \tag{8}$$

$$2e_\nu \sin\omega_t = \bar{\mathbf{t}} \cdot \mathbf{n} - \bar{\mathbf{n}} \cdot \mathbf{t}, \ 2e_t \sin\omega_t = \bar{\mathbf{n}} \cdot \boldsymbol{\nu} - \bar{\boldsymbol{\nu}} \cdot \mathbf{n},$$

$$2e_n \sin\omega_t = \bar{\boldsymbol{\nu}} \cdot \mathbf{t} - \bar{\mathbf{t}} \cdot \boldsymbol{\nu}. \tag{9}$$

Therefore, $\mathbf{e}$ and ω_t are known functions of $\mathbf{u}_{,\nu}$ and $\mathbf{u}'$ as well.

Taking the variation of (7) we obtain

$$-2\sin\omega_t \delta\omega_t = \delta\bar{\boldsymbol{\nu}} \cdot \boldsymbol{\nu} + \delta\bar{\mathbf{t}} \cdot \mathbf{t} + \delta\bar{\mathbf{n}} \cdot \mathbf{n}. \tag{10}$$

Thus in order to express $\delta\omega_t$ in terms of $\delta\mathbf{u}_{,\nu}$ and $\delta\mathbf{u}'$, such expressions for $\delta\bar{\boldsymbol{\nu}}$ and $\delta\bar{\mathbf{t}}$ should be given.

Since the variation of $\bar{a}_t^2 = \bar{\mathbf{r}}' \cdot \bar{\mathbf{r}}'$ leads to $\delta\bar{a}_t = \bar{\mathbf{t}} \cdot \delta\mathbf{u}'$ then

$$\delta\mathbf{u}' = (\bar{\mathbf{t}} \otimes \bar{\mathbf{t}}) \cdot \delta\mathbf{u}' + \bar{a}_t \delta\bar{\mathbf{t}}. \tag{11}$$

On the other hand, $\delta\mathbf{u}' \equiv \mathbf{1} \cdot \delta\mathbf{u}'$ in the basis $\bar{\boldsymbol{\nu}}$, $\bar{\mathbf{t}}$, $\bar{\mathbf{n}}$ reads

$$\delta\mathbf{u}' = (\bar{\boldsymbol{\nu}} \otimes \bar{\boldsymbol{\nu}}) \cdot \delta\mathbf{u}' + (\bar{\mathbf{t}} \otimes \bar{\mathbf{t}}) \cdot \delta\mathbf{u}' + (\bar{\mathbf{n}} \otimes \bar{\mathbf{n}}) \cdot \delta\mathbf{u}'. \tag{12}$$

From (11) and (12) it follows that

$$\delta\bar{\mathbf{t}} = \bar{a}_t^{-1}(\bar{\boldsymbol{\nu}} \otimes \bar{\boldsymbol{\nu}} + \bar{\mathbf{n}} \otimes \bar{\mathbf{n}}) \cdot \delta\mathbf{u}'. \tag{13}$$

[13]Professor, Polish Academy of Sciences, Institute of Fluid-Flow Machinery, ul. Fiszera 14, 80-952 Gdańsk, Poland.

Contributed by the Applied Mechanics Division of The American Society of Mechanical Engineers for publication in the ASME Journal of Applied Mechanics. Manuscript received by the ASME Applied Mechanics Division, Jan. 16, 1992; final revision, Oct. 23, 1990. Associate Technical Editor: F. M. Wan.

Then, (4) with (1*e*) leads to

$$\delta\bar{\mathbf{n}} = -\bar{a}_t j^{-1}(\bar{\nu}\otimes\bar{\mathbf{n}})\cdot\delta\mathbf{u}_{,\nu} + \bar{a}_t^{-1}(j^{-1}2\gamma_{\nu t}\bar{\nu}\otimes\bar{\mathbf{n}} - \bar{\mathbf{t}}\otimes\bar{\mathbf{n}})\cdot\delta\mathbf{u}'. \tag{14}$$

Finally, the variation of $\bar{\nu} = \bar{\mathbf{t}} \times \bar{\mathbf{n}}$ with the help of (13) and (14) yields

$$\delta\bar{\nu} = \bar{a}_t j^{-1}(\bar{\mathbf{n}}\otimes\bar{\mathbf{n}})\cdot\delta\mathbf{u}_{,\nu} - \bar{a}_t^{-1}(j^{-1}2\gamma_{\nu t}\bar{\mathbf{n}}\otimes\bar{\mathbf{n}} + \bar{\mathbf{t}}\otimes\bar{\nu})\cdot\delta\mathbf{u}'. \tag{15}$$

Including (15), (13), and (14) into (10) and using (9) we obtain

$$\delta\omega_t = -\bar{a}_t j^{-1} e_t(\bar{\mathbf{n}}\cdot\delta\mathbf{u}_{,\nu}) + \bar{a}_t^{-1}(e_\nu\bar{\mathbf{n}} + j^{-1}2\gamma_{\nu t}e_t\bar{\mathbf{n}} - e_n\bar{\nu})\cdot\delta\mathbf{u}'. \tag{16}$$

Now, from (16) we calculate $\bar{\mathbf{n}}\cdot\delta\mathbf{u}_{,\nu}$ expressed in terms of $\delta\omega_t$ and $\delta\mathbf{u}'$ only; this result introduced into (4) gives

$$\delta\bar{\mathbf{n}} = \mathbf{q}\delta\omega_t + \mathbf{L}\cdot\delta\mathbf{u}', \tag{17}$$

where

$$\mathbf{q} = \bar{a}_t^{-1} e_t^{-1} j\nu_\beta\bar{\mathbf{a}}^\beta, \tag{18a}$$

$$\mathbf{L} = \bar{a}_t^{-2} e_t^{-1} j\nu_\beta\bar{\mathbf{a}}^\beta\otimes(e_\nu\bar{\mathbf{n}} + j^{-1}2\gamma_{\nu t}e_t\bar{\mathbf{n}} - e_n\bar{\nu}) - t_\beta\bar{\mathbf{a}}^\beta\otimes\bar{\mathbf{n}}. \tag{18b}$$

Please note that by (17) $\delta\bar{\mathbf{n}}$ is now expressed entirely in terms of $\delta\omega_t$ and $\delta\mathbf{u}'$. The expression (17) provides a convenient alternative to earlier formulae for $\delta\bar{\mathbf{n}}$ reviewed by Pietraszkiewicz (1989).

Work-Conjugate Boundary Conditions

Let us introduce (17) into (2) and apply integration by parts to terms containing $\delta\mathbf{u}'$. This allows us to transform the line integral into the final form

$$\int_{C_f}[(\mathbf{P}-\mathbf{P}^*)\cdot\delta\mathbf{u} + (M-M^*)\delta\omega_t]ds + \sum_n(\mathbf{F}_n - \mathbf{F}_n^*)\cdot\delta\mathbf{u}_n, \tag{19}$$

where the effective force resultants and the bending couple resultants are defined by

$$\mathbf{P} = \mathbf{T}^\beta\nu_\beta + \mathbf{F}', \quad \mathbf{F} = -M^{\alpha\beta}\bar{\mathbf{a}}_\alpha\nu_\beta\cdot\mathbf{L}, \tag{20a}$$

$$\mathbf{P}^* = \mathbf{T} + \mathbf{F}^{*\prime}, \quad \mathbf{F}^* = -\mathbf{H}\cdot\mathbf{L}, \tag{20b}$$

$$M = M^{\alpha\beta}\bar{\mathbf{a}}_\alpha\nu_\beta\cdot\mathbf{q}, \quad M^* = \mathbf{H}\cdot\mathbf{q}, \tag{20c}$$

$$\mathbf{F}_n^* = \mathbf{F}^*(s_n+0) - \mathbf{F}^*(s_n-0), \quad \mathbf{u}_n = \mathbf{u}(s_n). \tag{20d}$$

From vanishing of (19) it follows that the static boundary and corner conditions take the form

$$\mathbf{P}(s) = \mathbf{P}^*(s), \quad M(s) = M^*(s) \text{ on } C_f, \tag{21a}$$

$$\mathbf{F}_n = \mathbf{F}_n^* \text{ at each corner } M_n \in C_f. \tag{21b}$$

It is also seen from (19) that the geometric boundary conditions which are work-conjugate to the static ones (21) are given by

$$\mathbf{u}(s) = \mathbf{u}^*(s), \quad \omega_t(s) = \omega_t^*(s) \text{ on } C_u, \tag{22}$$

where, by definition, $\omega_t(s) = \omega_t[\mathbf{u}_{,\nu}(s), \mathbf{u}'(s)]$ and $(\,)^*$ denotes the prescribed value. All the vector quantities in (20), (21), and (22) are understood to be expressed in components with respect to the known triad ν, $\mathbf{t}$, $\mathbf{n}$ of C.

The set of work-conjugate boundary conditions (21) and (22) is valid for unrestricted displacements, rotations, strains and/or changes of curvatures of the shell reference surface. In specific applications to nonlinear shell problems the boundary conditions (21), (22) may happen to be more convenient than two known alternative sets of work-conjugate boundary conditions derived earlier in (2.32) of Pietraszkiewicz (1984) and in (32), (33), and (41) of Makowski and Pietraszkiewicz (1989).

References

Makowski, J., and Pietraszkiewicz, W., 1989, "Work-Conjugate Boundary Conditions in the Nonlinear Theory of Thin Shells," ASME JOURNAL OF APPLIED MECHANICS, Vol. 56, pp. 395–401.

Pietraszkiewicz, W., 1979, *Finite Rotations and Lagrangean Description in the Non-Linear Theory of Shells*, Polish Scientific Publishers, Warszawa-Poznań.

Pietraszkiewicz, W., 1980, "Finite Rotations in the Non-Linear Theory of Thin Shells," *Thin Shell Theory, New Trends and Applications*, W. Olszak, ed., Springer-Verlag, Wien, pp. 153–208.

Pietraszkiewicz, W., 1984, "Lagrangian Description and Incremental Formulation in the Non-Linear Theory of Thin Shells," *International Journal of Non-Linear Mechanics*, Vol. 19, pp. 115–140.

Pietraszkiewicz, W., 1989, "Geometrically Nonlinear Theories of Thin Elastic Shells," *Advances in Mechanics*, Vol. 12, pp. 51–130.

Journal of Applied Mechanics

Discussion

The Effect of Compressibility on the Stress Distributions in Thin Elastomeric Blocks and Annular Bushings[1]

Charles W. Bert[2]. The authors are to be congratulated for obtaining a very interesting analysis of the behavior of a thin elastomeric block compressed between rigid plates to which it is bonded. Their paper clearly illustrates the quantitatively large effect of even small changes in Poisson's ratio from the incompressible value of 1/2.

Recently, the writer undertook the analysis of a thin elastic plate on a compressible foundation (Bert, 1992). This may be considered to be an extension of the previous work of Dillard (1989) to the compressible case. Equations (3), (4), (8), and (9) in the intermediate stops of this analysis are exactly equivalent to the author's Eq. (24). For the deflection influence coefficient due to a unit load applied at the center of a thin, square, isotropic plate, the result obtained was

$$K = (4a^4/D) \sum_m \sum_n \frac{\pi^2(m^2+n^2)+\overline{C}}{\pi^6(m^2+n^2)^3+\pi^4(m^2+n^2)^2\overline{C}+\overline{F}}$$

where $\overline{C} \equiv 18(a/h)^2(1-2\nu)/(1+\nu)$ and $F \equiv 144(a/h)^6(1-\nu_p^2)/(G+E_p)$. Here, a and h are length and thickness of the plate, G and ν are the shear modulus and Poisson's ratio of the interlayer, D is the plate flexural rigidity, E_p and ν_p are the elastic modulus and Poisson's ratio of the plate, and m and n are the longitudinal and transverse half-wave numbers. The above result reduces to that of Dillard (1989) if $\nu = 1/2$, since then $\overline{C}$ vanishes.

References

Bert, C. W., 1992, "Bending of Plates on Thin Compressible Foundations," unpublished manuscript.

Dillard, D. A., 1989, "Deformation of Plates on Elastomeric Foundations," ASME Journal of Applied Mechanics, Vol. 56, pp. 382–386.

Stress Distribution in an Edge-Stiffened Semi-infinite Elastic Plate Containing a Circular Hole[3]

X. Markenscoff[4]. As in all problems of geometries containing holes (or inclusions) and free boundaries, in which the solution is given by a series, the behavior of the solution is difficult to obtain numerically when the small parameter that describes the width of the ligament tends to zero, because, as the authors mention: "in the neighborhood of the straight boundary (i.e., for small α), σ_{zz} (0, y) cannot be accurately evaluated because of the slow convergence of the series solution, as was also mentioned by Jeffrey (1921)." However, this type of difficulty has been overcome (Callias and Markenscoff, 1989) by a singular perturbation analysis of the solution and the order of the stress amplification can be obtained. In the case of no stiffener (Mindlin problem) the stress was shown (Callias and Markenscoff, 1989) to be $\sigma_M \sim ((d-R)/R)^{-1/2}$, and it would be very interesting if the authors can show how the stiffener changes the $(-1/2)$ exponent of $(d-R)/R$. In the case, for instance, of the Koiter problem (Koiter, 1957), when a straight boundary is introduced on the other side of the hole, the exponent is (-1). The controlling effect of the stress distribution in the thin ligament is how the resultant force and moment transmitted by the ligament depend on $(d-R)/R$ (Markenscoff and Dundurs, 1992; Keller, 1993), which make the order of the stress amplification a function of both the loading and the geometry.

References

Callias, C. J., and Markenscoff, X., 1989, "Singular Asymptotic Analysis for the Singularity at a Hole Near a Boundary," *Quart. Appl. Math.*, Vol. 47, pp. 233–245.

Keller, J. B., 1993, "Stresses in Narrow Regions," ASME Journal of Applied Mechanics, in press.

Koiter, W. T., 1957, "Elementary Solution of Two Stress Concentration Problems in the Neighborhood of a Hole," *Quart. Appl. Math.*, Vol. 15, pp. 303–308.

Markenscoff, X., and Dundurs, J., 1992, "Amplification of Stresses in Thin Ligaments," *Int. J. Sol. Structures*, Vol.29, pp. 1883–1888.

Complex Modes and Solvability of Nonclassical Linear Systems[5]

S. M. Shahruz[6]. The authors consider the equation of motion of an n-degree-of-freedom linear system represented by

$$M\ddot{x}(t) + C\dot{x}(t) + Kx(t) = f(t), \qquad (1)$$

where the real $n \times n$ matrices M, C, and K do not necessarily satisfy symmetry, nonsingularity, and positive definiteness properties. The authors present conditions under which the system (1) is solvable. The system (1) is solvable when the matrices M, C, and K can be upper triangularized simultaneously, i.e., there exists a nonsingular real $n \times n$ matrix S that results in upper triangular matrices $S^{-1}MS$, $S^{-1}CS$, and

[1]By Y.-H. Lai, D. A. Dillard, and J. S. Thornton and published in the Dec. 1992 issue of the ASME Journal of Applied Mechanics, Vol. 59, pp. 902–908.

[2]Director and Perkinson Chair, School of Aerospace and Mechanical Engineering, The University of Oklahoma, Norman, OK 73019-0601, Fellow ASME.

[3]By E. J. Lee and E. C. Klang and published in the Dec. 1993 issue of the ASME Journal of Applied Mechanics, Vol. 59, pp. 789–795.

[4]Professor of Applied Mechanics, University of California, San Diego, LaJolla, CA 92092-0411.

[5]By T. K. Caughey and F. Ma and published in the Mar. 1993 issue of the ASME Journal of Applied Mechanics, Vol. 60, No. 1, pp. 26–28.

[6]Research Scientist, Berkeley Engineering Research Institute, P.O. Box 9984, Berkeley, CA 94709.

Journal of Applied Mechanics

Book Review

Applications of Potential Theory in Mechanics: A Selection of New Results, by V. I. Fabrikant, Kluwer Academic Publishers, Dordrecht, The Netherlands, 1989. 467 pages. Price: $119.00.

REVIEWED BY M. HANSON[1]

In a field as old and well defined as potential theory, it is seldom that a new idea or method can be developed which will have a significant impact on the way problems are approached and solved in the future. That is what the author claims to have accomplished with this book and this claim is well founded in the method he has developed to formulate and solve mixed boundary value problems in potential theory. This book develops the new method in the initial chapters and then applies it to various problems in the latter sections. The new results presented are those obtained by the author with reference to other research for comparative purposes when possible.

Chapter 1 presents a description of the new method for solving boundary value problems in potential theory. An integral representation for the reciprocal of the distance between two points is first developed, which is the foundation of his method. Chapter 2 moves on to mixed boundary value problems for a transversely isotropic half-space with a circular line dividing the boundary conditions while Chapter 3 addresses mixed-mixed boundary value problems. Chapters 4 and 5 apply the integral equation solutions developed in Chapter 2 to various crack and punch problems.

This book by Professor Fabrikant is a definite aid for researchers in elasticity as well as other fields in which the equations are reducible to those of potential theory. Furthermore, those interested in developing closed-form solutions to half-space problems with a circular line dividing the boundary conditions will find this book invaluable. Even with integral transform formulations, the final steps in piecing together closed-form solutions require the evaluation of formidable integrals for which this book has developed a systematic procedure. If Professor Fabrikant's method is adopted for solving mixed boundary value problems, his book can be used as a learning tool since it is rich with detail on the analysis and it contains many problems for exercises where the answers are also given. Although the method requires no knowledge of special functions, only integral and differential calculus, the manipulations are often formidable and this book is best suited to researchers or students who are well versed in the equations of potential theory and who are comfortable with the idea of mixed boundary value problems.

[1] Department of Engineering Mechanics, University of Kentucky, Lexington, KY 40506-0046.